Linked Interpolation and Strain Invariance in Finite-Element Modelling of Micropolar Continuum

Grbčić, Sara

Doctoral thesis / Disertacija

2018

Degree Grantor / Ustanova koja je dodijelila akademski / stručni stupanj: **University of Rijeka, Faculty of Civil Engineering in Rijeka / Sveučilište u Rijeci, Građevinski fakultet u Rijeci**

Repository / Repozitorij:

UNIN **DIGITALNA KNJIŽNICA**

University of Rijeka

Faculty of Civil Engineering

Sorbonne Universités

Université de Technologie de Compiègne

Sara Grbčić

Linked Interpolation and Strain Invariance in Finite-Element Modelling of Micropolar Continuum

Doctoral Thesis

Supervisors:

Prof. Gordan Jelenić, PhD

Prof. Adnan Ibrahimbegović, PhD

Rijeka, 2018

Supervisors:
>Prof. Gordan Jelenić, PhD
>Prof. Adnan Ibrahimbegović, PhD

The doctoral thesis is defended on 18th of December 2018 at the University of Rijeka, Faculty of Civil Engineering before the following committee:

1. Prof. Dragan Ribarić, PhD, University of Rijeka, Faculty of Civil Engineering, president

2. Prof. Zdenko Tonković, PhD, University of Zagreb, Faculty of Mechanical Engineering and Naval Architecture, external member

3. Prof. Boštjan Brank, PhD, University of Ljubljana, Faculty of Civil Engineering and Geodesy, external member

4. Prof. Adnan Ibrahimbegović, PhD, Sorbonne Universities, University of Technology of Compiegne, external member

5. Prof. Pierre Villon, PhD, Sorbonne Universities, University of Technology of Compiegne, external member

6. Maja Gaćeša, PhD, ANSYS, external member

7. Prof. Gulio Alfano, PhD, Brunel University London, external member

This thesis is dedicated to my mother.

You are the bravest, the strongest and
the most warmhearted person I know.

I am proud of being your daughter.

Acknowledgements

Personal:

Mother, thank you for your limitless love and support for all the, at the moment, crazy ideas and wishes that popped into my mind since I was a kid. Without your love and upbringing I wouldn't be what I am. Without your support and belief I wouldn't be writing this. Thank you for always giving me the best.

Milan, my love, my soulmate, my friend, my colleague, my everything. Without you, I am just a halve. Thank you for making me whole. I love you.

My friends Bati, Matea, Anja, Vladić, Matej, Čaki, Diana and Matija thank you for always jumping in to help me without asking questions. I know that no matter what, I can always lean on you. All the party, laughing, crying moments we spend together were my inspiration.

Thanks to Maja, Edita, Paulo, Leo, Nino, Miran, Dragan and Ivana, my colleagues and friends, for all the advices, hangouts, tutoring and supporting words.

Čina, thanks for the "push-pauses" filled with laughter and empathy that would always charge my batteries when I needed it the most.

Emina, Pablito, Ismar, Tea, Ivan, Emir, Abir, Nam Do, Adela, my dear Adnaners, thank you for always helping with the French administration, FEAP, missing public transportation and all the things that sometimes went wrong. With such a group of great people, you just cannot fail and you never feel alone.

My freakish dance girls Kmica, Blanša, Vale, Baabee and Mrva, thanks for supporting me regardless of how far I am and how long we didn't see. You always understood me and were here to encourage me. Wherever I will be, I will always miss your best silly humor in the world.

Nilda and Marina, thank you for your help, reminders and kindness you are selflessly giving on daily basis. You are a treasure.

Thanks to my supervisors:

Gordan, for your limitless support, understanding and empathy. First of all, you are a good man and you showed it to me more times than I can count. Thank you for always keeping your doors open and patiently answering millions of my questions. Thank you for your supporting words given in the moments I needed it the most. Thank you for recognizing those moments, without me saying anything. I am honored to be your student.

Adnan, for enabling me to experience the great synergy of your group. Without your effort and will none of it would exist. Your pushing over the limit always led to success.

Institutional:

Abstract

At the core of this thesis is an alternative continuum theory called the micropolar (Cosserat) continuum theory, developed in order to describe the phenomena which the classical continuum theory is not able to describe. In this theory, in addition to the displacement field, there also exists an independent microrotation field and, in order to completely describe such a material, six material parameters are needed. In the framework of the finite-element method, new finite elements based on the micropolar continuum theory in both linear and geometrically non-linear analysis are developed using the displacement-based approach.

In the linear analysis, both two- and three-dimensional set-ups are analysed. In 2D new families of triangular and quadrilateral finite elements with linked interpolation of the kinematic fields are derived. In order to assure convergence of the derived finite elements, they are modified using the Petrov-Galerkin approximation. Their performance is compared against existing conventional micropolar finite elements on a number of micropolar benchmark problems. It is observed that the linked interpolation shows enhanced accuracy in the bending test when compared against the conventional Lagrange micropolar finite element.

Next, the weak formulation is extended to 3D and a first-order hexahedral finite element enhanced with the incompatible modes is derived. The element performance is assessed by comparing the numerical results against the available analytical solutions for various boundary value problems, which are shown to be significant for the experimental verification of the micropolar material parameters. It is concluded that the proposed element is highly suitable for the validation of the methodology to determine the micropolar material parameters.

In the non-linear part, first- and second-order geometrically nonlinear hexahedral finite elements with Lagrange interpolation are derived. In order to test the performance of the presented finite elements, a pure-bending non-linear micropolar analytical solution is derived. It is observed that the elements converge to the derived solution. The elements are tested on three additional examples where the path-dependence and strain non-invariance phenomena are detected and assessed in the present context. A procedure to overcome the non-invariance anomaly is outlined.

Keywords: micropolar theory, microrotation, linked interpolation, incompatible modes, geometrical nonlinearity, strain invariance

Sažetak

Osnovu doktorske disertacije čini alternativna teorija kontinuuma poznata kao mikropolarna (Cosseratova) teorija kontinuuma koja je razvijena kako bi opisala fenomene koje nije moguće opisati klasičnom (Cauchyjevom) teorijom kontinuuma. U teoriji, osim polja pomaka postoji također i nezavisno polje mikrorotacija te kako bi se u potpunosti opisao takav materijal, potrebno je šest materijalnih parametera. U okviru metode konačnih elemenata razvijeni su novi konačni elementi temeljeni na mikropolarnoj teoriji u linearnoj i geometrijski nelinearnoj analizi korištenjem direktne metode temeljene na pomacima.

U linearnoj analizi provedena je dvodimenzionalna i trodimenzionalna analiza. U 2D razvijena je nova familija trokutnih i četverokutnih elemenata s vezanom interpolacijom kinematičkih polja. Kako bi se osigurala konvergencija razvijenih konačnih elemenata, elementi su modificirani Petrov-Galerkinovom aproksimacijom. Performanse elemenata uspoređene su s konvencionalnim mikropolarnim konačnim elementima na nekoliko referentnih mikropolarnih primjera. Uočeno je da vezana interpolacija pokazuje poboljšanu točnost u odnosu na konkvencionalne mikropolarne konačne elemente.

Nadalje, slaba forma proširena je na 3D analizu i razvijen je šesterostranični 3D konačni element prvog reda obogaćen nekompatibilnim oblicima. Performanse elementa ocijenjene su uspoređujući numeričke rezultate s dostupnim mikropolarnim referentnim rješenjima za koja je pokazano da su značajna za eksperimentalno utvrđivanje mikropolarnih parametara. Zaključeno je da je predloženi element izrazito pogodan za numeričku validaciju metodologije određivanja mikropolarnih parametara.

U nelinearnoj analizi razvijeni su geometrijski nelinearni šesterostranični 3D konačni elementi prvog i drugog reda. Kako bi se testirala valjanost izvedenih konačnih elemenata, razvijeno je i nelinearno mikropolarno analitičko rješenje za problem čistog savijanja. Uočeno je da razvijeni elementi konvergiraju ka izvedenom analitičkom rješenju. Elementi su također testirani na tri dodatna primjera gdje su uočeni fenomeni ovisnosti putanje ka rješenju te neinvarijantnosti deformacija. Predložen je postupak za eliminaciju anomalije neinvarijantnosti deformacija.

Ključne riječi: mikropolarna teorija, mikrorotacija, vezana interpolacija, nekompatibilni oblici, geometrijska nelinearnost, invarijantnost deformacija

Résumé

Au cœur de cette thèse est une théorie de continuum alternatif connue comme la théorie micropolaire (ou la théorie des Cosserats), qui est développée pour décrire des phénomènes lesquels on ne peut pas décrire en utilisant la théorie classique. Dans cette théorie, en complément du champ de déplacement, il existe aussi un autre champ independant, celui de microrotation, et afin de pouvoir décrire complètement un tel matériau, six paramètres des matriaux sont nécessaires. Dans le cadre de la modélisation par éléments finis, nouveaux éléments fondé sur la théorie micropolaire dans les régimes linéaire et géométriquement non linéaire sont dveloppes en utilisant l'approche basé au déplacements.

Dans le cadre de l'analyse linéaire, les problèmes bi- et tri-dimensionnels sont analysés. En 2D, les nouvelles familles des elements triangulaires et quadrilatères sont développes avec l'interpolation liée des champs cinématiques. Pour assurer la convergence des éléments finis développés, ils sont modifiés en utilisant l'approximation de Petrov-Galerkin. Leur performance est comparée avec celle des éléments finis micropolaires conventionnels dans un nombre des exemples de référence. Il est constaté que l'interpolation liée améliore la précision dans le cas de flexion, par rapport à la précision des éléments finis micropolaires conventionnels.

Ensuite, la forme faible est étendue aux trois dimensions, et un élément fini hexaédrique du premier ordre, avec le champ de déplacement enrichi avec des modes incompatibles est dérivé. La performance de l'élément est évaluée en faisant la comparaison des résultats numériques avec les solutions analytiques disponibles pour les divers problèmes des valeurs limites, lesquels ont une signification conséquente pour la vérification expérimentale des paramètres micropolaires. Enfin, il est conclu que l'élément proposé est très bien adaptè pour la validation de la méthodologie afin de déterminer les paramètres micropolaires.

Dans le part non-linéaire, les éléments de premier et deuxième ordre avec l'intepolation conventionnelle sont développes. Pour tester la performance des éléments présentes, une solution analytique non-linéaire de la flexion pure est dérivée. Il est observé que les éléments convergent vers la solution dérivée. Les éléments sont testes sur les trois autres exemples où la dépendance du sentier et l'invariance de deformation sont détectés. Une procedure pour résoudre ces anomalies est présentée.

Mots clés: théorie micropolaire, microrotation, l'interpolation liée, modes incompatibles, non-linéarité géométriques, invariance de deformation

Contents

iii

Chapter 1

Introduction

1.1 Motivaton

Most of the materials are heterogeneous in general, with a specific microstructure that can be represented at a scale particular for the material itself. When this scale is very small, these materials are usually considered as homogeneous (e.g. metals). In continuum mechanics, a material is modelled as a continuum which implies that the substance of an object completely fills the space it occupies. In other words, any microstructure detail is averaged, leading to a homogeneous continuum theory.

When we analyse a body in the state of rest on which loading is applied, in order to obtain the equilibrium, internal forces have to occur. The commonly used classical theory of continuum mechanics developed by Cauchy [3] is based on an ideal model of an elastic, continuous medium in which the loadings are transmitted through an area element in the body by means of one vector field called *the stress vector*. As the volume of the body tends to zero (which is the main postulate of any continuum theory), the moment of the stress vector with respect to any point within the volume in Cauchy's theory also tends to zero. It means that we cannot apply distributed moments. Consequently, in the classical theory, the response of the body to applied loading is described by means of two symmetric tensors, the so-called *strain tensor* and *stress tensor*. The classical continuum theory faithfully reproduces numerous experimental results carried out on many construction materials such as steel and aluminium [4]. However, in many cases remarkable discrepancies between theory and experiments have been observed [4]. When the microstructure scale becomes significantly large compared to the overall scale, representation based on the classical theory fails, as shown in experiments on materials with granular, fibrous or lattice structure [5, 6, 7]. A phenomenon called *size-effect* is experimentally observed in rods made of foam subject to torsion and bending, i.e. thin specimens are shown to be more stiff than thick specimens [5], which cannot be modelled using the classical continuum theory. In elastic region, the classical theory predicts that the torsional and

bending rigidity of circular rods are proportional to the fourth power of the diameter of the cross-section. Also, it is shown that in states which exhibit high stress gradients such as the neighbourhood of holes, notches and cracks, the stress concentration factor K_t in the classical theory is higher than experimentally observed [8]. Furthermore, the stresses computed in the vicinity of such material discontinuities also do not correspond to the experimental observations. Additional differences are observed in dynamical problems, e.g. in case of elastic vibrations characterized by high frequency and small wavelengths (i.e. ultrasonic waves) [4]. This discrepancy is a result of the fact that for high frequencies and small wave-lengths the influence of the body microstructure becomes significant, i.e. the microstructure of materials can develop new types of waves which change the behaviour of the material. In addition, since the classical continuum theory strictly relies on symmetry of the stress tensor, it is intrinsically unable to accommodate arbitrary natural boundary conditions. Due to such anomalies, an alternative continuum model, which should be able to describe the behavior of such materials accurately is highly needed.

In an attempt to answer to such demands, numerous alternative continuum theories have been developed, i.e. different approaches are developed to study the multi-scale nature of the material deformation by taking into account additional effects consistent with the observed behavior of heterogeneous materials. Within the limits of continuum mechanics some of them may be developed by introducing *higher-order field derivatives* in the strain-tensor definition, such as the so-called couple-stress theory [9] or higher-order strain-gradient theories [10]. An alternative approach is by introducing *additional degrees of freedom*, such as in the so-called micro-stretch or micro-morphic continuum theory [11], to name only a few. Among the latter class of theories, here we further elaborate upon the so-called *micropolar continuum theory*, usually attributed to the Cosserat brothers [12].

1.2   Micropolar continuum theory

Unlike the classical (Cauchy) continuum theory, in the micropolar continuum theory the interaction between two particles is described not only by means of the stress vector field but also an additional vector field which we call *the moment-stress vector*. Now, even when the volume of the body tends to zero, we can obtain moment vectors acting on the body. As a consequence, the stress tensor and an additional *couple-stress tensor* acting in the deformed body are obtained, both of which are asymmetric. Furthermore, in the micropolar continuum theory there exist two independent kinematic fields, the displacement field and the so-called *microrotation field*, which represents the local rotation of a point. Due to that, the particle becomes *orientable*. It is important to note that this microrotation is completely independent and in general different from the displacement-induced macrorotation known from the classical continuum theory [12]. Consequently,

we obtain two strain tensors, the *(micropolar) strain tensor* and the *curvature tensor*, both of which are again asymmetric. If we consider a linear, elastic, homogeneous and isotropic material it turns out to be described by *six independent material constants* [4], in contrast to only two constants present in a linear elastic, homogeneous and isotropic classical continuum. From a mathematical point of view, an isotropic micropolar material is a continuum in which rigid particles of infinitesimal size are uniformly distributed in an elastic matrix and in which homogeneity and isotropy are taken to be the macroproperties of the medium. The couple stresses physically originate from the bending and twisting moments transmitted between the rigid particles within the material, while the microrotation field describes their rotation. In terms of a physical picture, a material body may be envisioned as a collection of a large number of orientable particles that contribute to the macroscopic behavior of the body [11]. With this approach many new problems can be modelled, and the obtained results are much closer to the experimental results [4, 13, 8].

The concept of microrotation (as well as the even more general concept of *microcontinuum*) naturally brings *length scales* into continuum theories. In general microcontinuum theories, the orientation of material points is set by three local directors. A material point carrying three deformable directors belongs to the so-called *micromorphic continuum* and introduces nine extra degrees of freedom (three microrotations, three principal microstretches and three principal directions) over the classical theory. When the directors are constrained to have only breathing-type microdeformations, such a particle belongs to the so-called *microstretch continuum*, and the extra degrees of freedom are reduced to four: three microrotations and one microstretch. In our micropolar continuum, a point is endowed with three rigid directors only. A material point is then equipped with the degrees of freedom for rigid rotations only, in addition to the classical translational degrees of freedom [11].

The response of the body is influenced heavily by the ratio of the characteristic length λ (associated with the specimen size) to the internal characteristic length l associated with material structure. When $\dfrac{\lambda}{l} >> 1$, the classical theory gives reliable predictions. However, when $\dfrac{\lambda}{l} \approx 1$, the response of constituent subcontinua (deformable and/or orientable particle) becomes important, so that the axiom of locality underlying classical field theories fails [11].

1.2.1   Historical development of the theory

The micropolar nature of materials (e.g. crystalline solids) was first considered by Voigt [14] who assumed that the interaction between two parts of the body through an area element is transmitted not only by the force vector, but also by a moment vector. After establishing the differential equilibrium equations (including the moment equilibrium), Voigt obtained the stress and the couple-stress tensors as *asymmetric* [4]. Two

decades later, brothers E. and F. Cosserat [12] extended Voigt's theory and introduced the theory of non-symmetric elasticity. They assumed that to each particle a rigid trihedron is attached, which can translate and rotate during the deformation process. In this way, each material particle had as many as six degrees of freedom: three displacement components and three rotation components. The theory was originally presented as a unified theory which brings together mechanics, optics, magnetism and electrodynamics, but it did not provide the detail on the constitutive equations. The theory had remained dormant for nearly half a century and was reopened by Günther [15] in 1960s who gave the fundamentals of the linear Cosserat continuum and discussed in detail the 1D, 2D and 3D models. Six years later, Truesdell [16] and Toupin [17] present their analysis of the so-called *Cosserat pseudocontinuum* (nowadays also known as the couple-stress continuum), where the non-symmetric stress tensor is obtained, but the deformation is determined by the displacement vector only, using the macrorotation for the rotation field [11]. Further analysis of the linear Cosserat continuum was given by Schäfer [18], who focused only on the 2D case. The latest extension of the Cosserat theory was provided by Eringen [19], who published his theory of microfluids and introduced a new balance law: *the law of conservation of microinertia* and suggested the presently used denomination of the theory as the *micropolar theory of elasticity*. Other than Cosserat's or micropolar, this theory is in the literature also referred to as the asymmetric theory of elasticity [20].

1.2.2 Application of the theory

The micropolar continuum theory is still not widely used in the numerical analysis of structures. A possible reason may lie in the lack of reliable procedures to determine the material parameters. Even though there exist numerous works related to micropolar theory (see e.g. [20, 11, 21] among many others), relatively few experimental tests have been successfully conducted. The first analytical and experimental procedure to determine all six micropolar material parameters is given by Gauthier and Jahsman in [1], but without particular success in the experimental part since an opposite trend to the prediction has been observed. However, by subsequent refinement of Gauthier's and Jahsman's procedure, Lakes and his co-workers have given the most significant contribution to devising experimental procedures to determine the micropolar material parameters in their analysis of bones [22, 23, 24], polymeric foams [7, 25, 5, 6] and metal foams [26]. A different approach to determining the micropolar parameters is based on various homogenisation procedures applied to lattices, granular media, cellular structures and heterogeneus structures such as masonry structures [27, 28, 29, 30], which provide a more significant source of the actual values for the micropolar parameters. In contrast to the above experiments performed by Lakes and his co-workers, which involve specimen preparation on a very small scale, the idea of homogenisation is to replace a larger-scale composite material or

assembly of particles by an effective micropolar continuum model. Assuming a homogeneous Cosserat material that best approximates a heterogeneous Cauchy material, the material parameters of the observed specimen may be determined more easily. A comprehensive list of related works can be found in [21]. Several recent works of Wheel et al. [31, 32, 33] have determined the material parameters of highly heterogeneous materials on a larger-scale by comparing the results of experiments and the finite element simulation.

As mentioned in [34], newer, more comprehensive material models such as composite material models, are struggling with experimental verification and their corresponding conceptualisation and interpretation. We are faced with a situation where theory precedes experiment. Due to the lack of experimental verifications, we believe that the key to understanding and developing more precise experimental procedures lies in the comprehensive numerical analysis of the solution to a boundary value problem analysed. The numerical analysis should broaden the range of solvable problems and open up new possibilities for the numerical simulation of experimental set-ups. In particular, the development of the finite elements of high quality is important for the future progress and understanding of the micropolar continuum theory.

An early attempt to incorporate micropolar constitutive behaviour into a linear finite element formulation is presented in [35] with more authors working on numerical solutions of the micropolar continuum using different finite elements in the linear analysis (e.g. [36, 37, 38, 39, 40, 41]). In addition to the standard finite element procedures, non-standard finite element methods, such as the control volume-based finite element method have also been used to model micropolar finite elements, as presented in [42] and [31]. For the non-linear micropolar continuum, however, the theory is extensively analysed in [11, 43, 44, 45, 46], but the numerical implementation of the nonlinear finite elements is not as broadly given. The first attempt to numerically model the nonlinear behaviour in the geometrical and material framework is presented in [47], where the authors have analysed micropolar plasticity on one 2D problem. The nonlinear analysis presented by Ramezani et al. [48] also incorporated both material and geometrical nonlinearity but is restricted to planar configurations only. The first and only work familiar to us which has analysed pure micropolar geometrical non-linearity with a finite-element implementation in 3D is the work of Bauer et al. [49], where mostly linear benchmark problems have been presented in the nonlinear regime. Other related works which studied the geometrical non-linearity where based on the theoretical setting of deriving the material strain tensors [45] and parametrisation of large rotations [44] in the framework of the micropolar theory but without any finite element implementation. The formulation presented in [49] was extended to a material nonlinear regime in [50] and [51] where the authors analysed micropolar hyperelasticity and hyper-elastoplasticity. However, a set of representative problems to test the micropolar geometrical nonlinearity is still missing.

In this thesis we wish to contribute to the existing numerical models by introducing new finite elements in the finite element analysis of the micropolar continuum.

1.3   Thesis overview

Within the framework of this thesis the objectives are separated into two main domains:

(i) linear analysis of the micropolar continuum using the finite element method,

(ii) geometrically non-linear analysis of the micropolar continuum using the finite element method.

1.3.1   Linear analysis

In Chapter 2 we present the linear micropolar continuum model, where, after proving the existence of the stress and couple-stress tensors and setting the equilibrium of a differential volume and surface, we derive the kinematic equations using the geometric approach. We also define the constitutive equations and relate the derived equations to the alternative notations present in the literature. Next, in Chapter 3 we first set the finite element formulation in 2D and develop families of triangular and quadrilateral membrane finite elements enhanced with the so-called *linked interpolation* for the displacement field. After assuring convergence of the presented families of finite elements, their performance is tested against conventional micropolar finite elements interpolated using only Lagrange interpolation through two benchmark problems. Next we derive the finite element formulation in 3D and develop the micropolar hexahedral finite element where the conventional Lagrange displacement interpolation is enhanced with the so-called *incompatible modes*. The element performance is tested against the analytical boundary value problems and compared to the performance of the conventional Lagrange micropolar hexahedral finite element.

1.3.2   Non-linear analysis

In Chapter 4 we derive the three sets of equations needed to describe a geometrically non-linear micropolar continuum. At the beginning, a special treatment of spatial rotations is discussed. Next, the kinematic equations are derived with respect to the material description using Reissner's approach, while the constitutive equations are kept linear. In Chapter 5 we define the nonlinear residual force vector, by using the principle of virtual work and setting the first and second order hexahedral interpolation of the virtual fields. After performing the extensive linearization presented in detail in Appendix G, the condition that the residual should vanish at equilibrium is reduced to a system of linear equations which may be solved using the Newton-Raphson iterative method. In Section

5.2 the numerical analysis of the nonlinear hexahedral finite elements is presented. In order to test the validity of the derived elements, a pure-bending non-linear analytical solution is derived and presented in Section 5.2.1. Next we test the finite-element performance by comparing the obtained results against the derived analytical solution for the cantilever beam subject to pure bending. In a number of different 2D and 3D problems we further test the derived formulation and finite element implementation and detect the path-dependence and strain non-invariance anomalies. Finally, a brief comment on a possible solution how to overcome the strain non-invariance anomaly is proposed.

Chapter 2

Linear micropolar continuum model

In this Chapter the mechanical problem of a linear micropolar continuum is analysed and the three sets of equations (equilibrium, kinematic and constitutive) needed in order to describe the problem are derived. All the three sets of equations are presented using the matrix, tensor and summation-convention notation.

2.1 Existence of stress and couple-stress tensors

Mechanical interactions between parts of a body and between the body and the environment are described by forces. The forces are divided into three groups, as follows: (i) contact forces between particles of the body, (ii) contact forces exerted on the boundary of the body by its environment and (iii) body forces acting on the interior parts of the body. In order to define equilibrium equations of an infinitesimal volume and surface, first we need to prove existence of the stress tensor. The Euler–Cauchy stress principle states that "*upon any smooth, closed, orientable surface S, be it an imagined surface within the body or the bounding surface of the body itself, there exists an integrable field of traction vectors* **t** *equipollent to the action exerted by the matter exterior to S and contiguous to it on that interior to S*" [52].

We generalize this principle to a micropolar continuum, in which there exist an additional integrable field of moment traction vectors **m**.

Let the body $\mathcal{B}$ consisting of material particles $X, Y,...$ deform in the three-dimensional (3D) Euclidean space $\mathcal{E}$. We identify a generic particle of $\mathcal{B}$ by the label X. In the *reference (undeformed)* configuration the material particle $X \in \mathcal{B}$ is given through its position vector $\mathbf{X}$ relative to a point o at time t_0. The body deforms and is brought to a new position which defines the *current (deformed)* configuration of the body. Load is applied to the body in terms of a specific body force $\mathbf{p}_\mathrm{v}$, a specific body moment $\mathbf{m}_\mathrm{v}$, a specific surface force $\mathbf{p}_\mathrm{s}$ and a specific surface moment $\mathbf{m}_\mathrm{s}$. In the deformed placement the position vector of a material point $X \in \mathcal{B}$ relative to the same origin o at time t is defined

by $\mathbf{x}$. A single Cartesian coordinate system with associated vector basis $\{\mathbf{e}_1, \mathbf{e}_2, \mathbf{e}_3\}$ is used for both configurations of the body. The reference Cartesian coordinates of a material point are denoted by (X_1, X_2, X_3) and the current Cartesian coordinates are denoted by (x_1, x_2, x_3) (see Figure 2.1).
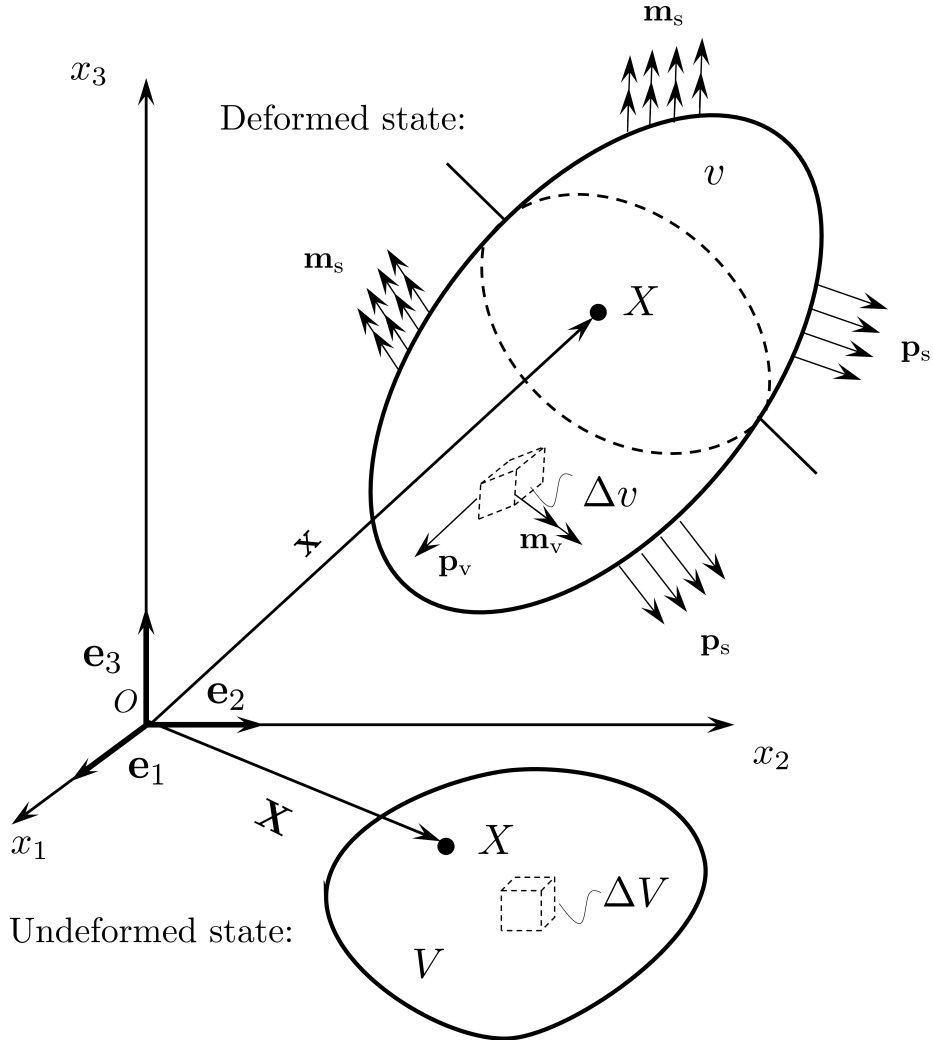
Figure 2.1: Continuous body with applied loading

For each configuration of the body $\mathcal{B}$ there exists a scalar field $\rho(\mathbf{x}, t)$ defined over $\mathcal{B}$ such that

$$m(\mathcal{B}) = \int_v \rho(\mathbf{x}, t)\mathrm{d}v, \tag{2.1}$$

where $\mathrm{d}v$ is the volume element in the current state, $m(\mathcal{B})$ is the *mass* of the body, independent of the configuration of the body and $\rho(\mathbf{x}, t)$ is the *mass density* of the material of the body dependent on the configuration. Since $m(\mathcal{B})$ is independent of the configuration we can write

$$\int_v \rho(\mathbf{x}, t)\mathrm{d}v = \int_V \rho_0(\mathbf{X})\mathrm{d}V \tag{2.2}$$

10

for an arbitrary choice of reference configuration, where $\rho_0(\mathbf{X})$ is the mass density of $\mathcal{B}$ in the reference configuration and $\mathrm{d}V$ is the volume element in the reference configuration ($\mathcal{B}_0$) [53]. Since the mass is conserved during motion we can write

$$\frac{\mathrm{d}}{\mathrm{d}t}(\rho\,\mathrm{d}v) = 0, \qquad (2.3)$$

known as the *law of conservation of mass*.

To generalise the Cauchy stress principle, we consider an imaginary surface s passing through an internal material point X dividing the continuous body into two segments (see Figure 2.2). The part of the body will remain in equilibrium under the assumption that, instead of the second part of the body, there exists a corresponding system of internal forces acting on the surface s. It means that on a small surface Δs only a part of the internal forces is acting. The resultant of this action on the small surface Δs are force and moment vectors $\Delta\mathbf{F}$ and $\Delta\mathbf{M}$.
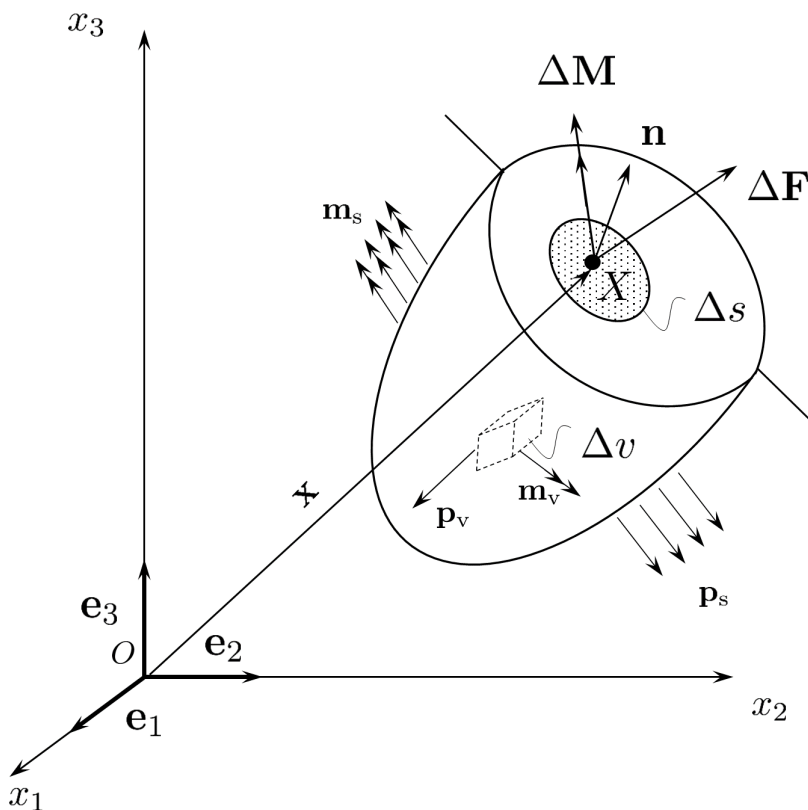
Figure 2.2: Part of the body with applied loading, internal forces and moments

In order to describe the action of the internal forces, we presume the existence of a mean stress vector $\bar{\mathbf{t}}$ and a mean couple stress vector $\overline{\mathbf{m}}$ defined as:

$$\bar{\mathbf{t}} = \frac{\Delta\mathbf{F}}{\Delta s}, \qquad \overline{\mathbf{m}} = \frac{\Delta\mathbf{M}}{\Delta s}. \qquad (2.4)$$

The limiting values, when $\Delta s \to 0$, represent the stress vector field $\mathbf{t}(\mathbf{x}, t, \mathbf{n})$ and the couple stress vector field $\mathbf{m}(\mathbf{x}, t, \mathbf{n})$ depending on the position $\mathbf{x}$ of the material point, time t and a unit vector $\mathbf{n}$, defining the outward normal to the chosen surface, as follows:

$$\mathbf{t} = \lim_{\Delta s \to 0} \overline{\mathbf{t}} = \lim_{\Delta s \to 0} \frac{\Delta \mathbf{F}}{\Delta s}, \tag{2.5}$$

$$\mathbf{m} = \lim_{\Delta s \to 0} \overline{\mathbf{m}} = \lim_{\Delta s \to 0} \frac{\Delta \mathbf{M}}{\Delta s}. \tag{2.6}$$

Physically, $\mathbf{t}(\mathbf{x}, t, \mathbf{n})$ represents the force per unit area exerted on the surface oriented with $\mathbf{n}$ at the position $\mathbf{x}$ and time t and $\mathbf{m}(\mathbf{x}, t, \mathbf{n})$ represents the moment per unit area exerted on the surface oriented with $\mathbf{n}$ at the position $\mathbf{x}$ and time t. The question is: What governs the motion of a small portion of the body surrounded by the small area Δs and the three areas obtained by cutting the body using three surfaces orthogonal at their intersection?

In order to answer that question, first we have to postulate the momentum and the moment of momentum conservation laws, which we use to prove the existence of the stress and the couple stress tensors.

Definition 1. Momentum balance

The rate of change of a translational momentum of any part of the body is equal to the vectorial sum of all forces acting on it, i.e.

$$\frac{\mathrm{d}}{\mathrm{d}t} \int_{v'} \rho \dot{\mathbf{x}} \, \mathrm{d}v = \int_{v'} \mathbf{p}_\mathrm{v}(\mathbf{x}, t) \, \mathrm{d}v + \int_{s'} \mathbf{t}(\mathbf{x}, t, \mathbf{n}) \, \mathrm{d}s, \tag{2.7}$$

where v' represents the current volume of the analysed part of the body and s' is the closed surface of that part of the body.

From the law of conservation of mass (2.3) we know that $\rho \, \mathrm{d}v$ is constant, i.e. we obtain

$$\int_{v'} \rho \ddot{\mathbf{x}} \, \mathrm{d}v = \int_{v'} \mathbf{p}_\mathrm{v}(\mathbf{x}, t) \, \mathrm{d}v + \int_{s'} \mathbf{t}(\mathbf{x}, t, \mathbf{n}) \, \mathrm{d}s. \tag{2.8}$$

Let us fix the time and focus on the neighbourhood of a material point $X \in s$ (on an arbitrary diaphragm within the body, through which we draw three curvilinear coordinate axes, which are orthogonal at X with coordinates ξ^α along the orthogonal and curved unit base vectors $\mathbf{g}_\alpha$, $\alpha = 1, 2, 3$. Let us draw a tetrahedron W with one edge of length l and others in fixed proportions to it. We denote the coordinate faces of the tetrahedron W by Σ_α ($\alpha = 1, 2, 3$) and the principal face by Σ. Let us put a unit normal $\mathbf{n}$ pointing from the origin, a force vector $\Delta \mathbf{F}$ and a moment vector $\Delta \mathbf{M}$ on the principal face Σ of the tetrahedron (see Figure 2.3a). Furthermore, force vectors $\Delta \mathbf{F}_\alpha$ together with moment

vectors $\Delta\mathbf{M}_\alpha$ act on each face Σ_α ($\alpha = 1, 2, 3$) of the tetrahedron. The orientation of the faces Σ_α are defined by the outward normals $\mathbf{n}_\alpha$ (see Figure 2.3b (*Note: To avoid cluttering, the force and moment acting on the principal side and the volume forces have been separated from the forces and moments acting on remaining sides of the tetrahedron W*).).
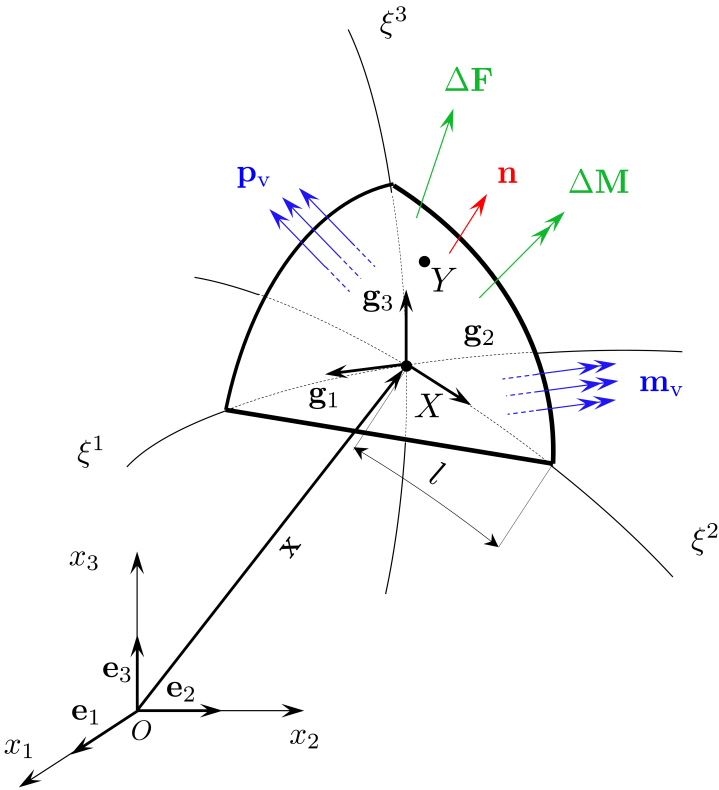
(a) Neighbourhood of point X with applied volume load and force and moment vectors on the principal side of the tetrahedron W
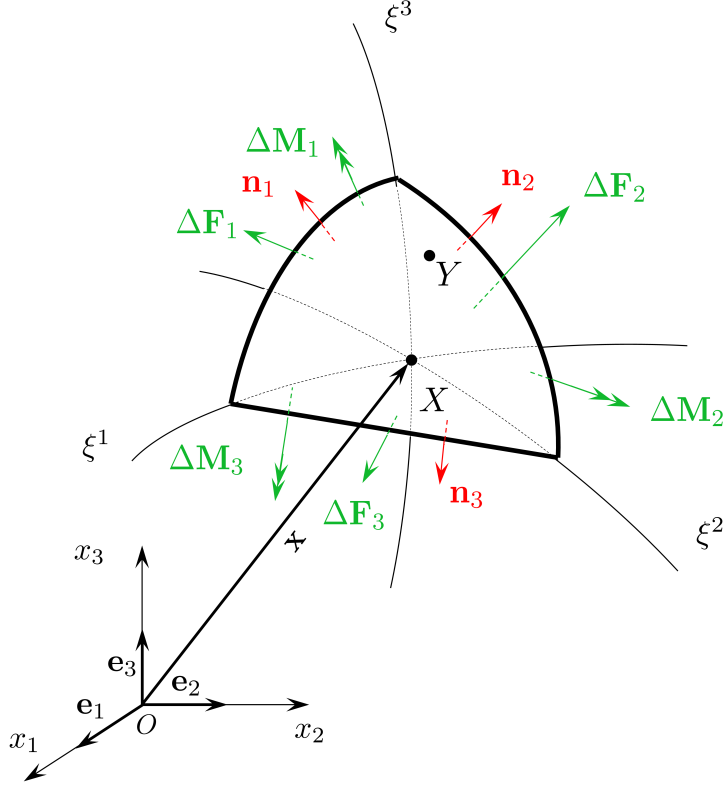
(b) Neighbourhood of point X with force and moment vectors on remaining sides of the tetrahedron W

Figure 2.3: Forces and moments on W

From the conservation of momentum of the tetrahedron W we have

$$\frac{\mathrm{d}}{\mathrm{d}t} \int_{\overline{v}} \rho \dot{\mathbf{x}} \, \mathrm{d}v = \int_{\overline{v}} \mathbf{p}_{\mathrm{v}}(\mathbf{x}, t) \, \mathrm{d}v + \overline{\mathbf{t}}\Sigma + \overline{\mathbf{t}}_1\Sigma_1 + \overline{\mathbf{t}}_2\Sigma_2 + \overline{\mathbf{t}}_3\Sigma_3, \tag{2.9}$$

i.e.

$$\int_{\overline{v}} \rho \ddot{\mathbf{x}} \, \mathrm{d}v = \int_{\overline{v}} \mathbf{p}_{\mathrm{v}}(\mathbf{x}, t) \, \mathrm{d}v + \overline{\mathbf{t}}\Sigma + \overline{\mathbf{t}}_1\Sigma_1 + \overline{\mathbf{t}}_2\Sigma_2 + \overline{\mathbf{t}}_3\Sigma_3 \tag{2.10}$$

and thus

$$\overline{\mathbf{t}}\Sigma + \overline{\mathbf{t}}_1\Sigma_1 + \overline{\mathbf{t}}_2\Sigma_2 + \overline{\mathbf{t}}_3\Sigma_3 + \int_{\overline{v}} (\mathbf{p}_{\mathrm{v}}(\mathbf{x}, t) - \rho\ddot{\mathbf{x}}) \, \mathrm{d}v = \mathbf{0}, \tag{2.11}$$

where $\overline{v}$ is the volume of the tetrahedron. The volume of the tetrahedron $\overline{v}$ and the area of its surface $\overline{s}$ ($\overline{s} = \Sigma_1 + \Sigma_2 + \Sigma_3 + \Sigma$) are functions of l, i. e. $\overline{v} = \overline{v}(l^3)$, and $\overline{s} = \overline{s}(l^2)$. As the side l goes towards zero, the volume of the tetrahedron approaches zero faster than the area of its surface, i.e.

$$\lim_{l \to 0} \frac{\overline{v}}{\overline{s}} = 0. \tag{2.12}$$

14

In equation (2.11) we will define a new value $\mathbf{p}_v^*$ and name it the effective body force:

$$\mathbf{p}_v^* = \mathbf{p}_v - \rho\ddot{\mathbf{x}}. \tag{2.13}$$

As $l \to 0$ the mean values of the stress vectors become equal to the total value of the stress vector $\mathbf{t}$. Furthermore, from equations (2.11), (2.12) and (2.13) we conclude that

$$\lim_{l\to 0} \frac{\int_{\bar{v}} \mathbf{p}_v^* \, dv}{\bar{s}} = -\lim_{l\to 0} \frac{\int_{\Sigma} \mathbf{t}\, ds + \int_{\Sigma_1} \bar{\mathbf{t}}_1 \, ds + \int_{\Sigma_2} \bar{\mathbf{t}}_2 \, ds + \int_{\Sigma_3} \bar{\mathbf{t}}_3 \, ds}{\bar{s}} \Rightarrow \lim_{l\to 0} \frac{\int_{\bar{s}} \mathbf{t}\, ds}{\bar{s}} = 0. \tag{2.14}$$

The mean value theorem for integrals [54] states that every integral can be written as a product of a certain function value within the area of integration and the area of integration so that there exists a point $Y \in \Sigma$ and points $Y_\alpha \in \Sigma_\alpha$ such that

$$\frac{1}{\bar{s}} \int_{\bar{s}} \mathbf{t}\, ds = \frac{1}{\bar{s}} \left[\mathbf{t}(\mathbf{x}_Y, \mathbf{n})(\text{area } \Sigma) + \sum_{\alpha=1}^{3} \mathbf{t}(\mathbf{x}_{Y_\alpha}, \mathbf{n}_\alpha)(\text{area } \Sigma_\alpha) \right], \tag{2.15}$$

where $\mathbf{n}_\alpha$ is the outward unit normal to Σ_α at Y_α and $\mathbf{n}$ is the outward unit normal to Σ at Y.

As the length l is approaching zero, the tetrahedron collapses into the point X and the position vectors $\mathbf{x}_Y$, $\mathbf{x}_{Y_\alpha}$ become equal to $\mathbf{x}$, and the unit normals become equal to the unit vectors $\mathbf{g}_\alpha$ but with opposite direction, i.e. $\mathbf{n}_\alpha = -\mathbf{g}_\alpha$. It means that, as $l \to 0$, $\frac{area\ \Sigma}{\bar{s}} \to \beta$, where β is a constant, and $\frac{area\ \Sigma_\alpha}{\bar{s}} \to n^\alpha \beta$, where $\mathbf{n} = n^\alpha \mathbf{g}_\alpha$. Equations (2.14) and (2.15) give

$$\mathbf{t}(\mathbf{x}, \mathbf{n}) + \sum_{\alpha=1}^{3} n^\alpha \mathbf{t}(\mathbf{x}, -\mathbf{g}_\alpha) = \mathbf{0}. \tag{2.16}$$

Noting that $\mathbf{n} = n^\alpha \mathbf{g}_\alpha$ multiplied by $\mathbf{g}_\beta$ gives

$$\mathbf{n} \cdot \mathbf{g}_\beta = n^\alpha \mathbf{g}_\alpha \cdot \mathbf{g}_\beta, \tag{2.17}$$

and thus

$$\mathbf{n} \cdot \mathbf{g}_\beta = n^\beta. \tag{2.18}$$

If we take that $\mathbf{n} = \mathbf{g}_\beta = \delta_{\alpha\beta}\mathbf{g}_\alpha$, where $\delta_{\alpha\beta}$ is the Kronecker symbol defined as

$$\delta_{ij} = \begin{cases} 0 & \text{if } i \neq j \\ 1 & \text{if } i = j \end{cases}, \tag{2.19}$$

and using equation (D.2) we obtain:

$$\mathbf{t}(\mathbf{x}, \mathbf{g}_\beta) + \sum_{\alpha=1}^{3} \delta_{\alpha\beta} \mathbf{t}(\mathbf{x}, -\mathbf{g}_\alpha) = \mathbf{0}, \tag{2.20}$$

$$\mathbf{t}(\mathbf{x}, \mathbf{g}_\beta) + \mathbf{t}(\mathbf{x}, -\mathbf{g}_\beta) = \mathbf{0}, \tag{2.21}$$

$$\mathbf{t}(\mathbf{x}, \mathbf{g}_\beta) = -\mathbf{t}(\mathbf{x}, -\mathbf{g}_\beta). \tag{2.22}$$

Equation (2.22) is known as *Cauchy's Fundamental Lemma* [55]. Using this and going back to the equation (D.2) we obtain:

$$\mathbf{t}(\mathbf{x}, \mathbf{n}) + \sum_{\alpha=1}^{3} n^\alpha \mathbf{t}(\mathbf{x}, -\mathbf{g}_\alpha) = \mathbf{0}, \tag{2.23}$$

$$\mathbf{t}(\mathbf{x}, \mathbf{n}) = \sum_{\alpha=1}^{3} \mathbf{g}_\alpha \cdot \mathbf{n} \; \mathbf{t}(\mathbf{x}, -\mathbf{g}_\alpha) = \mathbf{0}, \tag{2.24}$$

$$\mathbf{t}(\mathbf{x}, \mathbf{n}) = \sum_{\alpha=1}^{3} \mathbf{t}(\mathbf{x}, -\mathbf{g}_\alpha) \otimes \mathbf{g}_\alpha \cdot \mathbf{n}, \tag{2.25}$$

where "$\otimes$" is a *tensor* (or *outer*) product. The vector field $\mathbf{t}(\mathbf{x}, t, \mathbf{n})$ is therefore not just a function of the normal to an imaginary internal diaphragm within the body, it is *the linear function* of this normal:

$$\mathbf{t}(\mathbf{x}, t, \mathbf{n}) = \boldsymbol{\sigma}(\mathbf{x}, t) \cdot \mathbf{n}, \tag{2.26}$$

where

$$\boldsymbol{\sigma}(\mathbf{x}, t) = \sum_{\alpha=1}^{3} \mathbf{t}(\mathbf{x}, -\mathbf{g}_\alpha) \otimes \mathbf{g}_\alpha \tag{2.27}$$

is the *stress tensor*. Equation (2.26) is referred to as *the Cauchy theorem* [55]. The stress tensor $\boldsymbol{\sigma}$ is a second order tensor which in the classical continuum theory completely defines the state of stress at a point in the deformed configuration. The above proof of existence of such an object due to Cauchy is of fundamental importance for the development of all continuum theories. Since in the micropolar continuum theory the interaction between particles is described by an additional moment couple-stress vector, we may also prove existence of an additional stress tensor known as the *couple-stress tensor* as will be shown next.

Definition 2. Balance of Angular Momentum.

The rate of change of an angular momentum of any part of the body is equal to the vectorial sum of all moments acting on it, i.e.

$$\frac{\mathrm{d}}{\mathrm{d}t} \int_{v'} (\mathbf{x} \times \rho \dot{\mathbf{x}}) \, \mathrm{d}v = \int_{v'} [\mathbf{x} \times \mathbf{p}_v(\mathbf{x}, t) + \mathbf{m}_v(\mathbf{x}, t)] \, \mathrm{d}v + \int_{s'} [\mathbf{x} \times \mathbf{t}(\mathbf{x}, t, \mathbf{n}) + \mathbf{m}(\mathbf{x}, t, \mathbf{n})] \, \mathrm{d}s.$$

When this balance is applied to the tetrahedron W we have

$$\frac{\mathrm{d}}{\mathrm{d}t} \int_{\overline{v}} (\mathbf{x} \times \rho \dot{\mathbf{x}}) \, \mathrm{d}v = \int_{\overline{v}} [\mathbf{x} \times \mathbf{p}_v(\mathbf{x}, t) + \mathbf{m}_v(\mathbf{x}, t)] \, \mathrm{d}v + \int_{\overline{s}} [\mathbf{x} \times \mathbf{t}(\mathbf{x}, t, \mathbf{n})] \, \mathrm{d}s+$$
$$+ \overline{\mathbf{m}}\Sigma + \overline{\mathbf{m}}_1 \Sigma_1 + \overline{\mathbf{m}}_2 \Sigma_2 + \overline{\mathbf{m}}_3 \Sigma_3. \tag{2.28}$$

Replacing the stress vector $\mathbf{t}(\mathbf{x}, t, \mathbf{n}) = \boldsymbol{\sigma}(\mathbf{x}, t) \cdot \mathbf{n}$ and noting that

$$\mathbf{x} \times \mathbf{t} = \hat{\mathbf{x}} \cdot \mathbf{t}, \quad \forall \, \mathbf{x} \in \mathbb{R}^3, \tag{2.29}$$

where $\hat{\mathbf{x}}$ is a skew-symmetric vector-product operator given for the present vector base in the matrix form as

$$\hat{\mathbf{x}} = \begin{bmatrix} 0 & -x_3 & x_2 \\ x_3 & 0 & -x_1 \\ -x_2 & x_1 & 0 \end{bmatrix}, \tag{2.30}$$

we obtain

$$\int_{\overline{v}} (\dot{\mathbf{x}} \times \rho \dot{\mathbf{x}} + \mathbf{x} \times \rho \ddot{\mathbf{x}}) \, \mathrm{d}v = \int_{\overline{v}} [\mathbf{x} \times \mathbf{p}_v(\mathbf{x}, t) + \mathbf{m}_v(\mathbf{x}, t)] \, \mathrm{d}v + \int_{\overline{s}} [\hat{\mathbf{x}} \cdot \boldsymbol{\sigma}(\mathbf{x}, t) \cdot \mathbf{n}] \, \mathrm{d}s+$$
$$+ \overline{\mathbf{m}}\Sigma + \overline{\mathbf{m}}_1 \Sigma_1 + \overline{\mathbf{m}}_2 \Sigma_2 + \overline{\mathbf{m}}_3 \Sigma_3. \tag{2.31}$$

In order to further manipulate the equation (2.31) we introduce next the so-called divergence theorem [56].

Theorem 1 (Divergence Theorem, also known as Ostrogradsky-Gauss Theorem:)
The outward flux of a vector field $\mathbf{v}$ through a closed surface is equal to the integral over the volume inside the surface of the divergence of the vector field, i.e.

$$\int_V \mathrm{div} \, \mathbf{v} \, \mathrm{d}V = \oint_S \mathbf{v} \cdot \mathbf{n} \, \mathrm{d}S, \tag{2.32}$$

where V is a considered volume, S is a closed surface around it, $\mathbf{v}$ is an arbitrary differentiable vector field, $\mathbf{n}$ is an outward normal to S and $\mathrm{div} \, \mathbf{v} = \nabla \cdot \mathbf{v}$ with ∇ as the nabla operator.

17

The divergence theorem can be generalised to second order tensors as follows

$$\int_V \text{div } \mathbf{A} \, dV = \oint_S \mathbf{A} \cdot \mathbf{n} \, dS, \tag{2.33}$$

where $\mathbf{A}$ is a second order tensor. The proof of this theorem can be found in [54].

Divergence of a tensor is not an uniquely defined operation, i.e. written in a tensor form it can be understood as $\nabla \cdot \mathbf{A}$ either $\mathbf{A} \cdot \nabla$.

Here we define the *scalar product* (also known as the *dot product* or *inner product*) between a second-order tensor and a vector. Second-order tensor $\mathbf{A}$ is defined as

$$\mathbf{A} = A_{ij}\mathbf{e}_i \otimes \mathbf{e}_j, \tag{2.34}$$

where ∇ is defined as

$$\nabla = \frac{\partial}{\partial x_p}\mathbf{e}_p. \tag{2.35}$$

The first tensor-divergence form, i.e. $\nabla \cdot \mathbf{A}$ is thus equal to

$$\nabla \cdot \mathbf{A} = \frac{\partial}{\partial x_p}\mathbf{e}_p \cdot A_{ij}\mathbf{e}_i \otimes \mathbf{e}_j \tag{2.36}$$

$$= \frac{\partial}{\partial x_p}A_{ij}\mathbf{e}_p \cdot \mathbf{e}_i \otimes \mathbf{e}_j \tag{2.37}$$

$$= \frac{\partial}{\partial x_p}A_{ij}\delta_{pi} \otimes \mathbf{e}_j \tag{2.38}$$

$$= \frac{\partial}{\partial x_p}A_{pj}\mathbf{e}_j, \tag{2.39}$$

and the second form, i.e. $\mathbf{A} \cdot \nabla$ is equal to

$$\mathbf{A} \cdot \nabla = A_{ij}\mathbf{e}_i \otimes \mathbf{e}_j \cdot \frac{\partial}{\partial x_p}\mathbf{e}_p$$

$$= A_{ij}\frac{\partial}{\partial x_p}\mathbf{e}_i \otimes \mathbf{e}_j \cdot \mathbf{e}_p$$

$$= A_{ij}\frac{\partial}{\partial x_p}\mathbf{e}_i\delta_{jp}$$

$$= A_{ip}\frac{\partial}{\partial x_p}\mathbf{e}_i. \tag{2.40}$$

In this work we choose to use the second form for a tensor-divergence operation, i.e. $\text{div } \mathbf{A} = \mathbf{A} \cdot \nabla$ but, in order to compare the analytical model and the obtained numerical results in the linear analysis with numerous literature that uses the alternative convention [57, 20] $\text{div } \mathbf{A} = \nabla \cdot \mathbf{A}$, the linear micropolar analytical model is also derived using the former tensor-divergence definition and presented in Appendix A.

Applying the divergence theorem on equation (2.31) gives

$$\int_{\overline{v}} (\mathbf{x} \times \rho \ddot{\mathbf{x}}) \, \mathrm{d}v = \int_{\overline{v}} \left[\mathbf{x} \times \mathbf{p}_v(\mathbf{x}, t) + \mathbf{m}_v(\mathbf{x}, t) + \mathrm{div}(\hat{\mathbf{x}} \cdot \boldsymbol{\sigma}(\mathbf{x}, t)) \right] \mathrm{d}v +$$
$$+ \overline{\mathbf{m}}\Sigma + \overline{\mathbf{m}}_1 \Sigma_1 + \overline{\mathbf{m}}_2 \Sigma_2 + \overline{\mathbf{m}}_3 \Sigma_3. \tag{2.41}$$

We define a new effective body moment $\mathbf{p}_{\mathrm{m}}^*$:

$$\mathbf{p}_{\mathrm{m}}^* = \mathbf{x} \times \rho \ddot{\mathbf{x}} - \mathbf{x} \times \mathbf{p}_v(\mathbf{x}, t) - \mathbf{m}_v(\mathbf{x}, t) - \mathrm{div}(\hat{\mathbf{x}} \cdot \boldsymbol{\sigma}(\mathbf{x}, t)). \tag{2.42}$$

As the side l goes towards zero, the volume of the tetrahedron approaches zero faster than the area of its surface. Analogously, we can conclude that

$$\lim_{l \to 0} \frac{\int_{\overline{v}} \mathbf{p}_{\mathrm{m}}^* \, \mathrm{d}v}{\overline{s}} = \lim_{l \to 0} \frac{\int_{\Sigma} \mathbf{m} \, \mathrm{d}s + \int_{\Sigma_1} \mathbf{m}_1 \, \mathrm{d}s + \int_{\Sigma_2} \mathbf{m}_2 \, \mathrm{d}s + \int_{\Sigma_3} \mathbf{m}_3 \, \mathrm{d}s}{\overline{s}} \Rightarrow \lim_{l \to 0} \frac{\int_{\overline{s}} \mathbf{m} \, \mathrm{d}s}{\overline{s}} = 0. \tag{2.43}$$

According to the mean theorem:

$$\frac{1}{\overline{s}} \int_{\overline{s}} \mathbf{m} \, \mathrm{d}s = \frac{1}{\overline{s}} \left[\mathbf{m}(\mathbf{x}_Y, \mathbf{n})(\mathrm{area} \ \Sigma) + \sum_{\alpha=1}^{3} \mathbf{m}(\mathbf{x}_{Y_\alpha}, \mathbf{n}_\alpha)(\mathrm{area} \ \Sigma_\alpha) \right]. \tag{2.44}$$

As the length l is approaching zero, the tetrahedron reduces to the point X and the position vectors $\mathbf{x}_Y$, $\mathbf{x}_{Y_\alpha}$ become equal to $\mathbf{x}$, and the unit normals become equal to the unit vectors $\mathbf{g}_\alpha$ but with opposite direction, i.e. $\mathbf{n}_\alpha = -\mathbf{g}_\alpha$. It means that, as $l \to 0$, $\dfrac{\mathrm{area} \ \Sigma}{\overline{s}} \to \beta$, where β is a constant, and $\dfrac{\mathrm{area} \ \Sigma_\alpha}{\overline{s}} \to n^\alpha \beta$, where $\mathbf{n} = n^\alpha \mathbf{g}_\alpha$. Equations (2.43) and (2.44) give

$$\mathbf{m}(\mathbf{x}, \mathbf{n}) + \sum_{\alpha=1}^{3} n^\alpha \mathbf{m}(\mathbf{x}, -\mathbf{g}_\alpha) = \mathbf{0}. \tag{2.45}$$

We thus generalise the Cauchy Fundamental Lemma to the couple stress vector as

$$\mathbf{m}(\mathbf{x}, \mathbf{g}_\beta) = -\mathbf{m}(\mathbf{x}, -\mathbf{g}_\beta). \tag{2.46}$$

Using equations (2.45) and (2.46) we obtain

$$\mathbf{m}(\mathbf{x}, \mathbf{n}) = \sum_{\alpha=1}^{3} \mathbf{g}_\alpha \cdot \mathbf{n} \ \mathbf{m}(\mathbf{x}, -\mathbf{g}_\alpha) = \mathbf{0}, \tag{2.47}$$

$$\mathbf{m}(\mathbf{x}, \mathbf{n}) = \sum_{\alpha=1}^{3} \mathbf{m}(\mathbf{x}, -\mathbf{g}_\alpha) \otimes \mathbf{g}_\alpha \cdot \mathbf{n}. \tag{2.48}$$

The couple stress vector field $\mathbf{m}(\mathbf{x}, t, \mathbf{n})$ is therefore also *the linear function* of the

normal to an imaginary internal diaphragm within the body:

$$\mathbf{m}(\mathbf{x}, t, \mathbf{n}) = \boldsymbol{\mu}(\mathbf{x}, t) \cdot \mathbf{n}, \qquad (2.49)$$

where

$$\boldsymbol{\mu}(\mathbf{x}, t) = \sum_{\alpha=1}^{3} \mathbf{m}(\mathbf{x}, -\mathbf{g}_\alpha) \otimes \mathbf{g}_\alpha, \qquad (2.50)$$

is the *couple-stress tensor*. Since we have assumed that the interactions between particles occur by means of a force stress vector $\mathbf{t}$ and an additional couple-stress vector $\mathbf{m}$, the existence of an additional stress tensor is inevitable. The couple-stress tensor is also a tensor of order two. By proving the existence of both tensors, we have completely defined the state of stress of a point in the deformed configuration of a micropolar continuum.

In order to shorten and simplify the notation, the dot ("·") in the definition of the inner product (between two vectors, two second order tensors and between a second order tensor and a vector) will be generally omitted in the continuation of this thesis, i.e. $\mathbf{A} \cdot \mathbf{b} = \mathbf{A}\mathbf{b}$, $\mathbf{A} \cdot \mathbf{B} = \mathbf{A}\mathbf{B}$, $\mathbf{a} \cdot \mathbf{b} = \mathbf{a}^\mathrm{T}\mathbf{b}$ and $\mathbf{a} \cdot \mathbf{B} = \mathbf{a}^\mathrm{T}\mathbf{B}$ where $\mathbf{a}, \mathbf{b}$ represent vectors and $\mathbf{A}, \mathbf{B}$ represent second order tensors. Such a notation thus fully conforms with standard matrix multiplication.

2.2 Equations of equilibrium

Let us analyse the body in the deformed state under the influence of external actions consisting of a distributed volume load and a distributed surface load as defined in Section 2.1. In the linear analysis analysed here we assume that the body, when deformed, exhibit small displacements and small rotations. This assumption leads to the fact that the difference between the body volume and body surface in the undeformed and deformed configuration can be neglected. Thus the deformed body volume is referred to as V and the deformed body surface is referred to as S. The body surface S is divided into two parts: S_p with prescribed forces and couples and S_u with prescribed displacements and rotations where $S_u \cup S_p = S$ and $S_u \cap S_p = \varnothing$. Distributed surface loads $\mathbf{p}_s$ and $\mathbf{m}_s$ and distributed volume loads $\mathbf{p}_v$ and $\mathbf{m}_v$ are assumed to act on S_p and in the interior of the body as shown in Figure 2.4. The base vectors $\mathbf{e}_i, \ i = 1, 2, 3$ are here assumed to be orthogonal and straight.
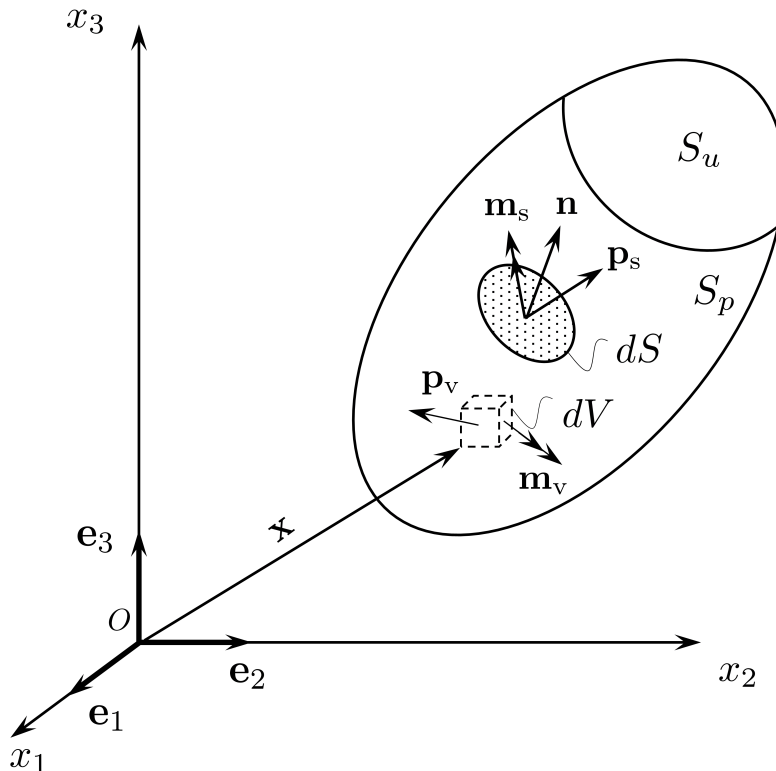
Figure 2.4: Body subject to applied volume load and surface traction

2.2.1 Differential equations of equilibrium within the body

Let us analyse the forces acting on the differential volume $\mathrm{d}V$ in the deformed configuration as shown in Figure 2.5, where stresses and loadings have been separated for clarity.

(a) Components of the force stress

(b) Components of the couple-stress

(c) Components of the applied volume load
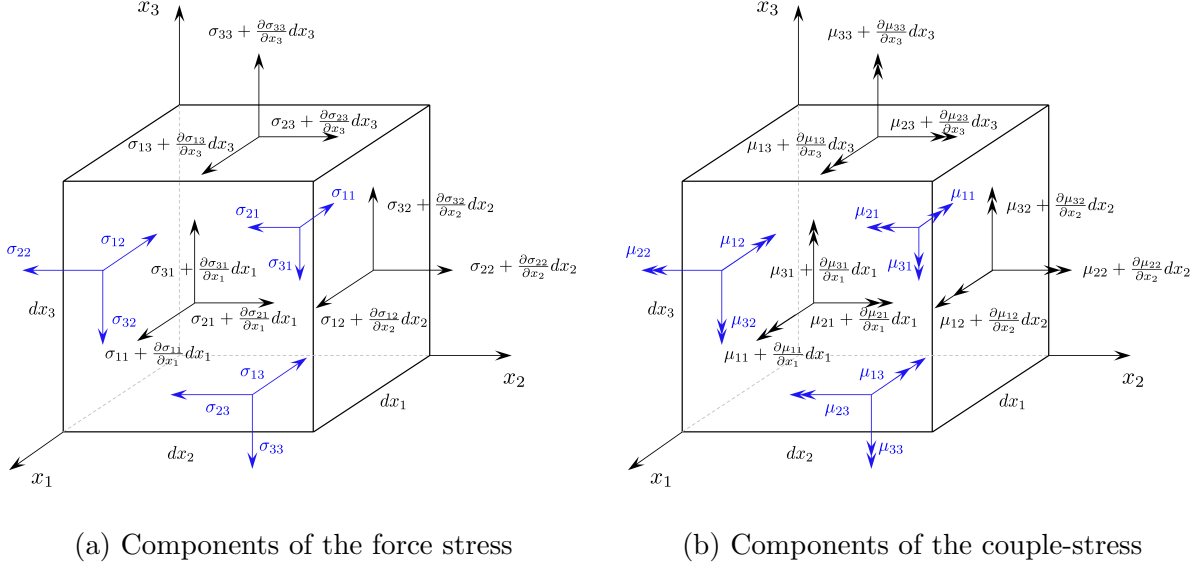
Figure 2.5: Equilibrium of a differential volume.

Summing all the components of the applied load and internal forces along the co-ordinate axis x_1 and dividing by dV gives:

$$\frac{\partial \sigma_{11}}{\partial x_1} + \frac{\partial \sigma_{12}}{\partial x_2} + \frac{\partial \sigma_{13}}{\partial x_3} + p_{v1} = 0. \tag{2.51}$$

Summing all the components of the applied load and internal forces along the co-ordinate axis x_2 and dividing by dV gives:

$$\frac{\partial \sigma_{21}}{\partial x_1} + \frac{\partial \sigma_{22}}{\partial x_2} + \frac{\partial \sigma_{23}}{\partial x_3} + p_{v2} = 0. \tag{2.52}$$

Summing all the components of the applied load and internal forces along the co-ordinate axis x_3 and dividing by dV gives:

$$\frac{\partial \sigma_{31}}{\partial x_1} + \frac{\partial \sigma_{32}}{\partial x_2} + \frac{\partial \sigma_{33}}{\partial x_3} + p_{v3} = 0. \tag{2.53}$$

Written in the matrix form equations (2.51), (2.52) and (2.53) read

$$\begin{bmatrix} \sigma_{11} & \sigma_{12} & \sigma_{13} \\ \sigma_{21} & \sigma_{22} & \sigma_{23} \\ \sigma_{31} & \sigma_{32} & \sigma_{33} \end{bmatrix} \begin{Bmatrix} \frac{\partial}{\partial x_1} \\ \frac{\partial}{\partial x_2} \\ \frac{\partial}{\partial x_3} \end{Bmatrix} + \begin{Bmatrix} p_{v1} \\ p_{v2} \\ p_{v3} \end{Bmatrix} = \begin{Bmatrix} 0 \\ 0 \\ 0 \end{Bmatrix}, \tag{2.54}$$

i.e.

$$\boldsymbol{\sigma}\nabla + \mathbf{p_v} = \mathbf{0}, \tag{2.55}$$

where ∇ is the nabla operator defined in the present vector base as

$$\nabla = \begin{Bmatrix} \frac{\partial}{\partial x_1} \\ \frac{\partial}{\partial x_2} \\ \frac{\partial}{\partial x_3} \end{Bmatrix}. \tag{2.56}$$

Defining the divergence of the stress tensor as div $\boldsymbol{\sigma} = \boldsymbol{\sigma}\nabla$, the tensor form of equations (2.51),(2.52) and (2.53) is

$$\text{div } \boldsymbol{\sigma} + \mathbf{p_v} = \mathbf{0}, \tag{2.57}$$

and using summation convention, equations (2.51), (2.52) and (2.53) can also be written as

$$\sigma_{ij,j} + p_{vi} = 0, \tag{2.58}$$

where the first index in the stress denotes the direction of the stress with respect to the coordinate base, the second index denotes the direction of the surface normal, comma denotes differentiation with respect to the spatial coordinates, and $i, j = 1, 2, 3$.

In order to completely define the equilibrium of the differential volume, we have to write the moment equilibrium equations around axes x_1, x_2 and x_3. Summing all the moments around the x_1 axis we obtain

$$\left(\sigma_{31} + \frac{\partial \sigma_{31}}{\partial x_1}\,dx_1\right)\frac{(dx_2)^2}{2}\,dx_3 - \left(\sigma_{21} + \frac{\partial \sigma_{21}}{\partial x_1}\,dx_1\right)dx_2\frac{(dx_3)^2}{2} - \left(\sigma_{22} + \frac{\partial \sigma_{22}}{\partial x_2}\,dx_2\right)dx_1\frac{(dx_3)^2}{2} +$$
$$+ \left(\sigma_{32} + \frac{\partial \sigma_{32}}{\partial x_2}\,dx_2\right)dx_1\,dx_2\,dx_3 + \sigma_{21}\,dx_2\frac{(dx_3)^2}{2} - \sigma_{31}\frac{(dx_2)^2}{2}\,dx_3 + \sigma_{22}\,dx_1\frac{(dx_3)^2}{2} +$$
$$- \sigma_{33}\,dx_1\frac{(dx_2)^2}{2} + \left(\sigma_{33} + \frac{\partial \sigma_{33}}{\partial x_3}\,dx_3\right)dx_1\frac{(dx_2)^2}{2} - \left(\sigma_{23} + \frac{\partial \sigma_{23}}{\partial x_3}\,dx_3\right)dx_1\,dx_2\,dx_3 + \tag{2.59}$$
$$+ \left(\mu_{11} + \frac{\partial \mu_{11}}{\partial x_1}\,dx_1\right)dx_2\,dx_3 + \left(\mu_{12} + \frac{\partial \mu_{12}}{\partial x_2}\,dx_2\right)dx_1\,dx_3 - \mu_{11}\,dx_2\,dx_3 - \mu_{12}\,dx_1\,dx_3 +$$
$$+ \left(\mu_{13} + \frac{\partial \mu_{13}}{\partial x_3}\,dx_3\right)dx_1\,dx_2 - \mu_{13}\,dx_1\,dx_2 + m_{v1}\,dV + p_{v3}\frac{dx_2}{2}\,dV - p_{v2}\frac{dx_3}{2}\,dV = 0.$$

Dividing this result by dV and letting $dx_2 \to 0$ and $dx_3 \to 0$ we obtain

$$\frac{\partial \mu_{11}}{\partial x_1} + \frac{\partial \mu_{12}}{\partial x_2} + \frac{\partial \mu_{13}}{\partial x_3} + \sigma_{32} - \sigma_{23} + m_{v1} = 0. \tag{2.60}$$

Summing all the moments around the axes x_2 and x_3 likewise gives

$$\frac{\partial \mu_{21}}{\partial x_1} + \frac{\partial \mu_{22}}{\partial x_2} + \frac{\partial \mu_{23}}{\partial x_3} + \sigma_{13} - \sigma_{31} + m_{v2} = 0, \tag{2.61}$$

$$\frac{\partial \mu_{31}}{\partial x_1} + \frac{\partial \mu_{32}}{\partial x_2} + \frac{\partial \mu_{33}}{\partial x_3} + \sigma_{21} - \sigma_{12} + m_{v3} = 0. \tag{2.62}$$

Written in the matrix form equations (2.60), (2.61) and (2.62) read

$$\begin{bmatrix} \mu_{11} & \mu_{12} & \mu_{13} \\ \mu_{21} & \mu_{22} & \mu_{23} \\ \mu_{31} & \mu_{32} & \mu_{33} \end{bmatrix} \begin{Bmatrix} \frac{\partial}{\partial x_1} \\ \frac{\partial}{\partial x_2} \\ \frac{\partial}{\partial x_3} \end{Bmatrix} + \begin{Bmatrix} \sigma_{32} - \sigma_{23} \\ -\sigma_{31} + \sigma_{13} \\ \sigma_{21} - \sigma_{12} \end{Bmatrix} + \begin{Bmatrix} m_{v1} \\ m_{v2} \\ m_{v3} \end{Bmatrix} = \begin{Bmatrix} 0 \\ 0 \\ 0 \end{Bmatrix}. \tag{2.63}$$

We will further split our stress tensor $\boldsymbol{\sigma}$ into its symmetric ($\boldsymbol{\sigma}_s$) and skew-symmetric ($\boldsymbol{\sigma}_a$) part as follows:

$$\begin{bmatrix} \sigma_{11} & \sigma_{12} & \sigma_{13} \\ \sigma_{21} & \sigma_{22} & \sigma_{23} \\ \sigma_{31} & \sigma_{32} & \sigma_{33} \end{bmatrix} = \underbrace{\begin{bmatrix} \sigma_{11} & \frac{1}{2}(\sigma_{12} + \sigma_{21}) & \frac{1}{2}(\sigma_{13} + \sigma_{31}) \\ \frac{1}{2}(\sigma_{21} + \sigma_{12}) & \sigma_{22} & \frac{1}{2}(\sigma_{23} + \sigma_{32}) \\ \frac{1}{2}(\sigma_{31} + \sigma_{13}) & \frac{1}{2}(\sigma_{32} + \sigma_{23}) & \sigma_{33} \end{bmatrix}}_{=\boldsymbol{\sigma}_s} + \underbrace{\begin{bmatrix} 0 & \frac{1}{2}(\sigma_{12} - \sigma_{21}) & \frac{1}{2}(\sigma_{13} - \sigma_{31}) \\ \frac{1}{2}(\sigma_{21} - \sigma_{12}) & 0 & \frac{1}{2}(\sigma_{23} - \sigma_{32}) \\ \frac{1}{2}(\sigma_{31} - \sigma_{13}) & \frac{1}{2}(\sigma_{32} - \sigma_{23}) & 0 \end{bmatrix}}_{=\boldsymbol{\sigma}_a = \frac{1}{2}\hat{\mathbf{a}}}. \tag{2.64}$$

As shown in equation (2.29), every skew-symmetric tensor of order two can be written in a vector form such that for every two vectors $\mathbf{v}, \mathbf{w} \in \mathbb{R}^3$

$$\hat{\mathbf{v}}\mathbf{w} = \mathbf{v} \times \mathbf{w}, \tag{2.65}$$

where $\hat{\mathbf{v}}$ is a skew-symmetric tensor and $\hat{v}$ is its *axial vector* [53]. In this way we obtain an axial vector $\mathbf{a}$ of the double skew-symmetric part of the stress tensor as

$$\mathbf{a} = \text{axial}(2\boldsymbol{\sigma}_a) = \begin{Bmatrix} \sigma_{32} - \sigma_{23} \\ -\sigma_{31} + \sigma_{13} \\ \sigma_{21} - \sigma_{12} \end{Bmatrix}. \tag{2.66}$$

Now we can write equation (2.63) in a matrix form as

$$\boldsymbol{\mu}\nabla + \mathbf{a} + \mathbf{m_v} = \mathbf{0}. \tag{2.67}$$

The tensor form of this equation is

$$\text{div } \boldsymbol{\mu} + \text{grad } \hat{\mathbf{x}} : \boldsymbol{\sigma} + \mathbf{m_v} = \mathbf{0}. \tag{2.68}$$

The second term of equation (2.68) represents a *double inner product* (or *double contraction*) between a third-order tensor and a second-order tensor. Using summation convention and setting any two indices equal (i.e. one pair of indices), tensors are said to be contracted and the order of the tensor is reduced by two [53]. It is not an uniquely defined operation, since any of the indices can be set as equal. Here we have a double contraction and, in order to obtain $\mathbf{a}$ from grad $\hat{\mathbf{x}}$ and $\boldsymbol{\sigma}$, we have to define which two pairs of indices we have to set as equal. First we will define

$$\text{grad } \hat{\mathbf{x}} = -\varepsilon_{ijk}x_i\mathbf{e}_j \otimes \mathbf{e}_k \otimes \nabla, \tag{2.69}$$

where ε_{ijk} is the permutation tensor or Levi-Civita symbol defined as

$$\varepsilon_{ijk} = \begin{cases} 1 & \text{if } (i,j,k) \text{ is a cyclic permutation of } (1,2,3), \\ -1 & \text{if } (i,j,k) \text{ is an anticyclic permutation of } (1,2,3), \\ 0 & \text{otherwise,} \end{cases} \tag{2.70}$$

and $\nabla = \dfrac{\partial}{\partial x_p}\mathbf{e}_p$. Furthermore, $\boldsymbol{\sigma}$ is a second-order tensor, i.e.

$$\boldsymbol{\sigma} = \sigma_{mn}\mathbf{e}_m \otimes \mathbf{e}_n. \tag{2.71}$$

From equation (2.69) we obtain:

$$\begin{aligned} \text{grad } \hat{\mathbf{x}} &= -\varepsilon_{ijk}\frac{\partial x_i}{\partial x_p}\mathbf{e}_j \otimes \mathbf{e}_k \otimes \mathbf{e}_p, \\ &= -\varepsilon_{ijk}\delta_{ip}\mathbf{e}_j \otimes \mathbf{e}_k \otimes \mathbf{e}_p, \\ &= -\varepsilon_{ijk}\mathbf{e}_j \otimes \mathbf{e}_k \otimes \mathbf{e}_i, \\ &= -\varepsilon_{ijk}\mathbf{e}_i \otimes \mathbf{e}_j \otimes \mathbf{e}_k. \end{aligned} \tag{2.72}$$

The double contraction between the third-order tensor grad $\hat{\mathbf{x}}$ and the second-order tensor $\boldsymbol{\sigma}$

$$\text{grad } \hat{\mathbf{x}} : \boldsymbol{\sigma} = (-\varepsilon_{ijk}\mathbf{e}_i \otimes \mathbf{e}_j \otimes \mathbf{e}_k) : (\sigma_{mn}\mathbf{e}_m \otimes \mathbf{e}_n) \tag{2.73}$$

is now defined such that the dot products apply to the adjacent set of the base vectors

(here the last pair) i.e.

$$\text{grad } \hat{\mathbf{x}} : \boldsymbol{\sigma} = -\varepsilon_{ijk}\sigma_{mn}\mathbf{e}_i \left(\mathbf{e}_j^{\mathrm{T}}\mathbf{e}_m\right) \left(\mathbf{e}_k^{\mathrm{T}}\mathbf{e}_n\right)$$
$$= -\varepsilon_{ijk}\sigma_{mn}\mathbf{e}_i\delta_{jm}\delta_{kn}$$
$$= -\varepsilon_{ijk}\sigma_{jk}\mathbf{e}_i. \tag{2.74}$$

A detailed analysis of the equality $\mathbf{a} = \text{grad } \hat{\mathbf{x}} : \boldsymbol{\sigma}$ is given in Appendix B.

As a result, using summation indices, equations (2.60), (2.61) and (2.62) can be written as follows:

$$\mu_{ij,j} - \varepsilon_{ijk}\sigma_{jk} + m_{vi} = 0, \tag{2.75}$$

where the first index in the couple-stress tensor denotes the direction of the axis of the couple stress with respect to the coordinate base and the second index denotes the direction of the surface normal. We can see that the stress tensor is generally *not symmetric*. The skew-symmetric part of the stress tensor is determined by the body couples and the divergence of the couple-stress tensor. When $\mu_{ij} = 0$, $m_{vi} = 0$ the stress tensor will be symmetric, which is the case of the classical continuum theory.

As already mentioned, in the development of the micropolar theory, two different conventions for representing the equilibrium equations exist. The more commonly used one is attributed to Eringen [57, 11] in which authors use alternative forms of the Cauchy theorem, i.e.

$$\mathbf{t}(\mathbf{x}, t, \mathbf{n}) = \mathbf{n}^{\mathrm{T}}\boldsymbol{\sigma}(\mathbf{x}, t), \tag{2.76}$$
$$\mathbf{m}(\mathbf{x}, t, \mathbf{n}) = \mathbf{n}^{\mathrm{T}}\boldsymbol{\mu}(\mathbf{x}, t), \tag{2.77}$$

and the alternative definition of divergence of the second-order tensor, i.e. $\text{div } \boldsymbol{\sigma} = \nabla^{\mathrm{T}}\boldsymbol{\sigma}$. As a result, the meaning of the indices in the stress and stress couple tensors (there denoted as t_{ij} and m_{ij}) is actually reversed – the first index denotes the direction of the surface normal, while the second index denotes the direction of the stress or axis of the couple-stress component with respect to the coordinate base (effectively meaning $t_{ij} = \sigma_{ji}$ and $m_{ij} = \mu_{ji}$). The convention we follow (see e.g. [58], p. 140) is motivated by its widespread use in modern classical theory of elasticity. However, for comparison with the present literature, in Appendix A.1 equilibrium of the same differential volume is written using the alternative notation.

2.2.2 Equations of equilibrium on surface

In order to fully define the boundary conditions on S_p, we need to relate the applied surface loads $\mathbf{p}_{\mathrm{s}}$ and $\mathbf{m}_{\mathrm{s}}$ to the inside of S_p which resist the action of $\mathbf{p}_{\mathrm{s}}$ and $\mathbf{m}_{\mathrm{s}}$ and keep the surface in equilibrium. To do that, we analyse equilibrium of a differential element

under the differential surface dS with a unit normal $\mathbf{n}$ as shown in Figure 2.6, where stresses and loadings are separated for clarity.
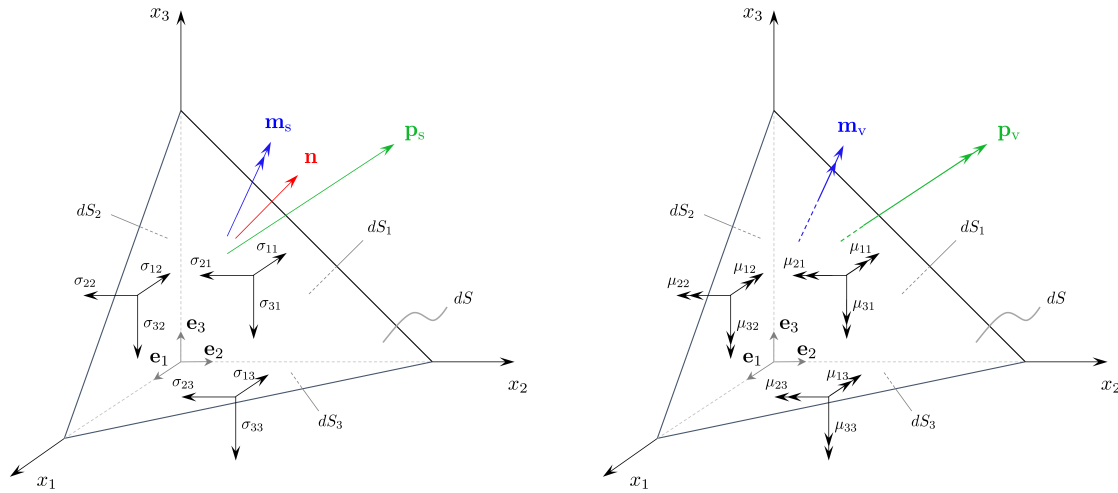
(a) Components of the force stress and the applied surface load   (b) Components of the moment stress and the applied volume load

Figure 2.6: Equilibrium of a differential surface element.

Summing all the forces in the directions $x_1,\ x_2$ and x_3 we obtain:

$$\sigma_{11}\,dS_1 + \sigma_{12}\,dS_2 + \sigma_{13}\,dS_3 = p_{s1}\,dS + p_{v1}\,dV, \tag{2.78}$$

$$\sigma_{21}\,dS_1 + \sigma_{22}\,dS_2 + \sigma_{23}\,dS_3 = p_{s2}\,dS + p_{v2}\,dV, \tag{2.79}$$

$$\sigma_{31}\,dS_1 + \sigma_{32}\,dS_2 + \sigma_{33}\,dS_3 = p_{s3}\,dS + p_{v3}\,dV. \tag{2.80}$$

Taking into account that here $\dfrac{dV}{dS}$ is a higher-order differential (which can be neglected) and

$$dS_i = dS\,n_i, \quad n_i = \cos(\mathbf{n}, \mathbf{e}_i), \quad i = 1, 2, 3, \tag{2.81}$$

where $\mathbf{n}$ is the unit normal to the surface element dS, equations (2.78)-(2.80) may be written in the matrix form to obtain the following:

$$\begin{bmatrix} \sigma_{11} & \sigma_{12} & \sigma_{13} \\ \sigma_{21} & \sigma_{22} & \sigma_{23} \\ \sigma_{31} & \sigma_{32} & \sigma_{33} \end{bmatrix} \begin{Bmatrix} n_1 \\ n_2 \\ n_3 \end{Bmatrix} = \begin{Bmatrix} p_{s1} \\ p_{s2} \\ p_{s3} \end{Bmatrix}, \tag{2.82}$$

i.e.

$$\boldsymbol{\sigma}\mathbf{n} = \mathbf{p_s}. \tag{2.83}$$

The previous equation can be written in the component form as

$$\sigma_{ij} n_j = p_{si}, \quad i, j = 1, 2, 3. \tag{2.84}$$

Summing all the moments around x_1, x_2 and x_3 and neglecting the contribution of the stresses, distributed forces and volume loads which involve differentials of a higher order, we obtain

$$\mu_{11} \, dS_1 + \mu_{12} \, dS_2 + \mu_{13} \, dS_3 = m_{s1} \, dS, \tag{2.85}$$

$$\mu_{21} \, dS_1 + \mu_{22} \, dS_2 + \mu_{23} \, dS_3 = m_{s2} \, dS, \tag{2.86}$$

$$\mu_{31} \, dS_1 + \mu_{32} \, dS_2 + \mu_{33} \, dS_3 = m_{s3} \, dS, \tag{2.87}$$

or, in the matrix form:

$$\begin{bmatrix} \mu_{11} & \mu_{12} & \mu_{13} \\ \mu_{21} & \mu_{22} & \mu_{23} \\ \mu_{31} & \mu_{32} & \mu_{33} \end{bmatrix} \begin{Bmatrix} n_1 \\ n_2 \\ n_3 \end{Bmatrix} = \begin{Bmatrix} m_{s1} \\ m_{s2} \\ m_{s3} \end{Bmatrix}, \tag{2.88}$$

i.e.

$$\boldsymbol{\mu}\mathbf{n} = \mathbf{m_s}. \tag{2.89}$$

The component form of this equation is

$$\mu_{ij} n_j = m_{si}, \quad i, j = 1, 2, 3. \tag{2.90}$$

Equations (2.84) and (2.90) give the *natural* (also known as the static, load or Neumann) boundary condition. In contrast, the boundary conditions on S_u are called *essential* (also known as the kinematic or Dirichlet) boundary conditions. Since the equilibrium equation is here a differential equation the associated essential boundary condition on S_u, as well as the natural boundary condition on S_p are considered to be the fundamental parts of the group of equilibrium equations. Again, in Appendix A.2 the same differential surface is analysed but using the alternative definition of the stress indices.

2.3 Kinematic equations - geometric approach in linear analysis

The second group of equations we need to provide in order to fully define the problem are the kinematic equations, which relate the strains to the displacements. In this section we will limit our attention only to linear analysis and derive the kinematic equations by

analysing geometry of the deformation process. A two-dimensional solid in the state of planar strain is shown in Figure 2.7.
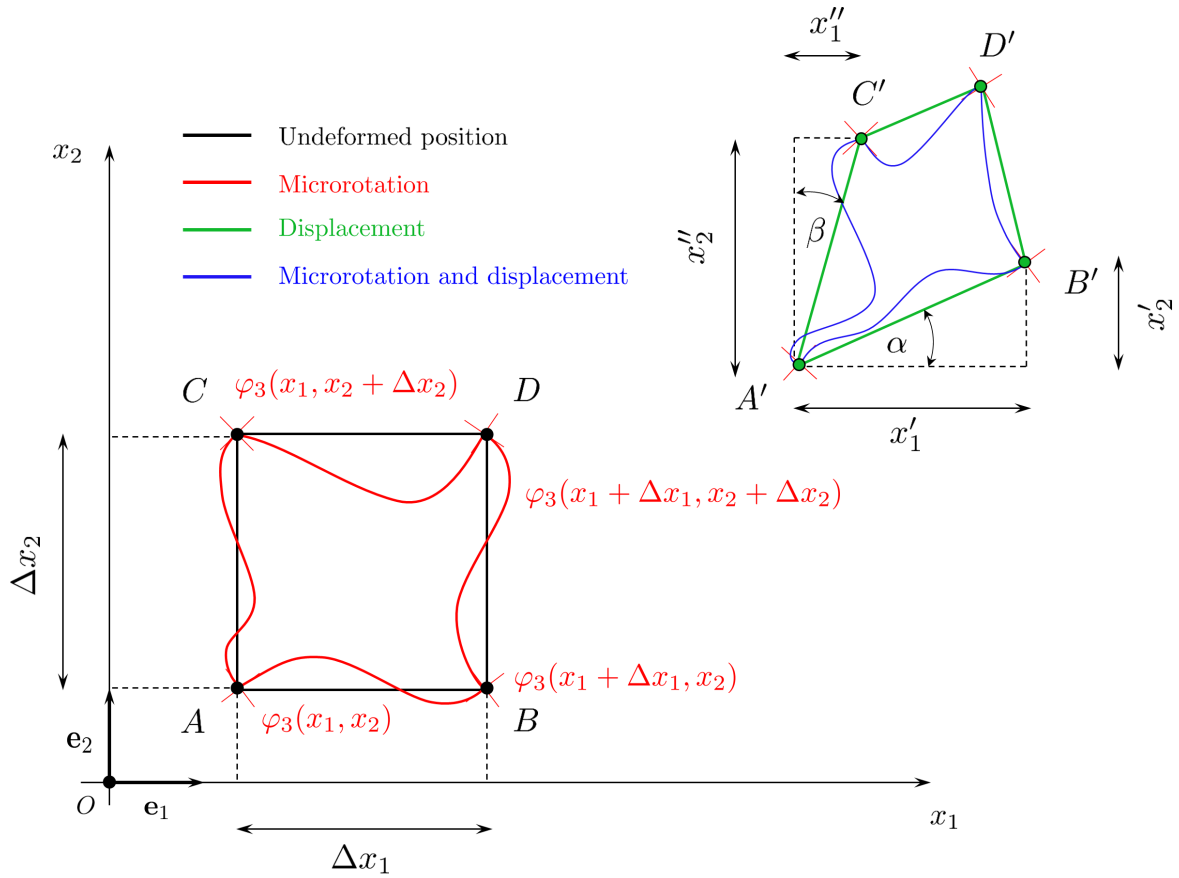
Figure 2.7: Kinematics

The difference between the deformed and the initial position is called *the displacement* and is denoted by $\mathbf{u}$. The components of displacement are denoted by u_1, u_2, u_3, all functions of x_1, x_2, x_3. In relation to the classical continuum theory, in the micropolar continuum theory we have an additional kinematic field $\boldsymbol{\varphi}(x_1, x_2, x_3)$ known as the *microrotation field* which represents the local rotation of the point with coordinates x_1, x_2, x_3 and is *completely independent* of the displacement field. For the planar situation shown in Figure 2.7 both $\mathbf{u}$ and $\boldsymbol{\varphi}$ depend only on x_1 and x_2, where also $u_3 = 0$ and $\varphi_1 = \varphi_2 = 0$. In the classical continuum theory, the deformed configuration will not involve the microrotation, i.e. the elements of the deformation process drawn in Figure 2.7 as red and blue will not exist. Any rotation left in the deformation process will in this case be completely defined by the change of the displacement field in space - the *macrorotation*.

In the classical continuum theory, the displacement gradient grad $\mathbf{u} = \mathbf{u} \otimes \nabla$ (for a 3D body) is decomposed into a symmetric part $\boldsymbol{\varepsilon}$ and a skew-symmetric part $\boldsymbol{\Omega}$, as follows:

$$\text{grad } \mathbf{u} = \boldsymbol{\varepsilon} + \boldsymbol{\Omega}, \tag{2.91}$$

i.e.

$$
\underbrace{\begin{bmatrix} \frac{\partial u_1}{\partial x_1} & \frac{\partial u_1}{\partial x_2} & \frac{\partial u_1}{\partial x_3} \\ \frac{\partial u_2}{\partial x_1} & \frac{\partial u_2}{\partial x_2} & \frac{\partial u_2}{\partial x_3} \\ \frac{\partial u_3}{\partial x_1} & \frac{\partial u_3}{\partial x_2} & \frac{\partial u_3}{\partial x_3} \end{bmatrix}}_{\text{grad } \mathbf{u}} = \underbrace{\begin{bmatrix} \frac{\partial u_1}{\partial x_1} & \frac{1}{2}\left(\frac{\partial u_1}{\partial x_2}+\frac{\partial u_2}{\partial x_1}\right) & \frac{1}{2}\left(\frac{\partial u_1}{\partial x_3}+\frac{\partial u_3}{\partial x_1}\right) \\ \frac{1}{2}\left(\frac{\partial u_1}{\partial x_2}+\frac{\partial u_2}{\partial x_1}\right) & \frac{\partial u_2}{\partial x_2} & \frac{1}{2}\left(\frac{\partial u_2}{\partial x_3}+\frac{\partial u_3}{\partial x_2}\right) \\ \frac{1}{2}\left(\frac{\partial u_1}{\partial x_3}+\frac{\partial u_3}{\partial x_1}\right) & \frac{1}{2}\left(\frac{\partial u_2}{\partial x_3}+\frac{\partial u_3}{\partial x_2}\right) & \frac{\partial u_3}{\partial x_3} \end{bmatrix}}_{\boldsymbol{\varepsilon}} +
$$
$$
+ \underbrace{\begin{bmatrix} 0 & -\frac{1}{2}\left(\frac{\partial u_2}{\partial x_1}-\frac{\partial u_1}{\partial x_2}\right) & \frac{1}{2}\left(\frac{\partial u_1}{\partial x_3}-\frac{\partial u_3}{\partial x_1}\right) \\ \frac{1}{2}\left(\frac{\partial u_2}{\partial x_1}-\frac{\partial u_1}{\partial x_2}\right) & 0 & -\frac{1}{2}\left(\frac{\partial u_3}{\partial x_2}-\frac{\partial u_2}{\partial x_3}\right) \\ -\frac{1}{2}\left(\frac{\partial u_1}{\partial x_3}-\frac{\partial u_3}{\partial x_1}\right) & \frac{1}{2}\left(\frac{\partial u_3}{\partial x_2}-\frac{\partial u_2}{\partial x_3}\right) & 0 \end{bmatrix}}_{\boldsymbol{\Omega}},
\tag{2.92}
$$

where $\boldsymbol{\varepsilon}$ is called the *strain tensor* and $\boldsymbol{\Omega}$ represents the rigid body rotation, also known as the *spin* or the *macrorotation tensor* [3]. The components of the vector $\boldsymbol{\Omega}\mathbf{v}$ are equal to the components of the vector product $\boldsymbol{\omega} \times \mathbf{v}$, where $\mathbf{v}$ is an arbitrary vector $\mathbf{v} \in \mathbb{R}^3$ [3]. Hence $\boldsymbol{\Omega} = \hat{\boldsymbol{\omega}}$ and $\boldsymbol{\omega} = \frac{1}{2}\nabla \times \mathbf{u}$, where the macrorotation vector $\boldsymbol{\omega}$ is

$$
\boldsymbol{\omega} = \left\{ \begin{array}{c} \frac{1}{2}\left(\frac{\partial u_3}{\partial x_2}-\frac{\partial u_2}{\partial x_3}\right) \\ \frac{1}{2}\left(\frac{\partial u_1}{\partial x_3}-\frac{\partial u_3}{\partial x_1}\right) \\ \frac{1}{2}\left(\frac{\partial u_2}{\partial x_1}-\frac{\partial u_1}{\partial x_2}\right) \end{array} \right\} = \left\{ \begin{array}{c} \omega_1 \\ \omega_2 \\ \omega_3 \end{array} \right\}.
\tag{2.93}
$$

It is important to note that the microrotation $\boldsymbol{\varphi}$ is completely independent and different from the rotational part $\boldsymbol{\Omega}$ of the displacement gradient, i.e. from the macrorotation $\boldsymbol{\omega}$.

Considering planar deformation shown in Figure 2.7, coordinates of the points A, B, C, D in the undeformed position are:

$$
\begin{aligned}
A &= (x_1, x_2), \\
B &= (x_1 + \Delta x_1, x_2), \\
C &= (x_1, x_2 + \Delta x_2), \\
D &= (x_1 + \Delta x_1, x_2 + \Delta x_2).
\end{aligned}
$$

As a result of external actions the body deforms and is brought to a new position. Coordinates of these points in the deformed position are:

$$
\begin{aligned}
A' &= \left(x_1 + u_1(x_1, x_2), x_2 + u_2(x_1, x_2)\right), \\
B' &= \left(x_1 + \Delta x_1 + u_1(x_1 + \Delta x_1, x_2), x_2 + u_2(x_1 + \Delta x_1, x_2)\right), \\
C' &= \left(x_1 + u_1(x_1, x_2 + \Delta x_2), x_2 + \Delta x_2 + u_2(x_1, x_2 + \Delta x_2)\right), \\
D' &= \left(x_1 + \Delta x_1 + u_1(x_1 + \Delta x_1, x_2 + \Delta x_2), x_2 + \Delta x_2 + u_2(x_1 + \Delta x_1, x_2 + \Delta x_2)\right).
\end{aligned}
$$

The *normal strains* of the linear micropolar continuum ϵ_{11} and ϵ_{22} are defined as the change in length of a material fibre per initial length when the initial length tends to zero. We are analysing the body on a differential level, i.e. when $\Delta x_1 = \mathrm{d}x_1$ and $\Delta x_2 = \mathrm{d}x_2$ and expand $u_1(x_1 + \mathrm{d}x_1, x_2)$, $u_1(x_1, x_2 + \mathrm{d}x_2)$, $u_1(x_1 + \mathrm{d}x_1, x_2 + \mathrm{d}x_2)$, $u_2(x_1 + \mathrm{d}x_1, x_2)$, $u_2(x_1, x_2 + \mathrm{d}x_2)$, $u_2(x_1 + \mathrm{d}x_1, x_2 + \mathrm{d}x_2)$ in Taylor series. The oriented length $\overrightarrow{A'B'}$ then follows as

$$\overrightarrow{A'B'} = (x_{1B'} - x_{1A'})\,\mathbf{e}_1 + (x_{2B'} - x_{2A'})\,\mathbf{e}_2 \tag{2.94}$$

$$= \left(\mathrm{d}x_1 + \frac{\partial u_1}{\partial x_1}\,\mathrm{d}x_1\right)\mathbf{e}_1 + \left(\frac{\partial u_2}{\partial x_1}\,\mathrm{d}x_1\right)\mathbf{e}_2, \tag{2.95}$$

where all the higher-order terms in $\mathrm{d}x_1$ (i.e. $\mathrm{d}x_1^2$, $\mathrm{d}x_1^3$,...) vanish in comparison to the terms with $\mathrm{d}x_1$. The normal strain ϵ_{11} is equal to

$$\epsilon_{11} = \frac{\|\overrightarrow{A'B'}\| - \mathrm{d}x_1}{\mathrm{d}x_1} \tag{2.96}$$

$$= \frac{1}{\mathrm{d}x_1}\,\mathrm{d}x_1 \left[\sqrt{\left(1 + \frac{\partial u_1}{\partial x_1}\right)^2 + \left(\frac{\partial u_2}{\partial x_1}\right)^2} - 1\right] \tag{2.97}$$

$$= \left[\sqrt{\left(1 + \frac{\partial u_1}{\partial x_1}\right)^2 + \left(\frac{\partial u_2}{\partial x_1}\right)^2} - 1\right]. \tag{2.98}$$

We will expand the function $\epsilon_{11} = f\left(\frac{\partial u_1}{\partial x_1}, \frac{\partial u_2}{\partial x_1}\right)$ into Taylor series around $\frac{\partial u_1}{\partial x_1} = 0$, $\frac{\partial u_2}{\partial x_1} = 0$ (the undeformed state) as follows

$$\epsilon_{11} = \left[\sqrt{\left(1 + \frac{\partial u_1}{\partial x_1}\right)^2 + \left(\frac{\partial u_2}{\partial x_1}\right)^2} - 1\right]\Bigg|_{(0,0)} + \frac{2\left(1 + \frac{\partial u_1}{\partial x_1}\right)}{2\sqrt{\left(1 + \frac{\partial u_1}{\partial x_1}\right)^2 + \left(\frac{\partial u_2}{\partial x_1}\right)^2}}\Bigg|_{(0,0)} \frac{\partial u_1}{\partial x_1} +$$

$$+ \frac{2\left(\frac{\partial u_2}{\partial x_1}\right)}{2\sqrt{\left(1 + \frac{\partial u_1}{\partial x_1}\right)^2 + \left(\frac{\partial u_2}{\partial x_1}\right)^2}}\Bigg|_{(0,0)} \frac{\partial u_2}{\partial x_1} + O\left(\left(\frac{\partial u_1}{\partial x_1}\right)^2, \frac{\partial u_1}{\partial x_1}\frac{\partial u_2}{\partial x_1}, \left(\frac{\partial u_2}{\partial x_1}\right)^2\right). \tag{2.99}$$

After neglecting the non-linear terms in u_1 and u_2 we obtain

$$\epsilon_{11} = \frac{\partial u_1}{\partial x_1} = \varepsilon_{11}, \tag{2.100}$$

where ε_{11} is the normal strain in the classical continuum theory (see equation (2.92)). Analogously, we compute $\overrightarrow{A'C'}$ as

$$\overrightarrow{A'C'} = (x_{1C'} - x_{1A'})\,\mathbf{e}_1 + (x_{2C'} - x_{2A'})\,\mathbf{e}_2 \tag{2.101}$$

$$= \left(\frac{\partial u_1}{\partial x_2} \mathrm{d}x_2 \right) \mathbf{e}_1 + \left(\mathrm{d}x_2 + \frac{\partial u_2}{\partial x_2} \mathrm{d}x_2 \right) \mathbf{e}_2, \qquad (2.102)$$

where again all the higher-order terms in $\mathrm{d}x_2$ (i.e. $\mathrm{d}x_2^2$, $\mathrm{d}x_2^3$, ...) vanish in comparison to the terms with $\mathrm{d}x_2$. The normal strain ϵ_{22} is thus equal to

$$\epsilon_{22} = \frac{\|\overrightarrow{A'C'}\| - \mathrm{d}x_2}{\mathrm{d}x_2} \qquad (2.103)$$

$$= \frac{1}{\mathrm{d}x_2} \mathrm{d}x_2 \left[\sqrt{\left(\frac{\partial u_1}{\partial x_2} \right)^2 + \left(1 + \frac{\partial u_2}{\partial x_2} \right)^2} - 1 \right]. \qquad (2.104)$$

After expanding the result into Taylor series as before and neglecting the non-linear terms in u_1 and u_2 we obtain

$$\epsilon_{22} = \frac{\partial u_2}{\partial x_2} = \varepsilon_{22}, \qquad (2.105)$$

where ε_{22} is the normal strain in the classical continuum theory as given in equation (2.92). It should be noted that the same result for ϵ_{11} and ϵ_{22} would be obtained if we considered deformation of the sides CD and BD rather than AB and AC. Analogously, in 3D we would obtain

$$\epsilon_{33} = \frac{\partial u_3}{\partial x_3} = \varepsilon_{33}, \qquad (2.106)$$

where ε_{33} is the normal strain in the classical continuum theory as given in equation (2.92).

We can see that the normal strains in the micropolar continuum theory are equal to those in the classical continuum theory, which means that the microrotation $\boldsymbol{\varphi}$ does not contribute to stretching or shortening of the generic fibre. The influence of the microrotation will become present in shear strains ϵ_{12} and ϵ_{21}. In contrast to the classical continuum theory, where the *tensor shear strain* ε_{12} is defined as half of the change in the right angle $\alpha + \beta$ (*the engineering shear strain*; see Figure (2.7)) initially formed by the sides parallel to x_1 and x_2 [3], in the micropolar continuum theory the shear strain components (ϵ_{12} and ϵ_{21}) are defined in a different manner. A micropolar shear strain is defined to be equal to the difference of the change of inclination of a generic fibre during deformation and the microrotation $\boldsymbol{\varphi}$.

The shear strain ϵ_{21} is thus equal to the difference between the angle α (see Figure 2.7) and the microrotation $\varphi_3(x_1, x_2)$ in the plane x_1, x_2, around axis x_3, i.e.

$$\epsilon_{12} = \alpha - \varphi_3. \qquad (2.107)$$

The angle α is computed from:

$$\tan \alpha = \frac{x_2'}{x_1'}, \qquad (2.108)$$

where

$$
\begin{aligned}
x_2' &= x_{2B'} - x_{2A'} \\
&= x_2 + u_2(x_1 + \Delta x_1, x_2) - x_2 - u_2(x_1, x_2).
\end{aligned}
$$

and

$$
\begin{aligned}
x_1' &= x_{1B'} - x_{1A'} \\
&= x_1 + \Delta x_1 + u_1(x_1 + \Delta x_1, x_2) - x_1 - u_1(x_1, x_2).
\end{aligned}
$$

It means that

$$\tan \alpha = \frac{u_2(x_1 + \Delta x_1, x_2) - u_2(x_1, x_2)}{\Delta x_1 + u_1(x_1 + \Delta x_1, x_2) - u_1(x_1, x_2)}, \qquad (2.109)$$

$$\alpha = \arctan \frac{u_2(x_1 + \Delta x_1, x_2) - u_2(x_1, x_2)}{\Delta x_1 + u_1(x_1 + \Delta x_1, x_2) - u_1(x_1, x_2)}. \qquad (2.110)$$

We expand functions u_1 and u_2 into Taylor series and obtain

$$
\begin{aligned}
\alpha &= \arctan \frac{u_2(x_1, x_2) + \dfrac{\partial u_2}{\partial x_1}\Delta x_1 + O(\Delta x_1^2) - u_2(x_1, x_2)}{\Delta x_1 + u_1(x_1, x_2) + \dfrac{\partial u_1}{\partial x_1}\Delta x_1 + O(\Delta x_1^2) - u_1(x_1, x_2)} \\[2mm]
&= \arctan \frac{\dfrac{\partial u_2}{\partial x_1}\Delta x_1 + O(\Delta x_1^2)}{\Delta x_1 + \dfrac{\partial u_1}{\partial x_1}\Delta x_1 + O(\Delta x_1^2)} \\[2mm]
&= \arctan \frac{\dfrac{\partial u_2}{\partial x_1} + O(\Delta x_1)}{1 + \dfrac{\partial u_1}{\partial x_1} + O(\Delta x_1)}
\end{aligned}
$$

When $\Delta x_1 \to 0$:

$$\alpha = \arctan \frac{\dfrac{\partial u_2}{\partial x_1}}{1 + \dfrac{\partial u_1}{\partial x_1}}. \qquad (2.111)$$

We will expand the obtained function α into Taylor series:

$$\alpha = \arctan \left. \frac{\frac{\partial u_2}{\partial x_1}}{1 + \frac{\partial u_1}{\partial x_1}} \right|_{(0,0)} + \frac{1}{1 + \left(\frac{\frac{\partial u_2}{\partial x_1}}{1 + \frac{\partial u_1}{\partial x_1}} \right)^2} \left. \frac{\left(1 + \frac{\partial u_1}{\partial x_1} \right) \cdot 0 - \frac{\partial u_2}{\partial x_1} \cdot 1}{\left(1 + \frac{\partial u_1}{\partial x_1} \right)^2} \right|_{(0,0)} \frac{\partial u_1}{\partial x_1} +$$

$$+ \frac{1}{1 + \left(\frac{\frac{\partial u_2}{\partial x_1}}{1 + \frac{\partial u_1}{\partial x_1}} \right)^2} \left. \frac{\left(1 + \frac{\partial u_1}{\partial x_1} \right) \cdot 1 - \frac{\partial u_2}{\partial x_1} \cdot 0}{\left(1 + \frac{\partial u_1}{\partial x_1} \right)^2} \right|_{(0,0)} \frac{\partial u_2}{\partial x_1} + O \left(\left(\frac{\partial u_1}{\partial x_1} \right)^2, \frac{\partial u_1}{\partial x_1} \frac{\partial u_2}{\partial x_1}, \left(\frac{\partial u_2}{\partial x_1} \right)^2 \right).$$

After neglecting non-linear terms in u_1 and u_2 we finally obtain

$$\alpha = \frac{\partial u_2}{\partial x_1}, \tag{2.112}$$

which means that the shear strain ϵ_{21} is equal to

$$\epsilon_{21} = \frac{\partial u_2}{\partial x_1} - \varphi_3. \tag{2.113}$$

Analogously, we define the shear strain ϵ_{12} as follows:

$$\epsilon_{12} = \beta + \varphi_3. \tag{2.114}$$

The angle β is computed from (see Figure 2.7):

$$\tan \beta = \frac{x_1''}{x_2''}, \tag{2.115}$$

where

$$x_1'' = x_{1C'} - x_{1A'}$$
$$= x_1 + u_1(x_1, x_2 + \Delta x_2) - x_1 - u_1(x_1, x_2)$$

and

$$x_2'' = x_{2C'} - x_{2A'}$$
$$= x_2 + \Delta x_2 + u_2(x_1, x_2 + \Delta x_2) - x_2 - u_2(x_1, x_2).$$

It means that

$$\tan \beta = \frac{u_1(x_1, x_2 + \Delta x_2) - u_1(x_1, x_2)}{\Delta x_2 + u_2(x_1, x_2 + \Delta x_2) - u_2(x_1, x_2)}, \tag{2.116}$$

$$\beta = \arctan \frac{u_1(x_1, x_2 + \Delta x_2) - u_1(x_1, x_2)}{\Delta x_2 + u_2(x_1, x_2 + \Delta x_2) - u_2(x_1, x_2)}. \tag{2.117}$$

After expanding the result into Taylor series as before and when $\Delta x_2 \to 0$ we obtain

$$\beta = \arctan \frac{\frac{\partial u_1}{\partial x_2}}{1 + \frac{\partial u_2}{\partial x_2}}. \tag{2.118}$$

We expand the obtained function β into Taylor series and neglect the non-linear terms in u_1 and u_2 and obtain

$$\beta = \frac{\partial u_1}{\partial x_2}, \tag{2.119}$$

which means that the shear strain ϵ_{21} is equal to

$$\epsilon_{12} = \frac{\partial u_1}{\partial x_2} + \varphi_3. \tag{2.120}$$

The strain tensor with its components for a planar state of strain is therefore equal to

$$\begin{bmatrix} \epsilon_{11} & \epsilon_{12} \\ \epsilon_{21} & \epsilon_{22} \end{bmatrix} = \begin{bmatrix} \frac{\partial u_1}{\partial x_1} & \frac{\partial u_1}{\partial x_2} + \varphi_3 \\ \frac{\partial u_2}{\partial x_1} - \varphi_3 & \frac{\partial u_2}{\partial x_2} \end{bmatrix}, \tag{2.121}$$

which can be generalised on a 3D continuum as follows:

$$\begin{bmatrix} \epsilon_{11} & \epsilon_{12} & \epsilon_{13} \\ \epsilon_{21} & \epsilon_{22} & \epsilon_{23} \\ \epsilon_{31} & \epsilon_{32} & \epsilon_{33} \end{bmatrix} = \begin{bmatrix} \frac{\partial u_1}{\partial x_1} & \frac{\partial u_1}{\partial x_2} + \varphi_3 & \frac{\partial u_1}{\partial x_3} - \varphi_2 \\ \frac{\partial u_2}{\partial x_1} - \varphi_3 & \frac{\partial u_2}{\partial x_2} & \frac{\partial u_2}{\partial x_3} + \varphi_1 \\ \frac{\partial u_3}{\partial x_1} + \varphi_2 & \frac{\partial u_3}{\partial x_2} - \varphi_1 & \frac{\partial u_3}{\partial x_3} \end{bmatrix}. \tag{2.122}$$

The component form of the micropolar strain tensor is thus equal to

$$\epsilon_{ij} = u_{i,j} + \varepsilon_{ijk}\varphi_k. \tag{2.123}$$

Since we have an additional kinematic field $\boldsymbol{\varphi}(x_1, x_2, x_3)$, we should also define a corresponding *angular strain* (referred to as *curvature*) of an arbitrary fibre element $\mathrm{d}x_i, i = 1, 2, 3$. The curvature effect is a result of the existence of couple-stresses proved in Section 2.1. For the planar deformation shown in Figure 2.7 curvature κ_{31} is defined as a change of rotation φ_3, which is a function of coordinates (x_1, x_2), along axis x_1. The first index denotes the axis around which the rotation is taking place and the second index denotes the direction of change of the rotation, i.e.

$$\kappa_{31} = \lim_{\Delta x_1 \to 0} \frac{\varphi_3(x_1 + \Delta x_1, x_2) - \varphi_3(x_1, x_2)}{\Delta x_1} = \frac{\partial \varphi_3(x_1, x_2)}{\partial x_1}. \tag{2.124}$$

The same result is obtained by observing the change of function $\varphi_3(x_1, x_2)$ between points

C' and D', i.e.

$$\kappa_{31} = \lim_{\Delta x_1 \to 0} \frac{\varphi_3(x_1 + \Delta x_1, x_2 + \Delta x_2) - \varphi_3(x_1, x_2 + \Delta x_2)}{\Delta x_1} = \frac{\partial \varphi_3(x_1, x_2 + \Delta x_2)}{\partial x_1} \quad (2.125)$$

When $\Delta x_2 \to 0$, therefore

$$\kappa_{31} = \frac{\partial \varphi_3(x_1, x_2)}{\partial x_1}. \quad (2.126)$$

Curvature in the direction x_2 is obtained analogously, i.e.

$$\kappa_{32} = \lim_{\Delta x_2 \to 0} \frac{\varphi_3(x_1, x_2 + \Delta x_2) - \varphi_3(x_1, x_2)}{\Delta x_2} = \frac{\partial \varphi_3(x_1, x_2)}{\partial x_2}. \quad (2.127)$$

The same result is obtained by observing the change of function $\varphi_3(x_1, x_2)$ between points B' and D', i.e.

$$\kappa_{32} = \lim_{\Delta x_2 \to 0} \frac{\varphi_3(x_1 + \Delta x_1, x_2 + \Delta x_2) - \varphi_3(x_1 + \Delta x_1, x_2)}{\Delta x_2} = \frac{\partial \varphi_3(x_1 + \Delta x_1, x_2)}{\partial x_2} \quad (2.128)$$

When $\Delta x_1 \to 0$, therefore

$$\kappa_{32} = \frac{\partial \varphi_3(x_1, x_2)}{\partial x_2}. \quad (2.129)$$

For two dimensional solids the curvature vector $\boldsymbol{\kappa}_3$ is equal to

$$\boldsymbol{\kappa}_3 = \left\{ \begin{matrix} \frac{\partial \varphi_3}{\partial x_1} \\ \frac{\partial \varphi_3}{\partial x_2} \end{matrix} \right\} = \operatorname{grad} \varphi_3 \quad (2.130)$$

Likewise, for the other two coordinate planes we would obtain

$$\boldsymbol{\kappa}_1 = \left\{ \begin{matrix} \frac{\partial \varphi_1}{\partial x_2} \\ \frac{\partial \varphi_1}{\partial x_3} \end{matrix} \right\} = \operatorname{grad} \varphi_1 \quad \text{and} \quad \boldsymbol{\kappa}_2 = \left\{ \begin{matrix} \frac{\partial \varphi_2}{\partial x_1} \\ \frac{\partial \varphi_2}{\partial x_3} \end{matrix} \right\} = \operatorname{grad} \varphi_2 \quad (2.131)$$

which enables us to define a *curvature tensor* in the 3D case as

$$\begin{bmatrix} \kappa_{11} & \kappa_{12} & \kappa_{13} \\ \kappa_{21} & \kappa_{22} & \kappa_{23} \\ \kappa_{31} & \kappa_{32} & \kappa_{33} \end{bmatrix} = \begin{bmatrix} \frac{\partial \varphi_1}{\partial x_1} & \frac{\partial \varphi_1}{\partial x_2} & \frac{\partial \varphi_1}{\partial x_3} \\ \frac{\partial \varphi_2}{\partial x_1} & \frac{\partial \varphi_2}{\partial x_2} & \frac{\partial \varphi_2}{\partial x_3} \\ \frac{\partial \varphi_3}{\partial x_1} & \frac{\partial \varphi_3}{\partial x_2} & \frac{\partial \varphi_3}{\partial x_3} \end{bmatrix} = \operatorname{grad} \boldsymbol{\varphi} = \boldsymbol{\varphi} \otimes \nabla. \quad (2.132)$$

The diagonal terms in $\boldsymbol{\kappa}$, which do not exist in $\boldsymbol{\kappa}_1, \boldsymbol{\kappa}_2$ and $\boldsymbol{\kappa}_3$ obtained from individual planar cases are in fact the *torsional strains* (axial curvatures) which are a genuine 3D phenomenon. The component form of the curvature tensor is thus equal to

$$\kappa_{ij} = \varphi_{i,j}. \quad (2.133)$$

We note that the so-called *couple-stress theory* (see [59]) is a special case of the mi-

cropolar continuum theory where the microrotation vector $\boldsymbol{\varphi}$ is equal to the macrorotation vector $\boldsymbol{\omega}$. When $\boldsymbol{\varphi} = \boldsymbol{\omega}$ is introduced into the micropolar strain tensor we obtain:

$$\epsilon_{12} = \frac{\partial u_1}{\partial x_2} + \varphi_3 \tag{2.134}$$

$$= \underbrace{\frac{1}{2}\left(\frac{\partial u_1}{\partial x_2} + \frac{\partial u_2}{\partial x_1}\right)}_{=\varepsilon_{12}} + \underbrace{\frac{1}{2}\left(\frac{\partial u_1}{\partial x_2} - \frac{\partial u_2}{\partial x_1}\right)}_{=-\Omega_{12}=\omega_3} + \varphi_3 \tag{2.135}$$

$$= \varepsilon_{12} + \omega_3 + \varphi_3 \tag{2.136}$$

$$= \varepsilon_{12}. \tag{2.137}$$

Analogously,

$$\epsilon_{21} = \frac{\partial u_2}{\partial x_1} - \varphi_3 \tag{2.138}$$

$$= \underbrace{\frac{1}{2}\left(\frac{\partial u_2}{\partial x_1} + \frac{\partial u_1}{\partial x_2}\right)}_{=\varepsilon_{21}} + \underbrace{\frac{1}{2}\left(\frac{\partial u_2}{\partial x_1} - \frac{\partial u_1}{\partial x_2}\right)}_{=-\Omega_{21}=-\omega_3} - \varphi_3 \tag{2.139}$$

$$= \varepsilon_{21} - \omega_3 - \varphi_3 \tag{2.140}$$

$$= \varepsilon_{21}. \tag{2.141}$$

In the couple-stress theory, the curvature tensor thus involves second derivatives of the displacement field. When these derivatives are neglected, the curvature tensor also vanishes and the couple-stress theory reduces to the classical continuum theory.

2.4 Constitutive equations

Constitutive equations of elastic materials are equations which relate stresses to strains in the structure, i.e. they describe the macroscopic behaviour resulting from the internal constitution of the material. We are analysing a *continuous, homogeneous* and *isotropic* material. In a general ideal elastic body we say that stress depends upon strain or deformation from a certain natural state, i.e.

$$\text{Stress Tensor} = f(\text{Strain Tensor}). \tag{2.142}$$

The functional relationship between the two tensors in equation (2.142) must express a one-to-one relationship between stress and strain (it means, for example, that the strain has to vanish whenever the stress does) and it may be nonlinear. In the scope of this work we refer only to the *linear theory of elasticity for isotropic materials*. For the classical continuum theory this means that the stress tensor $\boldsymbol{\sigma}$ is assumed to depend linearly on

the strain tensor $\boldsymbol{\varepsilon}$. The most general relationship between two second-order tensors $\boldsymbol{\sigma}$ and $\boldsymbol{\varepsilon}$ is via a fourth-order tensor know as the *constitutive tensor* or the *modulus tensor* $\mathbf{T}$. It can be written as

$$\boldsymbol{\sigma} = \mathbf{T} : \boldsymbol{\varepsilon} \tag{2.143}$$

or, in the component form relative to an orthogonal vector base,

$$\sigma_{ij} = T_{ijpq}\varepsilon_{pq}, \quad \text{where} \quad i, j, p, q = 1, 2, 3. \tag{2.144}$$

The property of material isotropy is a very important condition which we use while setting the constitutive equations, so we will define it.

Definition 3. Material isotropy.
A material is isotropic with respect to certain properties if these properties are the same in all directions [3]. In particular, this means that if a strain tensor $\boldsymbol{\varepsilon}$ results in the stress tensor $\boldsymbol{\sigma}$, then a rotated strain tensor $\mathbf{Q}\boldsymbol{\varepsilon}\mathbf{Q}^T$, where $\mathbf{Q} \in \mathrm{SO}(3)$ is an arbitrary orthogonal tensor (i.e. $\mathbf{Q}\mathbf{Q}^T = \mathbf{I}$ and $\det \mathbf{Q} = +1$), must result in the rotated stress tensor $\mathbf{Q}\boldsymbol{\sigma}\mathbf{Q}^T$. This then implies that the components of the constitutive tensor $\mathbf{T}$ remain unaffected by the orthogonal transformation ($T_{klmn} = Q_{ki}Q_{lj}Q_{mp}Q_{nq}T_{ijpq}$), i.e. $\mathbf{T}$ must be an *isotopic tensor*.

The most general fourth-order isotropic tensor T_{ijpq} has rectangular Cartesian components of the following form:

$$T_{ijpq} = \lambda\delta_{ij}\delta_{pq} + \mu(\delta_{ip}\delta_{jq} + \delta_{iq}\delta_{jp}) + \nu(\delta_{ip}\delta_{jq} - \delta_{iq}\delta_{jp}), \tag{2.145}$$

where λ, μ, and ν represent the material parameters (or material constants) and have the same value in all coordinate systems and δ_{ij} is the Kronecker symbol. The proof is given in [60]. The first two terms in equation (2.145) are symmetric with respect to the first and second or third and fourth indices and the third term is antisymmetric with respect to them. In the classical continuum theory we have only one stress tensor $\boldsymbol{\sigma}$ and one strain tensor $\boldsymbol{\varepsilon}$, both of which are symmetric. This requires the symmetry of the constitutive tensor with respect to the first and second or third and fourth indices. As a result, the third term of the general form of the fourth-order isotropic tensor in (2.145) vanishes and we obtain only two independent elastic parameters of the material model, μ and λ, known as *Lamè e's constants*.

In the micropolar continuum theory we have two independent stress tensors $\boldsymbol{\sigma}$ and $\boldsymbol{\mu}$ related to two independent strain tensors $\boldsymbol{\epsilon}$ and $\boldsymbol{\kappa}$. Both pairs of stress and strain tensors

are in general non-symmetric. Thus, we have to obtain two fourth-order isotropic tensors $\mathbf{T}$ and $\mathbf{D}$ such that

$$\sigma_{ij} = T_{ijpq}\epsilon_{pq}, \tag{2.146}$$

$$\mu_{ij} = D_{ijpq}\kappa_{pq}. \tag{2.147}$$

Since the stress and strain tensors are non-symmetric, the two constitutive tensors now have to have all three independent material parameters each, in contrast to the classical theory of elasticity. Furthermore, we have two independent constitutive equations (2.146) and (2.147) which means that we will obtain six independent material constants in total. The component form of the two constitutive tensors is thus equal to

$$T_{ijpq} = \lambda\delta_{ij}\delta_{pq} + \mu(\delta_{ip}\delta_{jq} + \delta_{iq}\delta_{jp}) + \nu(\delta_{ip}\delta_{jq} - \delta_{iq}\delta_{jp}), \tag{2.148}$$

$$D_{ijpq} = \alpha\delta_{ij}\delta_{pq} + \beta(\delta_{ip}\delta_{jq} + \delta_{iq}\delta_{jp}) + \gamma(\delta_{ip}\delta_{jq} - \delta_{iq}\delta_{jp}), \tag{2.149}$$

where λ, μ, ν, α, β and γ, are the independent material elastic constants of a micropolar material. Using equations (2.146) and (2.148) we obtain the first set of nine equations as follows:

$$\sigma_{11} = (\lambda + 2\mu)\epsilon_{11} + \lambda\epsilon_{22} + \lambda\epsilon_{33}, \tag{2.150}$$

$$\sigma_{12} = (\mu + \nu)\epsilon_{12} + (\mu - \nu)\epsilon_{21}, \tag{2.151}$$

$$\sigma_{13} = (\mu + \nu)\epsilon_{13} + (\mu - \nu)\epsilon_{31}, \tag{2.152}$$

$$\sigma_{21} = (\mu - \nu)\epsilon_{12} + (\mu + \nu)\epsilon_{21}, \tag{2.153}$$

$$\sigma_{22} = \lambda\epsilon_{11} + (\lambda + 2\mu)\epsilon_{22} + \lambda\epsilon_{33}, \tag{2.154}$$

$$\sigma_{23} = (\mu + \nu)\epsilon_{23} + (\mu - \nu)\epsilon_{32}, \tag{2.155}$$

$$\sigma_{31} = (\mu - \nu)\epsilon_{13} + (\mu + \nu)\epsilon_{31}, \tag{2.156}$$

$$\sigma_{32} = (\mu - \nu)\epsilon_{23} + (\mu + \nu)\epsilon_{32}, \tag{2.157}$$

$$\sigma_{33} = \lambda\epsilon_{11} + \lambda\epsilon_{22} + (\lambda + 2\mu)\epsilon_{33}, \tag{2.158}$$

or simply

$$\sigma_{ij} = \lambda\epsilon_{pp}\delta_{ij} + (\mu + \nu)\epsilon_{ij} + (\mu - \nu)\epsilon_{ji}, \tag{2.159}$$

where λ and μ are the Lamé constants, ν is another material constant and δ_{ij} is the Kronecker symbol. The set of nine equations can also be written in a tensor form, i.e.

$$\boldsymbol{\sigma} = \mathbf{T} : \boldsymbol{\epsilon}, \tag{2.160}$$

where

$$\mathbf{T} = \lambda\,\mathbf{I}\otimes\mathbf{I} + (\mu + \nu)\boldsymbol{\mathcal{I}} + (\mu - \nu)\boldsymbol{\mathcal{I}}^{\mathrm{T}}. \tag{2.161}$$

In equation (2.161) $\mathbf{I}$ represents a second order identity tensor and $\boldsymbol{\mathcal{I}}$ represents a fourth order identity tensor. The double contraction product between two second order identity tensors gives a fourth order tensor which may be presented in a matrix form as

$$\mathbf{I} \otimes \mathbf{I} = \begin{bmatrix} \begin{bmatrix} 1 & 0 & 0 \\ 0 & 1 & 0 \\ 0 & 0 & 1 \end{bmatrix} & \begin{bmatrix} 0 & 0 & 0 \\ 0 & 0 & 0 \\ 0 & 0 & 0 \end{bmatrix} & \begin{bmatrix} 0 & 0 & 0 \\ 0 & 0 & 0 \\ 0 & 0 & 0 \end{bmatrix} \\ \begin{bmatrix} 0 & 0 & 0 \\ 0 & 0 & 0 \\ 0 & 0 & 0 \end{bmatrix} & \begin{bmatrix} 1 & 0 & 0 \\ 0 & 1 & 0 \\ 0 & 0 & 1 \end{bmatrix} & \begin{bmatrix} 0 & 0 & 0 \\ 0 & 0 & 0 \\ 0 & 0 & 0 \end{bmatrix} \\ \begin{bmatrix} 0 & 0 & 0 \\ 0 & 0 & 0 \\ 0 & 0 & 0 \end{bmatrix} & \begin{bmatrix} 0 & 0 & 0 \\ 0 & 0 & 0 \\ 0 & 0 & 0 \end{bmatrix} & \begin{bmatrix} 1 & 0 & 0 \\ 0 & 1 & 0 \\ 0 & 0 & 1 \end{bmatrix} \end{bmatrix}, \tag{2.162}$$

or in component notation as

$$\mathbf{I} \otimes \mathbf{I} = \delta_{ij}\delta_{kl}\mathbf{e}_i \otimes \mathbf{e}_j \otimes \mathbf{e}_k \otimes \mathbf{e}_l = \mathbf{e}_i \otimes \mathbf{e}_i \otimes \mathbf{e}_k \otimes \mathbf{e}_k = \mathbf{e}_i \otimes \mathbf{e}_i \otimes \mathbf{e}_j \otimes \mathbf{e}_j. \tag{2.163}$$

The 4th order identity tensor $\boldsymbol{\mathcal{I}}$ may be presented in a matrix form as

$$\boldsymbol{\mathcal{I}} = \begin{bmatrix} \begin{bmatrix} 1 & 0 & 0 \\ 0 & 0 & 0 \\ 0 & 0 & 0 \end{bmatrix} & \begin{bmatrix} 0 & 1 & 0 \\ 0 & 0 & 0 \\ 0 & 0 & 0 \end{bmatrix} & \begin{bmatrix} 0 & 0 & 1 \\ 0 & 0 & 0 \\ 0 & 0 & 0 \end{bmatrix} \\ \begin{bmatrix} 0 & 0 & 0 \\ 1 & 0 & 0 \\ 0 & 0 & 0 \end{bmatrix} & \begin{bmatrix} 0 & 0 & 0 \\ 0 & 1 & 0 \\ 0 & 0 & 0 \end{bmatrix} & \begin{bmatrix} 0 & 0 & 0 \\ 0 & 0 & 1 \\ 0 & 0 & 0 \end{bmatrix} \\ \begin{bmatrix} 0 & 0 & 0 \\ 0 & 0 & 0 \\ 1 & 0 & 0 \end{bmatrix} & \begin{bmatrix} 0 & 0 & 0 \\ 0 & 0 & 0 \\ 0 & 1 & 0 \end{bmatrix} & \begin{bmatrix} 0 & 0 & 0 \\ 0 & 0 & 0 \\ 0 & 0 & 1 \end{bmatrix} \end{bmatrix} \tag{2.164}$$

or in component notation as

$$\boldsymbol{\mathcal{I}} = \mathcal{I}_{ijkl}\mathbf{e}_i \otimes \mathbf{e}_j \otimes \mathbf{e}_k \otimes \mathbf{e}_l = \delta_{ik}\delta_{jl}\mathbf{e}_i \otimes \mathbf{e}_j \otimes \mathbf{e}_k \otimes \mathbf{e}_l = \mathbf{e}_i \otimes \mathbf{e}_j \otimes \mathbf{e}_i \otimes \mathbf{e}_j, \tag{2.165}$$

which gives $\boldsymbol{\mathcal{I}} : \mathbf{A} = \mathbf{A}$, where $\mathbf{A}$ is an arbitrary second order tensor [61]. Transpose of a 4th order identity tensor $\boldsymbol{\mathcal{I}}$ is defined by swapping the second and the fourth index, i.e.

in a matrix form as

$$
\boldsymbol{\mathcal{I}}^{\mathrm{T}} =
\begin{bmatrix}
\begin{bmatrix} 1 & 0 & 0 \\ 0 & 0 & 0 \\ 0 & 0 & 0 \end{bmatrix} &
\begin{bmatrix} 0 & 0 & 0 \\ 1 & 0 & 0 \\ 0 & 0 & 0 \end{bmatrix} &
\begin{bmatrix} 0 & 0 & 0 \\ 0 & 0 & 0 \\ 1 & 0 & 0 \end{bmatrix} \\[12pt]
\begin{bmatrix} 0 & 1 & 0 \\ 0 & 0 & 0 \\ 0 & 0 & 0 \end{bmatrix} &
\begin{bmatrix} 0 & 0 & 0 \\ 0 & 1 & 0 \\ 0 & 0 & 0 \end{bmatrix} &
\begin{bmatrix} 0 & 0 & 0 \\ 0 & 0 & 0 \\ 0 & 1 & 0 \end{bmatrix} \\[12pt]
\begin{bmatrix} 0 & 0 & 1 \\ 0 & 0 & 0 \\ 0 & 0 & 0 \end{bmatrix} &
\begin{bmatrix} 0 & 0 & 0 \\ 0 & 0 & 1 \\ 0 & 0 & 0 \end{bmatrix} &
\begin{bmatrix} 0 & 0 & 0 \\ 0 & 0 & 0 \\ 0 & 0 & 1 \end{bmatrix}
\end{bmatrix}
\tag{2.166}
$$

or in component notation as

$$
\boldsymbol{\mathcal{I}}^{\mathrm{T}} = \delta_{il}\delta_{jk}\mathbf{e}_i \otimes \mathbf{e}_j \otimes \mathbf{e}_k \otimes \mathbf{e}_l = \mathbf{e}_i \otimes \mathbf{e}_j \otimes \mathbf{e}_j \otimes \mathbf{e}_i,
\tag{2.167}
$$

which gives $\boldsymbol{\mathcal{I}}^{\mathrm{T}} : \mathbf{A} = \mathbf{A}^{\mathrm{T}}$ [61].

By performing the double contraction product between the first constitutive tensor and the micropolar strain tensor we obtain the tensor form of the first constitutive equation as

$$
\boldsymbol{\sigma} = \lambda(\operatorname{tr}\boldsymbol{\epsilon})\mathbf{I} + (\mu + \nu)\boldsymbol{\epsilon} + (\mu - \nu)\boldsymbol{\epsilon}^{\mathrm{T}}.
\tag{2.168}
$$

Equation (2.168) may be presented in a matrix form as

$$
\underbrace{\begin{bmatrix} \sigma_{11} & \sigma_{12} & \sigma_{13} \\ \sigma_{21} & \sigma_{22} & \sigma_{23} \\ \sigma_{31} & \sigma_{32} & \sigma_{33} \end{bmatrix}}_{\boldsymbol{\sigma}-\text{ stress tensor}} =
\underbrace{\begin{bmatrix}
\begin{bmatrix} (\lambda+2\mu) & 0 & 0 \\ 0 & \lambda & 0 \\ 0 & 0 & \lambda \end{bmatrix} &
\begin{bmatrix} 0 & (\mu+\nu) & 0 \\ (\mu-\nu) & 0 & 0 \\ 0 & 0 & 0 \end{bmatrix} &
\begin{bmatrix} 0 & 0 & (\mu+\nu) \\ 0 & 0 & 0 \\ (\mu-\nu) & 0 & 0 \end{bmatrix} \\[12pt]
\begin{bmatrix} 0 & (\mu-\nu) & 0 \\ (\mu+\nu) & 0 & 0 \\ 0 & 0 & 0 \end{bmatrix} &
\begin{bmatrix} \lambda & 0 & 0 \\ 0 & (\lambda+2\mu) & 0 \\ 0 & 0 & \lambda \end{bmatrix} &
\begin{bmatrix} 0 & 0 & 0 \\ 0 & 0 & (\mu+\nu) \\ 0 & (\mu-\nu) & 0 \end{bmatrix} \\[12pt]
\begin{bmatrix} 0 & 0 & (\mu-\nu) \\ 0 & 0 & 0 \\ (\mu+\nu) & 0 & 0 \end{bmatrix} &
\begin{bmatrix} 0 & 0 & 0 \\ 0 & 0 & (\mu-\nu) \\ 0 & (\mu+\nu) & 0 \end{bmatrix} &
\begin{bmatrix} \lambda & 0 & 0 \\ 0 & \lambda & 0 \\ 0 & 0 & (\lambda+2\mu) \end{bmatrix}
\end{bmatrix}}_{\mathbf{T}-\text{ constitutive tensor}} :
\underbrace{\begin{bmatrix} \epsilon_{11} & \epsilon_{12} & \epsilon_{13} \\ \epsilon_{21} & \epsilon_{22} & \epsilon_{23} \\ \epsilon_{31} & \epsilon_{32} & \epsilon_{33} \end{bmatrix}}_{\boldsymbol{\epsilon}-\text{ strain tensor}}.
\tag{2.169}
$$

In the micropolar continuum theory the couple-stress tensor $\boldsymbol{\mu}$ is related to the curvature tensor $\boldsymbol{\kappa}$ in a completely analogous way involving three additional material constants.

Using equations (2.147) and (2.149) we obtain the second set of nine equations as:

$$\mu_{11} = (\alpha + 2\beta)\kappa_{11} + \alpha\kappa_{22} + \alpha\kappa_{33}, \tag{2.170}$$

$$\mu_{12} = (\beta + \gamma)\kappa_{12} + (\beta - \gamma)\kappa_{21}, \tag{2.171}$$

$$\mu_{13} = (\beta + \gamma)\kappa_{13} + (\beta - \gamma)\kappa_{31}, \tag{2.172}$$

$$\mu_{21} = (\beta - \gamma)\kappa_{12} + (\beta + \gamma)\kappa_{21}, \tag{2.173}$$

$$\mu_{22} = \alpha\kappa_{11} + (\alpha + 2\beta)\kappa_{22} + \alpha\kappa_{33}, \tag{2.174}$$

$$\mu_{23} = (\beta + \gamma)\kappa_{23} + (\beta - \gamma)\kappa_{32}, \tag{2.175}$$

$$\mu_{31} = (\beta - \gamma)\kappa_{13} + (\beta + \gamma)\kappa_{31}, \tag{2.176}$$

$$\mu_{32} = (\beta - \gamma)\kappa_{23} + (\beta + \gamma)\kappa_{32}, \tag{2.177}$$

$$\mu_{33} = \alpha\kappa_{11} + \alpha\kappa_{22} + (\alpha + 2\beta)\kappa_{33}, \tag{2.178}$$

or simply

$$\mu_{ij} = \alpha\kappa_{pp}\delta_{ij} + (\beta + \gamma)\kappa_{ij} + (\beta - \gamma)\kappa_{ji}, \tag{2.179}$$

where α, β, γ are additional material parameters of the linear isotropic micropolar continuum. The tensor form of the second independent constitutive equation is defined as

$$\boldsymbol{\mu} = \mathbf{D} : \boldsymbol{\kappa}, \tag{2.180}$$

where

$$\mathbf{D} = \alpha\, \mathbf{I} \otimes \mathbf{I} + (\beta + \gamma)\boldsymbol{\mathcal{I}} + (\beta - \gamma)\boldsymbol{\mathcal{I}}^{\mathrm{T}}. \tag{2.181}$$

Again, by performing the double contraction product between the second constitutive tensor and the curvature tensor we obtain the tensor form of the second constitutive equation as

$$\boldsymbol{\mu} = \alpha(\mathrm{tr}\ \boldsymbol{\kappa})\mathbf{I} + (\beta + \gamma)\boldsymbol{\kappa} + (\beta - \gamma)\boldsymbol{\kappa}^{\mathrm{T}}, \tag{2.182}$$

which may be written in a matrix form as

$$
\underbrace{\begin{bmatrix} \mu_{11} & \mu_{12} & \mu_{13} \\ \mu_{21} & \mu_{22} & \mu_{23} \\ \mu_{31} & \mu_{32} & \mu_{33} \end{bmatrix}}_{\boldsymbol{\mu}-\text{ couple stress tensor}} = \underbrace{\begin{bmatrix} \begin{bmatrix} (\alpha+2\beta) & 0 & 0 \\ 0 & \alpha & 0 \\ 0 & 0 & \alpha \end{bmatrix} & \begin{bmatrix} 0 & (\beta+\gamma) & 0 \\ (\beta-\gamma) & 0 & 0 \\ 0 & 0 & 0 \end{bmatrix} & \begin{bmatrix} 0 & 0 & (\beta+\gamma) \\ 0 & 0 & 0 \\ (\beta-\gamma) & 0 & 0 \end{bmatrix} \\ \begin{bmatrix} 0 & (\beta-\gamma) & 0 \\ (\beta+\gamma) & 0 & 0 \\ 0 & 0 & 0 \end{bmatrix} & \begin{bmatrix} \alpha & 0 & 0 \\ 0 & (\alpha+2\beta) & 0 \\ 0 & 0 & \alpha \end{bmatrix} & \begin{bmatrix} 0 & 0 & 0 \\ 0 & 0 & (\beta+\gamma) \\ 0 & (\beta-\gamma) & 0 \end{bmatrix} \\ \begin{bmatrix} 0 & 0 & (\beta-\gamma) \\ 0 & 0 & 0 \\ (\beta+\gamma) & 0 & 0 \end{bmatrix} & \begin{bmatrix} 0 & 0 & 0 \\ 0 & 0 & (\beta-\gamma) \\ 0 & (\beta+\gamma) & 0 \end{bmatrix} & \begin{bmatrix} \alpha & 0 & 0 \\ 0 & \alpha & 0 \\ 0 & 0 & (\alpha+2\beta) \end{bmatrix} \end{bmatrix}}_{\mathbf{D}-\text{ constitutive tensor}} : \underbrace{\begin{bmatrix} \kappa_{11} & \kappa_{12} & \kappa_{13} \\ \kappa_{21} & \kappa_{22} & \kappa_{23} \\ \kappa_{31} & \kappa_{32} & \kappa_{33} \end{bmatrix}}_{\boldsymbol{\kappa}-\text{ curvature tensor}} .
$$

$$(2.183)$$

2.4.1 Relation between material constants and technical constants

The choice of parameters in the constitutive equations is inspired by Nowacki [4]. As written in [34], the motivation to adopt Nowacki's choice of parameters lies in the fact that this notation allows for the description of the extra features of the micropolar elasticity in a form parallel to the commonly used classical theory of elasticity. The following restrictions on the material parameters hold true as a consequence of positive definiteness of the constitutive tensors: $3\lambda + 2\mu > 0$, $\mu > 0$, $\nu > 0$, $3\alpha + 2\beta > 0$, $\beta > 0$ and $\gamma > 0$.

An alternative representation of the micropolar constitutive equations, attributed to Eringen [11], is also present in the literature, whereby (see also [62])

$$
\begin{aligned}
t_{ij} &= \tilde{\lambda} e_{pp}\delta_{ij} + (2\tilde{\mu} + \tilde{\kappa})e_{ij} + \tilde{\kappa}\varepsilon_{ijk}(r_k - \phi_k), \\
m_{ij} &= \tilde{\alpha}\phi_{p,p}\delta_{ij} + \tilde{\beta}\varphi_{i,j} + \tilde{\gamma}\varphi_{j,i},
\end{aligned}
$$

$$(2.184)$$

in which $t_{ij} = \sigma_{ji}$, $m_{ij} = \mu_{ji}$, $e_{ij} = \frac{1}{2}(u_{i,j} + u_{j,i})$ is the classical symmetric strain tensor, $r_i = \frac{1}{2}\varepsilon_{ijk}u_{k,j}$ is the macrorotation and ϕ_k is the microrotation, while $\tilde{\alpha}$, $\tilde{\beta}$, $\tilde{\gamma}$, $\tilde{\kappa}$, $\tilde{\mu}$ and $\tilde{\nu}$ represent the corresponding material parameters.

The two sets of material parameters may be related to a set of technical (measurable) parameters consisting of shear modulus G, Poisson's ratio n, a dimensionless coupling number between the macrorotation and the microrotation $N \in \langle 0, 1\rangle$, a dimensionless polar ratio of rotation sensitivity (a quantity which relates the torsional strains in a way analogous to that in which Poisson's ratio relates the normal strains) $\psi \in \langle 0, \frac{3}{2}\rangle$, and the characteristic lengths for torsion and bending l_t and l_b as [62]

$$
\begin{aligned}
\lambda &= \frac{2n\,G}{1-2n}, & \mu &= G, & \nu &= \frac{G\,N^2}{1-N^2}, \\
\alpha &= \frac{2G\,l_t^2(1-\psi)}{\psi}, & \beta &= G\,l_t^2, & \gamma &= G(4l_b^2 - l_t^2).
\end{aligned}
$$

$$(2.185)$$

43

or in Eringen's notation as [62]

$$\tilde{\lambda} = \frac{2n\,G}{1-2n}, \qquad \tilde{\mu} = \frac{G(2N^2-1)}{N^2-1}, \qquad \tilde{\kappa} = \frac{2GN^2}{1-N^2},$$
$$\tilde{\alpha} = \frac{2G\,l_t^2(1-\psi)}{\psi}, \quad \tilde{\beta} = 2G(l_t^2 - 2l_b^2), \quad \tilde{\gamma} = 4Gl_b^2. \tag{2.186}$$

The relation between the two sets of material parameters is thus equal to

$$\lambda = \tilde{\lambda}, \quad \mu = \tilde{\mu} + \frac{\tilde{\kappa}}{2}, \qquad \nu = \frac{\tilde{\kappa}}{2},$$
$$\alpha = \tilde{\alpha}, \quad \beta = \frac{\tilde{\gamma}+\tilde{\beta}}{2}, \quad \gamma = \frac{\tilde{\gamma}-\tilde{\beta}}{2}. \tag{2.187}$$

In some of the older literature (e.g. [57]) $\tilde{\mu}$ is sometimes mistaken for the Lamé parameter μ (the shear modulus G), which is investigated in detail and revealed in the work of Cowin [63]. Equations $(2.185)_1$ and $(2.185)_2$ thus unambiguously identify λ and μ as the Lamé parameters.

The constitutive equations together with the equilibrium equations (along with the associated essential and natural boundary conditions) and the kinematic equations fully define the mechanical problem of a linear micropolar continuum with displacements and rotations as the basic unknowns of the problem.

Chapter 3

Linear finite element analysis

The formulation and numerical results presented in this chapter are presented in:
[64] Grbčić, S., Jelenić, G., Ribarić D., "Quadrilateral 2D linked-interpolation finite elements for micropolar continuum", submitted for publication, 2018.
[65] Grbčić, S., Ibrahimbegović, A., Jelenić, G. "Variational formulation of micropolar elasticity using 3D hexahedral finite-element interpolation with incompatible modes", Computers and Structures, 205, 1-14, 2018.

Many authors worked on finding the numerical solutions of the micropolar continuum theory using different finite element methods in the linear analysis [35, 39, 36, 40, 42, 41]. Here we present two different approaches in developing novel finite elements, assess their performance, and attempt to clarify some ambiguities present in the literature regarding the micropolar finite element method.

In this chapter new linear micropolar finite elements with enhanced interpolation of the kinematic fields are presented. In the first part, the families of triangular and quadrilateral finite elements enhanced with the so-called *linked interpolation* are developed. The newly presented membrane finite elements of different order are thus tested and compared against the conventional Lagrange micropolar finite elements through four numerical examples. The quadrilateral family of finite elements with linked interpolation is presented in [64].

In the second part of this chapter we move from 2D to 3D and present a first order micropolar hexahedral finite element enhanced with the so-called *incompatible modes*. Again, the performance of this newly presented finite element is compared against the conventional first order micropolar hexahedral finite element. The enhanced performance of the hexahedral finite element with incompatible modes is highlighted while modelling different boundary value problems which are shown to be significant for the experimental verification of micropolar material parameters. This part of this thesis is published in [65].

All the presented finite elements are coded within the Finite Element Analysis Program (FEAP) [66].

3.1 Weak form of equilibrium equations in 3D

To construct a numerical solution procedure of the boundary value problem, we abandon its strong (or differential) form in favor of the corresponding weak (or integral) form. The displacement-type weak formulation is obtained by means of the *principle of virtual work* stating that the difference between virtual works of external and internal forces should vanish, i.e.

$$G(\mathbf{u}, \boldsymbol{\varphi}; \overline{\mathbf{u}}, \overline{\boldsymbol{\varphi}}) = G^{int}(\mathbf{u}, \boldsymbol{\varphi}; \overline{\mathbf{u}}, \overline{\boldsymbol{\varphi}}) - G^{ext}(\overline{\mathbf{u}}, \overline{\boldsymbol{\varphi}}) = 0. \tag{3.1}$$

The virtual work of internal and external forces can be expressed as

$$\begin{aligned} G^{int}(\mathbf{u}, \boldsymbol{\varphi}; \overline{\mathbf{u}}, \overline{\boldsymbol{\varphi}}) &= \int_V (\overline{\boldsymbol{\epsilon}} : \boldsymbol{\sigma} + \overline{\boldsymbol{\kappa}} : \boldsymbol{\mu}) dV, \\ G^{ext}(\overline{\mathbf{u}}, \overline{\boldsymbol{\varphi}}) &= \int_V (\overline{\mathbf{u}} \cdot \mathbf{p}_\mathrm{v} + \overline{\boldsymbol{\varphi}} \cdot \mathbf{m}_\mathrm{v}) dV + \int_S (\overline{\mathbf{u}} \cdot \mathbf{p}_\mathrm{s} + \overline{\boldsymbol{\varphi}} \cdot \mathbf{m}_\mathrm{s}) dS, \end{aligned} \tag{3.2}$$

where $\mathbf{u}$ and $\boldsymbol{\varphi}$ are the real displacements and real microrotation vectors, $\overline{\mathbf{u}}$ and $\overline{\boldsymbol{\varphi}}$ are the virtual displacements and virtual microrotation vectors and $\overline{\boldsymbol{\epsilon}}$ and $\overline{\boldsymbol{\kappa}}$ are the corresponding tensors of virtual micropolar strains and curvatures, respectively. The algebraic equilibrium equations of the finite element method will be thus obtained from the following fundamental integral principle

$$\int_V (\overline{\boldsymbol{\epsilon}} : \boldsymbol{\sigma} + \overline{\boldsymbol{\kappa}} : \boldsymbol{\mu}) dV - \int_V (\overline{\mathbf{u}} \cdot \mathbf{p}_\mathrm{v} + \overline{\boldsymbol{\varphi}} \cdot \mathbf{m}_\mathrm{v}) dV - \int_S (\overline{\mathbf{u}} \cdot \mathbf{p}_\mathrm{s} + \overline{\boldsymbol{\varphi}} \cdot \mathbf{m}_\mathrm{s}) dS = 0. \tag{3.3}$$

In order to obtain the numerical solution of the problem, the kinematic fields have to be approximated using chosen interpolations. In general, the real and virtual kinematic fields interpolation are chosen the same leading to $\mathbf{u}^h = \mathbf{N}_\mathrm{u}\, \mathbf{d}^e$, $\boldsymbol{\varphi}^h = \mathbf{N}_\varphi\, \mathbf{d}^e$, $\overline{\mathbf{u}}^h = \mathbf{N}_\mathrm{u}\, \overline{\mathbf{d}}^e$, $\overline{\boldsymbol{\varphi}}^h = \mathbf{N}_\varphi\, \overline{\mathbf{d}}^e$. More precisely, $\mathbf{N}_\mathrm{u}$ and $\mathbf{N}_\varphi$ represent the matrices of interpolation functions over an element for the displacement and microrotation field and $\mathbf{d}^e$ and $\overline{\mathbf{d}}^e$ represent the real and virtual vector of element nodal degrees of freedom, respectively. Superscript h denotes the finite-dimensional approximation and e denotes the element to which the interpolation is applied. After introducing the chosen interpolation of the kinematic fields and their virtual counterparts into (3.2) we obtain the interpolated element internal and external virtual works as

$$G^{int,e}(\mathbf{d}^e; \overline{\mathbf{d}}^e) = \overline{\mathbf{d}}^{e\mathrm{T}}\mathbf{K}^e\mathbf{d}^e, \quad G^{ext,e}(\overline{\mathbf{d}}^e) = \overline{\mathbf{d}}^{e\mathrm{T}}\mathbf{f}^e, \tag{3.4}$$

where $\mathbf{K}^e$ and $\mathbf{f}^e$ represent the element stiffness matrix and external force vector. The global internal and external virtual works are obtained by assembly over n_{elem} as the total number of elements in the mesh, with $\mathbb{A}$ as the finite-element assembly operator [56] as

$$G^{int}(\mathbf{d};\overline{\mathbf{d}}) = \mathop{\mathbb{A}}_{e=1}^{n_{elem}} G^{int,e}(\mathbf{d}^e;\overline{\mathbf{d}}^e) \equiv \overline{\mathbf{d}}^{\mathrm{T}}\mathbf{K}\mathbf{d}, \quad G^{ext}(\overline{\mathbf{d}}) = \mathop{\mathbb{A}}_{e=1}^{n_{elem}} G^{ext,e}(\overline{\mathbf{d}}^e) \equiv \overline{\mathbf{d}}^{\mathrm{T}}\mathbf{f}, \qquad (3.5)$$

with $\mathbf{d}$ and $\overline{\mathbf{d}}$ being the global vectors of real and virtual displacements, and $\mathbf{K} = \mathop{\mathbb{A}}\limits_{e=1}^{n_{elem}} \mathbf{K}^e$ and $\mathbf{f} = \mathop{\mathbb{A}}\limits_{e=1}^{n_{elem}} \mathbf{f}^e$ the global stiffness matrix and external force vector. Finally, by substituting (3.4) in (3.1) we obtain the approximated weak form. For arbitrary values of virtual parameters, $\forall\ \overline{\mathbf{d}}$, the approximated principle of virtual work leads to the basic algebraic equations of the finite element method $\mathbf{K}\ \mathbf{d} = \mathbf{f}$.

3.2 Governing equations of a 2D micropolar continuum

In order to develop membrane finite elements, the presented boundary value problem is reduced from 3D to 2D. Consequently, the kinematic fields are in Cartesian coordinates reduced to only two independent displacements $\mathbf{u} = \langle u_x\ u_y\ 0 \rangle^{\mathrm{T}}$ and one microrotation $\boldsymbol{\varphi} = \langle 0\ 0\ \varphi_z \rangle^{\mathrm{T}}$, which represents an in-plane (or *drilling*) rotation. For sake of simplicity, the kinematic fields notation adopted for this 2D analysis is defined as: $\mathbf{u} = \langle u\ v \rangle^{\mathrm{T}}$, being reduced to only two components and $\boldsymbol{\varphi} = \varphi$, being reduced to only one component. Furthermore, assuming a plane-strain condition, the stress and strain tensors are reduced to $\boldsymbol{\sigma} = \langle \sigma_{11}\ \sigma_{12}\ \sigma_{21}\ \sigma_{22} \rangle^{\mathrm{T}}$, $\boldsymbol{\mu} = \langle \mu_{31}\ \mu_{32} \rangle^{\mathrm{T}}$ and $\boldsymbol{\epsilon} = \langle \epsilon_{11}\ \epsilon_{12}\ \epsilon_{21}\ \epsilon_{22} \rangle^{\mathrm{T}}$, $\boldsymbol{\kappa} = \langle \kappa_{31}\ \kappa_{32} \rangle^{\mathrm{T}}$ respectively with

$$\begin{Bmatrix} \sigma_{11} \\ \sigma_{12} \\ \sigma_{21} \\ \sigma_{22} \end{Bmatrix} = \begin{bmatrix} (\lambda + 2\mu) & 0 & 0 & \lambda \\ 0 & (\mu + \nu) & (\mu - \nu) & 0 \\ 0 & (\mu - \nu) & (\mu + \nu) & 0 \\ \lambda & 0 & 0 & (\lambda + 2\mu) \end{bmatrix} \begin{Bmatrix} \epsilon_{11} \\ \epsilon_{12} \\ \epsilon_{21} \\ \epsilon_{22} \end{Bmatrix} \quad \Leftrightarrow \quad \boldsymbol{\sigma} = \mathbf{C_1}\boldsymbol{\epsilon}, \qquad (3.6)$$

$$\begin{Bmatrix} \mu_{31} \\ \mu_{32} \end{Bmatrix} = \begin{bmatrix} (\beta + \gamma) & 0 \\ 0 & (\beta + \gamma) \end{bmatrix} \begin{Bmatrix} \kappa_{31} \\ \kappa_{32} \end{Bmatrix} \quad \Leftrightarrow \quad \boldsymbol{\mu} = \mathbf{C_2}\boldsymbol{\kappa}, \qquad (3.7)$$

where $\mathbf{C_1}$ and $\mathbf{C_2}$ stand for the 2D micropolar constitutive tensors. Therefore, the problem requires only four material parameters λ, μ, ν and $\beta + \gamma$, and the material parameter α does not exist anymore in the present 2D element formulations. By analysing the positive definiteness through the eigenvalues of the reduced 2D constitutive tensors in this plane-strain problem, in order to fulfill the necessary condition of the positiveness of strain

energy, the following restrictions on material parameters must hold: $\mu > 0$, $\nu > 0$, $\lambda > -\mu$ and $\beta + \gamma > 0$. Of course, the real material must satisfy this condition in any stress-strain state, such as the earlier 3D state in which the more stringent conditions $\beta > 0$, $\gamma > 0$ and $\lambda > -\frac{2}{3}\mu$ apply. The applied loading is likewise reduced to

$$\mathbf{p}_\mathrm{v} = \begin{Bmatrix} p_{vx} \\ p_{vy} \\ 0 \end{Bmatrix} = \begin{Bmatrix} \mathbf{q}_\mathrm{v} \\ 0 \end{Bmatrix}, \quad \mathbf{m}_\mathrm{v} = \begin{Bmatrix} 0 \\ 0 \\ m_{vz} \end{Bmatrix} = \begin{Bmatrix} 0 \\ 0 \\ m_v \end{Bmatrix}, \tag{3.8}$$

$$\mathbf{p}_\mathrm{s} = \begin{Bmatrix} p_{sx} \\ p_{sy} \\ 0 \end{Bmatrix} = \begin{Bmatrix} \mathbf{q}_\mathrm{s} \\ 0 \end{Bmatrix}, \quad \mathbf{m}_\mathrm{s} = \begin{Bmatrix} 0 \\ 0 \\ m_{sz} \end{Bmatrix} = \begin{Bmatrix} 0 \\ 0 \\ m_s \end{Bmatrix}. \tag{3.9}$$

The kinematic equations are reduced to

$$\underbrace{\begin{Bmatrix} \epsilon_{11} \\ \epsilon_{12} \\ \epsilon_{21} \\ \epsilon_{22} \end{Bmatrix}}_{\boldsymbol{\epsilon}} = \underbrace{\begin{bmatrix} \frac{\partial}{\partial x} & 0 \\ \frac{\partial}{\partial y} & 0 \\ 0 & \frac{\partial}{\partial x} \\ 0 & \frac{\partial}{\partial y} \end{bmatrix}}_{\mathbf{D}_\mathrm{u}^\mathrm{T}} \underbrace{\begin{Bmatrix} u \\ v \end{Bmatrix}}_{\mathbf{u}} + \varphi \underbrace{\begin{Bmatrix} 0 \\ 1 \\ -1 \\ 0 \end{Bmatrix}}_{\mathbf{I}_\varphi} \quad \Leftrightarrow \quad \boldsymbol{\epsilon} = \mathbf{D}_\mathrm{u}^\mathrm{T}\mathbf{u} + \varphi\mathbf{I}_\varphi, \tag{3.10}$$

while the curvatures are reduced to

$$\underbrace{\begin{Bmatrix} \kappa_{31} \\ \kappa_{32} \end{Bmatrix}}_{\boldsymbol{\kappa}} = \underbrace{\begin{Bmatrix} \frac{\partial}{\partial x} \\ \frac{\partial}{\partial y} \end{Bmatrix}}_{\mathbf{D}_\varphi^\mathrm{T}} \varphi = \mathbf{D}_\varphi^\mathrm{T}\varphi. \tag{3.11}$$

Next, the chosen interpolation of the kinematic fields is introduced, as described in the previous section, where, for a 2D problem the real and virtual vector of element nodal degrees of freedom are defined as $\mathbf{d}^e = \langle u_1\ v_1\ \varphi_1\ \cdots\ u_{n_{node}}\ v_{n_{node}}\ \varphi_{n_{node}} \rangle^\mathrm{T}$ and $\overline{\mathbf{d}}^e = \langle \overline{u}_1\ \overline{v}_1\ \overline{\varphi}_1\ \cdots\ \overline{u}_{n_{node}}\ \overline{v}_{n_{node}}\ \overline{\varphi}_{n_{node}} \rangle^\mathrm{T}$, respectively, where n_{node} represent the number of element nodes. For example, by using the conventional Lagrange interpolation [67] we approximate the real and virtual displacements as

$$\mathbf{u}^h = \mathbf{N}_\mathrm{u}\mathbf{d}^e, \quad \overline{\mathbf{u}}^h = \mathbf{N}_\mathrm{u}\overline{\mathbf{d}}^e, \tag{3.12}$$

and the real and virtual microrotation as

$$\varphi^h = \mathbf{N}_\varphi\,\mathbf{d}^e, \quad \overline{\varphi}^h = \mathbf{N}_\varphi\,\overline{\mathbf{d}}^e, \tag{3.13}$$

48

with

$$\mathbf{N}_{\mathrm{u}} = \begin{bmatrix} N_1 & 0 & 0 & \ldots & N_{n_{node}} & 0 & 0 \\ 0 & N_1 & 0 & \ldots & 0 & N_{n_{node}} & 0 \end{bmatrix} \quad \text{and} \qquad (3.14)$$

$$\mathbf{N}_{\varphi} = \langle 0 \quad 0 \quad N_1 \quad \ldots \quad 0 \quad 0 \quad N_{n_{node}} \rangle, \qquad (3.15)$$

where $N_i (i = 1, ..., n_{node})$ is the ith Lagrangian polynomial. After introducing the chosen type of interpolation of the kinematic fields and substituting the kinematic equations (3.10), (3.11) and constitutive equations (3.6), (3.7) in (3.1) we obtain the interpolated element internal and external virtual works in 2D as

$$G^{int,e}(\mathbf{d}^e; \overline{\mathbf{d}}^e) = \overline{\mathbf{d}}^{e\mathrm{T}} \int_V (\mathbf{N}_{\mathrm{u}}^{\mathrm{T}} \mathbf{D}_{\mathrm{u}} + \mathbf{N}_{\varphi}^{\mathrm{T}} \mathbf{I}_{\varphi}^{\mathrm{T}}) \mathbf{C_1} (\mathbf{D}_{\mathrm{u}}^{\mathrm{T}} \mathbf{N}_{\mathrm{u}} + \mathbf{I}_{\varphi} \mathbf{N}_{\varphi}) dV \mathbf{d}^e$$

$$+ \overline{\mathbf{d}}^{e\mathrm{T}} \int_V (\mathbf{N}_{\varphi}^{\mathrm{T}} \mathbf{D}_{\varphi}) \mathbf{C_2} (\mathbf{D}_{\varphi}^{\mathrm{T}} \mathbf{N}_{\varphi}) dV \mathbf{d}^e = \overline{\mathbf{d}}^{e\mathrm{T}} \mathbf{K}^e \mathbf{d}^e, \qquad (3.16)$$

$$G^{ext,e}(\overline{\mathbf{d}}^e) = \overline{\mathbf{d}}^{e\mathrm{T}} \int_V (\mathbf{N}_{\mathrm{u}}^{\mathrm{T}} \mathbf{q_v} + \mathbf{N}_{\varphi}^{\mathrm{T}} m_v) dV + \overline{\mathbf{d}}^{e\mathrm{T}} \int_S (\mathbf{N}_{\mathrm{u}}^{\mathrm{T}} \mathbf{q_s} + \mathbf{N}_{\varphi}^{\mathrm{T}} m_s) dS$$

$$= \overline{\mathbf{d}}^{e\mathrm{T}} \mathbf{f}^e. \qquad (3.17)$$

In order to obtain the global internal and external virtual works G^{int} and G^{ext} we apply the finite-element assembly operator as defined in (3.5). Finally, by substituting G^{int} and G^{ext} in (3.1) we obtain the approximated weak form. Recognising arbitrariness of $\overline{\mathbf{d}}$, we eventually obtain the basic set of algebraic equations of the finite element method as $\mathbf{K}\,\mathbf{d} = \mathbf{f}$.

3.3   Lagrangian and linked interpolation in 2D

Within this section two different interpolations are compared for the families of triangular and quadrilateral membrane finite elements. The first one is the conventional Lagrange interpolation presented in (3.12) and (3.13). The second interpolation analysed is the linked interpolation in which the displacement field in addition depends on the nodal microrotation. The linked interpolation for the displacement field consists of the conventional Lagrange interpolation (represented by matrix $\mathbf{N}_{\mathrm{u}}$) enhanced by the contribution due to the nodal microrotations. In general, the linked interpolation is therefore given as

$$\mathbf{u}^h = (\mathbf{N}_{\mathrm{u}} + \mathbf{N}_{\mathrm{enh}}) \mathbf{d}^e, \quad \overline{\mathbf{u}}^h = (\mathbf{N}_{\mathrm{u}} + \mathbf{N}_{\mathrm{enh}}) \overline{\mathbf{d}}^e, \qquad (3.18)$$

where $\mathbf{N}_{\mathrm{enh}}$ is the matrix of linked-interpolation enhancement to the Lagrangian interpolation. In the linked-interpolation framework, the microrotations are still interpolated conventionally, as defined in equation (3.13).

The linked interpolation is in [68] derived as the exact solution of differential equations of a 3D Timoshenko beam. For the present purposes let us limit our attention to its 2D

form [69, 70], where the displacement field along the in-plane axis z orthogonal to the centroidal line x of the beam is

$$w = \sum_{i=1}^{n_{node}} N_i w_i - \frac{L}{n_{node}} \sum_{i=1}^{n_{node}} \frac{\xi - \xi_i}{2} N_i \varphi_i, \tag{3.19}$$

while the rotation field around the out-of-plane axis y orthogonal to the centroidal line is simply

$$\varphi = \sum_{i=1}^{n_{node}} N_i \varphi_i, \tag{3.20}$$

where L is the finite-element length, $\xi \in [-1, 1]$ is the natural co-ordinate, n_{node} is the number of nodes on the element, φ_i and w_i are the rotation and the displacement at the ith node, N_i is the ith Lagrange polynomial of order $n_{node} - 1$, ξ_i is the natural co-ordinate of the ith node, and the axes x, y, z form a right-handed co-ordinate system. The displacement field is thus interpolated by a polynomial one order higher than that used for the rotations. The Lagrangian polynomials are given as

$$N_i = \prod_{\substack{j=1 \\ j \neq i}}^{n_{node}} \frac{(\xi_j - \xi)}{(\xi_j - \xi_i)}, \quad i = 1, ..., n_{node}. \tag{3.21}$$

In order to generalise the linked interpolation concept presented to 2D micropolar continuum, it is important to note that, in contrast to beams, for this continuum in general there does not exist a closed-form solution of the differential equations. The approach that we take is the following: (i) we apply interpolation (3.19) *to the element edges only*, i.e. we treat the element edges as beam finite elements and (ii) we average the edge results within the interior of the element depending on the actual position, so that that interpolation correctly describes rigid-body motion. To do this, we follow the approach proposed in [69, 70] for the Mindlin plate elements.

3.3.1 Triangular finite elements

The triangular finite element family with the related shape functions is defined in the natural coordinate system. The mapping from the natural coordinate system (ξ, η) to the Cartesian coordinate system (x, y) is defined as:

$$x = \sum_{a=1}^{n_{node}} N_a(\xi, \eta) x_a, \quad y = \sum_{a=1}^{n_{node}} N_a(\xi, \eta) y_a, \tag{3.22}$$

where n_{node} stands for the number of element nodes, (x_a, y_a) represent the element nodal coordinates in the Cartesian coordinate system and $N_a(\xi, \eta)$ represent the isoparametric

shape functions with arguments ξ, η which run between $[0, 1]$. The transformation between the global and natural coordinate system is shown in Figure 3.1.
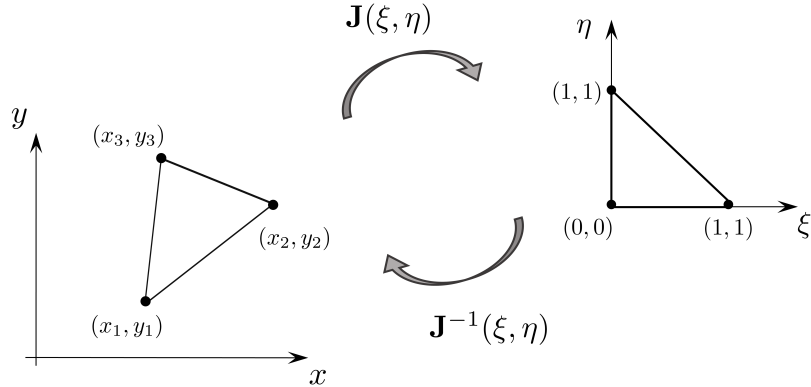
Figure 3.1: Transformation between the global and natural coordinate system for the first-order triangular element

The global derivatives of shape functions are given by the standard chain rule expressions using the so-called Jacobian matrix of transformation, which is for the present 2D problem defined as $\mathbf{J} = \dfrac{\partial(x, y)}{\partial(\xi, \eta)}$ [67], i.e.

$$\left\{ \begin{array}{c} \frac{\partial N_i}{\partial x} \\ \frac{\partial N_i}{\partial y} \end{array} \right\} = \underbrace{\begin{bmatrix} \frac{\partial \xi}{\partial x} & \frac{\partial \eta}{\partial x} \\ \frac{\partial \xi}{\partial y} & \frac{\partial \eta}{\partial y} \end{bmatrix}}_{\mathbf{J}^{-1}} \left\{ \begin{array}{c} \frac{\partial N_i}{\partial \xi} \\ \frac{\partial N_i}{\partial \eta} \end{array} \right\}. \tag{3.23}$$

Here we consider the elements with three, six or ten nodes, with a node-numbering convention as shown in Figure 3.2.

(a) Order 1 element (T3)   (b) Order 2 element (T6)   (c) Order 3 element (T10)
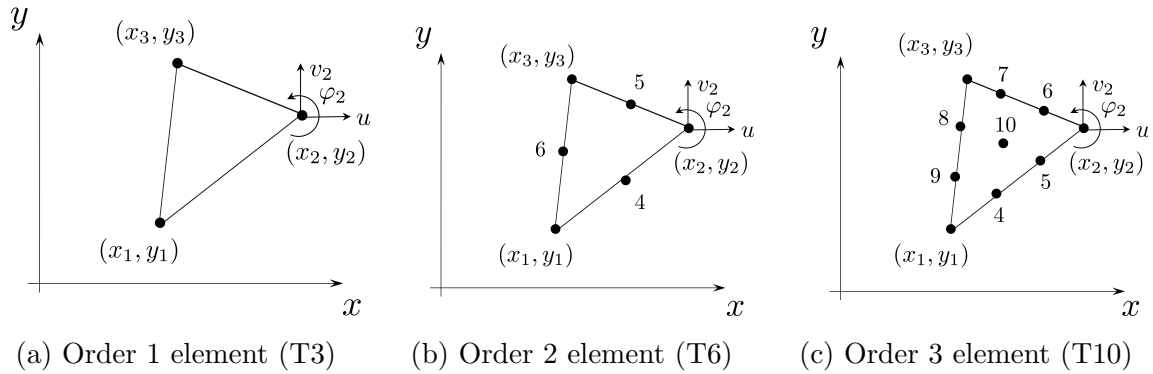
Figure 3.2: Triangular finite elements of different order

The shape functions in (3.22) are most easily expressed via a set of the so-called area coordinates

$$\zeta_1(\xi, \eta) = 1 - \xi - \eta, \quad \zeta_2(\xi, \eta) = \xi, \quad \zeta_3(\xi, \eta) = \eta. \tag{3.24}$$

51

For the edge nodes in Figure 3.2 taken at the edge halves in T6 and at the edge thirds in T10 and the inner node in T10 in its centroid they are given in Table 3.1.

Table 3.1: Triangular shape functions

Element	T3	T6	T10
Vertex shape functions $(a = 1, 2, 3)$	$N_a = \zeta_a$	$N_a = \zeta_a(2\zeta_a - 1)$	$N_a = \frac{1}{2}\zeta_a(3\zeta_a - 1)(3\zeta_a - 2)$
Edge shape functions $(i = 1, 2, 3,$ $j = \max(1; i + 1 < 4))$	-	$N_{i+3} = 4\zeta_i\zeta_j$	$N_{2i+2} = \frac{9}{2}\zeta_i\zeta_j(3\zeta_i - 1)$ $N_{2i+3} = \frac{9}{2}\zeta_i\zeta_j(3\zeta_j - 1)$
Centroid node shape function	-	-	$N_{10} = 27\zeta_1\zeta_2\zeta_3$

For the Lagrangian family of elements the same shape functions are used for the interpolation of real and virtual displacements and rotations as given in equations (3.12) and (3.13). For the family of elements with linked interpolation, the rotations are still interpolated using the Lagrange polynomials and (3.13), but in the displacement field we now have an enhancement in the displacement field as shown in equation (3.18). For the elements of different order, this enhancement is now defined following the approach given in [70].

3.3.1.1   Triangular membrane element with three nodes (T3LI)

In analogy with the linked interpolation for a beam element (3.19), when applied to a two-noded beam, we propose the linked interpolation for the triangular element with three nodes and three degrees of freedom per node, named T3LI and shown in Figure 3.2a) such that

$$
\begin{aligned}
\mathbf{u}^h = (\mathbf{N}_\mathrm{u} + \mathbf{N}_\mathrm{enh})\mathbf{d}^e = \sum_{a=1}^{3} N_a \begin{Bmatrix} u_a \\ v_a \end{Bmatrix} &+ \frac{1}{2}\zeta_2\zeta_3(\varphi_2 - \varphi_3) \begin{Bmatrix} y_2 - y_3 \\ x_3 - x_2 \end{Bmatrix} + \\
&+ \frac{1}{2}\zeta_3\zeta_1(\varphi_3 - \varphi_1) \begin{Bmatrix} y_3 - y_1 \\ x_1 - x_3 \end{Bmatrix} + \\
&+ \frac{1}{2}\zeta_1\zeta_2(\varphi_1 - \varphi_2) \begin{Bmatrix} y_1 - y_2 \\ x_2 - x_1 \end{Bmatrix} \\
= \sum_{a=1}^{3} N_a \mathbf{u}_a &+ \begin{Bmatrix} f_{1,x} \\ f_{1,y} \end{Bmatrix}(\varphi_2 - \varphi_3) + \begin{Bmatrix} f_{2,x} \\ f_{2,y} \end{Bmatrix}(\varphi_3 - \varphi_1) + \\
&+ \begin{Bmatrix} f_{3,x} \\ f_{3,y} \end{Bmatrix}(\varphi_1 - \varphi_2),
\end{aligned}
\tag{3.25}
$$

where $f_{i,x} = \frac{1}{2}\zeta_j\zeta_k(y_j - y_k)$, $f_{i,y} = \frac{1}{2}\zeta_j\zeta_k(x_k - x_j)$ and i, j, k is a cyclic permutation of $1, 2, 3$ resulting in $\mathbf{N}_{\text{enh}} = \begin{bmatrix} \mathbf{N}_{\text{enh},1} & \mathbf{N}_{\text{enh},2} & \mathbf{N}_{\text{enh},3} \end{bmatrix}$ where

$$\mathbf{N}_{\text{enh},i} = \begin{bmatrix} 0 & 0 & f_{k,x} - f_{j,x} \\ 0 & 0 & f_{k,y} - f_{j,y} \end{bmatrix}. \tag{3.26}$$

An analogous interpolation is proposed in [71] where a triangular element with three nodes based on the classical continuum theory and incorporating the so-called drilling degrees of freedom has been developed. The displacement interpolation in [71] has been also derived by linking the displacements with the drilling rotations obtaining a form analogous to (3.25). Due to the need for incorporating rotations in the finite element meshes involving 2D solids and beam elements, this work has generated considerable interest in the finite element community.

3.3.1.2 Triangular membrane element with six nodes (T6LI)

Now we generalise the linked interpolation of a beam element (3.19) applied to a three-noded beam to a triangular element with six nodes and three degrees of freedom per node, named T6LI and shown in Figure 3.2b). The displacement interpolation thus follows as

$$\begin{aligned}
\mathbf{u}^h = (\mathbf{N}_{\text{u}} + \mathbf{N}_{\text{enh}})\mathbf{d}^e = \sum_{a=1}^{6} N_a(\xi, \eta) \begin{Bmatrix} u_a \\ v_a \end{Bmatrix} + \\
+ \frac{1}{3}\zeta_1\zeta_2(\zeta_2 - \zeta_1)(\varphi_1 - 2\varphi_4 + \varphi_2) \begin{Bmatrix} y_2 - y_1 \\ x_1 - x_2 \end{Bmatrix} + \\
+ \frac{1}{3}\zeta_2\zeta_3(\zeta_3 - \zeta_2)(\varphi_2 - 2\varphi_5 + \varphi_3) \begin{Bmatrix} y_3 - y_2 \\ x_2 - x_3 \end{Bmatrix} + \\
+ \frac{1}{3}\zeta_3\zeta_1(\zeta_1 - \zeta_3)(\varphi_3 - 2\varphi_6 + \varphi_1) \begin{Bmatrix} y_1 - y_3 \\ x_3 - x_1 \end{Bmatrix},
\end{aligned} \tag{3.27}$$

from where $\mathbf{N}_{\text{enh}}$ immediately follows.

3.3.1.3 Triangular membrane element with ten nodes (T10LI)

Finally, we develop the triangular element with ten nodes shown in Figure 3.2c), which we name T10LI. Generalising the linked interpolation for a beam element (3.19) applied to a four-node element

$$\mathbf{u}^h = (\mathbf{N}_{\text{u}} + \mathbf{N}_{\text{enh}})\mathbf{d}^e = \sum_{a=1}^{10} N_a(\xi, \eta) \begin{Bmatrix} u_a \\ v_a \end{Bmatrix} +$$

$$+ \frac{1}{8}\zeta_1\zeta_2(3\zeta_1 - 1)(3\zeta_2 - 1)\begin{Bmatrix} y_2 - y_1 \\ x_1 - x_2 \end{Bmatrix}(\varphi_1 - 3\varphi_4 + 3\varphi_5 - \varphi_2) +$$

$$+ \frac{1}{8}\zeta_2\zeta_3(3\zeta_2 - 1)(3\zeta_3 - 1)\begin{Bmatrix} y_3 - y_2 \\ x_2 - x_3 \end{Bmatrix}(\varphi_2 - 3\varphi_6 + 3\varphi_7 - \varphi_3) + \qquad (3.28)$$

$$+ \frac{1}{8}\zeta_3\zeta_1(3\zeta_3 - 1)(3\zeta_1 - 1)\begin{Bmatrix} y_1 - y_3 \\ x_3 - x_1 \end{Bmatrix}(\varphi_3 - 3\varphi_8 + 3\varphi_9 - \varphi_1),$$

from where $\mathbf{N}_{\text{enh}}$ again immediately follows.

3.3.2 Quadrilateral finite elements

The second family of finite elements we develop are quadrilateral elements of order 1, 2 and 3 shown in Figure 3.4 with three degrees of freedom per node (horizontal and vertical displacements, microrotation). As for the triangular elements, the quadrilateral finite element family and the corresponding shape functions are defined in the natural coordinate system where the mapping is again defined by (3.22), where here we consider the elements with four, nine and sixteen nodes (Q4, Q9, Q16) and ξ and η run between $[-1, 1]$. The transformation between the global and natural coordinate system for the first-order quadrilateral finite element is shown in Figure 3.3.
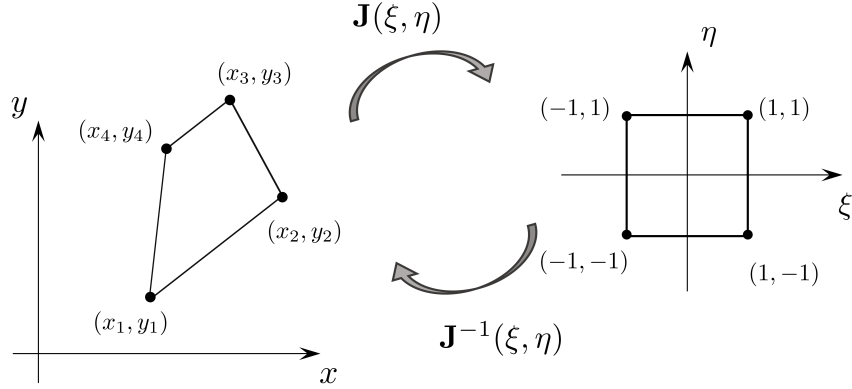
Figure 3.3: Transformation between the global and natural coordinate system for the first-order quadrilateral element

The node-numbering convention for the elements is shown in Figure 3.4.
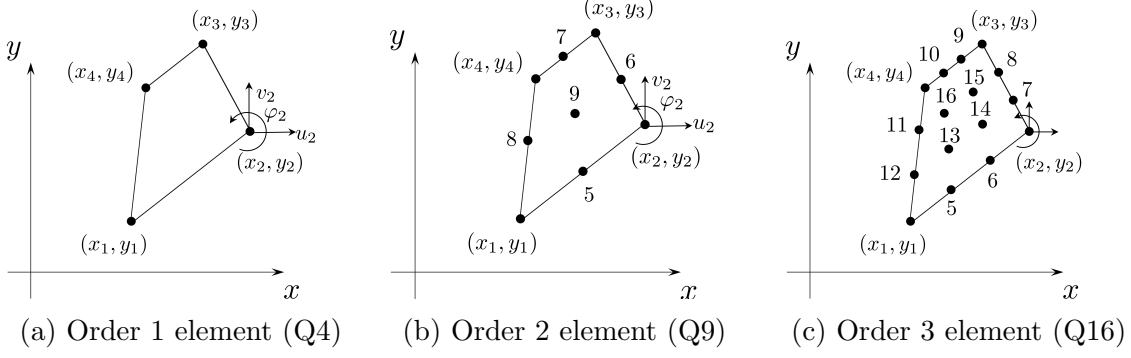
Figure 3.4: Quadrilateral finite elements of different order

The shape functions in (3.22) are given for $\xi_1 = \xi_4 = -1$, $\xi_2 = \xi_3 = +1$, $\eta_1 = \eta_2 = -1$, $\eta_3 = \eta_4 = +1$ as follows. For Q4, they are defined as $N_a(\xi, \eta) = \frac{1}{4}(1 + \xi_a \xi)(1 + \eta_a \eta)$. For Q9 with $\xi_8 = -1$, $\xi_5 = \xi_7 = \xi_9 = 0$, $\xi_6 = +1$, $\eta_5 = -1$, $\eta_6 = \eta_8 = \eta_9 = 0$ and $\eta_7 = +1$ they are given as

$$\text{Vertex nodes:} \qquad N_a = \frac{1}{4}\xi\eta(\xi + \xi_a)(\eta + \eta_a),$$

$$\text{Edge nodes 5 and 7:} \qquad N_a = \frac{1}{2}\eta(1 - \xi^2)(\eta + \eta_a),$$

$$\text{Edge nodes 6 and 8:} \qquad N_a = \frac{1}{2}\xi(\xi + \xi_a)(1 - \eta^2),$$

$$\text{Central node:} \qquad N_9 = (1 - \xi^2)(1 - \eta^2).$$

while for Q16 with $\xi_{11} = \xi_{12} = -1$, $\xi_5 = \xi_{10} = \xi_{13} = \xi_{16} = -\frac{1}{3}$, $\xi_6 = \xi_9 = \xi_{14} = \xi_{15} = +\frac{1}{3}$, $\xi_7 = \xi_8 = +1$, $\eta_5 = \eta_6 = -1$, $\eta_7 = \eta_{12} = \eta_{13} = \eta_{14} = -\frac{1}{3}$, $\eta_8 = \eta_{11} = \eta_{15} = \eta_{16} = +\frac{1}{3}$ and $\eta_9 = \eta_{10} = +1$ they are given as

Vertex nodes:
$$N_a = \frac{81}{256}(1 + \xi_a\xi)(1 + \eta_a\eta)(\frac{1}{9} - \xi^2)(\frac{1}{9} - \eta^2),$$

Edge nodes with $\xi_a = \pm 1$ and $\eta_a = \pm\frac{1}{3}$:
$$N_a = \frac{243}{256}(1 - \xi^2)(\eta^2 - \frac{1}{9})(\frac{1}{3} + 3\xi_a\xi)(1 + \eta_a\eta),$$

Edge nodes with $\xi_a = \pm\frac{1}{3}$ and $\eta_a = \pm 1$:
$$N_a = \frac{243}{256}(1 - \eta^2)(\xi^2 - \frac{1}{9})(\frac{1}{3} + 3\eta_a\eta)(1 + \xi_a\xi),$$

Internal nodes:
$$N_a = \frac{729}{256}(1 - \xi^2)(1 - \eta^2)(\frac{1}{3} + 3\eta_a\eta)(\frac{1}{3} + 3\xi_a\xi).$$

As in the family of triangular elements, for the quadrilateral elements of the Lagrangian type, the interpolation for the displacements and rotations are given by (3.12) and (3.13), the latter again also remaining valid for the quadrilateral family of elements with linked interpolation. The enhancement in the displacement field $\mathbf{N}_{\text{enh}}$ in (3.18) is now defined following the approach given in [69], based on the expression (3.19) for the linked interpolation in beams.

In [69] the authors have additionally enhanced the proposed finite elements with linked interpolation by introducing additional bubble modes. However, their numerical results have shown that the bubble mode contribution to the obtained result is negligible, except for the higher order patch test satisfaction. Therefore, the presented elements are not enhanced with additional modes.

3.3.2.1 Quadrilateral finite element with four nodes (Q4LI)

For the quadrilateral element with four nodes shown in Figure 3.4a), named Q4LI, we define the displacement interpolation as

$$
\mathbf{u}^h = (\mathbf{N}_\mathrm{u} + \mathbf{N}_\mathrm{enh})\mathbf{d}^e = \sum_{a=1}^{4} N_a(\xi, \eta) \begin{Bmatrix} u_a \\ v_a \end{Bmatrix} +
$$

$$
+ \frac{1}{8}\frac{1}{2}(1 - \xi^2)(1 - \eta) \begin{Bmatrix} y_2 - y_1 \\ x_1 - x_2 \end{Bmatrix} (\varphi_2 - \varphi_1) +
$$

$$
+ \frac{1}{8}\frac{1}{2}(1 + \xi)(1 - \eta^2) \begin{Bmatrix} y_3 - y_2 \\ x_2 - x_3 \end{Bmatrix} (\varphi_3 - \varphi_2) +
$$

$$
+ \frac{1}{8}\frac{1}{2}(1 - \xi^2)(1 + \eta) \begin{Bmatrix} y_4 - y_3 \\ x_3 - x_4 \end{Bmatrix} (\varphi_4 - \varphi_3) +
$$

$$
+ \frac{1}{8}\frac{1}{2}(1 - \xi)(1 - \eta^2) \begin{Bmatrix} y_1 - y_4 \\ x_4 - x_1 \end{Bmatrix} (\varphi_1 - \varphi_4)
$$

$$
= \sum_{a=1}^{4} N_a(\xi, \eta) \begin{Bmatrix} u_a \\ v_a \end{Bmatrix} +
$$

$$
+ \begin{Bmatrix} f_{1,x} \\ f_{1,y} \end{Bmatrix} (\varphi_1 - \varphi_2) + \begin{Bmatrix} f_{2,x} \\ f_{2,y} \end{Bmatrix} (\varphi_2 - \varphi_3) +
$$

$$
+ \begin{Bmatrix} f_{3,x} \\ f_{3,y} \end{Bmatrix} (\varphi_3 - \varphi_4) + \begin{Bmatrix} f_{4,x} \\ f_{4,y} \end{Bmatrix} (\varphi_4 - \varphi_1), \tag{3.29}
$$

where $f_{1,x} = \frac{1}{16}(1-\xi^2)(1-\eta)(y_1-y_2)$, $f_{2,x} = \frac{1}{16}(1+\xi)(1-\eta^2)(y_2-y_3)$, $f_{3,x} = \frac{1}{16}(1-\xi^2)(1+\eta)(y_3 - y_4)$, $f_{4,x} = \frac{1}{16}(1 - \xi)(1 - \eta^2)(y_4 - y_1)$ and $f_{1,y} = \frac{1}{16}(1 - \xi^2)(1 - \eta)(x_2 - x_1)$, $f_{2,y} = \frac{1}{16}(1+\xi)(1-\eta^2)(x_3-x_2)$, $f_{3,y} = \frac{1}{16}(1-\xi^2)(1+\eta)(x_4-x_3)$, $f_{4,y} = \frac{1}{16}(1-\xi)(1-\eta^2)(x_1-x_4)$ resulting in $\mathbf{N}_\mathrm{enh} = \begin{bmatrix} \mathbf{N}_\mathrm{enh,1} & \mathbf{N}_\mathrm{enh,2} & \mathbf{N}_\mathrm{enh,3} & \mathbf{N}_\mathrm{enh,4} \end{bmatrix}$ where

$$
\mathbf{N}_\mathrm{enh,1} = \begin{bmatrix} 0 & 0 & f_{1,x} - f_{4,x} \\ 0 & 0 & f_{1,y} - f_{4,y} \end{bmatrix}, \quad \mathbf{N}_\mathrm{enh,2} = \begin{bmatrix} 0 & 0 & f_{2,x} - f_{1,x} \\ 0 & 0 & f_{2,y} - f_{1,y} \end{bmatrix}, \tag{3.30}
$$

$$
\mathbf{N}_\mathrm{enh,3} = \begin{bmatrix} 0 & 0 & f_{3,x} - f_{2,x} \\ 0 & 0 & f_{3,y} - f_{2,y} \end{bmatrix}, \quad \mathbf{N}_\mathrm{enh,4} = \begin{bmatrix} 0 & 0 & f_{4,x} - f_{3,x} \\ 0 & 0 & f_{4,y} - f_{3,y} \end{bmatrix}.
$$

3.3.2.2 Quadrilateral finite element with nine nodes (Q9LI)

For the quadrilateral element with nine nodes shown in Figure 3.4b), named Q9LI, we define the displacement interpolation as

$$
\begin{aligned}
\mathbf{u}^h =&(\mathbf{N}_{\mathrm{u}} + \mathbf{N}_{\mathrm{enh}})\mathbf{d}^e = \sum_{a=1}^{9} N_a(\xi,\eta) \begin{Bmatrix} u_a \\ v_a \end{Bmatrix} + \\
&- \frac{1}{8}\frac{1}{3}\xi\eta(1-\xi^2)(1-\eta) \begin{Bmatrix} y_2 - y_1 \\ x_1 - x_2 \end{Bmatrix} (\varphi_1 - 2\varphi_5 + \varphi_2) + \\
&+ \frac{1}{4}\frac{1}{3}\xi(1-\xi^2)(1-\eta^2) \begin{Bmatrix} y_6 - y_8 \\ x_8 - x_6 \end{Bmatrix} (\varphi_8 - 2\varphi_9 + \varphi_6) + \\
&+ \frac{1}{8}\frac{1}{3}\xi\eta(1-\xi^2)(1+\eta) \begin{Bmatrix} y_3 - y_4 \\ x_4 - x_3 \end{Bmatrix} (\varphi_4 - 2\varphi_7 + \varphi_3) + \\
&+ \frac{1}{8}\frac{1}{3}\xi\eta(1-\xi)(1-\eta^2) \begin{Bmatrix} y_4 - y_1 \\ x_1 - x_4 \end{Bmatrix} (\varphi_1 - 2\varphi_8 + \varphi_4) + \\
&- \frac{1}{4}\frac{1}{3}\eta(1-\xi^2)(1-\eta^2) \begin{Bmatrix} y_7 - y_5 \\ x_5 - x_7 \end{Bmatrix} (\varphi_5 - 2\varphi_9 + \varphi_7) + \\
&- \frac{1}{8}\frac{1}{3}\xi\eta(1+\xi)(1-\eta^2) \begin{Bmatrix} y_3 - y_2 \\ x_2 - x_3 \end{Bmatrix} (\varphi_2 - 2\varphi_6 + \varphi_3)
\end{aligned}
\tag{3.31}
$$

from where $\mathbf{N}_{\mathrm{enh}}$ follows in a straight-forward way.

3.3.2.3 Quadrilateral finite element with sixteen nodes (Q16LI)

For the quadrilateral element with sixteen nodes shown in Figure 3.4c) and named Q16LI, we define the displacement interpolation as

$$
\begin{aligned}
\mathbf{u}^h =&(\mathbf{N}_{\mathrm{u}} + \mathbf{N}_{\mathrm{enh}})\mathbf{d}^e = \sum_{a=1}^{16} N_a(\xi,\eta) \begin{Bmatrix} u_a \\ v_a \end{Bmatrix} + \\
&+ \frac{1}{4}I_{1\eta}N_\xi \begin{Bmatrix} y_2 - y_1 \\ x_1 - x_2 \end{Bmatrix} (\varphi_1 - 3\varphi_5 + 3\varphi_6 - \varphi_2) + \\
&+ \frac{1}{4}I_{2\eta}N_\xi \begin{Bmatrix} y_7 - y_{12} \\ x_{12} - x_7 \end{Bmatrix} (\varphi_{12} - 3\varphi_{13} + 3\varphi_{14} - \varphi_7) + \\
&+ \frac{1}{4}I_{3\eta}N_\xi \begin{Bmatrix} y_8 - y_{11} \\ x_{11} - x_8 \end{Bmatrix} (\varphi_{11} - 3\varphi_{16} + 3\varphi_{15} - \varphi_8) + \\
&+ \frac{1}{4}I_{4\eta}N_\xi \begin{Bmatrix} y_3 - y_4 \\ x_4 - x_3 \end{Bmatrix} (\varphi_4 - 3\varphi_{10} + 3\varphi_9 - \varphi_3) +
\end{aligned}
\tag{3.32}
$$

$$-\frac{1}{4}I_{1\xi}N_\eta \begin{Bmatrix} y_4 - y_1 \\ x_1 - x_4 \end{Bmatrix} (\varphi_1 - 3\varphi_{12} + 3\varphi_{11} - \varphi_4) +$$

$$-\frac{1}{4}I_{2\xi}N_\eta \begin{Bmatrix} y_{10} - y_5 \\ x_5 - x_{10} \end{Bmatrix} (\varphi_5 - 3\varphi_{13} + 3\varphi_{16} - \varphi_{10}) +$$

$$-\frac{1}{4}I_{3\xi}N_\eta \begin{Bmatrix} y_9 - y_6 \\ x_6 - x_9 \end{Bmatrix} (\varphi_6 - 3\varphi_{14} + 3\varphi_{15} - \varphi_9) +$$

$$-\frac{1}{4}I_{4\xi}N_\eta \begin{Bmatrix} y_3 - y_2 \\ x_2 - x_3 \end{Bmatrix} (\varphi_2 - 3\varphi_7 + 3\varphi_8 - \varphi_3)$$

where $I_{1\xi} = -\frac{9}{16}(\xi^2 - \frac{1}{9})(\xi - 1)$, $I_{2\xi} = \frac{27}{16}(\xi^2 - 1)(\xi - \frac{1}{3})$, $I_{3\xi} = \frac{27}{16}(\xi^2 - 1)(\xi + \frac{1}{3})$, $I_{4\xi} = \frac{9}{16}(\xi^2 - \frac{1}{9})(\xi + 1)$, $N_\xi = \frac{9}{32}(\xi^2 - \frac{1}{9})(\xi^2 - 1)$, and analogously for $I_{1\eta}$, $I_{2\eta}$, $I_{3\eta}$, $I_{4\eta}$, N_η using the variable η. From here, $\mathbf{N}_{\text{enh}}$ again follows immediately.

3.4 Numerical examples in 2D

In this section the presented families of elements are analysed through four numerical examples. The convergence analysis is performed on a force patch test using a regular mesh in Section 3.4.1 and the conclusions drawn are implemented in the procedure to run the displacement patch test on an irregular mesh (Section 3.4.2) due to Providas and Kattis [36]. In Section 3.4.3, an infinite plate with a cylindrical hole subject to uniform tension is analysed and the results are compared to the analytical solution [13]. Finally, in Section 3.4.4, a cantilever beam in pure bending is analysed against the analytical solution [1]. In all the examples, both the standard Lagrange finite elements and the newly presented linked-interpolation finite elements are tested. Furthermore, it is important to note that all micropolar parameters are chosen to be greater than zero in all the presented examples, leading to fulfilment of the necessary condition of positiveness of the strain energy.

3.4.1 Force patch test in 2D: cantilever beam subject to pure tension

A force patch test shown in Figure 3.5 is performed on a cantilever beam of length $L = 10$ m, height $h = 2$ m and a unit thickness subject to pure axial distributed loading $p = 10$ N/m^2 using a number of regular meshes. The micropolar material parameters used are equal to $\mu = 1000$ N/m^2, $\lambda = 1000$ N/m^2, $\nu = 500$ N/m^2 and $\beta = \gamma = 20$ N.

In this example the analytical results for the stress fields (all components of the stress tensor and the couple-stress tensor equal to zero apart from the axial tension, which is equal to p) and the axial displacement at the free end (pL/E) are expected to be obtained

for an arbitrary number of finite elements in the mesh. The results of the test for triangular and quadrilateral finite elements with the conventional (Lagrange) interpolation and with the newly proposed linked interpolation are given in Table 3.2.
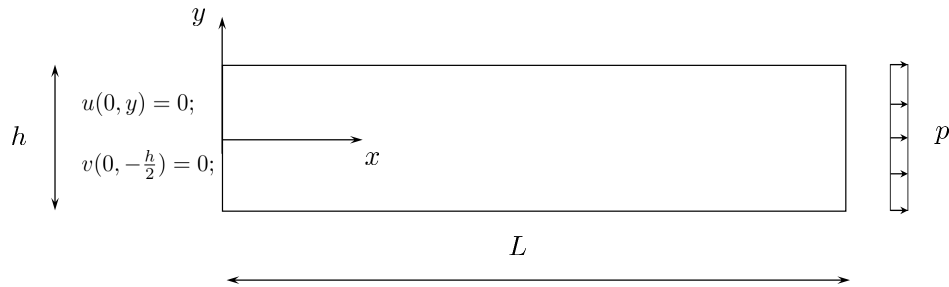
Figure 3.5: A cantilever beam subject to pure tension

To understand why most of the linked-interpolation elements fail this test and find the solution for how to modify them in order to pass it, an inversely posed problem has been studied which consists of the following: the correct nodal displacement and rotations have been prescribed to the elements with linked interpolation and the resulting stress and couple-stress tensors as well as the nodal load vector have been analysed. It turns out that all the stress and stress-couple components are exact but, in the nodal load vector, the incorrect moment components are generated by the linked interpolation applied to the virtual displacements. Interstingly, this does not happen in the quadratic elements T6LI and Q9LI.

Table 3.2: Results for the force patch test

Triangular elements		Quadrilateral elements	
Element	RESULT	Element	RESULT
T3	passed	Q4	passed
T3LI	failed	Q4LI	failed
T6	passed	Q9	passed
T6LI	passed	Q9LI	passed
T10	passed	Q16	passed
T10LI	failed	Q16LI	failed

Motivated by this observation, a solution is found by applying the *Petrov–Galerkin* finite-element method, which is based on *different interpolation* for the test and the trail functions – here the virtual and the actual displacement fields. To eliminate the anomalous

nodal moments caused by the linked interpolation of the virtual displacements $\overline{\mathbf{u}}$, here we choose to *interpolate them using the standard Lagrangian polynomials*, i.e.

$$\overline{\mathbf{u}} = \mathbf{N}_u \overline{\mathbf{d}}. \tag{3.33}$$

The real displacements, however, are still interpolated using the linked interpolation, i.e.

$$\mathbf{u} = (\mathbf{N}_u + \mathbf{N}_{enh})\mathbf{d}. \tag{3.34}$$

The microrotation interpolation remains unchanged in both its virtual and its real form, i.e. $\overline{\varphi} = \mathbf{N}_\varphi \overline{\mathbf{d}}$ and $\varphi = \mathbf{N}_\varphi \mathbf{d}$. The Petrov-Galerkin modification described is applied to those elements which fail the patch test. We refer to these elements as T3LI(PG), T10LI(PG), Q4LI(PG) and Q10LI(PG). When performing the same patch test using the elements based on the Petrov-Galerkin method, the patch test for all the elements is passed, as shown in Table 3.3.

Table 3.3: Results for the force patch test for the linked-interpolation finite elements based on the Petrov-Galerkin method

Triangular elements		Quadrilateral elements	
Element	RESULT	Element	RESULT
T3LI(PG)	passed	Q4LI(PG)	passed
T10LI(PG)	passed	Q16LI(PG)	passed

To understand why the quadratic elements with linked interpolation (T6LI and Q9LI) pass this patch test, while the linear and the cubic elements (T3LI, T10LI, Q4LI and Q16LI) do not, let us pinpoint the main difference between these two groups of elements in the *character of the enhanced shape functions* caused by the linked interpolation. In the linear and the cubic elements, the enhancement is symmetric, which, when integrated over the element domain, give a non-zero value, and thus provide non-desired nodal moments for the constant-stress state present here. On the other hand, the enhanced interpolation functions for the quadratic elements are antisymmetric and thus integrate to zero for the constant-stress state. Clearly, for quadrilaterals, this argument is applicable only to rectangular quadratic elements. For non-regular meshes, Q9LI should not be expected to retain this property and would have to be accordingly modified into Q9LI(PG). The general forms of the enhanced shape functions for triangular and quadrilateral elements are shown in Figures 3.6 and 3.7.
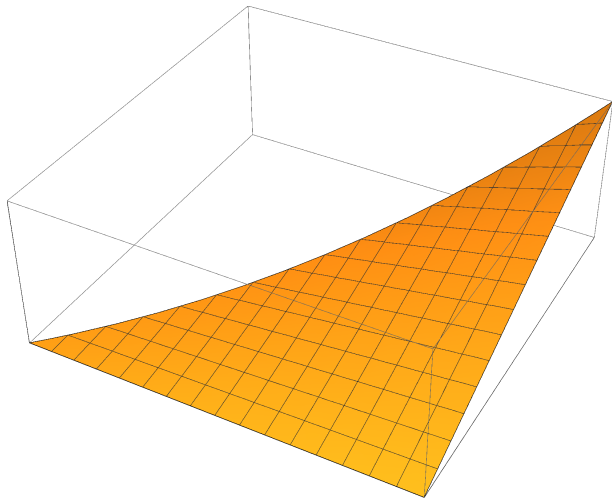
(a) Linked interpolation function character of T3LI elements
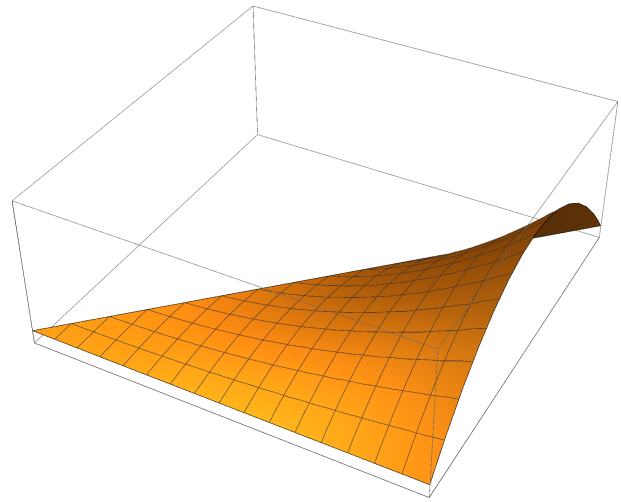
(b) Linked interpolation function character of T6LI elements
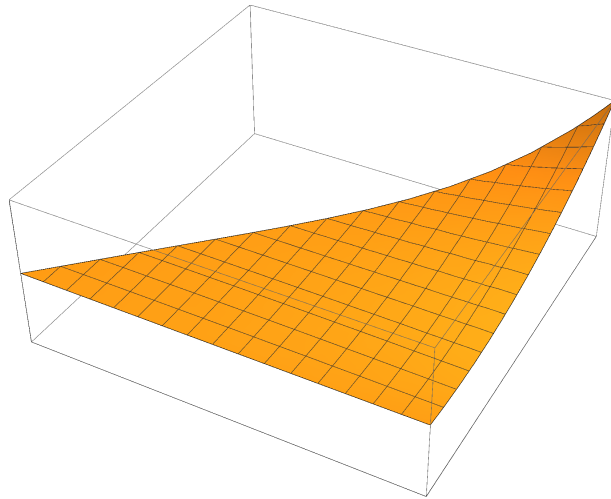
(c) Linked interpolation function character of T10LI elements

Figure 3.6: Character of the linked shape function of triangular family elements
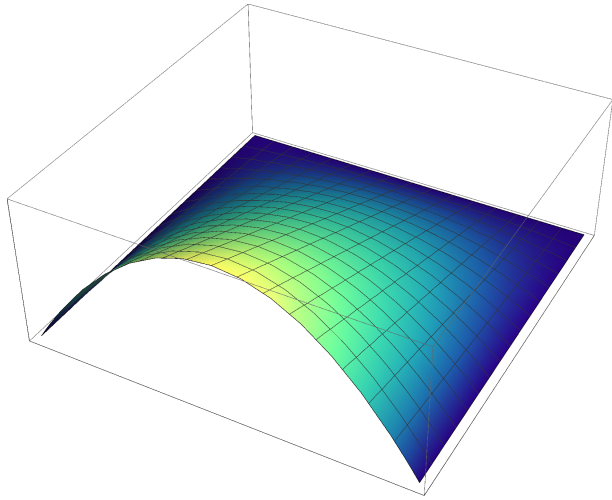
(a) Linked interpolation function character of Q4LI elements
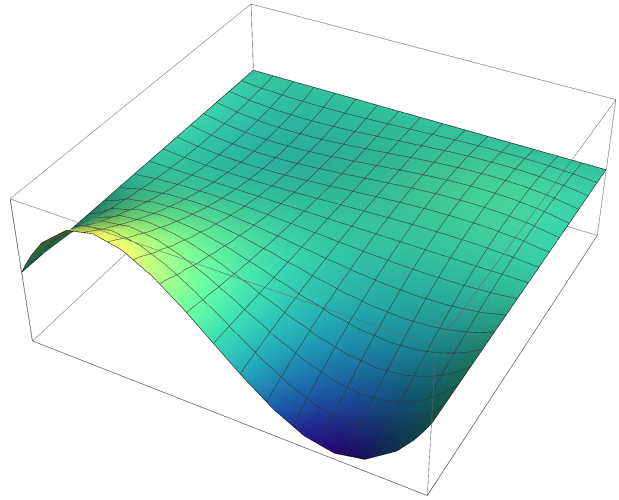
(b) Linked interpolation function character of Q9LI elements
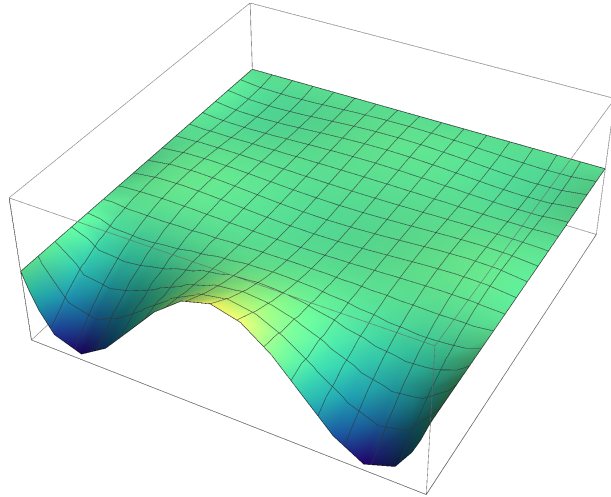
(c) Linked interpolation function character of Q16LI elements

Figure 3.7: Character of the linked shape function of quadrilateral family elements

Another approach to satisfy the convergence criteria may be provided along the lines of the modification of the matrix of enhanced interpolation proposed by Wilson and Ibrahimbegović [72]. In their work they impose the requirement that the enhanced part of the interpolation under the state of constant stress does not contribute to the strain energy. In order to satisfy this requirement, the matrix of enhanced interpolation has to be modified by adding a constant correction matrix, which makes the enhanced part to vanish for a state of constant stress. Even though in this part this approach is not analysed, we point out that it is a possible methodology for modifying the elements with linked interpolation to satisfy the patch test. This approach will be used in the next section, when developing the 3D hexahedral finite element with incompatible modes.

3.4.2 2D displacement patch tests for micropolar continuum

According to Providas and Kattis [36] the patch test for micropolar finite elements should consist of a set of three separate tests. The tests are performed on a rectangular domain bounded by the sides connecting the points 1–4 in Figure 3.8 and discretised using the distorted finite-element mesh shown. The length and height of the domain are $L = 0.24$ m, $H = 0.12$ m and the coordinates of the internal nodes 5–8 are the following 5=(0.04,0.02), 6=(0.18,0.03), 7=(0.08,0.08) and 8=(0.16,0.08). The material parameters used are the same as defined in the force patch test example. The displacements and microrotations are imposed on the external nodes, while the volume loading (if any) is imposed on the interior of the domain. The element passes a patch test if the internal nodes are capable of reproducing the analytical solution imposed by the boundary conditions.

(a) Displacement patch test: quadrilateral FE mesh

(b) Displacement patch test: triangular FE mesh
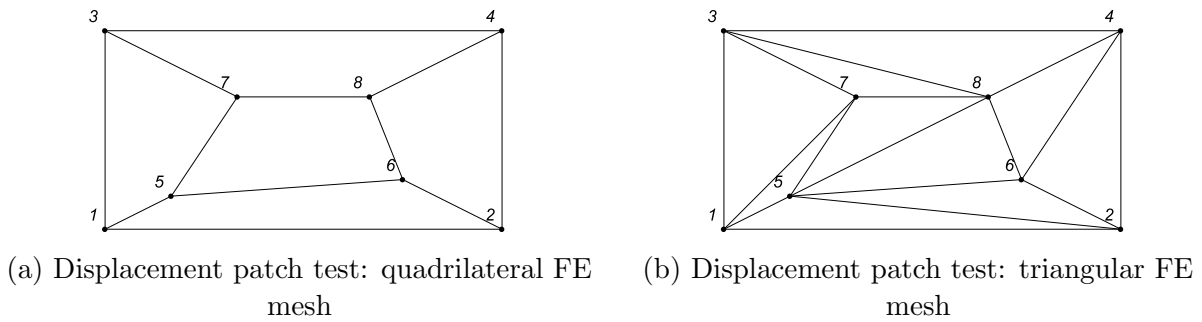
Figure 3.8: Finite element mesh for the displacement patch test

The first test is the standard patch test of the finite elements in the classical continuum theory, whereby imposing linearly varying displacement and a constant microrotation field via appropriate boundary conditions we obtain the state of *constant symmetric stress and strain*. The fields are defined as follows:

$$u = 10^{-3}(x + 0.5y), \quad v = 10^{-3}(x + y), \quad \varphi = 0.25 \cdot 10^{-3}. \tag{3.35}$$

The second test describes the state of *constant non-symmetric shear* (both in stress and strain), for which a constant body moment is needed. The actual input is given as

$$u = 10^{-3}(x + 0.5y), \quad v = 10^{-3}(x + y), \quad \varphi = 0.75 \cdot 10^{-3}, \quad m_v = 1. \tag{3.36}$$

The third test describes the state of constant curvature, whereby imposing linearly varying displacement, microrotation and body moment fields as well as a constant body force field we obtain linearly varying stresses and *constant couple-stresses*. Providas and Kattis consider the third patch test to be a necessary condition for finite-element convergence

even though in this test the shear stresses are *linearly varying*:

$$u = 10^{-3}(x + 0.5y), \quad v = 10^{-3}(x + y), \quad \varphi = 10^{-3}(0.25 + (x - y)),$$
$$p_{vx} = p_{vy} = 1, \quad m_v = 2(x - y). \tag{3.37}$$

According to [67], however, satisfaction of a patch test in which stress distribution is variable is not necessary for convergence and, for this reason, we consider this test to be a *higher-order patch test*, analogous to a pure bending test.

The constant stress tests are analysed first. As indicated earlier, when using an irregular mesh present here, the Q9LI element fails the first two patch tests. Its Petrov-Galerkin modification Q9LI(PG), however, passes them, as do also all the other proposed elements.

Regarding the third test, all the elements in which the standard Lagrangian interpolation has been utilised pass it (as does also the element given in [42]), which is expected even though it contradicts the results in the literature [36, 40]. For the highest-order elements T10 and Q16, however, the amount of data provided on the boundary has not been sufficient and four additional internal nodes have had to be additionally prescribed the field values to pass it. Concerning the family of elements with linked interpolation, T3LI(PG) and Q4LI(PG) fail to pass this test, while all the higher-order elements pass it. The results of the third test for the elements which do not pass it are presented in Table 3.4. Even though this patch test is not satisfied for the lower-order elements of finite size, we consider that all the proposed elements satisfy the convergence criteria since, as argued earlier, they are able to reproduce exactly any state of constant stress.

Table 3.4: Results for Patch test 3 [36]

(a) Displacements at node 6 and stresses in Gauss point at (0.0933, 0.006667)

Element	$u \cdot 10^{-3}$	$v \cdot 10^{-3}$	$\varphi \cdot 10^{-3}$	σ_{11}	σ_{12}	σ_{21}	μ_{31}	μ_{32}
T3	0.195	0.210	0.400	4.00	1.59	1.41	0.04	-0.040
T3LI(PG)	0.194	0.205	0.401	4.01	1.54	1.36	0.04	-0.041
Exact	0.195	0.210	0.400	4.00	1.59	1.41	0.04	-0.040

(b) Displacements at node 6 and stresses in Gauss point at (0.176027, 0.0281456)

Element	$u \cdot 10^{-3}$	$v \cdot 10^{-3}$	$\varphi \cdot 10^{-3}$	σ_{11}	σ_{12}	σ_{21}	μ_{31}	μ_{32}
Q4	0.1950	0.210	0.400	4.00	1.65	1.35	0.0400	-0.040
Q4LI(PG)	0.1946	0.205	0.401	4.03	1.70	1.44	0.0404	-0.038
Exact	0.1950	0.210	0.400	4.00	1.65	1.35	0.0400	-0.040

3.4.3 Stress concentration around a circular hole

To analyse the influence of the micropolar effect in a homogeneous and isotropic linear elastic solid, the so-called Kirsch problem [73] – an infinite plate with a circular hole subject to uniform tension – is considered next. We focus on the so-called *stress-concentration factor (K_t)* – the ratio between a maximum longitudinal stress at the edge of the hole and the applied surface loading. The classical theory predicts a constant stress concentration factor equal to three regardless of the hole size and the material parameters, i.e. $K_{t,CC} = \dfrac{\sigma_{max}}{\sigma_{avg}} = 3$ where σ_{max} is the maximum stress in the vicinity of the hole and σ_{avg} is the average stress in the sections far from the hole, as shown in Figure 3.9.
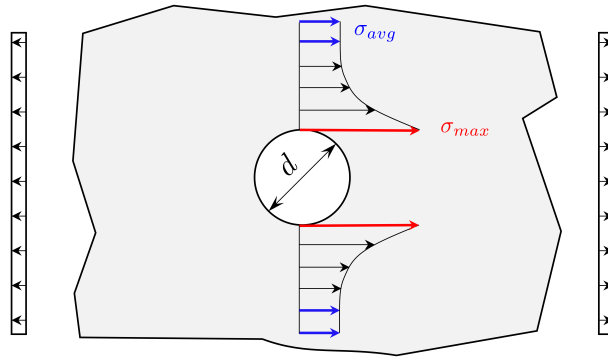
Figure 3.9: Distribution of stresses around a hole in an infinite plate – Kirsch problem

Experimental tests, e.g. [8], however, indicate a smaller stress-concentration factor than that. To model the Kirsch problem correctly, additional effects have to be taken into account, which is possible using the micropolar theory. The analytical solution of the problem using the micropolar theory [13], however, is dependent on the hole radius r, the coupling number N and the characteristic length l of the material and it returns the stress-concentration factor which is increasingly smaller than the one obtained by the classical theory as the diameter of the hole decreases.

In our numerical analysis, the plate is necessarily taken to be of a finite size and only a quarter of the plate is analysed. The square quarter is taken to be of unit thickness, $L = 16.2$ mm long and with a hole of radius $r = 0.216$ mm subject to uniform uniaxial tension $p_{sx} = 1$ N/mm² acting on one of its undented sides. The micropolar material parameters $\mu = 76923.1$ N/mm², $\lambda = 115385.0$ N/mm², $\beta = \gamma = 6352.25$ N, which correspond to the modulus of elasticity $E = 200000$ N/mm², Poisson's ratio $n = 0.3$ and a characteristic length $l = r/1.063 = 0.2031984948$ m are taken from [36]. The value of the micropolar material parameter ν is varied (indicating a variation in the coupling number N). The normal displacements and the microrotations along the dented sides are restrained. It is important to note that, since we are only analysing a quarter of the

plate, without restraining the microrotations the numerical results would not converge to the analytical solution given in [13].

(a) Triangular elements   (b) Quadrilateral elements
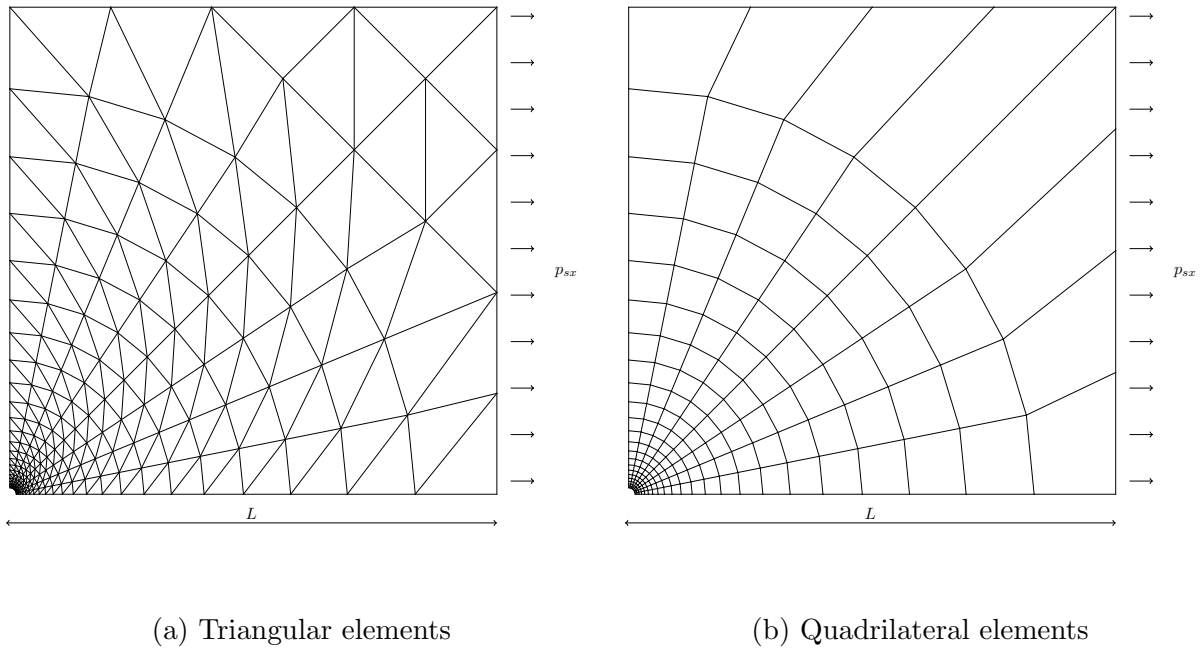
Figure 3.10: Finite-element mesh for the Kirsch problem

The results obtained by the proposed triangular and quadrilateral elements with linked interpolation are compared to those obtained by the finite elements with standard Lagrangian interpolation. The finite element meshes for triangular and quadrilateral elements, shown in Figure 3.10, consist of 360 and 176 elements, respectively, and are generated using software GMSH [74]. In the structured part of the mesh the finite elements project radially from the hole and are embedded within 22 concentric circles propagating in geometric progression with ratio between the radial increments of 1.2. The part of the mesh between the outermost band of the elements between the concentric circles and the undented edges is defined manually. The input file for GMSH can be found in the Appendix C.

The stresses are observed in the element containing the stress-concentration point P=(0.0, 0.216), where the analytical solution is provided. To avoid extrapolation of the computed stresses, the stress values for the numerical simulation are given at Gauss points closest to the edge of the hole, not at the exact edge, thus they can never exactly match the analytical result. For easier comparison with [36] the chosen integration for all triangular elements is 7 Gauss integration points per element, which brings us closer to the edge, where the analytical solution and Providas and Kattis's solutions are given. Considering quadrilateral finite elements, the minimum order of integration needed is used, i.e. 3×3 for order 1 elements, 4×4 for order 2 elements and 5×5 for order 3 elements. The Gauss points monitored have the co-ordinates equal to GP1=(0.00251643, 0.243476),

GP2=(0.0199002, 0.218483) and GP3=(0.0198966, 0.21843) for the triangular elements, and GP4=(0.0048953, 0.222164), GP5=(0.00300768, 0.220075) and GP6=(0.00201581, 0.218758) for the rectangular elements. The results for the stresses obtained using the triangular and the quadrilateral elements are shown in Tables 3.5 and 3.6, respectively.

Table 3.5: Triangular elements: Stress-concentration factor K_t

N	ν	K_t, [13]	Element	K_t, GP1	Element	K_t, GP2	Element	K_t, GP3
0.0	0.0	3.00	T3	2.846	T6	2.865	T10	2.849
			T3LI(PG)	2.846	T6LI	2.897	T10LI(PG)	2.849
0.25	5130.77	2.849	T3	2.737	T6	2.729	T10	2.715
			T3LI(PG)	2.740	T6LI	2.729	T10LI(PG)	2.715
0.50	25 638.5	2.555	T3	2.508	T6	2.466	T10	2.454
			T3LI(PG)	2.514	T6LI	2.466	T10LI(PG)	2.454
0.75	98 900.0	2.287	T3	2.267	T6	2.228	T10	2.219
			T3LI(PG)	2.273	T6LI	2.228	T10LI(PG)	2.219
0.90	327 938.0	2.158	T3	2.101	T6	2.117	T10	2.108
			T3LI(PG)	2.109	T6LI	2.117	T10LI(PG)	2.108

The numerical results for all the elements show that with the micropolar effect increased (through the coupling number N) the stress-concentration factor is reduced, as predicted theoretically. The predictive power of all the elements, however, decreases as the coupling number increases.

Table 3.6: Quadrilateral elements: Stress-concentration factor K_t

N	ν	K_t, [13]	Element	K_t, GP4	Element	K_t, GP5	Element	K_t, GP6
0.0	0.0	3.00	Q4	2.904	Q9	2.911	Q16	2.916
			Q4LI(PG)	2.904	Q9LI(PG)	2.911	Q16LI(PG)	2.916
0.25	5130.77	2.849	Q4	2.768	Q9	2.769	Q16	2.774
			Q4LI(PG)	2.769	Q9LI(PG)	2.769	Q16LI(PG)	2.774
0.50	25 638.5	2.555	Q4	2.496	Q9	2.492	Q16	2.498
			Q4LI(PG)	2.497	Q9LI(PG)	2.492	Q16LI(PG)	2.498
0.75	98 900.0	2.287	Q4	2.236	Q9	2.240	Q16	2.248
			Q4LI(PG)	2.236	Q9LI(PG)	2.240	Q16LI(PG)	2.248
0.90	327 938.0	2.158	Q4	2.104	Q9	2.119	Q16	2.129
			Q4LI(PG)	2.104	Q9LI(PG)	2.119	Q16LI(PG)	2.129

With the higher-order elements of both the triangular and the quadrilateral type, the linked-interpolation elements' behaviour is in this example exceedingly close to that of

the standard elements, i.e. these elements do not contribute to the faster convergence rate. In such a highly tension-dominated problem, expectedly, the linked-interpolation (incorporating polynomials of order 2 and higher) is not needed. Also, the stress values for the numerical simulation are given at Gauss points closest to the edge of the hole (whose position differs depending on the integration order) not at the exact edge, thus they can never exactly match the analytical result. Interestingly, the higher-order linked-interpolation element T6LI does behave marginally better than its Lagrangian counterparts when there is no micropolar effect present. With the low-order triangular elements, the linked-interpolation slightly improves the accuracy, this time however with an increasing micropolar effect. This behaviour is not observed in the low-order quadrilateral elements, though. Finally, as in [36], it is observed that in the triangular elements, depending on the value of the micropolar effects, the higher-order elements often produce results of lower accuracy than the low-order elements. This effect, however, is not observed in the quadrilateral elements.

By refining the finite element mesh in the vicinity of the hole, we expect to get closer to the analytical solution, due to two reasons. The first one is the expected convergence as a consequence of the mesh refinement, being in the spirit of the finite element method, while the second one lays in the simple fact that, as we refine the mesh in the vicinity of the hole, the position of the integration point also tends to the edge, where the analytical solution is provided. In order to demonstrate this, the problem is additionally solved using Q4LI(PG) by retaining the same number of elements, but by increasing the ratio between the radial increments in the mesh which makes the mesh finer in the vicinity of the hole. The ratios are chosen as 1.5 and 1.8 and the results for stresses are observed in Gauss points GP7 = (0.00475192, 0.215653) and GP8 = (0.00474938, 0.215536) and presented in Table 3.7. We can see that the obtained results are closer to the analytical solution due to the reasons mentioned above.

Table 3.7: Quadrilateral element Q4LI(PG): Stress-concentration factor K_t for meshes of different densities around the hole

| N | K_t, [13] | ratio = 1.2 | ratio = 1.5 | ratio = 1.8 |
		K_t, GP4	K_t, GP7	K_t, GP8
0.0	3.00	2.904	2.922	2.992
0.25	2.849	2.769	2.785	2.849
0.50	2.555	2.497	2.512	2.562
0.75	2.287	2.236	2.257	2.291
0.90	2.158	2.104	2.128	2.152

3.4.4 A cantilever beam subject to pure bending in 2D – higher-order patch test

In an attempt to determine the micropolar material constants experimentally, the analytical solution for stresses, displacements and microrotations of a micropolar elastic plate subject to pure bending has been derived by Gauthier and Jahsman [1]. Timoshenko and Goodier [75] showed that in three-dimensional classical elasticity, a plate subject to edge moments M_z acting per unit length will in general be deformed into an anticlastic shape. When transverse load is applied, the bending deformation occurs not only in the longitudinal direction, but also in the transverse direction, due to the Poisson's effect. This is defined as an anticlastic deformation.
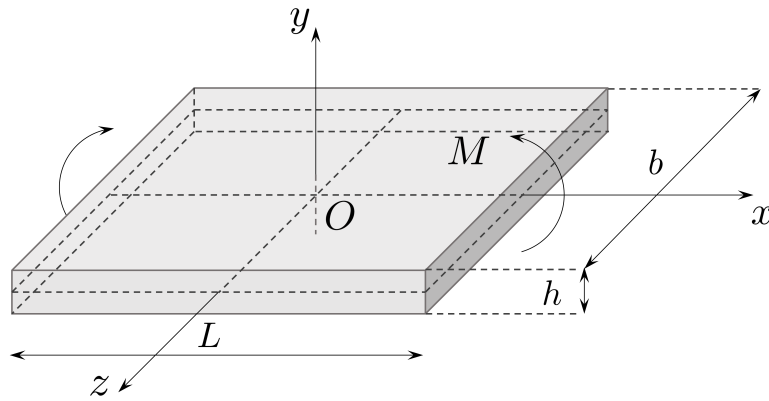
Figure 3.11: Bending of a plate

In the work of Gauthier and Jahsman the plate bending problem of length L, height h and thickness b, shown in Figure 3.11, is analysed by assuming lateral boundary conditions which prevent anticlastic distortion, turning it into cylindrical plane-strain bending problem. In other words, the only admissible displacements are $u_x(x,y)$ (denoted as $u(x,y)$ for the present 2D analysis) and $u_y(x,y)$ (denoted as $v(x,y)$ for the present 2D analysis) and the only admissible microrotation is $\varphi_z(x,y)$ (denoted as $\varphi(x,y)$ for the present 2D analysis). Furthermore, Gauthier and Jahsman imposed the requirement that the stresses and couple stresses are functions of y only, leading to a constant stress distribution in the x direction, and a linearly varying distribution in the y direction. Thus, the non-vanishing stresses are σ_{xx}, σ_{zz}, μ_{zx} and μ_{xz}.

We analyse a specimen of length L, thickness b and height h placed in the xy plane with x as its axis of centroids and assume an applied loading resulting in an in-plane bending moment M acting on the sides of the specimen orthogonal to the x-axis, as shown in Figure 3.12. While in the classical elasticity the only way to subject the specimen to

pure bending is via a linearly varying normal surface traction $p_{sx} = \frac{2y}{h}p_0$, Gauthier and Jahsman have shown that in the micropolar continuum the state of pure bending requires *both*, such a traction *and* a constant surface moment m_{sz} acting on the same sides of the specimen, i.e. $M = b \int_{-\frac{h}{2}}^{\frac{h}{2}}(y\,p_{sx} + m_{sz})dy$. Moreover, in order to produce pure bending of the specimen they have to be applied in *a unique proportion* given as

$$\frac{m_{sz}}{p_0} = \frac{1}{h}\frac{(\lambda + 2\mu)(\beta + \gamma)}{2\mu(\lambda + \mu)} \equiv \frac{h}{6}(1 - n)\delta, \tag{3.38}$$

with Poisson's coefficient n and $\delta = 24(l_b/h)^2$. Obviously, for a material with vanishing characteristic length $(l_b \to 0)$ the state of pure bending may not be achieved if the surface moment loading is present, while for a general micropolar material such a state is only possible when m_{sz} and p_0 are given in the proportion defined above resulting in $M = p_0 W_z + m_{sz}A$ with $A = bh$ and $W_z = bh^2/6$. As a result,

$$p_0 = -\frac{1}{1 + (1 - n)\delta}\frac{M}{W_z}, \quad m_{sz} = \frac{(1 - n)\delta}{1 + (1 - n)\delta}\frac{M}{A}, \tag{3.39}$$

the only non-vanishing stress components are

$$\sigma_{xx} = -\frac{1}{1 + (1 - n)\delta}\frac{M}{W_z}\frac{2y}{h}, \quad \mu_{zx} = \frac{(1 - n)\delta}{1 + (1 - n)\delta}\frac{M}{A}, \tag{3.40}$$

and, for the specimen fixed at the origin of the co-ordinate system, the displacement and rotation fields are

$$\varphi = \frac{1}{1 + (1 - n)\delta}\frac{Mx}{bD}, \quad u = -\frac{1}{1 + (1 - n)\delta}\frac{Mxy}{bD}, \tag{3.41}$$

$$v = \frac{1}{2}\frac{1}{1 + (1 - n)\delta}\frac{M}{bD}\left(x^2 + \frac{n}{1 - n}y^2\right), \tag{3.42}$$

where $D = \frac{Eh^3}{12(1-n^2)}$ is the flexural rigidity. This problem does not induce any non-symmetry in the stress tensor field, i.e. the solution does not depend on the coupling number N (and therefore also on the material parameter ν). For $l_b \to 0$, the classical solution is approached in all fields.

The numerical modelling of this problem is often misinterpreted in the literature, where authors often apply the external loading using only one of the surface tractions (e.g. [49], [39]) and compare the obtained numerical results against the analytical pure-bending solution, even though such loading cannot yield a pure bending state. If the precisely defined external loading proportion is not respected (equation (3.38), by refining the finite element mesh we converge to another, significantly different solution.

The solution demonstrates that all fields are obtained from their respective values in classical elasticity as *multiplied by the factor* $\frac{1}{1+(1-n)\delta}$, i.e. bending stiffness in micropolar elasticity increases with an increase in the material characteristic length l_b. In engineering

terms, bending resistance is not anymore proportional to the height of the specimen squared and we say that the micropolar elasticity exhibits the so-called *size-effect* with the solution increasingly departing from the classical solution when the characteristic length reaches the order of magnitude of a representative dimension of the specimen.
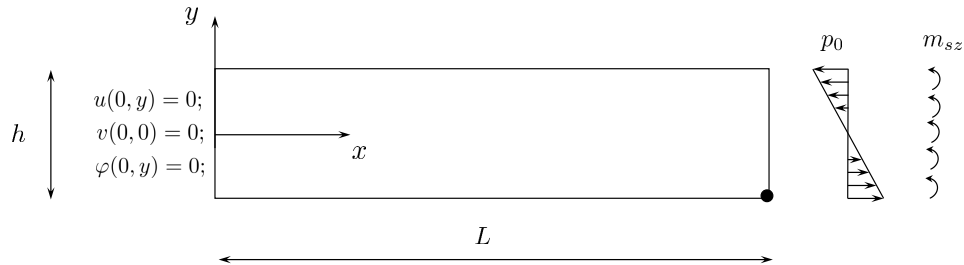
Figure 3.12: Cantilever beam subject to pure bending

The problem described (see Figure 3.12) is analysed using quadrilateral and triangular elements of different order, using both the proposed linked interpolation and the Lagrangian interpolation. The problem is solved while varying the value of the characteristic length $l_b = \frac{1}{2}\sqrt{\frac{\beta + \gamma}{G}}$, $l_b \in [0.1, 1.8]$ to capture the size-effect. The resultant bending moment $M = 20$ Nm is applied through a linearly varying surface loading and a constant surface moment as described above and summarised in Table 3.8. For the problem analysed, the analytical values of the external loading as a function of the characteristic length l_b are presented in Figure 3.13, where we can see that by increasing the characteristic length l_b, the contribution of p_0 in the external moment rapidly decreases, while the contribution of m_{sz} increases. In other words, when $l_b \to \infty$ the external moment is taken over by the distributed surface moment only, i.e. $p_0 = 0 \frac{\text{N}}{\text{m}^2}$, $m_{sz} = 10 \frac{\text{Nm}}{\text{m}^2}$, while for $l_b \to 0$ it is taken over by the linearly varying surface moment only, i.e. $p_0 = 30 \frac{\text{N}}{\text{m}^2}$, $m_{sz} = 0 \frac{\text{Nm}}{\text{m}^2}$.
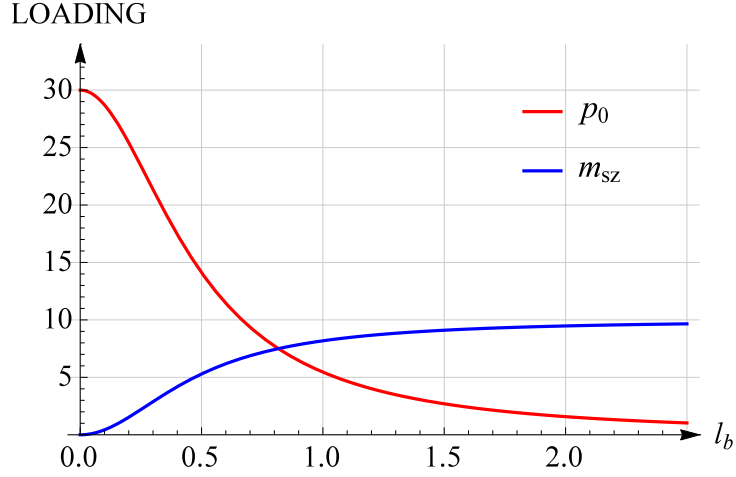
LOADING

Figure 3.13: Distributed external loading as a function of the characteristic length l_b

The distributed loading is applied through corresponding concentrated nodal forces and moments obtained by integration as defined in equation (3.5).

Table 3.8: Analytical values of the external loadings p_0 and m_{sz} as defined in (3.39) for different values of the characteristic length l_b and fixed values of the Poisson's coefficient and height of the cantilever, together giving the total external moment $M = 20$ Nm

l_b/h	l_b	$\beta + \gamma$	p_0	m_{sz}
0.05	0.1	24.0	28.708 133 971 291 860	0.430 622 009 569 378
0.15	0.3	216.0	21.352 313 167 259 780	2.882 562 277 580 070
0.30	0.6	864.0	11.450 381 679 389 320	6.183 206 106 870 228
0.60	1.2	3 456.0	4.010 695 187 165 778	8.663 101 604 278 070
0.90	1.8	7 776.0	1.925 545 571 245 185	9.358 151 476 251 610

The length of the cantilever is taken as $L = 10$ m, the height is $h = 2$ m and the engineering material parameters are $E = 1500$ N/m^2 and $n = 0.25$ which give the Lamé constants $\mu = 600$ N/m^2 and $\lambda = 600$ N/m^2. The material parameter $\nu = 200$ N/m^2 depends on the value of the coupling number, which is, in this example, chosen to be equal to $N = 0.5$, but in this example can have an arbitrary value, as discussed above. Along the left-hand edge of the cantilever all the horizontal displacements and microrotations are restrained. The vertical displacement at the left-hand edge is restrained only at the cantilever axis in order to preserve the symmetry of the system. Gauthier's and Jahsman's analytical solution is derived by assuming that the boundary value problem is symmetric, which has to be respected in order to obtain the analytical solution. Furthermore, because of the existence of external moment loads m_{sz} which have to be taken over as reactions along the clamped part, all microrotations along the left-hand edge have to be restrained.

(a) Q4 elements   (b) Q9 elements

(c) Q16 elements
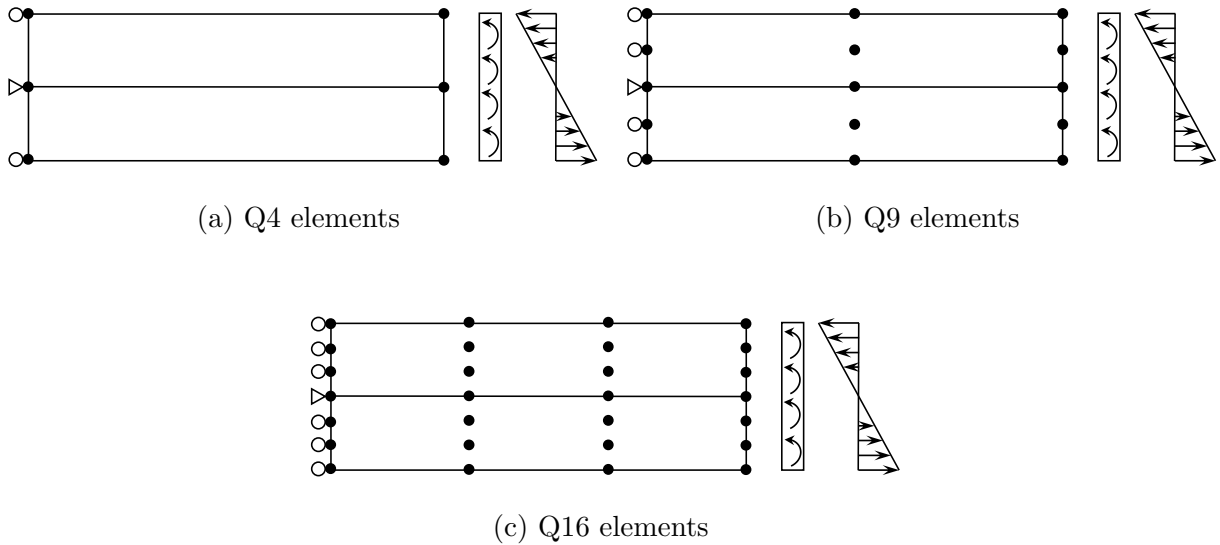
Figure 3.14: Quadrilateral finite element mesh, loading and boundary conditions

(a) T3 elements   (b) T6 elements

(c) T10 elements
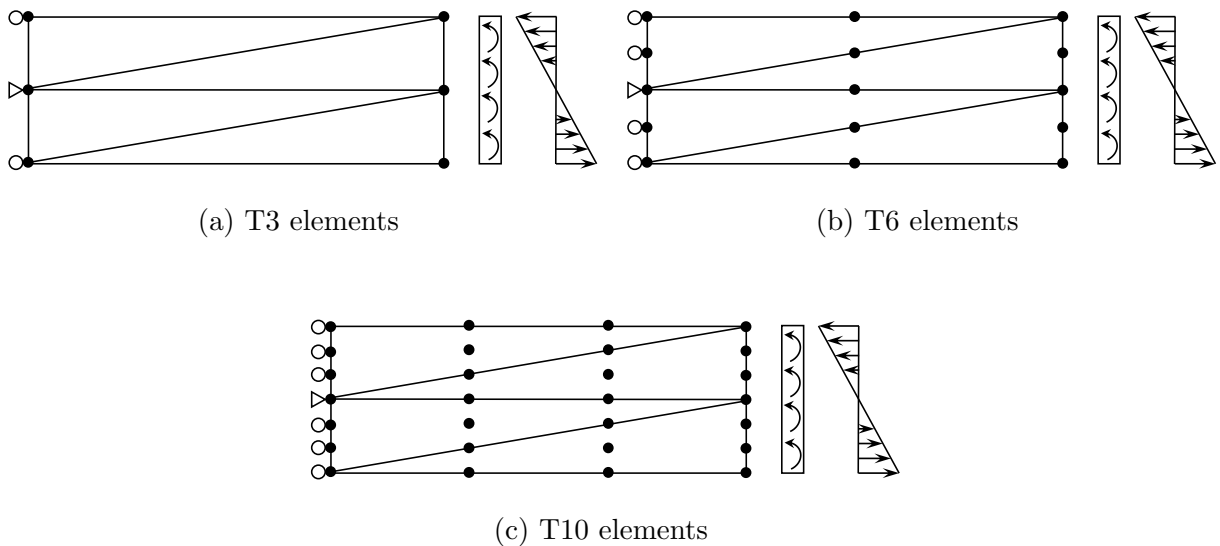
Figure 3.15: Triangular finite element mesh, loading and boundary conditions

The problem is solved using a mesh of two quadrilateral or four triangular elements of different order shown in Figures 3.14 and 3.15. The left-hand side nodes in the higher-order elements are restrained in the same way as the corner nodes. The results for the vertical displacement and microrotation v and φ at the bottom right-hand node and the stress σ_{xx} in the Gauss point nearest to this node obtained by the quadrilateral elements Q4 are compared to the analytical solution in Table 3.9 and Figure 3.16, while the same results obtained by the triangular elements T3 are shown in Table 3.10 and Figure 3.19.

Table 3.9: Results obtained using two quadrilateral elements (Q4), 3x3 integration points,
GP = (8.887298, -0.887298), A – Analytical solution, N – Numerical solution

Element	l_b/h	A v	N v	Error [%]	A φ	N φ	Error [%]	A $\sigma_{xx,GP}$	N $\sigma_{xx,GP}$	Error [%]
Q4	0.05	0.90012	0.06892	92.3	0.17943	0.01269	92.9	25.47267	2.22127	91.3
Q4LI(PG)			0.87402	2.9		0.17426	2.9		26.08884	2.4
Q4	0.15	0.66948	0.06740	89.9	0.13345	0.01296	90.3	18.94586	2.08130	89.0
Q4LI(PG)			0.65566	2.1		0.13071	2.1		19.56450	3.2
Q4	0.30	0.35902	0.06203	82.7	0.07157	0.01261	82.4	10.15990	1.88150	81.5
Q4LI(PG)			0.35518	1.1		0.07082	1.0		10.59720	4.1
Q4	0.60	0.12575	0.04624	63.2	0.02507	0.00978	70.0	3.55870	1.29741	65.5
Q4LI(PG)			0.12527	0.4		0.02498	0.4		3.73716	4.8
Q4	0.90	0.06037	0.03234	46.4	0.01204	0.00691	42.6	1.70853	0.89668	47.5
Q4LI(PG)			0.06025	0.2		0.01202	0.2		1.79747	4.9

(a) End node vertical displacements

(b) End node microrotation

(c) Stresses in Gauss point
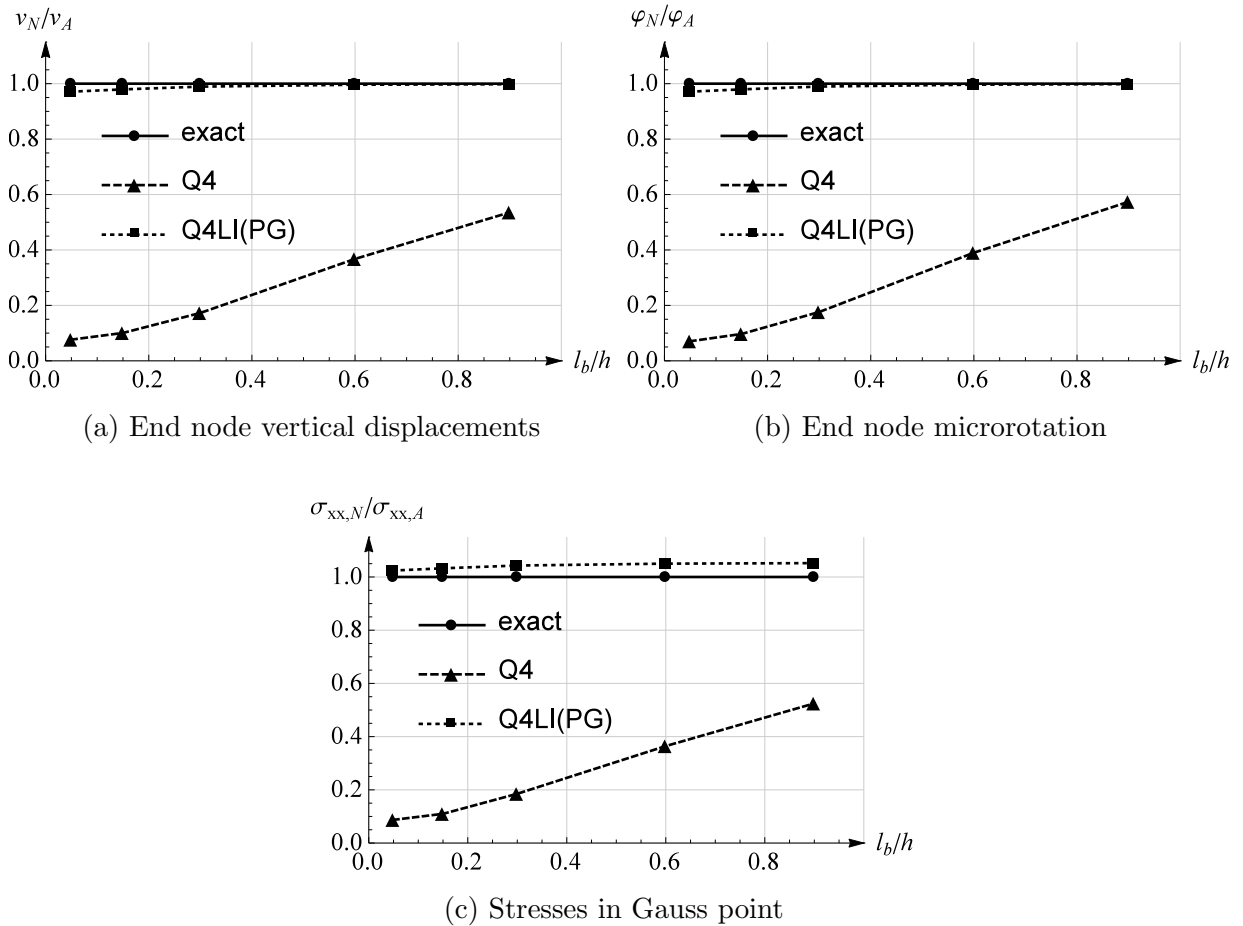
Figure 3.16: Cantilever beam subject to pure bending - Q4 elements

From Table 3.9 and Figure 3.16 we can see that Q4LI(PG) significantly improves the results of the conventional Lagrange Q4 element, in particular for the problems with exisiting, but less pronounced, micropolar effect. More precisely, for the smallest micropolar effects (i.e. $l_b/h = 0.05$) the error produced by the standard Q4 element is in average 92.2 %, while the error produced by the newly presented element Q4LI(PG) is in average 2.7%. For the largest micropolar effects (i.e. $l_b/h = 0.90$) the error produced by the standard Q4 element is in average 45.5 %, while the error produced by the newly presented element Q4LI(PG) is in average 1.8%, comparing against the analytical solution. In other words, the element Q4LI(PG) predicts the analytical solution significantly more accurate than the standard Q4 element. Furthermore, we want to point out that this improvement is accomplished without introducing additional (internal) nodes and degrees of freedom. Since the solution of Gauthier's and Jahsman's pure bending problem is describable by a quadratic polynomial, the use of the conventional quadrilateral Lagrangian finite elements of order 2 is sufficient to obtain the analytical solution. Consequently, as expected the quadrilateral Petrov-Galerkin linked interpolation finite elements of higher-order also reproduce the analytical solution to the level of computer accuracy. This is shown in Figures 3.17 and 3.18.

(a) End node vertical displacements

(b) End node microrotation

(c) Stresses in Gauss point
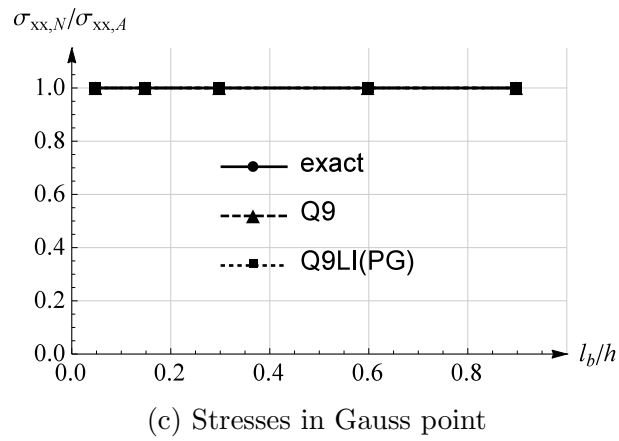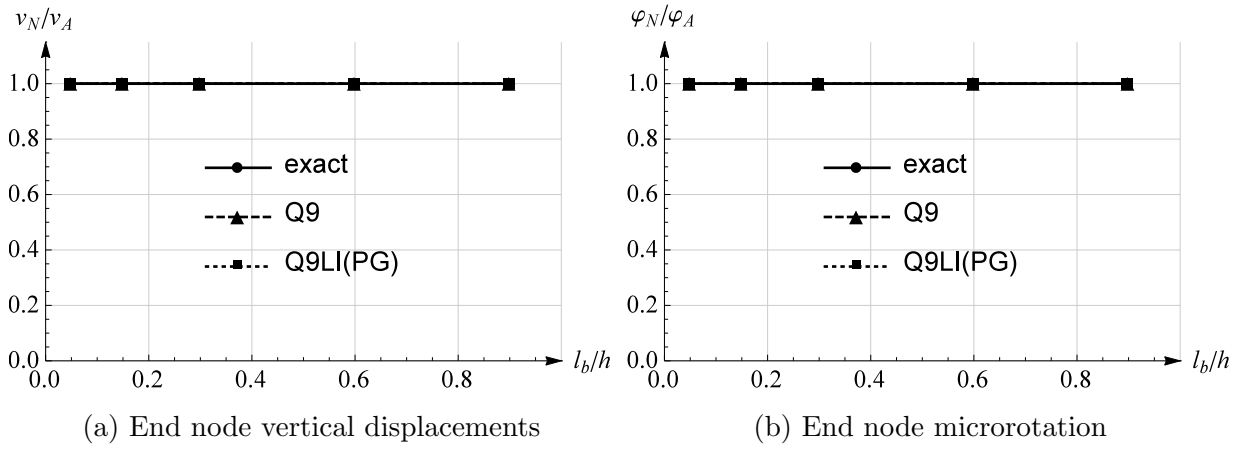
Figure 3.17: Cantilever beam subject to pure bending - Q9 elements

(a) End node vertical displacements

(b) End node microrotation

(c) Stresses in Gauss point
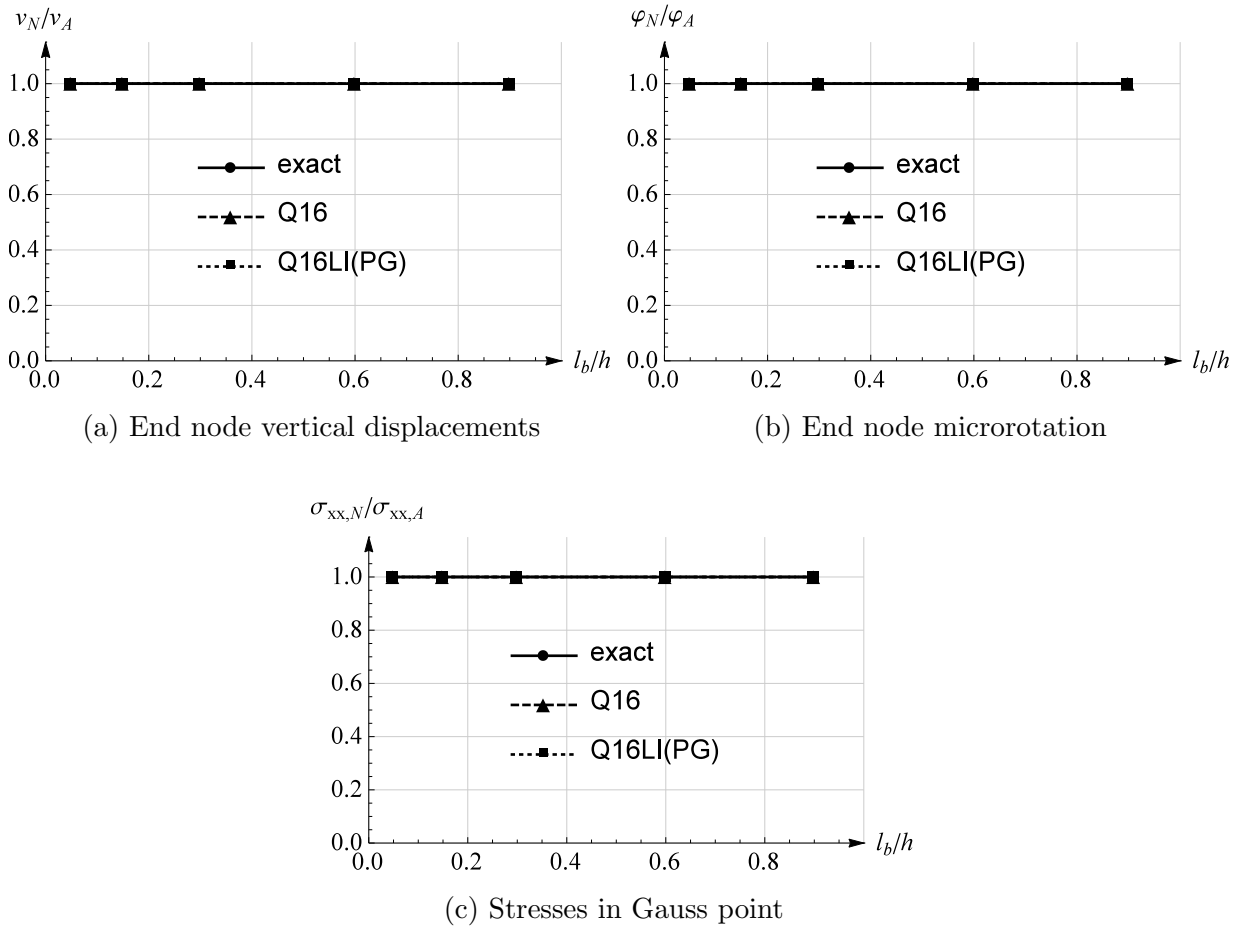
Figure 3.18: Cantilever beam subject to pure bending - Q16 elements

The improvement due to the linked interpolation in low-order triangulars is also present but it is far less significant than in the low-order quadrilaterals. More precisely, for the smallest micropolar effects (i.e. $l_b/h = 0.05$) the error produced by the standard T3 element is in average 97.2 %, while the error produced by the newly presented element T3LI(PG) is just around 8% smaller, i.e. 89.5% in average . By increasing the micropolar effects, the produced error decreases. For the largest micropolar effects (i.e. $l_b/h = 0.90$) the standard T3 element produces in average an error of 68.9 %, while the error produced by the newly presented element T3LI(PG) is half that value, i.e. 35.4% in average, comparing against the analytical solution. The reason why a significant enhancement as observed in the quadrilateral element in not achieved could lay in the strong locking character of the T3 element type, which is already highlighted in the classical [67] and micropolar [49] finite element analysis. Nevertheless, this type of element entails relatively low computational effort and is suitable in specific applications (e.g. error estimates in re-meshing) which is the reason why it should not be neglected. Moreover, this small improvement due to the linked interpolation could in such cases be beneficial.

Table 3.10: Results obtained using four triangular elements (T3), 7 integration points, GP=(5.29858, -0.9402841), A – Analytical solution, N – Numerical solution

Element	l_b/h	A v	N v	Error [%]	A φ	N φ	Error [%]	A $\sigma_{xx,GP}$	N $\sigma_{xx,GP}$	Error [%]
T3	0.05	0.90012	0.02359	97.4	0.17943	0.00542	97.0	26.9938	0.7583	97.2
T3LI(PG)			0.07463	91.7		0.01737	90.3		3.6797	86.4
T3	0.15	0.66948	0.02518	96.2	0.13345	0.00586	95.6	20.0772	0.7166	96.4
T3LI(PG)			0.08089	87.9		0.01765	86.8		2.8406	85.9
T3	0.30	0.35902	0.02645	92.6	0.07157	0.00650	90.9	10.7666	0.6447	94.0
T3LI(PG)			0.08296	76.9		0.01807	74.8		2.5249	76.5
T3	0.60	0.12575	0.02367	81.2	0.02507	0.00604	75.9	3.7712	0.5156	86.3
T3LI(PG)			0.05967	52.5		0.01307	47.9		1.7067	54.7
T3	0.90	0.06037	0.01891	68.7	0.01204	0.00487	60.0	1.8106	0.3993	77.9
T3LI(PG)			0.03844	36.3		0.00844	29.9		1.0842	40.1

(a) End node vertical displacements

(b) End node microrotation

(c) Stresses in Gauss point
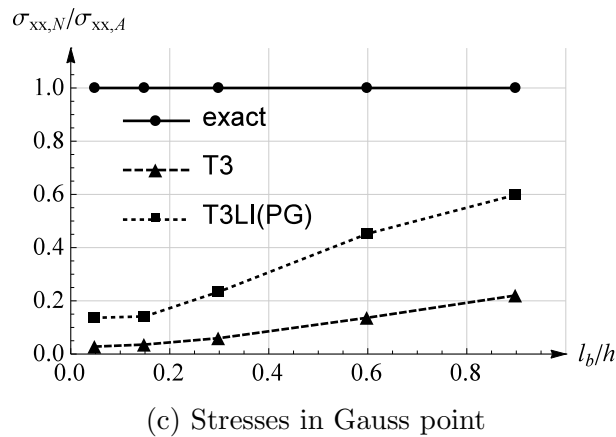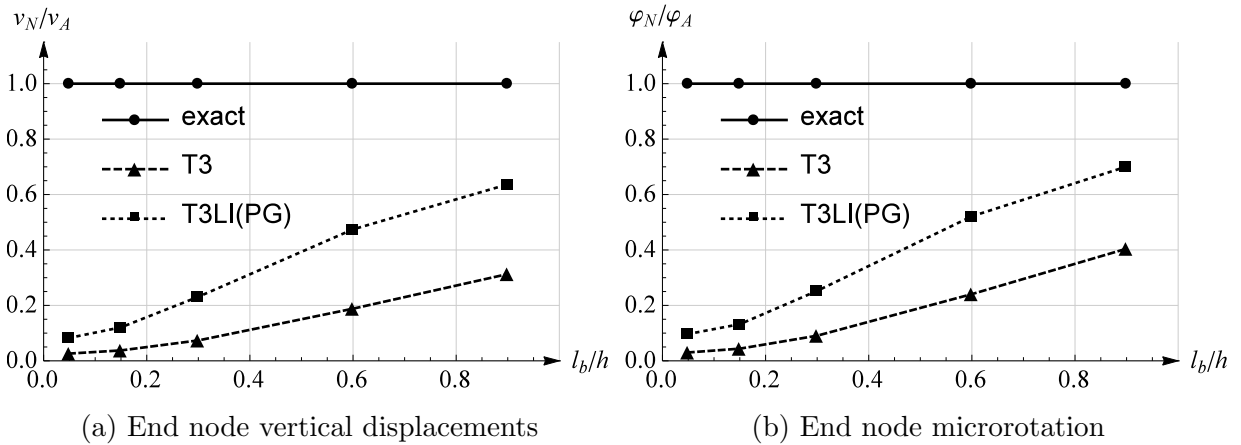
Figure 3.19: Cantilever beam subject to pure bending - T3 elements

As discussed before, the higher-order triangulars with both the Lagrangian interpolation as well as those with the Petrov-Galerkin linked interpolation again provide the analytical result, as expected, which is shown in Figures 3.20 and 3.21. However, when the Petrov-Galerkin interpolation in six-node triangulars is switched off (note that in these elements the Petrov-Galerkin interpolation is not necessary for convergence), the results deteriorate by at most 0.025% (for $l_b/h = 0.05$), the errors reducing rapidly as l_b/h increases and falling to below 0.003% for $l_b/h = 0.30$. The results are shown in Table 3.11.

Table 3.11: Results obtained using four triangular elements with six nodes (T6), 7 integration points, boundary conditions and loading as in Figure 3.15b, GP (5.29858,-0.9402841), A = Analytical, N = Numerical

Element	l_b/h	A v	N v	A φ	N φ	A $\sigma_{xx,GP}$	N $\sigma_{xx,GP}$
T6			0.90012		0.17943		26.9938
T6LI	0.1	0.900120	0.90066	0.179426	0.17986	26.9938	27.0008
T6LI(PG)			0.90012		0.17943		26.9938
T6			0.66948		0.13345		20.0772
T6LI	0.3	0.669484	0.66957	0.133452	0.13350	20.0772	20.0784
T6LI(PG)			0.66948		0.13345		20.0772
T6			0.35902		0.071565		10.7666
T6LI	0.6	0.359017	0.35903	0.0715649	0.071572	10.7666	10.7669
T6LI(PG)			0.35902		0.071565		10.7666
T6			0.12575		0.025067		3.81865
T6LI	1.2	0.125752	0.12575	0.0250668	0.025067	3.77119	3.77124
T6LI(PG)			0.12575		0.025067		3.81865
T6			0.060374		0.012035		1.81056
T6LI	1.8	0.0603739	0.060374	0.0120347	0.012035	1.81056	1.81057
T6LI(PG)			0.060374		0.012035		1.81056

(a) End node vertical displacements

(b) End node microrotation

(c) Stresses in Gauss point
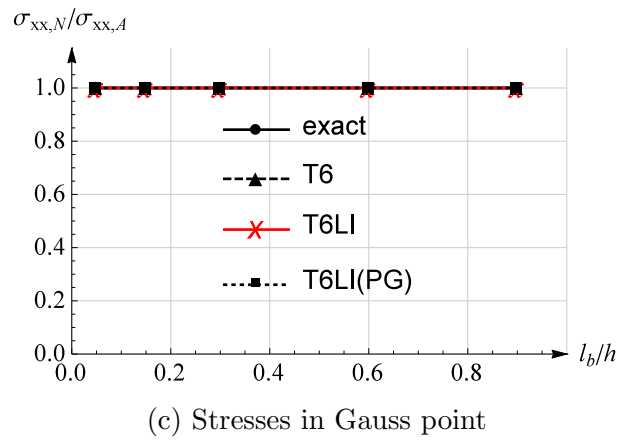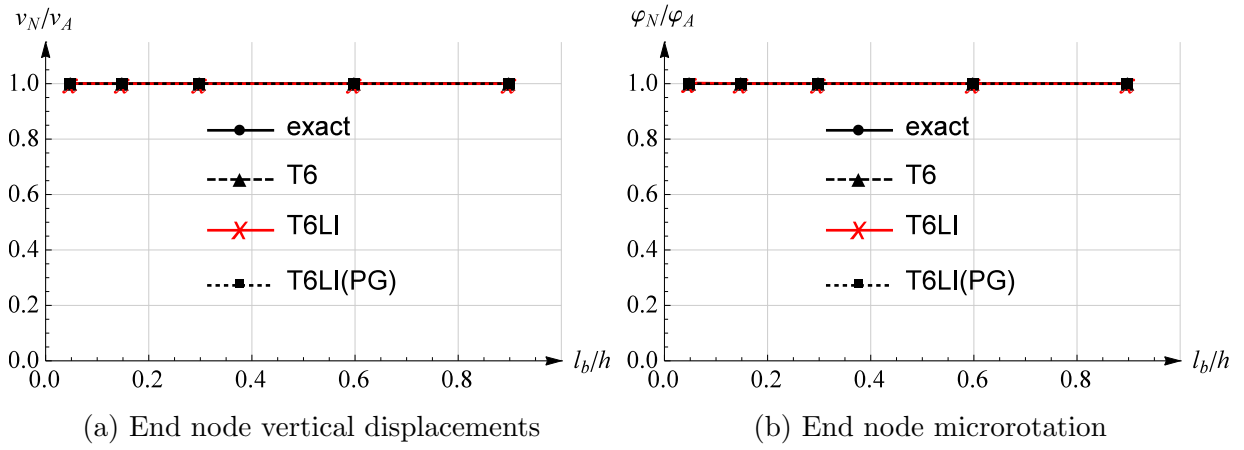
Figure 3.20: Cantilever beam subject to pure bending - T6 elements

(a) End node vertical displacements

(b) End node microrotation

(c) Stresses in Gauss point
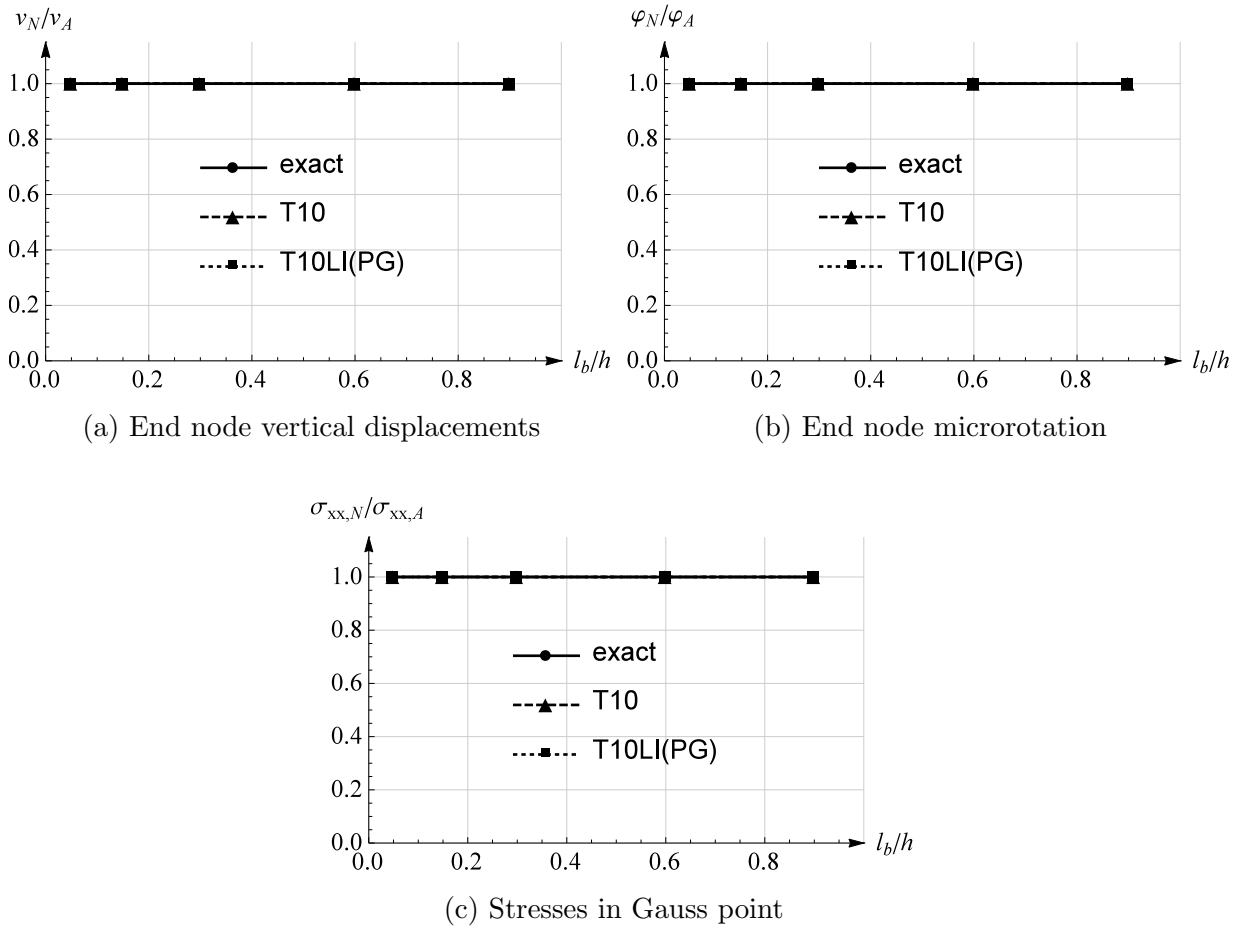
Figure 3.21: Cantilever beam subject to pure bending - T10 elements

Next we analyse h-convergence of the first-order elements with Lagrange and linked interpolation by modelling the same problem shown in Figure 3.12 for low $l_b/h = 0.05$ and high $l_b/h = 0.90$ micropolar effects. We perform the analysis on a number of meshes with equal number of uniform elements per length and height of the specimen and show the results in Table 3.12. We can see that Q4LI(PG) has a faster convergence rate than the Q4 element, but both elements converge to the exact solution. Again the comparative advantage of the linked-interpolation elements is more obvious for the lower value of l_b/h.

Table 3.12: h-convergence of first order quadrilateral elements for $l_b/h = 0.05$ and $l_b/h = 0.9$, 3×3 integration points used

Element	Mesh size	$l_b/h = 0.05$		$l_b/h = 0.9$	
		v	φ	v	φ
Q4	2×2	0.22336	0.04233	0.04976	0.01010
Q4LI(PG)		0.87402	0.17426	0.06024	0.01201
Q4	4×4	0.51163	0.09735	0.05730	0.01148
Q4LI(PG)		0.89340	0.17803	0.06034	0.01203
Q4	16×16	0.85921	0.16939	0.06017	0.01200
Q4LI(PG)		0.89970	0.17933	0.06037	0.01203
Q4	32×32	0.88951	0.17666	0.06032	0.01203
Q4LI(PG)		0.90001	0.17940	0.06037	0.01204
Q4	64×64	0.89744	0.17871	0.06036	0.01203
Q4LI(PG)		0.90009	0.17942	0.06037	0.01204
Q4	128×128	0.89945	0.17924	0.06037	0.01203
Q4LI(PG)		0.90011	0.17942	0.06037	0.01204
Q4	256×256	0.89995	0.17938	0.06037	0.01204
Q4LI(PG)		0.90012	0.17943	0.06037	0.01204
EXACT		0.90012	0.17943	0.06037	0.01204

As for the quadrilaterals, the h-refinement is also performed for the triangular elements of first order with Lagrange and linked interpolation. Even though the contribution of linked interpolation is small, from Table 3.13 we can see that it contributes to faster convergence rate.

Table 3.13: h-convergence of first order triangular elements for $l_b/h = 0.05$ and $l_b/h = 0.9$, 7 integration points used

Element	Mesh size	$l_b/h = 0.05$		$l_b/h = 0.9$	
		v	φ	v	φ
T3	$2\times2\times2$	0.00882	0.01817	0.03656	0.00813
T3LI(PG)		0.20132	0.04242	0.04976	0.01040
T3	$4\times4\times2$	0.26903	0.05235	0.05162	0.01058
T3LI(PG)		0.48812	0.09885	0.05705	0.01151
T3	$16\times16\times2$	0.78363	0.15460	0.05974	0.01193
T3LI(PG)		0.85617	0.17057	0.06015	0.01200
T3	$32\times32\times2$	0.86781	0.17232	0.06022	0.01205
T3LI(PG)		0.88874	0.17709	0.06032	0.01203
T3	$64\times64\times2$	0.89181	0.17755	0.06033	0.01203
T3LI(PG)		0.89725	0.17883	0.06036	0.01203
T3	$128\times128\times2$	0.89803	0.17895	0.06036	0.01203
T3LI(PG)		0.89940	0.17927	0.06037	0.01203
T3	$256\times256\times2$	0.89960	0.17930	0.06037	0.01203
T3LI(PG)		0.89994	0.17939	0.06037	0.01204
EXACT		0.90012	0.17943	0.06037	0.01204

In order to test the quadrilateral elements shape sensitivity, the cantilever beam problem was solved by modeling a distorted mesh with four elements as shown in Figure 3.22. The mesh distortion was accomplished using a distortion factor a and the behaviour of quadrilateral elements was observed for the distortion factor values $a = 1.0$, $a = 2.0$ and $a = 3.0$. The results for Q4LI(PG) are presented in Tables 3.15, 3.16 and 3.17.
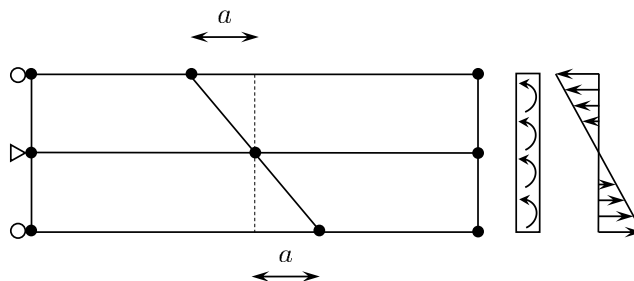
Figure 3.22: Irregular finite element mesh using a distortion factor a using quadrilateral elements

Table 3.14: Results obtained using four quadrilateral elements with four nodes (Q4) with a distortion factor a=0.0, 3×3 integration points, GP = (9.43649, -0.887298), A – Analytical solution, N – Numerical solution

Element	l_b/h	A v	N v	A φ	N φ	A $\sigma_{xx,GP}$	N $\sigma_{xx,GP}$
Q4LI(PG)	0.05	0.90012	0.87101	0.17943	0.29032	25.47267	26.0915
Q4LI(PG)	0.15	0.66948	0.65504	0.13345	0.13068	18.94586	19.5663
Q4LI(PG)	0.30	0.35902	0.35484	0.07157	0.07079	10.15990	10.5874
Q4LI(PG)	0.60	0.12575	0.12522	0.02507	0.02497	3.55870	3.7300
Q4LI(PG)	0.90	0.06037	0.060243	0.01204	0.01201	1.70853	1.7935

Table 3.15: Results obtained using four quadrilateral elements with four nodes (Q4) with a distortion factor a=1.0, 3×3 integration points, GP = (9.53649, -0.887298), A – Analytical solution, N – Numerical solution

Element	l_b/h	A v	N v	A φ	N φ	A $\sigma_{xx,GP}$	N $\sigma_{xx,GP}$
Q4LI(PG)	0.05	0.90012	0.71840	0.17943	0.14379	25.47267	20.9734
Q4LI(PG)	0.15	0.66948	0.61098	0.13345	0.12216	18.94586	18.1872
Q4LI(PG)	0.30	0.35902	0.34811	0.07157	0.06953	10.15990	10.3103
Q4LI(PG)	0.60	0.12575	0.12462	0.02507	0.02487	3.55870	3.69186
Q4LI(PG)	0.90	0.06037	0.06010	0.01204	0.01199	1.70853	1.77886

Table 3.16: Results obtained using four quadrilateral elements with four nodes (Q4) with a distortion factor a=2.0, 3×3 integration points, GP = (9.63649, -0.887298), A – Analytical solution, N – Numerical solution

Element	l_b/h	A v	N v	A φ	N φ	A $\sigma_{xx,GP}$	N $\sigma_{xx,GP}$
Q4LI(PG)	0.05	0.90012	0.60929	0.17943	0.12360	25.47267	18.1202
Q4LI(PG)	0.15	0.66948	0.58865	0.13345	0.11824	18.94586	16.9814
Q4LI(PG)	0.30	0.35902	0.34897	0.07157	0.069718	10.15990	9.8081
Q4LI(PG)	0.60	0.12575	0.12513	0.02507	0.02495	3.55870	3.35576
Q4LI(PG)	0.90	0.06037	0.06027	0.01204	0.012013	1.70853	1.67486

Table 3.17: Results obtained using four quadrilateral elements with four nodes (Q4) with a distortion factor a=3.0, 3×3 integration points, GP = (9.73649, -0.887298), A – Analytical solution, N – Numerical solution

		A	N	A	N	A	N
Element	l_b/h	v	v	φ	φ	$\sigma_{xx,GP}$	$\sigma_{xx,GP}$
Q4LI(PG)	0.05	0.90012	0.57816	0.17943	0.12048	25.47267	16.9026
Q4LI(PG)	0.15	0.66948	0.60406	0.13345	0.12184	18.94586	15.2828
Q4LI(PG)	0.30	0.35902	0.35799	0.07157	0.07131	10.15990	8.4683
Q4LI(PG)	0.60	0.12575	0.12671	0.02507	0.02515	3.55870	2.9403
Q4LI(PG)	0.90	0.06037	0.060791	0.01204	0.01206	1.70853	1.4063

In general, it is observed that the 1st order quadrilateral finite element Q4LI(PG) is sensitive to mesh distortion. However, for low micropolar effects the distortion significantly affects the obtained results, i.e. the accuracy of obtained results is reduced by increasing the distortion factor. On the other hand, for high micropolar effects the obtained results are still close to the analytical solution. Furthermore, the obtained results for higher distortion factor are in some cases even more accurate than for lower distortion factor (for example, compare the results for a=1.0 and a=2.0). However, by further increasing the distortion factor (a=3.0) the obtained results diverge from the exact solution. The higher order quadrilateral elements Q9LI(PG) and Q16LI(PG) are not sensitive to mesh distortion, i.e. they exactly reproduce the analytical result, independently of the value of the distortion factor.

3.5   Lagrangian interpolation and incompatible modes in 3D

After a detailed analysis of 2D problems using membrane finite elements, here we extend the finite element formulation to general 3D problems. After setting the weak form in 3D as described in Section 3.1, the interpolation of the kinematic fields has to be specified in order to obtain the numerical solution. In this section we again test two different interpolations. Both interpolations are applied on an isoparametric trilinear hexahedral finite element with eight nodes and six degrees of freedom per node (three displacements u_x, u_y, u_z and three microrotations φ_x, φ_y, φ_z) with the numbering convention as shown in Figure 3.23. The first type is the conventional trilinear Lagrange interpolation defined in the natural coordinate system, chosen for both displacement and microrotation fields, and the corresponding finite element is called Hex8. The second interpolation consists of the Lagrange interpolations for displacement and microrotation

fields, but with the displacement interpolation additionally enriched by the so-called *incompatible modes*. The derived finite element is referred to as Hex8IM. In the framework of the classical elasticity the incompatible displacement modes are first added to the isoparametric elements in [72], [76],[77],[56]. The main benefit of incompatible modes in the classical continuum framework is to avoid shear locking, as shown already in early 1970s [78]. In bending of isoparametric 4-node 2D or 8-node 3D finite elements, the absence of quadratic polynomials in the displacement field approximation predicts the shear strain in pure bending incorrectly. This is called the *shear-locking effect* [67]. Even with higher-order elements producing better results in pure-bending tests, the maximum possible reduction of computational cost is always a worthwhile goal. The proposed solution is to enrich the displacement interpolation of the corresponding element with quadratic displacement interpolation modes, requiring internal element degrees of freedom and leading to incompatibility of the displacement field. When first introduced into 2D quadrilateral isoparametric finite elements [78], the method was received with skepticism in the finite element method research community, since the displacement compatibility between finite elements was at that time considered to be absolutely mandatory [79]. The use of the incompatible-mode method for low-order elements in both two- and three-dimensional problems is nowadays common, leading to the most impressive performance not only in bending, but also elsewhere, e.g. when modelling cracking [80, 56] and two-phase materials [81]. A detailed exposition of 1D, 2D and 3D finite elements with incompatible modes in classical elasticity is presented in [82]. In the framework of micropolar elasticity, the idea of enhancing the displacement field of standard finite element is already recognised in [38], where authors analyzed straight and curved beam problems subject to shear loading. Only 2D problems have been analyzed in [38] and the numerical results have not always converged to the reference analytical solution.
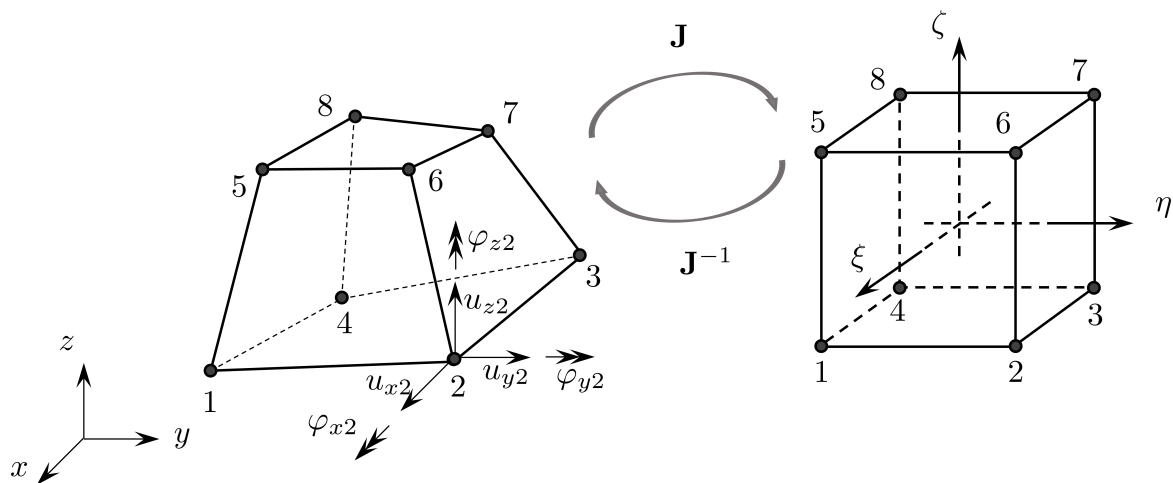
Figure 3.23: Hexahedral finite element with eight nodes

For the element Hex8IM the real and virtual displacement field interpolations are defined as

$$\mathbf{u}^h = \sum_{i=1}^{8} N_i(\xi, \eta, \zeta)\mathbf{u}_i^e + \sum_{i=1}^{3} M_i(\xi, \eta, \zeta)\boldsymbol{\alpha}_i^e = \mathbf{N}_{\mathrm{u}}\mathbf{d}^e + \mathbf{N}_{\mathrm{enh}}\boldsymbol{\alpha}^e,$$
$$\overline{\mathbf{u}}^h = \sum_{i=1}^{8} N_i(\xi, \eta, \zeta)\overline{\mathbf{u}}_i^e + \sum_{i=1}^{3} M_i(\xi, \eta, \zeta)\overline{\boldsymbol{\alpha}}_i^e = \mathbf{N}_{\mathrm{u}}\overline{\mathbf{d}}^e + \mathbf{N}_{\mathrm{enh}}\overline{\boldsymbol{\alpha}}^e,$$
(3.43)

where

$$N_i(\xi, \eta, \zeta) = \frac{1}{8}(1+\xi_a\xi)(1+\eta_a\eta)(1+\zeta_a\zeta), \ \ \xi_a = \pm 1, \ \eta_a = \pm 1, \ \zeta_a = \pm 1, \ i = 1, .., 8, \ (3.44)$$

represent the Lagrange trilinear isoparametric shape functions [67], $\mathbf{u}_i^e = \langle u_{xi} \ u_{yi} \ u_{zi}\rangle^{\mathrm{T}}$ is the vector of element nodal displacements at node i, and $\boldsymbol{\alpha}_i^e = \langle \alpha_{1i} \ \alpha_{2i} \ \alpha_{3i}\rangle^{\mathrm{T}}$ is the vector of the element parameters for the incompatible shape functions chosen as: $M_1 = 1 - \xi^2$, $M_2 = 1 - \eta^2$, and $M_3 = 1 - \zeta^2$. From (3.43) we can see that the displacement field interpolation consists of the conventional (compatible) part $\mathbf{N}_{\mathrm{u}}\mathbf{d}^e$ and the enhanced (incompatible) part $\mathbf{N}_{\mathrm{enh}}\boldsymbol{\alpha}^e$. In the compatible part, defining the complete displacement field interpolation of the Hex8 element, the vector of element nodal degrees of freedom is defined as $\mathbf{d}^e = \langle \mathbf{d}_1^e \ \mathbf{d}_2^e \ \ldots \ \mathbf{d}_8^e \rangle$, where $\mathbf{d}_i^e = \langle u_{xi} \ u_{yi} \ u_{zi} \ \varphi_{xi} \ \varphi_{yi} \ \varphi_{zi}\rangle^{\mathrm{T}}$, i being the node number, and the matrix of Lagrange interpolation functions is defined as $\mathbf{N}_{\mathrm{u}} = [\mathbf{N}_1 \ \mathbf{0} \ \ldots \ \mathbf{N}_8 \ \mathbf{0}]$, with explicit form of the sub-matrix of Lagrange interpolation functions as

$$\mathbf{N}_i = \begin{bmatrix} N_i & 0 & 0 \\ 0 & N_i & 0 \\ 0 & 0 & N_i \end{bmatrix},$$
(3.45)

and $\mathbf{0}$ as a 3×3 zero-matrix. Similarly, in the enhanced part with $\boldsymbol{\alpha}^e = \langle \boldsymbol{\alpha}_1^e \ \boldsymbol{\alpha}_2^e \ \boldsymbol{\alpha}_3^e \rangle^{\mathrm{T}}$ as the element vector of additional degrees of freedom, the matrix of incompatible shape functions is written as

$$\mathbf{N}_{\mathrm{enh}} = \begin{bmatrix} M_1 & 0 & 0 & M_2 & 0 & 0 & M_3 & 0 & 0 \\ 0 & M_1 & 0 & 0 & M_2 & 0 & 0 & M_3 & 0 \\ 0 & 0 & M_1 & 0 & 0 & M_2 & 0 & 0 & M_3 \end{bmatrix}.$$
(3.46)

The virtual fields $\overline{\mathbf{u}}_i^e$, $\overline{\boldsymbol{\alpha}}_i^e$, $\overline{\mathbf{d}}^e$ and $\overline{\boldsymbol{\alpha}}^e$ are defined analogously.

The real and virtual microrotation fields for both Hex8 and Hex8IM are interpolated by using only the standard Lagrange interpolation:

$$\boldsymbol{\varphi}^h = \sum_{i=1}^{8} N_i(\xi, \eta, \zeta)\boldsymbol{\varphi}_i^e = \mathbf{N}_\varphi \, \mathbf{d}^e, \qquad \overline{\boldsymbol{\varphi}}^h = \sum_{i=1}^{8} N_i(\xi, \eta, \zeta) \, \overline{\boldsymbol{\varphi}}_i^e = \mathbf{N}_\varphi \, \overline{\mathbf{d}}^e,$$
(3.47)

where $\boldsymbol{\varphi}_i^e = \langle \varphi_{xi} \ \varphi_{yi} \ \varphi_{zi}\rangle^{\mathrm{T}}$ is the vector of nodal microrotations at node i and $\mathbf{N}_\varphi = [\mathbf{0} \ \mathbf{N}_1 \ldots \mathbf{0} \ \mathbf{N}_8]$.

It is important to note that the reference configuration of the isoparametric element is still defined only with the compatible shape functions, i.e. the mapping between the natural coordinate system and the global coordinate system is defined as $\mathbf{x}^h = \sum_{i=1}^{8} N_i(\xi, \eta, \zeta)\, \mathbf{x}_i^e$ where $\mathbf{x}_i^e = \langle x_i\ y_i\ z_i \rangle^\mathrm{T}$ represents the vector of element nodal coordinates at node i.

By introducing the interpolation into the kinematic equations we obtain the vector of interpolated micropolar strain field

$$\boldsymbol{\epsilon}^h = \langle \epsilon_{11}\ \epsilon_{12}\ \epsilon_{13}\ \epsilon_{21}\ \epsilon_{22}\ \epsilon_{23}\ \epsilon_{31}\ \epsilon_{32}\ \epsilon_{33} \rangle^\mathrm{T} = \sum_{i=1}^{8} \mathbf{B}_{\mathrm{u}_i} \mathbf{d}_i^e + \sum_{i=1}^{8} \mathbf{Q}_{\varphi_i} \mathbf{d}_i^e + \sum_{i=1}^{3} \mathbf{G}_i \boldsymbol{\alpha}_i^e, \quad (3.48)$$

and the vector of interpolated curvature field

$$\boldsymbol{\kappa}^h = \langle \kappa_{11}\ \kappa_{12}\ \kappa_{13}\ \kappa_{21}\ \kappa_{22}\ \kappa_{23}\ \kappa_{31}\ \kappa_{32}\ \kappa_{33} \rangle^\mathrm{T} = \sum_{i=1}^{8} \mathbf{B}_{\varphi_i} \mathbf{d}_i^e, \quad (3.49)$$

where matrices $\mathbf{B}_{\mathrm{u}_i} = [\mathbf{B}_i\ \mathbf{0}]$ and $\mathbf{B}_{\varphi_i} = [\mathbf{0}\ \mathbf{B}_i]$ represent the matrices of global derivatives of the compatible shape functions, matrix $\mathbf{Q}_{\varphi_i} = [\mathbf{0}\ \mathbf{Q}_i]$ is the matrix of compatible shape functions defining the presence of microrotations in the definition of micropolar strains, matrix $\mathbf{G}_i$ is the matrix of global derivatives of incompatible shape functions and $\mathbf{0}$ is a 9×3 zero matrix, where the sub-matrices are defined as

$$\mathbf{B}_i = \begin{bmatrix} \frac{\partial N_i}{\partial x} & 0 & 0 \\ \frac{\partial N_i}{\partial y} & 0 & 0 \\ \frac{\partial N_i}{\partial z} & 0 & 0 \\ 0 & \frac{\partial N_i}{\partial x} & 0 \\ 0 & \frac{\partial N_i}{\partial y} & 0 \\ 0 & \frac{\partial N_i}{\partial z} & 0 \\ 0 & 0 & \frac{\partial N_i}{\partial x} \\ 0 & 0 & \frac{\partial N_i}{\partial y} \\ 0 & 0 & \frac{\partial N_i}{\partial z} \end{bmatrix}, \quad \mathbf{Q}_i = \begin{bmatrix} 0 & 0 & 0 \\ 0 & 0 & N_i \\ 0 & -N_i & 0 \\ 0 & 0 & -N_i \\ 0 & 0 & 0 \\ N_i & 0 & 0 \\ 0 & N_i & 0 \\ -N_i & 0 & 0 \\ 0 & 0 & 0 \end{bmatrix}, \quad \mathbf{G}_i = \begin{bmatrix} \frac{\partial M_i}{\partial x} & 0 & 0 \\ \frac{\partial M_i}{\partial y} & 0 & 0 \\ \frac{\partial M_i}{\partial z} & 0 & 0 \\ 0 & \frac{\partial M_i}{\partial x} & 0 \\ 0 & \frac{\partial M_i}{\partial y} & 0 \\ 0 & \frac{\partial M_i}{\partial z} & 0 \\ 0 & 0 & \frac{\partial M_i}{\partial x} \\ 0 & 0 & \frac{\partial M_i}{\partial y} \\ 0 & 0 & \frac{\partial M_i}{\partial z} \end{bmatrix}. \quad (3.50)$$

The global derivatives of compatible and incompatible shape functions are given by the usual chain rule expressions using the Jacobian matrix $\mathbf{J} = \dfrac{\partial(x, y, z)}{\partial(\xi, \eta, \zeta)}$ [67], i.e.

$$\left\{ \begin{array}{c} \frac{\partial N_i}{\partial x} \\ \frac{\partial N_i}{\partial y} \\ \frac{\partial N_i}{\partial z} \end{array} \right\} = \underbrace{\begin{bmatrix} \frac{\partial \xi}{\partial x} & \frac{\partial \eta}{\partial x} & \frac{\partial \zeta}{\partial x} \\ \frac{\partial \xi}{\partial y} & \frac{\partial \eta}{\partial y} & \frac{\partial \zeta}{\partial y} \\ \frac{\partial \xi}{\partial z} & \frac{\partial \eta}{\partial z} & \frac{\partial \zeta}{\partial z} \end{bmatrix}}_{\mathbf{J}^{-1}} \left\{ \begin{array}{c} \frac{\partial N_i}{\partial \xi} \\ \frac{\partial N_i}{\partial \eta} \\ \frac{\partial N_i}{\partial \zeta} \end{array} \right\}, \quad \left\{ \begin{array}{c} \frac{\partial M_i}{\partial x} \\ \frac{\partial M_i}{\partial y} \\ \frac{\partial M_i}{\partial z} \end{array} \right\} = \underbrace{\begin{bmatrix} \frac{\partial \xi}{\partial x} & \frac{\partial \eta}{\partial x} & \frac{\partial \zeta}{\partial x} \\ \frac{\partial \xi}{\partial y} & \frac{\partial \eta}{\partial y} & \frac{\partial \zeta}{\partial y} \\ \frac{\partial \xi}{\partial z} & \frac{\partial \eta}{\partial z} & \frac{\partial \zeta}{\partial z} \end{bmatrix}}_{\mathbf{J}^{-1}} \left\{ \begin{array}{c} \frac{\partial M_i}{\partial \xi} \\ \frac{\partial M_i}{\partial \eta} \\ \frac{\partial M_i}{\partial \zeta} \end{array} \right\}. \quad (3.51)$$

Before proceeding to the derivation of the element stiffness matrix, we have to take into account the finite element convergence criteria which states that any enhancement beyond the standard definition of the strain field has to vanish for a state of constant strain. In other words, any enhanced strain field must satisfy the stress orthogonality condition [56]. When enhancing the conventional interpolation functions, the condition which has to be satisfied when performing a patch test of order n, is that all the enhancement of order $(n + 1)$ has to vanish. By imposing the requirement that the strain energy associated with the incompatible modes under the state of constant stress has to vanish we obtain the following equation [72]:

$$\frac{1}{2}\boldsymbol{\sigma}^{\mathrm{T}} \int_{V^e} \mathbf{G}_i \ dV \boldsymbol{\alpha}^e = 0 \quad \Rightarrow \int_{V^e} \mathbf{G}_i \ dV = 0, \tag{3.52}$$

where V^e is the element volume and $\boldsymbol{\sigma} = \langle \sigma_{11} \ \sigma_{12} \ \sigma_{13} \ \sigma_{21} \ \sigma_{22} \ \sigma_{23} \ \sigma_{31} \ \sigma_{32} \ \sigma_{33} \rangle^{\mathrm{T}}$ is the element stress vector. This can be satisfied by adding a constant correction matrix $\mathbf{G}_{\mathbf{c}i}$ to the matrix $\mathbf{G}_i$, i.e. $\tilde{\mathbf{G}}_i = \mathbf{G}_i + \mathbf{G}_{\mathbf{c}i}$ such that

$$\int_{V^e} \tilde{\mathbf{G}}_i \ dV = \int_{V^e} (\mathbf{G}_{\mathbf{c}i} + \mathbf{G}_i) \ dV = 0, \tag{3.53}$$

which, by the fact that $\mathbf{G}_{\mathbf{c}i}$ is constant, leads to the following modification of matrix $\mathbf{G}_i$ [72]:

$$\tilde{\mathbf{G}}_i = \mathbf{G}_i - \frac{1}{V^e} \int_{V^e} \mathbf{G}_i \ dV. \tag{3.54}$$

By introducing the interpolation of the kinematic fields into the weak formulation we obtain a system of two equations defined at the element level, i.e.

$$\left\langle \overline{\mathbf{d}}^{e\mathrm{T}} \ \overline{\boldsymbol{\alpha}}^{e\mathrm{T}} \right\rangle \left(\begin{bmatrix} \mathbf{K}^e & \mathbf{F}^{e\mathrm{T}} \\ \mathbf{F}^e & \mathbf{H}^e \end{bmatrix} \begin{Bmatrix} \mathbf{d}^e \\ \boldsymbol{\alpha}^e \end{Bmatrix} \right) = \left\langle \overline{\mathbf{d}}^{e\mathrm{T}} \ \overline{\boldsymbol{\alpha}}^{e\mathrm{T}} \right\rangle \begin{Bmatrix} \mathbf{f}^e \\ \mathbf{0} \end{Bmatrix}, \tag{3.55}$$

where the obtained matrices are equal to

$$\mathbf{K}^e = \int_{V^e} \left(\ (\mathbf{B}_{\mathrm{u}}^{\mathrm{T}} + \mathbf{Q}_{\varphi}^{\mathrm{T}}) \, \mathbf{T_1} \, (\mathbf{B}_{\mathrm{u}} + \mathbf{Q}_{\varphi}) + \mathbf{B}_{\varphi}^{\mathrm{T}} \mathbf{T_2} \mathbf{B}_{\varphi} \ \right) \ dV, \tag{3.56}$$

$$\mathbf{F}^e = \int_{V^e} \tilde{\mathbf{G}}^{\mathrm{T}} \mathbf{T_1} \, (\mathbf{B}_{\mathrm{u}} + \mathbf{Q}_{\varphi}) \ dV, \tag{3.57}$$

$$\mathbf{H}^e = \int_{V^e} \tilde{\mathbf{G}}^{\mathrm{T}} \mathbf{T_1} \tilde{\mathbf{G}} \ dV, \tag{3.58}$$

where $\mathbf{B}_{\mathrm{u}} = [\mathbf{B}_{\mathrm{u}_1} \ \mathbf{B}_{\mathrm{u}_2} \ \ldots \ \mathbf{B}_{\mathrm{u}_8}]^{\mathrm{T}}$, $\mathbf{Q}_{\varphi} = [\mathbf{Q}_{\varphi_1} \ \mathbf{Q}_{\varphi_2} \ \ldots \ \mathbf{Q}_{\varphi_8}]$, $\mathbf{B}_{\varphi} = [\mathbf{B}_{\varphi_1} \ \mathbf{B}_{\varphi_2} \ \ldots \ \mathbf{B}_{\varphi_8}]^{\mathrm{T}}$, $\tilde{\mathbf{G}} = [\tilde{\mathbf{G}}_1 \ \tilde{\mathbf{G}}_2 \ \tilde{\mathbf{G}}_3]^{\mathrm{T}}$, and $\mathbf{T_1}$ and $\mathbf{T_2}$ are 9×9 constitutive

matrices defined as

$$\mathbf{T_1} = \begin{bmatrix} (\lambda + 2\mu) & 0 & 0 & 0 & \lambda & 0 & 0 & 0 & \lambda \\ 0 & (\mu + \nu) & 0 & (\mu - \nu) & 0 & 0 & 0 & 0 & 0 \\ 0 & 0 & (\mu + \nu) & 0 & 0 & 0 & (\mu - \nu) & 0 & 0 \\ 0 & (\mu - \nu) & 0 & (\mu + \nu) & 0 & 0 & 0 & 0 & 0 \\ \lambda & 0 & 0 & 0 & (\lambda + 2\mu) & 0 & 0 & 0 & \lambda \\ 0 & 0 & 0 & 0 & 0 & (\mu + \nu) & 0 & (\mu - \nu) & 0 \\ 0 & 0 & (\mu - \nu) & 0 & 0 & 0 & (\mu + \nu) & 0 & 0 \\ 0 & 0 & 0 & 0 & 0 & (\mu - \nu) & 0 & (\mu + \nu) & 0 \\ \lambda & 0 & 0 & 0 & \lambda & 0 & 0 & 0 & (\lambda + 2\mu) \end{bmatrix} , \quad (3.59)$$

with a corresponding result for $\mathbf{T_2}$ in which α, β, γ replace λ, μ, ν. In order to eliminate the presence of unknown incompatible-mode parameters $\boldsymbol{\alpha}^e$, we have to perform the so-called static condensation [77]. The static condensation is accomplished by first expressing $\boldsymbol{\alpha}^e = -\mathbf{H}^{e^{-1}}\mathbf{F}^e\,\mathbf{d}^e$ from equation $(3.55)_2$ and then introducing $\boldsymbol{\alpha}^e$ into equation $(3.55)_1$. Consequently, we obtain the reduced form of the element stiffness matrix

$$\tilde{\mathbf{K}}^e = \mathbf{K}^e - \mathbf{F}^{e^{\mathrm{T}}}\mathbf{H}^{e^{-1}}\mathbf{F}^e. \tag{3.60}$$

From this point on, we can proceed towards the standard finite element assembly accounting for all element contributions, i.e.

$$\mathbf{K}\,\mathbf{d} = \mathbf{f} \quad \Rightarrow \quad \mathbf{d}; \quad \mathbf{K} = \underset{e=1}{\overset{n_{elem}}{\mathbb{A}}}\,\tilde{\mathbf{K}}^e; \quad \mathbf{f} = \underset{e=1}{\overset{n_{elem}}{\mathbb{A}}}\,\mathbf{f}^e. \tag{3.61}$$

Having the nodal displacement values obtained, we can recover the corresponding element displacements $\mathbf{d}^e$ through the connectivity matrix $\mathbf{d} = \mathbf{L}^e\mathbf{d}^e$ which allows to obtain the incompatible mode parameters $\boldsymbol{\alpha}^e = -\mathbf{H}^{e^{-1}}\mathbf{F}^e\,\mathbf{d}^e$ and recover the micropolar strains $\boldsymbol{\epsilon}^h$ in (3.48). Stresses $\boldsymbol{\sigma}^h$ in Gauss points are then obtained from the constitutive equations. The curvatures $\boldsymbol{\kappa}^h$ are obtained in a conventional manner, directly from the element displacements, as shown in equation (3.49) and again, using the constitutive equation, we obtain the couple-stresses in Gauss points $\boldsymbol{\mu}^h$.

3.6   Numerical examples in 3D

In this section the performance of the conventional eight-node hexahedral micropolar finite element Hex8 and the enhanced element with incompatible modes Hex8IM is tested in four numerical examples. In the first example (Section 3.6.1), the finite-element verification is performed through the patch test [67] on a regular mesh, which represents a standard method for testing the finite element convergence. In the second example (Section 3.6.2) a set of displacement patch tests for a 2D micropolar continuum proposed in [36] and presented in subsection 3.4.2 are generalised to 3D and the elements are tested

on an irregular mesh. The finite elements are also tested on two boundary value problems that are important for the experimental determination of the micropolar material parameters, showing the size-effect phenomenon. In Section 3.6.3, the cylindrical bending of a cantilever beam (also referred to as the higher-order patch test) is analysed and compared to the analytical solution [1]. This pure bending example is already analysed using 2D finite elements and presented in detail in Section 3.4.4. Finally, in the last numerical example, presented in Section 3.6.4, an axisymmetric boundary-value problem consisting of a solid cylinder subject to torsion in two different configurations (two sets of material parameters) is analysed. In the second configuration, the obtained numerical results are compared against the experimental results given in [5].

3.6.1 Force patch test in 3D

We perform the force patch test [67] on a cantilever beam subject to pure tension, as shown in Figure 3.24, and check if for an arbitrary number of finite elements in the mesh the exact solution for the state of constant stress is returned. The geometry of the cantilever beam is chosen as $L = 5$ m, $h = 2$ m, $b = 1$ m. The free-end of the cantilever beam is subjected to constant axial distributed loading $p_y = 10$ N/m^2, leading to a constant stress field. The constant distributed surface loading is applied through corresponding concentrated nodal forces obtained by integration, which, for a single-element mesh gives $F = \dfrac{1}{4} p_y bh$, as shown in Figure 3.24. At the left-hand end of the cantilever all the displacements in the longitudinal direction are fixed, i.e. $u_y(x, 0, z) = 0$, while $u_z(x, 0, 0) = 0$, and $u_x(0, 0, 0) = 0$ for $x \in [0, b]$, $z \in [0, h]$. The patch test is performed on two regular meshes by equally increasing the number of uniform elements in the x, y and z direction for the chosen material parameters $\mu = 1000$ N/mm^2, $\lambda = 1000$ N/mm^2, $\nu = 500$ N/mm^2, $\alpha = 20$ N, $\beta = 20$ N and $\gamma = 20$ N, where the boundary conditions and external loading are correspondingly defined.
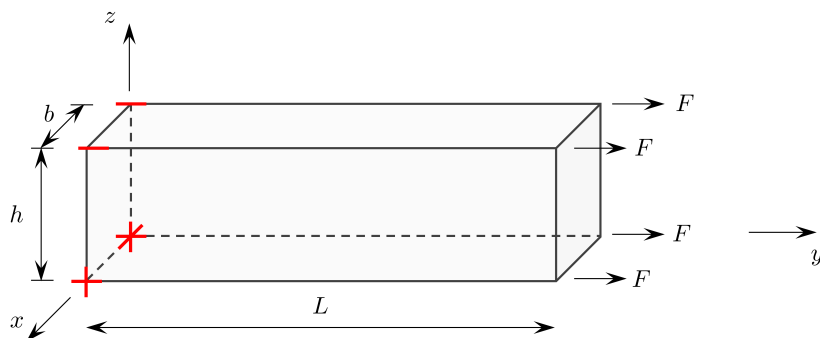
Figure 3.24: Cantilever beam subject to constant distributed axial load

It is observed that, even without the matrix modification defined in equation (3.54), for a regular mesh the micropolar trilinear hexahedral element with incompatible modes

reproduces the analytical results to the highest computer accuracy, which ensures that the element will converge to the exact solution when refining the mesh.

3.6.2 Generalized 3D displacement patch tests for micropolar continuum

As mentioned before, according to Providas and Kattis [36] the patch test for micropolar finite elements should consist of a set of three separate tests. In this section, the tests given in [36] and presented in Section 3.4.2 for 2D finite elements are generalized to 3D and performed on a cuboid domain of length $L = 0.24$, height $h = 0.12$, width $b = 0.06$ and internal nodes with the following co-ordinates: $1 = (0.04, 0.04, 0.02)$, $2 = (0.04, 0.18, 0.03)$, $3 = (0.02, 0.18, 0.03)$, $4 = (0.02, 0.04, 0.02)$, $5 = (0.04, 0.08, 0.08)$, $6 = (0.04, 0.16, 0.08)$, $7 = (0.02, 0.16, 0.08)$ and $8 = (0.02, 0.08, 0.08)$. The domain is discretized with 7 arbitrarily distorted hexahedral finite-elements as shown in Figure 3.25. It is important to note that the generalization of Providas' and Kattis' tests to 3D is not unique and, in this thesis one possible generalization of it is presented. The material parameters used are the same as defined in the 3D force patch test.
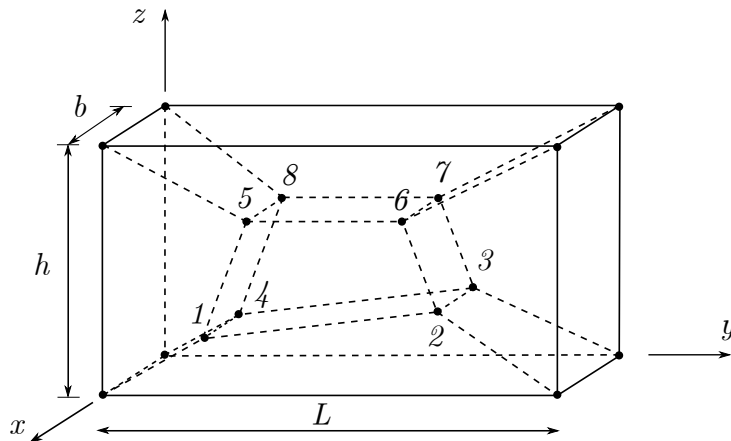
Figure 3.25: Finite element mesh for the displacement patch test

The patch tests are performed as in the 2D analysis, i.e. the displacements and microrotations are imposed on the external nodes, while the volume loading (if any) is imposed in the interior of the domain. Again, the element passes a patch test if the internal nodes are capable of reproducing the analytical solution imposed by the boundary conditions.

The first test is the standard patch test of the finite elements in the classical continuum theory, whereby imposing linearly varying displacement and constant microrotation fields via appropriate boundary conditions without any volume and surface loading we obtain the state of *constant symmetric stress and strain.* The kinematic fields of the generalised

first test are defined as follows:

$$
\begin{aligned}
u_x &= 10^{-3}(x + 0.5y + z), & u_y &= 10^{-3}(x + y + 0.5z), \\
u_z &= 10^{-3}(0.5x + y + z), & \varphi_x = \varphi_y &= \varphi_z = 0.25 \cdot 10^{-3},
\end{aligned}
\tag{3.62}
$$

leading to the following theoretical solution:

$$
\begin{aligned}
\sigma_{xx} = \sigma_{yy} = \sigma_{zz} &= 5.0, & \sigma_{xy} = \sigma_{yx} = \sigma_{yz} = \sigma_{zy} = \sigma_{xz} = \sigma_{zx} &= 1.5, \\
\epsilon_{xx} = \epsilon_{yy} = \epsilon_{zz} &= 10^{-3}, & \epsilon_{xy} = \epsilon_{yx} = \epsilon_{yz} = \epsilon_{zy} = \epsilon_{xz} = \epsilon_{zx} &= 0.75 \cdot 10^{-3},
\end{aligned}
\tag{3.63}
$$

with all the couple-stress and curvature components equal to zero.

The second test describes the state of *constant non-symmetric shear stresses and strains*, for which a constant body moment is needed in order to preserve equilibrium. The kinematic fields and body moments of the generalised second test are defined as follows:

$$
\begin{aligned}
u_x &= 10^{-3}(x + 0.5y + z), & u_y &= 10^{-3}(x + y + 0.5z), \\
u_z &= 10^{-3}(0.5x + y + z), & \varphi_x = \varphi_y &= \varphi_z = 0.75 \cdot 10^{-3}, \\
m_{vx} = m_{vy} &= m_{vz} = 1.0,
\end{aligned}
\tag{3.64}
$$

giving the following theoretical solution

$$
\begin{aligned}
\sigma_{xx} = \sigma_{yy} = \sigma_{zz} &= 5.0, & \sigma_{xz} = \sigma_{yx} = \sigma_{zy} &= 1.0, \\
\sigma_{zx} = \sigma_{xy} = \sigma_{yz} &= 2.0, & \epsilon_{xx} = \epsilon_{yy} = \epsilon_{zz} &= 10^{-3}, \\
\epsilon_{xz} = \epsilon_{yx} = \epsilon_{zy} &= 0.25 \cdot 10^{-3}, & \epsilon_{zx} = \epsilon_{xy} = \epsilon_{yz} &= 1.25 \cdot 10^{-3},
\end{aligned}
\tag{3.65}
$$

with all the couple-stress and curvature components again equal to zero. The third test describes the state of *constant curvature*, whereby imposing linearly varying displacement, microrotation and body-moment fields as well as a constant body-force field we obtain linearly varying stresses and *constant couple-stresses*. The input of the generalised third test is defined as:

$$
\begin{aligned}
u_x &= 10^{-3}(x + 0.5y + z), & u_y &= 10^{-3}(x + y + 0.5z), \\
u_z &= 10^{-3}(0.5x + y + z), & \varphi_x = \varphi_y &= \varphi_z = 10^{-3}(0.25 + (x - y - z)), \\
p_{vx} &= 0, \; p_{vy} = 2, \; p_{vz} = -2, & m_{vx} = m_{vy} &= m_{vz} = 2(x - y - z).
\end{aligned}
\tag{3.66}
$$

giving the following theoretical solution

$$
\begin{aligned}
\sigma_{xx} = \sigma_{yy} = \sigma_{zz} = 5.0, \quad \sigma_{xz} = \sigma_{yx} = \sigma_{zy} = 1.5 - (x - y - z), \\
\sigma_{zx} = \sigma_{xy} = \sigma_{yz} = 1.5 + (x - y - z), \quad \epsilon_{xx} = \epsilon_{yy} = \epsilon_{zz} = 10^{-3}, \\
\epsilon_{xz} = \epsilon_{yx} = \epsilon_{zy} = 10^{-3}(0.75 - (x - y - z)), \\
\epsilon_{zx} = \epsilon_{xy} = \epsilon_{yz} = 10^{-3}(0.75 + (x - y - z)), \\
\mu_{xx} = 0.02, \; \mu_{yy} = \mu_{zz} = -0.06, \; \mu_{xy} = \mu_{xz} = \mu_{yz} = \mu_{zy} = -0.04, \\
\mu_{yx} = \mu_{zx} = 0.04, \; \kappa_{xx} = \kappa_{yx} = \kappa_{zx} = 10^{-3}, \\
\kappa_{yy} = \kappa_{zz} = \kappa_{xy} = \kappa_{xz} = \kappa_{yz} = \kappa_{zy} = -10^{-3}.
\end{aligned}
\tag{3.67}
$$

Table 3.18: Results for Patch test 3 [36] using the Hex8IM element

	$u_x \cdot 10^{-4}$	$u_y \cdot 10^{-4}$	$u_z \cdot 10^{-4}$	$\varphi_x \cdot 10^{-4}$	σ_{xx}	μ_{xx}	μ_{xy}
	0.604	0.699	0.698	2.102	5.013	0.019	-0.039
Exact	0.600	0.700	0.700	2.100	5.000	0.020	-0.040

All three tests are first performed using the conventional Hex8 finite element and the obtained results correspond to the analytical solution to within the computer accuracy (10^{-16}). When analysing the first two tests using the enhanced finite element Hex8IM it is observed that, for a distorted mesh analysed here, the matrix modification as presented in (3.54) is necessary for the element to pass the patch tests. When applying the matrix modification, both tests are satisfied to within the computer accuracy. However, the third test which we treat as higher-order patch test is not satisfied either way and the obtained results are presented in Table 3.18. Even though the third patch test is not satisfied, we consider that Hex8IM satisfies the convergence criteria since, as argued above, the finite element is able to reproduce exactly any state of constant stress.

3.6.3 A cantilever beam subject to pure bending in 3D – higher-order patch test

In order to test the accuracy of the hexahedral element enhanced with incompatible modes, a cantilever beam shown in Figure 3.26 submitted to cylindrical bending is analysed. The chosen geometry is the same as in the 2D numerical analysis of this problem presented in Section 3.4.4, i.e. $L = 10$ m, $h = 2$ m and $b = 1$ m. In order to model correctly this problem, we follow the steps described in Section 3.4.4. Again, the problem is solved while varying the value of the characteristic length $l_b \in [0.0, 1.8]$ to capture the size-effect. The resultant bending moment $M = 20$ Nm is applied through a linearly varying surface loading p_{sx} and a constant surface moment loading m_{sz} in the proportion defined in equation (3.38), which has to be strictly respected in order to obtain a pure

bending state. The analytical values of the external loadings for different l_b are presented in Table 3.8. The distributed loading is applied through corresponding concentrated nodal forces and moments obtained by integration as defined by (3.1)-(3.4).
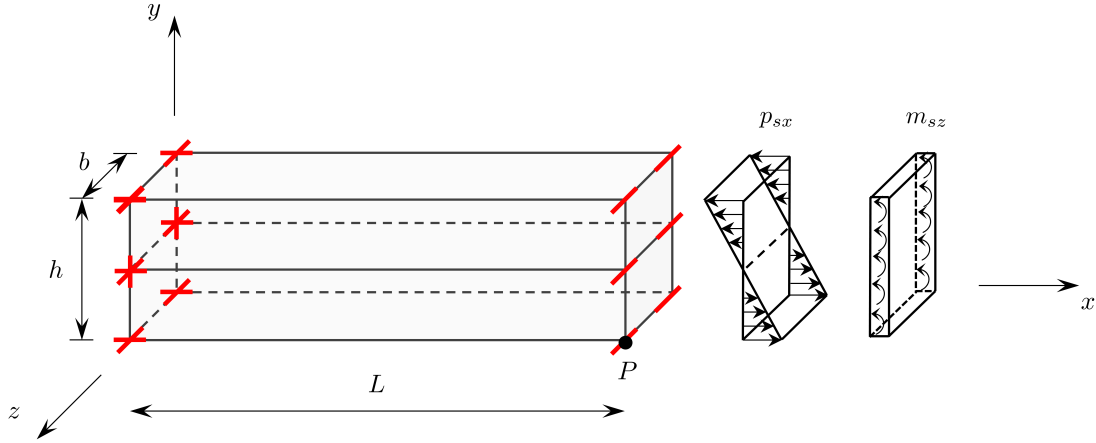
Figure 3.26: Cantilever beam subject to pure bending in 3D

The engineering material parameters are taken the same as defined in Section 3.4.4, i.e. $E = 1500$ N/m^2 and $n = 0.25$ which give the Lamé constants $\mu = 600$ N/m^2 and $\lambda = 600$ N/m^2. The parameter ν is chosen to be equal to $\nu = 200$ N/m^2, corresponding to $N = 0.5$, but in this example it can have an arbitrary value, as argued before. The remaining engineering parameters which exist only in the 3D analysis are chosen as $\psi = 0$ and $l_t = 0.1$, but, since they do not affect the solution, they can also have arbitrary values. Along the left-hand edge of the specimen all the horizontal displacements and microrotations are restrained, i.e. $u_x(0, y, z) = \varphi_x(0, y, z) = \varphi_y(0, y, z) = \varphi_z(0, y, z) = 0$, for $y \in [0, h]$ and $z \in [0, b]$. The vertical displacement at the left-hand edge is restrained only at the cantilever axis, i.e. $u_y(0, \frac{h}{2}, z) = 0$ for $z \in [0, b]$. Furthermore, the cylindrical bending of the specimen is accomplished by additionally restraining the displacements in the z direction along the whole cantilever, i.e. $u_z(x, y, z) = 0$ for $x \in [0, L]$, $y \in [0, h]$ and $z \in [0, b]$.

The problem is solved using a mesh of two hexahedral elements as shown in Figure 3.26. The results for the vertical displacement and microrotation u_y and φ_z at node P and the stress σ_{xx} at the Gauss point with coordinates $GP = (7.88675, 0.211325, 0.788675)$ obtained by Hex8 and Hex8IM are compared to the analytical solution and shown in Table 3.19 and Figure 3.27.

Table 3.19: Results obtained using two hexahedral elements with eight nodes (Hex8 and Hex8IM), $2 \times 2 \times 2$ integration points, A = Analytical, N = Numerical

Element	l_b	$\beta + \gamma$	A u_y	N u_y	A φ_z	N φ_z	A $\sigma_{xx,GP}$	N $\sigma_{xx,GP}$
Hex8	0.0	0.0	0.94063	0.06910	0.18750	0.01260	23.6603	1.9684
Hex8IM				0.94063		0.18750		23.6603
Hex8	0.1	24.0	0.90012	0.06892	0.17943	0.01269	22.6414	1.9503
Hex8IM				0.90012		0.17943		22.6414
Hex8	0.3	216.0	0.66948	0.06740	0.13345	0.01296	21.3523	1.8345
Hex8IM				0.66948		0.13345		21.3523
Hex8	0.6	864.0	0.35902	0.06203	0.07157	0.01261	11.4504	1.5997
Hex8IM				0.35902		0.07157		11.4504
Hex8	1.2	3456.0	0.12575	0.04624	0.02507	0.00977	3.1631	1.1436
Hex8IM				0.12575		0.02507		3.1631
Hex8	1.8	7776.0	0.06037	0.03234	0.01204	0.00691	1.5186	0.7904
Hex8IM				0.06037		0.01204		1.5186

(a) Normalised end-node vertical displacements

(b) Normalised end-node microrotation

(c) Normalised stresses in Gauss point
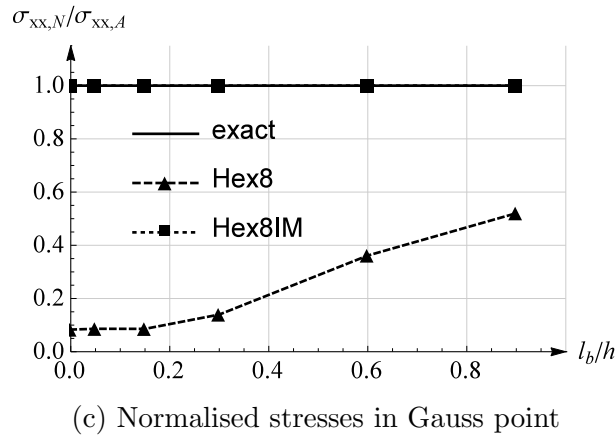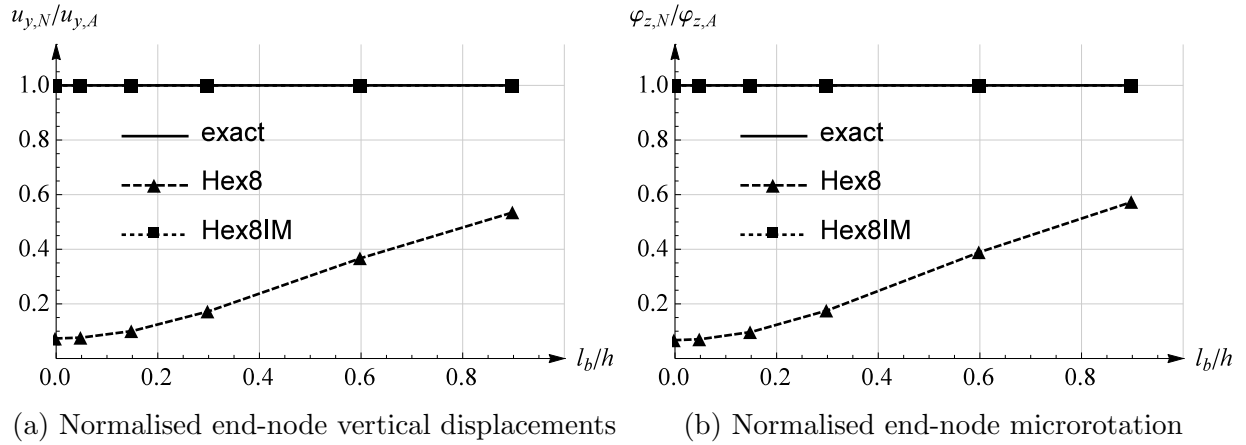
Figure 3.27: Cantilever beam subject to pure bending - results for Hex8 and Hex8IM

From the obtained results we can see that Hex8IM reproduces the analytical solution to within the computer accuracy, while the conventional element with Lagrange interpolation Hex8 shows very poor results, especially for smaller micropolar effects. The improvement due to the incompatible modes is highly significant. Even with a very coarse mesh, the analytical solution of this higher-order patch test is precisely reproduced.

3.6.4 Micropolar solid cylinder under torsional load

An axisymmetric solid micropolar cylinder subject to pure torsion shown in Figure 3.28 is analyzed in this example. Gauthier and Jahsman derived the analytical solution for a cylindrical specimen of height c and cross-section radius a in the cylindrical coordinate system $(r,\ \theta,\ z)$ subject to torsional load [1]. The stresses and couple stresses are axisymmetric, and independent of z. Furthermore, all non-vanishing variables are independent of the angle θ. By further imposing a traction-free surface for $r = a$, prescribing the appropriate resultant torque T on end surfaces $z = 0$ and $z = c$ and taking into account the compatibility conditions, the analytical solution for stresses, displacements and microrotations are obtained.

98
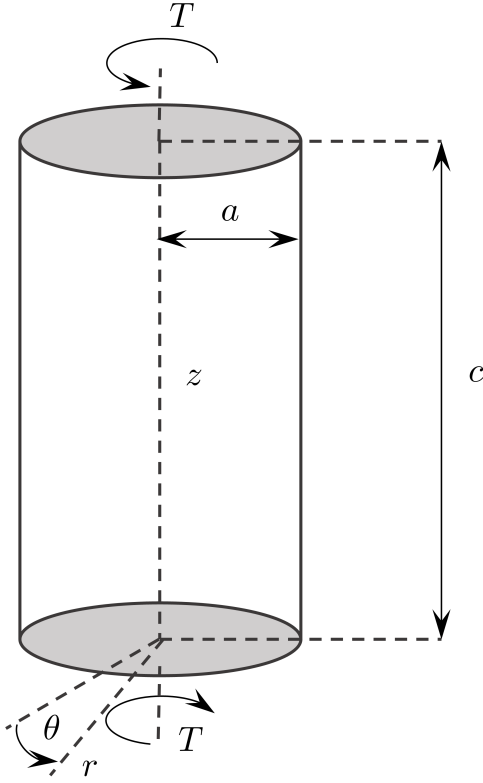
Figure 3.28: Solid cylinder in torsion

The first comprehensive numerical study of the problem is presented in [37], where linear beam finite elements are tested for a range of micropolar material parameters and the obtained results are compared to the analytical solution. Furthermore, in [49] three-dimensional non-linear finite elements are developed and their performance is tested by modeling this linear-elastic problem. A good agreement between the numerical and analytical results is shown in both references. However, as in the pure-bending case from Section 3.6.3, Gauthier and Jahsman have shown that in the micropolar theory the state of axisymmetric torsion of a circular cylinder can be achieved only by applying both a normal surface traction $p_{s\theta}$ and a surface moment traction m_{sz}. In other words, to correctly model the problem in 3D, the external torque T should be applied as

$$\int_A (r\ p_{s\theta} + m_{sz})\ dA = T, \tag{3.68}$$

where $A = r^2\pi$ is the cylinder cross-section area, r is the variable in the radial direction, $p_{s\theta}$ is the tangential surface loading and m_{sz} is the moment surface loading, as presented in [1]. The Neumann boundary condition is then $2\pi \int_0^a (r^2\ \sigma_{\theta z} + r\ \mu_{zz})\ dr = T$ where a represents the cross-section radius and $\sigma_{\theta z}$ and μ_{zz} represent the stress and couple-stress components, respectively, with the first index denoting the direction and the second index

denoting the surface normal. According to the analytical solution, both $\sigma_{\theta z}$ and μ_{zz} are described by the modified Bessel functions of the first kind $I_n(r)$ [83] depending on r and multiplied by constants of integration C_1 and C_9, as follows:

$$\sigma_{\theta z} = p_{s\theta} = \mu\ C_1\ r + 2\nu C_9 I_1(pr), \qquad \mu_{zz} = m_{sz} = \alpha\ p\ C_9\ I_0(pr) + 2\beta C_1, \qquad (3.69)$$

where

$$p = \sqrt{\frac{4\nu}{\alpha + 2\beta}}, \quad C_9 = \frac{T}{2\pi a^2} \left[(\frac{\mu a^2}{4\beta} + 1.5)\,(\alpha + 2\beta)\ p\ I_0(pa) - (\frac{\mu a^2}{4\beta} + 2)\frac{2\beta}{a}\ I_1(pa) \right]^{-1}$$

and $C_1 = 2C_9 \left(\dfrac{\alpha + 2\beta}{2\beta}\ p\ I_0(pa) - \dfrac{1}{a}\ I_1(pa) \right)$, I_0 and I_1 being the modified Bessel functions of the first kind. In other words, the distribution of the external loading is directly dependent on material parameters. The remaining non-vanishing variables are $\sigma_{z\theta}$, μ_{rr}, $\mu_{\theta\theta}$, u_θ, φ_r and φ_z, where the displacement and rotation fields are defined as

$$u_\theta = C_1 r z, \qquad \varphi_r = -\frac{C_1 r}{2} + C_9 I_1(pr), \qquad \varphi_z = C_1 z, \qquad (3.70)$$

u_θ being linear in r and z and φ_z linear in z as in the classical elasticity. Since u_z vanishes, no warping of surfaces is predicted.

In order to relate the classical and micropolar torsional problem, Gauthier and Jahsman introduce a parameter Ω which defines the ratio of the micropolar torsional rigidity to the classical torsional rigidity $J = \dfrac{G\pi a^4}{2}$. The ratio Ω is given as a function of engineering micropolar material parameters as:

$$\Omega = 1 + \frac{6}{a^2}l_t^2\,\frac{1 - \frac{4}{3}\psi\chi}{1 - \psi\chi}, \quad \text{where} \quad \chi = \frac{I_1(pa)}{p\,a\,I_0(pa)} \quad \text{and} \quad p = \sqrt{\frac{2\psi N^2}{l_t^2(1 - N^2)}}. \qquad (3.71)$$

It can be seen that for the limiting case $l_t \to 0$ the micropolar rigidity approaches the classical-elasticity value, since the ratio $\Omega \to 1$. On the other hand, for the limiting case $\psi \to 0$, the ratio of micropolar rigidity approaches its maximum value of $\Omega = 1 + 6(\dfrac{l_t}{a})^2$. In general, as the characteristic length approaches the specimen radius, the micropolar rigidity increases and it can be as many as seven times bigger than the classical rigidity.

In the first part of this analysis the problem is solved using both Hex8 and Hex8IM elements and the finite elements are tested by comparing the numerical results against the analytical solution. The radius of the cylinder is taken as $a = 0.2$ mm, its height is $c = 1$ mm, and it is subjected to a resultant torque $T = 1$ Nmm. The chosen material parameters are $\mu = 10\ 500$ N/mm^2, $\lambda = 157\ 500$ N/mm^2, $\nu = 3\ 500$ N/mm^2, $\alpha = 0$ N, $\beta = 105$ N and $\gamma = -105$ N , which corresponds to the following engineering material parameters $E = 30\ 843.8$ N/mm^2, $n = 0.46875$, $N = 0.5$, $l_b = 0$ mm, $l_t = 0.1$ mm,

$\psi = 1.0$. Since $\alpha = 0$, the first term in $(4.64)_2$ vanishes, i.e. m_{sz} becomes constant and we obtain the external loading as shown in Figure 3.29.

(a) $p_{s\theta}$ for $r \in [0, 1.0]$

(b) $p_{s\theta}$ for $r \in [0, a]$

(c) m_{sz} for $r \in [0, a]$
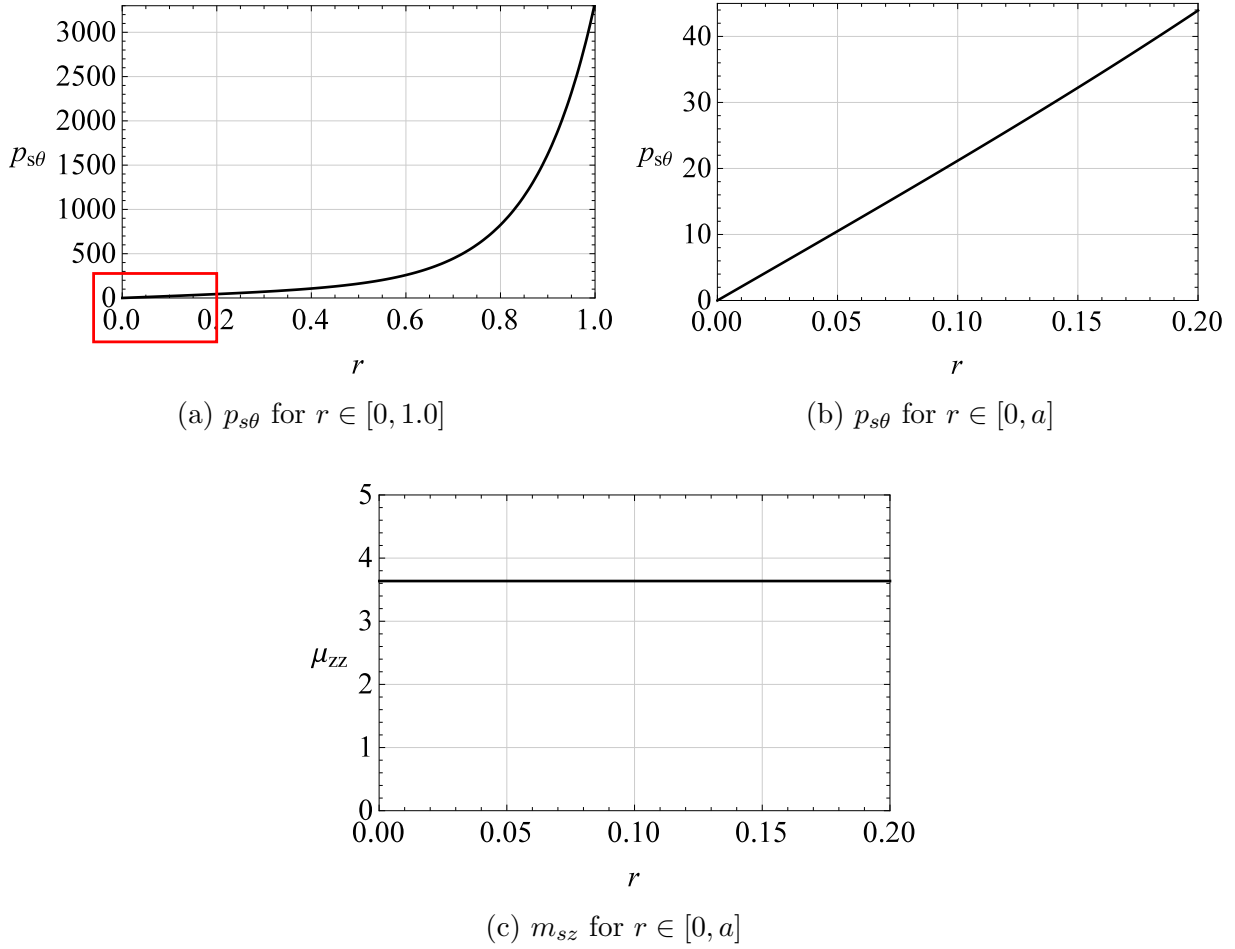
Figure 3.29: Distribution of the external loading

The surface traction is in general a non-linear function, as shown in Figure 3.29a. By extracting an initial part of that diagram (the detail in Figure 3.29a), we can see that as r gets smaller, the shape of $p_{s\theta}$ approaches a linear function, as blown up in Figure 3.29b. We can thus say that $p_{s\theta}$ is nearly linear for $r \in [0, a]$ and the resultant torque T is modelled as a linearly varying surface loading $p_{s\theta}$ where $p_{s\theta}(0, \theta, c) = 0$ N/mm^2, $p_{s\theta}(r, \theta, c) = 43.93046972$ N/mm^2, $\theta \in [0, 2\pi]$, along with a constant distributed moment surface loading $m_{sz} = 3.636829403$ Nmm/mm^2 shown in Figure 3.29c.

For the problem analysed, the analytical curves of the external loading as a function of the characteristic length l_t for $r = a$ are presented in Figure 3.30, where we can see that, as in the pure bending example, by increasing the characteristic length l_t, the contribution of $p_{s\theta}$ in the external moment rapidly decreases, while the contribution of m_{sz} increases. In other words, when $l_t \to \infty$ the external moment is taken over by the distributed surface moment only, i.e. $p_{s\theta} = 0$ $\frac{\text{N}}{\text{m}^2}$, $m_{sz} = 7.95775$ $\frac{\text{Nm}}{\text{m}^2}$, while for $l_t \to 0$ it is taken over by the linearly varying surface moment only, i.e. $p_{s\theta 0} = 79.5775$ $\frac{\text{N}}{\text{m}^2}$, $m_{sz} = 0$ $\frac{\text{Nm}}{\text{m}^2}$.
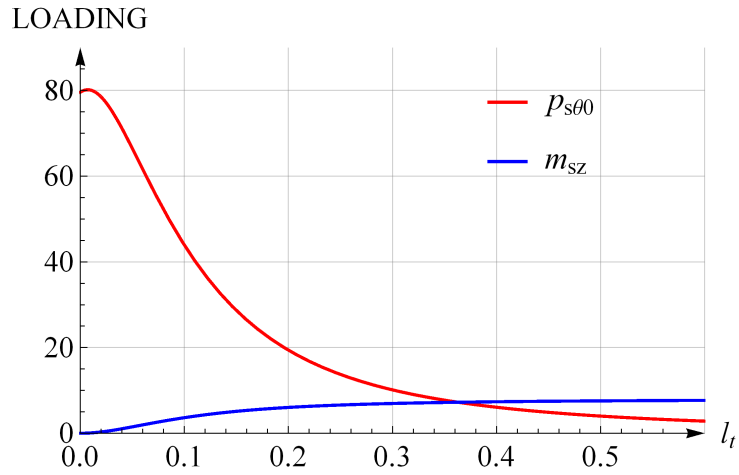
Figure 3.30: Distributed external loading as a function of the characteristic length l_t

Along the bottom side of the cylinder ($z = 0$) all the displacements and microrotation φ_z are restrained. The problem is solved for two different mesh densities, with 24 and 144 elements, as shown in Figures 3.31a and 3.31b, respectively.

(a) 24 elements   (b) 144 elements   (c) 1536 elements
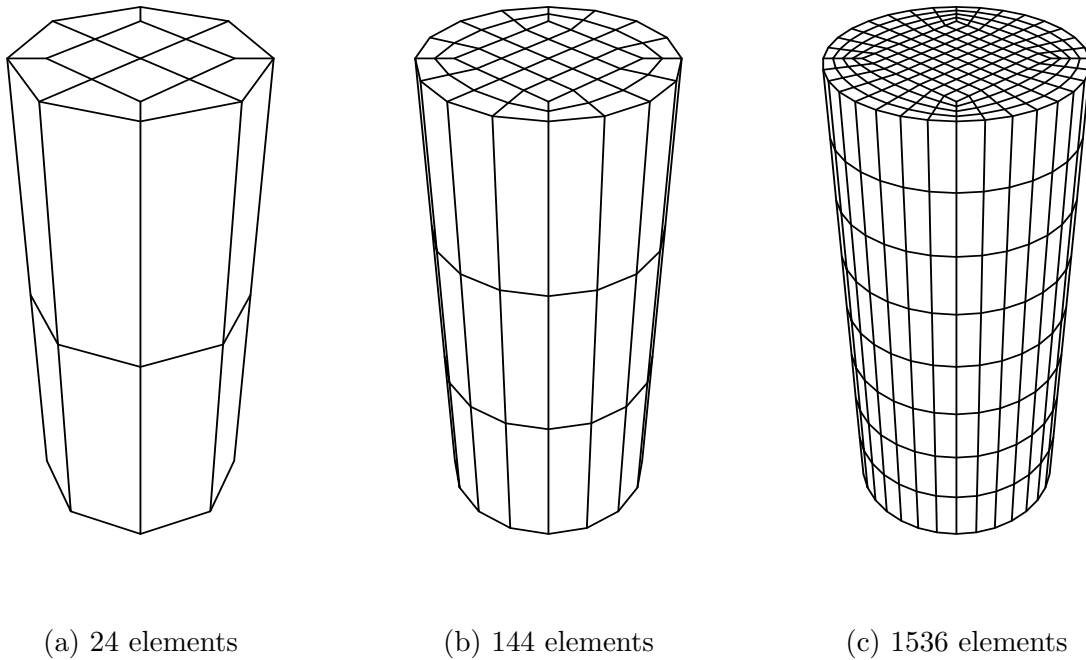
Figure 3.31: Finite element mesh for the axisymmetric problem

The results obtained by Hex8 and Hex8IM for microrotation φ_z along the cylinder axis z for $r = a$, and microrotation φ_r and displacement u_θ at the upper edge ($z = c$) along r are compared against the analytical solution, as shown in Figures 3.32, 3.33 and 3.34.
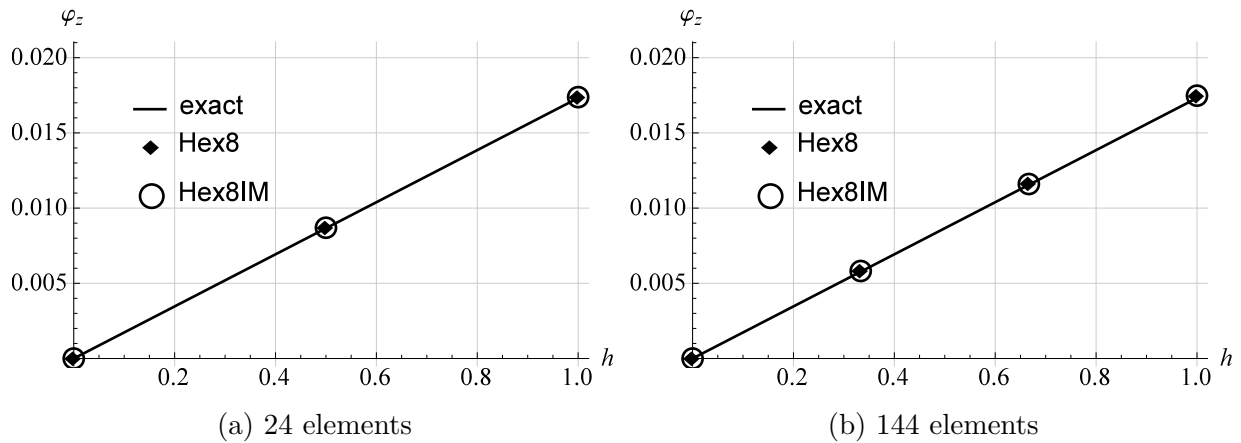
Figure 3.32: Distribution of φ_z along z - results for Hex8 and Hex8IM for different mesh densities
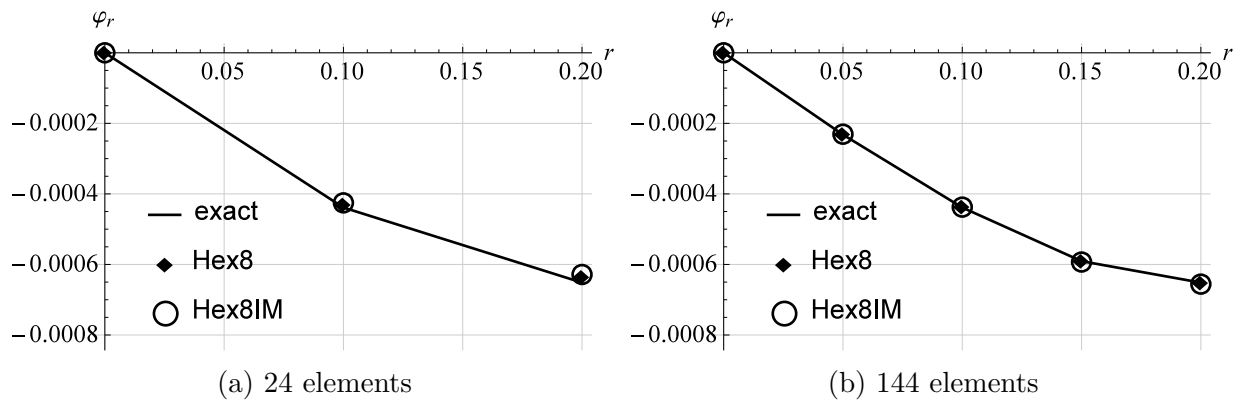
Figure 3.33: Distribution of φ_r along r - results for Hex8 and Hex8IM for different mesh densities
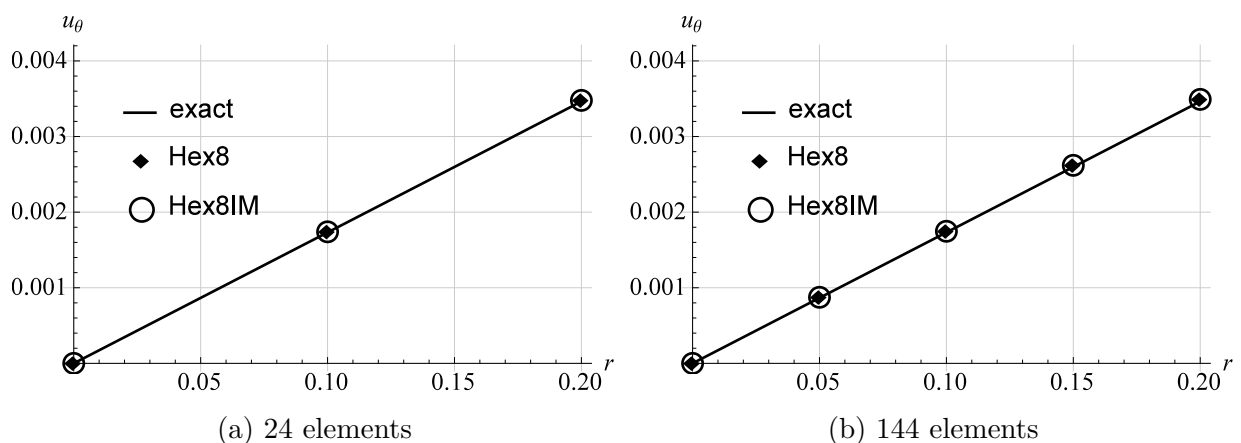
Figure 3.34: Distribution of u_θ along r for $z = c$ - results for Hex8 and Hex8IM for different mesh densities

We can see that both the Lagrange element Hex8 and the enhanced element Hex8IM follow the analytical solution, and the numerical results are in good agreement with the

analytical solution even for a coarse mesh. The numerical analysis correctly predicts the linear distribution of the axial microrotation component φ_z and the displacement component u_θ. The results for the radial microrotation component φ_r correctly follow the analytical trend. Because of the presence of the characteristic length for torsion, the rigidity of this micropolar cylinder is 2.19 times larger than expected classically. However, the enhancement due to incompatible modes does not improve the convergence rate.

As in the cylindrical bending example from Section 3.6.3, it is important to note that when the resultant moment T is modeled as a constant distributed moment surface loading $T = \int_A m_{sz} dA$, or a linearly varying surface loading $T = \int_A r\ p_{s\theta} dA$ only, an axisymmetric torsion state is not obtained. Consequently, such a problem does not converge to the analytical solution given in [1] but to another different solution. Such a problem is analysed in [49].

In the second part of this numerical example the results of the numerical analysis are compared with the experiments performed on a micropolar material. The first successful attempt to experimentally validate all six micropolar material parameters is conducted by Lakes [5] who has studied experimentally the size-effect phenomenon, which is analytically predicted to occur in torsion and bending [1]. His study consists of a set of quasi-static torsion and bending tests performed on circular cylinder specimens and dynamic tests performed on rectangular bars made of low-density polymeric foam. A characteristic dimension of the specimens is taken to be small enough for the size effect to be observable, approaching the value of the material characteristic length (diameters 13 mm, 20 mm, 28 mm, 35 mm and 40 mm with the length-to-diameter ratio $c/d = 5$). The end-point torsional rotation θ is measured for a given torque value and the resulting torsional rigidity is computed from $J = \dfrac{T\ c}{\theta}$. The results of $\dfrac{J}{d^2}$ against d^2 obtained in this way in [5] are reproduced as dots in Figure 3.35. Analytically, on the other hand, the micropolar torsional rigidity follows from $(3.70)_3$ as

$$J = \frac{T}{C_1} = \pi a^2 \frac{\left(\dfrac{\mu a^2}{2\beta} + 3\right)\left(\dfrac{\alpha}{2} + \beta\right)\ pa\ I_0(pa) - \left(\dfrac{\mu a^2}{2\beta} + 4\right)\beta\ I_1(pa)}{\left(1 + \dfrac{\alpha}{2\beta}\right)\ pa\ I_0(pa) - I_1(pa)}, \qquad (3.72)$$

with $a = \frac{d}{2}$ and $p = 2\sqrt{\frac{\nu}{\alpha + 2\beta}}$, i.e. it is a function of the micropolar material parameters μ, ν, α, β and the cross-section radius a. Lakes has determined these material parameters [5] by drawing the best-fit curve to the experimental results, plotted using a solid line in Figure 3.35. The micropolar engineering parameters G, l_t, N, and ψ can then be obtained from equation (2.185). Lakes refers to this approach as the method of size effects which makes use of the analytical solution [1] to describe the dependence of rigidity upon size. For the case of the polymeric-foam specimens, the experimental data are fitted well by $G = 0.6$ N/mm^2, $\psi = 1.5$, $l_t = 3.8$ mm and $N = 0.3$. The remaining

engineering parameters are obtained from the tension and bending test and are equal to $n = 0.07$ and $l_b = 5$ mm. The corresponding continuum material parameters are $\mu = 0.6$ N/mm^2, $\lambda = 0.0976744$ N/mm^2, $\nu = 0.0593407$ N/mm^2, $\alpha = -5.776$ N, $\beta = 8.664$ N and $\gamma = 51.336$ N. Let us note that here the restriction on positive definiteness of the strain energy is not strictly satisfied since $3\alpha + 2\beta = 0$. The dashed line in Figure 3.35 represents the theoretical solution in the classical-elasticity theory, $\dfrac{J}{d^2} = \dfrac{1}{32}\pi G d^2$.
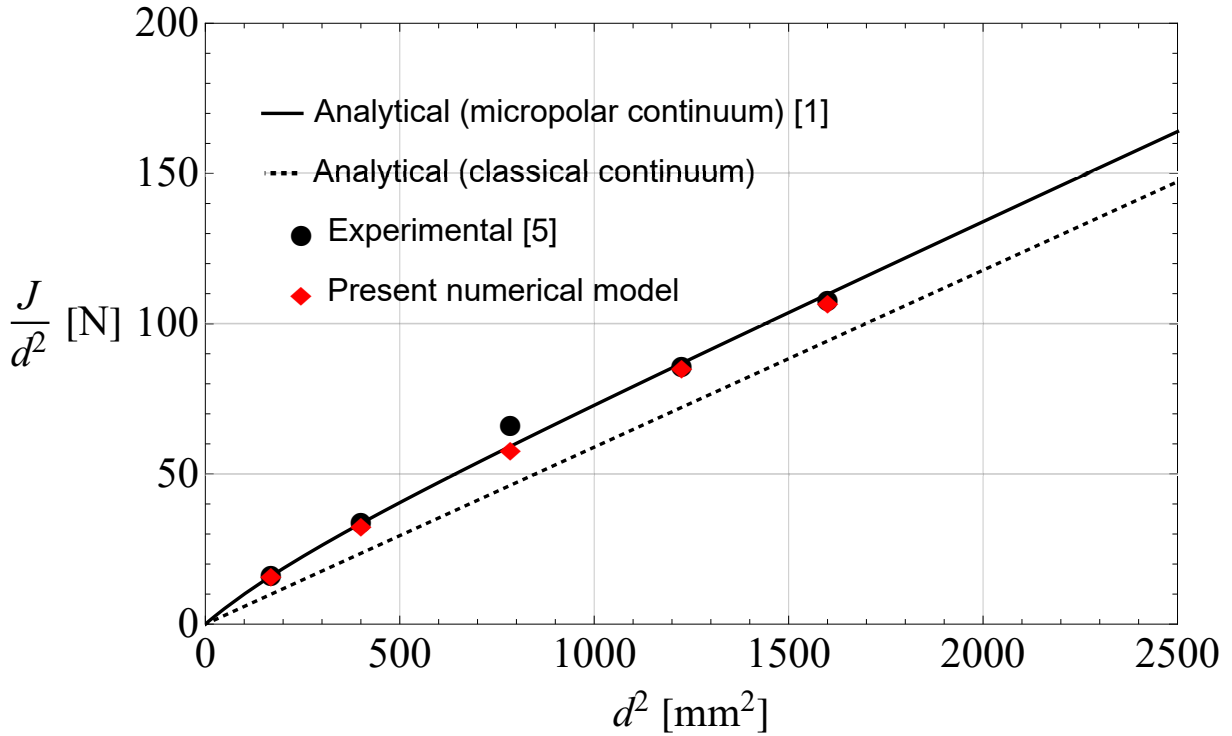
Figure 3.35: Analytical, experimental and numerical representation of a size-effect behaviour of a polymeric foam

In our numerical model proper external loading should be applied as argued earlier. For the micropolar parameters given and a unit torque moment $T = 1$ Nmm, the distributed surface loading is represented by a quasi-linearly varying surface loading $p_{s\theta}$ and, since $\psi \neq 0$, a non-constant distributed surface moment loading m_{sz}. For the specimen with $d = 13$ mm, this is shown in Figure 3.36.

(a) $p_{s\theta}$ for $r \in [0, 50.0]$

(b) $p_{s\theta}$ for $r \in [0, a]$

(c) m_{sz} for $r \in [0, a]$
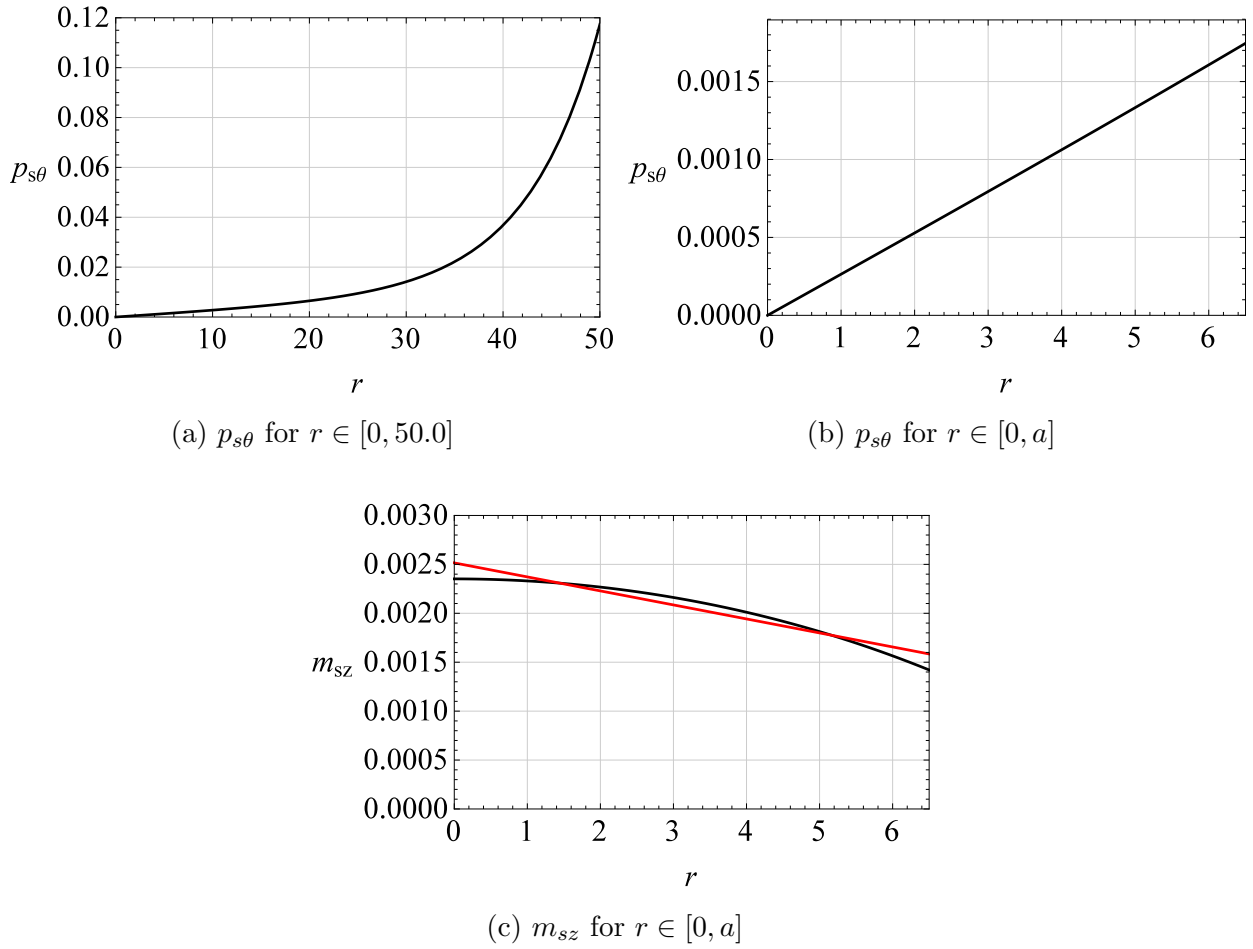
Figure 3.36: Distribution of the external loading for the specimen with $d = 13$ mm

By analysing the definition of the resultant torque T from equation (3.68), we can see from Figure 3.36 that for the specimen with diameter $d = 13$ mm the contribution of the distributed surface load m_{sz} in the resultant unit torque moment is 25.15 % while the contribution of $p_{s\theta}$ is 74.85 %. Furthermore, the contribution of the constant part of the surface moment loading, having the value of $m_{sz} = 0.001420949939$ Nmm/mm² is 18.86 % while the contribution of the non-linear part of the surface moment loading is 6.28 %, all computed using the *Wolfram Mathematica* package. Thus, the applied moment loading is simplified to a sum of the constant part of the moment surface loading equal to $m_{sz} = 0.001420949939$ Nmm/mm² and a radially linear distribution obtaining the value of 0.001094166286 Nmm/mm² for $r = 0$ and 0.0001634 Nmm/mm² for $r = a$. This distribution is shown in Figure 3.36c, represented by the straight line such that the areas under the analytical result (curved line) and the approximated result (straight line) are the same. Finally, the surface loading is applied as approximately linearly varying to obtain the value $p_{s\theta} = 0.001745546194$ N/mm² for $r = a$. The external loading for the remaining specimens is applied analogously, with the corresponding values obtained from (4.64). For the remaining specimens, the contribution of the distributed surface load m_{sz} in the resultant unit torque moment is decreasing by increasing the specimen diameter.

The problem is solved using Hex8IM elements for a fine mesh of 1536 elements shown in Figure 3.31c), and the obtained numerical results for u_θ at point $P(a, 0, c)$ for all specimens are introduced into the definition of the rigidity $J = \dfrac{T\, a\, c}{u_\theta}$ and plotted as diamonds in Figure 3.35. Even with the applied external loading simplified as described, very good agreement with the experiments conducted in [5] is achieved. Finally, in this example it is observed that, according to the experiments shown in Figure 3.35, the rigidity of the specimen with $d = 13$ mm is approximately 60% higher, while the rigidity of the specimen with $d = 20$ mm is approximately 16.5% higher than predicted by the classical-elasticity theory, which is now also numerically proven.

Chapter 4

Non-linear micropolar continuum model

The assumption of small or infinitesimal displacements and rotations in the linear micropolar continuum theory significantly simplifies derivation of the balance equations due to the fact that the difference between the undeformed and deformed configuration can be neglected in the equilibrium equations. However, this assumption is not always appropriate for a realistic description of the structural response. In general, we distinguish between two forms of non-linearity: material non-linearity and geometric non-linearity. In the specific case of an elastic material, the term material non-linearity implies that the stress is no longer proportional to the strain, as in the linear elasticity. In our work we focus explicitly on the *geometric non-linearity* where we do not restrict ourselves to small displacements and small rotations as assumed in the linear regime, i.e. we observe a body which, when deformed, exhibits large displacement and large rotations. Consequently, the difference between the deformed and initial (undeformed) configurations in the equilibrium equations cannot be neglected anymore, as assumed in the linear analysis. Thus, the equilibrium equations are no longer represented in a unique manner, i.e. we are obliged to choose a specific configuration to further work with. In that sense we can choose to express all the unknown variables as functions of coordinates in the initial (undeformed) configuration (in the literature also known as the *Lagrangian formulation*) or as functions of coordinates in the deformed configuration (in the literature also known as the *Eulerian formulation*) [56]. In solid mechanics the most commonly used formulation is Lagrangian, since it allows to express the variables with respect to a known configuration. Another challenge which arises in the non-linear analysis lies in the use of 3D finite rotations which are non-additive and non-commutative and as such require a special mathematical treatment, which is significantly more complex than that of displacements.

In this Chapter the mechanical problem of a non-linear micropolar continuum is analysed and the three sets of equations (equilibrium, kinematic and constitutive) with the corresponding boundary conditions needed in order to describe the problem are derived.

4.1 Orthonormal bases

The 3D Euclidean space $\mathbb{E}$ is a real vector space V with a basis defined by a set of three linearly independent vectors. An orthonormal basis is a set of three vectors, here denoted $\mathbf{e}_1$, $\mathbf{e}_2$ and $\mathbf{e}_3$ and collectively by $\{\mathbf{e}_i\}$ such that $\mathbf{e}_i \cdot \mathbf{e}_j = \delta_{ij}$, $i, j = 1, 2, 3$. [53]. Any point P in $\mathbb{E}$ is determined by three coordinates (X_1, X_2, X_3) and any vector $\mathbf{v}$ belonging to it can be represented with its components along the base vectors as

$$\mathbf{v} = v_1 \mathbf{e}_1 + v_2 \mathbf{e}_2 + v_3 \mathbf{e}_3, \tag{4.1}$$

where v_1, v_2, v_3 are the components of $\mathbf{v}$ relative to the given basis [53]. It is assumed here that the orthonormal basis $\{\mathbf{e}_i\}$ forms a right-handed triad of unit vectors, i.e. [53]

$$\mathbf{e}_1 \times \mathbf{e}_2 = \mathbf{e}_3, \quad \mathbf{e}_2 \times \mathbf{e}_3 = \mathbf{e}_1, \quad \mathbf{e}_3 \times \mathbf{e}_1 = \mathbf{e}_2. \tag{4.2}$$

4.1.1 Change of basis

We now consider another right-handed orthonormal basis $\{\mathbf{t}_i\}$ oriented with respect to $\{\mathbf{e}_i\}$, as shown in Figure 4.1.
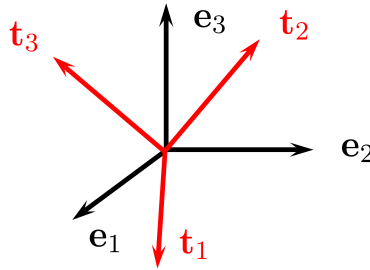
Figure 4.1: Change of basis

As shown in (4.1), since $\{\mathbf{e}_i\}$ is a basis, each $\mathbf{t}_i$ ($i = 1, 2, 3$) can be expressed as a linear combination of $\mathbf{e}_1$, $\mathbf{e}_2$ and $\mathbf{e}_3$, i.e. [53]

$$\mathbf{t}_i = Q_{ip} \mathbf{e}_p, \quad i, p = 1, 2, 3. \tag{4.3}$$

By taking the dot product of (4.3) with $\mathbf{e}_j$, we obtain the coefficients Q_{ij} as

$$Q_{ij} = \mathbf{t}_i \cdot \mathbf{e}_j. \tag{4.4}$$

By recalling the definition of the vector scalar product [53]

$$\mathbf{a} \cdot \mathbf{b} = |\mathbf{a}| \, |\mathbf{b}| \cos \sphericalangle(\mathbf{a}, \mathbf{b}), \tag{4.5}$$

we see that the coefficients Q_{ij} represent the direction cosines of the vectors $\mathbf{t}_i$ relative to $\mathbf{e}_j$. Furthermore, all the direction cosines Q_{ij} can be written in a matrix form $\mathbf{Q}$, which represents the *orientation matrix* or the *rotation matrix*. Due to orthonormality and (4.3) we obtain

$$\delta_{ij} = \mathbf{t}_i \cdot \mathbf{t}_j = Q_{ik}\mathbf{e}_k \cdot \mathbf{t}_j = Q_{ik}Q_{jk}, \tag{4.6}$$

leading to the conclusion that

$$\mathbf{Q}^{\mathrm{T}} = \mathbf{Q}^{-1}. \tag{4.7}$$

Any matrix satisfying (4.7) is said to be an *orthogonal matrix*, i.e. $\mathbf{Q}^{\mathrm{T}}\mathbf{Q} = \mathbf{Q}\mathbf{Q}^{\mathrm{T}} = \mathbf{I}$. Furthermore, by taking the determinant of $\mathbf{Q}\mathbf{Q}^{\mathrm{T}}$ we arrive at the following conclusion:

$$\det(\mathbf{Q}\mathbf{Q}^{\mathrm{T}}) = \det\mathbf{Q}\det\mathbf{Q}^{\mathrm{T}} = \det\mathbf{I} = (\det\mathbf{Q})^2 = 1, \;\; \Rightarrow \;\; \det(\mathbf{Q}) = \pm 1. \tag{4.8}$$

Orthogonal matrices with $\det(\mathbf{Q}) = +1$ represent a pure rotation of the basis, while orthogonal matrices with $\det(\mathbf{Q}) = -1$ represent a reflection of the basis. In this thesis we restrict our attention to the situations in which $\det(\mathbf{Q}) = +1$, which preserve the right-handedness of the basis vectors [53]. Such matrices are referred to as *proper orthogonal matrices*. In general, the matrix $\mathbf{Q}$ can be understood as a rotation operator which transforms linearly and isometrically (i.e. preserves the length and orientation) an orthonormal basis of $\mathbb{R}^3$ to another orthonormal basis in the Euclidean space. In the literature these matrices are also referred to as *special orthogonal*, and are classified to belong to the so-called special orthogonal rotation group SO(3), being also o Lie group and a subset of a larger matrix Lie group [84, 85]. A detailed exposition of this subject can be found in [86].

4.2 Frames of reference

In order to describe phenomena qualitatively and quantitatively, a *frame of reference* (location of an observer), which may be used as a basis for the description, is needed [53]. A frame is determined by its orientation and its placement. In general, by choosing different independent variables, different descriptions are attributed to the observed object. However, in continuum mechanics the only two descriptions of practical use are the *reference (material) description*, in which the independent variables are the position of a material particle in a chosen referential state and time and the *relative (spatial) description*, in which the independent variables are the position of a material particle in a current state and time.

Here we define a so-called *material frame of reference* by means of an associated base $\{\mathbf{E}_i\}$ at a chosen position relative to the body, which allows us to precisely define the position of a material point X within it. This is shown in Figure 4.2.
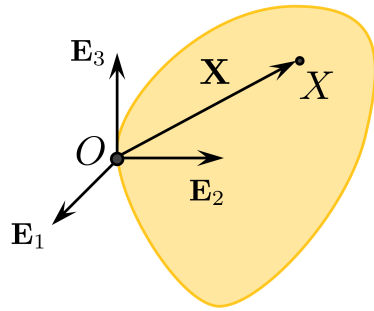
Figure 4.2: The material frame of reference

Next we define a so-called *spatial frame of reference* by means of another base $\{\mathbf{e}_i\}$ at a chosen position in space, with respect to which we are able to precisely define the position which the body takes when deformed, as shown in Figure 4.3.
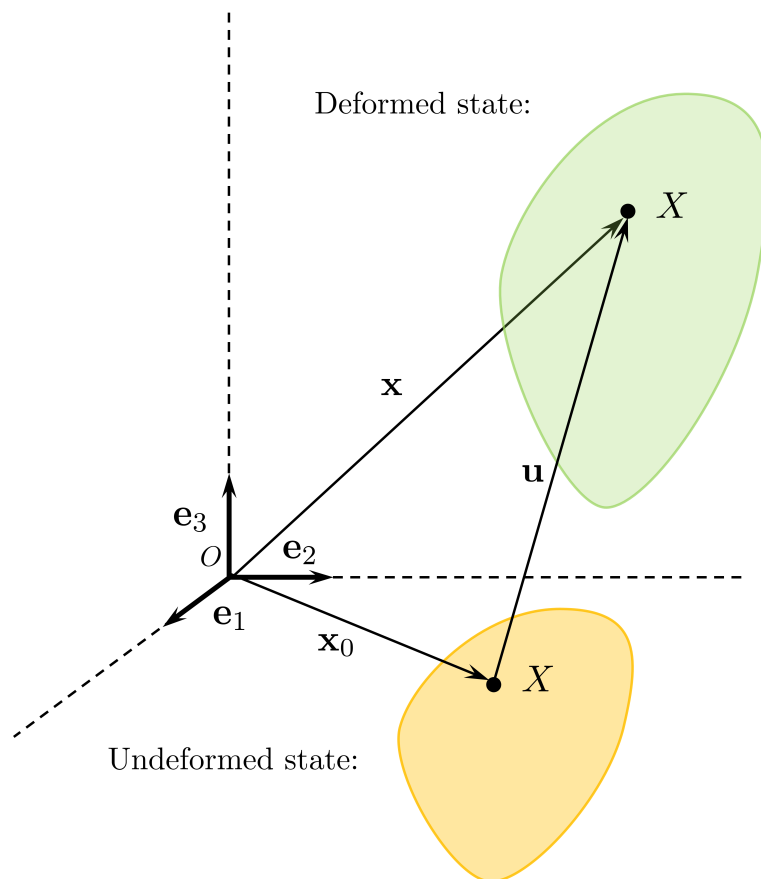
Figure 4.3: The spatial frame of reference

In Figure 4.3 the yellow body represents the reference state, which is here taken as the undeformed state, but can be taken as an arbitrary state of the body. The position

vectors $\mathbf{x}_0$, $\mathbf{x}$ together with the displacement vector $\mathbf{u}$ belong to this ambient space, which is why we refer to them as *spatial vectors*. In contrast, the position vector $\mathbf{X}$ lives in a different space, which we call the material space, and is thus called a *material vector*.

The relationship between spatial and material objects is defined by the so-called pull-back/push-forward mapping [56] by means of an orthogonal transformation $\mathbf{Q}$ which serves to define the relative orientation between the two respective domains (body and ambient space). For example, an arbitrary spatial vector $\mathbf{a}$ is related to its material counterpart $\mathbf{A}$ through

$$\mathbf{A} = \mathbf{Q}^{\mathrm{T}}\mathbf{a} \quad \Leftrightarrow \quad \mathbf{a} = \mathbf{Q}\mathbf{A}. \tag{4.9}$$

Geometrically, the vector $\mathbf{A}$ is a rotated version of the vector $\mathbf{a}$ by $\mathbf{Q}^{\mathrm{T}}$.

The pull-back/push-forward mapping is an inevitable tool in order to derive the balance equations in the known configuration in either description. In the process of deriving the balance equations it is important to keep in mind that the *body* and the *space* are distinct vector spaces, even though it is usually assumed (as we will also do here) that the material frame and spatial frame coincide. Nevertheless, it is useful to retain a notational distinction between the objects belonging to the two different spaces. As a rule we will use capital letters for the material objects and lower-case letters for the spatial objects.

4.3 On finite rotations

The two main features of the rotation group which have to be taken into account are:

1. Its elements (rotation matrices) are *not commutative* in general, i.e. $\mathbf{Q}_1\mathbf{Q}_2 \neq \mathbf{Q}_2\mathbf{Q}_1$ where $\mathbf{Q}_1$, $\mathbf{Q}_2 \in \mathrm{SO}(3)$, i.e. changing the order of two successive rotations a different result is obtained;

2. Its elements are *not additive*, i.e. $\mathbf{Q}_1 + \mathbf{Q}_2 \notin \mathrm{SO}(3)$.

Consequently, the mathematical treatment of finite rotations in a numerical analysis is significantly more complex than that of displacements.

As already mentioned, the finite rotations in 3D are represented by an orthogonal tensor $\mathbf{Q} \in \mathrm{SO}(3)$, i.e. $\mathbf{Q}^{-1} = \mathbf{Q}^{\mathrm{T}}$, $\det\mathbf{Q} = +1$. However, difficulties of such a representation arise due to the fact that $\mathrm{SO}(3)$ is not a linear space, but a non-linear differentiable manifold. The non-linearity of the rotational manifold $\mathrm{SO}(3)$ turns out to be incompatible with the standard additive interpolation techniques in the finite element method, which is a technique designed to respect the properties of the linear vector space [85]. Thus, the treatment of the 3D rotations becomes nontrivial primarily because of the nonlinear character of the manifold to which they belong.

4.3.1 Parametrization of finite rotation

In order to describe a three-dimensional finite rotation, a number of forms incorporating different parameters are developed. In general, they can be divided into two main groups: *the vector-like parametrizations* (such as Euler-Rodrigues and Cayley-Rodrigues), which are te most commonly used ones, and *the non vector-like parametrization* (such as the Euler's angles, quaternions ect.). The outline of different types of parametrizations of rotations can be found in e.g. [87], [84], [88], [89].

4.3.1.1 Vectorial parametrization of finite rotation

For plane problems, the rotations are trivially defined. In a plane, the only information needed is the magnitude (or angle) of rotation, i.e. rotations are represented as scalar quantities, which means that they commute, i.e. $\vartheta_1 + \vartheta_2 = \vartheta_2 + \vartheta_1$. Consequently, in plane problems, rotations are describable as a sequence of additive rotations. However, in order to define a finite spatial rotation, two informations are needed: the magnitude and direction (or axis of rotation). These two attributes describe vectors. However, contrary to infinitesimal rotations, finite spatial rotations do not obey the laws of vector calculus. Consequently, a rotational vector $\boldsymbol{\vartheta}$ is in the literature referred to as a rotational *pseudovector*, where the attribute *pseudo* signifies that it does not obey certain properties of classical vectors.

It is shown by Argiris [2] that two orientations represented by orientation matrices $\mathbf{Q}_1$ and $\mathbf{Q}_2$ are related through the exponential map of the skew-symmetric matrix $\widehat{\boldsymbol{\vartheta}}$ of the rotational vector $\boldsymbol{\vartheta}$ as

$$\mathbf{Q}_1 = \exp\widehat{\boldsymbol{\vartheta}}\mathbf{Q}_2, \tag{4.10}$$

where

$$\exp\widehat{\boldsymbol{\vartheta}} = \mathbf{I} + \frac{\sin\vartheta}{\vartheta}\hat{\boldsymbol{\vartheta}} + \frac{1-\cos\vartheta}{\vartheta^2}\hat{\boldsymbol{\vartheta}}^2. \tag{4.11}$$

Equation (4.11) is also know as the *Euler-Rodrigues formula*. As in [2], the detailed derivation of this result using the geometric approach is presented in Appendix D.

4.3.1.2 Quaternion parametrization of finite rotation

Some attempts to represent $\mathbf{Q}$ by some other sets of only three parameters (e.g. *Euler angles* [87]) has shown to be suffering from the so-called *non-uniqueness problem* [87], [89]. However, according to *Euler's rotation theorem* [87], any spatial rotation can be represented by a rotation of a given angle ϑ about a fixed axis. Therefore it can be represented as a combination of a unit vector $\mathbf{v}$ and a scalar ϑ. This idea led to the development of a 4-parameter representation of finite rotations based on the so-called *quaternions* which has shown to be practical and in favor of the computational cost saving in the numerical analysis. Compared to rotation matrices, they need less computational

space and are shown to be more numerically stable [89]. In order to establish a unique bijective global representation of finite rotations, a minimum of five parameters is needed [90]. However, even though strictly speaking, the quaternion parametrisation is not a 1-1 but rather a 2-1 representation, it is useful for practical purposes [89]. If a unit vector about which the rotation is taking place is defined as $\mathbf{v} = v_x\mathbf{i} + v_y\mathbf{j} + v_z\mathbf{k}$ and the angle of rotation is defined by a scalar ϑ, the quaternion representation of such a rotation is defined as [84]

$$\mathbf{q}^* = \cos\frac{\vartheta}{2} + (v_x\mathbf{i} + v_y\mathbf{j} + v_z\mathbf{k})\sin\frac{\vartheta}{2} = \{q_0, \mathbf{q}\}, \tag{4.12}$$

where

$$q_0 = \cos\frac{\vartheta}{2}, \quad \mathbf{q} = sin\frac{\vartheta}{2}\frac{\boldsymbol{\vartheta}}{||\boldsymbol{\vartheta}||}. \tag{4.13}$$

It is important to note that rotations can be represented only by unit quaternions. The parametrization of rotations via quaternions, i.e. $\{q_0, \mathbf{q}\} \in S^3 \mapsto \mathbf{Q} \in \mathrm{SO}(3)$ is defined through the relation

$$\mathbf{Q} = (2q_0^2 - 1)\mathbf{I} + 2q_0\hat{\mathbf{q}} + 2\mathbf{q} \otimes \mathbf{q}, \tag{4.14}$$

where $\hat{\mathbf{q}} = \mathbf{q} \times \mathbf{I}$ [84]. In general, if we define a unit quaternion as $\mathbf{q}^* = a + b\mathbf{i} + c\mathbf{j} + d\mathbf{k}$, the orthogonal matrix corresponding to a rotation by the unit quaternion $\mathbf{q}^*$ is equal to

$$\mathbf{Q} = \begin{bmatrix} a^2 + b^2 - c^2 - d^2 & 2bc - 2ad & 2bd + 2ac \\ 2bc + 2ad & a^2 - b^2 + c^2 - d^2 & 2cd - 2ab \\ 2bd - 2ac & 2cd + 2ab & a^2 - b^2 - c^2 + d^2 \end{bmatrix}. \tag{4.15}$$

The inverse mapping $\mathbf{Q} \in \mathrm{SO}(3) \mapsto \{q_0, \mathbf{q}\}$ is defined as

$$q_0 = \frac{1}{2}\sqrt{1 + \mathrm{tr}\mathbf{Q}}, \quad \mathbf{q} = \frac{1}{4q_0}[\widehat{\mathbf{Q} - \mathbf{Q}^\mathrm{T}}]. \tag{4.16}$$

However, this relation is not numerically stable due to sensitivity of the magnitude of rotation. In order to avoid singularities, it is suggested to use the so-called Spurrier algorithm [91]: If the trace of the orientation matrix is larger than any of the components on the diagonal of the orientation matrix, i.e. $\mathrm{tr}(\mathbf{Q}) > Q_{ii}$ compute the quaternion using the following expressions:

$$q_0 = \frac{1}{2}\sqrt{1 + \mathrm{tr}(Q)}, \quad q_i = \frac{(Q_{kj} - Q_{jk})}{4q_0}, \tag{4.17}$$

where j and k are chosen so that i, j, k is a cyclic permutation of 1,2,3. If any of the components on the diagonal is larger than the trace of the orientation matrix, i.e. $Q_{ii} > \mathrm{tr}(\mathbf{Q})$ use the following expressions:

$$q_i = \sqrt{\frac{Q_{ii}}{2} + \frac{(1 - \mathrm{tr}(Q))}{4}}, \quad q_0 = \frac{(Q_{kj} - Q_{jk})}{4q_i}, \quad q_l = \frac{(Q_{li} + Q_{il})}{4q_i}, \ (l = j, k), \tag{4.18}$$

115

where i, j, k is a cyclic permutation of 1,2,3 such that Q_{ii} is the largest.

4.4 Derivation of nonlinear micropolar equilibrium equations

In the following, the balance equations are derived with respect to both the *spatial* and *material* frame of reference. For the sake of clarity, the quantities pertaining to the material frame of reference are written using the upper-case letters, whereas those pertaining to the spatial frame of reference are written using the lower-case letters.

4.4.1 Strong form of equilibrium equations in spatial description

Let us analyse the body $\mathcal{B}$ in the deformed state under the influence of external actions consisting of distributed loadings $\mathbf{p}_\mathrm{v}$ as a specific volume force, $\mathbf{m}_\mathrm{v}$ as a specific body moment, a specific surface force $\mathbf{p}_\mathrm{s}$ and a specific surface moment $\mathbf{m}_\mathrm{s}$ as shown in Figure 4.4. The body surface S is divided into two parts: S_p with prescribed loading and S_u with prescribed displacements and rotations. Next, we observe an arbitrary part of the body, denoted as $\mathcal{B}'$ of a volume v' and with a closed surface s' in the deformed configuration. In order to preserve equilibrium, by following *Cauchy's theorem* as described in Section 2.1 there exist a mean stress vector $\overline{\mathbf{t}}$ and a mean couple-stress vector $\overline{\mathbf{m}}$ on the surface of the extracted body. When the body part $\mathcal{B}'$ becomes infinitesimally small, the mean stress and couple-stress vectors are represented by the stress vector field $\mathbf{t}$ and the couple-stress vector field $\mathbf{m}$.

By establishing equilibrium in the deformed configuration, we obtain the force equilibrium equation in the integral form

$$\int_{v'} \mathbf{p}_\mathrm{v} \, dv + \oint_{s'} \mathbf{t} \, ds = \mathbf{0}, \tag{4.19}$$

where by applying the Cauchy theorem $\boldsymbol{\sigma} \, \mathbf{n} = \mathbf{t}$ as defined in equation (2.26), we obtain

$$\int_{v'} \mathbf{p}_\mathrm{v} \, dv + \oint_{s'} \boldsymbol{\sigma} \, \mathbf{n} \, ds = \mathbf{0}, \tag{4.20}$$

where $\mathbf{n}$ is now a unit normal to s' in the deformed configuration.
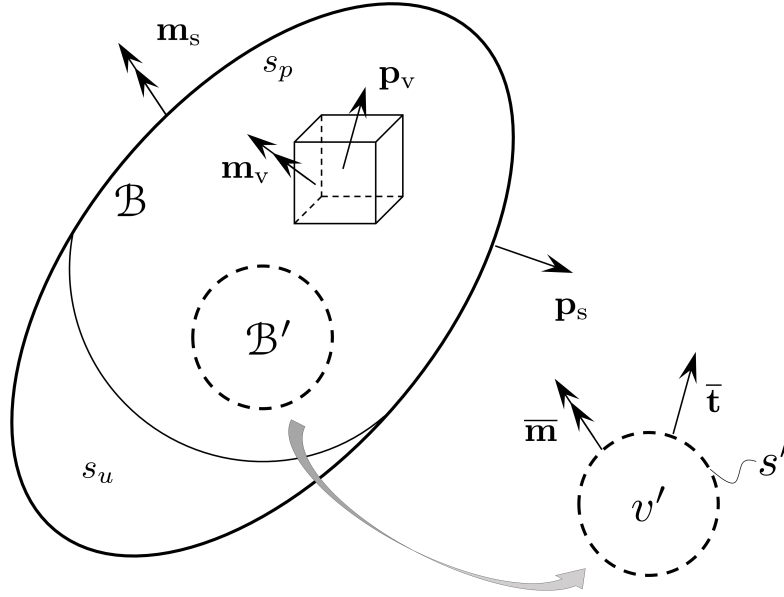
Figure 4.4: Body subject to applied volume load and surface traction in a deformed configuration

In order to obtain a differential equilibrium equation we have to apply divergence theorem defined in Theorem 1. (see Section 2.1). Applying the divergence theorem on equation (4.20) gives

$$\int_{v'} \mathbf{p}_\mathrm{v} \; dv + \int_{v'} \mathrm{div} \; \boldsymbol{\sigma} \; dv = \mathbf{0}, \tag{4.21}$$

$$\int_{v'} (\mathbf{p}_\mathrm{v} + \mathrm{div} \; \boldsymbol{\sigma}) \; dv = \mathbf{0}. \tag{4.22}$$

Since equation (4.22) has to be valid for an arbitrary volume v', we conclude that

$$\mathbf{p}_\mathrm{v} + \mathrm{div} \; \boldsymbol{\sigma} = \mathbf{0}, \tag{4.23}$$

which is the so-called strong (or differential) form of the force equilibrium. By summing all the moments acting on the part $\mathcal{B}'$ of the body $\mathcal{B}$ we obtain

$$\int_{v'} (\mathbf{m}_\mathrm{v} + \mathbf{x} \times \mathbf{p}_\mathrm{v}) \; dv + \oint_{s'} (\mathbf{x} \times \mathbf{t} + \mathbf{m}) \; ds = \mathbf{0}, \tag{4.24}$$

where $\mathbf{x}$ is the position vector in the deformed configuration of a material point with respect to the spatial frame and $\times$ denotes the cross product. Again, by applying the Cauchy theorem $\boldsymbol{\sigma} \; \mathbf{n} = \mathbf{t}$ as defined in equation (2.26) and a generalisation of the Cauchy theorem regarding the moment part as $\boldsymbol{\mu} \; \mathbf{n} = \mathbf{m}$ as defined in equation (2.49) we obtain

$$\int_{v'} (\mathbf{m}_\mathrm{v} + \mathbf{x} \times \mathbf{p}_\mathrm{v}) \ dv + \oint_{s'} (\mathbf{x} \times \boldsymbol{\sigma} \ \mathbf{n} + \boldsymbol{\mu} \ \mathbf{n}) \ ds = \mathbf{0}. \tag{4.25}$$

We introduce the identity $\mathbf{x} \times \mathbf{t} = \hat{\mathbf{x}}\mathbf{t}$ as defined in equation (2.29). Equation (4.25) may be thus written as

$$\int_{v'} (\mathbf{m}_\mathrm{v} + \hat{\mathbf{x}}\mathbf{p}_\mathrm{v}) \ dv + \oint_{s'} (\hat{\mathbf{x}}\boldsymbol{\sigma} + \boldsymbol{\mu}) \ \mathbf{n} \ ds = \mathbf{0}. \tag{4.26}$$

Now, we apply the divergence theorem and obtain

$$\int_{v'} (\mathbf{m}_\mathrm{v} + \hat{\mathbf{x}}\mathbf{p}_\mathrm{v}) \ dv + \int_{v'} \mathrm{div} \, (\hat{\mathbf{x}}\boldsymbol{\sigma} + \boldsymbol{\mu}) \ dv = \mathbf{0}. \tag{4.27}$$

By expressing $\mathbf{p}_\mathrm{v} = -\mathrm{div}\boldsymbol{\sigma}$ from (4.23) and expressing the divergence of a sum on the second integral in (4.27) as a sum of the corresponding divergences we obtain

$$\int_{v'} (\mathbf{m}_\mathrm{v} - \hat{\mathbf{x}}\mathrm{div}\boldsymbol{\sigma} + \mathrm{div}(\hat{\mathbf{x}}\boldsymbol{\sigma}) + \mathrm{div}\boldsymbol{\mu}) \ dv = \mathbf{0}. \tag{4.28}$$

Let us express the nabla operator componentially as $\nabla = \mathbf{e}_1\frac{\partial}{\partial x_1} + \mathbf{e}_2\frac{\partial}{\partial x_2} + \mathbf{e}_3\frac{\partial}{\partial x_3}$ with $(\mathbf{e}_1, \mathbf{e}_2, \mathbf{e}_3)$ as the spatial frame with respect to which (x_1, x_2, x_3) are the components of the position vector $\mathbf{x}$. Let us now analyse the term $\mathrm{div}(\hat{\mathbf{x}}\boldsymbol{\sigma})$, where the summation over repeated indices is implied:

$$\begin{aligned} \mathrm{div}(\hat{\mathbf{x}}\boldsymbol{\sigma}) &= (\hat{\mathbf{x}}\boldsymbol{\sigma})\nabla \\ &= \frac{\partial}{\partial x_p}(\hat{\mathbf{x}}\boldsymbol{\sigma})\mathbf{e}_p \\ &= \frac{\partial \hat{\mathbf{x}}}{\partial x_p}\boldsymbol{\sigma}\mathbf{e}_p + \hat{\mathbf{x}}\underbrace{\frac{\partial \boldsymbol{\sigma}}{\partial x_p}\mathbf{e}_p}_{\mathrm{div}\boldsymbol{\sigma}} \\ &= \frac{\partial \mathbf{x}}{\partial x_p} \times \boldsymbol{\sigma}\mathbf{e}_p + \hat{\mathbf{x}}\mathrm{div}\boldsymbol{\sigma} \end{aligned} \tag{4.29}$$

By applying the identities (E.2) and (E.7) on the first term of the right-hand side we obtain:

$$\begin{aligned} \widehat{\frac{\partial \mathbf{x}}{\partial x_p}} \times \boldsymbol{\sigma}\mathbf{e}_p &= (\boldsymbol{\sigma}\mathbf{e}_p) \otimes \frac{\partial \mathbf{x}}{\partial x_p} - \frac{\partial \mathbf{x}}{\partial x_p} \otimes (\boldsymbol{\sigma}\mathbf{e}_p) \\ &= \boldsymbol{\sigma}\mathbf{e}_p \left(\frac{\partial \mathbf{x}}{\partial x_p}\right)^\mathrm{T} - \left(\frac{\partial \mathbf{x}}{\partial x_p}\right)\mathbf{e}_p^\mathrm{T}\boldsymbol{\sigma}^\mathrm{T} \\ &= \boldsymbol{\sigma}\mathbf{e}_p \otimes \left(\frac{\partial \mathbf{x}}{\partial x_p}\right) - \left(\frac{\partial \mathbf{x}}{\partial x_p}\right) \otimes \mathbf{e}_p\boldsymbol{\sigma}^\mathrm{T} \end{aligned} \tag{4.30}$$

$$= \boldsymbol{\sigma} \mathbf{e}_p \otimes \underbrace{\frac{\partial x_i}{\partial x_p} \mathbf{e}_i}_{\delta_{pi}} - \underbrace{\frac{\partial x_i}{\partial x_p} \mathbf{e}_i}_{\delta_{pi}} \otimes \mathbf{e}_p \boldsymbol{\sigma}^{\mathrm{T}}$$

$$= \boldsymbol{\sigma} \mathbf{I} - \mathbf{I} \boldsymbol{\sigma}^{\mathrm{T}}$$

$$= \boldsymbol{\sigma} - \boldsymbol{\sigma}^{\mathrm{T}},$$

where $\mathbf{I} = \mathbf{e}_p \otimes \mathbf{e}_p$ is the identity tensor. Since in (4.28) we have $\mathrm{div}(\hat{\mathbf{x}}\boldsymbol{\sigma}) = \hat{\mathbf{x}}\mathrm{div}\boldsymbol{\sigma} + \frac{\partial \mathbf{x}}{\partial x_p} \times \boldsymbol{\sigma}\mathbf{e}_p$, i.e. we need a vector $\frac{\partial \mathbf{x}}{\partial x_p} \times \boldsymbol{\sigma}\mathbf{e}_p$, we employ an *axial operator* $\mathrm{ax}\,\widehat{(\cdot)} = (\cdot)$, as an inverse operation of $\widehat{(\cdot)}\mathbf{v} = (\cdot) \times \mathbf{v}$ in order to obtain a vector from a skew-symmetric matrix. Thus, we have

$$\frac{\partial \mathbf{x}}{\partial x_p} \times \boldsymbol{\sigma}\mathbf{e}_p = \mathrm{ax}\left(\boldsymbol{\sigma} - \boldsymbol{\sigma}^{\mathrm{T}}\right), \tag{4.31}$$

and substituting (4.29) and (4.31) in (4.28) we obtain

$$\int_{v'} \left(\mathbf{m}_{\mathrm{v}} - \hat{\mathbf{x}}\mathrm{div}\boldsymbol{\sigma} + \mathrm{ax}(\boldsymbol{\sigma} - \boldsymbol{\sigma}^{\mathrm{T}}) + \hat{\mathbf{x}}\mathrm{div}\boldsymbol{\sigma} + \mathrm{div}\boldsymbol{\mu}\right)\, dv = \mathbf{0}, \tag{4.32}$$

and finally

$$\int_{v'} \left(\mathrm{div}\boldsymbol{\mu} + \mathrm{ax}(\boldsymbol{\sigma} - \boldsymbol{\sigma}^{\mathrm{T}}) + \mathbf{m}_{\mathrm{v}}\right)\, dv = \mathbf{0}. \tag{4.33}$$

Since equation (4.33) is valid for an arbitrary part of the body, it has to be valid for the whole body. By taking this observation into account we obtain the strong form of the second equilibrium equation in the deformed configuration as

$$\mathrm{div}\boldsymbol{\mu} + \mathrm{ax}(\boldsymbol{\sigma} - \boldsymbol{\sigma}^{\mathrm{T}}) + \mathbf{m}_{\mathrm{v}} = \mathbf{0}. \tag{4.34}$$

The boundary conditions are defined as

$$\boldsymbol{\sigma}\,\mathbf{n} = \mathbf{p}_{\mathrm{s}}, \quad \boldsymbol{\mu}\,\mathbf{n} = \mathbf{m}_{\mathrm{s}} \ \text{ on } S_p. \tag{4.35}$$

The stress $\boldsymbol{\sigma}$ is in the literature referred to as the *true (Cauchy) stress*, since in reality it is the only stress that occurs in a deformed solid body undergoing large strains, displacements and rotations [56]. The same holds for the couple stress $\boldsymbol{\mu}$, referred to as the *true couple-stress*. We can see that the equilibrium equations (4.23) and (4.34) in the deformed configuration of a non-linear micropolar continuum obtain the same form as the equilibrium equations (2.57) and (2.68) in the linear analysis, with grad $\hat{\mathbf{x}} : \boldsymbol{\sigma} = \mathrm{ax}(\boldsymbol{\sigma} - \boldsymbol{\sigma}^{\mathrm{T}})$. However, in contrast to the linear analysis, the domain and its boundary, as well as the position vector and orientation of a material point are now unknown. In order to find the solution of a boundary value problem posed in such a way, we need to establish the equilibrium equations in a known configuration.

4.4.2 Strong form of equilibrium equations in material description

Let an undeformed body $\mathcal{B}_0$ deforms in the three-dimensional Euclidean space to a new placement $\mathcal{B}$. In the micropolar continuum theory, each material particle can translate and rotate independently, leading to the conclusion that each material point has six degrees of freedom (three translations and three rotations). Consequently, in the reference placement, taken to be the undeformed state, each material point (or particle) is defined by its position vector $\mathbf{X} = X_i \mathbf{E}_i$ relative to the origin and by three orthonormal vectors $\{\mathbf{W}_i\}$, defining the orientation of the material point. In the deformed placement, referred to as $\mathcal{B}$, the position of the particle is now defined by another position vector $\mathbf{x} = x_i \mathbf{e}_i$ relative to the origin and its orientation is defined by three new orthonormal vectors $\{\mathbf{k}_i\}$. The relation between the two sets of orthonormal vectors is defined by a proper orthogonal microrotation tensor $\mathbf{Q} \in \mathrm{SO}(3)$ i.e. $\mathbf{Q}^{-1} = \mathbf{Q}^{\mathrm{T}}$, $\det \mathbf{Q} = +1$, i.e. $\mathbf{k}_i = \mathbf{Q} \mathbf{W}_i$. Even though the vector bases $\mathbf{E}_i$ and $\mathbf{e}_i$ are here taken to be equal (Figure 4.5) we keep notational distinction between them and call the fields defined over $\mathcal{B}_0$ *material* and those defined over $\mathcal{B}$ *spatial*. In order to distinguish between these two sets, fields belonging to the material frame are written using upper-case letters, while fields belonging to the spatial frame are written using lower-case letters.
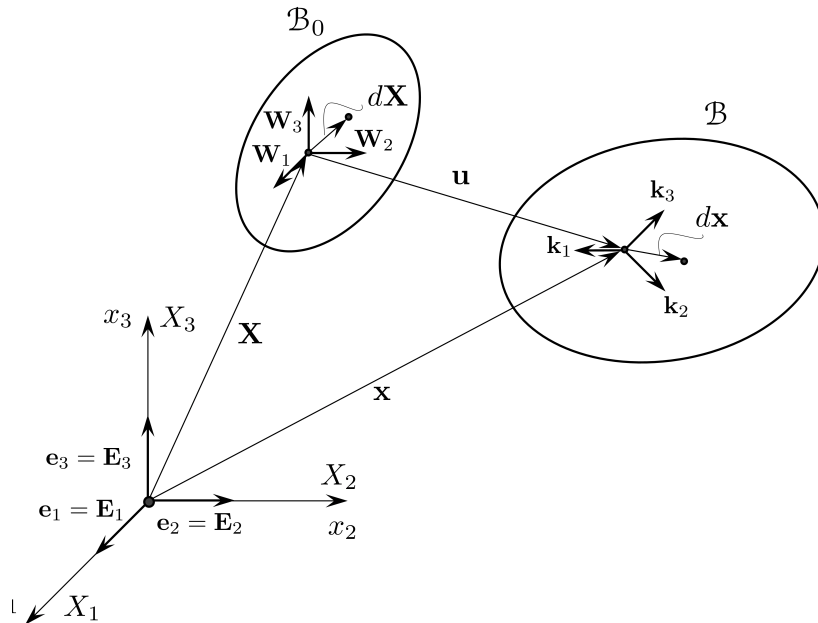
Figure 4.5: Initial and deformed configuration of a micropolar solid body in Euclidean space

The relation between an infinitesimal vector in the spatial reference $d\mathbf{x}$ and an infinitesimal vector in the material reference $d\mathbf{X}$ is described by the so-called deformation

gradient $\mathbf{F}$ as $d\mathbf{x} = \mathbf{F} \ d\mathbf{X}$. The deformation gradient is a two-point tensor defined as follows [56]:

$$\mathbf{F} = \text{GRAD } \mathbf{x} = \mathbf{x} \otimes \nabla_X = \frac{\partial \mathbf{x}}{\partial X_I} \otimes \mathbf{E}_I = \frac{\partial x_i}{\partial X_I} \mathbf{e}_i \otimes \mathbf{E}_I, \qquad (4.36)$$

where ∇_X represents the partial differential operator with respect to the material frame of reference. The deformation gradient tensor, besides infinitesimal vectors, defines also the transformation of an infinitesimal surface and an infinitesimal volume element from the material to the deformed configuration.

An infinitesimal surface element ds can be constructed as the vector product of two infinitesimal vectors $d\mathbf{x}$ and $d\mathbf{y}$ where the unit normal to that surface is defined as $\mathbf{n} = \dfrac{(d\mathbf{x} \times d\mathbf{y})}{\| \ d\mathbf{x} \times d\mathbf{y} \ \|}$. By using the transformation between infinitesimal vectors via the deformation gradient $d\mathbf{x} = \mathbf{F}d\mathbf{X}$ we obtain

$$\begin{aligned}
ds\mathbf{n} &= d\mathbf{x} \times d\mathbf{y} \\
&= (\mathbf{F}d\mathbf{X}) \times (\mathbf{F}d\mathbf{Y}) \\
&= (\det\mathbf{F} \ \mathbf{F}^{-\text{T}})(d\mathbf{X} \times d\mathbf{Y}) \\
&= (\det\mathbf{F} \ \mathbf{F}^{-\text{T}})dS\mathbf{N} \\
&= dS(\text{cof } \mathbf{F})\mathbf{N}.
\end{aligned} \qquad (4.37)$$

The equation (4.37) is referred to as Nanson formula [56].

By defining the infinitesimal volume as a scalar product between the surface vector $ds\mathbf{n}$ and the infinitesimal vector $d\mathbf{z}$, i.e. $dv = d\mathbf{z} \cdot ds\mathbf{n}$ and using (4.37) we obtain the relation between the infinitesimal volume in the initial and the deformed configuration as follows:

$$\begin{aligned}
dv &= d\mathbf{z} \cdot ds\mathbf{n} \\
&= \mathbf{F}d\mathbf{Z} \cdot (\det\mathbf{F} \ \mathbf{F}^{-\text{T}})dS\mathbf{N} = |\det\mathbf{F} = J| \\
&= d\mathbf{Z}^{\text{T}}\mathbf{F}^{\text{T}}\mathbf{F}^{-\text{T}}\mathbf{N}JdS \\
&= d\mathbf{Z}^{\text{T}}(\mathbf{F}^{-1}\mathbf{F})^{\text{T}}\mathbf{N}JdS \\
&= d\mathbf{Z}^{\text{T}}\mathbf{N}JdS \\
&= J \ d\mathbf{Z} \cdot dS\mathbf{N} \\
&= J \ dV.
\end{aligned} \qquad (4.38)$$

The equation confirms that the change of an infinitesimal volume is governed by the determinant of the deformation gradient J [56].

In order to obtain the strong form of the equilibrium equations in the material description, we start by writing the differential equilibrium equations in the weak form and apply the so-called change of variables theorem [92]. First we multiply equation (4.23)

and the force boundary condition $(4.35)_1$ by an arbitrary weighting (test) function $\overline{\mathbf{u}}$ and equation (4.34) and its corresponding boundary condition $(4.35)_2$ by another arbitrary weighting (test) function $\overline{\boldsymbol{\varphi}}$, as follows:

$$\overline{\mathbf{u}} \cdot (-\mathbf{p}_{\mathrm{v}} - \operatorname{div} \boldsymbol{\sigma}) = 0, \qquad \overline{\mathbf{u}} \cdot (\boldsymbol{\sigma}\mathbf{n} - \mathbf{p}_{\mathrm{s}}) = 0, \tag{4.39}$$

$$\overline{\boldsymbol{\varphi}} \cdot \left(-\operatorname{div}\boldsymbol{\mu} - \operatorname{ax}(\boldsymbol{\sigma} - \boldsymbol{\sigma}^{\mathrm{T}}) - \mathbf{m}_{\mathrm{v}}\right) = 0, \qquad \overline{\boldsymbol{\varphi}} \cdot (\boldsymbol{\mu}\mathbf{n} - \mathbf{m}_{\mathrm{s}}) = 0. \tag{4.40}$$

The test functions have to be sufficiently many times differentiable and identically equal to zero on the part of the surface with prescribed essential (kinematic) boundary conditions s_u. Now we integrate the equations over their respective domains of definition:

$$\int_v \left[\overline{\mathbf{u}} \cdot (-\mathbf{p}_{\mathrm{v}} - \operatorname{div} \boldsymbol{\sigma})\right] dv + \int_v \left[\overline{\boldsymbol{\varphi}} \cdot \left(-\operatorname{div}\boldsymbol{\mu} - \operatorname{ax}(\boldsymbol{\sigma} - \boldsymbol{\sigma}^{\mathrm{T}}) - \mathbf{m}_{\mathrm{v}}\right)\right] dv$$
$$+ \int_{s_p} \overline{\mathbf{u}} \cdot (\boldsymbol{\sigma}\mathbf{n} - \mathbf{p}_{\mathrm{s}})\, ds + \int_{s_p} \overline{\boldsymbol{\varphi}} \cdot (\boldsymbol{\mu}\mathbf{n} - \mathbf{m}_{\mathrm{s}})\, ds = 0. \tag{4.41}$$

Next, we analyse the terms containing the divergence of stress and couple-stress tensors, as follows:

$$\begin{aligned}
\overline{\mathbf{u}} \cdot \operatorname{div} \boldsymbol{\sigma} &= \overline{\mathbf{u}} \cdot (\boldsymbol{\sigma} \cdot \nabla_{\mathrm{x}}) \\
&= \overline{\mathbf{u}} \cdot \frac{\partial \boldsymbol{\sigma}}{\partial x_i} \mathbf{e}_i \\
&= \frac{\partial}{\partial x_i} (\overline{\mathbf{u}} \cdot \boldsymbol{\sigma})\, \mathbf{e}_i - \frac{\partial \overline{\mathbf{u}}}{\partial x_i} \cdot \boldsymbol{\sigma}\mathbf{e}_i \\
&= \frac{\partial}{\partial x_i} (\overline{\mathbf{u}}^{\mathrm{T}} \boldsymbol{\sigma})\, \mathbf{e}_i - \frac{\partial \overline{\mathbf{u}}}{\partial x_i} \cdot (\boldsymbol{\sigma}\mathbf{e}_i) & (4.42) \\
&= \frac{\partial}{\partial x_i} \mathbf{e}_i^{\mathrm{T}} (\boldsymbol{\sigma}^{\mathrm{T}}\overline{\mathbf{u}}) - \operatorname{tr}\left(\frac{\partial \overline{\mathbf{u}}}{\partial x_i} \otimes \boldsymbol{\sigma}\mathbf{e}_i\right) & (4.43) \\
&= \nabla_{\mathrm{x}}^{\mathrm{T}} (\boldsymbol{\sigma}^{\mathrm{T}}\overline{\mathbf{u}}) - \operatorname{tr}\left(\frac{\partial \overline{\mathbf{u}}}{\partial x_i} \mathbf{e}_i^{\mathrm{T}} \boldsymbol{\sigma}^{\mathrm{T}}\right) \\
&= \nabla_{\mathrm{x}} \cdot (\boldsymbol{\sigma}^{\mathrm{T}}\overline{\mathbf{u}}) - \operatorname{tr}\left(\frac{\partial \overline{\mathbf{u}}}{\partial x_i} \otimes \mathbf{e}_i \boldsymbol{\sigma}^{\mathrm{T}}\right) \\
&= \operatorname{div}(\boldsymbol{\sigma}^{\mathrm{T}}\overline{\mathbf{u}}) - \operatorname{grad}\overline{\mathbf{u}} : \boldsymbol{\sigma}.
\end{aligned}$$

By analogy we obtain:

$$\overline{\boldsymbol{\varphi}} \cdot \operatorname{div}\boldsymbol{\mu} = \operatorname{div}(\boldsymbol{\mu}^{\mathrm{T}}\overline{\boldsymbol{\varphi}}) - \operatorname{grad}\overline{\boldsymbol{\varphi}} : \boldsymbol{\mu}. \tag{4.44}$$

$$\tag{4.45}$$

Next we analyse the surface integral term $\int_{s_p} \overline{\mathbf{u}} \cdot (\boldsymbol{\sigma} \mathbf{n})\, ds$:

$$\int_{s_p} \overline{\mathbf{u}} \cdot (\boldsymbol{\sigma}\mathbf{n})\, ds = \int_{s_p} \overline{\mathbf{u}}^{\mathrm{T}}(\boldsymbol{\sigma}\mathbf{n}) = \int_{s_p} (\boldsymbol{\sigma}\mathbf{n})^{\mathrm{T}}\overline{\mathbf{u}}\, ds = \int_{s_p} \mathbf{n}^{\mathrm{T}}\boldsymbol{\sigma}^{\mathrm{T}}\overline{\mathbf{u}}\, ds = \int_{s_p} \mathbf{n} \cdot \boldsymbol{\sigma}^{\mathrm{T}}\overline{\mathbf{u}}\, ds$$

$$= \int_{s_p} \mathbf{n} \cdot \boldsymbol{\sigma}^{\mathrm{T}}\overline{\mathbf{u}}\, ds + \underbrace{\int_{s_u} \mathbf{n} \cdot \boldsymbol{\sigma}^{\mathrm{T}}\overline{\mathbf{u}}\, ds}_{=0}$$

$$= \oint_s \mathbf{n} \cdot \boldsymbol{\sigma}^{\mathrm{T}}\overline{\mathbf{u}}\, ds. \qquad (4.46)$$

where $\overline{\mathbf{u}}$ is identically equal to zero on s_u. By applying the divergence theorem we obtain

$$\oint_s \mathbf{n} \cdot \boldsymbol{\sigma}^{\mathrm{T}}\overline{\mathbf{u}}\, ds = \int_v \mathrm{div}(\boldsymbol{\sigma}^{\mathrm{T}}\overline{\mathbf{u}})\, dv. \qquad (4.47)$$

Analogously, for the surface integral term $\int_{s_p} \overline{\boldsymbol{\varphi}} \cdot (\boldsymbol{\mu}\mathbf{n})\, ds$ we obtain

$$\int_{s_p} \overline{\boldsymbol{\varphi}} \cdot (\boldsymbol{\mu}\mathbf{n})\, ds = \int_{s_p} \overline{\boldsymbol{\varphi}}^{\mathrm{T}}(\boldsymbol{\mu}\mathbf{n}) = \int_{s_p} (\boldsymbol{\mu}\mathbf{n})^{\mathrm{T}}\overline{\boldsymbol{\varphi}}\, ds = \int_{s_p} \mathbf{n}^{\mathrm{T}}\boldsymbol{\mu}^{\mathrm{T}}\overline{\boldsymbol{\varphi}}\, ds = \oint_s \mathbf{n} \cdot \boldsymbol{\mu}^{\mathrm{T}}\overline{\boldsymbol{\varphi}}\, ds, \quad (4.48)$$

where, by applying the divergence theorem we obtain

$$\oint_s \mathbf{n} \cdot \boldsymbol{\mu}^{\mathrm{T}}\overline{\boldsymbol{\varphi}}\, ds = \int_v \mathrm{div}(\boldsymbol{\mu}^{\mathrm{T}}\overline{\boldsymbol{\varphi}})\, dv. \qquad (4.49)$$

By introducing the derived terms (4.47) and (4.49) into the weak formulation (4.41) we obtain

$$\int_v [-\mathrm{div}(\boldsymbol{\sigma}^{\mathrm{T}}\overline{\mathbf{u}}) + \mathrm{grad}\overline{\mathbf{u}} : \boldsymbol{\sigma} - \overline{\mathbf{u}} \cdot \mathbf{p}_{\mathrm{v}}]dv + \int_v [-\mathrm{div}(\boldsymbol{\mu}^{\mathrm{T}}\overline{\boldsymbol{\varphi}}) + \mathrm{grad}\overline{\boldsymbol{\varphi}} : \boldsymbol{\mu} - \overline{\boldsymbol{\varphi}} \cdot \mathrm{ax}(\boldsymbol{\sigma} - \boldsymbol{\sigma}^{\mathrm{T}})$$

$$-\overline{\boldsymbol{\varphi}} \cdot \mathbf{m}_{\mathrm{v}}]\, dv + \int_v \mathrm{div}(\boldsymbol{\sigma}^{\mathrm{T}}\overline{\mathbf{u}})\, dv + \int_v \mathrm{div}(\boldsymbol{\mu}^{\mathrm{T}}\overline{\boldsymbol{\varphi}})\, dv - \int_{s_p} (\overline{\mathbf{u}} \cdot \mathbf{p}_{\mathrm{s}} + \overline{\boldsymbol{\varphi}} \cdot \mathbf{m}_{\mathrm{s}})\, ds = 0,$$

$$(4.50)$$

and finally we obtain the principle of virtual work in the spatial description as:

$$\int_v [\mathrm{grad}\overline{\mathbf{u}} : \boldsymbol{\sigma} - \overline{\boldsymbol{\varphi}} \cdot \mathrm{ax}(\boldsymbol{\sigma} - \boldsymbol{\sigma}^{\mathrm{T}}) + \mathrm{grad}\overline{\boldsymbol{\varphi}} : \boldsymbol{\mu}]\, dv = \int_v (\overline{\mathbf{u}} \cdot \mathbf{p}_{\mathrm{v}} + \overline{\boldsymbol{\varphi}} \cdot \mathbf{m}_{\mathrm{v}})\, dv + \int_{s_p} (\overline{\mathbf{u}} \cdot \mathbf{p}_{\mathrm{s}} + \overline{\boldsymbol{\varphi}} \cdot \mathbf{m}_{\mathrm{s}})\, ds.$$

$$(4.51)$$

Now, we apply the change of variables theorem [56] to find the relations between spatial entities (which we denote by lower-case letters) and corresponding material entities (upper-case letters). As shown in equation (4.38), the relation between the deformed differential volume dv and the undeformed differential volume is described by the determinant of the deformation gradient denoted by $\det\mathbf{F} = J$, as $dv = J\, dV$. We introduce

this relation into the first integral of the principle of virtual work (equation (4.51)):

$$\int_v \left[\text{grad}\overline{\mathbf{u}} : \boldsymbol{\sigma} - \overline{\boldsymbol{\varphi}} \cdot \text{ax}(\boldsymbol{\sigma} - \boldsymbol{\sigma}^{\text{T}}) + \text{grad}\overline{\boldsymbol{\varphi}} : \boldsymbol{\mu} \right] dv$$

$$= \int_V \left[\text{grad}\overline{\mathbf{u}} : \boldsymbol{\sigma} - \overline{\boldsymbol{\varphi}} \cdot \text{ax}(\boldsymbol{\sigma} - \boldsymbol{\sigma}^{\text{T}}) + \text{grad}\overline{\boldsymbol{\varphi}} : \boldsymbol{\mu} \right] J \, dV \qquad (4.52)$$

$$= \int_V \left[\text{grad}\overline{\mathbf{u}} : J\boldsymbol{\sigma} - \overline{\boldsymbol{\varphi}} \cdot \text{ax}(J\boldsymbol{\sigma} - J\boldsymbol{\sigma}^{\text{T}}) + \text{grad}\overline{\boldsymbol{\varphi}} : J\boldsymbol{\mu} \right] \, dV$$

where V represents the body volume in the material configuration. In the above equation we recognise new stress tensors, in the literature known as nominal or Kirchhoff-like stress tensors [56], which are spatial quantities, but are measured per material (undeformed) body volume, as

$$J\boldsymbol{\sigma} = \boldsymbol{\tau} = \tau_{ij}\mathbf{e}_i \otimes \mathbf{e}_j, \qquad (4.53)$$

$$J\boldsymbol{\mu} = \boldsymbol{\eta} = \eta_{ij}\mathbf{e}_i \otimes \mathbf{e}_j. \qquad (4.54)$$

The remaining problem in the first integral is that $\text{grad}\overline{\mathbf{u}}$ and $\text{grad}\overline{\boldsymbol{\varphi}}$ are still unknown, since they require differentiation with respect to the spatial coordinates. To resolve that problem we introduce the relation between the nabla operator in the spatial and material frame [56]

$$\nabla_{\text{X}} = \mathbf{F}^{\text{T}}\nabla_{\text{x}} \quad \Leftrightarrow \quad \nabla_{\text{x}} = \mathbf{F}^{\text{-T}}\nabla_{\text{X}}, \qquad (4.55)$$

where ∇_{X} represents the nabla operator in the material description, while ∇_{x} represents the nabla operator in the spatial description. By introducing this relation into $\text{grad}\overline{\mathbf{u}}$ we obtain:

$$\text{grad}\overline{\mathbf{u}} = \overline{\mathbf{u}} \otimes \nabla_{\text{x}} = \overline{\mathbf{u}}\nabla_{\text{x}}^{\text{T}} = \overline{\mathbf{u}}(\nabla_{\text{X}}^{\text{T}}\mathbf{F}^{-1}) = (\overline{\mathbf{u}} \otimes \nabla_{\text{X}})\mathbf{F}^{-1} = \text{GRAD}\overline{\mathbf{u}} \, \mathbf{F}^{-1}. \qquad (4.56)$$

Equation (4.56) gives the gradient of the virtual displacement field with respect to the material coordinates X_i. By using the same approach we obtain the relation between the gradients of the virtual microrotation field with respect to the spatial and material coordinates, as

$$\text{grad}\overline{\boldsymbol{\varphi}} = \text{GRAD}\overline{\boldsymbol{\varphi}} \, \mathbf{F}^{-1}. \qquad (4.57)$$

By additional mathematical manipulation of $\text{grad}\overline{\mathbf{u}} : J\boldsymbol{\sigma}$ in (4.52) we obtain

$$\text{grad}\overline{\mathbf{u}} : J\boldsymbol{\sigma} = \text{GRAD}\overline{\mathbf{u}} \, \mathbf{F}^{-1} : J\boldsymbol{\sigma}$$

$$= \text{tr}(\text{GRAD}\overline{\mathbf{u}}J\mathbf{F}^{-1}\boldsymbol{\sigma}^{\text{T}})$$

$$= \text{tr}(\text{GRAD}\overline{\mathbf{u}}J(\boldsymbol{\sigma}\mathbf{F}^{-\text{T}})^{\text{T}})$$

$$= \text{GRAD}\overline{\mathbf{u}} : (J\boldsymbol{\sigma}\mathbf{F}^{-\text{T}}), \qquad (4.58)$$

i.e.

$$\text{grad}\overline{\mathbf{u}} : J\boldsymbol{\sigma} = \text{GRAD}\overline{\mathbf{u}} : \mathbf{P}, \tag{4.59}$$

where $\mathbf{P} = J\boldsymbol{\sigma}\mathbf{F}^{-\text{T}} = \boldsymbol{\tau}\mathbf{F}^{-\text{T}} = P_{iI}\mathbf{e}_i \otimes \mathbf{E}_I$ represents the 1st Piola-Kirchhoff stress tensor which is a two-point tensor. Analogously, we analyse the third term under the first integral in (4.51) in order to obtain a corresponding two-point couple-stress tensor:

$$\begin{aligned}
\text{grad}\overline{\boldsymbol{\varphi}} : J\boldsymbol{\mu} &= \text{GRAD}\overline{\boldsymbol{\varphi}} \ \mathbf{F}^{-1} : J\boldsymbol{\mu} \\
&= \text{tr}(\text{GRAD}\overline{\boldsymbol{\varphi}}J\mathbf{F}^{-1}\boldsymbol{\mu}^{\text{T}}) \\
&= \text{tr}(\text{GRAD}\overline{\boldsymbol{\varphi}}J(\boldsymbol{\mu}\mathbf{F}^{-\text{T}})^{\text{T}}) \\
&= \text{GRAD}\overline{\boldsymbol{\varphi}} : (J\boldsymbol{\mu}\mathbf{F}^{-\text{T}}),
\end{aligned} \tag{4.60}$$

i.e.

$$\text{grad}\overline{\boldsymbol{\varphi}} : J\boldsymbol{\mu} = \text{GRAD}\overline{\boldsymbol{\varphi}} : \mathbf{M}, \tag{4.61}$$

where $\mathbf{M} = J\boldsymbol{\mu}\mathbf{F}^{-\text{T}} = \boldsymbol{\eta}\mathbf{F}^{-\text{T}} = M_{iI}\mathbf{e}_i \otimes \mathbf{E}_I$ represents the 1st Piola-Kirchhoff-like couple-stress tensor which is also a two point tensor defined with a mixed base and is related to the true couple stress via the deformation gradient.

By expressing the divergence of the true stress tensors with respect to the coordinates in the initial configuration we obtain:

$$J\text{div}\boldsymbol{\sigma} = J\boldsymbol{\sigma}\nabla_{\text{x}} = J\boldsymbol{\sigma}\mathbf{F}^{-\text{T}}\nabla_{\text{X}} = \mathbf{P}\nabla_{\text{X}} = \text{DIV}\mathbf{P}, \tag{4.62}$$

$$J\text{div}\boldsymbol{\mu} = J\boldsymbol{\mu}\nabla_{\text{x}} = J\boldsymbol{\mu}\mathbf{F}^{-\text{T}}\nabla_{\text{X}} = \mathbf{M}\nabla_{\text{X}} = \text{DIV}\mathbf{M}. \tag{4.63}$$

Finally we introduce

$$\mathbf{p}_{\text{v}} \, dv = \mathbf{P}_{\text{V}} \, dV, \tag{4.64}$$

$$\mathbf{p}_{\text{s}} \, ds = \mathbf{P}_{\text{S}} \, dS, \tag{4.65}$$

$$\mathbf{m}_{\text{v}} \, dv = \mathbf{M}_{\text{V}} \, dV, \tag{4.66}$$

$$\mathbf{m}_{\text{s}} \, ds = \mathbf{M}_{\text{S}} \, dS, \tag{4.67}$$

where $\mathbf{P}_{\text{V}}$, $\mathbf{P}_{\text{S}}$, $\mathbf{M}_{\text{V}}$ and $\mathbf{M}_{\text{S}}$ are the distributed volume and surface forces and couples measured per initial volume and surface. By introducing the presented transformations we obtain the principle of virtual work in terms of the 1st Piola-Kirchhoff stress tensor $\mathbf{P}$ and the 1st Piola-Kirchhoff-like couple-stress tensor $\mathbf{M}$ as:

$$\begin{aligned}
\int_V \left[\text{GRAD}\overline{\mathbf{u}} : \mathbf{P} - \overline{\boldsymbol{\varphi}} \cdot \text{ax}(\mathbf{P}\mathbf{F}^{\text{T}} - \mathbf{F}\mathbf{P}^{\text{T}}) + \text{GRAD}\overline{\boldsymbol{\varphi}} : \mathbf{M} \right] dV = \\
= \int_V (\overline{\mathbf{u}} \cdot \mathbf{P}_{\text{V}} + \overline{\boldsymbol{\varphi}} \cdot \mathbf{M}_{\text{V}}) \, dV + \int_{S_p} (\overline{\mathbf{u}} \cdot \mathbf{P}_{\text{S}} + \overline{\boldsymbol{\varphi}} \cdot \mathbf{M}_{\text{S}}) \, dS,
\end{aligned} \tag{4.68}$$

from where the strong form of equilibrium equations on V follows as

$$\mathrm{DIV}\mathbf{P} + \mathbf{P}_\mathrm{V} = \mathbf{0}, \tag{4.69}$$

$$\mathrm{DIV}\mathbf{M} + \mathrm{ax}(\mathbf{PF}^\mathrm{T} - \mathbf{FP}^\mathrm{T}) + \mathbf{M}_\mathrm{V} = \mathbf{0}, \tag{4.70}$$

with the corresponding boundary conditions $\mathbf{PN} = \mathbf{P}_\mathrm{S}$ and $\mathbf{MN} = \mathbf{M}_\mathrm{S}$ on S_p.

In this work we seek to obtain the stress tensors defined completely in the material frame. To do that we additionally "pull-back" the 1st Piola-Kirrchoff-like stress tensor and the 1st Piola-Kirrchoff-like couple-stress tensor by multiplying the tensors with a (micro)rotation (or (micro)orientation) matrix $\mathbf{Q} \in \mathrm{SO}(3)$, i.e. $\mathbf{Q}^{-1} = \mathbf{Q}^\mathrm{T}$, $\det\mathbf{Q} = +1$ and introduce new Biot-like stress and couple-stress tensors as:

$$\mathbf{B} = \mathbf{Q}^\mathrm{T}\mathbf{P} = \mathbf{Q}^\mathrm{T}\boldsymbol{\tau}\mathbf{F}^{-\mathrm{T}} = J\mathbf{Q}^\mathrm{T}\boldsymbol{\sigma}\mathbf{F}^{-\mathrm{T}} = B_{IJ}\mathbf{E}_I \otimes \mathbf{E}_J$$
$$\mathbf{G} = \mathbf{Q}^\mathrm{T}\mathbf{M} = \mathbf{Q}^\mathrm{T}\boldsymbol{\eta}\mathbf{F}^{-\mathrm{T}} = J\mathbf{Q}^\mathrm{T}\boldsymbol{\mu}\mathbf{F}^{-\mathrm{T}} = G_{IJ}\mathbf{E}_I \otimes \mathbf{E}_J$$

where $\mathbf{B}$ represents the Biot-like stress tensor and $\mathbf{G}$ represents the Biot-like couple-stress tensor. We call $\mathbf{B}$ the Biot-like, rather than Biot stress tensor as the latter is defined as $\mathbf{R}^\mathrm{T}\mathbf{P}$ where $\mathbf{R}$ is the macrorotation tensor in the polar decomposition of the deformation gradient $\mathbf{F} = \mathbf{RU} = \mathbf{VR}$, with $\mathbf{U}$, $\mathbf{V}$ as the right and left stretch tensors, respectively [56].

By substituting $\mathbf{P} = \mathbf{QB}$ and $\mathbf{M} = \mathbf{QG}$ into (4.68) we obtain the virtual work equation in terms of the Biot-like stress tensors as

$$\int_V \left[\mathrm{GRAD}\overline{\mathbf{u}} : (\mathbf{QB}) - \overline{\boldsymbol{\varphi}} \cdot \mathrm{ax}(\mathbf{QBF}^\mathrm{T} - \mathbf{FB}^\mathrm{T}\mathbf{Q}^\mathrm{T}) + \mathrm{GRAD}\overline{\boldsymbol{\varphi}} : (\mathbf{QG}) \right] dV =$$
$$= \int_V (\overline{\mathbf{u}} \cdot \mathbf{P}_\mathrm{V} + \overline{\boldsymbol{\varphi}} \cdot \mathbf{M}_\mathrm{V})\, dV + \int_{S_p} (\overline{\mathbf{u}} \cdot \mathbf{P}_\mathrm{S} + \overline{\boldsymbol{\varphi}} \cdot \mathbf{M}_\mathrm{S})\, dS. \tag{4.71}$$

The strong form of equilibrium equations on V expressed in terms of Biot-like stress and couple stress tensors is thus

$$\mathrm{DIV}(\mathbf{QB}) + \mathbf{P}_\mathrm{V} = \mathbf{0}, \tag{4.72}$$

$$\mathrm{DIV}(\mathbf{QG}) + \mathrm{ax}(\mathbf{QBF}^\mathrm{T} - \mathbf{FB}^\mathrm{T}\mathbf{Q}^\mathrm{T}) + \mathbf{M}_\mathrm{V} = \mathbf{0}, \tag{4.73}$$

with the boundary conditions on S_p

$$(\mathbf{QB})\mathbf{N} = \mathbf{P}_\mathrm{S} \quad \text{and} \quad (\mathbf{QG})\mathbf{N} = \mathbf{M}_\mathrm{S}. \tag{4.74}$$

4.5 Non-linear kinematic equations - derivation of Biot-like strain tensors by using Reissner's approach

Reissner derived the material strain measures of a 3D beam from the condition that the virtual work equation must be equal to the equations of motion integrated over the same domain [93]. By following Reissner's approach, in order to derive the strain tensors, we enforce the equivalence between the strong form of equilibrium equations and the principle of virtual work. Firstly, we assume that there exist work-conjugate Biot-like strain tensors to Biot-like stress tensors. The virtual work equation is given as

$$V_i - Ve = \int_V \left(\overline{\mathbf{E}} : \mathbf{B} + \overline{\mathbf{K}} : \mathbf{G}\right) dV - \int_V \left(\overline{\mathbf{u}} \cdot \mathbf{P}_{\mathrm{V}} + \overline{\boldsymbol{\varphi}} \cdot \mathbf{M}_{\mathrm{V}}\right) dV - \int_{S_p} \left(\overline{\mathbf{u}} \cdot \mathbf{P}_{\mathrm{S}} + \overline{\boldsymbol{\varphi}} \cdot \mathbf{M}_{\mathrm{S}}\right) dS = 0,$$
(4.75)

where $\overline{\mathbf{E}}$ represents the material virtual micropolar Biot-like strain tensor and $\overline{\mathbf{K}}$ represents the material virtual Biot-like curvature tensor which are work-conjugate to the Biot-like stress tensors $\mathbf{B}$ and $\mathbf{G}$. The virtual displacement field $\overline{\mathbf{u}}$ and the virtual microrotation field $\overline{\boldsymbol{\varphi}}$ are assumed to be kinematically admissible and such that the internal virtual work is linear in terms of them. The virtual strain tensors then follow as the strain tensors for linearized kinematics.

We start by expressing the external loading from the equilibrium equations and introducing them into the virtual work equation, i.e. we introduce the following equalities from (4.72), (4.73) and (4.74):

$$\mathbf{P}_{\mathrm{V}} = -\mathrm{DIV}(\mathbf{QB}),$$
(4.76)

$$\mathbf{M}_{\mathrm{V}} = -\mathrm{DIV}(\mathbf{QG}) - \mathrm{ax}(\mathbf{QBF}^{\mathrm{T}} - \mathbf{FB}^{\mathrm{T}}\mathbf{Q}^{\mathrm{T}}),$$
(4.77)

$$\mathbf{P}_{\mathrm{S}} = (\mathbf{QB})\mathbf{N},$$
(4.78)

$$\mathbf{M}_{\mathrm{S}} = (\mathbf{QG})\mathbf{N},$$
(4.79)

into (4.75) and obtain

$$\int_V \left(\overline{\mathbf{E}} : \mathbf{B} + \overline{\mathbf{K}} : \mathbf{G}\right) dV$$

$$= -\int_V \left(\overline{\mathbf{u}} \cdot \mathrm{DIV}(\mathbf{QB}) + \overline{\boldsymbol{\varphi}} \cdot \left(\mathrm{DIV}(\mathbf{QG}) + \mathrm{ax}(\mathbf{QBF}^{\mathrm{T}} - \mathbf{FB}^{\mathrm{T}}\mathbf{Q}^{\mathrm{T}})\right)\right) dV$$

$$+ \int_{S_p} \left(\overline{\mathbf{u}} \cdot (\mathbf{QB})\mathbf{N} + \overline{\boldsymbol{\varphi}} \cdot (\mathbf{QG})\mathbf{N}\right) dS.$$
(4.80)

As shown before, the following identities hold:

$$\mathbf{\bar{u}} \cdot \mathrm{DIV}(\mathbf{QB}) = \mathrm{DIV}\left((\mathbf{QB})^{\mathrm{T}}\mathbf{\bar{u}}\right) - \mathrm{GRAD}\mathbf{\bar{u}} : (\mathbf{QB}), \tag{4.81}$$

$$\mathbf{\overline{\varphi}} \cdot \mathrm{DIV}(\mathbf{QG}) = \mathrm{DIV}\left((\mathbf{QG})^{\mathrm{T}}\mathbf{\overline{\varphi}}\right) - \mathrm{GRAD}\mathbf{\overline{\varphi}} : (\mathbf{QG}). \tag{4.82}$$

By using identities (E.10) and (E.11) defined in Appendix E we rewrite double contraction terms from equations (4.81) and (4.82) as

$$\mathrm{GRAD}\mathbf{\bar{u}} : (\mathbf{QB}) = \mathrm{tr}\left(\mathrm{GRAD}\mathbf{\bar{u}}\mathbf{B}^{\mathrm{T}}\mathbf{Q}^{\mathrm{T}}\right) = \mathbf{Q}^{\mathrm{T}}\mathrm{GRAD}\mathbf{\bar{u}} : \mathbf{B},$$

$$\mathrm{GRAD}\mathbf{\overline{\varphi}} : (\mathbf{QG}) = \mathrm{tr}\left(\mathrm{GRAD}\mathbf{\overline{\varphi}}\mathbf{G}^{\mathrm{T}}\mathbf{Q}^{\mathrm{T}}\right) = \mathbf{Q}^{\mathrm{T}}\mathrm{GRAD}\mathbf{\overline{\varphi}} : \mathbf{G}. \tag{4.83}$$

Futhermore, we apply identity (E.13) valid for any 2nd order tensor $\mathbf{A}$ on $\mathrm{ax}(\mathbf{QBF}^{\mathrm{T}} - \mathbf{FB}^{\mathrm{T}}\mathbf{Q}^{\mathrm{T}})$ from (4.80) and obtain

$$\mathbf{\overline{\varphi}} \cdot \mathrm{ax}(\mathbf{QBF}^{\mathrm{T}} - \mathbf{FB}^{\mathrm{T}}\mathbf{Q}^{\mathrm{T}}) = -\mathbf{\overline{\varphi}} \cdot \boldsymbol{\epsilon} : (\mathbf{QBF}^{\mathrm{T}}) = -\widehat{\mathbf{\overline{\varphi}}} : (\mathbf{QBF}^{\mathrm{T}}), \tag{4.84}$$

where $\widehat{\mathbf{\overline{\varphi}}}$ is the skew-symmetric tensor of vector $\mathbf{\overline{\varphi}}$. By applying the identities (E.10), (E.11) and (E.8) and we obtain

$$\widehat{\mathbf{\overline{\varphi}}}^{\mathrm{T}} : (\mathbf{QBF}^{\mathrm{T}}) = \mathrm{tr}(\widehat{\mathbf{\overline{\varphi}}}\mathbf{QBF}^{\mathrm{T}}) = (\mathbf{F}^{\mathrm{T}}\widehat{\mathbf{\overline{\varphi}}}\mathbf{Q}) : \mathbf{B}^{\mathrm{T}} = (\mathbf{F}^{\mathrm{T}}\widehat{\mathbf{\overline{\varphi}}}\mathbf{Q})^{\mathrm{T}} : \mathbf{B} = (\mathbf{Q}^{\mathrm{T}}\widehat{\mathbf{\overline{\varphi}}}^{\mathrm{T}}\mathbf{F}) : \mathbf{B} \tag{4.85}$$

Finally, we apply the divergence theorem on terms under the surface integral in (4.80) and by using (E.1) and recognising that $\mathbf{\bar{u}}$ and $\mathbf{\overline{\varphi}}$ vanish on S_u we obtain:

$$\int_{S_p} \mathbf{\bar{u}} \cdot \mathbf{QBN}dS = \int_{S} \mathbf{\bar{u}} \cdot \mathbf{QBN}dS = \int_{V} \mathrm{DIV}\left((\mathbf{QB})^{\mathrm{T}}\mathbf{\bar{u}}\right) dV,$$

$$\int_{S} \mathbf{\overline{\varphi}} \cdot \mathbf{QGN}dS = \int_{S_p} \mathbf{\overline{\varphi}} \cdot \mathbf{QGN}dS = \int_{V} \mathrm{DIV}\left((\mathbf{QG})^{\mathrm{T}}\mathbf{\overline{\varphi}}\right) dV. \tag{4.86}$$

By introducing (4.81), (4.82), (4.83), (4.85) and (4.86) into (4.80) and using identity (E.11) we obtain

$$\int_{V} \left(\mathbf{\overline{E}} : \mathbf{B} + \mathbf{\overline{K}} : \mathbf{G} - \mathbf{Q}^{\mathrm{T}}\mathrm{GRAD}\mathbf{\bar{u}} : \mathbf{B} - \mathbf{Q}^{\mathrm{T}}\mathrm{GRAD}\mathbf{\overline{\varphi}} : \mathbf{G} - (\mathbf{Q}^{\mathrm{T}}\widehat{\mathbf{\overline{\varphi}}}^{\mathrm{T}}\mathbf{F}) : \mathbf{B}\right) dV = 0, \tag{4.87}$$

i.e.

$$\int_{V} \left(\mathbf{\overline{E}} - \mathbf{Q}^{\mathrm{T}}\mathrm{GRAD}\mathbf{\bar{u}} - (\mathbf{Q}^{\mathrm{T}}\widehat{\mathbf{\overline{\varphi}}}^{\mathrm{T}}\mathbf{F})\right) : \mathbf{B} \, dV + \int_{V} \left(\mathbf{\overline{K}} - \mathbf{Q}^{\mathrm{T}}\mathrm{GRAD}\mathbf{\overline{\varphi}}\right) : \mathbf{G} \, dV = 0. \tag{4.88}$$

For arbitrary $\mathbf{B}$ and $\mathbf{G}$ equation (4.88) is identically satisfied only for

$$\mathbf{\overline{E}} = \mathbf{Q}^{\mathrm{T}}(\mathrm{GRAD}\mathbf{\bar{u}} + \widehat{\mathbf{\overline{\varphi}}}^{\mathrm{T}}\mathbf{F}), \tag{4.89}$$

$$\overline{\mathbf{K}} = \mathbf{Q}^{\mathrm{T}} \mathrm{GRAD}\overline{\boldsymbol{\varphi}}, \tag{4.90}$$

where equations (4.89) and (4.90) represent the virtual Biot-like strain tensors of a micropolar continuum in the geometrically non-linear regime. In order to obtain the total Biot-like strain tensors, we recognise the total-differential character of the virtual strain tensors $\overline{\mathbf{E}}$ and $\overline{\mathbf{K}}$ and integrate equations (4.89) and (4.90). By making use of directional derivative of the orientation matrix $\overline{\mathbf{Q}} = \widehat{\overline{\boldsymbol{\varphi}}}\mathbf{Q}$ derived in Appendix G.1, equation (G.1) we obtain from (4.89)

$$\begin{aligned}
\overline{\mathbf{E}} &= \mathbf{Q}^{\mathrm{T}} \mathrm{GRAD}\overline{\mathbf{u}} + \overline{\mathbf{Q}}^{\mathrm{T}} \mathbf{F} \\
&= \mathbf{Q}^{\mathrm{T}} \mathrm{GRAD}\overline{\mathbf{u}} + \overline{\mathbf{Q}}^{\mathrm{T}} \mathrm{GRAD}\mathbf{x} \\
&= \mathbf{Q}^{\mathrm{T}} \mathrm{GRAD}\overline{\mathbf{x}} + \overline{\mathbf{Q}}^{\mathrm{T}} \mathrm{GRAD}\mathbf{x} \\
&= \mathbf{Q}^{\mathrm{T}} \overline{\mathrm{GRAD}\mathbf{x}} + \overline{\mathbf{Q}}^{\mathrm{T}} \mathrm{GRAD}\mathbf{x} \\
&= \overline{(\mathbf{Q}^{\mathrm{T}} \mathrm{GRAD}\mathbf{x})} \\
&= \overline{(\mathbf{Q}^{\mathrm{T}} \mathbf{F})}.
\end{aligned} \tag{4.91}$$

We now integrate $\overline{\mathbf{E}} = \overline{(\mathbf{Q}^{\mathrm{T}}\mathbf{F})}$ and obtain

$$\mathbf{E} = \mathbf{Q}^{\mathrm{T}}\mathbf{F} + \mathbf{C_1} \tag{4.92}$$

where $\mathbf{C_1}$ is an integration constant. By taking into account that the initial configuration is undeformed (i.e. $\mathbf{E}_0 = \mathbf{0}$) we obtain

$$\mathbf{C_1} = -\mathbf{Q}_0^{\mathrm{T}}\mathbf{F}_0 = -\mathbf{Q}_0^{\mathrm{T}}\mathrm{GRAD}\mathbf{X} = -\mathbf{I}. \tag{4.93}$$

Finally, we obtain the Biot-like translational strain tensor as

$$\mathbf{E} = \mathbf{Q}^{\mathrm{T}}\mathbf{F} - \mathbf{I}. \tag{4.94}$$

In order to derive the real curvature from (4.90), we start by extracting a curvature vector $\overline{\mathbf{K}}_i$ from $\overline{\mathbf{K}} = \overline{\mathbf{K}}_i \otimes \mathbf{E}_i$ such that $\overline{\mathbf{K}}_i = \overline{\mathbf{K}}\mathbf{E}_i$ as

$$\overline{\mathbf{K}}_i = \mathbf{Q}^{\mathrm{T}}\frac{\partial \overline{\boldsymbol{\varphi}}}{\partial X_i} \tag{4.95}$$

where $\dfrac{\partial \overline{\boldsymbol{\varphi}}}{\partial X_i} = \mathrm{GRAD}\overline{\boldsymbol{\varphi}} \cdot \mathbf{E}_i$. By using the identities $\widehat{\mathbf{Qv}} = \mathbf{Q}\hat{\mathbf{v}}\mathbf{Q}^{\mathrm{T}} \ \forall \ \mathbf{v} \in \mathbb{R}^3$ and $\hat{\mathbf{v}} = -\hat{\mathbf{v}}^{\mathrm{T}} \ \forall \ \hat{\mathbf{v}} \in \mathrm{so}(3)$ [94] we obtain

$$\widehat{\overline{\mathbf{K}}}_i = \widehat{\overline{\mathbf{K}}\mathbf{E}}_i = \mathbf{Q}^{\mathrm{T}}\frac{\partial \widehat{\overline{\boldsymbol{\varphi}}}}{\partial X_i}\mathbf{Q}. \tag{4.96}$$

By writing the equation using the integration by parts rule we obtain

$$\widehat{\overline{\mathbf{K}}}_i = \mathbf{Q}^{\mathrm{T}} \frac{\partial \widehat{\overline{\boldsymbol{\varphi}}}}{\partial X_i} \mathbf{Q}$$

$$= \mathbf{Q}^{\mathrm{T}} \frac{\partial}{\partial X_i}(\widehat{\overline{\boldsymbol{\varphi}}}\mathbf{Q}) - \mathbf{Q}^{\mathrm{T}}\widehat{\overline{\boldsymbol{\varphi}}} \frac{\partial}{\partial X_i}\mathbf{Q}$$

$$= \mathbf{Q}^{\mathrm{T}} \frac{\partial}{\partial X_i}(\widehat{\overline{\boldsymbol{\varphi}}}\mathbf{Q}) + \mathbf{Q}^{\mathrm{T}}\widehat{\overline{\boldsymbol{\varphi}}}^{\mathrm{T}} \frac{\partial}{\partial X_i}\mathbf{Q}$$

$$= \mathbf{Q}^{\mathrm{T}} \frac{\partial}{\partial X_i}(\widehat{\overline{\boldsymbol{\varphi}}}\mathbf{Q}) + (\widehat{\overline{\boldsymbol{\varphi}}}\mathbf{Q})^{\mathrm{T}} \frac{\partial}{\partial X_i}\mathbf{Q}. \tag{4.97}$$

We recognize the directional derivative of the microrotation matrix $\overline{\mathbf{Q}} = \widehat{\overline{\boldsymbol{\varphi}}}\mathbf{Q}$ and obtain

$$\widehat{\overline{\mathbf{K}}}_i = \mathbf{Q}^{\mathrm{T}} \frac{\partial}{\partial X_i}\overline{\mathbf{Q}} + \overline{\mathbf{Q}}^{\mathrm{T}} \frac{\partial}{\partial X_i}\mathbf{Q} = \overline{\left(\mathbf{Q}^{\mathrm{T}} \frac{\partial \mathbf{Q}}{\partial X_i} \right)}. \tag{4.98}$$

By introducing the axial operator (E.4) into (4.98) we obtain

$$\overline{\mathbf{K}}_i = \mathrm{ax}\left(\overline{\mathbf{Q}^{\mathrm{T}} \frac{\partial \mathbf{Q}}{\partial X_i}} \right)$$

$$\overline{\mathbf{K}}\mathbf{E}_i = \mathrm{ax}\left(\overline{\mathbf{Q}^{\mathrm{T}} \frac{\partial \mathbf{Q}}{\partial X_i}} \right) \quad / \otimes \mathbf{E}_i$$

$$\overline{\mathbf{K}} \underbrace{\mathbf{E}_i \otimes \mathbf{E}_i}_{\mathbf{I}} = \mathrm{ax}\left(\overline{\mathbf{Q}^{\mathrm{T}} \frac{\partial \mathbf{Q}}{\partial X_i}} \right) \otimes \mathbf{E}_i$$

$$\overline{\mathbf{K}} = \mathrm{ax}\left(\overline{\mathbf{Q}^{\mathrm{T}} \frac{\partial \mathbf{Q}}{\partial X_i}} \right) \otimes \mathbf{E}_i. \tag{4.99}$$

Furthermore, as shown in (E.4), the axial vector of a skew-symmetric tensor can be written as a negative double contraction between the third-order permutation tensor $\boldsymbol{\epsilon}$ and the skew-symmetric tensor halved. By expressing the axial vector from (4.99) in this way, i.e.

$$\overline{\mathbf{K}} = -\frac{1}{2}\boldsymbol{\epsilon} : \left(\overline{\mathbf{Q}^{\mathrm{T}} \frac{\partial \mathbf{Q}}{\partial X_i}} \right) \otimes \mathbf{E}_i \tag{4.100}$$

and recognizing that $\left(\overline{\mathbf{Q}^{\mathrm{T}} \frac{\partial \mathbf{Q}}{\partial X_i}} \right) \otimes \mathbf{E}_i = \overline{\mathbf{Q}^{\mathrm{T}} \frac{\partial \mathbf{Q}}{\partial X_i} \otimes \mathbf{E}_i} = \overline{\mathbf{Q}^{\mathrm{T}}\mathrm{GRAD}\mathbf{Q}}$, we obtain an easily integrable expression

$$\overline{\mathbf{K}} = -\frac{1}{2}\boldsymbol{\epsilon} : \left(\overline{\mathbf{Q}^{\mathrm{T}}\mathrm{GRAD}\mathbf{Q}} \right). \tag{4.101}$$

By treating the overlined entities as total differentials and integrating the equation (4.101) we obtain

$$\mathbf{K} = -\frac{1}{2}\boldsymbol{\epsilon} : \left(\mathbf{Q}^{\mathrm{T}}\mathrm{GRAD}\mathbf{Q} \right) + \mathbf{C_2} \tag{4.102}$$

where $\mathbf{C_2}$ is an integration constant. By taking into account that the initial configuration is undeformed (i.e. $\mathbf{K}_0 = \mathbf{0}$) we obtain $\mathbf{C_2} = \mathbf{0}$. Finally, the total Biot-like curvature

tensor is obtained as

$$\mathbf{K} = -\frac{1}{2}\boldsymbol{\epsilon} : \left(\mathbf{Q}^{\mathrm{T}}\mathrm{GRAD}\mathbf{Q}\right),\tag{4.103}$$

where $\mathbf{K} = \mathbf{K}_i \otimes \mathbf{E}_i$ with $\mathbf{K}_i = \mathrm{ax}\left(\mathbf{Q}^{\mathrm{T}}\dfrac{\partial \mathbf{Q}}{\partial X_i}\right)$.

The derived Biot-like strain tensors coincide with the micropolar material strain measures derived in [45], where the strain tensor is referred to as the stretch tensor, while the curvature tensor is referred to as the wryness tensor. Furthermore, when the Biot-like strain tensors are reduced to 1D, the same form of equations are obtained as the material strain measures of the geometrically exact 3D beam theory, e.g. [94].

4.6 Constitutive equations

In the scope of this thesis only geometric nonlinearity is analysed, keeping the constitutive equations linear, as presented in Section 2.4. The first constitutive equation may thus be applied to the present Biot-like stress and strain tensors and written in matrix form as

$$\underbrace{\begin{bmatrix} B_{11} & B_{12} & B_{13} \\ B_{21} & B_{22} & B_{23} \\ B_{31} & B_{32} & B_{33} \end{bmatrix}}_{\mathbf{B}} = \underbrace{\begin{bmatrix} \begin{bmatrix} (\lambda+2\mu) & 0 & 0 \\ 0 & \lambda & 0 \\ 0 & 0 & \lambda \end{bmatrix} & \begin{bmatrix} 0 & (\mu+\nu) & 0 \\ (\mu-\nu) & 0 & 0 \\ 0 & 0 & 0 \end{bmatrix} & \begin{bmatrix} 0 & 0 & (\mu+\nu) \\ 0 & 0 & 0 \\ (\mu-\nu) & 0 & 0 \end{bmatrix} \\ \begin{bmatrix} 0 & (\mu-\nu) & 0 \\ (\mu+\nu) & 0 & 0 \\ 0 & 0 & 0 \end{bmatrix} & \begin{bmatrix} \lambda & 0 & 0 \\ 0 & (\lambda+2\mu) & 0 \\ 0 & 0 & \lambda \end{bmatrix} & \begin{bmatrix} 0 & 0 & 0 \\ 0 & 0 & (\mu+\nu) \\ 0 & (\mu-\nu) & 0 \end{bmatrix} \\ \begin{bmatrix} 0 & 0 & (\mu-\nu) \\ 0 & 0 & 0 \\ (\mu+\nu) & 0 & 0 \end{bmatrix} & \begin{bmatrix} 0 & 0 & 0 \\ 0 & 0 & (\mu-\nu) \\ 0 & (\mu+\nu) & 0 \end{bmatrix} & \begin{bmatrix} \lambda & 0 & 0 \\ 0 & \lambda & 0 \\ 0 & 0 & (\lambda+2\mu) \end{bmatrix} \end{bmatrix}}_{\mathbf{T}} : \underbrace{\begin{bmatrix} E_{11} & E_{12} & E_{13} \\ E_{21} & E_{22} & E_{23} \\ E_{31} & E_{32} & E_{33} \end{bmatrix}}_{\mathbf{E}},$$

$$\tag{4.104}$$

where $\mathbf{T}$ is given in a tensor form in (2.161). This leads to

$$\mathbf{B} = \lambda(\mathrm{tr}\ \mathbf{E})\mathbf{I} + (\mu+\nu)\mathbf{E} + (\mu-\nu)\mathbf{E}^{\mathrm{T}},\tag{4.105}$$

a result equivalent to (2.168).

The second constitutive equation likewise follows as

$$
\underbrace{\begin{bmatrix} G_{11} & G_{12} & G_{13} \\ G_{21} & G_{22} & G_{23} \\ G_{31} & G_{32} & G_{33} \end{bmatrix}}_{\mathbf{G}} = \underbrace{\begin{bmatrix} \begin{bmatrix} (\alpha+2\beta) & 0 & 0 \\ 0 & \alpha & 0 \\ 0 & 0 & \alpha \end{bmatrix} & \begin{bmatrix} 0 & (\beta+\gamma) & 0 \\ (\beta-\gamma) & 0 & 0 \\ 0 & 0 & 0 \end{bmatrix} & \begin{bmatrix} 0 & 0 & (\beta+\gamma) \\ 0 & 0 & 0 \\ (\beta-\gamma) & 0 & 0 \end{bmatrix} \\ \begin{bmatrix} 0 & (\beta-\gamma) & 0 \\ (\beta+\gamma) & 0 & 0 \\ 0 & 0 & 0 \end{bmatrix} & \begin{bmatrix} \alpha & 0 & 0 \\ 0 & (\alpha+2\beta) & 0 \\ 0 & 0 & \alpha \end{bmatrix} & \begin{bmatrix} 0 & 0 & 0 \\ 0 & 0 & (\beta+\gamma) \\ 0 & (\beta-\gamma) & 0 \end{bmatrix} \\ \begin{bmatrix} 0 & 0 & (\beta-\gamma) \\ 0 & 0 & 0 \\ (\beta+\gamma) & 0 & 0 \end{bmatrix} & \begin{bmatrix} 0 & 0 & 0 \\ 0 & 0 & (\beta-\gamma) \\ 0 & (\beta+\gamma) & 0 \end{bmatrix} & \begin{bmatrix} \alpha & 0 & 0 \\ 0 & \alpha & 0 \\ 0 & 0 & (\alpha+2\beta) \end{bmatrix} \end{bmatrix}}_{\mathbf{D}} : \underbrace{\begin{bmatrix} K_{11} & K_{12} & K_{13} \\ K_{21} & K_{22} & K_{23} \\ K_{31} & K_{32} & K_{33} \end{bmatrix}}_{\mathbf{K}},
$$

(4.106)

where the tensor form of $\mathbf{D}$ is given in (2.181) and leads to

$$
\mathbf{G} = \alpha(\operatorname{tr} \mathbf{K})\mathbf{I} + (\beta+\gamma)\mathbf{K} + (\beta-\gamma)\mathbf{K}^{\mathrm{T}},
$$

(4.107)

a result equivalent to (2.182).

Chapter 5

Non-linear micropolar finite element analysis in 3D

We start by writing the weak formulation obtained by the virtual work principle (4.75)

$$V_i - V_e = G(\mathbf{u}, \mathbf{Q}; \overline{\mathbf{u}}, \overline{\boldsymbol{\varphi}}) = \int_V \left(\overline{\mathbf{E}} : \mathbf{B} + \overline{\mathbf{K}} : \mathbf{G} \right) dV - \int_V (\overline{\mathbf{u}} \cdot \mathbf{P}_\mathrm{V} + \overline{\boldsymbol{\varphi}} \cdot \mathbf{M}_\mathrm{V}) \, dV$$
$$- \int_{S_p} (\overline{\mathbf{u}} \cdot \mathbf{P}_\mathrm{S} + \overline{\boldsymbol{\varphi}} \cdot \mathbf{M}_\mathrm{S}) \, dS = 0.$$

and introduce the the virtual strain tensors (4.89) and (4.90) to obtain

$$G(\mathbf{u}, \mathbf{Q}, \overline{\mathbf{u}}, \overline{\boldsymbol{\varphi}}) = \int_V \left(\left(\mathbf{Q}^\mathrm{T}(\mathrm{GRAD}\overline{\mathbf{u}} + \widehat{\overline{\boldsymbol{\varphi}}}^\mathrm{T}\mathbf{F}) \right) : \mathbf{B} + (\mathbf{Q}^\mathrm{T}\mathrm{GRAD}\overline{\boldsymbol{\varphi}}) : \mathbf{G} \right) dV$$
$$- \int_V (\overline{\mathbf{u}} \cdot \mathbf{P}_\mathrm{V} + \overline{\boldsymbol{\varphi}} \cdot \mathbf{M}_\mathrm{V}) \, dV - \int_{S_p} (\overline{\mathbf{u}} \cdot \mathbf{P}_\mathrm{S} + \overline{\boldsymbol{\varphi}} \cdot \mathbf{M}_\mathrm{S}) \, dS = 0. \tag{5.1}$$

In order to discretise the problem and to obtain the residual load vector (the out-of-balance load vector), the virtual kinematic fields have to be approximated using chosen interpolations. In general, the virtual fields can be interpolated as $\overline{\mathbf{u}}^h = \mathbf{N_u}\overline{\mathbf{d}}^e$ and $\overline{\boldsymbol{\varphi}}^h = \mathbf{N}_\varphi\overline{\mathbf{d}}^e$. The matrices $\mathbf{N_u}$ and $\mathbf{N}_\varphi$ represent the matrices of interpolation functions for the virtual displacement and microrotation field and $\overline{\mathbf{d}}^e$ represents the virtual vector of element nodal degrees of freedom. For the domain discretization we choose two finite elements, hexahedral finite elements with 8 and 27 nodes, both of which have six degrees of freedom per node. We refer to them as Hex8NL and Hex27NL. The numbering convention we follow is the one defined in FEAP [95], which for Hex8NL is shown in Figure 3.23, while for Hex27NL is shown in Figure 5.1 (*Note: To avoid cluttering, the nodes have been shown in three separate images.*).
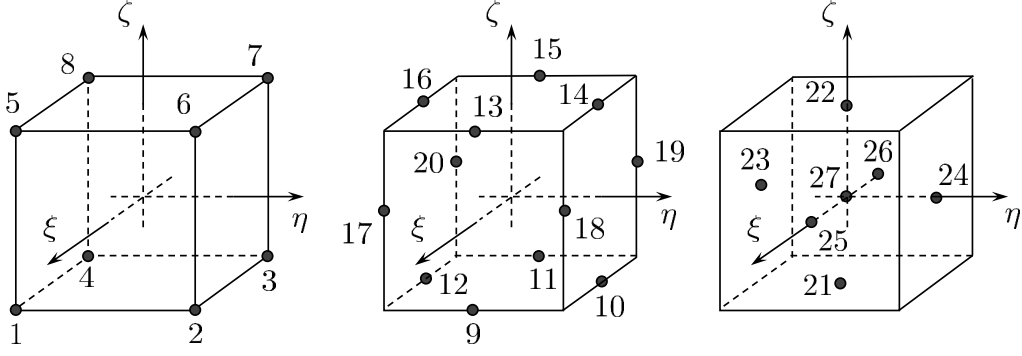
Figure 5.1: Isoparametric hexahedral finite element with 27 nodes

The virtual vector of element nodal degrees of freedom is thus defined as $\overline{\mathbf{d}}^e = \langle \overline{\mathbf{d}}_1^e \ \overline{\mathbf{d}}_2^e \ \ldots \ \overline{\mathbf{d}}_{n_{node}}^e \rangle$, where $\overline{\mathbf{d}}_i^e = \left\langle \overline{\mathbf{d}}_{\mathbf{u}_i}^e \ \overline{\mathbf{d}}_{\boldsymbol{\varphi}_i}^e \right\rangle^{\mathrm{T}} = \langle \overline{u}_{1i} \ \overline{u}_{2i} \ \overline{u}_{3i} \ \overline{\varphi}_{1i} \ \overline{\varphi}_{2i} \ \overline{\varphi}_{3i} \rangle^{\mathrm{T}}$, i being the node number. The matrix of Lagrange interpolation functions in the displacement field approximation is $\mathbf{N_u} = [\mathbf{N}_1 \ \ \mathbf{0} \ \ldots \ \mathbf{N}_{n_{node}} \ \ \mathbf{0}]$, with explicit form of the sub-matrix of Lagrange interpolation functions as (3.45). The isoparametric shape functions for the Hex8NL element are defined in (3.44), while for the Hex27NL they are defined as [67]:

1. For vertex nodes: (3.44)

2. For mid-edge nodes:

$$N_i = \frac{1}{4} \begin{cases} (1 - \xi_a \xi)(1 + \eta^2)(1 + \zeta_a \zeta), & i = 9, 11, 13, 15, \\ (1 - \xi^2)(1 + \eta_a \eta)(1 + \zeta_a \zeta), & i = 10, 12, 14, 16, \\ (1 - \xi_a \xi)(1 + \eta_a \eta)(1 + \zeta^2), & i = 17, 18, 19, 20. \end{cases} \tag{5.2}$$

3. For mid-face nodes:

$$N_i = \frac{1}{2} \begin{cases} (1 - \xi^2)(1 - \eta^2)(1 + \zeta_a \zeta), & i = 21, 22, \\ (1 - \xi^2)(1 + \eta_a \eta)(1 - \zeta^2), & i = 23, 24, \\ (1 + \xi_a \xi)(1 - \eta^2)(1 - \zeta^2), & i = 25, 26. \end{cases} \tag{5.3}$$

4. For the interior node

$$N_{27} = (1 - \xi^2)(1 - \eta^2)(1 - \zeta^2). \tag{5.4}$$

The matrix of interpolation functions in the microrotation field approximation is defined in an analogous way, i.e. $\mathbf{N}_\varphi = [\mathbf{0} \ \ \mathbf{N}_1 \ldots \ \mathbf{0} \ \ \mathbf{N}_{n_{node}}]$, with $\mathbf{N}_i$ and $\mathbf{0}$ in the switched position compared to those in $\mathbf{N_u}$. The interpolated virtual fields are now introduced into (5.1). For the sake of simplicity, each term in the weak formulation is treated separately.

By introducing the interpolation into the term $\left(\mathbf{Q}^\mathrm{T}\mathrm{GRAD}\overline{\mathbf{u}}^h\right):\mathbf{B}$ we obtain:

$$\left(\mathbf{Q}^\mathrm{T}\mathrm{GRAD}\overline{\mathbf{u}}^h\right):\mathbf{B} = \overline{\mathbf{d}}^{e\,\mathrm{T}}\mathbf{A}\,\mathbf{N_u}^\mathrm{T}\nabla_X, \tag{5.5}$$

where

$$\mathbf{A} = \begin{bmatrix} \mathbf{QB} & \mathbf{0} & \mathbf{0} & \mathbf{0} & \cdots & \mathbf{0} & \mathbf{0} \\ \mathbf{0} & \mathbf{0} & \mathbf{0} & \mathbf{0} & \cdots & \mathbf{0} & \mathbf{0} \\ \mathbf{0} & \mathbf{0} & \mathbf{QB} & \mathbf{0} & \cdots & \mathbf{0} & \mathbf{0} \\ \mathbf{0} & \mathbf{0} & \mathbf{0} & \mathbf{0} & \cdots & \mathbf{0} & \mathbf{0} \\ \vdots & \vdots & \vdots & \vdots & \ddots & \vdots & \vdots \\ \mathbf{0} & \mathbf{0} & \mathbf{0} & \mathbf{0} & \cdots & \mathbf{QB} & \mathbf{0} \\ \mathbf{0} & \mathbf{0} & \mathbf{0} & \mathbf{0} & \cdots & \mathbf{0} & \mathbf{0} \end{bmatrix}, \tag{5.6}$$

i.e. a square matrix assembled of $n_{node} \times n_{node}$ 6×6 blocks $\begin{bmatrix} \mathbf{QB} & \mathbf{0} \\ \mathbf{0} & \mathbf{0} \end{bmatrix}$ along the diagonal region and zero elsewhere. The detailed exposition of the derivation is presented in Appendix G.10.1. Analogously, we obtain

$$\left(\mathbf{Q}^\mathrm{T}\mathrm{GRAD}\overline{\boldsymbol{\varphi}}^h\right):\mathbf{G} = \overline{\mathbf{d}}^{e\,\mathrm{T}}\mathbf{L}\,\mathbf{N}_\varphi^\mathrm{T}\nabla_X, \tag{5.7}$$

where

$$\mathbf{L} = \begin{bmatrix} \mathbf{0} & \mathbf{0} & \mathbf{0} & \mathbf{0} & \cdots & \mathbf{0} & \mathbf{0} \\ \mathbf{0} & \mathbf{QG} & \mathbf{0} & \mathbf{0} & \cdots & \mathbf{0} & \mathbf{0} \\ \mathbf{0} & \mathbf{0} & \mathbf{0} & \mathbf{0} & \cdots & \mathbf{0} & \mathbf{0} \\ \mathbf{0} & \mathbf{0} & \mathbf{0} & \mathbf{QG} & \cdots & \mathbf{0} & \mathbf{0} \\ \vdots & \vdots & \vdots & \vdots & \ddots & \vdots & \vdots \\ \mathbf{0} & \mathbf{0} & \mathbf{0} & \mathbf{0} & \cdots & \mathbf{0} & \mathbf{0} \\ \mathbf{0} & \mathbf{0} & \mathbf{0} & \mathbf{0} & \cdots & \mathbf{0} & \mathbf{QG} \end{bmatrix} \tag{5.8}$$

represents a matrix made of $n_{node} \times n_{node}$ blocks equal to 6×6 matrices $\begin{bmatrix} \mathbf{0} & \mathbf{0} \\ \mathbf{0} & \mathbf{QG} \end{bmatrix}$ along the diagonal region and zero matrices elsewhere. Furthermore, by introducing interpolation of the virtual fields into $\left(\mathbf{Q}^\mathrm{T}\widehat{\boldsymbol{\varphi}}^\mathrm{T}\mathbf{F}\right):\mathbf{B}$, we obtain

$$\left(\mathbf{Q}^\mathrm{T}\widehat{\overline{\boldsymbol{\varphi}}^h}^\mathrm{T}\mathbf{F}\right):\mathbf{B} = 2\overline{\mathbf{d}}^{e\,\mathrm{T}}\mathbf{N}_\varphi^\mathrm{T}\mathrm{ax}\left(\mathrm{skew}\left(\mathbf{FB}^\mathrm{T}\mathbf{Q}^\mathrm{T}\right)\right), \tag{5.9}$$

where $\mathrm{skew}\left(\mathbf{FB}^\mathrm{T}\mathbf{Q}^\mathrm{T}\right) = \frac{1}{2}\left(\mathbf{FB}^\mathrm{T}\mathbf{Q}^\mathrm{T} - \mathbf{QBF}^\mathrm{T}\right)$. The detailed exposition of the derivation of (5.9) can be found in Appendix G.10.3. Finally, the interpolated principle of virtual

work (in terms of virtual fields only) is equal to

$$\int_V \left(\overline{\mathbf{d}}^{e^T} \mathbf{A}\, \mathbf{N_u}^T \nabla_X + 2\overline{\mathbf{d}}^{e^T} \mathbf{N}_\varphi^{\,T} \mathrm{ax}\left(\mathrm{skew}\left(\mathbf{FB^TQ^T} \right) \right) + \overline{\mathbf{d}}^{e^T} \mathbf{L}\, \mathbf{N}_\varphi^{\,T} \nabla_X \right) dV -$$
$$\int_V \left(\overline{\mathbf{d}}^{e^T} \mathbf{N_u}^T \mathbf{P_V} + \overline{\mathbf{d}}^{e^T} \mathbf{N}_\varphi^{\,T} \mathbf{M_V} \right) dV - \int_{S_p} \left(\overline{\mathbf{d}}^{e^T} \mathbf{N_u}^T \mathbf{P_S} + \overline{\mathbf{d}}^{e^T} \mathbf{N}_\varphi^{\,T} \mathbf{M_S} \right) dS = 0. \tag{5.10}$$

By extracting the vector of virtual nodal displacements and microrotations out of the integral we obtain

$$\overline{\mathbf{d}}^{e^T} \left\{ \int_V \left(\mathbf{A}\, \mathbf{N_u}^T \nabla_X + 2\mathbf{N}_\varphi^{\,T} \mathrm{ax}\left(\mathrm{skew}\left(\mathbf{FB^TQ^T} \right) \right) + \mathbf{L}\, \mathbf{N}_\varphi^{\,T} \nabla_X \right) dV - \right.$$
$$\left. \int_V \left(\mathbf{N_u}^T \mathbf{P_V} + \mathbf{N}_\varphi^{\,T} \mathbf{M_V} \right) dV - \int_{S_p} \left(\mathbf{N_u}^T \mathbf{P_S} + \mathbf{N}_\varphi^{\,T} \mathbf{M_S} \right) dS \right\} = 0.$$

Now we can introduce the element residual force vector $\mathbf{g}^e$ as

$$\overline{\mathbf{d}}^{e^T} \mathbf{g}^e = \overline{\mathbf{d}}^{e^T} \left(\mathbf{q}^{int,e} - \mathbf{q}^{ext,e} \right) = 0, \tag{5.11}$$

where

$$\mathbf{g}^e = \int_V \left(\mathbf{A}\, \mathbf{N_u}^T \nabla_X + 2\mathbf{N}_\varphi^{\,T} \mathrm{ax}\left(\mathrm{skew}\left(\mathbf{FB^TQ^T} \right) \right) + \mathbf{L}\, \mathbf{N}_\varphi^{\,T} \nabla_X \right) dV +$$
$$- \int_V \left(\mathbf{N_u}^T \mathbf{P_V} + \mathbf{N}_\varphi^{\,T} \mathbf{M_V} \right) dV - \int_{S_p} \left(\mathbf{N_u}^T \mathbf{P_S} + \mathbf{N}_\varphi^{\,T} \mathbf{M_S} \right) dS = 0,$$

while $\mathbf{q}^{int,e}$ represents the element vector of internal forces and $\mathbf{q}^{ext,e}$ represents the element vector of external forces, which follow from (5.11) as

$$\mathbf{q}^{int,e} = \int_V \left(\mathbf{A}\, \mathbf{N_u}^T \nabla_X + 2\mathbf{N}_\varphi^{\,T} \mathrm{ax}\left(\mathrm{skew}\left(\mathbf{FB^TQ^T} \right) \right) + \mathbf{L}\, \mathbf{N}_\varphi^{\,T} \nabla_X \right) dV, \tag{5.12}$$

$$\mathbf{q}^{ext,e} = \int_V \left(\mathbf{N_u}^T \mathbf{P_V} + \mathbf{N}_\varphi^{\,T} \mathbf{M_V} \right) dV + \int_{S_p} \left(\mathbf{N_u}^T \mathbf{P_S} + \mathbf{N}_\varphi^{\,T} \mathbf{M_S} \right) dS. \tag{5.13}$$

The element internal force vector at node i thus follows from (5.6), (5.8), (5.9) and the structure of $\mathbf{N_u}$ and $\mathbf{N}_\varphi$ as

$$\mathbf{q}_i^{int,e} = \int_V \left\{ \begin{array}{c} \mathbf{QB}(N_i \nabla_X) \\ 2N_i \mathrm{ax}(\mathrm{skew}(\mathbf{FB^TQ^T})) + \mathbf{QG}(N_i \nabla_X) \end{array} \right\} dV. \tag{5.14}$$

5.1   Linearization of the element residual force vector

To solve a nonlinear boundary-value problem, the nonlinear equations have to be linearized and solved as a sequence of linear problems, i.e. in order to proceed to finding

the solution of this problem, the residual force has to be linearized as follows

$$\text{Lin}\left[\mathbf{g}(\mathbf{u}, \mathbf{Q})\right]) = \mathbf{g}(\mathbf{u}, \mathbf{Q}) + \Delta\mathbf{g}$$

$$= \mathbf{g}(\mathbf{u}, \mathbf{Q}) + \left.\frac{\mathrm{d}}{\mathrm{d}\epsilon}\right|_{\epsilon=0} \mathbf{g}\left(\mathbf{u} + \epsilon\Delta\mathbf{u},\ \exp(\epsilon\widehat{\Delta\boldsymbol{\varphi}})\mathbf{Q}\right) = \mathbf{0}, \qquad (5.15)$$

with $\Delta(\bullet) = \left.\dfrac{\mathrm{d}}{\mathrm{d}\epsilon}\right|_{\epsilon=0} (\bullet)_\epsilon$ as the directional derivative in the direction of the infinitesimally small perturbations $\Delta\mathbf{u}$ and $\Delta\boldsymbol{\varphi}$, where making $\text{Lin}(\mathbf{g})$ vanish in a series of iterative solutions provides an algoritmic basis for the solution process.

When the linearization of the element residual is performed, the following general form is obtained:

$$\mathbf{g}^e(\mathbf{u}, \mathbf{Q}) + \Delta\mathbf{g}^e = \mathbf{q}^{int,e} - \mathbf{q}^{ext,e} + \mathbf{K}^e\Delta\mathbf{d}^e = \mathbf{0}, \qquad (5.16)$$

where $\mathbf{K}^e$ represents the element tangent stiffness matrix. In the nonlinear analysis $\mathbf{K}^e$ consists of two parts:

$$\mathbf{K}^e = \mathbf{K_M}^e + \mathbf{K_G}^e. \qquad (5.17)$$

The matrix $\mathbf{K_M}^e$ is referred to as the element material stiffness matrix and $\mathbf{K_G}^e$ is referred to as the element geometric stiffness matrix. The part $\mathbf{K_M}^e$ depends on material properties, while the part $\mathbf{K_G}^e$ depends on stresses and is a characteristic of large displacement/rotation problems and consequently does not exist in the linear analysis.

The linearization of each term in the element residual is derived and presented in detail in Appendix G. By introducing the linearized terms derived there and substituting $\boldsymbol{\ell} = \text{ax}(\text{skew}(\mathbf{FQ}^{\mathrm{T}}))$ we obtain the element incremental residual

$$\Delta\mathbf{g}^e = \left\{\begin{array}{c} \Delta\mathbf{g}_1^e \\ \Delta\mathbf{g}_2^e \\ \vdots \\ \Delta\mathbf{g}_{n_{node}}^e \end{array}\right\}. \qquad (5.18)$$

The element incremental nodal residual $\Delta\mathbf{g}_i^e$ is thus

$$\Delta\mathbf{g}_i^e = \int \left\{\begin{array}{c} \Delta\mathbf{g}_i^{e1} \\ \Delta\mathbf{g}_i^{e2} \end{array}\right\} dV, \qquad (5.19)$$

where vectors $\Delta\mathbf{g}_i^{e1}$ and $\Delta\mathbf{g}_i^{e2}$ are equal to

$$\Delta\mathbf{g}_i^{e1} = \left(\widehat{\Delta\boldsymbol{\varphi}}\mathbf{QB} + \mathbf{Q}\left(\mathbf{T} : \Delta\mathbf{E}\right)\right)(N_i\nabla_X),$$

$$\Delta\mathbf{g}_i^{e2} = \left(\widehat{\Delta\boldsymbol{\varphi}}\mathbf{QG} + \mathbf{Q}\left(\mathbf{D} : \Delta\mathbf{K}\right)\right)(N_i\nabla_X)$$

$$- N_i\boldsymbol{\epsilon} : \left(\text{GRAD}\Delta\mathbf{u}\mathbf{B}^{\mathrm{T}}\mathbf{Q}^{\mathrm{T}} + \mathbf{F}(\mathbf{T} : \Delta\mathbf{E})^{\mathrm{T}}\mathbf{Q}^{\mathrm{T}} + \mathbf{FB}^{\mathrm{T}}\mathbf{Q}^{\mathrm{T}}\widehat{\Delta\boldsymbol{\varphi}}^{\mathrm{T}}\right). \qquad (5.20)$$

Here, we introduce the equalities derived in Sections G.10.1, G.10.2 and G.10.3 of Appendix G, as follows:

$$
\begin{aligned}
&\left(\widehat{\Delta\boldsymbol{\varphi}}\mathbf{Q}\mathbf{B} + \mathbf{Q}\left(\mathbf{T}:\Delta\mathbf{E}\right)\right)(N_i\nabla_X) \\
&= \left(\lambda\mathbf{Q}(N_i\nabla_X)\nabla_X^{\mathrm{T}}\mathbf{Q}^{\mathrm{T}} + (\mu+\nu)\nabla_X^{\mathrm{T}}(N_i\nabla_X)\mathbf{I} + (\mu-\nu)\mathbf{Q}\nabla_X(N_i\nabla_X)^{\mathrm{T}}\mathbf{Q}^{\mathrm{T}}\right)\Delta\mathbf{u} \\
&+ \left(-\widehat{\mathbf{Q}\mathbf{B}(N_i\nabla_X)} + \lambda\mathbf{Q}(N_i\nabla_X)2\left[\mathrm{ax}(\mathrm{skew}(\mathbf{F}\mathbf{Q}^{\mathrm{T}}))\right]^{\mathrm{T}} + (\mu+\nu)\widehat{\mathbf{F}(N_i\nabla_X)}\right. \\
&\left. -(\mu-\nu)\mathbf{Q}\mathbf{F}^{\mathrm{T}}\widehat{\mathbf{Q}(N_i\nabla_X)}\right)\Delta\boldsymbol{\varphi}, \tag{5.21}
\end{aligned}
$$

where free ∇_X in the factor multiplying $\Delta\mathbf{u}$ operates exclusively on $\Delta\mathbf{u}$,

$$
\begin{aligned}
&\left(\widehat{\Delta\boldsymbol{\varphi}}\mathbf{Q}\mathbf{G} + \mathbf{Q}\left(\mathbf{D}:\Delta\mathbf{K}\right)\right)(N_i\nabla_X) \tag{5.22} \\
&= \left(-\widehat{\mathbf{Q}\mathbf{G}(N_i\nabla_X)} + \alpha\mathbf{Q}(N_i\nabla_X)\nabla_X^{\mathrm{T}}\mathbf{Q}^{\mathrm{T}} + (\beta+\gamma)\nabla_X^{\mathrm{T}}(N_i\nabla_X) + (\beta-\gamma)\mathbf{Q}\nabla_X(N_i\nabla_X)^{\mathrm{T}}\mathbf{Q}^{\mathrm{T}}\right)\Delta\boldsymbol{\varphi},
\end{aligned}
$$

where free ∇_X in the factor multiplying $\Delta\boldsymbol{\varphi}$ operates exclusively on $\Delta\boldsymbol{\varphi}$ and

$$
\begin{aligned}
&-N_i\boldsymbol{\epsilon}:\left(\mathrm{GRAD}\Delta\mathbf{u}\mathbf{B}^{\mathrm{T}}\mathbf{Q}^{\mathrm{T}} + \mathbf{F}(\mathbf{T}:\Delta\mathbf{E})^{\mathrm{T}}\mathbf{Q}^{\mathrm{T}} + \mathbf{F}\mathbf{B}^{\mathrm{T}}\mathbf{Q}^{\mathrm{T}}\widehat{\Delta\boldsymbol{\varphi}}^{\mathrm{T}}\right) \\
&= N_i\widehat{\mathbf{Q}\mathbf{B}\nabla_X}\Delta\mathbf{u} + 4\lambda N_i\,\mathrm{ax}(\mathrm{skew}(\mathbf{F}\mathbf{Q}^{\mathrm{T}}))\left[\mathrm{ax}(\mathrm{skew}(\mathbf{F}\mathbf{Q}^{\mathrm{T}}))\right]^{\mathrm{T}}\Delta\boldsymbol{\varphi} \\
&+ 2\lambda N_i\,\mathrm{ax}(\mathrm{skew}(\mathbf{F}\mathbf{Q}^{\mathrm{T}}))\nabla_X^{\mathrm{T}}\mathbf{Q}^{\mathrm{T}}\Delta\mathbf{u} - (\mu+\nu)N_i\left(\mathbf{F}\mathbf{F}^{\mathrm{T}} - \mathrm{tr}(\mathbf{F}\mathbf{F}^{\mathrm{T}})\mathbf{I}\right)\Delta\boldsymbol{\varphi} \\
&- (\mu+\nu)N_i\widehat{\mathbf{F}\nabla_X}\Delta\mathbf{u} \\
&+ (\mu-\nu)N_i\left[\mathbf{m_1}\quad\mathbf{m_2}\quad\mathbf{m_3}\right]\Delta\boldsymbol{\varphi} \\
&+ (\mu-\nu)N_i\widehat{\mathbf{Q}\nabla_X}\mathbf{F}\mathbf{Q}^{\mathrm{T}}\Delta\mathbf{u} + N_i\left[\left(\mathbf{F}\mathbf{B}^{\mathrm{T}}\mathbf{Q}^{\mathrm{T}}\right)^{\mathrm{T}} - \mathrm{tr}\left(\mathbf{F}\mathbf{B}^{\mathrm{T}}\mathbf{Q}^{\mathrm{T}}\right)\mathbf{I}\right]\Delta\boldsymbol{\varphi}, \tag{5.23}
\end{aligned}
$$

where $\mathbf{m_i} = \mathrm{ax}(2\mathrm{skew}(\mathbf{F}\mathbf{Q}^{\mathrm{T}}\boldsymbol{\epsilon_i}\mathbf{F}\mathbf{Q}^{\mathrm{T}}))$ and $\boldsymbol{\epsilon_i}$ is a submatrix of the Levi-Civita tensor, as presented in equation (G.38). In (5.23) all ∇_X operate on $\Delta\mathbf{u}$.

Finally, we obtain the vectors $\Delta\mathbf{g}_i^{e1}$ and $\Delta\mathbf{g}_i^{e2}$ as

$$
\begin{aligned}
\Delta\mathbf{g}_i^{e1} = &-\widehat{\mathbf{Q}\mathbf{B}(N_i\nabla_X)}\Delta\boldsymbol{\varphi} + \lambda\mathbf{Q}(N_i\nabla_X)2\boldsymbol{\ell}^{\mathrm{T}}\Delta\boldsymbol{\varphi} + \lambda\mathbf{Q}(N_i\nabla_X)\nabla_X^{\mathrm{T}}\mathbf{Q}^{\mathrm{T}}\Delta\mathbf{u} \\
&+ (\mu+\nu)\widehat{\mathbf{F}(N_i\nabla_X)}\Delta\boldsymbol{\varphi} + (\mu+\nu)\nabla_X^{\mathrm{T}}(N_i\nabla_X)\Delta\mathbf{u} \\
&- (\mu-\nu)\mathbf{Q}\mathbf{F}^{\mathrm{T}}\widehat{\mathbf{Q}(N_i\nabla_X)}\Delta\boldsymbol{\varphi} + (\mu-\nu)\mathbf{Q}\nabla_X(N_i\nabla_X^{\mathrm{T}})\mathbf{Q}^{\mathrm{T}}\Delta\mathbf{u}, \tag{5.24}
\end{aligned}
$$

$$
\begin{aligned}
\Delta\mathbf{g}_i^{e2} = &-\widehat{\mathbf{Q}\mathbf{G}(N_i\nabla_X)}\Delta\boldsymbol{\varphi} + \alpha\mathbf{Q}(N_i\nabla_X)\nabla_X^{\mathrm{T}}\mathbf{Q}^{\mathrm{T}}\Delta\boldsymbol{\varphi} + (\beta+\gamma)\nabla_X^{\mathrm{T}}(N_i\nabla_X)\Delta\boldsymbol{\varphi} \\
&+ (\beta-\gamma)\mathbf{Q}\nabla_X(N_i\nabla_X^{\mathrm{T}})\mathbf{Q}^{\mathrm{T}}\Delta\boldsymbol{\varphi} + N_i\widehat{\mathbf{Q}\mathbf{B}\nabla_X}\Delta\mathbf{u} + 4\lambda N_i\,\boldsymbol{\ell}\boldsymbol{\ell}^{\mathrm{T}}\Delta\boldsymbol{\varphi} \\
&+ 2\lambda N_i\,\boldsymbol{\ell}\nabla_X^{\mathrm{T}}\mathbf{Q}^{\mathrm{T}}\Delta\mathbf{u} - (\mu+\nu)N_i\left(\mathbf{F}\mathbf{F}^{\mathrm{T}} - \mathrm{tr}(\mathbf{F}\mathbf{F}^{\mathrm{T}})\mathbf{I}\right)\Delta\boldsymbol{\varphi} - (\mu+\nu)N_i\widehat{\mathbf{F}\nabla_X}\Delta\mathbf{u} \\
&+ (\mu-\nu)N_i\left[\mathbf{m_1}\,\mathbf{m_2}\,\mathbf{m_3}\right]\Delta\boldsymbol{\varphi} + (\mu-\nu)N_i\widehat{\mathbf{Q}\nabla_X}\mathbf{F}\mathbf{Q}^{\mathrm{T}}\Delta\mathbf{u} \\
&+ N_i\left[\left(\mathbf{F}\mathbf{B}^{\mathrm{T}}\mathbf{Q}^{\mathrm{T}}\right)^{\mathrm{T}} - \mathrm{tr}\left(\mathbf{F}\mathbf{B}^{\mathrm{T}}\mathbf{Q}^{\mathrm{T}}\right)\mathbf{I}\right]\Delta\boldsymbol{\varphi}. \tag{5.25}
\end{aligned}
$$

Next, we split the element incremental nodal residual $\Delta \mathbf{g}_i^e$ into its geometric and material part as:

$$\Delta \mathbf{g}_i^e = \Delta \mathbf{g}_{\mathrm{G}_i}^e + \Delta \mathbf{g}_{\mathrm{M}_i}^e. \tag{5.26}$$

In order to obtain the geometric element stiffness matrix, we observe the part of the element incremental residual $\mathbf{g}_{\mathrm{G}_i}^e$ which depends on stresses $\mathbf{B}$ and/or $\mathbf{G}$ which is equal to:

$$\Delta \mathbf{g}_{\mathrm{G}_i}^e = \int_V \left\{ \begin{matrix} \Delta \mathbf{g}_{\mathrm{G}_i}^{e1} \\ \Delta \mathbf{g}_{\mathrm{G}_i}^{e2} \end{matrix} \right\} dV, \tag{5.27}$$

where vectors $\Delta \mathbf{g}_{\mathrm{G}_i}^{e1}$ and $\Delta \mathbf{g}_{\mathrm{G}_i}^{e2}$ are equal to

$$\Delta \mathbf{g}_{\mathrm{G}_i}^{e1} = \left(-\widehat{\mathbf{Q}\mathbf{B}(N_i \nabla_X)} + 2\lambda \mathbf{Q}(N_i \nabla_X) \boldsymbol{\ell}^{\mathrm{T}} \right) \Delta \boldsymbol{\varphi}, \tag{5.28}$$

$$\Delta \mathbf{g}_{\mathrm{G}_i}^{e2} = \left(-\widehat{\mathbf{Q}\mathbf{G}(N_i \nabla_X)} + 4\lambda N_i \boldsymbol{\ell}\boldsymbol{\ell}^{\mathrm{T}} + N_i \left[(\mathbf{F}\mathbf{B}^{\mathrm{T}}\mathbf{Q}^{\mathrm{T}})^{\mathrm{T}} - \mathrm{tr}(\mathbf{F}\mathbf{B}^{\mathrm{T}}\mathbf{Q}^{\mathrm{T}})\mathbf{I} \right] \right) \Delta \boldsymbol{\varphi}$$
$$+ \left(N_i \widehat{\mathbf{Q}\mathbf{B}\nabla_X} + 2\lambda N_i \boldsymbol{\ell}\nabla_X^{\mathrm{T}}\mathbf{Q}^{\mathrm{T}} \right) \Delta \mathbf{u}. \tag{5.29}$$

It is important to note that terms $\lambda \mathbf{Q}(N_i \nabla_X) \boldsymbol{\ell}^{\mathrm{T}} \Delta \boldsymbol{\varphi}$, $4\lambda N_i \boldsymbol{\ell}\boldsymbol{\ell}^{\mathrm{T}}$ and $2\lambda N_i \boldsymbol{\ell}\nabla_X^{\mathrm{T}}\mathbf{Q}^{\mathrm{T}} \Delta \mathbf{u}$ contain the material parameter λ and as such is more intuitive to be classified as terms belonging to the material part. However, in the linear analysis of the present formulation these three terms vanish, as proven in Appendix H, which is the reason why we classified them as a part of the geometric stiffness. By extracting the vector of incremental displacements and microrotations we obtain

$$\Delta \mathbf{g}_{\mathrm{G}_i}^e = \int_V \left[\begin{matrix} \mathbf{0} & -\widehat{\mathbf{Q}\mathbf{B}(N_i \nabla_X)} + 2\lambda \mathbf{Q}(N_i \nabla_X) \boldsymbol{\ell}^{\mathrm{T}} \\ N_i \widehat{\mathbf{Q}\mathbf{B}\nabla_X} + 2\lambda N_i \boldsymbol{\ell}\nabla_X^{\mathrm{T}}\mathbf{Q}^{\mathrm{T}} & -\widehat{\mathbf{Q}\mathbf{G}(N_i \nabla_X)} + 4\lambda N_i \boldsymbol{\ell}\boldsymbol{\ell}^{\mathrm{T}} + N_i \left[(\mathbf{F}\mathbf{B}^{\mathrm{T}}\mathbf{Q}^{\mathrm{T}})^{\mathrm{T}} - \mathrm{tr}(\mathbf{F}\mathbf{B}^{\mathrm{T}}\mathbf{Q}^{\mathrm{T}})\mathbf{I} \right] \end{matrix} \right] \left\{ \begin{matrix} \Delta \mathbf{u} \\ \Delta \boldsymbol{\varphi} \end{matrix} \right\} dV, \tag{5.30}$$

where $\mathbf{0}$ is a 3×3 zero matrix. Now we introduce into (5.30) the interpolation of the kinematic field increments defined earlier as

$$\Delta \mathbf{u}^h = \sum_{j=1}^{n_{node}} N_j(\xi, \eta, \zeta) \Delta \mathbf{u}_j, \qquad \Delta \boldsymbol{\varphi}^h = \sum_{j=1}^{n_{node}} N_j(\xi, \eta, \zeta) \Delta \boldsymbol{\varphi}_j, \tag{5.31}$$

and by extracting the interpolated vector of incremental nodal degrees of freedom $\Delta \mathbf{d}_j^e = \left\{ \begin{matrix} \Delta \mathbf{u} \\ \Delta \boldsymbol{\varphi} \end{matrix} \right\}$ we obtain

$$\Delta \mathbf{g}_{\mathrm{G}_i}^e = \sum_{j=1}^{n_{node}} \mathbf{K}_{\mathrm{G}_{ij}}^e \Delta \mathbf{d}_j^e, \tag{5.32}$$

where the 6×6 element block geometric stiffness matrix $\mathbf{K}_{\mathrm{G}_{ij}}^e$ follows as

$$\mathbf{K}_{\mathrm{G}ij}^{e} = \int_{V} \begin{bmatrix} \mathbf{0} & \mathbf{K}_{\mathrm{G}ij}^{e1} \\ \mathbf{K}_{\mathrm{G}ij}^{e2} & \mathbf{K}_{\mathrm{G}ij}^{e3} \end{bmatrix} dV, \tag{5.33}$$

where the submatrices are

$$\mathbf{K}_{\mathrm{G}ij}^{e1} = -\widehat{\mathbf{QB}(N_i\nabla_X)}N_j + 2\lambda\mathbf{Q}(N_i\nabla_X)\boldsymbol{\ell}^{\mathrm{T}}N_j, \tag{5.34}$$

$$\mathbf{K}_{\mathrm{G}ij}^{e2} = N_i\widehat{\mathbf{QB}(N_j\nabla_X)} + 2\lambda N_i\boldsymbol{\ell}(N_j\nabla_X)^{\mathrm{T}}\mathbf{Q}^{\mathrm{T}}, \tag{5.35}$$

$$\mathbf{K}_{\mathrm{G}ij}^{e3} = -\widehat{\mathbf{QG}(N_i\nabla_X)}N_j + 4\lambda N_iN_j\boldsymbol{\ell}\boldsymbol{\ell}^{\mathrm{T}} + N_iN_j\left[(\mathbf{FB}^{\mathrm{T}}\mathbf{Q}^{\mathrm{T}})^{\mathrm{T}} - \mathrm{tr}(\mathbf{FB}^{\mathrm{T}}\mathbf{Q}^{\mathrm{T}})\mathbf{I}\right]. \tag{5.36}$$

Next we define the element nodal incremental material residual $\Delta\mathbf{g}_{\mathrm{M}_i}^{e}$ as

$$\Delta\mathbf{g}_{\mathrm{M}_i}^{e} = \int_{V} \begin{Bmatrix} \Delta\mathbf{g}_{\mathrm{M}_i}^{e1} \\ \Delta\mathbf{g}_{\mathrm{M}_i}^{e2} \end{Bmatrix} dV, \tag{5.37}$$

where vectors $\Delta\mathbf{g}_{\mathrm{M}_i}^{e1}$ and $\Delta\mathbf{g}_{\mathrm{M}_i}^{e2}$ are equal to

$$\begin{aligned} \Delta\mathbf{g}_{\mathrm{M}_i}^{e1} = &\left(\lambda\mathbf{Q}(N_i\nabla_X)\nabla_X^{\mathrm{T}}\mathbf{Q}^{\mathrm{T}} + (\mu+\nu)\nabla_X^{\mathrm{T}}(N_i\nabla_X)\mathbf{I} + (\mu-\nu)\mathbf{Q}\nabla_X(N_i\nabla_X)^{\mathrm{T}}\mathbf{Q}^{\mathrm{T}}\right)\Delta\mathbf{u} \\ &+ \left((\mu+\nu)\widehat{\mathbf{F}(N_i\nabla_X)} - (\mu-\nu)\mathbf{QF}^{\mathrm{T}}\widehat{\mathbf{Q}(N_i\nabla_X)}\right)\Delta\boldsymbol{\varphi}, \end{aligned} \tag{5.38}$$

$$\begin{aligned} \Delta\mathbf{g}_{\mathrm{M}_i}^{e2} = &\left(-(\mu+\nu)N_i\widehat{\mathbf{F}\nabla_X} + (\mu-\nu)N_i\widehat{\mathbf{Q}\nabla_X}\mathbf{FQ}^{\mathrm{T}}\right)\Delta\mathbf{u} \\ &+ \big(\alpha\mathbf{Q}(N_i\nabla_X)\nabla_X^{\mathrm{T}}\mathbf{Q}^{\mathrm{T}} + (\beta+\gamma)\nabla_X^{\mathrm{T}}(N_i\nabla_X)\mathbf{I} + (\beta-\gamma)\mathbf{Q}\nabla_X(N_i\nabla_X^{\mathrm{T}})\mathbf{Q}^{\mathrm{T}} \\ &-(\mu+\nu)N_i\left(\mathbf{FF}^{\mathrm{T}} - \mathrm{tr}(\mathbf{FF}^{\mathrm{T}})\mathbf{I}\right) + (\mu-\nu)N_i\left[\mathbf{m_1}\ \mathbf{m_2}\ \mathbf{m_3}\right]\big)\Delta\boldsymbol{\varphi}. \end{aligned} \tag{5.39}$$

By extracting the vector of incremental displacements and microrotations and introducing the interpolation of the kinematic field increments defined in equation (5.31) into (5.37) and extracting $\Delta\mathbf{d}_j^e$ we obtain

$$\Delta\mathbf{g}_{\mathrm{M}_i}^{e} = \sum_{j=1}^{n_{node}} \mathbf{K}_{\mathrm{M}ij}^{e}\Delta\mathbf{d}_j^e, \tag{5.40}$$

where the 6×6 element block material stiffness matrix $\mathbf{K}_{\mathrm{M}ij}^{e}$ follows as

$$\mathbf{K}_{\mathrm{M}ij}^{e} = \int_{V} \begin{bmatrix} \mathbf{K}_{\mathrm{M}ij}^{e1} & \mathbf{K}_{\mathrm{M}ij}^{e2} \\ \mathbf{K}_{\mathrm{M}ij}^{e3} & \mathbf{K}_{\mathrm{M}ij}^{e4} \end{bmatrix} dV, \tag{5.41}$$

where the submatrices are

$$\mathbf{K}_{\mathrm{M}ij}^{e1} = \lambda\mathbf{Q}(N_i\nabla_X)(N_j\nabla_X)^{\mathrm{T}}\mathbf{Q}^{\mathrm{T}} + (\mu+\nu)(N_j\nabla_X)^{\mathrm{T}}(N_i\nabla_X)\mathbf{I}$$

$$+ (\mu - \nu)\mathbf{Q}(N_j\nabla_X)(N_i\nabla_X)^{\mathrm{T}}\mathbf{Q}^{\mathrm{T}} \tag{5.42}$$

$$\mathbf{K}_{\mathrm{M}_{ij}}^{e2} = (\mu + \nu)\widehat{\mathbf{F}(N_i\nabla_X)}N_j - (\mu - \nu)\mathbf{Q}\mathbf{F}^{\mathrm{T}}\widehat{\mathbf{Q}(N_i\nabla_X)}N_j, \tag{5.43}$$

$$\mathbf{K}_{\mathrm{M}_{ij}}^{e3} = -(\mu + \nu)N_i\widehat{\mathbf{F}(N_j\nabla_X)} + (\mu - \nu)N_i\widehat{\mathbf{Q}(N_j\nabla_X)}\mathbf{F}\mathbf{Q}^{\mathrm{T}}, \tag{5.44}$$

$$\mathbf{K}_{\mathrm{M}_{ij}}^{e4} = \alpha\mathbf{Q}(N_i\nabla_X)(N_j\nabla_X^{\mathrm{T}})\mathbf{Q}^{\mathrm{T}} + (\beta + \gamma)(N_j\nabla_X^{\mathrm{T}})(N_i\nabla_X)\mathbf{I} + (\beta - \gamma)\mathbf{Q}(N_j\nabla_X)(N_i\nabla_X^{\mathrm{T}})\mathbf{Q}^{\mathrm{T}}$$
$$- (\mu + \nu)N_iN_j\left(\mathbf{F}\mathbf{F}^{\mathrm{T}} - \mathrm{tr}(\mathbf{F}\mathbf{F}^{\mathrm{T}})\mathbf{I}\right) + (\mu - \nu)N_iN_j\left[\mathbf{m_1}\ \mathbf{m_2}\ \mathbf{m_3}\right]. \tag{5.45}$$

Finally, the element stiffness matrix is the sum of geometric and material stiffness block matrices in the following form

$$\mathbf{K}^e = \begin{bmatrix} [\mathbf{K}_{\mathrm{M}11}^e] + [\mathbf{K}_{\mathrm{G}11}^e] & [\mathbf{K}_{\mathrm{M}12}^e] + [\mathbf{K}_{\mathrm{G}12}^e] & \cdots & [\mathbf{K}_{\mathrm{M}1n}^e] + [\mathbf{K}_{\mathrm{G}1n}^e] \\ [\mathbf{K}_{\mathrm{M}21}^e] + [\mathbf{K}_{\mathrm{G}21}^e] & [\mathbf{K}_{\mathrm{M}22}^e] + [\mathbf{K}_{\mathrm{G}22}^e] & \cdots & [\mathbf{K}_{\mathrm{M}2n}^e] + [\mathbf{K}_{\mathrm{G}2n}^e] \\ \vdots & \vdots & \ddots & \vdots \\ [\mathbf{K}_{\mathrm{M}n1}^e] + [\mathbf{K}_{\mathrm{G}n1}^e] & [\mathbf{K}_{\mathrm{M}n2}^e] + [\mathbf{K}_{\mathrm{G}n2}^e] & \cdots & [\mathbf{K}_{\mathrm{M}nn}^e] + [\mathbf{K}_{\mathrm{G}nn}^e] \end{bmatrix}, \tag{5.46}$$

where n in (5.46) represents the number of nodes on the element (here introduced instead of n_node for the sake of clarity).

The derived formulation is tested by comparing the stiffness matrix with the stiffness matrix obtained in the linear analysis. This is presented in Appendix H.

From this point on, we can proceed towards the standard finite element assembly accounting for all element contributions, i.e.

$$\mathbf{K} = \mathop{\mathbb{A}}_{e=1}^{n_{elem}} \mathbf{K}^e, \quad \mathbf{q}^{int} = \mathop{\mathbb{A}}_{e=1}^{n_{elem}} \mathbf{q}^{int,e}, \quad \mathbf{q}^{ext} = \mathop{\mathbb{A}}_{e=1}^{n_{elem}} \mathbf{q}^{ext,e}. \tag{5.47}$$

After performing the finite element assembly procedure and introducing the boundary conditions we obtain the global system of equations we need to solve as

$$\Delta\mathbf{d} = -\mathbf{K}^{-1}\left(\mathbf{q}^{int} - \mathbf{q}^{ext}\right), \tag{5.48}$$

where $\Delta\mathbf{d}$ represents the global vector of nodal incremental displacements and incremental microrotations, which are the basic unknowns of our problem, $\mathbf{K}$ is the global stiffness matrix, $\mathbf{q}^{int}$ is the global internal force vector and $\mathbf{q}^{ext}$ is the global external force vector.

By linearizing the residual the initial non-linear system of equations is reduced to a system of linear equations which we can solve using the rapidly convergent Newton-Raphson iterative method. The basic steps of the Newton-Raphson method are outlined as follows:

DO $k = 1, 2, ..., niter$

- Compute the stiffness matrix and obtain the iterative correction:

$$\Delta \mathbf{d}^{(k)} = -\mathbf{K}^{-1}(\mathbf{d}^{(k)}) \left(\mathbf{q}^{int}(\mathbf{d}^{(k)}) - \mathbf{q}^{ext} \right) \tag{5.49}$$

- Update the displacement vector and orientation matrix

- Test convergence

$$\text{IF} \quad ||\mathbf{q}^{ext} - \mathbf{q}^{int}(\mathbf{d}^{(k+1)})|| \leq \text{tol} \ \Rightarrow \text{CONVERGED SOLUTION}$$
$$\text{ELSE} \quad \Rightarrow \text{NEXT ITERATION } (k+1)$$

In the 1st iteration we assume that the system is undeformed, i.e.

$$\mathbf{u} = \mathbf{0}, \qquad \mathbf{Q} = \mathbf{I}, \quad \Rightarrow \quad \mathbf{F} = \mathbf{I}, \quad \mathbf{B} = \mathbf{0}, \quad \mathbf{G} = \mathbf{0}, \tag{5.50}$$

and by solving the system of equations (5.48) we obtain the first increments of the displacement field $\Delta \mathbf{u}^{(1)}$ and increments of the microrotation field $\Delta \boldsymbol{\varphi}^{(1)}$. The obtained results correspond to the results obtained in the linear analysis. Then we update the value of the displacement field as

$$\mathbf{u}^{(2)} := \mathbf{u}^{(1)} + \Delta \mathbf{u}^{(1)}. \tag{5.51}$$

In general, the update of the displacement field is defined as

$$\mathbf{u}^{(k+1)} := \mathbf{u}^{(k)} + \Delta \mathbf{u}^{(k)} \tag{5.52}$$

where the superscript (k) define the iteration number.

As mentioned earlier, due to non-linearity of the finite rotation space, the update of the orientation matrix $\mathbf{Q}$ must be performed differently. In our work we choose the quaternion parametrization of orientation matrices. In general, after obtaining the vector increment of the microrotation field $\Delta \boldsymbol{\varphi}^{(k)}$ in the k-th iteration we form the corresponding quaternion increment as

$$\mathbf{q}'^{(k)}_{\Delta \boldsymbol{\varphi}} = \left\{ q^{(k)}_{\Delta \varphi}, \ \mathbf{q}^{(k)}_{\Delta \varphi} \right\} = \left\{ \cos \left(\frac{\Delta \varphi^{(k)}}{2} \right), \frac{\sin \left(\dfrac{\Delta \varphi^{(k)}}{2} \right)}{\Delta \varphi^{(k)}} \Delta \boldsymbol{\varphi}^{(k)} \right\}, \tag{5.53}$$

where $\Delta \varphi^{(k)}$ represents the norm of vector $\Delta \boldsymbol{\varphi}^{(k)}$, i.e. $\Delta \varphi^{(k)} = \sqrt{\Delta \boldsymbol{\varphi}^{(k)} \cdot \Delta \boldsymbol{\varphi}^{(k)}}$. The quaternion update is defined through the quaternion multiplication, i.e.

$$\mathbf{q}'^{(k+1)} = \mathbf{q}'^{(k)}_{\Delta \boldsymbol{\varphi}} \circ \mathbf{q}'^{(k)} = \left\{ q_0^{(k+1)}, \ \mathbf{q}^{(k+1)} \right\}, \tag{5.54}$$

where $\mathbf{q}'^{(k)} = \left\{ q_0^{(k)}, \ \mathbf{q}^{(k)} \right\}$ is the quaternion obtained in the previous ($k-$th) iteration. The updated quaternion is obtained as [88]

$$\mathbf{q}'^{(k+1)} = \left\{ q_{\Delta\varphi}^{(k)} \cdot q_0^{(k)} - \mathbf{q}_{\Delta\varphi}^{(k)} \cdot \mathbf{q}^{(k)}, \ \mathbf{q}_{\Delta\varphi}^{(k)} \times \mathbf{q}^{(k)} + q_0^{(k)} \cdot \mathbf{q}_{\Delta\varphi}^{(k)} + q_{\Delta\varphi}^{(k)} \cdot \mathbf{q}^{(k)} \right\}. \qquad (5.55)$$

Next, by following (4.14) we form the updated orientation matrix $\mathbf{Q}_{\text{new}}$ as

$$\mathbf{Q}_{\text{new}} = (2q_0^{(k+1)^2} - 1)\mathbf{I} + 2q_0^{(k+1)}\widehat{\mathbf{q}^{(k+1)}} + 2\mathbf{q}^{(k+1)} \otimes \mathbf{q}^{(k+1)}. \qquad (5.56)$$

Update of Biot-like strain and curvature tensors

In order to update the Biot-like strain and curvature tensors $\mathbf{E}$ and $\mathbf{K}$ we have to compute the values of the displacement field and orientation matrix at the integration points. For the deformation gradient $\mathbf{F}$, these values are easily obtained by finding the derivative of the interpolated values in the corresponding Gauss point l as follows:

$$\mathbf{F} = \mathbf{I} + \text{GRAD} \left(\sum_{j=1}^{n_{node}} N_i(\xi_l, \eta_l, \zeta_l)\mathbf{u}_i \right) \qquad (5.57)$$

$$= \mathbf{I} + \sum_{j=1}^{n_{node}} \begin{Bmatrix} u_{i1} \\ u_{i2} \\ u_{i3} \end{Bmatrix} \otimes \begin{Bmatrix} \frac{\partial N_i(\xi_l, \eta_l, \zeta_l)}{\partial X_1} \\ \frac{\partial N_i(\xi_l, \eta_l, \zeta_l)}{\partial X_2} \\ \frac{\partial N_i(\xi_l, \eta_l, \zeta_l)}{\partial X_3} \end{Bmatrix}, \qquad (5.58)$$

and the values of the orientation matrix are obtained as $\mathbf{Q} = \exp(\widehat{\Delta\varphi})\mathbf{Q}_{\text{old}}$ where $\mathbf{Q}_{\text{old}}$ represents the orientation matrix in the previous iteration. Then, the current strain tensor is evaluated by substituting the obtained matrices $\mathbf{F}$ and $\mathbf{Q}$ into equation (4.94).

In order to update the curvature tensor, we start by extracting the curvature vector $\mathbf{K}_i$ from $\mathbf{K} = [\mathbf{K}_1 \ \mathbf{K}_2 \ \mathbf{K}_3]$. As shown in equation (4.98) for its virtual form, the curvature vector $\mathbf{K}_i$ is defined as

$$\mathbf{K}_i = \text{ax}(\widehat{\mathbf{K}_i}) = \text{ax} \left(\mathbf{Q}^{\text{T}} \frac{\partial \mathbf{Q}}{\partial X_i} \right). \qquad (5.59)$$

Next, we introduce $\mathbf{Q} = \exp(\widehat{\Delta\varphi})\mathbf{Q}_{\text{old}}$ into $\widehat{\mathbf{K}_i} = \mathbf{Q}^{\text{T}} \dfrac{\partial \mathbf{Q}}{\partial X_i}$ and obtain

$$\widehat{\mathbf{K}_i} = \mathbf{Q}_{\text{old}}^{\text{T}} \exp(\widehat{\Delta\varphi})^{\text{T}} \frac{\partial \left(\exp(\widehat{\Delta\varphi})\mathbf{Q}_{\text{old}} \right)}{\partial X_i}.$$

We further obtain

$$\widehat{\mathbf{K}}_i = \mathbf{Q}_{\text{old}}^{\text{T}}\exp(\widehat{\Delta\boldsymbol{\varphi}})^{\text{T}}\frac{\partial\exp(\widehat{\Delta\boldsymbol{\varphi}})}{\partial X_i}\mathbf{Q}_{\text{old}} + \mathbf{Q}_{\text{old}}^{\text{T}}\underbrace{\exp(\widehat{\Delta\boldsymbol{\varphi}})^{\text{T}}\exp(\widehat{\Delta\boldsymbol{\varphi}})}_{\mathbf{I}}\frac{\partial\mathbf{Q}_{\text{old}}}{\partial X_i}.$$

Here, we recognize that $\mathbf{Q}_{\text{old}}^{\text{T}}\dfrac{\partial\mathbf{Q}_{\text{old}}}{\partial X_i} = \widehat{\mathbf{K}}_{i\text{old}}$ and obtain

$$\widehat{\mathbf{K}}_i = \mathbf{Q}_{\text{old}}^{\text{T}}\exp(\widehat{\Delta\boldsymbol{\varphi}})^{\text{T}}\frac{\partial\exp(\widehat{\Delta\boldsymbol{\varphi}})}{\partial X_i}\mathbf{Q}_{\text{old}} + \widehat{\mathbf{K}}_{i\text{old}}.$$

Next, we rewrite $\mathbf{Q}_{\text{old}} = \exp(\widehat{\Delta\boldsymbol{\varphi}})^{\text{T}}\mathbf{Q}$ and obtain

$$\widehat{\mathbf{K}}_i = \mathbf{Q}^{\text{T}}\underbrace{\exp(\widehat{\Delta\boldsymbol{\varphi}})\exp(\widehat{\Delta\boldsymbol{\varphi}})^{\text{T}}}_{\mathbf{I}}\frac{\partial\exp(\widehat{\Delta\boldsymbol{\varphi}})}{\partial X_i}\exp(\widehat{\Delta\boldsymbol{\varphi}})^{\text{T}}\mathbf{Q} + \widehat{\mathbf{K}}_{i\text{old}}$$

$$= \mathbf{Q}^{\text{T}}\frac{\partial\exp(\widehat{\Delta\boldsymbol{\varphi}})}{\partial X_i}\exp(\widehat{\Delta\boldsymbol{\varphi}})^{\text{T}}\mathbf{Q} + \widehat{\mathbf{K}}_{i\text{old}}.$$

After a lengthy, but otherwise straightforward algebraic manipulation of the term $\dfrac{\partial\exp(\widehat{\Delta\boldsymbol{\varphi}})}{\partial X_i}\exp(\widehat{\Delta\boldsymbol{\varphi}})^{\text{T}}$ (which is presented in detail in [85]) we obtain

$$\widehat{\mathbf{K}}_i = \mathbf{Q}^{\text{T}}\widehat{\mathbf{H}(\Delta\boldsymbol{\varphi})\frac{\partial\Delta\boldsymbol{\varphi}}{\partial X_i}}\mathbf{Q} + \widehat{\mathbf{K}}_{i\text{old}}$$

$$= \widehat{\mathbf{K}}_{i\text{old}} + \Delta\widehat{\mathbf{K}}_i, \tag{5.60}$$

where

$$\mathbf{H}(\Delta\boldsymbol{\varphi}) = \mathbf{I} + \frac{1 - \cos(\Delta\varphi)}{(\Delta\varphi)^2}\widehat{\Delta\boldsymbol{\varphi}} + \frac{\Delta\varphi - \sin(\Delta\varphi)}{(\Delta\varphi)^3}\widehat{\Delta\boldsymbol{\varphi}}^2, \tag{5.61}$$

and $\Delta\varphi$ represents the norm of the iterative change in the microrotation vector. Finally, by using the identity $\widehat{\mathbf{Qv}} = \mathbf{Q}\hat{\mathbf{v}}\mathbf{Q}^{\text{T}} \; \forall \; \mathbf{v} \in \mathbb{R}^3, \; \mathbf{Q} \in \text{SO}(3)$, we obtain the update of the material curvature vector as

$$\mathbf{K}_i = \mathbf{Q}^{\text{T}}\mathbf{H}(\Delta\boldsymbol{\varphi})\frac{\partial\Delta\boldsymbol{\varphi}}{\partial X_i} + \mathbf{K}_{i\text{old}}. \tag{5.62}$$

Finally, the update of the curvature tensor can be regarded as the update of the three curvature vectors, i.e. $\mathbf{K} = [\mathbf{K}_1\ \mathbf{K}_2\ \mathbf{K}_3]$ where

$$\mathbf{K}_1 = \mathbf{Q}^{\text{T}}\mathbf{H}(\Delta\boldsymbol{\varphi})\frac{\partial\Delta\boldsymbol{\varphi}}{\partial X_1}+\mathbf{K}_{1\text{old}}, \;\; \mathbf{K}_2 = \mathbf{Q}^{\text{T}}\mathbf{H}(\Delta\boldsymbol{\varphi})\frac{\partial\Delta\boldsymbol{\varphi}}{\partial X_2}+\mathbf{K}_{2\text{old}}, \;\; \mathbf{K}_3 = \mathbf{Q}^{\text{T}}\mathbf{H}(\Delta\boldsymbol{\varphi})\frac{\partial\Delta\boldsymbol{\varphi}}{\partial X_3}+\mathbf{K}_{3\text{old}},$$
$$\tag{5.63}$$

which can be written as

$$\mathbf{K} = \mathbf{K}_{\mathrm{old}} + \Delta\mathbf{K}$$
$$= \mathbf{K}_{\mathrm{old}} + \mathbf{Q}^{\mathrm{T}}\mathbf{H}(\Delta\boldsymbol{\varphi})\mathrm{GRAD}(\Delta\boldsymbol{\varphi}). \tag{5.64}$$

5.2   Numerical examples - nonlinear analysis

In the framework of micropolar elasticity, to the best of our knowledge the only work dealing with pure geometrical nonlinearity of 3D solids including finite-element implementation is due to Bauer et al. [49]. This work encompasses mostly benchmark problems for which an analytical solution only in the linear regime is provided, since, as also stated in that work, no analytical solutions for large-deformation micropolar elasticity is available. To the best of our knowledge, this is indeed so and here a pure-bending non-linear micropolar analytical solution is derived in order to test the validity of the presented finite elements and is presented in Section 5.2.1. Next, in Section 5.2.2 the non-linear hexahedral finite elements are tested by modelling the cantilever beam problem subject to pure bending and the obtained results are compared against the derived analytical solution. Their performance is further tested in three additional numerical examples. In Section 5.2.3, a T-shape structure subject to bending and torsion is modelled by following the approach presented in [49]. So far as we are aware, this problem represents the only geometrically nonlinear numerical example documented in the literature. Its capacity to test the elements in 3D is limited, though, and next a real three-dimensional problem consisting of a in-plane curved beam subject to out-of-the-plane loading is analysed in Section 5.2.4 and the obtained results are compared against a reference solution given in the classical theory of elasticity. Finally, the elbow cantilever subject to point load and prescribed rotation is analysed in Section 5.2.5. All the presented numerical examples are modeled within the finite element analysis program FEAP [66] where the so-called energy-convergence criterion $\Delta\mathbf{d}^{\mathrm{T}}(\mathbf{q}^{int} - \mathbf{q}^{ext}) \leq tol_e$ is prescribed with $tol_e = 10^{-16}$.

5.2.1   Derivation of non-linear analytical solution for a cantilever beam subjected to pure bending

The pure bending state of a cantilever beam is a state of stress where a bending moment which is applied to the beam does not produce any internal axial and/or shear forces, i.e. the axis of the beam is bent into a circular curve. Consequently, the beam cross-sections remain planar and perpendicular to the axis (and all the lines parallel with it) of the beam. The problem is presented in Figure 5.2 and the following boundary conditions are applied: all displacements and microrotation components in the plane $x = 0$ are equal to zero and all displacements and microrotation components other than u, v and φ_z in the

plane $z = \mp\frac{b}{2}$ are equal to zero. Also, $\frac{m_{sz}}{p_0} = \frac{h\delta}{6}$. The micropolar linear analytical solution of this problem is derived by Gauthier and Jahsman [1] and presented in Section 3.4.4. In the existing literature to the best of our knowledge no non-linear micropolar analytical solutions of this problem can be found and in this Section, such a solution is derived. A full comprehension of the linear analytical solution by Gauthier and Jahsman applied to the case of vanishing Poisson's ratio ($n = 0$), as well as the standard nonlinear solution for Euler elastica given below represent the basis for the development of this result.
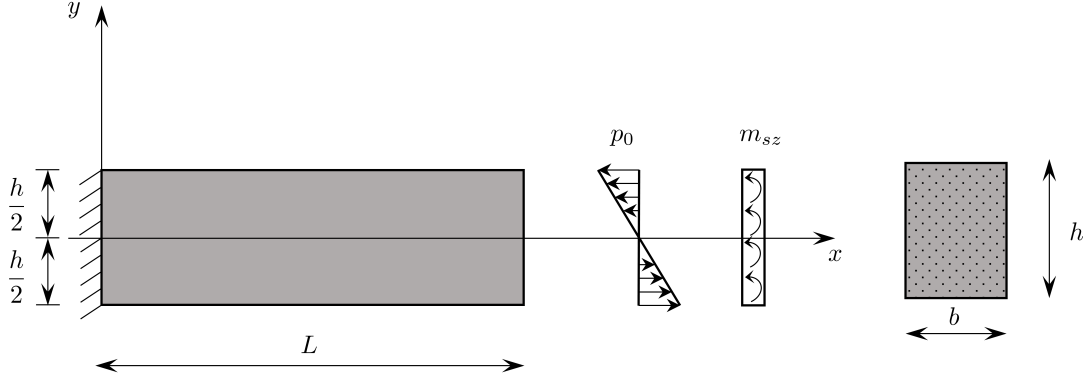
Figure 5.2: Pure bending of a cantilever beam

5.2.1.1 Linear micropolar analytical solution for $n = 0$ (Gauthier and Jahsman [1])

This solution is given in (3.41) and (3.42) for arbitrary n and in the present special case reads

$$\varphi_z = \frac{1}{1+\delta} \frac{M_z x}{EI_z}, \tag{5.65}$$

$$u = -\frac{1}{1+\delta} \frac{M_z xy}{EI_z}, \tag{5.66}$$

$$v = \frac{1}{1+\delta} \frac{M_z x^2}{2EI_z}, \tag{5.67}$$

where $M_z = p_0 W_z + m_{sz} A$, $A = bh$, $W_z = \dfrac{bh^2}{6}$, $I_z = \dfrac{bh^3}{12}$, while $\delta = 24 \left(\dfrac{l_b}{h}\right)^2 = 6\dfrac{\beta+\gamma}{\mu h^2}$, $\dfrac{m_{sz}}{p_0 h} = \dfrac{\delta}{6}$ and $E = 2\mu$. All the strain and curvature components are equal to zero other than

$$\epsilon_{xx} = -\frac{p_0}{\mu} \frac{y}{h}, \tag{5.68}$$

$$\kappa_{zx} = \frac{m_{sz}}{\beta+\gamma}, \tag{5.69}$$

and all the stress and couple-stress components are equal to zero other than

$$\sigma_{xx} = -p_0 \frac{2y}{h} = -\frac{1}{1+\delta} \frac{M_z}{W_z} \frac{2y}{h}, \tag{5.70}$$

$$\mu_{zx} = m_{sz} = \frac{\delta}{1+\delta} \frac{M_z}{A}. \tag{5.71}$$

5.2.1.2 Non-linear beam solution

This solution follows from the equilibrium

$$\frac{d\varphi_{z0}}{dx} = \frac{M_z}{EI_z}, \tag{5.72}$$

which shows that the beam reference axis turns into a circular arc of curvature $\dfrac{M_z}{EI_z}$ with

$$\varphi_{z0} = \varphi_z(x,0) = \frac{M_z x}{EI_z}, \tag{5.73}$$

$$u_0 = u(x,0) = -x + \frac{EI_z}{M_z} \sin \varphi_{z0} = -x + \frac{EI_z}{M_z} \sin \frac{M_z x}{EI_z}, \tag{5.74}$$

$$v_0 = v(x,0) = \frac{EI_z}{M_z} \left(1 - \cos \varphi_{z0}\right) = \frac{EI_z}{M_z} \left(1 - \cos \frac{M_z x}{EI_z}\right). \tag{5.75}$$

The deformation is illustrated in Figure 5.3 from where the following solution is obtained

$$\varphi_z = \frac{M_z x}{EI_z}, \tag{5.76}$$

$$u = u_0 - y \sin \varphi_z = \left(\frac{EI_z}{M_z} - y\right) \sin \frac{M_z x}{EI_z} - x, \tag{5.77}$$

$$v = v_0 - y \left(1 - \cos \varphi_z\right) = \left(\frac{EI_z}{M_z} - y\right) \left(1 - \cos \frac{M_z x}{EI_z}\right), \tag{5.78}$$

since in the beam theory the cross-sections remain rigid and for the present pure-bending state they also remain orthogonal to the deformed beam axis. The lowest-order expansion of the above displacements gives

$$u = -\frac{M_z x y}{EI_z} \quad \text{and} \quad v = \frac{M_z x^2}{2EI_z}. \tag{5.79}$$
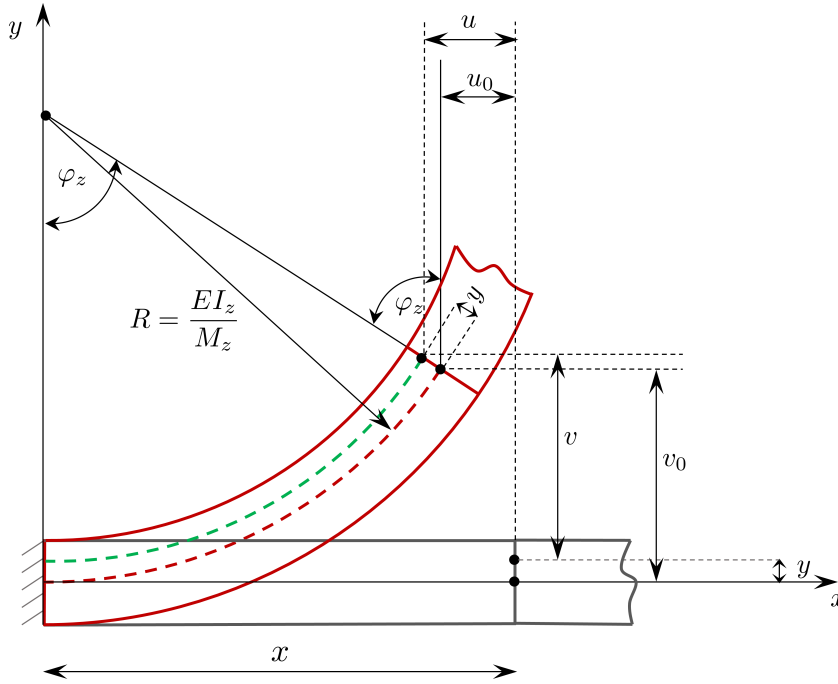
Figure 5.3: Deformation of a cantilever in pure bending

5.2.1.3 Non-linear micropolar analytical solution for $n = 0$

The existing analytical solutions given in 5.2.1.1 and 5.2.1.2 inspire us to assume that in the micropolar elasticity the bending stiffness increases by the factor $1+\delta$ in comparison to the following micropolar non-linear pure-bending solution:

$$\varphi_z = \frac{1}{1+\delta}\frac{M_z x}{EI_z}, \tag{5.80}$$

$$u = \left((1+\delta)\frac{EI_z}{M_z} - y\right)\sin\frac{M_z x}{(1+\delta)EI_z} - x, \tag{5.81}$$

$$v = \left((1+\delta)\frac{EI_z}{M_z} - y\right)\left(1 - \cos\frac{M_z x}{(1+\delta)EI_z}\right), \tag{5.82}$$

where $M_z = p_0 W_z + m_{sz}A$ is the resultant bending moment in which in the present geometrically non-linear case it has to be recognised that the applied load traction p_0 has to stay orthogonal to the cross-section at all times, i.e. it ought to point in the direction of

$$\mathbf{t}_{1L} = \mathbf{Q}_L\mathbf{e_1}, \tag{5.83}$$

with $\mathbf{Q}_L = \begin{bmatrix} \cos\varphi_{zL} & -\sin\varphi_{zL} & 0 \\ \sin\varphi_{zL} & \cos\varphi_{zL} & 0 \\ 0 & 0 & 1 \end{bmatrix}$ as the rotation matrix of the cross-section at $x = L$.

Then, instead of the components $p_x = -p_0 \dfrac{2y}{h}$ and $p_y = 0$ present in the linear analysis, we now have $p_x = -p_0 \dfrac{2y}{h} \cos\varphi_{zL}$ and $p_y = -p_0 \dfrac{2y}{h} \sin\varphi_{zL}$ with $\varphi_{zL} = \dfrac{1}{1+\delta} \dfrac{M_z L}{EI_z}$ and $p_0 = \dfrac{1}{1+\delta} \dfrac{M_z}{W_z}$, while $msz = \dfrac{\delta}{1+\delta} \dfrac{M_z}{A}$. Note that the presumed solution reduces to both the linear micropolar solution in 5.2.1.1 for small φ_z (i.e. for the lowest-order expansion of $\sin\varphi_z$ and $\cos\varphi_z$) and the non-linear beam solution in 5.2.1.2 for vanishing micropolar effects ($\delta = 0$).

In order to check if this solution actually is the analytical solution sought, we use a semi-inverse method, i.e. we check if it satisfies the governing equations of the problem (4.72) and (4.73). Since in 2D the rotation matrix is

$$\mathbf{Q} = \begin{bmatrix} \cos\varphi_z & -\sin\varphi_z & 0 \\ \sin\varphi_z & \cos\varphi_z & 0 \\ 0 & 0 & 1 \end{bmatrix}. \tag{5.84}$$

and the deformation gradient $\mathbf{F} = \mathrm{GRAD}\mathbf{u} + \mathbf{I}$ is

$$\mathbf{F} = \begin{bmatrix} \dfrac{\partial u}{\partial x} + 1 & \dfrac{\partial u}{\partial y} & 0 \\ \dfrac{\partial v}{\partial x} & \dfrac{\partial v}{\partial y} + 1 & 0 \\ 0 & 0 & 1 \end{bmatrix}. \tag{5.85}$$

the Biot-like strain tensor $\mathbf{E} = \mathbf{Q}^{\mathrm{T}}\mathbf{F} - \mathbf{I}$ follows as

$$
\begin{aligned}
\mathbf{E} &= \begin{bmatrix} E_{11} & E_{12} & 0 \\ E_{21} & E_{22} & 0 \\ 0 & 0 & 0 \end{bmatrix} \\
&= \begin{bmatrix} \cos\varphi_z\left(\dfrac{\partial u}{\partial x}+1\right) + \sin\varphi_z \dfrac{\partial v}{\partial x} - 1 & \cos\varphi_z \dfrac{\partial u}{\partial y} + \sin\varphi_z\left(\dfrac{\partial v}{\partial y}+1\right) & 0 \\ -\sin\varphi_z\left(\dfrac{\partial u}{\partial x}+1\right) + \cos\varphi_z \dfrac{\partial v}{\partial x} & -\sin\varphi_z \dfrac{\partial u}{\partial y} + \cos\varphi_z\left(\dfrac{\partial v}{\partial y}+1\right) - 1 & 0 \\ 0 & 0 & 0 \end{bmatrix},
\end{aligned}
\tag{5.86}
$$

and the Biot-like curvature tensor $\mathbf{K} = \mathbf{Q}^{\mathrm{T}}\mathrm{GRAD}\mathbf{Q}$ as

$$\mathbf{K} = \begin{bmatrix} 0 & 0 & 0 \\ 0 & 0 & 0 \\ K_{31} & K_{32} & 0 \end{bmatrix} = \begin{bmatrix} 0 & 0 & 0 \\ 0 & 0 & 0 \\ \dfrac{\partial \varphi_z}{\partial x} & \dfrac{\partial \varphi_z}{\partial y} & 0 \end{bmatrix}. \tag{5.87}$$

By taking the partial derivatives of the presumed solution:

$$\frac{\partial u}{\partial x} = -1 + \cos\left(\frac{x}{R}\right)\left(1 - \frac{y}{R}\right), \qquad \frac{\partial u}{\partial y} = -\sin\left(\frac{x}{R}\right), \tag{5.88}$$

$$\frac{\partial v}{\partial x} = \sin\left(\frac{x}{R}\right)\left(1 - \frac{y}{R}\right), \qquad \frac{\partial v}{\partial y} = \cos\frac{x}{R} - 1, \tag{5.89}$$

$$\frac{\partial \varphi_z}{\partial x} = \frac{1}{R}, \qquad \frac{\partial \varphi_z}{\partial y} = 0, \tag{5.90}$$

where $R = (1 + \delta)\dfrac{EI}{M_z}$, the strain tensor and the curvature tensor turn into

$$\mathbf{E} = \begin{bmatrix} -\frac{y}{R} & 0 & 0 \\ 0 & 0 & 0 \\ 0 & 0 & 0 \end{bmatrix}, \qquad \mathbf{K} = \begin{bmatrix} 0 & 0 & 0 \\ 0 & 0 & 0 \\ \frac{1}{R} & 0 & 0 \end{bmatrix}, \tag{5.91}$$

and the non-zero components of the stress tensor and the couple-stress tensor turn into

$$B_{11} = (\lambda + 2\mu)E_{11} = -\frac{1}{1+\delta}\frac{M_z}{W_z}\frac{2y}{h}, \tag{5.92}$$

$$G_{31} = (\beta + \gamma)K_{31} = \frac{\delta}{1+\delta}\frac{M_z}{A}, \tag{5.93}$$

which obviously satisfy the non-linear differential equilibrium equations (4.72) and (4.73).

Finally, we analyse the boundary conditions $(\mathbf{QB})\mathbf{N} = \mathbf{P}_{\mathrm{S}}$, $(\mathbf{QG})\mathbf{N} = \mathbf{M}_{\mathrm{S}}$ at $x = L$ and obtain

$$\begin{bmatrix} \cos\varphi_z B_{11} & 0 & 0 \\ \sin\varphi_z B_{11} & 0 & 0 \\ 0 & 0 & 0 \end{bmatrix} \begin{Bmatrix} 1 \\ 0 \\ 0 \end{Bmatrix} = \begin{Bmatrix} P_{S1} \\ P_{S2} \\ 0 \end{Bmatrix} \quad \Rightarrow \quad \begin{aligned} P_{S1} &= \cos\varphi_L B_{11}, \\ P_{S2} &= \sin\varphi_L B_{11}, \end{aligned} \tag{5.94}$$

$$\begin{bmatrix} 0 & 0 & 0 \\ 0 & 0 & 0 \\ G_{31} & 0 & 0 \end{bmatrix} \begin{Bmatrix} 1 \\ 0 \\ 0 \end{Bmatrix} = \begin{Bmatrix} 0 \\ 0 \\ M_{S3} \end{Bmatrix} \quad \Rightarrow \quad M_{S3} = G_{31}, \tag{5.95}$$

i.e.

$$P_{S1} = -\frac{1}{1+\delta}\frac{M_z}{W_z}\cos\varphi_L\frac{2y}{h} = -p_0\frac{2y}{h}\cos\varphi_L, \tag{5.96}$$

$$P_{S2} = -\frac{1}{1+\delta}\frac{M_z}{W_z}\sin\varphi_L\frac{2y}{h} = -p_0\frac{2y}{h}\sin\varphi_L, \qquad (5.97)$$

$$M_{S3} = \frac{\delta}{1+\delta}\frac{M_z}{A} = m_{sz}, \qquad (5.98)$$

which satisfies the boundary conditions applied.

In this way we have derived a possible micropolar non-linear solution for the cantilever beam problem subject to pure bending.

5.2.2 Non-linear cantilever beam subject to pure bending

In order to test the accuracy of the newly presented nonlinear finite elements Hex8NL and Hex27NL we model a thin cantilever beam (with height to length ratio $\frac{h}{L} \leq 0.01$) subject to pure bending as shown in Figure 5.4 and observe its nonlinear behavior. The chosen geometry of the cantilever is $L = 10$ m, $h = 0.1$ m and $b = 1$ m, and, in order to capture the size-effect the value of the characteristic length is varied in the region $l_b \in [0.01, 0.08]$. The resultant bending moment chosen as $M_z = 0.01\pi$ Nm is applied through a linearly varying surface loading P_{S1} and a constant surface moment loading M_{S3} in the proportion defined in equation (3.38), which has to be strictly respected in order to obtain a pure bending state. In addition, the linearly varying surface loading P_{S1} has to be applied as a follower load, i.e. it has to remain orthogonal to the cantilever cross-section during the whole deformation process. The analytical values of the loading magnitudes p_0 and M_{S3} for different l_b are presented in Table 5.1. The distributed loadings (5.96)-(5.98) are applied through corresponding concentrated nodal forces and moments obtained by integration as defined by (3.1)-(3.4).

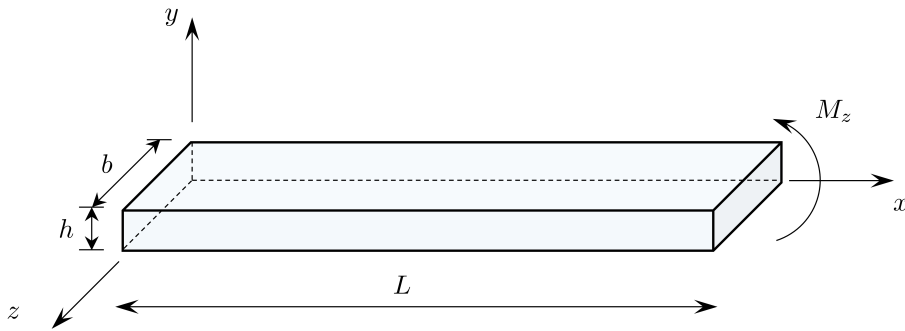Figure 5.4: Thin cantilever beam subject to bending

The engineering material parameters are taken as $E = 1200$ N/m^2 and $n = 0.0$ which give the Lamé constants $\mu = 600$ N/m^2 and $\lambda = 0$ N/m^2. The parameter ν is chosen to be equal to $\nu = 200$ N/m^2, corresponding to $N = 0.5$, but in this example it can have an arbitrary value since it does not affect the solution. The remaining engineering

parameters which exist only in the 3D analysis are chosen as $\psi = 0$ and $l_t = 0.02$ m, but, since they also do not affect the solution, they can also have arbitrary values. Along the left-hand edge of the specimen all the displacements and microrotations are restrained, i.e. $u_1(0, y, z) = u_2(0, y, z) = u_3(0, y, z) = \varphi_1(0, y, z) = \varphi_2(0, y, z) = \varphi_3(0, y, z) = 0$, for $y \in [0, h]$ and $z \in [0, b]$. Furthermore, the cylindrical bending is accomplished by additionally restraining the displacements in the z direction along the whole cantilever, i.e. $u_3(x, y, z) = 0$ for $x \in [0, L]$, $y \in [0, h]$ and $z \in [0, b]$.

Table 5.1: Analytical values of the external loadings P_0 and M_{S3} in the undeformed configuration as defined in (3.39) for different values of the characteristic length l_b, $n = 0.0$, $h = 0.1$, together giving the total external moment $M = 0.01\pi$ Nm

l_b/h	l_b	$\beta + \gamma$	p_0	M_{S3}
0.1	0.01	0.24	15.201 254 775 434 490	0.060 805 019 101 737 940
0.2	0.02	0.96	9.617 120 368 132 020	0.153 873 925 890 112 300
0.4	0.04	3.84	3.894 536 347 425 364	0.249 250 326 235 223 300
0.8	0.08	15.36	1.152 173 344 837 332	0.294 956 376 278 357 100

First, the problem is solved using a mesh of 64 hexahedral finite elements Hex8NL and Hex27NL propagating in the x direction. The obtained numerical results for the horizontal and vertical displacements u_1 and u_2 and microrotation φ_3 at node $P(10.0, 0.1, 1.0)$ using both elements are compared against the analytical solution derived in Section 5.2.1. The results obtained using the Hex8NL element are shown in Table 5.2, while the results obtained using the Hex27NL element are shown in Table 5.3.

Table 5.2: Results in node $P = (10.0, 0.1, 1.0)$ obtained using $64 \times 1 \times 1$ Hex8NL elements, A = Analytical, N = Numerical, LS = Number of load steps

l_b	LS	A u_1	N u_1	A u_2	N u_2	A φ_3	N φ_3	niter	CPU time
0.01	1	-7.774	-1.927	7.096	4.923	2.534	1.094	18	2 sec
0.02	1	-3.814	-1.268	6.387	4.088	1.603	0.876	14	1.5 sec
0.04	1	-0.718	-0.412	3.123	2.376	0.650	0.486	11	1 sec
0.08	1	-0.071	-0.059	0.956	0.870	0.192	0.175	5	0.5 sec

Table 5.3: Results in node $P = (10.0, 0.1, 1.0)$ obtained using $64 \times 1 \times 1$ Hex27NL element, A = Analytical, N = Numerical, LS = Number of load steps

l_b	LS	A u_1	N u_1	A u_2	N u_2	A φ_3	N φ_3	niter	CPU time
0.01	5	-7.774	-7.773	7.096	7.096	2.534	2.533	5*11	4 min 09 sec
0.02	2	-3.814	-3.814	6.387	6.387	1.603	1.603	2*14	2 min 38 sec
0.04	1	-0.718	-0.718	3.123	3.123	0.649	0.649	12	57 sec
0.08	1	-0.071	-0.071	0.956	0.956	0.192	0.192	6	30 sec

As in the linear analysis, it is again observed that, by increasing the value of the characteristic length, the cantilever becomes stiffer. Hex8NL shows quite poor results, especially for small micropolar effects, which is also observed in the linear analysis, while Hex27NL shows results which are in agreement with the derived analytical results in three significant digits. For the Hex8NL element, the finite element mesh is further refined to 1024 and 2048 elements and the obtained results are presented in Tables 5.4 and 5.5. The analytical result is approached in all the observed results, and for the mesh of 2048 elements the accuracy is achieved in two significant digits. The deformed configuration for the softest configuration ($l_b = 0.01$) for different load steps obtained by 64 Hex27NL finite element is shown in Figure 5.5.

Table 5.4: Results in node $P = (10.0, 0.1, 1.0)$ obtained using $1024 \times 1 \times 1$ Hex8NL element, A = Analytical, N = Numerical, LS = Number of load steps

l_b	LS	A u_1	N u_1	A u_2	N u_2	A φ_3	N φ_3	niter	CPU time
0.01	5	-7.774	-7.721	7.096	7.103	2.534	2.521	5*11	73 min 13 sec
0.02	2	-3.814	-3.793	6.387	6.376	1.603	1.598	16+26	51 min 22 sec
0.04	1	-0.718	-0.716	3.123	3.120	0.650	0.648	11	11 min 19 sec
0.08	1	-0.071	-0.071	0.956	0.956	0.192	0.192	6	5 min 14 sec

Table 5.5: Results in node $P = (10.0, 0.1, 1.0)$ obtained using $2048 \times 1 \times 1$ Hex8NL element, A = Analytical, N = Numerical, LS = Number of load steps

l_b	LS	A u_1	N u_1	A u_2	N u_2	A φ_3	N φ_3	niter	CPU time
0.01	5	-7.774	-7.776	7.096	7.097	2.534	2.530	5*11	524 min 44 sec
0.02	5	-3.814	-3.809	6.387	6.385	1.603	1.602	5*9	428 min 34 sec
0.04	1	-0.718	-0.717	3.121	3.121	0.650	0.649	11	103 min 45 sec
0.08	1	-0.071	-0.071	0.956	0.956	0.192	0.192	5	45 min 08 sec

By introducing the follower loads (i.e. keeping the nodal forces orthogonal to the cantilever cross-section during the whole deformation process), the external loading ceases to be constant, since it becomes dependent on the orientation matrix $\mathbf{Q}$. Consequently, when linearizing the residual $\mathbf{g}^e = \mathbf{q}^{int,e} - \mathbf{q}^{ext,e}$ in equation (5.12), the linearized non-constant external loading becomes non-zero and also contributes to the element stiffness matrix $\mathbf{K}^e$ in equation (5.46). For each loaded node i the contribution of the linearized external force vector thus follows as

$$\mathbf{K}^e_{\text{EXT}ij} = \delta_{ij} \begin{bmatrix} \mathbf{0} & \widehat{\mathbf{Q}_i \mathbf{F}_i} \\ \mathbf{0} & \mathbf{0} \end{bmatrix}, \tag{5.99}$$

where $\mathbf{Q}_i$ represent the nodal orientation matrix, $\mathbf{F}_i$ the nodal force vector and $\mathbf{0}$ is a 3×3 zero matrix and the summation convention does not apply. The ij block of the element stiffness matrix $\mathbf{K}^e$ is then computed as $[\mathbf{K}^e_{ij}] = [\mathbf{K}^e_{\text{M}ij}] + [\mathbf{K}^e_{\text{G}ij}] + [\mathbf{K}^e_{\text{EXT}i}]$. It is very important to take this into account in order to keep the quadratic convergence rate during the Newton-Raphson solution procedure. In order to demonstrate this, the problem is solved using 64 Hex8NL and 64 Hex27NL finite elements for $l_b = 0.02$. The convergence rate using both elements with and without $\mathbf{K}^e_{\text{EXT}ij}$ is given in Tables 5.6 and 5.7. We can see that without proper linearization of the residual, the number of iterations increases from 14 to 19 for both elements.. Moreover, the quadratic convergence rate of the Newton-Raphson method is lost, in contrast to the case when $\mathbf{K}^e_{\text{EXT}ij}$ is taken into account. However, in both cases we converge to the same solution, as expected. All the examples presented in Tables 5.3, 5.4 and 5.5 are solved with proper linearization of the residual which is manifested in the presence of the quadratic convergence rate.

Table 5.6: Convergence rate of the Newton-Raphson scheme using 64 Hex8NL elements for $l_b = 0.02$; absolute norm of the residual and energy

	with $\mathbf{K}^e_{\mathrm{EXT}ij}$		without $\mathbf{K}^e_{\mathrm{EXT}ij}$	
It	Residual	Energy	Residual	Energy
0	$1.60 \cdot 10^{-1}$	$2.75 \cdot 10^{-2}$	$1.60 \cdot 10^{-1}$	$2.75 \cdot 10^{-2}$
1	$2.25 \cdot 10^{2}$	$6.17 \cdot 10^{1}$	$2.25 \cdot 10^{2}$	$6.17 \cdot 10^{1}$
2	$3.36 \cdot 10^{1}$	$2.75 \cdot 10^{0}$	$3.36 \cdot 10^{1}$	$2.75 \cdot 10^{0}$
3	$3.00 \cdot 10^{0}$	$2.25 \cdot 10^{-2}$	$3.05 \cdot 10^{1}$	$2.44 \cdot 10^{-2}$
4	$9.41 \cdot 10^{-1}$	$3.28 \cdot 10^{-3}$	$9.67 \cdot 10^{-1}$	$3.79 \cdot 10^{-3}$
5	$2.10 \cdot 10^{0}$	$5.32 \cdot 10^{-3}$	$2.34 \cdot 10^{0}$	$6.40 \cdot 10^{-3}$
6	$4.92 \cdot 10^{-1}$	$3.69 \cdot 10^{-4}$	$5.05 \cdot 10^{-1}$	$3.83 \cdot 10^{-4}$
7	$6.46 \cdot 10^{-2}$	$3.30 \cdot 10^{-4}$	$5.98 \cdot 10^{-2}$	$2.08 \cdot 10^{-4}$
8	$9.23 \cdot 10^{-1}$	$9.26 \cdot 10^{-4}$	$9.91 \cdot 10^{-1}$	$1.06 \cdot 10^{-3}$
9	$3.42 \cdot 10^{-3}$	$1.59 \cdot 10^{-4}$	$2.90 \cdot 10^{-3}$	$8.68 \cdot 10^{-5}$
10	$8.62 \cdot 10^{-1}$	$7.99 \cdot 10^{-4}$	$8.67 \cdot 10^{-1}$	$8.08 \cdot 10^{-4}$
11	$5.75 \cdot 10^{-5}$	$4.73 \cdot 10^{-7}$	$3.56 \cdot 10^{-5}$	$1.84 \cdot 10^{-7}$
12	$2.73 \cdot 10^{-3}$	$8.04 \cdot 10^{-9}$	$1.99 \cdot 10^{-3}$	$4.37 \cdot 10^{-9}$
13	$6.76 \cdot 10^{-10}$	$4.88 \cdot 10^{-17}$	$3.66 \cdot 10^{-6}$	$2.46 \cdot 10^{-11}$
14			$3.70 \cdot 10^{-6}$	$3.60 \cdot 10^{-14}$
15			$8.72 \cdot 10^{-8}$	$3.28 \cdot 10^{-15}$
16			$4.25 \cdot 10^{-8}$	$7.06 \cdot 10^{-18}$
17			$1.51 \cdot 10^{-9}$	$4.52 \cdot 10^{-19}$

Table 5.7: Convergence rate of the Newton-Raphson scheme using 64 Hex27NL elements for $l_b = 0.02$ and load increment 1 ; absolute norm of the residual and energy

It	with $\mathbf{K}^e_{\mathrm{EXT}ij}$		without $\mathbf{K}^e_{\mathrm{EXT}ij}$	
	Residual	Energy	Residual	Energy
0	$8.02 \cdot 10^{-2}$	$1.25 \cdot 10^{-2}$	$8.02 \cdot 10^{-2}$	$1.25 \cdot 10^{-2}$
1	$1.45 \cdot 10^{2}$	$4.37 \cdot 10^{1}$	$1.45 \cdot 10^{2}$	$4.37 \cdot 10^{1}$
2	$1.41 \cdot 10^{1}$	$9.29 \cdot 10^{-1}$	$1.41 \cdot 10^{1}$	$9.29 \cdot 10^{-1}$
3	$3.50 \cdot 10^{0}$	$3.10 \cdot 10^{-2}$	$3.73 \cdot 10^{0}$	$3.50 \cdot 10^{-2}$
4	$1.90 \cdot 10^{0}$	$9.90 \cdot 10^{-3}$	$2.19 \cdot 10^{0}$	$1.26 \cdot 10^{-2}$
5	$6.80 \cdot 10^{0}$	$8.94 \cdot 10^{-2}$	$7.39 \cdot 10^{0}$	$1.05 \cdot 10^{-1}$
6	$5.87 \cdot 10^{-1}$	$6.76 \cdot 10^{-4}$	$6.55 \cdot 10^{-1}$	$8.34 \cdot 10^{-4}$
7	$1.37 \cdot 10^{-2}$	$2.86 \cdot 10^{-4}$	$1.34 \cdot 10^{-2}$	$2.02 \cdot 10^{-4}$
8	$1.48 \cdot 10^{0}$	$4.19 \cdot 10^{-3}$	$1.67 \cdot 10^{0}$	$5.31 \cdot 10^{-3}$
9	$4.57 \cdot 10^{-4}$	$6.95 \cdot 10^{-5}$	$4.11 \cdot 10^{-4}$	$4.46 \cdot 10^{-5}$
10	$5.91 \cdot 10^{-1}$	$6.67 \cdot 10^{-4}$	$6.40 \cdot 10^{-1}$	$7.84 \cdot 10^{-4}$
11	$2.98 \cdot 10^{-6}$	$2.21 \cdot 10^{-9}$	$1.89 \cdot 10^{-5}$	$1.92 \cdot 10^{-9}$
12	$1.89 \cdot 10^{-5}$	$6.84 \cdot 10^{-13}$	$2.78 \cdot 10^{-5}$	$2.67 \cdot 10^{-12}$
13	$6.14 \cdot 10^{-12}$	$4.38 \cdot 10^{-26}$	$4.19 \cdot 10^{-7}$	$1.33 \cdot 10^{-12}$
14			$5.80 \cdot 10^{-7}$	$5.08 \cdot 10^{-15}$
15			$3.17 \cdot 10^{-8}$	$1.44 \cdot 10^{-15}$
16			$1.90 \cdot 10^{-8}$	$1.13 \cdot 10^{-17}$
17			$1.59 \cdot 10^{-9}$	$1.65 \cdot 10^{-18}$
18			$6.43 \cdot 10^{-10}$	$2.10 \cdot 10^{-20}$

(a) No loading

(b) Load step 1

(c) Load step 2
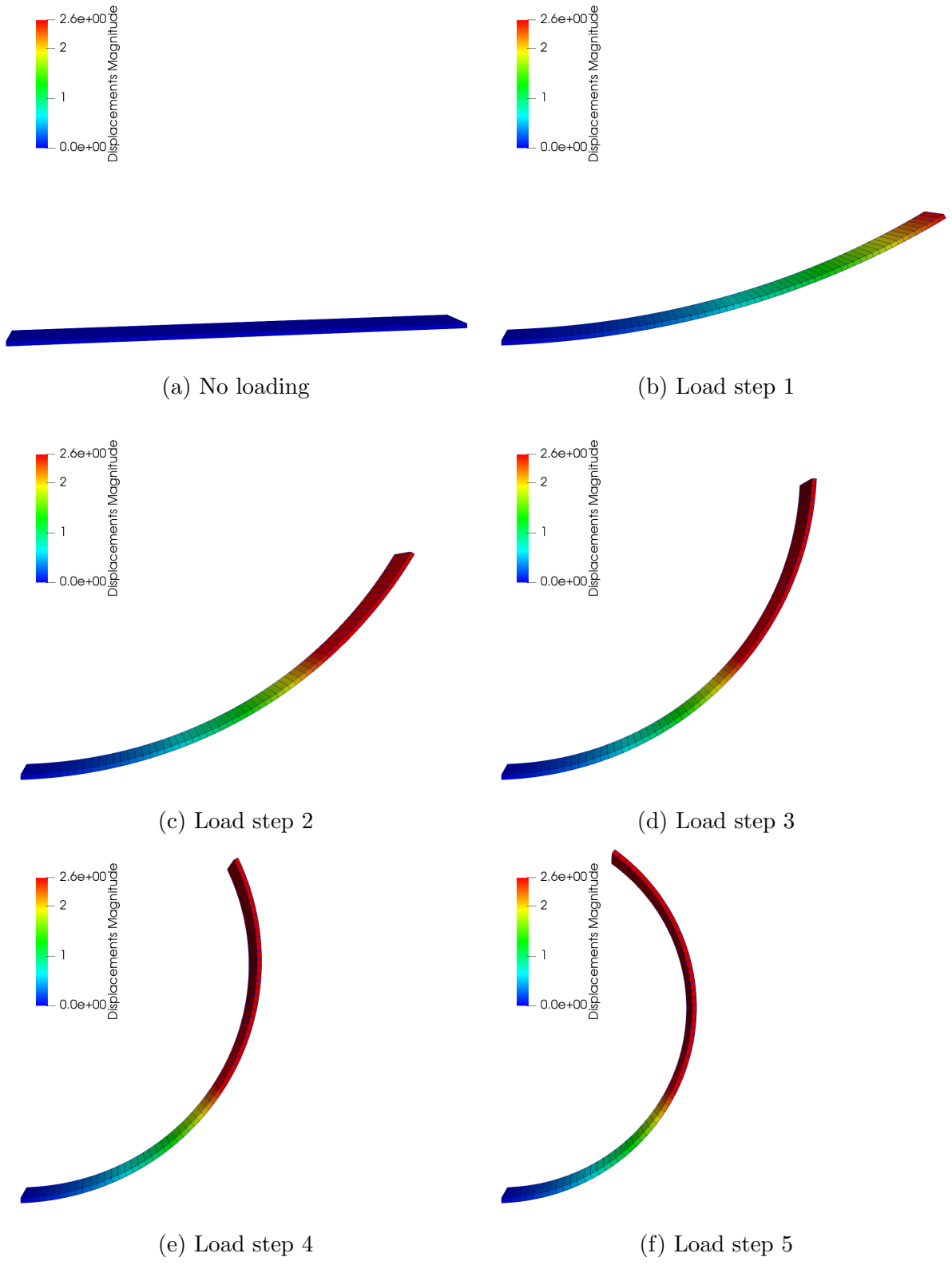
(d) Load step 3

(e) Load step 4

(f) Load step 5

Figure 5.5: Deformed configuration of the cantilever beam for $l_b = 0.01$ for different load steps obtained using a mesh of $64 \times 1 \times 1$ Hex27NL elements

5.2.3 T-shaped structure subject to bending and torsion

In this example a T-shaped structure shown in Figure 5.6 subject to bending and torsion moments is modelled. This structure is presented in [96] in the framework of the classical theory, and in [49] in the framework of the micropolar theory, which is also the only geometrically nonlinear numerical example without the material nonlinearity effects solved using micropolar finite elements with large displacements and large rotations we have been able to find in the literature. In [49], however, only the obtained deformed configurations for selected load steps are plotted, without any numerical results for displacements and/or microrotations. The micropolar material parameters are here taken as in [49], i.e. $\mu = 10\ 500$ N/mm^2, $\lambda = 15\ 750$ N/mm^2, $\nu = 3\ 500$ N/mm^2, $\alpha = 0$ N, $\beta = 52.5$ N and $\gamma = 52.5$ N , which corresponds to the following engineering material parameters: $E = 27\ 300$ N/mm^2, $n = 0.3$, $N = 0.5$, $l_b = 0.05$ mm, $l_t = \sqrt{2}l_b$, $\psi = 0$. The rib of the structure is submitted to a resultant torsional moment M_1 at the free end and both ends of the flange are submitted to a resultant bending moments M_2 chosen in the same proportion as in [49], i.e. $\frac{M_1}{M_2} = \frac{8}{15}$ while the material points in the plane where the rib touches the flange are completely fixed. The problem is modelled using two sets of different moment values chosen as $M_1 = 1200$ Nmm, $M_2 = 2250$ Nmm and $M_1 = 600$ Nmm, $M_2 = 1125$ Nmm. The chosen values of the applied moments differ from the ones specified in [49] ($M_1 = 300\ 000$ and $M_2 = 562\ 500$), which produce a deformation that is way above the theoretical predictions. The order of magnitude of moments chosen here correspond to the ones defined in [96]. The resultant moments are assumed to follow from a constant distributed surface moment loads and are thus applied through corresponding concentrated nodal moments obtained by integration as defined by (3.1)-(3.4). The structure is clamped at the points between the rib and the flange, i.e. all the displacements and microrotations are restrained $(u_1(x,1,z) = u_2(x,1,z) = u_3(x,1,z) = \varphi_1(x,1,z) = \varphi_2(x,1,z) = \varphi_3(x,1,z) = 0,$ for $x \in [5,6]$ and $z \in [0,1])$. The domain is discretised using 21 cube-shaped elements as shown in Figure 5.7. First the torsional load is applied in 20 equal load increments, keeping the flange free of any loading. Then, the two bending moments M_2 are applied at each end of the flange in another 20 equal load increments, while the torsional moment is kept constant. The displacements and microrotations at the nodes $P_1 = (0.0, 1.0, 1.0)$, $P_2 = (11.0, 1.0, 1.0)$, $P_3 = (5.0, 11.0, 1.0)$ and $P_4 = (6.0, 11.0, 1.0)$ obtained using both the Hex8NL and Hex27NL elements are shown in Tables 5.8 and 5.9 for $M_1 = 1200$ Nmm, $M_2 = 2250$ Nmm and in Tables 5.10 and 5.11 for $M_1 = 600$ Nmm, $M_2 = 1125$ Nmm. Note that the rotations of the points at the edges of the flange in the xy plane obtained using the Hex27NL elements are in the order of magnitude of $\dfrac{M_2 l}{EI}$ for $l = 5$ mm and $I = 0.8\dot{3}$ mm^4, while the rotations of the points at the edge of the rib around the y axis

obtained using the same element are in the order of magnitude of $\dfrac{M_1 L}{G I_t}$ for $L = 10$ mm,

$G = \dfrac{E}{2(1+n)}$ and $I_t \approx 0.141$ mm^4.

Figure 5.6: Top view of the T-shape structure [49]
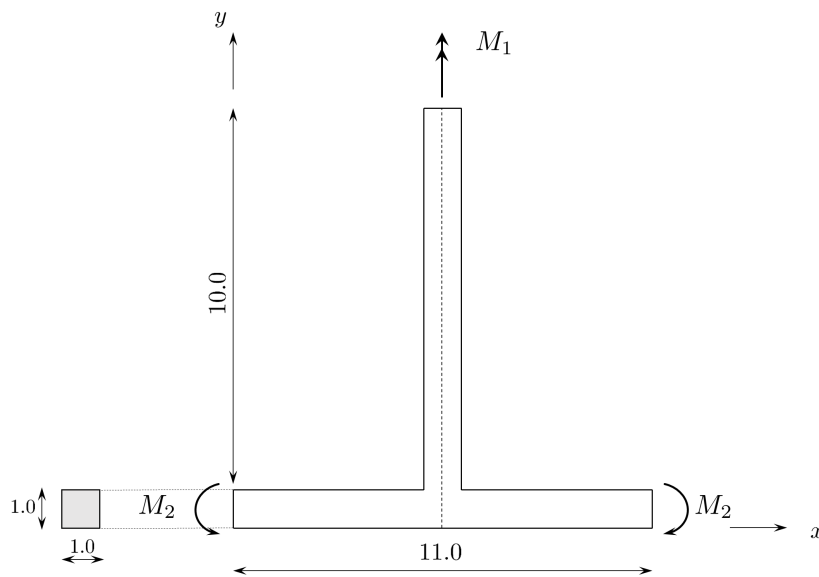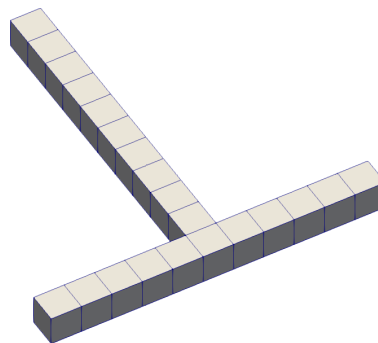

Figure 5.7: Finite element mesh of the T-shape structure

The various stages of deformation of the T-shape structure are presented in Figures 5.8 and 5.10 for Hex8NL and in Figures 5.9 and 5.11 for Hex27NL. In the present formulation the elements are not checked against and prevented from penetrating one another, which is present in the final configurations in Figure 5.9.

Table 5.8: Results obtained using $21 \times 1 \times 1$ Hex8NL elements for $M_1 = 1200$ Nmm, $M_2 = 2250$ Nmm in the last load step

Node	u_1	u_2	u_3	φ_1	φ_2	φ_3
P_1	4.8248	-4.4767	-9.3183 $\cdot 10^{-3}$	-1.9970 $\cdot 10^{-2}$	-1.8987 $\cdot 10^{-2}$	3.4405
P_2	-4.8248	-4.4767	-9.3183 $\cdot 10^{-3}$	-1.9970 $\cdot 10^{-2}$	1.8987 $\cdot 10^{-2}$	-3.4405
P_3	-1.5678 $\cdot 10^{-1}$	1.2410 $\cdot 10^{-2}$	-1.7078 $\cdot 10^{-1}$	-1.5980 $\cdot 10^{-3}$	6.2279	1.6213 $\cdot 10^{-2}$
P_4	-1.7078 $\cdot 10^{-1}$	1.2410 $\cdot 10^{-2}$	1.5678 $\cdot 10^{-1}$	1.6213 $\cdot 10^{-2}$	6.2279	1.5980 $\cdot 10^{-3}$

Table 5.9: Results obtained using $21 \times 1 \times 1$ Hex27NL elements for $M_1 = 1200$ Nmm, $M_2 = 2250$ Nmm in the last load step

Node	u_1	u_2	u_3	φ_1	φ_2	φ_3
P_1	6.2540	-5.0208 $\cdot 10^{-1}$	-8.1916 $\cdot 10^{-3}$	-1.5776 $\cdot 10^{-2}$	-1.2772 $\cdot 10^{-2}$	6.3059
P_2	-6.2540	-5.0208 $\cdot 10^{-1}$	-8.1916 $\cdot 10^{-3}$	-1.5766 $\cdot 10^{-2}$	-1.2772 $\cdot 10^{-2}$	-6.3059
P_3	4.2582 $\cdot 10^{-2}$	-2.6253 $\cdot 10^{-2}$	7.9328 $\cdot 10^{-2}$	1.0446 $\cdot 10^{-2}$	6.9310	8.2121 $\cdot 10^{-3}$
P_4	7.9328 $\cdot 10^{-2}$	-2.6253 $\cdot 10^{-2}$	-4.2582 $\cdot 10^{-2}$	8.2121 $\cdot 10^{-3}$	6.9310	-1.0446 $\cdot 10^{-2}$

Table 5.10: Results obtained using $21 \times 1 \times 1$ Hex8NL elements for $M_1 = 600$ Nmm, $M_2 = 1125$ Nmm in the last load step

Point	u_1	u_2	u_3	φ_1	φ_2	φ_3
P_1	1.2182	-3.6278	-1.1277 $\cdot 10^{-2}$	-1.4940 $\cdot 10^{-2}$	-5.2237 $\cdot 10^{-3}$	1.7303
P_2	-1.2182	-3.6278	-1.1277 $\cdot 10^{-2}$	-1.4940 $\cdot 10^{-2}$	5.2237 $\cdot 10^{-3}$	-1.7303
P_3	1.0335	2.7191 $\cdot 10^{-3}$	-9.7484 $\cdot 10^{-1}$	-4.5819 $\cdot 10^{-2}$	3.2176	-4.5027 $\cdot 10^{-2}$
P_4	-9.7484 $\cdot 10^{-1}$	2.7191 $\cdot 10^{-3}$	-1.0335	-4.5027 $\cdot 10^{-2}$	3.2176	4.5819 $\cdot 10^{-2}$

Table 5.11: Results obtained using $21 \times 1 \times 1$ Hex27NL elements for $M_1 = 600$ Nmm, $M_2 = 1125$ Nmm in the last load step
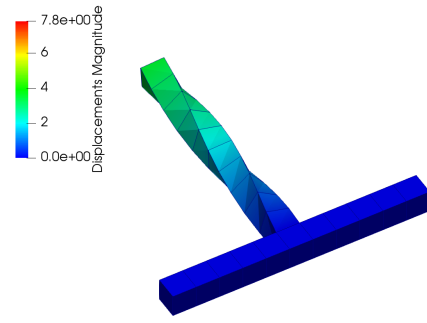
Point	u_1	u_2	u_3	φ_1	φ_2	φ_3
P_1	3.6130	-4.5842	-1.0906 $\cdot 10^{-2}$	-1.5587 $\cdot 10^{-2}$	-1.8711 $\cdot 10^{-2}$	3.0388
P_2	-3.6130	-4.5842	-1.0906 $\cdot 10^{-2}$	-1.5587 $\cdot 10^{-2}$	-1.8711 $\cdot 10^{-2}$	-3.0388
P_3	1.0051	-6.7156 $\cdot 10^{-3}$	-1.0078	-4.0736 $\cdot 10^{-2}$	3.4236	-4.2163 $\cdot 10^{-2}$
P_4	-1.0078	-6.7156 $\cdot 10^{-3}$	-1.0051	-4.2163 $\cdot 10^{-2}$	3.4236	4.0736 $\cdot 10^{-2}$
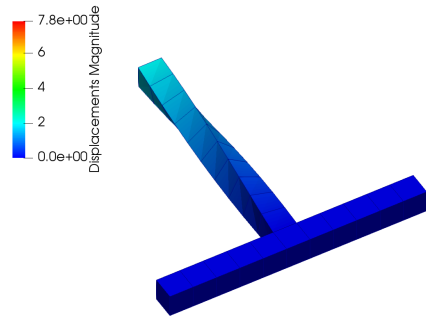
(a) Load step 5

(b) Load step 10
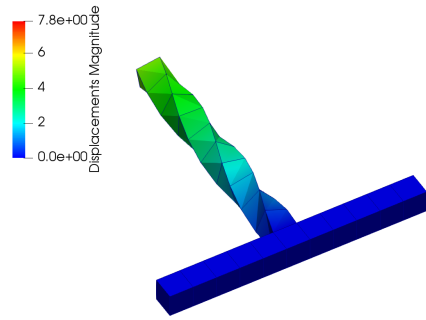
(c) Load step 15

(d) Load step 20

(e) Load step 25

(f) Load step 30

(g) Load step 35

(h) Load step 40

Figure 5.8: Deformed configuration of the T-shape structure for different load steps obtained using $21 \times 1 \times 1$ Hex8NL for $M_1 = 1200$ Nmm, $M_2 = 2250$ Nmm

(a) Load step 5

(b) Load step 10

(c) Load step 15

(d) Load step 20

(e) Load step 25

(f) Load step 30

(g) Load step 35

(h) Load step 40

Figure 5.9: Deformed configuration of the T-shape structure for different load steps obtained using a mesh of $21 \times 1 \times 1$ Hex27NL elements, $M_1 = 1200$ Nmm, $M_2 = 2250$ Nmm

(a) Load step 5   (b) Load step 10

(c) Load step 15   (d) Load step 20
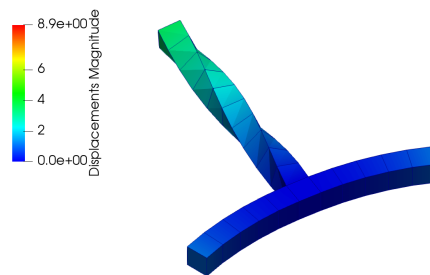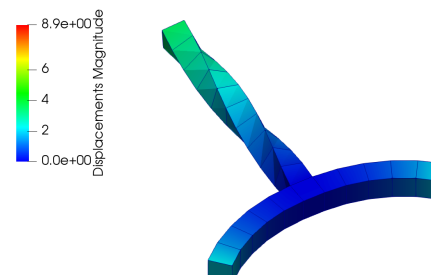
(e) Load step 25   (f) Load step 30
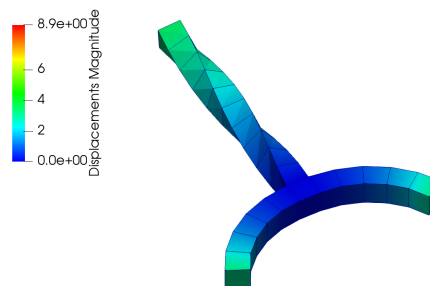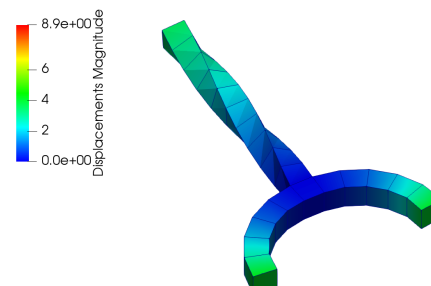
(g) Load step 35   (h) Load step 40

Figure 5.10: Deformed configuration of the T-shape structure for different load steps obtained using a mesh of $21 \times 1 \times 1$ Hex8NL elements for $M_1 = 600$ Nmm, $M_2 = 1125$ Nmm
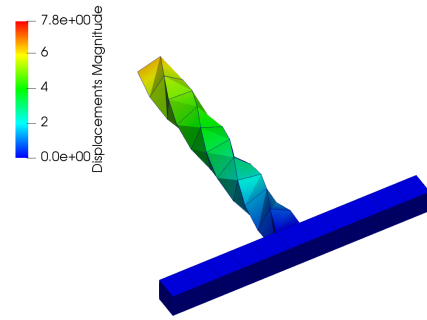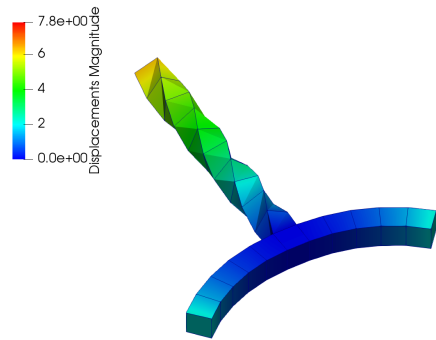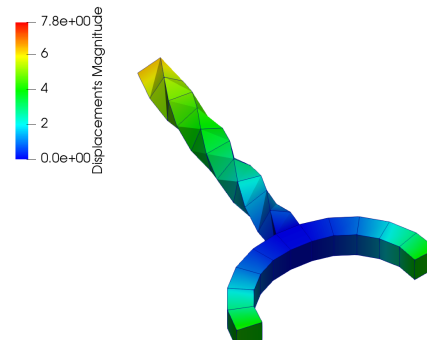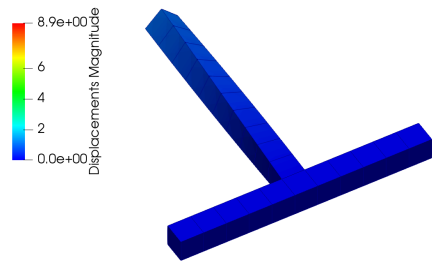
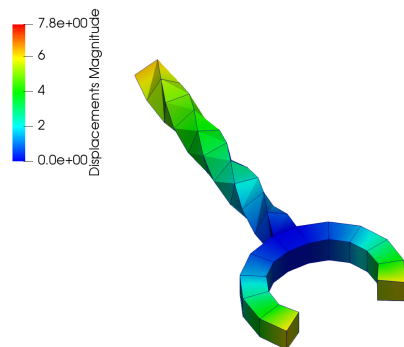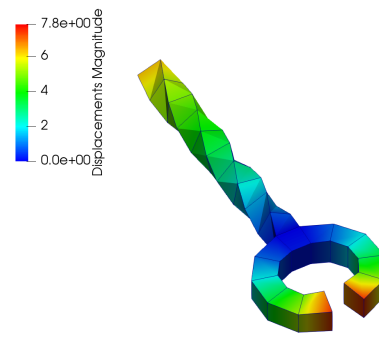(a) Load step 5   (b) Load step 10
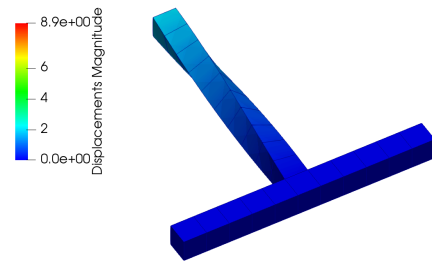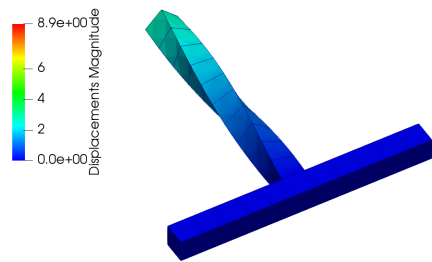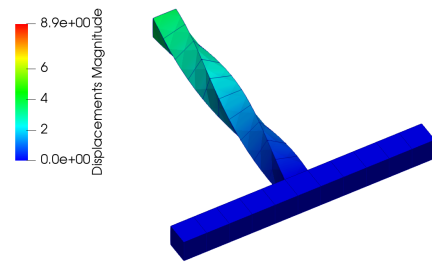
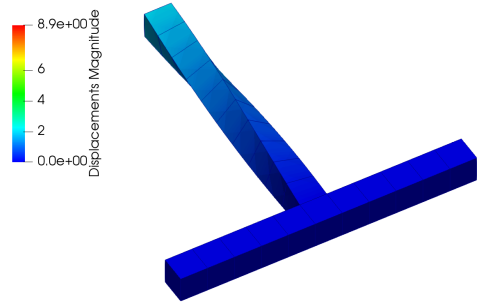(c) Load step 15   (d) Load step 20
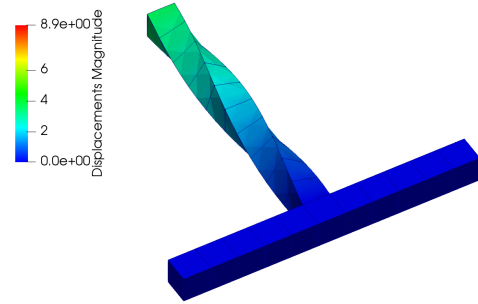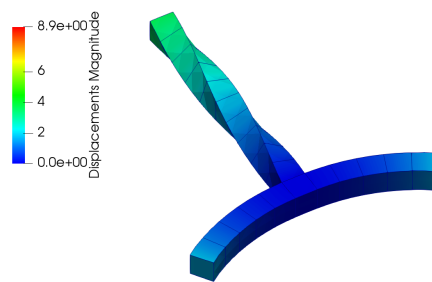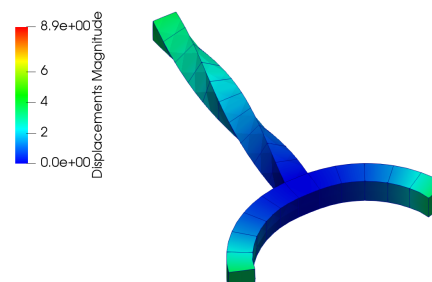
(e) Load step 25   (f) Load step 30
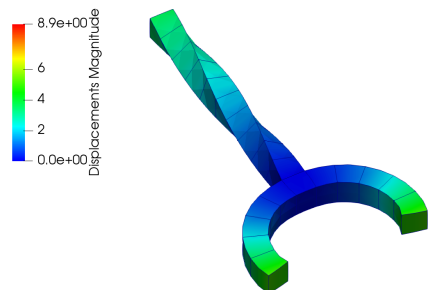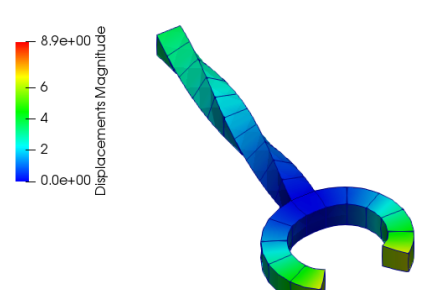
(g) Load step 35   (h) Load step 40
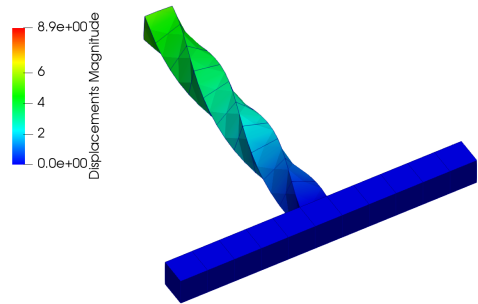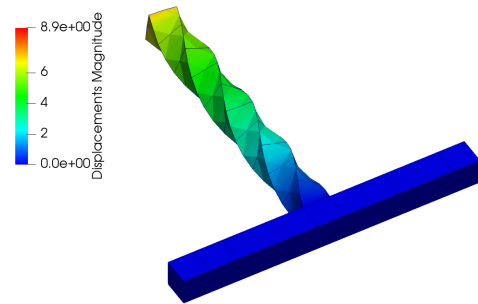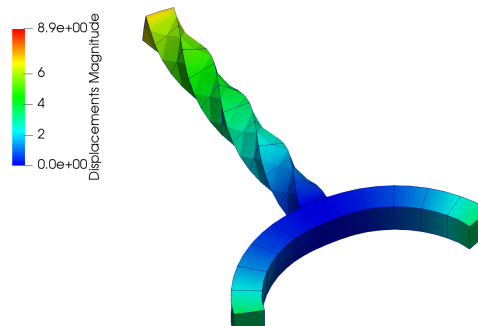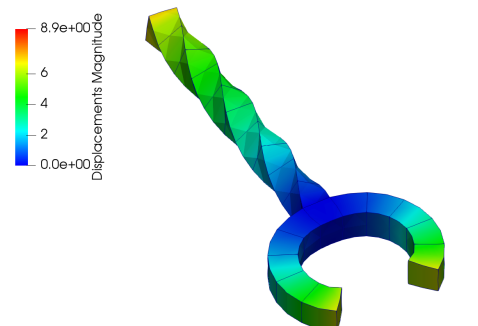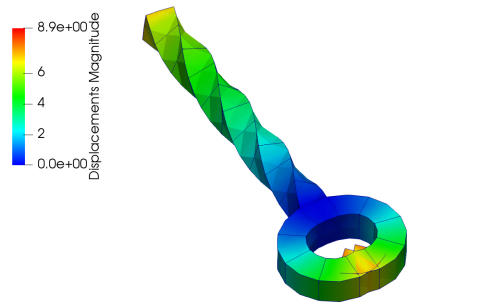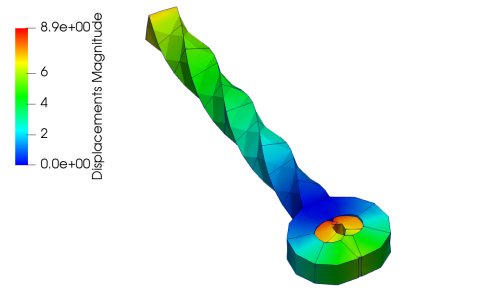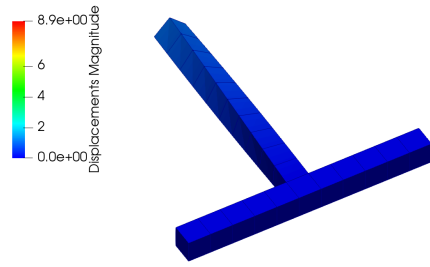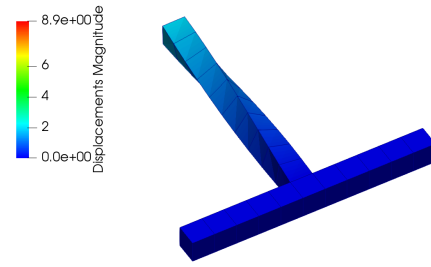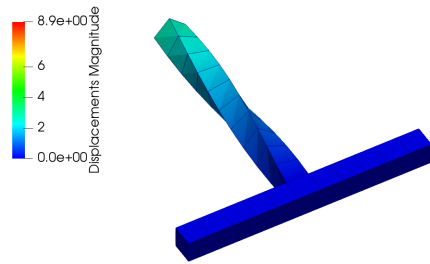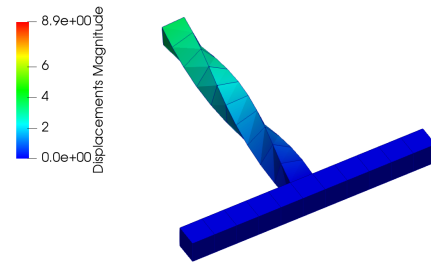
Figure 5.11: Deformed configuration of the T-shape structure for different load steps obtained using a mesh of $21 \times 1 \times 1$ Hex27NL elements for $M_1 = 600$ Nmm, $M_2 = 1125$ Nmm

5.2.4 45° curved cantilever bend

In the previous two examples only predominantly two-dimensional problems have been analysed. Since we have implemented a fully geometrically non-linear formulation capable of describing large 3D rotations, it is essential to test the elements in an appropriate example in which there exist large rotation components in all three dimensions. One such example is the problem of a curved cantilever beam with out-of-plane loading first presented by Bathe and Bolourchi [97] and very often analysed in the framework of the classical elasticity (see e.g. [96]). However, no literature is found in which this problem has been modelled in the framework of the 3D micropolar elasticity. Here, we take this problem in order to test the three-dimensional large rotation performance of the derived micropolar finite elements.

The beam lies in a horizontal plane and is curved by a radius of $R = 100$ and angle of 45°, i.e. it represents one eighth of a circle, as shown in Figure 5.12. The cantilever is loaded normally to that plane at the free end by a constant distributed surface loading in the x_3 direction $p_3 = 600$ along the square-shaped cross-section of the side $a = 1$. The distributed surface loading is applied through corresponding concentrated nodal forces obtained by integration as defined by (3.1)-(3.4) in a number of load increments. The cantilever is clamped at the left-hand side end, i.e. all the displacements and microrotations are restrained $(u_1(0, x_2, x_3) = u_2(0, x_2, x_3) = u_3(0, x_2, x_3) = \varphi_1(0, x_2, x_3) = \varphi_2(0, x_2, x_3) = \varphi_3(0, x_2, x_3) = 0$, for $x_2 \in [R - 0.5a, R + 0.5a]$, and $x_3 \in [0, a])$.

First, in order to compare the obtained results against a reference solution of the classical theory, Lamé constants are taken as in [96], i.e. $\mu = 5 \cdot 10^6$, $\lambda = 0$, while the micropolar parameters are taken as very small (but ν, β, γ necessarily larger than zero in order to satisfy the condition of the positiveness of strain energy). It is important to note that, as observed in all the numerical examples already analysed, the bigger the micropolar parameters are, the stiffer the structure is. Thus, even for small micropolar parameters, we expect a bit stiffer behavior of the micropolar problem, compared against the classical elasticity model. The remaining material parameters are chosen as $\nu = 50\ 505.1$, $\alpha = 0$, $\beta = 12\ 500$ and $\gamma = 37\ 500$, which correspond to the following engineering material parameters: $E = 10^7$, $n = 0.0$, $N = 0.1$, $l_b = 0.05$, $l_t = 0.05$, $\psi = 0$. This problem is in [96] modelled by using a mesh of 16 solid elements with 8 nodes enhanced by the incompatible modes. The obtained results in nodes $P_1 = (70.357, 70.357, 0.0)$, $P_2 = (71.064, 71.064, 0.0)$, $P_3 = (70.357, 70.357, 1.0)$ and $P_4 = (71.064, 71.064, 1.0)$ are then averaged and the reference solution for the displacements u_1, u_2 and u_3 is given. Here, the obtained results using Hex8NL and Hex27NL elements for different mesh densities are compared against the results in [96] and presented in Table 5.12 for Hex8NL and in Table 5.13 for Hex27NL. We can see that the results converge towards the reference solution with both h- and p-refinement.

From Table 5.13c we can see that the results obtained using Hex27NL are very close to the results obtained using the classical theory of elasticity for the same mesh density. However, due to the presence of the micropolar effects, the structure is slightly stiffer, as expected. As already observed in other numerical examples in both linear and nonlinear regime, the first order element Hex8NL shows quite poor results for a coarse mesh, which is here shown in Table 5.12a. However, by refining the mesh, the obtained results are getting closer to the reference result [96]. To verify the correct implementation of the discrete Newton-Raphson solution procedure, the evolution of the residual and energy norms have been observed. The solution procedure in the limit gives a quadratic convergence rate for both elements in all load steps. The residual and energy norms for both elements and an arbitrarily chosen load step are presented in Tables 5.14 and 5.15.
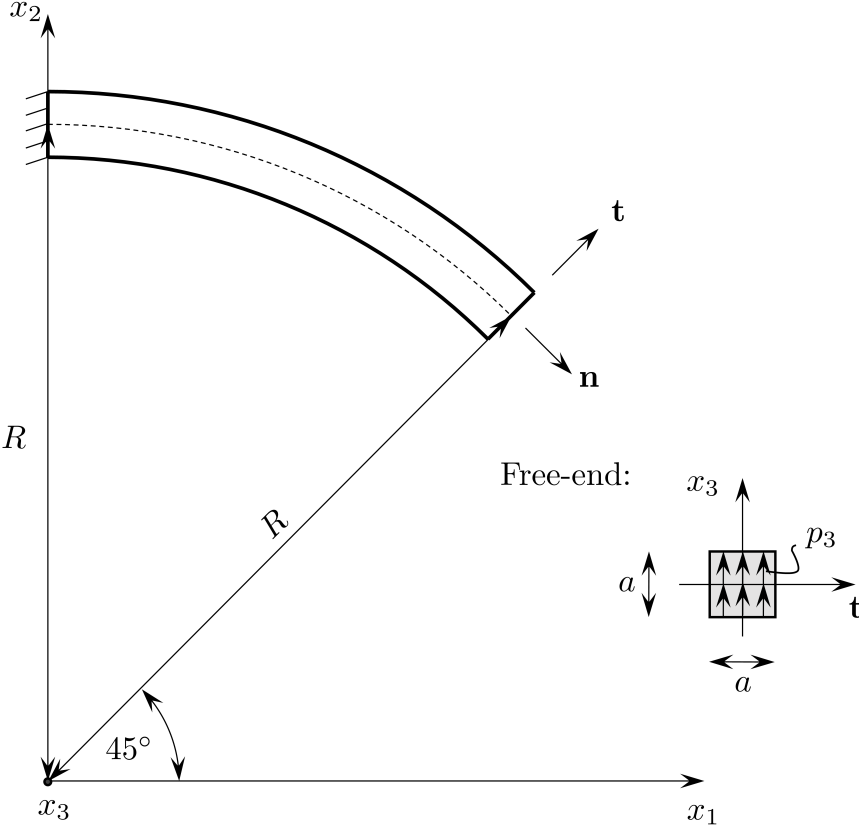
Figure 5.12: Top view of the curved cantilever beam

Table 5.12: Results obtained using Hex8NL elements

(a) $16 \times 1 \times 1$ Hex8NL elements

LS	Node	u_1	u_2	u_3	$\varphi_1 \cdot 10^{-1}$	$\varphi_2 \cdot 10^{-2}$	$\varphi_3 \cdot 10^{-2}$
1	P_1	-1.28	1.91	16.06	-5.08	-6.06	-3.56
	P_2	-1.24	1.80	15.76	-5.08	-6.06	-3.57
	P_3	-1.32	2.40	15.93	-5.08	-6.06	-3.57
	P_4	-1.28	2.29	15.63	-5.08	-6.06	-3.57
Averaged results		-1.28	2.10	15.85	-5.08	-6.06	-3.57
Ref. solution [96]		-23.30	13.64	53.21	-	-	-

(b) $128 \times 1 \times 1$ Hex8NL elements

LS	Node	u_1	u_2	u_3	$\varphi_1 \cdot 10^{-1}$	$\varphi_2 \cdot 10^{-1}$	$\varphi_3 \cdot 10^{-2}$
4	P_1	-19.60	11.38	50.21	-5.64	-9.08	2.40
	P_2	-19.72	11.46	50.40	-5.65	-9.07	2.45
	P_3	-20.35	11.83	49.69	-5.63	-9.08	2.37
	P_4	-20.47	11.91	49.89	-5.65	-9.07	2.52
Averaged results		-20.04	11.65	50.04	-5.64	-9.08	2.44
Ref. solution [96]		-23.30	13.64	53.21	-	-	-

(c) $256 \times 1 \times 1$ Hex8NL elements

LS	Node	u_1	u_2	u_3	$\varphi_1 \cdot 10^{-1}$	$\varphi_2 \cdot 10^{-1}$	$\varphi_3 \cdot 10^{-2}$
10	P_1	-21.53	12.48	52.20	-5.67	-9.66	4.78
	P_2	-21.68	12.58	52.42	-5.67	-9.66	4.77
	P_3	-22.32	12.91	51.64	-5.67	-9.66	4.78
	P_4	-22.48	13.00	51.85	-5.67	-9.66	4.77
Averaged results		-22.00	12.74	52.03	-5.67	-9.66	4.78
Ref. solution [96]		-23.30	13.64	53.21	-	-	-

*LS - number of load steps

Table 5.13: Results obtained using Hex27NL elements

(a) $6 \times 1 \times 1$ Hex27NL elements

LS	Node	u_1	u_2	u_3	$\varphi_1 \cdot 10^{-1}$	$\varphi_2 \cdot 10^{-1}$	$\varphi_3 \cdot 10^{-2}$
5	P_1	-16.30	14.15	47.87	-5.48	-9.04	9.38
	P_2	-16.47	14.26	48.05	-5.49	-9.03	9.33
	P_3	-17.07	14.55	47.37	-5.48	-9.04	9.39
	P_4	-17.24	14.67	47.54	-5.49	-9.03	9.35
Averaged results		-16.77	14.50	47.63	-5.48	-9.04	9.36
Ref. solution [96]		-23.30	13.64	53.21	-	-	-

(b) $12 \times 1 \times 1$ Hex27NL elements

LS	Node	u_1	u_2	u_3	$\varphi_1 \cdot 10^{-1}$	$\varphi_2 \cdot 10^{-1}$	$\varphi_3 \cdot 10^{-2}$
7	P_1	-21.60	12.94	52.31	-5.64	-9.81	5.74
	P_2	-21.77	13.05	52.53	-5.64	-9.81	5.73
	P_3	-22.40	13.36	51.74	-5.64	-9.81	5.75
	P_4	-22.57	13.47	51.95	-5.64	-9.81	5.73
Averaged results		-22.09	13.21	52.13	-5.64	-9.81	5.74
Ref. solution [96]		-23.30	13.64	53.21	-	-	-

(c) $16 \times 1 \times 1$ Hex27NL elements

LS	Node	u_1	u_2	u_3	$\varphi_1 \cdot 10^{-1}$	$\varphi_2 \cdot 10^{-1}$	$\varphi_3 \cdot 10^{-2}$
7	P_1	-22.05	12.85	52.70	-5.65	-9.87	5.56
	P_2	-22.22	12.96	52.92	-5.65	-9.87	5.58
	P_3	-22.86	13.27	52.12	-5.65	-9.87	5.58
	P_4	-23.03	13.37	52.34	-5.65	-9.87	5.57
Averaged results		-22.54	13.11	52.52	-5.65	-9.87	5.57
Ref. solution [96]		-23.30	13.64	53.21	-	-	-

*LS - number of load steps

Table 5.14: Convergence rate of the Newton-Raphson scheme for the mesh of 256 Hex8NL elements for load increment 1 ; absolute norm of the residual and energy

It	Residual	Energy
0	$3.0{\cdot}10^1$	$6.22{\cdot}10^2$
1	$6.34{\cdot}10^5$	$2.52{\cdot}10^5$
2	$1.27{\cdot}10^4$	$2.32{\cdot}10^3$
3	$5.67{\cdot}10^3$	$1.43{\cdot}10^1$
4	$9.51{\cdot}10^0$	$3.11{\cdot}10^{-2}$
5	$3.68{\cdot}10^1$	$7.24{\cdot}10^{-4}$
6	$3.64{\cdot}10^{-3}$	$6.65{\cdot}10^{-9}$
7	$8.72{\cdot}10^{-6}$	$3.77{\cdot}10^{-17}$

Table 5.15: Convergence rate of the Newton-Raphson scheme for the mesh of 16 Hex27NL elements for load increment 6 ; absolute norm of the residual and energy

It	Residual	Energy
0	$4.28{\cdot}10^1$	$3.34{\cdot}10^2$
1	$5.05{\cdot}10^5$	$1.82{\cdot}10^4$
2	$3.64{\cdot}10^2$	$3.76{\cdot}10^0$
3	$4.98{\cdot}10^3$	$1.79{\cdot}10^0$
4	$5.21{\cdot}10^{-2}$	$1.21{\cdot}10^{-3}$
5	$5.89{\cdot}10^{-3}$	$2.26{\cdot}10^{-12}$
6	$1.16{\cdot}10^{-6}$	$3.66{\cdot}10^{-20}$

Next, we vary the micropolar material parameters and observe the behavior of the curved beam using both Hex8NL and Hex27NL for a fine mesh of 256 Hex8NL and 16 Hex27NL elements. First, the following five micropolar parameters are kept as previously defined, i.e. $\mu = 5 \cdot 10^6$, $\lambda = 0.$, $\alpha = 0$, $\beta = 12\ 500$ and $\gamma = 37\ 500$ and the value of the coupling number $N \in \{0.1,\ 0.5, 0.9\}$ is varied. Remember that N can obtain values between 0 and 1. The results in node P_1 are presented in Tables 5.16 and 5.17. Both elements show that by increasing the value of the coupling number, the values of displacements reduce. However, even for $N = 0.9$, quite close results to the case with the smallest value of N are obtained, leading to the conclusion that N does not significantly affect the solution. Interestingly, the solution does become more robust with an increase in N, i.e. a converged solution has been obtained in fewer load steps.

Table 5.16: Results obtained using $256 \times 1 \times 1$ Hex8NL while varying the value of the coupling number N

LS	N	$\nu \cdot 10^6$	u_1	u_2	u_3	$\varphi_1 \cdot 10^{-1}$	$\varphi_2 \cdot 10^{-1}$	$\varphi_3 \cdot 10^{-2}$
10	0.1	0.0505051	-21.53	12.48	52.20	-5.67	-9.66	4.78
8	0.5	1.66667	-21.15	12.27	51.83	-5.65	-9.56	4.46
5	0.9	21.3158	-18.74	10.89	49.27	-5.60	-8.82	1.78

Table 5.17: Results obtained using $16 \times 1 \times 1$ Hex27NL while varying the value of the coupling number N

LS	N	$\nu \cdot 10^6$	u_1	u_2	u_3	$\varphi_1 \cdot 10^{-1}$	$\varphi_2 \cdot 10^{-1}$	$\varphi_3 \cdot 10^{-2}$
7	0.1	0.0505051	-22.05	12.85	52.70	-5.65	-9.87	5.56
5	0.5	1.66667	-21.89	12.76	52.55	-5.63	-9.84	5.60
5	0.9	21.3158	-21.81	12.73	52.48	-5.58	-9.85	5.95

Next, we fix another set of five micropolar parameters, i.e. we take $\mu = 5 \cdot 10^6$, $\lambda = 0.$, $\nu = 50\ 505.1$, $\beta = 12\ 500$ and $\gamma = 37\ 500$ (which correspond to $E = 10^7$, $n = 0.0$, $l_b = 0.05$, $l_t = 0.05$, $N = 0.1$) and vary the value of the polar ratio $\psi \in \{0.0,\ 0.7,\ 1.4\}$, which otherwise ranges between 0 and 1.5. The results are presented in Tables 5.18 and 5.19.

Table 5.18: Results in node P_1 obtained using $256 \times 1 \times 1$ Hex8NL, while varying the value of the polar ratio ψ

LS	ψ	α	u_1	u_2	u_3	$\varphi_1 \cdot 10^{-1}$	$\varphi_2 \cdot 10^{-1}$	$\varphi_3 \cdot 10^{-2}$
10	0.0	0.0	-21.53	12.48	52.20	-5.67	-9.66	4.78
10	0.7	10 714.3	-21.52	12.48	52.20	-5.67	-9.66	4.81
15	1.4	-7142.86	-21.54	12.48	52.21	-5.68	-9.66	4.71

Table 5.19: Results in node P_1 obtained using $16 \times 1 \times 1$ Hex27NL, while varying the value of the polar ratio ψ

LS	ψ	α	u_1	u_2	u_3	$\varphi_1 \cdot 10^{-1}$	$\varphi_2 \cdot 10^{-1}$	$\varphi_3 \cdot 10^{-2}$
7	0.0	0.0	-22.05	12.85	52.70	-5.65	-9.87	5.56
7	0.7	10 714.3	-22.05	12.85	52.69	-5.64	-9.87	5.61
7	1.4	-7142.86	-22.06	12.85	52.70	-5.65	-9.86	5.53

From Tables 5.18 and 5.19 we can see that the influence of the increase in the polar ratio on the obtained numerical results is even more negligible than that of the coupling number. However, for Hex8NL it influences the robustness of the solution procedure adversely, since 5 more load increments are needed in order to obtain convergence.

Next we analyse the problem using the original set of micropolar material parameters with a coarse mesh of either elements using different load incrementation and present the results in Tables 5.20 and 5.21. By increasing the number of load increments it is observed that the results are *path dependent*, i.e. different solution is obtained by using different number of load increments, as shown in Tables 5.20 and 5.21. Furthermore, it is observed that the difference between the obtained results is decreased by increasing the number of load steps. Moreover, it is observed that the influence of the path dependence decreases by refining the finite element mesh.

Table 5.20: Results obtained using Hex8NL elements in node P_1

(a) $2 \times 1 \times 1$ Hex8NL

LS	$u_1 \cdot 10^{-2}$	$u_2 \cdot 10^{-2}$	u_3	$\varphi_1 \cdot 10^{-1}$	$\varphi_2 \cdot 10^{-2}$	$\varphi_3 \cdot 10^{-3}$
1	3.22380217	8.96615334	1.74092068	-1.03530509	1.84385002	-0.66557417
2	3.22676004	8.97012158	1.74111321	-1.03573693	1.80196104	0.47039203
5	3.22705926	8.97031812	1.74114303	-1.03575263	1.79484997	1.17387104
10	3.22707549	8.97031665	1.74114503	-1.03577725	1.79347336	1.18231451
20	3.22707481	8.97030970	1.74114528	-1.03578291	1.79319065	1.17890116

(b) $6 \times 1 \times 1$ Hex8NL

LS	$u_1 \cdot 10^{-2}$	u_2	u_3	$\varphi_1 \cdot 10^{-1}$	$\varphi_2 \cdot 10^{-2}$	$\varphi_3 \cdot 10^{-2}$
1	-1.54324172	1.09651610	8.38923296	-4.28271918	6.67664458	-1.16604438
2	-1.54331271	1.09651335	8.38924174	-4.27986499	6.86755695	-1.14437321
5	-1.54330559	1.09651097	8.38923862	-4.27908140	6.91957968	-1.12668659
10	-1.54330942	1.09651068	8.38923850	-4.27899174	6.92523667	-1.12570753
20	-1.54331048	1.09651060	8.38923846	-4.27896957	6.92662771	-1.12542920

Table 5.21: Results obtained using Hex27NL elements in node P_1

(a) $2 \times 1 \times 1$ Hex27NL elements

LS	u_1	$u_2 \cdot 10^1$	$u_3 \cdot 10^1$	$\varphi_1 \cdot 10^{-1}$	$\varphi_2 \cdot 10^{-1}$	$\varphi_3 \cdot 10^{-1}$
3	-1.08925956	1.87489260	3.04600207	-4.89368066	-5.70177365	2.90681231
5	-1.08907145	1.87484513	3.04595205	-4.81874622	-5.85796503	2.92898286
10	-1.08905931	1.87485319	3.04595412	-4.82084221	-5.84180543	3.08608508
20	-1.08912083	1.87485184	3.04596409	-4.80630082	-5.85892294	3.09886429

(b) $6 \times 1 \times 1$ Hex27NL elements

LS	$u_1 \cdot 10^1$	$u_2 \cdot 10^1$	$u_3 \cdot 10^1$	$\varphi_1 \cdot 10^{-1}$	$\varphi_2 \cdot 10^{-1}$	$\varphi_3 \cdot 10^{-2}$
4	-1.63027650	1.41467267	4.78738606	-5.20977432	-8.84584561	7.67777834
5	-1.63018568	1.41468357	4.78733127	-5.48391877	-9.03790569	9.37819012
10	-1.63018550	1.41468445	4.78733128	-5.46593568	-9.04844694	9.43080561
20	-1.63018576	1.41468368	4.78733127	-5.46178681	-9.05091989	9.44184672

5.2.5 Elbow cantilever subject to point load and prescribed rotation - detection of non-invariance

The last numerical example analysed was first presented in [98] in the framework of the geometrically exact 3D beam theory. In this example an in-plane rectangular elbow cantilever subject to out-of-the-plane vertical loading at its free end and a prescribed rotation at its fixed end is analysed, as shown in Figure 5.13. The frame is composed of two equally long mutually perpendicular legs, with a square cross section and axial length $L = 10$. At the free end of the cantilever, a surface load $p_3 = 5.0$ is applied in the negative z direction. The relation between the cross-sections and length of the elbows is $\frac{L}{h} \approx 10^3$ given in [98], which in this 3D analysis represents a problem due to the big aspect ratio of the 3D finite elements. Consequently, in this work we choose a square cross-section of height and width $h = b = 1$, i.e. with a cross-section area $A = 1$. The geometry of the problem is presented in Figure 5.14. The material parameters are chosen as $E = 2 \cdot 10^4$ and $n = 0.0$ which give Lamé constants $\mu = 10\,000$ and $\lambda = 0$. The remaining micropolar material parameters are taken as very small (but again ν, β, γ necessarily larger than zero in order to satisfy that the strain energy should remain positive): $\nu = 101.01$, $\alpha = 0$, $\beta = 25$ and $\gamma = 75$, which correspond to the following engineering material parameters $N = 0.1$, $l_b = 0.05$, $l_t = 0.05$, $\psi = 0$.
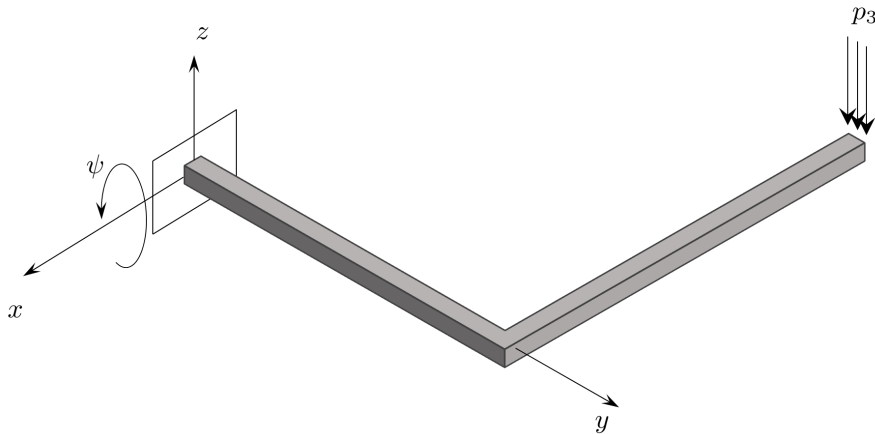
Figure 5.13: Elbow cantilever subject to a fixed loading in the z direction and a prescribed rotation around x axis
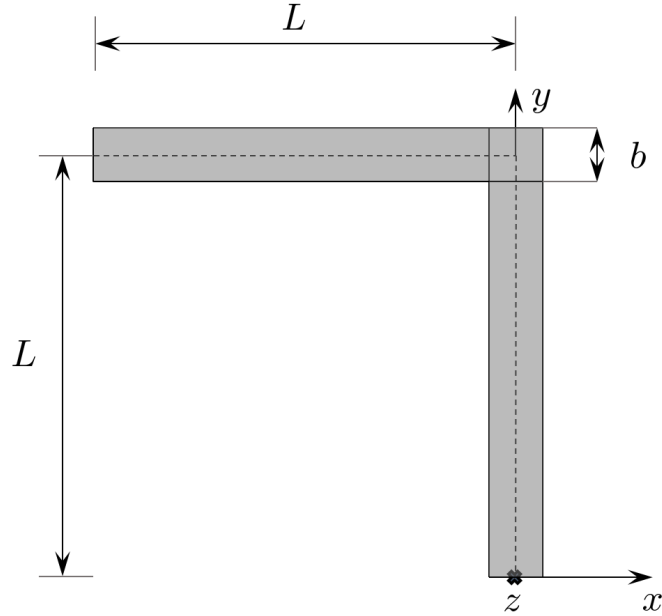
Figure 5.14: Top view: Geometry of the elbow cantilever

The problem is first solved with Hex27NL elements, which make a mesh with nodes which lie on the elbow axis, which facilitates the analysis and discussion. For Hex27NL the external loading on the free end is first applied as a concentrated force $F = 5$ in the central node with coordinates $N_1(-10, 10, 0)$. The junction between the legs is modelled as one cube-shaped finite element, while the number of elements in each leg is varied equally for each leg from one to ten. The obtained displacements in the central node of the free end for different mesh densities are presented in Table 5.22, where a clear trend towards a converged solution with h-refinement is observed.

Table 5.22: Tip displacements u_1, u_2 and u_3 in node $N_1(-10, 10, 0)$ after applying the surface loading $p_3 = 5$ in one load step using Hex27NL

Number of elements	u_1	u_2	u_3
3	0.606605534	-0.198732899	-3.87449424
5	0.670944949	-0.177990694	-4.21443597
7	0.683678903	-0.175167899	-4.27641520

As in [98], after applying the force, a prescribed rotation of $\psi = \dfrac{\pi}{2}$ is applied to the fixed end which rotates the elbow around axis x, as shown in Figure 5.13. However, the direction of the applied force remains constant during the whole deformation process. Consequently, in this configuration we expect the deformation to take place only in the vertical plane, i.e. we expect the absolute value of the vertical displacement u_2 to be exactly equal to $L = 10$. For this 3D finite element analysis, in order to accomplish the

174

Newton-Raphson convergence, the rotation $\psi = \dfrac{\pi}{2}$ has to be applied in 5 equal increments, in contrast to only one increment needed in [98] for the geometrically exact 3D beam finite elements. The results for different mesh densities are presented in Table 5.23.

Table 5.23: Tip displacements u_1, u_2 and u_3 in node $N_1(-10, 10, 0)$ after applying the force $F = 5$ in one increment and the rotation $\psi = \dfrac{\pi}{2}$ in five increments (while keeping the force constant) using Hex27NL

Num elements	u_1	u_2	u_3
3	-0.788605849	-10.0000327	6.83459122
5	-0.821452713	-9.99996897	6.31307382
7	-0.818525647	-9.99995938	6.25229118
11	No convergence		

From Table 5.23 we can see that the obtained numerical results for u_2 with all mesh densities differ from the expected displacement $u_2 = -10.0$ in the fifth decimal place, i.e. the error is of order of magnitude of 10^{-5}. In the work of Crisfield and Jelenić [94] and Jelenić and Crisfield [98] this is taken as an indication of the strain *non-invariance* of a formulation and the corresponding interpolated strain measures are referred to as *non-objective*. Further discussion is presented in the following section.

Table 5.24: Tip displacements u_1, u_2 and u_3 in node $N_1(-10, 10, 0)$ after applying the force $F = 5$ in one increment and a rotation $\psi = 2\pi$ in 20 increments (while keeping the force constant) using Hex27NL

Num elements	u_1	u_2	u_3
3	0.606857046	-0.198121914	-3.87481501
5	No convergence		
7	No convergence		

An even clearer perception of this anomaly is obtained by first observing the free-end displacements after applying just the force $F = 5$, and then rigidly rotating the elbow for $\psi = 2\pi$ around the fixed end while keeping the force constant, and then observing the free-end displacement. We thus expect to obtain the same displacements as obtained when applying just the force. The problem is solved by first applying the force in one increment and then by applying the rotation $\psi = 2\pi$ in 20 increments for three different meshes and the results are shown in Table 5.24. However, convergence is not accomplished for the meshes of 5 and 7 elements. For the mesh of 3 elements, comparing the results

from Tables 5.22 and 5.24 we notice that the obtained displacements differ, i.e. for a mesh of 3 Hex27NL elements the difference between the obtained dominant displacements u_3 is $3.2077 \cdot 10^{-4}$. For the Hex8NL element, the external load is applied via concentrated forces $\frac{F}{4}$ in all the four nodes at the free end. Again, the procedure is shown not to be as robust as in [98], since in our formulation 20 rotation increments are needed in contrast to only 4 needed in [98] in order to assure the Newton-Raphson convergence. The displacements of the node $N_2(-10, 10.5, 0.5)$ at the free end obtained for different mesh densities when just a force is applied are presented in Table 5.25 while the displacements of this node when both a force and a rotation of 2π are applied are presented in Table 5.26. We can see that again we do not obtain the same results (as we should), i.e. the strain non-invariance anomaly is present. However, by observing the dominant displacement u_3 we can see that by refining the finite-element mesh, the error is reduced, i.e. for a mesh of 3 Hex8NL elements the difference between the obtained displacements is $1.5366 \cdot 10^{-3}$, while for a mesh of 11 Hex8NL elements $1.9336 \cdot 10^{-4}$, i.e. around 10 times smaller. This trend was also observed in [98]. Also, as in [98] we can see that the error is more severe for the lower-order element for the same mesh density.

Table 5.25: Tip displacements u_1, u_2 and u_3 in node $N_2(-10, 10.5, 0.5)$ after applying the surface loading $p_3 = 5$ in one increment using Hex8NL

Num elements	u_1	u_2	u_3
3	0.0959976851	0.0213167905	-1.99265510
5	0.228107001	-0.0153211998	-2.77538949
7	0.255114516	-0.0407865218	-2.97662570
11	0.301094975	-0.0804784620	-3.32302580
21	0.398404983	-0.112628011	-3.88206822

Table 5.26: Tip displacements u_1, u_2 and u_3 in node $N_2(-10, 10.5, 0.5)$ after applying the surface loading $p_3 = 5$ in one increment and a rotation $\psi = 2\pi$ in 20 increments (while keeping the surface load constant) using Hex8NL

Num elements	u_1	u_2	u_3
3	0.0962737524	0.0219238490	-1.99419076
5		No convergence	
7	0.255134160	-0.0408355629	-2.97683495
11	0.301116332	-0.0804918162	-3.32321916
21		No convergence	

As shown in [98], the strain-invariance anomaly comes to the fore for low-order elements, coarse meshes and large increments and vanishes with a refinement in any of these. However, the 3D geometrically nonlinear micropolar formulation presented in this work is shown not to be as robust as the geometrically exact 3D beam formulation since a significantly larger number of increments is needed in order to assure the Newton-Raphson convergence. Moreover, in order to obtain a converged solution of the problem analysed, much finer meshes are needed than in the 3D beam formulation. Therefore, the implementation of a strain-invariant formulation would not be as significantly beneficial in the presented formulation as it was in [98]. However, in the next section a procedure to overcome the non-invariance anomaly is outlined, without its finite element implementation.

5.3 Comments on strain invariance in finite-element implementation of problems with large 3D rotations

In the work of Crisfield and Jelenić [94] it is stated that the *objectivity* of material strain measures at a particular configuration is understood as their inherent ability to remain unaffected by a constant motion of the configuration. Such strain measures are also referred to as *invariant* under a superimposed rigid-body motion, i.e. they remain unchanged when exhibiting a rigid motion. The proof of invariance of the material strain measures in the geometrically exact three-dimensional beam theory can be found in [94].

In order to prove invariance of the Biot-like strain and curvature tensors, we observe a configuration defined by its position vector and orientation matrix $(\mathbf{x}, \mathbf{Q})$. Next, we superimpose a rigid motion $(\mathbf{x}_R, \mathbf{Q}_R)$ consisting of a rigid translation and a rigid rotation and obtain a new configuration $(\underline{\mathbf{x}}, \underline{\mathbf{Q}})$ defined as

$$\underline{\mathbf{x}} = \mathbf{Q}_R \left(\mathbf{x}_R + \mathbf{x} \right), \tag{5.100}$$

$$\underline{\mathbf{Q}} = \mathbf{Q}_R \mathbf{Q}. \tag{5.101}$$

The material strain and curvature tensors are invariant if they are equal in both configurations $(\mathbf{x}, \mathbf{Q})$ and $(\underline{\mathbf{x}}, \underline{\mathbf{Q}})$ and independent of the history of deformation [94]. By evaluating the strain and curvature tensors $\mathbf{E} = \mathbf{Q}^{\mathrm{T}}\mathbf{F} - \mathbf{I}$ and $\mathbf{K} = -\frac{1}{2}\boldsymbol{\epsilon} : \left(\mathbf{Q}^{\mathrm{T}}\mathrm{GRAD}\mathbf{Q} \right)$ at the new configuration $\underline{\mathbf{E}}(\underline{\mathbf{x}}, \underline{\mathbf{Q}})$, $\underline{\mathbf{K}}(\underline{\mathbf{x}}, \underline{\mathbf{Q}})$ we obtain:

$$
\begin{aligned}
\underline{\mathbf{E}} &= \underline{\mathbf{Q}}^{\mathrm{T}}\underline{\mathbf{F}} - \mathbf{I} \\
&= \mathbf{Q}^{\mathrm{T}}\mathbf{Q}_R^{\mathrm{T}}\mathrm{GRAD}\underline{\mathbf{x}} - \mathbf{I} \\
&= \mathbf{Q}^{\mathrm{T}}\mathbf{Q}_R^{\mathrm{T}} \left(\mathrm{GRAD}\mathbf{Q}_R \left(\mathbf{x}_R + \mathbf{x} \right) + \mathbf{Q}_R\mathrm{GRAD} \left(\mathbf{x}_R + \mathbf{x} \right) \right) - \mathbf{I}.
\end{aligned}
\tag{5.102}
$$

Since $\mathbf{x}_R$ and $\mathbf{Q}_R$ are constant and $\mathbf{Q}_R^{\mathrm{T}}\mathbf{Q}_R = \mathbf{Q}_R\mathbf{Q}_R^{\mathrm{T}} = \mathbf{I}$ we obtain

$$\underline{\mathbf{E}} = \mathbf{Q}^{\mathrm{T}}\mathrm{GRAD}\mathbf{x} - \mathbf{I} = \mathbf{E}. \tag{5.103}$$

Next, we evaluate the curvature tensor in the new configuration as

$$\begin{aligned}
\underline{\mathbf{K}} &= -\frac{1}{2}\boldsymbol{\epsilon} : \left(\underline{\mathbf{Q}}^{\mathrm{T}}\mathrm{GRAD}\underline{\mathbf{Q}}\right) \\
&= -\frac{1}{2}\boldsymbol{\epsilon} : \left(\mathbf{Q}^{\mathrm{T}}\mathbf{Q}_R^{\mathrm{T}}\left(\mathrm{GRAD}\mathbf{Q}_R\mathbf{Q} + \mathbf{Q}_R\mathrm{GRAD}\mathbf{Q}\right)\right) \\
&= -\frac{1}{2}\boldsymbol{\epsilon} : \left(\mathbf{Q}^{\mathrm{T}}\mathrm{GRAD}\mathbf{Q}\right) \\
&= \mathbf{K}. \tag{5.104}
\end{aligned}$$

As in [94], equations (5.103) and (5.104) prove that the material Biot-like strain and curvature tensors depend only on the current configuration $(\mathbf{x}, \mathbf{Q})$, which makes them independent of the history of deformation. However, as stated in [94], even when the strain and curvature tensors are invariant, their approximated (interpolated) values do not necessarily inherit this property.

In our nonlinear finite element implementation, we chose to interpolate the iterative rotation, i.e. we interpolate the rotations between the last known, but not necessarily converged configuration and the current configuration. Different other approaches exist in the literature, such as the interpolation of incremental rotations (the rotations between the last converged configuration and the current configuration) or interpolation of total rotations (the rotations between the initial configuration and the current configuration) [84]. However, regardless of the manner in which rotations are interpolated, all of these formulations interpolate the rotations between a particular reference configuration and the current configuration. The rotations interpolated in this way in general include rigid-body rotations, so that error introduced by the interpolation makes the resulting strains and curvatures dependent on the rigid-body rotations [94]. In particular, the presently used interpolation of iterative rotations makes this formulation *non-invariant*, which is actually detected in Section 5.2.5.

In order to overcome the non-invariance anomaly, a procedure which eliminates the rigid-body rotations from the interpolation of the rotational variables is proposed in [94]. For the 3D geometrically exact beam finite elements this was achieved by decomposing the rotational matrix $\mathbf{Q}$ into a reference orientation matrix $\mathbf{Q}_{ref}$ which is unique for the whole element and a relative orientation matrix $\mathbf{Q}_{rel}$ which represents the actual orientation with respect to $\mathbf{Q}_{ref}$, i.e. $\mathbf{Q} = \mathbf{Q}_{ref}\mathbf{Q}_{rel}$. For the reference orientation matrix, the rotation of one of the beam nodes may be taken, while the relative orientation is obtained by exponentiation of an interpolated relative rotation with respect to $\mathbf{Q}_{ref}$. Consequently, only local rotations have been interpolated. With this intervention, the

geometrically exact 3D beam finite-element formulation is shown to be strain-invariant and path-dependent [98].

The procedure presented in [94] and tested in [98] may be generalised to the present 3D geometrically nonlinear micropolar finite element formulation by using the same approach. The element orientation matrix may be again decomposed into a reference orientation matrix and a relative orientation matrix. For the hexahedral finite elements derived, the reference orientation matrix may be taken as the orientation matrix in one of the chosen nodes (for example $\mathbf{Q}_j$, where j represents the number of the node taken as the reference node) while the relative orientation is obtained by interpolation as $\mathbf{Q}_{rel} = \exp(\overline{\sum_{i=1}^{n_{node}} N_i(\xi, \eta, \zeta)\mathbf{\Psi}_i})$ where the local nodal rotation $\mathbf{\Psi}_i$ is calculated from $\exp\widehat{\mathbf{\Psi}_i} = \mathbf{Q}_{ref}^{\mathrm{T}}\mathbf{Q}_i$.

However, as already mentioned in the previous section, the presented micropolar formulation requires a large number of increments in order to obtain the Newton-Raphson convergence and a fine finite-element mesh in order to obtain representative numerical results and both of these effects reduce the actual amount of non-invariance. Consequently, the numerical error obtained in the present formulation in this respect can be considered as negligible.

Chapter 6

Conclusions and future work

Linear analysis

In linear analysis, new finite elements enhanced with the so-called linked interpolation in 2D [64] and the incompatible modes in 3D [65] are presented and implemented within the Finite Element Analysis Program (FEAP) [66]. Some ambiguities in the existing literature regarding the finite-element method in the linear micropolar continuum theory are resolved. The conclusions for the linked-interpolation finite elements in 2D and the incompatible-mode finite elements in 3D are drawn below.

Triangular and quadrilateral linked interpolation finite elements

A new family of membrane finite elements developed using the linked-interpolation concept for the analysis of the micropolar continuum theory is presented. Triangular and quadrilateral elements of different order are developed and tested via four numerical examples and compared to the conventional elements with the Lagrangian interpolation. We observe the pattern of the element's behavior and reveal the importance of the enhanced shape functions in the force-patch-test example. It is concluded that, in order to assure convergence, the proposed linked-interpolation finite elements should be modified and here this is performed using Petrov-Galerkin interpolation. Furthermore, it is shown that all the Lagrange finite elements pass Providas and Kattis's patch tests [36], while only the higher-order finite elements with linked interpolation pass their test #3. The character of this test is sometimes misinterpreted in the literature [40]. In the benchmark problem regarding the infinite plate with circular hole [13], the newly proposed finite elements correctly reproduce the amount of stress concentration predicted by the micropolar theory. However, they do not converge significantly faster their Lagrangian counterparts, which is explained by the fact that a satisfying result is already obtained with low-order elements. Consequently, the higher-order polynomial contribution incorporated via the linked interpolation in this example does not come to the fore. The last numerical example considers

a cantilever beam subject to pure bending, for which there exist an analytical solution (Gauthier and Jahsman's [1]). It is observed that this problem is sometimes incorrectly modelled in the literature [39], and a detailed explanation of the necessary approach is presented in the work and in [64, 65]. It is shown that the first-order quadrilateral element with linked interpolation converges significantly faster than the conventional Lagrange Q4 element. Interestingly, this improvement is reduced as the ratio between the characteristic length of the micropolar material and a characteristic specimen dimension increases. The contribution of the linked interpolation in the first-order triangular element remains present, but is far less significant. Due to the fact that the analytical solution is described by at most a quadratic polynomial, both conventional and newly presented higher-order triangular and quadrilateral finite elements reproduce the analytical solution to within the computer accuracy, as expected.

Hexahedral finite element with incompatible modes

In 3D, the performance of a 1st order hexahedral finite element enhanced with incompatible modes is analysed. The element is tested in four numerical examples and compared to the conventional hexahedral element interpolated using the standard Lagrange interpolation. The motivation for the choice of the numerical examples is found in the available analytical solutions for various boundary value problems, which are significant for experimental determination of the micropolar material parameters. After assuring convergence of the finite element against the patch test for constant stresses [65], a cylindrical bending test [1] is performed, where it is shown that the enhancement due to incompatible modes is significant. The resulting element is able to correctly reproduce the analytical solution, while the conventional element gives poor results. Finally, pure torsion tests [1] on circular cylinders of different geometry are performed and the numerical results are assessed against those of the experimental analysis on a polymeric foam. It is shown that the finite element correctly describes the size-effect phenomenon predicted analytically [1] and observed experimentally [5]. An excellent agreement between theory, experiments and the numerical analysis is achieved. However, it is observed that the enhancement due to incompatible modes does not increase the convergence rate present in the conventional finite element with Lagrange interpolation. It is concluded that the incompatible modes are not needed for the pure torsion problem (contrary to the pure bending test).

It can be concluded that Hex8IM highly reduces the computational cost in the cylindrical bending problem and correctly predicts the size-effect phenomenon in bending and torsion. Owing to that, the use of the presented element as a part of the numerical validation of the methodology to determine the micropolar material parameters can be considered to be highly efficient [65].

Nonlinear analysis

In the geometrically nonlinear regime, the equilibrium equations of a micropolar continuum are derived with respect to the material and the spatial frame of reference. The material Biot-like strain and curvature tensors are derived by following Reissner's approach [93]. By introducing the interpolation of the virtual fields in the weak form, the nonlinear residual equation is obtained. In order to solve this equation, the extensive linearization of the residual force vector is performed, and a base for the Newton-Raphson solution procedure is set.

Geometrically nonlinear hexahedral finite elements with Lagrange interpolation

The geometrically nonlinear micropolar hexahedral finite elements interpolated using Lagrange interpolation of order one and two are derived and implemented within the Finite Element Analysis Program (FEAP) [66]. In order to test the validity of the derived formulation, a micropolar analytical nonlinear pure-bending problem has been derived, which, to the best of our knowledge, represents the only analytical large-deformation micropolar elasticity solution present in the literature. It is observed that both presented finite elements converge to the derived analytical solution, with an enhanced performance of the second-order finite element. The elements are tested on three additional numerical examples. A T-shaped structure subject to bending and torsion is modelled, which represents the only pure geometrically nonlinear micropolar numerical example (without material nonlinearity) we have been able to find in the literature [49]. It is observed that the derived finite elements are able to model large displacements and large rotations and the obtained results are in the order of magnitude of those obtained by the beam theory, again with an enhanced performance of the second-order hexahedral finite element. Next, a genuine three-dimensional problem consisting of a curved cantilever beam with out-of-plane loading is modelled. Since we have found no micropolar reference solution in the literature, the problem is modelled by taking very small micropolar parameters. The obtained results are compared against a reference solution of the classical theory. It is observed that the results converge towards the reference solution with both h- and p-refinement. However, due to the presence of the micropolar effects, the structure behaves slightly stiffer, which is also observed in all the numerical examples previously analysed. Moreover, a micropolar parameter sensitivity analysis is performed within this example, where the values of the coupling number and polar ratio have been varied. It is concluded that neither of the varied parameters affect the results significantly. However, both parameters influence the robustness of the solution procedure. In addition, by increasing the number of load increments, the results are shown to be path-dependent. Finally, an

elbow cantilever subject to point load and prescribed rotation has been analysed. It is observed that, in addition to path-dependence, the derived finite elements suffer from the strain non-invariance phenomenon, which is most significantly manifested in low-order elements, coarse meshes and a small number of increments. However, compared against the geometrically exact 3D beam formulation, where this anomaly was detected first, the present formulation needs a significantly larger number of increments in order to assure convergence of the Newton-Raphson solution procedure. In addition, in order to obtain sufficiently accurate results, much finer meshes are needed. Consequently, the error due to the strain non-invariance is not significant. However, a procedure to overcome the strain non-invariance anomaly is outlined, without its finite-element implementation.

Future work

Further research in the micropolar continuum framework will be performed within the project *Fixed-pole concept in numerical modelling of Cosserats' continuum* (FIMCOS) financed by the Croatian Science Foundation, where new finite elements for linear and non-linear static and dynamic analysis in the so-called fixed-pole description will be developed. In addition, motivated by some observations during this thesis, a set of laboratory tests will be conducted on a number of specimens in an attempt to identify the micropolar material parameters of chosen materials.

Appendix A

Micropolar continuum model – alternative convention

A.1   Equilibrium of a differential volume $\mathrm{d}V$

Let us analyse the forces acting on the differential volume $\mathrm{d}V$ as shown in Figure A.1. Here, the components of the stress tensor and those of the couple-stress tensor are written in the alternative form where

$$\mathbf{t}(\mathbf{x}, t, \mathbf{n}) = \mathbf{n} \cdot \boldsymbol{\sigma}(\mathbf{x}, t), \tag{A.1}$$

$$\mathbf{m}(\mathbf{x}, t, \mathbf{n}) = \mathbf{n} \cdot \boldsymbol{\mu}(\mathbf{x}, t), \tag{A.2}$$

which are not in agreement with (2.26) and (2.49), but are very common in the literature, and for full reference here we derive the equilibrium equations from them.
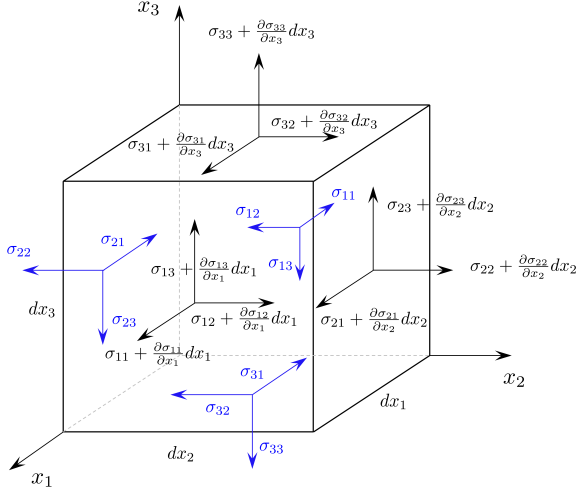
(a) Components of the force stress
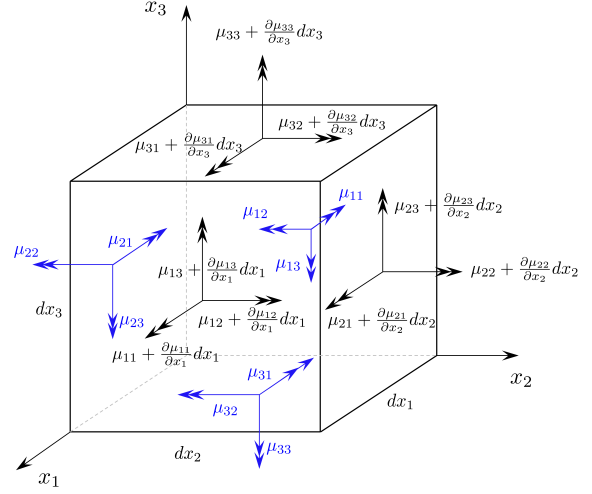
(b) Components of the moment stress
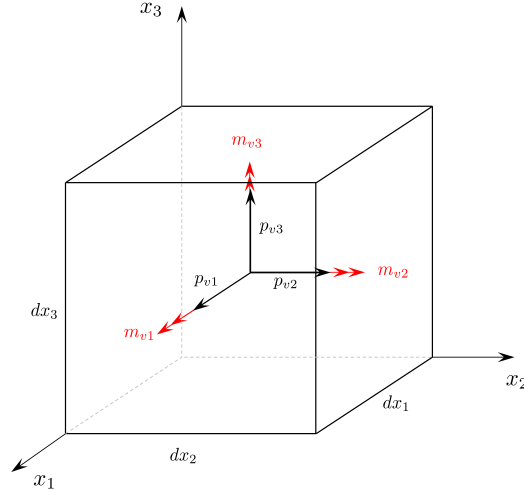
(c) Components of the applied volume load

Figure A.1: Equilibrium of a differential volume.

Summing all the components of the applied load and internal forces along the coordinate axis x_1 gives

$$\frac{\partial \sigma_{11}}{\partial x_1} + \frac{\partial \sigma_{21}}{\partial x_2} + \frac{\partial \sigma_{31}}{\partial x_3} + p_{v1} = 0. \tag{A.3}$$

Summing all the components of the applied load and internal forces along the coordinate axis x_2 gives

$$\frac{\partial \sigma_{12}}{\partial x_1} + \frac{\partial \sigma_{22}}{\partial x_2} + \frac{\partial \sigma_{32}}{\partial x_3} + p_{v2} = 0. \tag{A.4}$$

Summing all the components of the applied load and internal forces along the coordinate axis x_3 gives

$$\frac{\partial \sigma_{13}}{\partial x_1} + \frac{\partial \sigma_{23}}{\partial x_2} + \frac{\partial \sigma_{33}}{\partial x_3} + p_{v3} = 0. \tag{A.5}$$

Written in the matrix form equations (A.3), (A.4) and (A.5) read

$$\left\langle \frac{\partial}{\partial x_1} \quad \frac{\partial}{\partial x_2} \quad \frac{\partial}{\partial x_3} \right\rangle \begin{bmatrix} \sigma_{11} & \sigma_{12} & \sigma_{13} \\ \sigma_{21} & \sigma_{22} & \sigma_{23} \\ \sigma_{31} & \sigma_{32} & \sigma_{33} \end{bmatrix} + \left\langle p_{v1} \quad p_{v2} \quad p_{v3} \right\rangle = \left\langle 0 \quad 0 \quad 0 \right\rangle, \tag{A.6}$$

or

$$\nabla^{\mathrm{T}} \boldsymbol{\sigma} + \mathbf{p_v}^{\mathrm{T}} = \mathbf{0}^{\mathrm{T}}. \tag{A.7}$$

If we now define divergence as

$$\mathrm{div}\ \boldsymbol{\sigma} = \nabla \cdot \boldsymbol{\sigma}, \tag{A.8}$$

the tensor form of the equations (A.3), (A.4) and (A.5) becomes

$$\mathrm{div}\ \boldsymbol{\sigma} + \mathbf{p_v} = \mathbf{0}. \tag{A.9}$$

Using summation indices, equations (A.3),(A.4) and (A.5) can also be written as

$$\sigma_{ji,j} + p_{vi} = 0. \tag{A.10}$$

Summing all the moments around the x_1 axis we obtain:

$$\frac{\partial \mu_{11}}{\partial x_1} + \frac{\partial \mu_{21}}{\partial x_2} + \frac{\partial \mu_{31}}{\partial x_3} + \sigma_{23} - \sigma_{32} + m_{v1} = 0. \tag{A.11}$$

Summing all the moments around the x_2 axis we obtain:

$$\frac{\partial \mu_{12}}{\partial x_1} + \frac{\partial \mu_{22}}{\partial x_2} + \frac{\partial \mu_{32}}{\partial x_3} + \sigma_{31} - \sigma_{13} + m_{v2} = 0. \tag{A.12}$$

Summing all the moments around the x_3 axis we obtain:

$$\frac{\partial \mu_{13}}{\partial x_1} + \frac{\partial \mu_{23}}{\partial x_2} + \frac{\partial \mu_{33}}{\partial x_3} + \sigma_{12} - \sigma_{21} + m_{v3} = 0. \tag{A.13}$$

Written in the matrix form equations (A.11), (A.12) and (A.13) read

$$\left\langle \frac{\partial}{\partial x_1} \quad \frac{\partial}{\partial x_2} \quad \frac{\partial}{\partial x_3} \right\rangle \begin{bmatrix} \mu_{11} & \mu_{12} & \mu_{13} \\ \mu_{21} & \mu_{22} & \mu_{23} \\ \mu_{31} & \mu_{32} & \mu_{33} \end{bmatrix} - \left\langle \sigma_{32} - \sigma_{23} \quad -\sigma_{31} + \sigma_{13} \quad \sigma_{21} - \sigma_{12} \right\rangle +$$
$$+ \left\langle m_{v1} \quad m_{v2} \quad m_{v3} \right\rangle = \left\langle 0 \quad 0 \quad 0 \right\rangle, \tag{A.14}$$

or

$$\nabla^{\mathrm{T}}\boldsymbol{\mu} - \mathbf{a}^{\mathrm{T}} + \mathbf{m_v}^{\mathrm{T}} = \mathbf{0}^{\mathrm{T}}. \tag{A.15}$$

The tensor form of this equation is

$$\mathrm{div}\,\boldsymbol{\mu} - \mathrm{grad}\,\hat{\mathbf{x}} : \boldsymbol{\sigma} + \mathbf{m_v} = \mathbf{0}. \tag{A.16}$$

The proof of this result is given in Appendix B. Using summation indices, equations (A.11), (A.12) and (A.13) can be written as

$$\mu_{ji,j} + \varepsilon_{ijk}\sigma_{jk} + m_{vi} = 0. \tag{A.17}$$

A.2   Equilibrium of a differential surface $\mathrm{d}S$

For the stress-indexing convention introduced in Appendix A.1, we also need to define the natural boundary conditions. To do this, we need to relate the applied surface loads $\mathbf{p_s}$ and $\mathbf{m_s}$ to the stresses on S_p which resists the action of $\mathbf{p_s}$ and $\mathbf{m_s}$ and keep the surface in equilibrium. To do that, we analyse equilibrium of a differential element under the differential surface $\mathrm{d}S$ with a unit normal $\mathbf{n}$ as shown in Figure A.2.

(a) Components of the force stress and the applied surface load

(b) Components of the moment stress and applied volume load
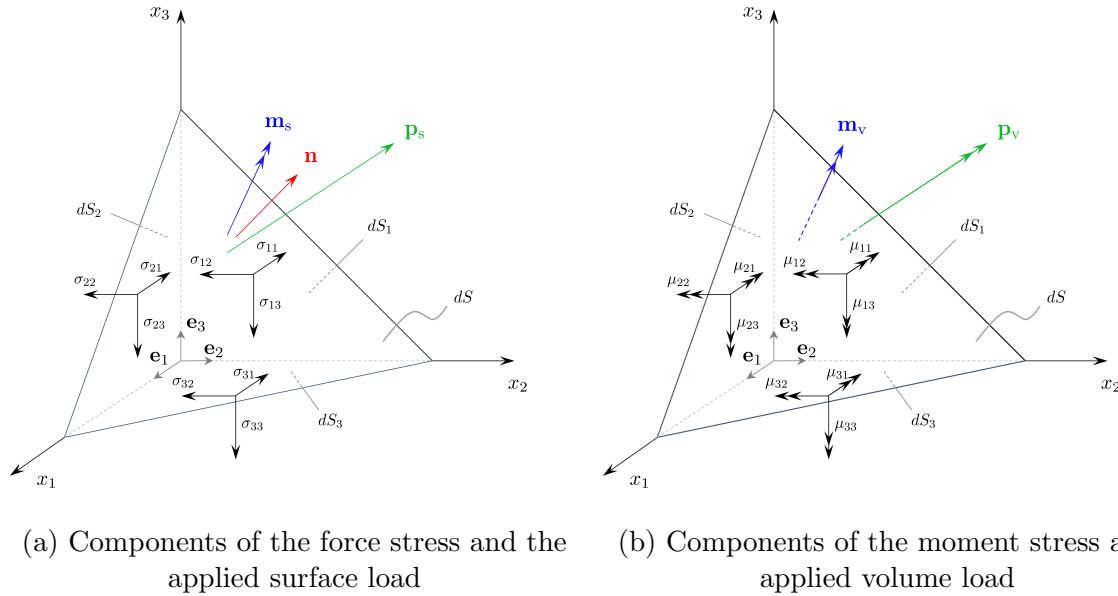
Figure A.2: Equilibrium of a differential surface element.

Summing all the forces in the directions x_1, x_2 and x_3 we obtain:

$$\sigma_{11}\,\mathrm{d}S_1 + \sigma_{21}\,\mathrm{d}S_2 + \sigma_{31}\,\mathrm{d}S_3 = p_{s1}\,\mathrm{d}S + p_{v1}\,\mathrm{d}V, \tag{A.18}$$

$$\sigma_{12}\,\mathrm{d}S_1 + \sigma_{22}\,\mathrm{d}S_2 + \sigma_{32}\,\mathrm{d}S_3 = p_{s2}\,\mathrm{d}S + p_{v2}\,\mathrm{d}V, \tag{A.19}$$

$$\sigma_{13}\,\mathrm{d}S_1 + \sigma_{23}\,\mathrm{d}S_2 + \sigma_{33}\,\mathrm{d}S_3 = p_{s3}\,\mathrm{d}S + p_{v3}\,\mathrm{d}V. \tag{A.20}$$

Taking into account that $\dfrac{\mathrm{d}V}{\mathrm{d}S}$ is a first-order differential which can be neglected and

$$\mathrm{d}S_i = \mathrm{d}S n_i, \quad n_i = \cos(\mathbf{n}, \mathbf{e}_i), \quad i = 1, 2, 3, \tag{A.21}$$

where $\mathbf{n}$ is the unit normal to the surface element $\mathrm{d}S$, equations (A.18) may be written in the matrix form to obtain the following:

$$\left\langle n_1 \quad n_2 \quad n_3 \right\rangle \begin{bmatrix} \sigma_{11} & \sigma_{12} & \sigma_{13} \\ \sigma_{21} & \sigma_{22} & \sigma_{23} \\ \sigma_{31} & \sigma_{32} & \sigma_{33} \end{bmatrix} = \left\langle p_{s1} \quad p_{s2} \quad p_{s3} \right\rangle, \tag{A.22}$$

i.e.

$$\mathbf{n}^{\mathrm{T}} \boldsymbol{\sigma} = \mathbf{p_s}^{\mathrm{T}}. \tag{A.23}$$

The previous equation can be written in a tensor form as follows:

$$\mathbf{n} \cdot \boldsymbol{\sigma} = \mathbf{p_s}, \tag{A.24}$$

and in the component form as follows:

$$\sigma_{ji} n_j = p_{si}, \quad i, j = 1, 2, 3. \tag{A.25}$$

Summing all the moments around x_1, x_2 and x_3 and after neglecting the contribution of the stress forces and volume loads which represent differentials of a higher order we obtain the following:

$$\mu_{11} dS_1 + \mu_{21} dS_2 + \mu_{31} dS_3 = m_{s1} dS, \tag{A.26}$$
$$\mu_{12} dS_1 + \mu_{22} dS_2 + \mu_{32} dS_3 = m_{s2} dS, \tag{A.27}$$
$$\mu_{13} dS_1 + \mu_{23} dS_2 + \mu_{33} dS_3 = m_{s3} dS, \tag{A.28}$$
$$\tag{A.29}$$

or in the matrix form:

$$\left\langle n_1 \quad n_2 \quad n_3 \right\rangle \begin{bmatrix} \mu_{11} & \mu_{12} & \mu_{13} \\ \mu_{21} & \mu_{22} & \mu_{23} \\ \mu_{31} & \mu_{32} & \mu_{33} \end{bmatrix} = \left\langle m_{s1} \quad m_{s2} \quad m_{s3} \right\rangle, \tag{A.30}$$

i.e.

$$\mathbf{n}^{\mathrm{T}} \boldsymbol{\mu} = \mathbf{m_s}^{\mathrm{T}}. \tag{A.31}$$

The tensor form of this equation is

$$\mathbf{n} \cdot \boldsymbol{\mu} = \mathbf{m_s}, \tag{A.32}$$

while its component form is

$$\mu_{ji} n_j = m_{si}, \quad i, j = 1, 2, 3. \tag{A.33}$$

Appendix B

Tensor form of the vector a

In order to write the tensor form of equation (2.67) we need to express vector $\mathbf{a}$ from equation (2.66) using tensorial operations. This has been performed in Section 2.2.1 (equations (2.68)-(2.74)), but here we illustrate these results using a matrix representation of tensors.

The following identity holds for every vector $\mathbf{v} \in \mathbb{R}$

$$\mathbf{x} \times \mathbf{v} = \hat{\mathbf{x}} \cdot \mathbf{v}, \quad \text{where } \hat{\mathbf{x}} = \begin{bmatrix} 0 & -x_3 & x_2 \\ x_3 & 0 & -x_1 \\ -x_2 & x_1 & 0 \end{bmatrix}. \tag{B.1}$$

Since $\hat{\mathbf{x}}$ is a tensor of order 2, its gradient is a tensor of order 3, i.e. we may represent it in a matrix form as

$$\text{grad } \hat{\mathbf{x}} = \begin{bmatrix} 0 & -x_3 & x_2 \\ x_3 & 0 & -x_1 \\ -x_2 & x_1 & 0 \end{bmatrix} \otimes \left\{ \begin{array}{c} \dfrac{\partial}{\partial x_1} \\ \dfrac{\partial}{\partial x_2} \\ \dfrac{\partial}{\partial x_3} \end{array} \right\} = \left\{ \begin{array}{c} \begin{bmatrix} 0 & 0 & 0 \\ 0 & 0 & -1 \\ 0 & 1 & 0 \end{bmatrix} \\ \begin{bmatrix} 0 & 0 & 1 \\ 0 & 0 & 0 \\ -1 & 0 & 0 \end{bmatrix} \\ \begin{bmatrix} 0 & -1 & 0 \\ 1 & 0 & 0 \\ 0 & 0 & 0 \end{bmatrix} \end{array} \right\}, \tag{B.2}$$

where the sub-matrices in the right-hand side should be understood as "pages" of the third-order tensor grad $\hat{\mathbf{x}}$.

From here, then,

$$
\text{grad } \hat{\mathbf{x}} : \boldsymbol{\sigma} =
\left\{
\begin{bmatrix} 0 & 0 & 0 \\ 0 & 0 & -1 \\ 0 & 1 & 0 \end{bmatrix} \\
\begin{bmatrix} 0 & 0 & 1 \\ 0 & 0 & 0 \\ -1 & 0 & 0 \end{bmatrix} \\
\begin{bmatrix} 0 & -1 & 0 \\ 1 & 0 & 0 \\ 0 & 0 & 0 \end{bmatrix}
\right\}
:
\begin{bmatrix} \sigma_{11} & \sigma_{12} & \sigma_{13} \\ \sigma_{21} & \sigma_{22} & \sigma_{23} \\ \sigma_{31} & \sigma_{32} & \sigma_{33} \end{bmatrix}
=
\left\{
\begin{array}{c} \sigma_{32} - \sigma_{23} \\ -\sigma_{31} + \sigma_{13} \\ \sigma_{21} - \sigma_{12} \end{array}
\right\},
\qquad \text{(B.3)}
$$

i.e.

$$
\mathbf{a} = \text{grad}(\hat{\mathbf{x}}) : \boldsymbol{\sigma}.
\qquad \text{(B.4)}
$$

Appendix C

Input file to generate the finite element mesh for the plate with hole problem for GMSH software package

C.1 Input file for triangular finite elements

```
// Gmsh project created on Wed Sep 27 21:48:45 2017
// Sara Grbcic, sara.grbcic@uniri.hr

L=16.2; //domain length and height
r=0.216; //hole radius
a = 1.2; // ratio between the radial increments
n=22; // number of divisions
p=(a-1)/(a^(n)-1)*(L-r);
alpha=90/8*Pi/180; // angle in radians to obtain boundary nodes

Point(1) = {0, 0, 0, 0};
Point(2) = {r, 0, 0, 0};
Point(3) = {0, r, 0, 0};


j=4;
k=1;

For i In {0:n-1}

Point(j) = {r+p*(1-a^i)/(1-a), 0, 0, 0};
Point(j+1) = {0, r+p*(1-a^i)/(1-a), 0, 0};

Circle(k) = {j-1, 1, j-2};
Transfinite Line {k} = 9;

Line (k+1) ={j-2,j};
Transfinite Line {k+1} = 2;

Circle(k+2) = {j, 1, j+1};
Transfinite Line {k+2} = 9;

Line (k+3) ={j+1,j-1};
Transfinite Line {k+3} = 2;

Line Loop (k+4)={k,k+1,k+2,k+3};

Plane Surface (k+5) = {(k+4)};

Transfinite Surface {k+5} = {j-2,j,j+1,j-1} Right;

p1=k;
p2=j;
j=j+2;
k=k+5;

EndFor


// THE OTHER STRUCTURED PART
// SURFACE 1
Point(2*n+4) = {L, 0, 0, 0};
```

```
Line (5*n+2) = {p2,2*n+4};
Transfinite Line {5*n+2} = 2;


Point(2*n+5) = {L, L*Tan(alpha), 0, 0};
Point(2*n+6) = {L, L*Tan(2*alpha), 0, 0};
Line (5*n+3) = {2*n+4,2*n+5,2*n+6};
Transfinite Line {5*n+3} = 3;


Point(2*n+7) = {(r+p*(1-a^(n-1))/(1-a))*Cos(2*alpha),
(r+p*(1-a^(n-1))/(1-a))*Sin(2*alpha), 0, 0};
Line (5*n+4) = {2*n+6,2*n+7};
Transfinite Line {5*n+4} = 2;


Circle (5*n+5) = {2*n+7,1,p2};
Transfinite Line {5*n+5} = 3;


Line Loop(5*n+6)={5*n+2,5*n+3,5*n+4,5*n+5}; //Line
Loop(5*n+6)={5*n+2,5*n+3,5*n+4,5*n+5};


Plane Surface (5*n+7) = {5*n+6};
Transfinite Surface {5*n+7} = {p2,2*n+4,2*n+6,2*n+7} Right;


// SURFACE 2
Point(2*n+9) = {L*Tan(2*alpha),L, 0, 0};
Line (5*n+8) = {2*n+6,2*n+9};
Transfinite Line {5*n+8} = 5;


Point(2*n+10) = {(r+p*(1-a^(n-1))/(1-a))*Sin(2*alpha),
(r+p*(1-a^(n-1))/(1-a))*Cos(2*alpha), 0, 0};
Line (5*n+9) = {2*n+9,2*n+10};
Transfinite Line {5*n+9} = 2;


Circle (5*n+10) = {2*n+10,1,2*n+7};
Transfinite Line {5*n+10} = 5;


Line Loop(5*n+11)={-(5*n+4),5*n+8,5*n+9,5*n+10};


Plane Surface (5*n+12) = {5*n+11};
Transfinite Surface {5*n+12};


// SURFACE 3
Point(2*n+11) = {0, L, 0, 0};
Line (5*n+13) = {2*n+9,2*n+11};
Transfinite Line {5*n+13} = 3;


Line (5*n+14) = {2*n+11,p2+1};
Transfinite Line {5*n+14} = 2;


Circle (5*n+15) = {p2+1,1,2*n+10};
Transfinite Line {5*n+15} = 3;


Line Loop(5*n+16)={-(5*n+9),5*n+13,5*n+14,5*n+15};
```

```
Plane Surface (5*n+17) = {5*n+16};
Transfinite Surface {5*n+17};


// SURFACE 4
Point(2*n+12) = {L,0.5*(L-L*Tan(2*alpha))+L*Tan(2*alpha),0, 0};
Line (5*n+18) = {2*n+6,2*n+12};
Transfinite Line {5*n+18} = 2;


y_108 = 0.5*(L-L*Tan(2*alpha))+L*Tan(2*alpha);
y_102 = L*Tan(2*alpha);


Point(2*n+13) = {0.5*(L+y_108),0.5*(y_108-y_102)+y_102,0, 0};
x_109 = 0.5*(L+y_108);
y_109 = 0.5*(y_108-y_102)+y_102;
Line (5*n+19) = {2*n+12,2*n+13};
Transfinite Line {5*n+19} = 2;


Line (5*n+20) = {2*n+13,2*n+6};
Transfinite Line {5*n+20} = 2;


Line Loop(5*n+21)={5*n+18,5*n+19,5*n+20};


Plane Surface (5*n+22) = {5*n+21};
Transfinite Surface {5*n+22};




// SURFACE 5
Point(2*n+16) = {y_108, L, 0, 0};
Line (5*n+23) = {2*n+12,2*n+16};
Transfinite Line {5*n+23} = 3;


Point(2*n+17) = {y_109, x_109, 0, 0};

Line (5*n+24) = {2*n+16,2*n+17};
Transfinite Line {5*n+24} = 2;

Line (5*n+25) = {2*n+17,2*n+13};
Transfinite Line {5*n+25} = 3;

Line Loop(5*n+26)={-(5*n+19),5*n+23,5*n+24,5*n+25};

Plane Surface (5*n+27) = {5*n+26};
Transfinite Surface {5*n+27};

// SURFACE 6

Line (5*n+28) = {2*n+16,2*n+9};
Transfinite Line {5*n+28} = 2;

Line (5*n+29) = {2*n+9,2*n+17};
```

Page 3

196

```
Transfinite Line {5*n+29} = 2;

Line Loop (5*n+30)={-(5*n+24),5*n+28,5*n+29};
Plane Surface (5*n+31) = {5*n+30};
Transfinite Surface {5*n+31} Right;

// SURFACE 7

Point(2*n+15) = {L, L, 0, 0};

Line (5*n+32) = {2*n+12,2*n+15};
Transfinite Line {5*n+32} = 2;

Line (5*n+33) = {2*n+15,2*n+16};
Transfinite Line {5*n+33} = 2;

Line Loop (5*n+34)={-(5*n+23),5*n+32,5*n+33};
Plane Surface (5*n+35) = {5*n+34};
//Transfinite Surface {5*n+35};


//this needs to be done manually, use CTRL+MOUSE to select all
Physical Surface("triangles") = {26, 21, 16, 11, 6, 31, 91, 145, 141, 137, 132,
127, 122, 117, 111, 106, 101, 96, 86, 81, 76, 71, 66, 61, 56, 51, 46, 41, 36};


Mesh.Algorithm = 1;

Mesh.ElementOrder = 1; //Set element order

Mesh 2;  // Generate 2D mesh
Coherence Mesh;  // Remove duplicate entities
//Save "plate-with-hole-T3-a=1.2.msh";  // Save mesh in MSH format
```

C.2   Input file for quadrilateral finite elements

```
// Gmsh project created on Wed Sep 27 21:48:45 2017
// Sara Grbcic, sara.grbcic@uniri.hr

L=16.2; //domain length and height
r=0.216; //hole radius
a = 1.2; // ratio between the radial increments
n=22; // number of divisions
p=(a-1)/(a^(n)-1)*(L-r);
alpha=90/8*Pi/180; // angle in radians to obtain boundary nodes

Point(1) = {0, 0, 0, 0};
Point(2) = {r, 0, 0, 0};
Point(3) = {0, r, 0, 0};


j=4;
k=1;

For i In {0:n-1}

Point(j) = {r+p*(1-a^i)/(1-a), 0, 0, 0};
Point(j+1) = {0, r+p*(1-a^i)/(1-a), 0, 0};

Circle(k) = {j-1, 1, j-2};
Transfinite Line {k} = 9; // 9 = number of nodes per line

Line (k+1) ={j-2,j};
Transfinite Line {k+1} = 2;  // 2 = number of nodes per line

Circle(k+2) = {j, 1, j+1};
Transfinite Line {k+2} = 9;  // 9 = number of nodes per line

Line (k+3) ={j+1,j-1};
Transfinite Line {k+3} = 2;

Line Loop (k+4)={k,k+1,k+2,k+3};

Plane Surface (k+5) = {(k+4)};

Transfinite Surface {k+5} = {j-2,j,j+1,j-1} Right;
Recombine Surface {k+5};

p1=k;
p2=j;
j=j+2;
k=k+5;

EndFor


// THE OTHER STRUCTURED PART
// SURFACE 1
```

```
Point(2*n+4) = {L, 0, 0, 0};
Line (5*n+2) = {p2,2*n+4};
Transfinite Line {5*n+2} = 2;


Point(2*n+5) = {L, L, 0, 0}; //101
Point(2*n+6) = {L, (r+p*(1-a^(n-1))/(1-a))*Sin(alpha), 0, 0};
Point(2*n+7) = {L, (r+p*(1-a^(n-1))/(1-a))*Sin(2*alpha), 0, 0};
Point(2*n+8) = {L, (r+p*(1-a^(n-1))/(1-a))*Sin(3*alpha), 0, 0};
Line (5*n+3) = {2*n+4,2*n+6,2*n+7,2*n+8,2*n+5};
Transfinite Line {5*n+3} = 5;


Point(2*n+9) = {(r+p*(1-a^(n-1))/(1-a))*Cos(4*alpha),
(r+p*(1-a^(n-1))/(1-a))*Sin(4*alpha), 0, 0};
Line (5*n+4) = {2*n+5,2*n+9};
Transfinite Line {5*n+4} = 2;


Circle (5*n+5) = {2*n+9,1,p2};
Transfinite Line {5*n+5} = 5;


Line Loop(5*n+6)={5*n+2,5*n+3,5*n+4,5*n+5};


Plane Surface (5*n+7) = {5*n+6};
Transfinite Surface {5*n+7};
Recombine Surface {5*n+7};


// SURFACE 2
Point(2*n+10) = {0, L, 0, 0};
Line (5*n+8) = {2*n+5,2*n+10};
Transfinite Line {5*n+8} = 5;


Line (5*n+9) = {2*n+10,p2+1};
Transfinite Line {5*n+9} = 2;


Circle (5*n+10) = {p2+1,1,2*n+9};
Transfinite Line {5*n+10} = 5;


Line Loop(5*n+11)={5*n+8,5*n+9,5*n+10,-(5*n+4)};


Plane Surface (5*n+12) = {5*n+11};
Transfinite Surface {5*n+12};
Recombine Surface {5*n+12};


Mesh.Algorithm = 1;


Mesh.ElementOrder = 1; //Set element order


//Physical Surface("quads") = {66, 210, 205, 111, 106, 101, 96, 91, 86, 81, 76,
71, 11, 61, 56, 51, 46, 41, 36, 31, 26, 21, 16}; //This needs to be done
manually


Mesh 2;  // Generate 2D mesh
```

```
Coherence Mesh;  // Remove duplicate entities

//Save "plate-with-hole-Q4-a=1.2.msh";  // Save mesh in MSH format
```

Appendix D

Geometric derivation of the exponential map as given by Argyris [2]

Any three-dimensional rotation can be interpreted as a 2D rotation (defined by the angle of rotation ϑ) that takes place in a plane orthogonal to the axis of rotation, which can be identified by a unit rotation vector $\mathbf{e}$. The two quantities $(\mathbf{e}, \vartheta)$ are referred tu as the principal axis of rotation and the principal angle of rotation, which completely define the rotation represented by the rotation tensor $\boldsymbol{\Lambda}$. In order to express the rotation tensor in terms of the rotation vector we choose the geometric approach presented by Argyris [2]. We introduce a rotational *pseudovector* $\boldsymbol{\vartheta} = \vartheta\, \mathbf{e}$ along the axis of rotation as shown in figure, where ϑ is the vector norm, and $\mathbf{e}$ is the unit vector. Written in the Cartesian coordinate system, the vector is described as $\boldsymbol{\vartheta} = \{\varphi \;\; \chi \;\; \psi\}$, where the vector norm is defined as $\vartheta = \sqrt{\varphi^2 + \chi^2 + \psi^2}$. We want to rotate a vector $\mathbf{p}$ by applying a rotation expressed as $\boldsymbol{\vartheta}$ (defining the axis of rotation- direction of the vector and angle of rotation defined by the vector norm) from its initial position to a new position referred to as $\hat{\mathbf{p}}$, as shown in Figure D.1.
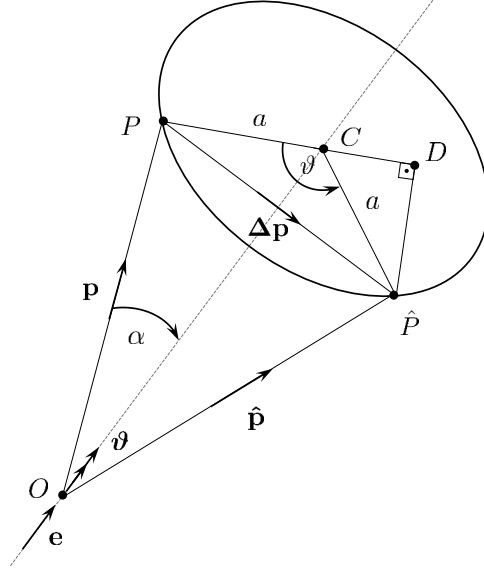
Figure D.1: Construction of a transformation matrix $\mathbf{T}(\boldsymbol{\vartheta}) = \boldsymbol{\Lambda}$ for an arbitrary rotational pseudovector $\boldsymbol{\vartheta}$ [2]

In other words, the aim is to establish the following transformation:

$$\hat{\mathbf{p}} = \mathbf{T}(\boldsymbol{\vartheta})\ \mathbf{p}. \tag{D.1}$$

We refer to $\mathbf{T}(\boldsymbol{\vartheta})$ as the transformation rotation matrix, which is a nonlinear function of $\boldsymbol{\vartheta}$. The rotation matrix is orthogonal, i.e. $\mathbf{T}^{\mathrm{T}} = \mathbf{T}^{-1}$, $\mathbf{T} \in \mathrm{SO}(3)$. By analysing the geometry of the rotation process we define the following:

$$\hat{\mathbf{p}} = \mathbf{p} + \Delta\mathbf{p}. \tag{D.2}$$

We seek to express the right hand side of equation (D.2) as in equation (D.1). From Figure D.1, we obtain $\Delta\mathbf{p} = \overrightarrow{PD} + \overrightarrow{D\hat{P}}$. First we proceed to the definition of the vector $\overrightarrow{D\hat{P}}$, pointing in the direction of $\mathbf{e} \times \mathbf{p}$. The norm of vector $|\overrightarrow{D\hat{P}}|$ is equal to

$$|\overrightarrow{D\hat{P}}| = a\ \sin\vartheta. \tag{D.3}$$

Since we know the direction, we have to calculate the norm of $\mathbf{e} \times \mathbf{p}$, as follows:

$$|\mathbf{e} \times \mathbf{p}| = |\mathbf{e}|\ |\mathbf{p}| \sin \sphericalangle(\mathbf{e}, \mathbf{p}) \tag{D.4}$$

$$= 1\ p\ \sin\alpha \tag{D.5}$$

$$= a. \tag{D.6}$$

202

By further introducing $\boldsymbol{\vartheta} = \vartheta \mathbf{e}$, the vector $\overrightarrow{D\hat{P}}$ is defined as

$$\overrightarrow{D\hat{P}} = a \ \sin \vartheta \ \frac{1}{a} \ (\mathbf{e} \times \mathbf{p}) \tag{D.7}$$

$$= (\mathbf{e} \times \mathbf{p}) \ \sin \vartheta \tag{D.8}$$

$$= \frac{\sin \vartheta}{\vartheta}(\boldsymbol{\vartheta} \times \mathbf{p}). \tag{D.9}$$

Now we have to define the vector $\overrightarrow{PD}$. We know that it is orthogonal to the plane in which lies the vector $\overrightarrow{D\hat{P}}$. Furthermore, we know that it is also orthogonal to the unit vector $\mathbf{e}$. Due to that, we assign the direction $\mathbf{e} \times (\mathbf{e} \times \mathbf{p})$. First we calculate the norm of the assigned direction as

$$|\mathbf{e} \times (\mathbf{e} \times \mathbf{p})| = |\mathbf{e}| \ |(\mathbf{e} \times \mathbf{p})| \ \sin 90°$$

$$= 1 \ a \ 1$$

$$= a. \tag{D.10}$$

Furthermore, from Figure D.1, we obtain

$$|\overrightarrow{PD}| = |\overrightarrow{PC}| + |\overrightarrow{CD}|$$

$$= a + (- \cos \vartheta \ a)$$

$$= a(1 - \cos \vartheta)$$

$$= a(\sin^2 \frac{\vartheta}{2} + \cos^2 \frac{\vartheta}{2} - \cos^2 \frac{\vartheta}{2} + \sin^2 \frac{\vartheta}{2})$$

$$= 2a \sin^2 \frac{\vartheta}{2}. \tag{D.11}$$

Finally, by introducing (D.10) and (D.11) into the definition of $\overrightarrow{PD}$ we obtain

$$\overrightarrow{PD} = 2a \sin^2 \frac{\vartheta}{2} \frac{1}{a}(\mathbf{e} \times (\mathbf{e} \times \mathbf{p}))$$

$$= \frac{1}{\vartheta} \frac{1}{\vartheta} 2 \sin^2 \frac{\vartheta}{2}(\boldsymbol{\vartheta} \times (\boldsymbol{\vartheta} \times \mathbf{p}))$$

$$= \frac{1}{2} \frac{\sin^2 \frac{\vartheta}{2}}{(\frac{\vartheta}{2})^2}(\boldsymbol{\vartheta} \times (\boldsymbol{\vartheta} \times \mathbf{p})) \tag{D.12}$$

Now we go back to equation (D.2) and define:

$$\hat{\mathbf{p}} = \mathbf{p} + \frac{\sin \vartheta}{\vartheta}(\boldsymbol{\vartheta} \times \mathbf{p}) + \frac{1}{2} \frac{\sin^2 \frac{\vartheta}{2}}{(\frac{\vartheta}{2})^2}(\boldsymbol{\vartheta} \times (\boldsymbol{\vartheta} \times \mathbf{p}))$$

$$= \mathbf{p} + \frac{\sin \vartheta}{\vartheta}(\boldsymbol{\vartheta} \times \mathbf{p}) + \frac{1 - \cos \vartheta}{\vartheta^2}(\boldsymbol{\vartheta} \times (\boldsymbol{\vartheta} \times \mathbf{p})).$$

We convert the cross product to a matrix multiplication by presenting a skew-symmetric matrix obtained from a vector, as follows:

$$\hat{\boldsymbol{\vartheta}} = \mathbf{S} = \begin{bmatrix} 0 & -\psi & \chi \\ \psi & 0 & -\varphi \\ -\chi & \varphi & 0 \end{bmatrix}, \tag{D.13}$$

i.e.

$$\boldsymbol{\vartheta} \times \mathbf{p} = \hat{\boldsymbol{\vartheta}}\mathbf{p} = \mathbf{S}\mathbf{p}, \tag{D.14}$$

$$\boldsymbol{\vartheta} \times (\boldsymbol{\vartheta} \times \mathbf{p}) = \hat{\boldsymbol{\vartheta}}^2\mathbf{p} = \mathbf{S}^2\mathbf{p}. \tag{D.15}$$

Finally, we obtain

$$\hat{\mathbf{p}} = \left(\mathbf{I} + \frac{\sin \vartheta}{\vartheta}\mathbf{S} + \frac{1}{2}\frac{\sin^2 \frac{\vartheta}{2}}{(\frac{\vartheta}{2})^2}\mathbf{S}^2\right)\mathbf{p}$$

$$= \left(\mathbf{I} + \frac{\sin \vartheta}{\vartheta}\mathbf{S} + \frac{1 - \cos \vartheta}{\vartheta^2}\mathbf{S}^2\right)\mathbf{p}$$

$$= \mathbf{T}(\boldsymbol{\vartheta})\,\mathbf{p},$$

where $\mathbf{T}(\boldsymbol{\vartheta})$ represents the rotation matrix. By expanding the trigonometric functions in terms multiplying $\mathbf{S}$ in the above equation into Taylor series as

$$\sin \vartheta = \vartheta - \frac{\vartheta^3}{3!} + \frac{\vartheta^5}{5!} - ..., \quad \cos \vartheta = 1 - \frac{\vartheta^2}{2!} + \frac{\vartheta^4}{4!} - ..., \tag{D.16}$$

we obtain the following

$$\mathbf{T}(\boldsymbol{\vartheta}) = \mathbf{I} + \left(1 - \frac{1}{3!}\vartheta^2 + \frac{1}{5!}\vartheta^4 + ...\right)\mathbf{S} + \left(\frac{1}{2!} - \frac{1}{4!}\vartheta^2 + \frac{1}{6!}\vartheta^4 + ...\right)\mathbf{S}^2. \tag{D.17}$$

By recognizing the recursive properties of the skew-symmetric matrix $\mathbf{S}$ as

$$\mathbf{S}^{2n-1} = (-1)^{n-1}\vartheta^{2(n-1)}\mathbf{S} \tag{D.18}$$

$$\mathbf{S}^{2n} = (-1)^{n-1}\vartheta^{2(n-1)}\mathbf{S}^2 \tag{D.19}$$

we prove the so-called *exponential map*, as

$$\mathbf{T}(\boldsymbol{\vartheta}) = \mathbf{I} + \mathbf{S} + \frac{1}{2!}\mathbf{S}^2 + \frac{1}{3!}\mathbf{S}^3 + ... + \frac{1}{n!}\mathbf{S}^n = e^{\mathbf{S}} = \exp \mathbf{S} = \exp \hat{\boldsymbol{\vartheta}}, \tag{D.20}$$

which represents a specific operation between a Lie group and a related Lie algebra (for

example so(n)$\Leftrightarrow$ SO(n)). In conclusion, the following equation

$$\mathbf{T}(\boldsymbol{\vartheta}) = \mathbf{I} + \frac{\sin\vartheta}{\vartheta}\hat{\boldsymbol{\vartheta}} + \frac{1 - \cos\vartheta}{\vartheta^2}\hat{\boldsymbol{\vartheta}}^2 \tag{D.21}$$

defines the relation between the total rotation vector $\boldsymbol{\vartheta}$ and the rotation tensor $\mathbf{T}$. Furthermore, it represents the so-called *Euler rotation vector parametrization of the rotation tensor*, also known as the *Euler-Rodrigues formula*.

Appendix E

Tensor identities

In the present Appendix some of the identities used in this thesis are outlined. The proof for the commonly used ones can be found in [53], while for identities derived in this work the proof is also given.

Vectors:

The following identities hold for any vectors $\mathbf{a}$, $\mathbf{b}$, $\mathbf{c}$:

$$\mathbf{a} \cdot \mathbf{b} = \mathbf{b} \cdot \mathbf{a} = \mathbf{a}^{\mathrm{T}}\mathbf{b} = \mathbf{b}^{\mathrm{T}}\mathbf{a}, \tag{E.1}$$

$$\mathbf{a}\mathbf{b}^{\mathrm{T}} = \mathbf{a} \otimes \mathbf{b}, \tag{E.2}$$

$$\mathrm{tr}(\mathbf{a} \otimes \mathbf{b}) = \mathbf{a} \cdot \mathbf{b} = \mathbf{a}^{\mathrm{T}}\mathbf{b}, \tag{E.3}$$

$$\mathbf{v} = -\frac{1}{2}\boldsymbol{\epsilon} : \hat{\mathbf{v}} = \mathrm{ax}(\hat{\mathbf{v}}), \tag{E.4}$$

$$\widehat{\mathbf{a}}\ \mathbf{b} = -\widehat{\mathbf{b}}\ \mathbf{a}, \tag{E.5}$$

$$\mathrm{tr}(\widehat{\mathbf{a}}\widehat{\mathbf{b}}) = -2\mathbf{a} \cdot \mathbf{b} = -2\mathbf{a}^{\mathrm{T}}\mathbf{b}, \tag{E.6}$$

$$\widehat{\mathbf{v} \times \mathbf{w}} = \mathbf{w} \otimes \mathbf{v} - \mathbf{v} \otimes \mathbf{w}. \tag{E.7}$$

Tensors of order 2:

The following identities hold for any 2nd order tensors $\mathbf{A}$, $\mathbf{B}$, $\mathbf{C}$:

$$\mathbf{A} : \mathbf{B}^{\mathrm{T}} = \mathbf{A}^{\mathrm{T}} : \mathbf{B}, \tag{E.8}$$

$$\mathbf{A} : \mathbf{B} = \mathbf{B} : \mathbf{A}, \tag{E.9}$$

$$\mathbf{A} : \mathbf{B} = \mathrm{tr}(\mathbf{A}\mathbf{B}^{\mathrm{T}}), \tag{E.10}$$

$$\mathrm{tr}(\mathbf{A}\mathbf{B}\mathbf{C}) = (\mathbf{A}\mathbf{B}) : \mathbf{C}^{\mathrm{T}} = (\mathbf{B}\mathbf{C}) : \mathbf{A}^{\mathrm{T}} = (\mathbf{C}\mathbf{A}) : \mathbf{B}^{\mathrm{T}}, \tag{E.11}$$

$$(\mathbf{A}\mathbf{B}\mathbf{C}) : \mathbf{D}^{\mathrm{T}} = (\mathbf{B}\mathbf{C}\mathbf{D}) : \mathbf{A}^{\mathrm{T}} = (\mathbf{C}\mathbf{D}\mathbf{A}) : \mathbf{B}^{\mathrm{T}}, \tag{E.12}$$

$$\mathrm{ax}(\mathbf{A} - \mathbf{A}^{\mathrm{T}}) = -\boldsymbol{\epsilon} : \mathbf{A} \tag{E.13}$$

PROOF of (E.13)

$$
\begin{aligned}
\mathrm{ax}&(\mathbf{A} - \mathbf{A}^{\mathrm{T}}) \\
&= \mathrm{ax}\left(\begin{bmatrix} A_{11} & A_{12} & A_{13} \\ A_{21} & A_{22} & A_{23} \\ A_{31} & A_{32} & A_{33} \end{bmatrix} - \begin{bmatrix} A_{11} & A_{21} & A_{31} \\ A_{12} & A_{22} & A_{32} \\ A_{13} & A_{23} & A_{33} \end{bmatrix} \right) \\
&= \mathrm{ax}\left(\begin{bmatrix} 0 & A_{12} - A_{21} & A_{13} - A_{31} \\ A_{21} - A_{12} & 0 & A_{23} - A_{32} \\ A_{31} - A_{13} & A_{32} - A_{23} & 0 \end{bmatrix} \right) \\
&= \begin{Bmatrix} A_{32} - A_{23} \\ A_{13} - A_{31} \\ A_{21} - A_{12} \end{Bmatrix}
\end{aligned} \tag{E.14}
$$

$$- \boldsymbol{\epsilon} : \mathbf{A}$$

$$= - \left[\begin{bmatrix} 0 & 0 & 0 \\ 0 & 0 & 1 \\ 0 & -1 & 0 \end{bmatrix} \\ \begin{bmatrix} 0 & 0 & -1 \\ 0 & 0 & 0 \\ 1 & 0 & 0 \end{bmatrix} \\ \begin{bmatrix} 0 & 1 & 0 \\ -1 & 0 & 0 \\ 0 & 0 & 0 \end{bmatrix} \right] : \begin{bmatrix} A_{11} & A_{12} & A_{13} \\ A_{21} & A_{22} & A_{23} \\ A_{31} & A_{32} & A_{33} \end{bmatrix}$$

$$= \begin{Bmatrix} A_{32} - A_{23} \\ A_{13} - A_{31} \\ A_{21} - A_{12} \end{Bmatrix} , \tag{E.15}$$

i.e.

$$\mathrm{ax}(\mathbf{A} - \mathbf{A}^{\mathrm{T}}) = -\boldsymbol{\epsilon} : \mathbf{A}. \tag{E.16}$$

Appendix F

Derivation of terms needed in the finite element formulation of the residual vector

F.1 Introduction of the interpolation of virtual displacements into $\left(\mathbf{Q}^{\mathrm{T}}\mathbf{GRAD}\overline{\mathbf{u}}^h\right) : \mathbf{B}$

$$
\begin{aligned}
\left(\mathbf{Q}^{\mathrm{T}}\mathrm{GRAD}\overline{\mathbf{u}}^h\right) : \mathbf{B} &= \left(\mathbf{Q}^{\mathrm{T}}(\overline{\mathbf{u}}^h \otimes \nabla_X)\right) : \mathbf{B} \\
&= \left(\mathbf{Q}^{\mathrm{T}}(\mathbf{N_u}\overline{\mathbf{d}}^e \otimes \nabla_X)\right) : \mathbf{B} \\
&= \left(\mathbf{Q}^{\mathrm{T}}\sum_{i=1}^{n_{node}}[\mathbf{N}_i \ \ \mathbf{0}]\overline{\mathbf{d}}_i^e \left\langle \frac{\partial}{\partial X_1} \ \ \frac{\partial}{\partial X_2} \ \ \frac{\partial}{\partial X_3} \ \right\rangle\right) : \mathbf{B} \\
&= \left(\mathbf{Q}^{\mathrm{T}}\sum_{i=1}^{n_{node}}\mathbf{N}_i \left\{\begin{matrix}\overline{u}_{1i}\\\overline{u}_{2i}\\\overline{u}_{3i}\end{matrix}\right\} \left\langle \frac{\partial}{\partial X_1} \ \ \frac{\partial}{\partial X_2} \ \ \frac{\partial}{\partial X_3} \ \right\rangle\right) : \mathbf{B} \\
&= \left(\mathbf{Q}^{\mathrm{T}}\sum_{i=1}^{n_{node}}N_i \ \mathbf{I} \ \overline{\mathbf{d}}_{\mathbf{u}_i}^e \left\langle \frac{\partial}{\partial X_1} \ \ \frac{\partial}{\partial X_2} \ \ \frac{\partial}{\partial X_3} \ \right\rangle\right) : \mathbf{B} \\
&= \left(\mathbf{Q}^{\mathrm{T}}\sum_{i=1}^{n_{node}} \overline{\mathbf{d}}_{\mathbf{u}_i}^e N_i \nabla_X^{\mathrm{T}}\right) : \mathbf{B} \\
&= \left(\mathbf{Q}^{\mathrm{T}}\sum_{i=1}^{n_{node}} \overline{\mathbf{d}}_{\mathbf{u}_i}^e \otimes (N_i \nabla_X)\right) : \mathbf{B} \\
&= \sum_{i=1}^{n_{node}} \left(\left(\mathbf{Q}^{\mathrm{T}} \ \overline{\mathbf{d}}_{\mathbf{u}_i}^e \otimes (N_i \nabla_X)\right) : \mathbf{B}\right), \quad \text{and by using (E.10),}
\end{aligned}
$$

$$= \sum_{i=1}^{n_{node}} \mathrm{tr}\left(\left(\mathbf{Q}^{\mathrm{T}}\,\overline{\mathbf{d}}_{\mathbf{u}_i}^{e} \otimes (N_i \nabla_X)\right) \mathbf{B}^{\mathrm{T}}\right)$$

$$= \sum_{i=1}^{n_{node}} \mathrm{tr}\left(\mathbf{Q}^{\mathrm{T}}\,\overline{\mathbf{d}}_{\mathbf{u}_i}^{e}\left(N_i \nabla_X^{\mathrm{T}}\right)\mathbf{B}^{\mathrm{T}}\right), \qquad \text{and by using (E.2),}$$

$$= \sum_{i=1}^{n_{node}} \mathrm{tr}\left(\mathbf{Q}^{\mathrm{T}}\,\overline{\mathbf{d}}_{\mathbf{u}_i}^{e} \otimes (\mathbf{B}(N_i \nabla_X))\right), \qquad \text{and by using (E.3),}$$

$$= \sum_{i=1}^{n_{node}} \left(\left(\overline{\mathbf{d}}_{\mathbf{u}_i}^{e\,\mathrm{T}}\mathbf{Q}\right)(\mathbf{B}(N_i \nabla_X))\right)$$

$$= \overline{\mathbf{d}}_{\mathbf{u}_1}^{e\,\mathrm{T}}\mathbf{Q}\mathbf{B}(N_1 \nabla_X) + \overline{\mathbf{d}}_{\mathbf{u}_2}^{e\,\mathrm{T}}\mathbf{Q}\mathbf{B}(N_2 \nabla_X) + \ldots + \overline{\mathbf{d}}_{\mathbf{u}_{n_{node}}}^{e\,\mathrm{T}}\mathbf{Q}\mathbf{B}(N_{n_{node}} \nabla_X)$$

$$= \left\langle \overline{\mathbf{d}}_{\mathbf{u}_1}^{e\,\mathrm{T}}\,\overline{\mathbf{d}}_{\mathbf{u}_2}^{e\,\mathrm{T}}\,\ldots\,\overline{\mathbf{d}}_{\mathbf{u}_{n_{node}}}^{e\,\mathrm{T}}\right\rangle \left\{\begin{array}{c} \mathbf{Q}\mathbf{B}(N_1 \nabla_X) \\ \mathbf{Q}\mathbf{B}(N_2 \nabla_X) \\ \vdots \\ \mathbf{Q}\mathbf{B}(N_{n_{node}} \nabla_X) \end{array}\right\}$$

$$= \left\langle \left\langle \overline{\mathbf{d}}_{\mathbf{u}_1}^{e\,\mathrm{T}}\,\overline{\mathbf{d}}_{\boldsymbol{\varphi}_1}^{e\,\mathrm{T}}\right\rangle \left\langle \overline{\mathbf{d}}_{\mathbf{u}_2}^{e\,\mathrm{T}}\,\overline{\mathbf{d}}_{\boldsymbol{\varphi}_2}^{e\,\mathrm{T}}\right\rangle\,\ldots\,\left\langle \overline{\mathbf{d}}_{\mathbf{u}_{n_{node}}}^{e\,\mathrm{T}}\,\overline{\mathbf{d}}_{\boldsymbol{\varphi}_{n_{node}}}^{e\,\mathrm{T}}\right\rangle\right\rangle \left\{\begin{array}{c} \left\{\begin{array}{c} \mathbf{Q}\mathbf{B}(N_1 \nabla_X) \\ \mathbf{0} \end{array}\right\} \\[4pt] \left\{\begin{array}{c} \mathbf{Q}\mathbf{B}(N_2 \nabla_X) \\ \mathbf{0} \end{array}\right\} \\[4pt] \vdots \\[4pt] \left\{\begin{array}{c} \mathbf{Q}\mathbf{B}(N_{n_{node}} \nabla_X) \\ \mathbf{0} \end{array}\right\} \end{array}\right\}$$

$$= \left\langle \overline{\mathbf{d}}_1^{e\,\mathrm{T}}\,\overline{\mathbf{d}}_2^{e\,\mathrm{T}}\,\ldots\,\overline{\mathbf{d}}_{n_{node}}^{e\,\mathrm{T}}\right\rangle \underbrace{\begin{bmatrix} \mathbf{QB} & \mathbf{0} & \mathbf{0} & \mathbf{0} & \cdots & \mathbf{0} & \mathbf{0} \\ \mathbf{0} & \mathbf{0} & \mathbf{0} & \mathbf{0} & \cdots & \mathbf{0} & \mathbf{0} \\ \mathbf{0} & \mathbf{0} & \mathbf{QB} & \mathbf{0} & \cdots & \mathbf{0} & \mathbf{0} \\ \mathbf{0} & \mathbf{0} & \mathbf{0} & \mathbf{0} & \cdots & \mathbf{0} & \mathbf{0} \\ \vdots & \vdots & \vdots & \vdots & \ddots & \vdots & \vdots \\ \mathbf{0} & \mathbf{0} & \mathbf{0} & \mathbf{0} & \cdots & \mathbf{QB} & \mathbf{0} \\ \mathbf{0} & \mathbf{0} & \mathbf{0} & \mathbf{0} & \cdots & \mathbf{0} & \mathbf{0} \end{bmatrix}}_{\mathbf{A}} \left\{\begin{array}{c} N_1 \nabla_X \\ \mathbf{0} \\ N_2 \nabla_X \\ \mathbf{0} \\ \vdots \\ N_{n_{node}} \nabla_X \\ \mathbf{0} \end{array}\right\}$$

$$= \overline{\mathbf{d}}^{e\,\mathrm{T}}\mathbf{A}\left\{\begin{array}{c} \begin{bmatrix} \mathbf{N_1} \\ \mathbf{0} \end{bmatrix}\nabla_X \\[8pt] \begin{bmatrix} \mathbf{N_2} \\ \mathbf{0} \end{bmatrix}\nabla_X \\[8pt] . \\ . \\[4pt] \begin{bmatrix} \mathbf{N_{n_{node}}} \\ \mathbf{0} \end{bmatrix}\nabla_X \end{array}\right\}$$

$$
= \overline{\mathbf{d}}^{e^{\mathrm{T}}} \mathbf{A} \left(\begin{bmatrix} \mathbf{N_1} \\ \mathbf{0} \\ \mathbf{N_2} \\ \mathbf{0} \\ \vdots \\ \mathbf{N_{n_{node}}} \\ \mathbf{0} \end{bmatrix} \nabla_X \right)
$$

$$
= \overline{\mathbf{d}}^{e^{\mathrm{T}}} \mathbf{A} \left(\mathbf{N_u}^{\mathrm{T}} \nabla_X \right). \tag{F.1}
$$

F.2 Introduction of the interpolation of virtual rotations into $\left(\mathbf{Q}^{\mathrm{T}} \widehat{\overline{\boldsymbol{\varphi}^h}}^{\mathrm{T}} \mathbf{F} \right) : \mathbf{B}$

By using (E.12), (E.10), (E.9) and by noticing that a double-contraction product (scalar product) between a skew-symmetric and a symmetric 2nd order tenor is zero, the term $\left(\mathbf{Q}^{\mathrm{T}} \widehat{\overline{\boldsymbol{\varphi}^h}}^{\mathrm{T}} \mathbf{F} \right) : \mathbf{B}$ can be written as

$$
\left(\mathbf{Q}^{\mathrm{T}} \widehat{\overline{\boldsymbol{\varphi}^h}}^{\mathrm{T}} \mathbf{F} \right) : \mathbf{B} = \left(\widehat{\overline{\boldsymbol{\varphi}^h}}^{\mathrm{T}} \mathbf{F} \mathbf{B}^{\mathrm{T}} \right) : \mathbf{Q} = \left(\mathbf{F} \mathbf{B}^{\mathrm{T}} \mathbf{Q}^{\mathrm{T}} \right) : \widehat{\overline{\boldsymbol{\varphi}^h}} = \widehat{\overline{\boldsymbol{\varphi}^h}} : \left(\mathbf{F} \mathbf{B}^{\mathrm{T}} \mathbf{Q}^{\mathrm{T}} \right) =
$$

$$
= \widehat{\overline{\boldsymbol{\varphi}^h}} : \mathrm{skew} \left(\mathbf{F} \mathbf{B}^{\mathrm{T}} \mathbf{Q}^{\mathrm{T}} \right) = \mathrm{tr} \left(\widehat{\overline{\boldsymbol{\varphi}^h}} \, \mathrm{skew} \left(\mathbf{F} \mathbf{B}^{\mathrm{T}} \mathbf{Q}^{\mathrm{T}} \right)^{\mathrm{T}} \right) =
$$

$$
= -\mathrm{tr} \left(\widehat{\overline{\boldsymbol{\varphi}^h}} \, \mathrm{skew} \left(\mathbf{F} \mathbf{B}^{\mathrm{T}} \mathbf{Q}^{\mathrm{T}} \right) \right), \tag{F.2}
$$

where $\mathrm{skew} \left(\mathbf{F} \mathbf{B}^{\mathrm{T}} \mathbf{Q}^{\mathrm{T}} \right) = \frac{1}{2} \left(\mathbf{F} \mathbf{B}^{\mathrm{T}} \mathbf{Q}^{\mathrm{T}} - \mathbf{Q} \mathbf{B} \mathbf{F}^{\mathrm{T}} \right)$. The trace of a dot product of two skew-symmetric matrices $\hat{\mathbf{a}}$ and $\hat{\mathbf{b}}$ is equal to

$$
\mathrm{tr} \left(\hat{\mathbf{a}} \, \hat{\mathbf{b}} \right) = \mathrm{tr} \left(\begin{bmatrix} 0 & -a_3 & a_2 \\ a_3 & 0 & -a_1 \\ -a_2 & a_1 & 0 \end{bmatrix} \begin{bmatrix} 0 & -b_3 & b_2 \\ b_3 & 0 & -b_1 \\ -b_2 & b_1 & 0 \end{bmatrix} \right)
$$

$$
= \mathrm{tr} \begin{bmatrix} -a_3 b_3 - a_2 b_2 & a_2 b_1 & a_3 b_1 \\ a_1 b_2 & -a_3 b_3 - a_1 b_1 & a_3 b_2 \\ a_1 b_3 & a_2 b_3 & -a_2 b_2 - a_1 b_1 \end{bmatrix}
$$

$$
= -2(a_1 b_1 + a_2 b_2 + a_3 b_3)
$$

$$
= -2\mathbf{a} \cdot \mathbf{b}
$$

$$
= -2\mathbf{a}^{\mathrm{T}} \mathbf{b}. \tag{F.3}
$$

By introducing (F.3) into (F.2) we obtain

$$-\mathrm{tr}\left(\widehat{\overline{\boldsymbol{\varphi}^h}}\,\mathrm{skew}\left(\mathbf{F}\mathbf{B}^{\mathrm{T}}\mathbf{Q}^{\mathrm{T}}\right)\right) = 2\overline{\boldsymbol{\varphi}^h}\cdot\mathrm{ax}\left(\mathrm{skew}\left(\mathbf{F}\mathbf{B}^{\mathrm{T}}\mathbf{Q}^{\mathrm{T}}\right)\right) = 2\overline{\boldsymbol{\varphi}^h}^{\mathrm{T}}\mathrm{ax}\left(\mathrm{skew}\left(\mathbf{F}\mathbf{B}^{\mathrm{T}}\mathbf{Q}^{\mathrm{T}}\right)\right).$$
(F.4)

Finally,

$$\left(\mathbf{Q}^{\mathrm{T}}\widehat{\overline{\boldsymbol{\varphi}}}^{\mathrm{T}}\mathbf{F}\right):\mathbf{B} = 2\overline{\mathbf{d}}^{e^{\mathrm{T}}}\mathbf{N}_{\varphi}{}^{\mathrm{T}}\mathrm{ax}\left(\mathrm{skew}\left(\mathbf{F}\mathbf{B}^{\mathrm{T}}\mathbf{Q}^{\mathrm{T}}\right)\right)$$
$$= \overline{\mathbf{d}}^{e^{\mathrm{T}}}\mathbf{N}_{\varphi}{}^{\mathrm{T}}\mathrm{ax}\left(\mathbf{F}\mathbf{B}^{\mathrm{T}}\mathbf{Q}^{\mathrm{T}} - \mathbf{Q}\mathbf{B}\mathbf{F}^{\mathrm{T}}\right).$$
(F.5)

Appendix G

Linearization

G.1 Directional derivative of Q in the direction of $\widehat{\overline{\varphi}}$

We consider the orientation (or rotation) tensor $\mathbf{Q} \in \mathrm{SO}(3)$ and denote its kinematically admissible perturbation by $\widehat{\overline{\varphi}} \in \mathrm{so}(3)$ as $\left.\dfrac{\mathrm{d}}{\mathrm{d}\epsilon}\right|_{\epsilon=0} \mathbf{Q}_\epsilon = \overline{\mathbf{Q}}$. The variation of the orientation matrix is thus defined as its directional derivative in the direction of a superimposed infinitesimally small perturbation $\overline{\varphi}$, i.e.

$$
\begin{aligned}
\overline{\mathbf{Q}} &= \left.\frac{\mathrm{d}}{\mathrm{d}\epsilon}\right|_{\epsilon=0} \exp\left(\epsilon\widehat{\overline{\varphi}}\right)\mathbf{Q} \\
&= \left.\frac{\mathrm{d}}{\mathrm{d}\epsilon}\right|_{\epsilon=0} \left(\mathbf{I} + \frac{\sin\epsilon\overline{\varphi}}{\epsilon\overline{\varphi}}\epsilon\widehat{\overline{\varphi}} + \frac{1-\cos\epsilon\overline{\varphi}}{(\epsilon\overline{\varphi})^2}\epsilon^2\widehat{\overline{\varphi}}^2\right)\mathbf{Q} \\
&= \left.\left(\cos(\epsilon\overline{\varphi})\widehat{\overline{\varphi}} + \frac{\sin(\epsilon\overline{\varphi})}{\overline{\varphi}}\widehat{\overline{\varphi}}^2\right)\mathbf{Q}\,\right|_{\epsilon=0} \\
&= \widehat{\overline{\varphi}}\mathbf{Q}
\end{aligned}
\tag{G.1}
$$

G.2 Directional derivative of Q in the direction of $\widehat{\Delta\varphi}$

$$
\begin{aligned}
\Delta\mathbf{Q} &= \left.\frac{\mathrm{d}}{\mathrm{d}\epsilon}\right|_{\epsilon=0} \exp\left(\epsilon\widehat{\Delta\varphi}\right)\mathbf{Q} \\
&= \left.\frac{\mathrm{d}}{\mathrm{d}\epsilon}\right|_{\epsilon=0} \left(\mathbf{I} + \frac{\sin(\epsilon\Delta\varphi)}{\epsilon\Delta\varphi}\epsilon\widehat{\Delta\varphi} + \frac{1-\cos(\epsilon\Delta\varphi)}{(\epsilon\Delta\varphi)^2}\epsilon^2\widehat{\Delta\varphi}^2\right)\mathbf{Q} \\
&= \left.\left(\cos(\epsilon\Delta\varphi)\widehat{\Delta\varphi} + \frac{\sin((\epsilon\Delta\varphi))}{\Delta\varphi}\widehat{\Delta\varphi}^2\right)\mathbf{Q}\,\right|_{\epsilon=0} \\
&= \widehat{\Delta\varphi}\mathbf{Q}.
\end{aligned}
\tag{G.2}
$$

G.3 Directional derivative of **F** in the direction of Δ**u**

$$
\begin{aligned}
\Delta \mathbf{F} &= \left.\frac{\mathrm{d}}{\mathrm{d}\epsilon}\right|_{\epsilon=0} \mathbf{F}\left(\mathbf{u} + \epsilon \Delta \mathbf{u}\right) \\
&= \left.\frac{\mathrm{d}}{\mathrm{d}\epsilon}\right|_{\epsilon=0} \left(\mathrm{GRAD}\left(\epsilon \Delta \mathbf{u}\right) + \mathbf{I}\right) \\
&= \left.\frac{\mathrm{d}}{\mathrm{d}\epsilon}\right|_{\epsilon=0} \left(\left(\epsilon \Delta \mathbf{u}\right) \otimes \nabla_X + \mathbf{I}\right) \\
&= \mathrm{GRAD}\Delta \mathbf{u}
\end{aligned}
\tag{G.3}
$$

G.4 Directional derivative of **E** in the direction of Δ**u** and $\widehat{\Delta\varphi}$

$$
\begin{aligned}
\Delta \mathbf{E} &= \left.\frac{\mathrm{d}}{\mathrm{d}\epsilon}\right|_{\epsilon=0} \mathbf{E}_\epsilon \\
&= \left.\frac{\mathrm{d}}{\mathrm{d}\epsilon}\right|_{\epsilon=0} \mathbf{E}\left(\mathbf{u} + \epsilon \Delta \mathbf{u}, \; \exp(\epsilon \widehat{\Delta\varphi})\mathbf{Q}\right) \\
&= \left.\frac{\mathrm{d}}{\mathrm{d}\epsilon}\right|_{\epsilon=0} \left(\mathbf{Q}^{\mathrm{T}}\mathbf{F} - \mathbf{I}\right)_\epsilon \\
&= \left.\frac{\mathrm{d}}{\mathrm{d}\epsilon}\right|_{\epsilon=0} \mathbf{Q}_\epsilon^{\mathrm{T}}\mathbf{F} + \mathbf{Q}^{\mathrm{T}} \left.\frac{\mathrm{d}}{\mathrm{d}\epsilon}\right|_{\epsilon=0} \mathbf{F}_\epsilon \\
&= \mathbf{Q}^{\mathrm{T}}\left(\widehat{\Delta\varphi}^{\mathrm{T}}\mathbf{F} + \mathrm{GRAD}\Delta \mathbf{u}\right)
\end{aligned}
\tag{G.4}
$$

G.5 Directional derivative of **K** in the direction of $\widehat{\Delta\varphi}$

The curvature matrix has been derived in (4.103) as:

$$
\mathbf{K} = -\frac{1}{2}\epsilon : \left(\mathbf{Q}^{\mathrm{T}}\mathrm{GRAD}\mathbf{Q}\right),
\tag{G.5}
$$

where each column represents a curvature vector $\mathbf{K}_i$ such that $\mathbf{K}_i = \mathbf{K}\mathbf{E}_i = \mathrm{ax}\left(\mathbf{Q}^{\mathrm{T}}\dfrac{\partial \mathbf{Q}}{\partial X_i}\right)$. The directional derivative of $\mathbf{K}_i$ is equal to

$$
\left.\frac{\mathrm{d}}{\mathrm{d}\epsilon}\right|_{\epsilon=0} \mathbf{K}_i\left(\exp(\epsilon\widehat{\Delta\varphi})\mathbf{Q}\right) = \left.\frac{\mathrm{d}}{\mathrm{d}\epsilon}\right|_{\epsilon=0} \left(\mathbf{K}_i\right)_\epsilon
$$

$$
= \left.\frac{\mathrm{d}}{\mathrm{d}\epsilon}\right|_{\epsilon=0} \mathrm{ax}\left(\mathbf{Q}^{\mathrm{T}}\frac{\partial \mathbf{Q}}{\partial X_i}\right)_{\epsilon}
$$

$$
= \mathrm{ax}\left(\left.\frac{\mathrm{d}}{\mathrm{d}\epsilon}\right|_{\epsilon=0}\mathbf{Q}_{\epsilon}^{\mathrm{T}}\frac{\partial \mathbf{Q}}{\partial X_i} + \mathbf{Q}^{\mathrm{T}}\left.\frac{\mathrm{d}}{\mathrm{d}\epsilon}\right|_{\epsilon=0}\frac{\partial \mathbf{Q}_{\epsilon}}{\partial X_i}\right)
$$

$$
= \mathrm{ax}\left(\mathbf{Q}^{\mathrm{T}}\widehat{\Delta\boldsymbol{\varphi}}^{\mathrm{T}}\frac{\partial \mathbf{Q}}{\partial X_i} + \mathbf{Q}^{\mathrm{T}}\frac{\partial}{\partial X_i}(\widehat{\Delta\boldsymbol{\varphi}}\mathbf{Q})\right)
$$

$$
= \mathrm{ax}\left(\mathbf{Q}^{\mathrm{T}}\left(\widehat{\Delta\boldsymbol{\varphi}}^{\mathrm{T}}\frac{\partial \mathbf{Q}}{\partial X_i} + \frac{\partial}{\partial X_i}(\widehat{\Delta\boldsymbol{\varphi}}\mathbf{Q})\right)\right). \tag{G.6}
$$

Since $\dfrac{\partial}{\partial X_i}(\widehat{\Delta\boldsymbol{\varphi}}\mathbf{Q}) = \dfrac{\partial\widehat{\Delta\boldsymbol{\varphi}}}{\partial X_i}\mathbf{Q} + \widehat{\Delta\boldsymbol{\varphi}}\dfrac{\partial \mathbf{Q}}{\partial X_i} \Rightarrow -\widehat{\Delta\boldsymbol{\varphi}}\dfrac{\partial \mathbf{Q}}{\partial X_i} = \dfrac{\partial\widehat{\Delta\boldsymbol{\varphi}}}{\partial X_i}\mathbf{Q} - \dfrac{\partial}{\partial X_i}(\widehat{\Delta\boldsymbol{\varphi}}\mathbf{Q})$ and $\widehat{\Delta\boldsymbol{\varphi}}^{\mathrm{T}} = -\widehat{\Delta\boldsymbol{\varphi}}$ (G.6) can be written as

$$
\left.\frac{\mathrm{d}}{\mathrm{d}\epsilon}\right|_{\epsilon=0}(\mathbf{K}_i)_{\epsilon} = \mathrm{ax}\left(\mathbf{Q}^{\mathrm{T}}\left(-\widehat{\Delta\boldsymbol{\varphi}}\frac{\partial \mathbf{Q}}{\partial X_i} + \frac{\partial}{\partial X_i}(\widehat{\Delta\boldsymbol{\varphi}}\mathbf{Q})\right)\right)
$$

$$
= \mathrm{ax}\left(\mathbf{Q}^{\mathrm{T}}\left(\frac{\partial\widehat{\Delta\boldsymbol{\varphi}}}{\partial X_i}\mathbf{Q} - \frac{\partial}{\partial X_i}(\widehat{\Delta\boldsymbol{\varphi}}\mathbf{Q}) + \frac{\partial}{\partial X_i}(\widehat{\Delta\boldsymbol{\varphi}}\mathbf{Q})\right)\right)
$$

$$
= \mathrm{ax}\left(\mathbf{Q}^{\mathrm{T}}\frac{\partial\widehat{\Delta\boldsymbol{\varphi}}}{\partial X_i}\mathbf{Q}\right). \tag{G.7}
$$

By recognizing that $\widehat{\mathbf{Q}\mathbf{v}} = \mathbf{Q}\hat{\mathbf{v}}\mathbf{Q}^{\mathrm{T}} \ \forall \ \mathbf{v} \in \mathbb{R}^3$, i.e. $\mathbf{Q}^{\mathrm{T}}\widehat{\dfrac{\partial\Delta\boldsymbol{\varphi}}{\partial X_i}} = \mathbf{Q}^{\mathrm{T}}\dfrac{\partial\widehat{\Delta\boldsymbol{\varphi}}}{\partial X_i}\mathbf{Q}$ and introducing it into (G.7) we obtain

$$
\left.\frac{\mathrm{d}}{\mathrm{d}\epsilon}\right|_{\epsilon=0}(\mathbf{K}_i)_{\epsilon} = \mathrm{ax}\left(\mathbf{Q}^{\mathrm{T}}\frac{\partial\widehat{\Delta\boldsymbol{\varphi}}}{\partial X_i}\mathbf{Q}\right)
$$

$$
= \mathrm{ax}\left(\widehat{\mathbf{Q}^{\mathrm{T}}\frac{\partial\Delta\boldsymbol{\varphi}}{\partial X_i}}\right)
$$

$$
= \mathbf{Q}^{\mathrm{T}}\frac{\partial\Delta\boldsymbol{\varphi}}{\partial X_i} \tag{G.8}
$$

In order to obtain the directional derivative of the whole curvature matrix, we recognise that $\mathbf{K} = \mathbf{K}_i \otimes \mathbf{E}_i$ from where it follows

$$
\Delta\mathbf{K} = \left.\frac{\mathrm{d}}{\mathrm{d}\epsilon}\right|_{\epsilon=0}\mathbf{K}_{\epsilon}
$$

$$
= \left.\frac{\mathrm{d}}{\mathrm{d}\epsilon}\right|_{\epsilon=0}(\mathbf{K}_i)_{\epsilon} \otimes \mathbf{E}_i
$$

$$
= \mathbf{Q}^{\mathrm{T}}\frac{\partial\Delta\boldsymbol{\varphi}}{\partial X_i} \otimes \mathbf{E}_i
$$

$$
= \mathbf{Q}^{\mathrm{T}}\mathrm{GRAD}\,\Delta\boldsymbol{\varphi} \tag{G.9}
$$

G.6 Directional derivative of B in the direction of $\Delta\mathbf{u}$ and $\widehat{\Delta\varphi}$

$$
\begin{aligned}
\Delta\mathbf{B} &= \left.\frac{\mathrm{d}}{\mathrm{d}\epsilon}\right|_{\epsilon=0} \mathbf{B}_\epsilon \\
&= \left.\frac{\mathrm{d}}{\mathrm{d}\epsilon}\right|_{\epsilon=0} \mathbf{B}\left(\mathbf{u}+\epsilon\Delta\mathbf{u},\ \exp(\epsilon\widehat{\Delta\varphi})\mathbf{Q}\right) \\
&= \left.\frac{\mathrm{d}}{\mathrm{d}\epsilon}\right|_{\epsilon=0} (\mathbf{T}:\mathbf{E})_\epsilon \\
&= \mathbf{T}:\left.\frac{\mathrm{d}}{\mathrm{d}\epsilon}\right|_{\epsilon=0} \mathbf{E}_\epsilon \\
&= \mathbf{T}:\mathbf{Q}^{\mathrm{T}}\left(\widehat{\Delta\varphi}^{\mathrm{T}}\mathbf{F}+\mathrm{GRAD}\Delta\mathbf{u}\right)
\end{aligned}
\tag{G.10}
$$

G.7 Directional derivative of G in the direction of $\widehat{\Delta\varphi}$

$$
\begin{aligned}
\Delta\mathbf{G} &= \left.\frac{\mathrm{d}}{\mathrm{d}\epsilon}\right|_{\epsilon=0} \mathbf{G}_\epsilon \\
&= \left.\frac{\mathrm{d}}{\mathrm{d}\epsilon}\right|_{\epsilon=0} (\mathbf{D}:\mathbf{K})_\epsilon \\
&= \mathbf{D}:\mathbf{Q}^{\mathrm{T}}\mathrm{GRAD}\Delta\varphi
\end{aligned}
\tag{G.11}
$$

G.8 Directional derivative of A in the direction of $\Delta\mathbf{u}$ and $\widehat{\Delta\varphi}$

The directional derivative of the block matrix $\mathbf{A}$ derived in (5.6) is equal to

$$
\begin{aligned}
\Delta\mathbf{A} &= \left.\frac{\mathrm{d}}{\mathrm{d}\epsilon}\right|_{\epsilon=0} \mathbf{A}_\epsilon \\
&= \left.\frac{\mathrm{d}}{\mathrm{d}\epsilon}\right|_{\epsilon=0} \mathbf{A}\left(\mathbf{u}+\epsilon\Delta\mathbf{u},\ \exp(\epsilon\widehat{\Delta\varphi})\mathbf{Q}\right)
\end{aligned}
$$

$$
=
\begin{bmatrix}
\left.\dfrac{\mathrm{d}}{\mathrm{d}\epsilon}\right|_{\epsilon=0}(\mathbf{QB})_\epsilon & \mathbf{0} & \mathbf{0} & \mathbf{0} & \cdots & \mathbf{0} & \mathbf{0} \\
\mathbf{0} & \mathbf{0} & \mathbf{0} & \mathbf{0} & \cdots & \mathbf{0} & \mathbf{0} \\
\mathbf{0} & \mathbf{0} & \left.\dfrac{\mathrm{d}}{\mathrm{d}\epsilon}\right|_{\epsilon=0}(\mathbf{QB})_\epsilon & \mathbf{0} & \cdots & \mathbf{0} & \mathbf{0} \\
\mathbf{0} & \mathbf{0} & \mathbf{0} & \mathbf{0} & \cdots & \mathbf{0} & \mathbf{0} \\
\vdots & \vdots & \vdots & \vdots & \ddots & \vdots & \vdots \\
\mathbf{0} & \mathbf{0} & \mathbf{0} & \mathbf{0} & \cdots & \left.\dfrac{\mathrm{d}}{\mathrm{d}\epsilon}\right|_{\epsilon=0}(\mathbf{QB})_\epsilon & \mathbf{0} \\
\mathbf{0} & \mathbf{0} & \mathbf{0} & \mathbf{0} & \cdots & \mathbf{0} & \mathbf{0}
\end{bmatrix}
\tag{G.12}
$$

where the directional derivative of the product $\mathbf{QB}$ is equal to

$$
\begin{aligned}
\left.\frac{\mathrm{d}}{\mathrm{d}\epsilon}\right|_{\epsilon=0}(\mathbf{QB})_\epsilon &= \left.\frac{\mathrm{d}}{\mathrm{d}\epsilon}\right|_{\epsilon=0}\mathbf{Q}_\epsilon\mathbf{B} + \mathbf{Q}\left.\frac{\mathrm{d}}{\mathrm{d}\epsilon}\right|_{\epsilon=0}\mathbf{B}_\epsilon \\
&= \widehat{\Delta\boldsymbol{\varphi}}\,\mathbf{QB} + \mathbf{Q}\,(\mathbf{T}:\Delta\mathbf{E}) \\
&= \widehat{\Delta\boldsymbol{\varphi}}\,\mathbf{Q}\left(\mathbf{T}:(\mathbf{Q}^{\mathrm{T}}\mathbf{F}-\mathbf{I})\right) + \mathbf{Q}\left(\mathbf{T}:\left(\mathbf{Q}^{\mathrm{T}}\left(\widehat{\Delta\boldsymbol{\varphi}}^{\mathrm{T}}\mathbf{F}+\mathrm{GRAD}\Delta\mathbf{u}\right)\right)\right).
\end{aligned}
\tag{G.13}
$$

G.9   Directional derivative of L in the direction of $\widehat{\Delta\boldsymbol{\varphi}}$

The directional derivative of the block matrix $\mathbf{L}$ derived in (5.8) is equal to

$$
\begin{aligned}
\Delta\mathbf{L} &= \left.\frac{\mathrm{d}}{\mathrm{d}\epsilon}\right|_{\epsilon=0}\mathbf{L}_\epsilon \\
&= \left.\frac{\mathrm{d}}{\mathrm{d}\epsilon}\right|_{\epsilon=0}\mathbf{L}\left(\exp(\epsilon\widehat{\Delta\boldsymbol{\varphi}})\mathbf{Q}\right) \\
&=
\begin{bmatrix}
\mathbf{0} & \mathbf{0} & \mathbf{0} & \mathbf{0} & \cdots & \mathbf{0} & \mathbf{0} \\
\mathbf{0} & \left.\dfrac{\mathrm{d}}{\mathrm{d}\epsilon}\right|_{\epsilon=0}(\mathbf{QG})_\epsilon & \mathbf{0} & \mathbf{0} & \cdots & \mathbf{0} & \mathbf{0} \\
\mathbf{0} & \mathbf{0} & \mathbf{0} & \mathbf{0} & \cdots & \mathbf{0} & \mathbf{0} \\
\mathbf{0} & \mathbf{0} & \mathbf{0} & \left.\dfrac{\mathrm{d}}{\mathrm{d}\epsilon}\right|_{\epsilon=0}(\mathbf{QG})_\epsilon & \cdots & \mathbf{0} & \mathbf{0} \\
\vdots & \vdots & \vdots & \vdots & \ddots & \vdots & \vdots \\
\mathbf{0} & \mathbf{0} & \mathbf{0} & \mathbf{0} & \cdots & \mathbf{0} & \mathbf{0} \\
\mathbf{0} & \mathbf{0} & \mathbf{0} & \mathbf{0} & \cdots & \mathbf{0} & \left.\dfrac{\mathrm{d}}{\mathrm{d}\epsilon}\right|_{\epsilon=0}(\mathbf{QG})_\epsilon
\end{bmatrix}
\end{aligned}
\tag{G.14}
$$

where the directional derivative of the product $\mathbf{QG}$ is equal to

$$
\left.\frac{\mathrm{d}}{\mathrm{d}\epsilon}\right|_{\epsilon=0}(\mathbf{QG})_\epsilon = \left.\frac{\mathrm{d}}{\mathrm{d}\epsilon}\right|_{\epsilon=0}\mathbf{Q}_\epsilon\mathbf{G} + \mathbf{Q}\left.\frac{\mathrm{d}}{\mathrm{d}\epsilon}\right|_{\epsilon=0}\mathbf{G}_\epsilon
$$

$$= \widehat{\Delta \varphi} \mathbf{Q} \mathbf{G} + \mathbf{Q} \left(\mathbf{D} : \Delta \mathbf{K} \right)$$

$$= \widehat{\Delta \varphi} \mathbf{Q} \left(\mathbf{D} : \left(-\frac{1}{2} \epsilon : \left(\mathbf{Q}^{\mathrm{T}} \mathrm{GRAD} \mathbf{Q} \right) \right) \right) + \mathbf{Q} \left(\mathbf{D} : \left(\mathbf{Q}^{\mathrm{T}} \mathrm{GRAD} \Delta \varphi \right) \right).$$

$$\text{(G.15)}$$

G.10 Linearized residual $\Delta \mathbf{g}$

In order to derive the linearized residual, the directional derivatives derived in (G.1)-(G.9) are used.

G.10.1 Term $\left. \dfrac{\mathrm{d}}{\mathrm{d}\epsilon} \right|_{\epsilon=0} \left(\mathbf{A} \, \left(\mathbf{N_u}^{\mathbf{T}} \nabla_X \right) \right)_{\epsilon}$

$$\mathbf{A} \left(\mathbf{N_u}^{\mathrm{T}} \nabla_X \right) = \left\{ \begin{array}{c} \mathbf{Q} \mathbf{B} (N_1 \nabla_X) \\ \mathbf{0} \\ \mathbf{Q} \mathbf{B} (N_2 \nabla_X) \\ \mathbf{0} \\ \vdots \\ \mathbf{Q} \mathbf{B} (N_{n_{node}} \nabla_X) \\ \mathbf{0} \end{array} \right\}, \qquad \text{(G.16)}$$

Since from (G.13) $\left. \dfrac{\mathrm{d}}{\mathrm{d}\epsilon} \right|_{\epsilon=0} (\mathbf{Q} \mathbf{B})_{\epsilon} = \widehat{\Delta \varphi} \mathbf{Q} \mathbf{B} + \mathbf{Q} \left(\mathbf{T} : \Delta \mathbf{E} \right)$ we obtain

$$\left. \frac{\mathrm{d}}{\mathrm{d}\epsilon} \right|_{\epsilon=0} \left(\mathbf{A} \, \left(\mathbf{N_u}^{\mathrm{T}} \nabla_X \right) \right)_{\epsilon} = \left\{ \begin{array}{c} \left(\widehat{\Delta \varphi} \mathbf{Q} \mathbf{B} + \mathbf{Q} \left(\mathbf{T} : \Delta \mathbf{E} \right) \right) (N_1 \nabla_X) \\ \mathbf{0} \\ \left(\widehat{\Delta \varphi} \mathbf{Q} \mathbf{B} + \mathbf{Q} \left(\mathbf{T} : \Delta \mathbf{E} \right) \right) (N_2 \nabla_X) \\ \mathbf{0} \\ \vdots \\ \left(\widehat{\Delta \varphi} \mathbf{Q} \mathbf{B} + \mathbf{Q} \left(\mathbf{T} : \Delta \mathbf{E} \right) \right) (N_{n_{node}} \nabla_X) \\ \mathbf{0} \end{array} \right\} \qquad \text{(G.17)}$$

$$
= \left\{ \begin{array}{c} \widehat{\Delta\varphi}\mathbf{QB}(N_1\nabla_X) \\ \mathbf{0} \\ \widehat{\Delta\varphi}\mathbf{QB}(N_2\nabla_X) \\ \mathbf{0} \\ \vdots \\ \widehat{\Delta\varphi}\mathbf{QB}(N_{n_{node}}\nabla_X) \\ \mathbf{0} \end{array} \right\} + \left\{ \begin{array}{c} \mathbf{Q}\left(\mathbf{T}:\Delta\mathbf{E}\right)(N_1\nabla_X) \\ \mathbf{0} \\ \mathbf{Q}\left(\mathbf{T}:\Delta\mathbf{E}\right)(N_2\nabla_X) \\ \mathbf{0} \\ \vdots \\ \mathbf{Q}\left(\mathbf{T}:\Delta\mathbf{E}\right)(N_{n_{node}}\nabla_X) \\ \mathbf{0} \end{array} \right\}.
$$

$$(G.18)$$

By using $\widehat{\mathbf{a}}\,\mathbf{b} = -\widehat{\mathbf{b}}\,\mathbf{a}$, the term $\widehat{\Delta\varphi}\mathbf{QB}(N_i\nabla_X)$ can be written as $-\widehat{\mathbf{QB}(N_i\nabla_X)}\Delta\varphi$. In order to manipulate the term $\mathbf{Q}\left(\mathbf{T}:\Delta\mathbf{E}\right)(N_i\nabla_X)$, we substitute $\mathbf{T} = \lambda\,\mathbf{I}\otimes\mathbf{I} + (\mu+\nu)\boldsymbol{\mathcal{I}} + (\mu-\nu)\boldsymbol{\mathcal{I}}^{\mathrm{T}}$ and obtain:

$$
\begin{aligned}
\mathbf{Q}\left(\mathbf{T}:\Delta\mathbf{E}\right)(N_i\nabla_X) &= \mathbf{Q}\left(\left(\lambda\,\mathbf{I}\otimes\mathbf{I} + (\mu+\nu)\boldsymbol{\mathcal{I}} + (\mu-\nu)\boldsymbol{\mathcal{I}}^{\mathrm{T}}\right):\Delta\mathbf{E}\right)(N_i\nabla_X) \\
&= \mathbf{Q}\left(\lambda\,\underbrace{\mathbf{I}\otimes\mathbf{I}:\Delta\mathbf{E}}_{\mathrm{tr}(\Delta\mathbf{E})\mathbf{I}} + (\mu+\nu)\underbrace{\boldsymbol{\mathcal{I}}:\Delta\mathbf{E}}_{\Delta\mathbf{E}} + (\mu-\nu)\underbrace{\boldsymbol{\mathcal{I}}^{\mathrm{T}}:\Delta\mathbf{E}}_{\Delta\mathbf{E}^{\mathrm{T}}}\right)(N_i\nabla_X) \\
&= \lambda\mathbf{Q}\mathrm{tr}(\Delta\mathbf{E})\underbrace{\mathbf{I}\,(N_i\nabla_X)}_{N_i\nabla_X} + (\mu+\nu)\mathbf{Q}\Delta\mathbf{E}\,(N_i\nabla_X) + (\mu-\nu)\mathbf{Q}\Delta\mathbf{E}^{\mathrm{T}}\,(N_i\nabla_X) \\
&= \lambda\mathbf{Q}\mathrm{tr}(\Delta\mathbf{E})\,(N_i\nabla_X) + (\mu+\nu)\mathbf{Q}\Delta\mathbf{E}\,(N_i\nabla_X) + (\mu-\nu)\mathbf{Q}\Delta\mathbf{E}^{\mathrm{T}}\,(N_i\nabla_X) \\
&= \lambda\mathbf{Q}\,(N_i\nabla_X)\,\mathrm{tr}(\Delta\mathbf{E}) + (\mu+\nu)\mathbf{Q}\Delta\mathbf{E}\,(N_i\nabla_X) + (\mu-\nu)\mathbf{Q}\Delta\mathbf{E}^{\mathrm{T}}\,(N_i\nabla_X).
\end{aligned}
$$

$$(G.19)$$

The three terms in this equation will be now analysed separately.

G.10.1.1 $\quad \lambda\mathbf{tr}(\Delta\mathbf{E})\mathbf{Q}\,(N_i\nabla_X)$

Using (G.4) we have

$$
\begin{aligned}
\mathrm{tr}(\Delta\mathbf{E}) &= \mathrm{tr}\left(\mathbf{Q}^{\mathrm{T}}\left(\widehat{\Delta\varphi}^{\mathrm{T}}\mathbf{F} + \mathrm{GRAD}\Delta\mathbf{u}\right)\right) \\
&= \mathrm{tr}\left(\mathbf{Q}^{\mathrm{T}}\widehat{\Delta\varphi}^{\mathrm{T}}\mathbf{F}\right) + \mathrm{tr}\left(\mathbf{Q}^{\mathrm{T}}\mathrm{GRAD}\Delta\mathbf{u}\right),
\end{aligned}
$$

$$(G.20)$$

with

$$
\begin{aligned}
\mathrm{tr}\left(\mathbf{Q}^{\mathrm{T}}\widehat{\Delta\varphi}^{\mathrm{T}}\mathbf{F}\right) &= \mathbf{Q}^{\mathrm{T}}\widehat{\Delta\varphi}^{\mathrm{T}}:\mathbf{F}^{\mathrm{T}} = \widehat{\Delta\varphi}^{\mathrm{T}}\mathbf{F}:\mathbf{Q} = \mathbf{F}\mathbf{Q}^{\mathrm{T}}:\widehat{\Delta\varphi} = \mathrm{skew}(\mathbf{F}\mathbf{Q}^{\mathrm{T}}):\widehat{\Delta\varphi} = \\
&= \mathrm{tr}(\mathrm{skew}(\mathbf{F}\mathbf{Q}^{\mathrm{T}})\widehat{\Delta\varphi}^{\mathrm{T}}) = -\mathrm{tr}(\mathrm{skew}(\mathbf{F}\mathbf{Q}^{\mathrm{T}})\widehat{\Delta\varphi}) = 2\left[\mathrm{ax}(\mathrm{skew}(\mathbf{F}\mathbf{Q}^{\mathrm{T}}))\right]^{\mathrm{T}}\Delta\varphi,
\end{aligned}
$$

$$(G.21)$$

and

$$\mathrm{tr}\left(\mathbf{Q}^{\mathrm{T}}\mathrm{GRAD}\Delta\mathbf{u}\right) = \mathrm{tr}\left(\mathbf{Q}^{\mathrm{T}}\left(\Delta\mathbf{u}\otimes\nabla_X\right)\right) = \mathrm{tr}\left(\mathbf{Q}^{\mathrm{T}}\left(\Delta\mathbf{u}\nabla_X^{\mathrm{T}}\right)\right) = \nabla_X\cdot(\mathbf{Q}^{\mathrm{T}}\Delta\mathbf{u}) = \nabla_X^{\mathrm{T}}\mathbf{Q}^{\mathrm{T}}\Delta\mathbf{u},$$
(G.22)

where ∇_X^{T} in (G.22) operates exclusively on $\Delta\mathbf{u}$. Finally, we obtain for the first term in (G.19)

$$\lambda\mathrm{tr}(\Delta\mathbf{E})\mathbf{Q}\left(N_i\nabla_X\right) = \left(2\left[\mathrm{ax}(\mathrm{skew}(\mathbf{F}\mathbf{Q}^{\mathrm{T}}))\right]^{\mathrm{T}}\Delta\boldsymbol{\varphi} + \nabla_X^{\mathrm{T}}\mathbf{Q}^{\mathrm{T}}\Delta\mathbf{u}\right)\lambda\mathbf{Q}\left(N_i\nabla_X\right).$$
(G.23)

G.10.1.2 $(\mu + \nu)\mathbf{Q}\Delta\mathbf{E}\left(N_i\nabla_X\right)$

$$\begin{aligned}
(\mu + \nu)\mathbf{Q}\Delta\mathbf{E}(N_i\nabla_X) &= (\mu + \nu)\underbrace{\mathbf{Q}\mathbf{Q}^{\mathrm{T}}}_{\mathbf{I}}\left(\widehat{\Delta\boldsymbol{\varphi}}^{\mathrm{T}}\mathbf{F} + \mathrm{GRAD}\Delta\mathbf{u}\right)(N_i\nabla_X) \\
&= (\mu + \nu)\widehat{\Delta\boldsymbol{\varphi}}^{\mathrm{T}}\mathbf{F}(N_i\nabla_X) + (\mu + \nu)\mathrm{GRAD}\Delta\mathbf{u}(N_i\nabla_X) \\
&= -(\mu + \nu)\widehat{\Delta\boldsymbol{\varphi}}\mathbf{F}(N_i\nabla_X) + (\mu + \nu)(\Delta\mathbf{u}\otimes\nabla_X)(N_i\nabla_X) \\
&= (\mu + \nu)\widehat{\mathbf{F}(N_i\nabla_X)}\Delta\boldsymbol{\varphi} + (\mu + \nu)(\Delta\mathbf{u}\underbrace{\nabla_X^{\mathrm{T}})(N_i\nabla_X)}_{\mathrm{scalar}} \\
&= (\mu + \nu)\widehat{\mathbf{F}(N_i\nabla_X)}\Delta\boldsymbol{\varphi} + (\mu + \nu)\nabla_X^{\mathrm{T}}(N_i\nabla_X)\Delta\mathbf{u},
\end{aligned}$$
(G.24)

where ∇_X^{T} in (G.24) operates exclusively on $\Delta\mathbf{u}$.

G.10.1.3 $(\mu - \nu)\mathbf{Q}\Delta\mathbf{E}^{\mathbf{T}}(N_i\nabla_X)$

$$\begin{aligned}
(\mu - \nu)\mathbf{Q}\Delta\mathbf{E}^{\mathrm{T}}(N_i\nabla_X) &= (\mu - \nu)\mathbf{Q}\left(\mathbf{F}^{\mathrm{T}}\widehat{\Delta\boldsymbol{\varphi}} + (\Delta\mathbf{u}\otimes\nabla_X)^{\mathrm{T}}\right)\mathbf{Q}(N_i\nabla_X) \\
&= (\mu - \nu)\mathbf{Q}\mathbf{F}^{\mathrm{T}}\widehat{\Delta\boldsymbol{\varphi}}\mathbf{Q}(N_i\nabla_X) + (\mu - \nu)\mathbf{Q}(\nabla_X\otimes\Delta\mathbf{u})\mathbf{Q}(N_i\nabla_X) \\
&= -(\mu - \nu)\mathbf{Q}\mathbf{F}^{\mathrm{T}}\widehat{\mathbf{Q}(N_i\nabla_X)}\Delta\boldsymbol{\varphi} + (\mu - \nu)\mathbf{Q}\nabla_X\underbrace{\Delta\mathbf{u}^{\mathrm{T}}\mathbf{Q}}_{\mathbf{a}^{\mathrm{T}}}\underbrace{(N_i\nabla_X)}_{\mathbf{b}} \\
&= -(\mu - \nu)\mathbf{Q}\mathbf{F}^{\mathrm{T}}\widehat{\mathbf{Q}(N_i\nabla_X)}\Delta\boldsymbol{\varphi} + (\mu - \nu)\mathbf{Q}\nabla_X\underbrace{(N_i\nabla_X)^{\mathrm{T}}}_{\mathbf{b}^{\mathrm{T}}}\underbrace{\mathbf{Q}^{\mathrm{T}}\Delta\mathbf{u}}_{\mathbf{a}} \\
&= -(\mu - \nu)\mathbf{Q}\mathbf{F}^{\mathrm{T}}\widehat{\mathbf{Q}(N_i\nabla_X)}\Delta\boldsymbol{\varphi} + (\mu - \nu)\mathbf{Q}\nabla_X(N_i\nabla_X)^{\mathrm{T}}\mathbf{Q}^{\mathrm{T}}\Delta\mathbf{u},
\end{aligned}$$
(G.25)

where ∇_X in (G.25) operates exclusively on $\Delta\mathbf{u}$. Finally, substituting (G.23)-(G.25) in (G.19) and the result in (G.18) for each subvector we obtain

$$\left(\widehat{\Delta\boldsymbol{\varphi}}\mathbf{Q}\mathbf{B} + \mathbf{Q}\left(\mathbf{T}:\Delta\mathbf{E}\right)\right)\left(N_i\nabla_X\right)$$

$$= -\widehat{\mathbf{QB}(N_i\nabla_X)}\Delta\boldsymbol{\varphi} + \lambda\mathbf{Q}(N_i\nabla_X)\left(2\left[\mathrm{ax}(\mathrm{skew}(\mathbf{FQ}^{\mathrm{T}}))\right]^{\mathrm{T}}\Delta\boldsymbol{\varphi} + \nabla_X^{\mathrm{T}}\mathbf{Q}^{\mathrm{T}}\Delta\mathbf{u}\right)$$

$$+ (\mu+\nu)\widehat{\mathbf{F}(N_i\nabla_X)}\Delta\boldsymbol{\varphi} + (\mu+\nu)\nabla_X^{\mathrm{T}}(N_i\nabla_X)\Delta\mathbf{u} - (\mu-\nu)\mathbf{QF}^{\mathrm{T}}\widehat{\mathbf{Q}(N_i\nabla_X)}\Delta\boldsymbol{\varphi}$$

$$+ (\mu-\nu)\mathbf{Q}\nabla_X(N_i\nabla_X)^{\mathrm{T}}\mathbf{Q}^{\mathrm{T}}\Delta\mathbf{u}, \tag{G.26}$$

i.e.

$$\left(\widehat{\Delta\boldsymbol{\varphi}}\mathbf{QB} + \mathbf{Q}\left(\mathbf{T}:\Delta\mathbf{E}\right)\right)(N_i\nabla_X)$$

$$= \left(\lambda\mathbf{Q}(N_i\nabla_X)\nabla_X^{\mathrm{T}}\mathbf{Q}^{\mathrm{T}} + (\mu+\nu)\nabla_X^{\mathrm{T}}(N_i\nabla_X)\mathbf{I} + (\mu-\nu)\mathbf{Q}\nabla_X(N_i\nabla_X)^{\mathrm{T}}\mathbf{Q}^{\mathrm{T}}\right)\Delta\mathbf{u}$$

$$+ \left(-\widehat{\mathbf{QB}(N_i\nabla_X)} + \lambda\mathbf{Q}(N_i\nabla_X)2\left[\mathrm{ax}(\mathrm{skew}(\mathbf{FQ}^{\mathrm{T}}))\right]^{\mathrm{T}} + (\mu+\nu)\widehat{\mathbf{F}(N_i\nabla_X)}\right.$$

$$\left. -(\mu-\nu)\mathbf{QF}^{\mathrm{T}}\widehat{\mathbf{Q}(N_i\nabla_X)}\right)\Delta\boldsymbol{\varphi}, \tag{G.27}$$

where free ∇_X in the factor multiplying $\Delta\mathbf{u}$ operates only on $\Delta\mathbf{u}$.

G.10.2   Term $\left.\dfrac{\mathrm{d}}{\mathrm{d}\epsilon}\right|_{\epsilon=0}\left(\mathbf{L}\ \left(\mathbf{N_\varphi}^{\mathrm{T}}\nabla_X\right)\right)_\epsilon$

The term $\mathbf{L}\ \left(\mathbf{N_\varphi}^{\mathrm{T}}\nabla_X\right)$ is derived in (5.7) as

$$\mathbf{L}\left(\mathbf{N_\varphi}^{\mathrm{T}}\nabla_X\right) = \left\{\begin{array}{c} \mathbf{0} \\ \mathbf{QG}(N_1\nabla_X) \\ \mathbf{0} \\ \mathbf{QG}(N_2\nabla_X) \\ \mathbf{0} \\ \vdots \\ \mathbf{0} \\ \mathbf{QG}(N_{n_{node}}\nabla_X) \end{array}\right\}. \tag{G.28}$$

Since from (G.15)

$$\left.\frac{\mathrm{d}}{\mathrm{d}\epsilon}\right|_{\epsilon=0}(\mathbf{QG})_\epsilon = \widehat{\Delta\boldsymbol{\varphi}}\mathbf{QG} + \mathbf{Q}\left(\mathbf{D}:\Delta\mathbf{K}\right)$$

$$= \widehat{\Delta\boldsymbol{\varphi}}\mathbf{QG} + \mathbf{Q}\left(\mathbf{D}:\left(\mathbf{Q}^{\mathrm{T}}\mathrm{GRAD}\Delta\boldsymbol{\varphi}\right)\right) \tag{G.29}$$

we obtain

$$\frac{\mathrm{d}}{\mathrm{d}\epsilon}\bigg|_{\epsilon=0}\left(\mathbf{L}\left(\mathbf{N}_{\varphi}{}^{\mathrm{T}}\nabla_X\right)\right)_\epsilon = \begin{Bmatrix} \mathbf{0} \\ \left(\widehat{\Delta\boldsymbol{\varphi}}\mathbf{QG} + \mathbf{Q}\left(\mathbf{D}:\left(\mathbf{Q}^{\mathrm{T}}\mathrm{GRAD}\Delta\boldsymbol{\varphi}\right)\right)\right)(N_1\nabla_X) \\ \mathbf{0} \\ \left(\widehat{\Delta\boldsymbol{\varphi}}\mathbf{QG} + \mathbf{Q}\left(\mathbf{D}:\left(\mathbf{Q}^{\mathrm{T}}\mathrm{GRAD}\Delta\boldsymbol{\varphi}\right)\right)\right)(N_2\nabla_X) \\ \mathbf{0} \\ \vdots \\ \mathbf{0} \\ \left(\widehat{\Delta\boldsymbol{\varphi}}\mathbf{QG} + \mathbf{Q}\left(\mathbf{D}:\left(\mathbf{Q}^{\mathrm{T}}\mathrm{GRAD}\Delta\boldsymbol{\varphi}\right)\right)\right)(N_{n_{node}}\nabla_X) \end{Bmatrix} \quad \text{(G.30)}$$

$$= \begin{Bmatrix} \mathbf{0} \\ \widehat{\Delta\boldsymbol{\varphi}}\mathbf{QG}(N_1\nabla_X) \\ \mathbf{0} \\ \widehat{\Delta\boldsymbol{\varphi}}\mathbf{QG}(N_2\nabla_X) \\ \mathbf{0} \\ \vdots \\ \mathbf{0} \\ \widehat{\Delta\boldsymbol{\varphi}}\mathbf{QG}(N_{n_{node}}\nabla_X) \end{Bmatrix} + \begin{Bmatrix} \mathbf{0} \\ \mathbf{Q}\left(\mathbf{D}:\left(\mathbf{Q}^{\mathrm{T}}\mathrm{GRAD}\Delta\boldsymbol{\varphi}\right)\right)(N_1\nabla_X) \\ \mathbf{0} \\ \mathbf{Q}\left(\mathbf{D}:\left(\mathbf{Q}^{\mathrm{T}}\mathrm{GRAD}\Delta\boldsymbol{\varphi}\right)\right)(N_2\nabla_X) \\ \mathbf{0} \\ \vdots \\ \mathbf{0} \\ \mathbf{Q}\left(\mathbf{D}:\left(\mathbf{Q}^{\mathrm{T}}\mathrm{GRAD}\Delta\boldsymbol{\varphi}\right)\right)(N_{n_{node}}\nabla_X) \end{Bmatrix},$$

$$\text{(G.31)}$$

where the term $\widehat{\Delta\boldsymbol{\varphi}}\mathbf{QG}(N_i\nabla_X)$ can be written as $-\widehat{\mathbf{QG}(N_i\nabla_X)}\Delta\boldsymbol{\varphi}$. We substitute the constitutive tensor $\mathbf{D} = \alpha\,\mathbf{I}\otimes\mathbf{I} + (\beta+\gamma)\boldsymbol{\mathcal{I}} + (\beta-\gamma)\boldsymbol{\mathcal{I}}^{\mathrm{T}}$ and obtain the following result using the same method as in (G.19):

$$\mathbf{Q}\left(\mathbf{D}:\Delta\mathbf{K}\right)(N_i\nabla_X) = \mathbf{Q}\left(\left(\alpha\,\mathbf{I}\otimes\mathbf{I} + (\beta+\gamma)\boldsymbol{\mathcal{I}} + (\beta-\gamma)\boldsymbol{\mathcal{I}}^{\mathrm{T}}\right):\Delta\mathbf{K}\right)(N_i\nabla_X)$$
$$= \alpha\mathbf{Q}(N_i\nabla_X)\mathrm{tr}(\Delta\mathbf{K}) + (\beta+\gamma)\mathbf{Q}\Delta\mathbf{K}(N_i\nabla_X) + (\beta-\gamma)\mathbf{Q}\Delta\mathbf{K}^{\mathrm{T}}(N_i\nabla_X).$$
$$\text{(G.32)}$$

G.10.2.1 $\alpha\mathbf{tr}(\Delta\mathbf{K})\mathbf{Q}(N_i\nabla_X)$

Using (G.9) we obtain

$$\mathrm{tr}(\Delta\mathbf{K}) = \mathrm{tr}(\mathbf{Q}^{\mathrm{T}}\mathrm{GRAD}\Delta\boldsymbol{\varphi})$$
$$= \mathrm{tr}\left(\mathbf{Q}^{\mathrm{T}}\left(\Delta\boldsymbol{\varphi}\otimes\nabla_X\right)\right)$$
$$= \nabla_X\cdot\mathbf{Q}^{\mathrm{T}}\Delta\boldsymbol{\varphi}$$
$$= \nabla_X^{\mathrm{T}}\mathbf{Q}^{\mathrm{T}}\Delta\boldsymbol{\varphi}, \quad\quad\quad\quad \text{(G.33)}$$

where ∇_X^{T} in (G.33) operates exclusively on $\Delta\boldsymbol{\varphi}$.

Thus $\alpha\mathbf{Q}(N_i\nabla_X)\mathrm{tr}(\Delta\mathbf{K}) = \alpha\mathbf{Q}(N_i\nabla_X)\nabla_X^{\mathrm{T}}\mathbf{Q}^{\mathrm{T}}\Delta\boldsymbol{\varphi}$.

G.10.2.2 $(\beta+\gamma)\mathbf{Q}\Delta\mathbf{K}(N_i\nabla_X)$

$$
\begin{aligned}
(\beta+\gamma)\mathbf{Q}\Delta\mathbf{K}(N_i\nabla_X) &= (\beta+\gamma)\underbrace{\mathbf{Q}\mathbf{Q}^{\mathrm{T}}}_{\mathbf{I}}\mathrm{GRAD}\Delta\boldsymbol{\varphi}(N_i\nabla_X) \\
&= (\beta+\gamma)(\Delta\boldsymbol{\varphi}\otimes\nabla_X)(N_i\nabla_X) \\
&= (\beta+\gamma)\Delta\boldsymbol{\varphi}\underbrace{\nabla_X^{\mathrm{T}}(N_i\nabla_X)}_{\text{scalar}} \\
&= (\beta+\gamma)\nabla_X^{\mathrm{T}}(N_i\nabla_X)\Delta\boldsymbol{\varphi}, && \text{(G.34)}
\end{aligned}
$$

where ∇_X^{T} in (G.34) operates exclusively on $\Delta\boldsymbol{\varphi}$.

G.10.2.3 $(\beta-\gamma)\mathbf{Q}\Delta\mathbf{K}^{\mathbf{T}}(N_i\nabla_X)$

$$
\begin{aligned}
(\beta-\gamma)\mathbf{Q}\Delta\mathbf{K}^{\mathrm{T}}(N_i\nabla_X) &= (\beta-\gamma)\mathbf{Q}\left(\mathrm{GRAD}\Delta\boldsymbol{\varphi}\right)^{\mathrm{T}}\mathbf{Q}(N_i\nabla_X) \\
&= (\beta-\gamma)\mathbf{Q}\left(\Delta\boldsymbol{\varphi}\otimes\nabla_X\right)^{\mathrm{T}}\mathbf{Q}(N_i\nabla_X) \\
&= (\beta-\gamma)\mathbf{Q}\left(\Delta\boldsymbol{\varphi}\nabla_X^{\mathrm{T}}\right)^{\mathrm{T}}\mathbf{Q}(N_i\nabla_X) \\
&= (\beta-\gamma)\mathbf{Q}\nabla_X\underbrace{\Delta\boldsymbol{\varphi}^{\mathrm{T}}\mathbf{Q}}_{\mathbf{a}^{\mathrm{T}}}\underbrace{(N_i\nabla_X)}_{\mathbf{b}} && \text{by using (E.1)} \\
&= (\beta-\gamma)\mathbf{Q}\nabla_X(N_i\nabla_X)^{\mathrm{T}}\mathbf{Q}^{\mathrm{T}}\Delta\boldsymbol{\varphi}, && \text{(G.35)}
\end{aligned}
$$

where ∇_X in (G.35) operates exclusively on $\Delta\boldsymbol{\varphi}$.

Finally, for each subvector in (G.31) we obtain

$$
\begin{aligned}
\widehat{\Delta\boldsymbol{\varphi}}\mathbf{Q}\mathbf{G}(N_i\nabla_X) &+ \mathbf{Q}\left(\mathbf{D}:\left(\mathbf{Q}^{\mathrm{T}}\mathrm{GRAD}\Delta\boldsymbol{\varphi}\right)\right)(N_i\nabla_X) \\
&= -\widehat{\mathbf{Q}\mathbf{G}(N_i\nabla_X)}\Delta\boldsymbol{\varphi} + \alpha\mathbf{Q}(N_i\nabla_X)\nabla_X^{\mathrm{T}}\mathbf{Q}^{\mathrm{T}}\Delta\boldsymbol{\varphi} + (\beta+\gamma)\nabla_X^{\mathrm{T}}(N_i\nabla_X)\Delta\boldsymbol{\varphi} \\
&\quad + (\beta-\gamma)\mathbf{Q}\nabla_X(N_i\nabla_X)^{\mathrm{T}}\mathbf{Q}^{\mathrm{T}}\Delta\boldsymbol{\varphi}, && \text{(G.36)}
\end{aligned}
$$

i.e.

$$
\begin{aligned}
\widehat{\Delta\boldsymbol{\varphi}}\mathbf{Q}\mathbf{G}(N_i\nabla_X) &+ \mathbf{Q}\left(\mathbf{D}:\left(\mathbf{Q}^{\mathrm{T}}\mathrm{GRAD}\Delta\boldsymbol{\varphi}\right)\right)(N_i\nabla_X) \\
&= \left(-\widehat{\mathbf{Q}\mathbf{G}(N_i\nabla_X)} + \alpha\mathbf{Q}(N_i\nabla_X)\nabla_X^{\mathrm{T}}\mathbf{Q}^{\mathrm{T}} + (\beta+\gamma)\nabla_X^{\mathrm{T}}(N_i\nabla_X)\mathbf{I} + (\beta-\gamma)\mathbf{Q}\nabla_X(N_i\nabla_X)^{\mathrm{T}}\mathbf{Q}^{\mathrm{T}}\right)\Delta\boldsymbol{\varphi}.
\end{aligned}
$$
$$\text{(G.37)}$$

G.10.3 Term $\dfrac{\mathrm{d}}{\mathrm{d}\epsilon}\Big|_{\epsilon=0} \left(2\mathbf{N_\varphi}^{\mathbf{T}}\mathbf{ax}\left(\mathbf{skew}\left(\mathbf{FB^T Q^T}\right)\right)\right)_\epsilon$

Consider $2\mathbf{N_\varphi}^{\mathrm{T}}\mathrm{ax}\left(\mathrm{skew}\left(\mathbf{FB^T Q^T}\right)\right)$ derived in (F.5):

$$2\mathbf{N_\varphi}^{\mathrm{T}}\mathrm{ax}\left(\mathrm{skew}\left(\mathbf{FB^T Q^T}\right)\right) = \left\{\begin{array}{c} \mathbf{0} \\ 2N_1\mathrm{ax}\left(\mathrm{skew}\left(\mathbf{FB^T Q^T}\right)\right) \\ \mathbf{0} \\ 2N_2\mathrm{ax}\left(\mathrm{skew}\left(\mathbf{FB^T Q^T}\right)\right) \\ \cdot \\ \cdot \\ \mathbf{0} \\ 2N_{n_{node}}\mathrm{ax}\left(\mathrm{skew}\left(\mathbf{FB^T Q^T}\right)\right) \end{array}\right\}$$

Since $\mathrm{ax}\left(\mathrm{skew}\left(\mathbf{A}\right)\right) = -\dfrac{1}{2}\boldsymbol{\epsilon} : \mathbf{A}$ where $\boldsymbol{\epsilon}$ is the third-order permutation tensor (or Levi-Civita) which may be represented as

$$\boldsymbol{\epsilon} = \begin{bmatrix} \begin{bmatrix} 0 & 0 & 0 \\ 0 & 0 & 1 \\ 0 & -1 & 0 \end{bmatrix} \\ \begin{bmatrix} 0 & 0 & -1 \\ 0 & 0 & 0 \\ 1 & 0 & 0 \end{bmatrix} \\ \begin{bmatrix} 0 & 1 & 0 \\ -1 & 0 & 0 \\ 0 & 0 & 0 \end{bmatrix} \end{bmatrix} = \begin{bmatrix} \boldsymbol{\epsilon_1} \\ \boldsymbol{\epsilon_2} \\ \boldsymbol{\epsilon_3} \end{bmatrix}, \tag{G.38}$$

the vector $2N_i\mathrm{ax}\left(\mathrm{skew}\left(\mathbf{FB^T Q^T}\right)\right)$ can be written as

$$2N_i\mathrm{ax}\left(\mathrm{skew}\left(\mathbf{FB^T Q^T}\right)\right) = 2N_i\left(-\dfrac{1}{2}\boldsymbol{\epsilon}\right) : \left(\mathbf{FB^T Q^T}\right)$$

$$= -N_i\boldsymbol{\epsilon} : \left(\mathbf{FB^T Q^T}\right). \tag{G.39}$$

Next we perform the linearization and obtain

$$\dfrac{\mathrm{d}}{\mathrm{d}\epsilon}\Big|_{\epsilon=0} \left(-N_i\boldsymbol{\epsilon} : \left(\mathbf{FB^T Q^T}\right)\right)_\epsilon$$

$$= -N_i\boldsymbol{\epsilon} : \left(\Delta\mathbf{FB^T Q^T} + \mathbf{F}(\Delta\mathbf{B})^{\mathrm{T}}\mathbf{Q^T} + \mathbf{FB^T}(\Delta\mathbf{Q})^{\mathrm{T}}\right)$$

$$= -N_i\boldsymbol{\epsilon} : \left(\mathrm{GRAD}\Delta\mathbf{u}\mathbf{B^T Q^T} + \mathbf{F}(\mathbf{T} : \Delta\mathbf{E})^{\mathrm{T}}\mathbf{Q^T} + \mathbf{FB^T Q^T}\widehat{\Delta\boldsymbol{\varphi}}^{\mathrm{T}}\right)$$

$$= -N_i\boldsymbol{\epsilon} : \left(\mathrm{GRAD}\Delta\mathbf{u}\mathbf{B}^{\mathrm{T}}\mathbf{Q}^{\mathrm{T}}\right) - N_i\boldsymbol{\epsilon} : \left(\mathbf{F}(\mathbf{T} : \Delta\mathbf{E})^{\mathrm{T}}\mathbf{Q}^{\mathrm{T}}\right) - N_i\boldsymbol{\epsilon} : \left(\mathbf{F}\mathbf{B}^{\mathrm{T}}\mathbf{Q}^{\mathrm{T}}\widehat{\Delta\boldsymbol{\varphi}}^{\mathrm{T}}\right).$$

$$(G.40)$$

G.10.3.1 $\quad -N_i\boldsymbol{\epsilon} : \left(\mathbf{GRAD}\Delta\mathbf{u}\mathbf{B}^{\mathbf{T}}\mathbf{Q}^{\mathbf{T}}\right)$

$$
\begin{aligned}
-N_i\boldsymbol{\epsilon} : \left(\mathrm{GRAD}\Delta\mathbf{u}\mathbf{B}^{\mathrm{T}}\mathbf{Q}^{\mathrm{T}}\right) &= -N_i\boldsymbol{\epsilon} : \left(\left(\Delta\mathbf{u}\nabla_X^{\mathrm{T}}\right)\mathbf{B}^{\mathrm{T}}\mathbf{Q}^{\mathrm{T}}\right) \\
&= -N_i\boldsymbol{\epsilon} : \left(\Delta\mathbf{u} \otimes \left(\mathbf{Q}\mathbf{B}\nabla_X\right)\right) \\
&= N_i\widehat{\mathbf{Q}\mathbf{B}\nabla_X}\Delta\mathbf{u},
\end{aligned}
$$

$$(G.41)$$

where ∇_X in (G.41) operates exclusively on $\Delta\mathbf{u}$, because for any $\mathbf{a},\ \mathbf{b} \in \mathbb{R}^3$

$$\boldsymbol{\epsilon} : (\mathbf{a} \otimes \mathbf{b}) = -\widehat{\mathbf{b}}\mathbf{a} = \widehat{\mathbf{a}}\mathbf{b}.$$

$$(G.42)$$

PROOF:

$$
\mathbf{a} \otimes \mathbf{b} = \begin{Bmatrix} a_1 \\ a_2 \\ a_3 \end{Bmatrix} \begin{Bmatrix} b_1 & b_2 & b_3 \end{Bmatrix} = \begin{bmatrix} a_1 b_1 & a_1 b_2 & a_1 b_3 \\ a_2 b_1 & a_2 b_2 & a_2 b_3 \\ a_3 b_1 & a_3 b_2 & a_3 b_3 \end{bmatrix},
$$

$$(G.43)$$

$$
\begin{aligned}
\boldsymbol{\epsilon} : (\mathbf{a} \otimes \mathbf{b}) &= \begin{bmatrix} \begin{bmatrix} 0 & 0 & 0 \\ 0 & 0 & 1 \\ 0 & -1 & 0 \end{bmatrix} \\ \begin{bmatrix} 0 & 0 & -1 \\ 0 & 0 & 0 \\ 1 & 0 & 0 \end{bmatrix} \\ \begin{bmatrix} 0 & 1 & 0 \\ -1 & 0 & 0 \\ 0 & 0 & 0 \end{bmatrix} \end{bmatrix} : \begin{bmatrix} a_1 b_1 & a_1 b_2 & a_1 b_3 \\ a_2 b_1 & a_2 b_2 & a_2 b_3 \\ a_3 b_1 & a_3 b_2 & a_3 b_3 \end{bmatrix} \\
&= \begin{Bmatrix} a_2 b_3 - a_3 b_2 \\ -a_1 b_3 + a_3 b_1 \\ a_1 b_2 - a_2 b_1 \end{Bmatrix} \\
&= \begin{bmatrix} 0 & -a_3 & a_2 \\ a_3 & 0 & -a_1 \\ -a_2 & a_1 & 0 \end{bmatrix} \begin{Bmatrix} b_1 \\ b_2 \\ b_3 \end{Bmatrix} \\
&= \widehat{\mathbf{a}}\mathbf{b}.
\end{aligned}
$$

$$(G.44)$$

Therefore,

$$\boldsymbol{\epsilon} : (\mathbf{a} \otimes \mathbf{b}) = -\widehat{\mathbf{b}\mathbf{a}} = \widehat{\mathbf{a}\mathbf{b}}. \tag{G.45}$$

G.10.3.2 $\quad -N_i\boldsymbol{\epsilon} : \left(\mathbf{F}(\mathbf{T} : \Delta\mathbf{E})^{\mathbf{T}}\mathbf{Q}^{\mathbf{T}}\right)$

We introduce the following relations presented earlier:

$$\mathbf{T} : \Delta\mathbf{E} = \lambda \, \mathrm{tr}(\Delta\mathbf{E})\mathbf{I} + (\mu + \nu)\Delta\mathbf{E} + (\mu - \nu)\Delta\mathbf{E}^{\mathrm{T}},$$

$$(\mathbf{T} : \Delta\mathbf{E})^{\mathrm{T}} = \left(\lambda \, \mathrm{tr}(\Delta\mathbf{E})\mathbf{I} + (\mu + \nu)\Delta\mathbf{E} + (\mu - \nu)\Delta\mathbf{E}^{\mathrm{T}}\right)^{\mathrm{T}}$$

$$= \lambda \, \mathrm{tr}(\Delta\mathbf{E})\mathbf{I} + (\mu + \nu)\Delta\mathbf{E}^{\mathrm{T}} + (\mu - \nu)\Delta\mathbf{E},$$

$$\Delta\mathbf{E} = \mathbf{Q}^{\mathrm{T}}\widehat{\Delta\boldsymbol{\varphi}}^{\mathrm{T}}\mathbf{F} + \mathbf{Q}^{\mathrm{T}}\mathrm{GRAD}(\Delta\mathbf{u})$$

$$\Delta\mathbf{E}^{\mathrm{T}} = \mathbf{F}^{\mathrm{T}}\widehat{\Delta\boldsymbol{\varphi}}\mathbf{Q} + [\mathrm{GRAD}(\Delta\mathbf{u})]^{\mathrm{T}}\mathbf{Q},$$

$$\mathrm{tr}(\Delta\mathbf{E}) = 2\left[\mathrm{ax}(\mathrm{skew}(\mathbf{F}\mathbf{Q}^{\mathrm{T}}))\right]^{\mathrm{T}}\Delta\boldsymbol{\varphi} + \nabla_X^{\mathrm{T}}\mathbf{Q}^{\mathrm{T}}\Delta\mathbf{u},$$

into $-N_i\boldsymbol{\epsilon} : \left(\mathbf{F}(\mathbf{T} : \Delta\mathbf{E})^{\mathrm{T}}\mathbf{Q}^{\mathrm{T}}\right)$ and obtain

$$- N_i\boldsymbol{\epsilon} : \left(\mathbf{F}(\mathbf{T} : \Delta\mathbf{E})^{\mathrm{T}}\mathbf{Q}^{\mathrm{T}}\right)$$

$$= -N_i\boldsymbol{\epsilon} : \left(\mathbf{F}(\lambda \, \mathrm{tr}(\Delta\mathbf{E})\mathbf{I} + (\mu + \nu)\Delta\mathbf{E}^{\mathrm{T}} + (\mu - \nu)\Delta\mathbf{E})\mathbf{Q}^{\mathrm{T}}\right)$$

$$= -N_i\boldsymbol{\epsilon} : \left(\mathbf{F}(\lambda \, \mathrm{tr}(\Delta\mathbf{E})\mathbf{I}\mathbf{Q}^{\mathrm{T}}\right) - N_i\boldsymbol{\epsilon} : \left(\mathbf{F}(\mu + \nu)\Delta\mathbf{E}^{\mathrm{T}}\mathbf{Q}^{\mathrm{T}}\right) - N_i\boldsymbol{\epsilon} : \left(\mathbf{F}(\mu - \nu)\Delta\mathbf{E}\mathbf{Q}^{\mathrm{T}}\right).$$
$$\tag{G.46}$$

First term in (G.46):

$$- N_i\boldsymbol{\epsilon} : \left(\mathbf{F}(\underbrace{\lambda \, \mathrm{tr}(\Delta\mathbf{E})}_{\text{scalar}}\mathbf{I}\mathbf{Q}^{\mathrm{T}}\right)$$

$$= -N_i\boldsymbol{\epsilon} : \left(\mathbf{F}\mathbf{Q}^{\mathrm{T}}\right)\lambda \, \mathrm{tr}(\Delta\mathbf{E})$$

$$= -N_i\boldsymbol{\epsilon} : \left(\mathbf{F}\mathbf{Q}^{\mathrm{T}}\right)\lambda \, \left(2\left[\mathrm{ax}(\mathrm{skew}(\mathbf{F}\mathbf{Q}^{\mathrm{T}}))\right]^{\mathrm{T}}\Delta\boldsymbol{\varphi} + \nabla_X^{\mathrm{T}}\mathbf{Q}^{\mathrm{T}}\Delta\mathbf{u}\right)$$

$$\left|\text{since}\quad \boldsymbol{\epsilon} : \left(\mathbf{F}\mathbf{Q}^{\mathrm{T}}\right) = -2\,\mathrm{ax}(\mathrm{skew}(\mathbf{F}\mathbf{Q}^{\mathrm{T}}))\right|$$

$$= 4\lambda N_i \, \mathrm{ax}(\mathrm{skew}(\mathbf{F}\mathbf{Q}^{\mathrm{T}}))\left[\mathrm{ax}(\mathrm{skew}(\mathbf{F}\mathbf{Q}^{\mathrm{T}}))\right]^{\mathrm{T}}\Delta\boldsymbol{\varphi} + 2\lambda N_i \, \mathrm{ax}(\mathrm{skew}(\mathbf{F}\mathbf{Q}^{\mathrm{T}}))\nabla_X^{\mathrm{T}}\mathbf{Q}^{\mathrm{T}}\Delta\mathbf{u},$$
$$\tag{G.47}$$

where ∇_X^{T} in (G.47) operates exclusively on $\Delta\mathbf{u}$.

Second term in (G.46):

$$-N_i\boldsymbol{\epsilon} : \left(\mathbf{F}(\mu + \nu)\Delta\mathbf{E}^{\mathrm{T}}\mathbf{Q}^{\mathrm{T}}\right) = -N_i\boldsymbol{\epsilon} : \left(\mathbf{F}(\mu + \nu)\left(\mathbf{F}^{\mathrm{T}}\widehat{\Delta\boldsymbol{\varphi}}\mathbf{Q} + [\mathrm{GRAD}\Delta\mathbf{u}]^{\mathrm{T}}\mathbf{Q}\right)\mathbf{Q}^{\mathrm{T}}\right)$$

$$= -(\mu + \nu)N_i\boldsymbol{\epsilon} : \left(\mathbf{F}\mathbf{F}^{\mathrm{T}}\widehat{\Delta\boldsymbol{\varphi}}\mathbf{Q}\mathbf{Q}^{\mathrm{T}} + \mathbf{F}[\mathrm{GRAD}\Delta\mathbf{u}]^{\mathrm{T}}\mathbf{Q}\mathbf{Q}^{\mathrm{T}}\right)$$

$$= -(\mu + \nu)N_i\boldsymbol{\epsilon} : \left(\mathbf{F}\mathbf{F}^{\mathrm{T}}\widehat{\Delta\boldsymbol{\varphi}} + \mathbf{F}\left[\mathrm{GRAD}\Delta\mathbf{u}\right]^{\mathrm{T}}\right)$$

$$= -(\mu + \nu)N_i\boldsymbol{\epsilon} : \left(\mathbf{F}\mathbf{F}^{\mathrm{T}}\widehat{\Delta\boldsymbol{\varphi}}\right) - (\mu + \nu)N_i\boldsymbol{\epsilon} : \left(\mathbf{F}\left[\mathrm{GRAD}\Delta\mathbf{u}\right]^{\mathrm{T}}\right).$$

The term $-(\mu + \nu)N_i\boldsymbol{\epsilon} : \left(\mathbf{F}\mathbf{F}^{\mathrm{T}}\widehat{\Delta\boldsymbol{\varphi}}\right)$ can be written as

$$-(\mu + \nu)N_i\boldsymbol{\epsilon} : \left(\mathbf{F}\mathbf{F}^{\mathrm{T}}\widehat{\Delta\boldsymbol{\varphi}}\right) = -(\mu + \nu)N_i\left(\mathbf{F}\mathbf{F}^{\mathrm{T}} - \mathrm{tr}(\mathbf{F}\mathbf{F}^{\mathrm{T}})\mathbf{I}\right)\Delta\boldsymbol{\varphi}, \tag{G.48}$$

because for any $\mathbf{A}$, $\widehat{\mathbf{b}}$

$$\boldsymbol{\epsilon} : \left(\mathbf{A}\widehat{\mathbf{b}}\right) = \left(\mathbf{A}^{\mathrm{T}} - \mathrm{tr}(\mathbf{A})\mathbf{I}\right)\mathbf{b}. \tag{G.49}$$

PROOF:

$$\mathbf{A}\widehat{\mathbf{b}} = \begin{bmatrix} A_{11} & A_{12} & A_{13} \\ A_{21} & A_{22} & A_{23} \\ A_{31} & A_{32} & A_{33} \end{bmatrix} \begin{bmatrix} 0 & -b_3 & b_2 \\ b_3 & 0 & -b_1 \\ -b_2 & b_1 & 0 \end{bmatrix}$$

$$= \begin{bmatrix} A_{12}b_3 - A_{13}b_2 & -A_{11}b_3 + A_{13}b_1 & A_{11}b_2 - A_{12}b_1 \\ A_{22}b_3 - A_{23}b_2 & -A_{21}b_3 + A_{23}b_1 & A_{21}b_2 - A_{22}b_1 \\ A_{32}b_3 - A_{33}b_2 & -A_{31}b_3 + A_{33}b_1 & A_{31}b_2 - A_{32}b_1 \end{bmatrix}$$

$$\boldsymbol{\epsilon} : \left(\mathbf{A}\widehat{\mathbf{b}}\right) = \begin{bmatrix} \begin{bmatrix} 0 & 0 & 0 \\ 0 & 0 & 1 \\ 0 & -1 & 0 \end{bmatrix} \\ \begin{bmatrix} 0 & 0 & -1 \\ 0 & 0 & 0 \\ 1 & 0 & 0 \end{bmatrix} \\ \begin{bmatrix} 0 & 1 & 0 \\ -1 & 0 & 0 \\ 0 & 0 & 0 \end{bmatrix} \end{bmatrix} : \begin{bmatrix} A_{12}b_3 - A_{13}b_2 & -A_{11}b_3 + A_{13}b_1 & A_{11}b_2 - A_{12}b_1 \\ A_{22}b_3 - A_{23}b_2 & -A_{21}b_3 + A_{23}b_1 & A_{21}b_2 - A_{22}b_1 \\ A_{32}b_3 - A_{33}b_2 & -A_{31}b_3 + A_{33}b_1 & A_{31}b_2 - A_{32}b_1 \end{bmatrix}$$

$$= \left\{ \begin{array}{c} A_{21}b_2 - A_{22}b_1 + A_{31}b_3 - A_{33}b_1 \\ -A_{11}b_2 + A_{12}b_1 + A_{32}b_3 - A_{33}b_2 \\ -A_{11}b_3 + A_{13}b_1 - A_{22}b_3 + A_{23}b_2 \end{array} \right\}$$

$$= \left\{ \begin{array}{c} (-A_{22} - A_{33})b_1 + A_{21}b_2 + A_{31}b_3 \\ A_{12}b_1 + (-A_{11} - A_{33})b_2 + A_{32}b_3 \\ A_{13}b_1 + A_{23}b_2 + (-A_{11} - A_{22})b_3 \end{array} \right\}$$

$$= \begin{bmatrix} (-A_{22} - A_{33}) & A_{21} & A_{31} \\ A_{12} & (-A_{11} - A_{33}) & A_{32} \\ A_{13} & A_{23} & (-A_{11} - A_{22}) \end{bmatrix} \begin{Bmatrix} b_1 \\ b_2 \\ b_3 \end{Bmatrix}$$

$$= \left(\underbrace{\begin{bmatrix} A_{11} & A_{21} & A_{31} \\ A_{12} & A_{22} & A_{32} \\ A_{13} & A_{23} & A_{33} \end{bmatrix}}_{\mathbf{A}^{\mathrm{T}}} - \underbrace{\begin{bmatrix} A_{11} + A_{22} + A_{33} & 0 & 0 \\ 0 & A_{11} + A_{22} + A_{33} & 0 \\ 0 & 0 & A_{11} + A_{22} + A_{33} \end{bmatrix}}_{\mathrm{tr}(\mathbf{A})\mathbf{I}} \right) \begin{Bmatrix} b_1 \\ b_2 \\ b_3 \end{Bmatrix}$$

$$= \left(\mathbf{A}^{\mathrm{T}} - \mathrm{tr}(\mathbf{A})\mathbf{I} \right) \mathbf{b}$$

Furthermore, since

$$
\begin{aligned}
-(\mu + \nu)N_i\boldsymbol{\epsilon} : \left(\mathbf{F}\left[\mathrm{GRAD}\Delta\mathbf{u} \right]^{\mathrm{T}} \right) &= -(\mu + \nu)N_i\boldsymbol{\epsilon} : \left(\mathbf{F}\left(\Delta\mathbf{u} \otimes \nabla_X \right)^{\mathrm{T}} \right) \\
&= -(\mu + \nu)N_i\boldsymbol{\epsilon} : \left(\mathbf{F}\left(\nabla_X \otimes \Delta\mathbf{u} \right) \right) \\
&\quad |\text{since} \quad \boldsymbol{\epsilon} : \mathbf{A} = -\boldsymbol{\epsilon} : \mathbf{A}^{\mathrm{T}}| \\
&= (\mu + \nu)N_i\boldsymbol{\epsilon} : \left(\mathbf{F}\left(\nabla_X \otimes \Delta\mathbf{u} \right) \right)^{\mathrm{T}} \\
&= (\mu + \nu)N_i\boldsymbol{\epsilon} : \left(\Delta\mathbf{u} \otimes \mathbf{F}\nabla_X \right) \\
&\quad |\text{by using (G.45)}| \\
&= -(\mu + \nu)N_i\widehat{\mathbf{F}\nabla_X}\Delta\mathbf{u}, \quad\quad\quad\quad (\text{G.50})
\end{aligned}
$$

where ∇_X in (G.50) operates exclusively on $\Delta\mathbf{u}$, we obtain for the second term in (G.46)

$$-N_i\boldsymbol{\epsilon} : \left(\mathbf{F}(\mu + \nu)\Delta\mathbf{E}^{\mathrm{T}}\mathbf{Q}^{\mathrm{T}} \right) = -(\mu + \nu)N_i \left(\mathbf{F}\mathbf{F}^{\mathrm{T}} - \mathrm{tr}(\mathbf{F}\mathbf{F}^{\mathrm{T}})\mathbf{I} \right) \Delta\boldsymbol{\varphi} - (\mu + \nu)N_i\widehat{\mathbf{F}\nabla_X}\Delta\mathbf{u}. \quad (\text{G.51})$$

Third term in (G.46):

$$
\begin{aligned}
-N_i\boldsymbol{\epsilon} : \left(\mathbf{F}(\mu - \nu)\Delta\mathbf{E}\mathbf{Q}^{\mathrm{T}} \right) &= -(\mu - \nu)N_i\boldsymbol{\epsilon} : \left(\mathbf{F}\left(\mathbf{Q}^{\mathrm{T}}\widehat{\Delta\boldsymbol{\varphi}}^{\mathrm{T}}\mathbf{F} + \mathbf{Q}^{\mathrm{T}}\mathrm{GRAD}\Delta\mathbf{u} \right) \mathbf{Q}^{\mathrm{T}} \right) \\
&= -(\mu - \nu)N_i\boldsymbol{\epsilon} : \left(\mathbf{F}\mathbf{Q}^{\mathrm{T}}\widehat{\Delta\boldsymbol{\varphi}}^{\mathrm{T}}\mathbf{F}\mathbf{Q}^{\mathrm{T}} + \mathbf{F}\mathbf{Q}^{\mathrm{T}}\mathrm{GRAD}\Delta\mathbf{u}\mathbf{Q}^{\mathrm{T}} \right) \\
&= -(\mu - \nu)N_i\boldsymbol{\epsilon} : \left(\mathbf{F}\mathbf{Q}^{\mathrm{T}}\widehat{\Delta\boldsymbol{\varphi}}^{\mathrm{T}}\mathbf{F}\mathbf{Q}^{\mathrm{T}} \right) - (\mu - \nu)N_i\boldsymbol{\epsilon} : \left(\mathbf{F}\mathbf{Q}^{\mathrm{T}}\mathrm{GRAD}\Delta\mathbf{u}\mathbf{Q}^{\mathrm{T}} \right) \\
&\quad\quad\quad\quad\quad\quad\quad\quad\quad\quad\quad\quad\quad\quad\quad\quad\quad\quad\quad\quad\quad\quad (\text{G.52})
\end{aligned}
$$

First term in (G.52):

$$- (\mu - \nu) N_i \boldsymbol{\epsilon} : \left(\mathbf{FQ}^{\mathrm{T}} \widehat{\Delta \boldsymbol{\varphi}}^{\mathrm{T}} \mathbf{FQ}^{\mathrm{T}} \right)$$

$$= (\mu - \nu) N_i \boldsymbol{\epsilon} : \left(\mathbf{FQ}^{\mathrm{T}} \widehat{\Delta \boldsymbol{\varphi}} \mathbf{FQ}^{\mathrm{T}} \right)$$

$$= (\mu - \nu) N_i \left[\mathrm{ax}(2\mathrm{skew}(\mathbf{FQ}^{\mathrm{T}} \boldsymbol{\epsilon_1} \mathbf{FQ}^{\mathrm{T}})) \ \ \mathrm{ax}(2\mathrm{skew}(\mathbf{FQ}^{\mathrm{T}} \boldsymbol{\epsilon_2} \mathbf{FQ}^{\mathrm{T}})) \ \ \mathrm{ax}(2\mathrm{skew}(\mathbf{FQ}^{\mathrm{T}} \boldsymbol{\epsilon_3} \mathbf{FQ}^{\mathrm{T}})) \right] \Delta \boldsymbol{\varphi}$$

where $\mathrm{skew}(\mathbf{FQ}^{\mathrm{T}} \boldsymbol{\epsilon_i} \mathbf{FQ}^{\mathrm{T}}) = \dfrac{1}{2} \left(\mathbf{FQ}^{\mathrm{T}} \boldsymbol{\epsilon_i} \mathbf{FQ}^{\mathrm{T}} - (\mathbf{FQ}^{\mathrm{T}} \boldsymbol{\epsilon_i} \mathbf{FQ}^{\mathrm{T}})^{\mathrm{T}} \right)$, since

$$\boldsymbol{\epsilon} : \left(\mathbf{A}\widehat{\mathbf{b}}\mathbf{A} \right) = \underbrace{\left[\mathrm{ax}(2\mathrm{skew}(\mathbf{A}\boldsymbol{\epsilon_1}\mathbf{A})) \ \ \mathrm{ax}(2\mathrm{skew}(\mathbf{A}\boldsymbol{\epsilon_2}\mathbf{A})) \ \ \mathrm{ax}(2\mathrm{skew}(\mathbf{A}\boldsymbol{\epsilon_3}\mathbf{A})) \right]}_{\text{2nd order tensor}} \mathbf{b} \qquad \text{(G.53)}$$

for any second-order 3D tensor $\mathbf{A}$ and a first order 3D tensor b with $\boldsymbol{\epsilon_i}$ as a second order 3D tensor forming a part of the third order permutation tensor $\boldsymbol{\epsilon}$ as shown in (G.38).

PROOF:

$$
\mathbf{A}\widehat{\mathbf{b}}\mathbf{A} =
\begin{bmatrix}
A_{11} & A_{12} & A_{13} \\
A_{21} & A_{22} & A_{23} \\
A_{31} & A_{32} & A_{33}
\end{bmatrix}
\begin{bmatrix}
0 & -b_3 & b_2 \\
b_3 & 0 & -b_1 \\
-b_2 & b_1 & 0
\end{bmatrix}
\begin{bmatrix}
A_{11} & A_{12} & A_{13} \\
A_{21} & A_{22} & A_{23} \\
A_{31} & A_{32} & A_{33}
\end{bmatrix}
$$

$$
=
\begin{bmatrix}
A_{12}b_3 - A_{13}b_2 & -A_{11}b_3 + A_{13}b_1 & A_{11}b_2 - A_{12}b_1 \\
A_{22}b_3 - A_{23}b_2 & -A_{21}b_3 + A_{23}b_1 & A_{21}b_2 - A_{22}b_1 \\
A_{32}b_3 - A_{33}b_2 & -A_{31}b_3 + A_{33}b_1 & A_{31}b_2 - A_{32}b_1
\end{bmatrix}
\begin{bmatrix}
A_{11} & A_{12} & A_{13} \\
A_{21} & A_{22} & A_{23} \\
A_{31} & A_{32} & A_{33}
\end{bmatrix}
$$

$$
=
\begin{bmatrix}
(A_{12}b_3 - A_{13}b_2)A_{11} + (-A_{11}b_3 + A_{13}b_1)A_{21} + (A_{11}b_2 - A_{12}b_1)A_{31} & (A_{12}b_3 - A_{13}b_2)A_{12} + (-A_{11}b_3 + A_{13}b_1)A_{22} + (A_{11}b_2 - A_{12}b_1)A_{32} & (A_{12}b_3 - A_{13}b_2)A_{13} + (-A_{11}b_3 + A_{13}b_1)A_{23} + (A_{11}b_2 - A_{12}b_1)A_{33} \\
(A_{22}b_3 - A_{23}b_2)A_{11} + (-A_{21}b_3 + A_{23}b_1)A_{21} + (A_{21}b_2 - A_{22}b_1)A_{31} & (A_{22}b_3 - A_{23}b_2)A_{12} + (-A_{21}b_3 + A_{23}b_1)A_{22} + (A_{21}b_2 - A_{22}b_1)A_{32} & (A_{22}b_3 - A_{23}b_2)A_{13} + (-A_{21}b_3 + A_{23}b_1)A_{23} + (A_{21}b_2 - A_{22}b_1)A_{33} \\
(A_{32}b_3 - A_{33}b_2)A_{11} + (-A_{31}b_3 + A_{33}b_1)A_{21} + (A_{31}b_2 - A_{32}b_1)A_{31} & (A_{32}b_3 - A_{33}b_2)A_{12} + (-A_{31}b_3 + A_{33}b_1)A_{22} + (A_{31}b_2 - A_{32}b_1)A_{32} & (A_{32}b_3 - A_{33}b_2)A_{13} + (-A_{31}b_3 + A_{33}b_1)A_{23} + (A_{31}b_2 - A_{32}b_1)A_{33}
\end{bmatrix}
$$

$$
\boldsymbol{\epsilon} : \left(\mathbf{A}\widehat{\mathbf{b}}\mathbf{A}\right) =
\left\{
\begin{array}{l}
(A_{22}b_3 - A_{23}b_2)A_{13} + (-A_{21}b_3 + A_{23}b_1)A_{23} + (A_{21}b_2 - A_{22}b_1)A_{33} - [(A_{32}b_3 - A_{33}b_2)A_{12} + (-A_{31}b_3 + A_{33}b_1)A_{22} + (A_{31}b_2 - A_{32}b_1)A_{32}] \\
- [(A_{12}b_3 - A_{13}b_2)A_{13} + (-A_{11}b_3 + A_{13}b_1)A_{23} + (A_{11}b_2 - A_{12}b_1)A_{33}] + (A_{32}b_3 - A_{33}b_2)A_{11} + (-A_{31}b_3 + A_{33}b_1)A_{21} + (A_{31}b_2 - A_{32}b_1)A_{31} \\
(A_{12}b_3 - A_{13}b_2)A_{12} + (-A_{11}b_3 + A_{13}b_1)A_{22} + (A_{11}b_2 - A_{12}b_1)A_{32} - [(A_{22}b_3 - A_{23}b_2)A_{11} + (-A_{21}b_3 + A_{23}b_1)A_{21} + (A_{21}b_2 - A_{22}b_1)A_{31}]
\end{array}
\right\}
$$

$$
=
\left\{
\begin{array}{l}
(A_{23}^2 + A_{32}^2 - 2A_{22}A_{33})b_1 + (A_{33}(A_{12} + A_{21}) - A_{23}A_{13} - A_{31}A_{32})b_2 + (A_{22}(A_{13} + A_{31}) - A_{21}A_{23} - A_{32}A_{12})b_3 \\
(A_{33}(A_{12} + A_{21}) - A_{13}A_{23} - A_{32}A_{31})b_1 + (A_{13}^2 + A_{31}^2 - 2A_{11}A_{33})b_2 + (A_{11}(A_{23} + A_{32}) - A_{12}A_{13} - A_{31}A_{21})b_3 \\
(A_{22}(A_{13} + A_{31}) - A_{12}A_{32} - A_{23}A_{21})b_1 + (A_{11}(A_{32} + A_{23}) - A_{12}A_{13} - A_{31}A_{21})b_2 + (A_{12}^2 + A_{21}^2 - 2A_{11}A_{22})b_3
\end{array}
\right\}
$$

$$
=
\begin{bmatrix}
A_{23}^2 + A_{32}^2 - 2A_{22}A_{33} & A_{33}(A_{12} + A_{21}) - A_{23}A_{13} - A_{31}A_{32} & A_{22}(A_{13} + A_{31}) - A_{21}A_{23} - A_{32}A_{12} \\
A_{33}(A_{12} + A_{21}) - A_{13}A_{23} - A_{32}A_{31} & A_{13}^2 + A_{31}^2 - 2A_{11}A_{33} & A_{11}(A_{23} + A_{32}) - A_{12}A_{13} - A_{31}A_{21} \\
A_{22}(A_{13} + A_{31}) - A_{12}A_{32} - A_{23}A_{21} & A_{11}(A_{32} + A_{23}) - A_{12}A_{13} - A_{31}A_{21} & A_{12}^2 + A_{21}^2 - 2A_{11}A_{22}
\end{bmatrix}
\left\{
\begin{array}{c}
b_1 \\
b_2 \\
b_3
\end{array}
\right\}
$$

Now we analyse the term

$$2\mathrm{skew}(\mathbf{A}\boldsymbol{\epsilon_1}\mathbf{A}) = \mathbf{A}\boldsymbol{\epsilon_1}\mathbf{A} - \mathbf{A}^{\mathrm{T}}\boldsymbol{\epsilon_1^{\mathrm{T}}}\mathbf{A}^{\mathrm{T}}$$

$$\mathbf{A}\boldsymbol{\epsilon_1}\mathbf{A} = \begin{bmatrix} A_{11} & A_{12} & A_{13} \\ A_{21} & A_{22} & A_{23} \\ A_{31} & A_{32} & A_{33} \end{bmatrix} \begin{bmatrix} 0 & 0 & 0 \\ 0 & 0 & 1 \\ 0 & -1 & 0 \end{bmatrix} \begin{bmatrix} A_{11} & A_{12} & A_{13} \\ A_{21} & A_{22} & A_{23} \\ A_{31} & A_{32} & A_{33} \end{bmatrix}$$

$$= \begin{bmatrix} -A_{13}A_{21}+A_{12}A_{31} & -A_{13}A_{22}+A_{12}A_{32} & -A_{13}A_{23}+A_{12}A_{33} \\ -A_{23}A_{21}+A_{22}A_{31} & -A_{23}A_{22}+A_{22}A_{32} & -A_{23}^2+A_{22}A_{33} \\ -A_{33}A_{21}+A_{32}A_{31} & -A_{33}A_{22}+A_{32}^2 & -A_{33}A_{23}+A_{32}A_{33} \end{bmatrix},$$

$$\mathbf{A}^{\mathrm{T}}\boldsymbol{\epsilon_1^{\mathrm{T}}}\mathbf{A}^{\mathrm{T}} = (\mathbf{A}\boldsymbol{\epsilon_1}\mathbf{A})^{\mathrm{T}}$$

$$= \begin{bmatrix} A_{31}A_{12}-A_{21}A_{13} & A_{31}A_{22}-A_{21}A_{23} & A_{31}A_{32}-A_{21}A_{33} \\ A_{32}A_{12}-A_{22}A_{13} & A_{32}A_{22}-A_{22}A_{23} & A_{32}^2-A_{22}A_{33} \\ A_{33}A_{12}-A_{23}A_{13} & A_{33}A_{22}-A_{23}^2 & A_{33}A_{32}-A_{23}A_{33} \end{bmatrix},$$

$2\mathrm{skew}(\mathbf{A}\boldsymbol{\epsilon_1}\mathbf{A})$

$= \mathbf{A}\boldsymbol{\epsilon_1}\mathbf{A} - \mathbf{A}^{\mathrm{T}}\boldsymbol{\epsilon_1^{\mathrm{T}}}\mathbf{A}^{\mathrm{T}}$

$$= \begin{bmatrix} -A_{13}A_{21}+A_{12}A_{31} & -A_{13}A_{22}+A_{12}A_{32} & -A_{13}A_{23}+A_{12}A_{33} \\ -A_{23}A_{21}+A_{22}A_{31} & -A_{23}A_{22}+A_{22}A_{32} & -A_{23}^2+A_{22}A_{33} \\ -A_{33}A_{21}+A_{32}A_{31} & -A_{33}A_{22}+A_{32}^2 & -A_{33}A_{23}+A_{32}A_{33} \end{bmatrix} - \begin{bmatrix} A_{31}A_{12}-A_{21}A_{13} & A_{31}A_{22}-A_{21}A_{23} & A_{31}A_{32}-A_{21}A_{33} \\ A_{32}A_{12}+A_{22}A_{13} & A_{32}A_{22}-A_{22}A_{23} & A_{32}^2-A_{22}A_{33} \\ A_{33}A_{12}+A_{23}A_{13} & A_{33}A_{22}-A_{23}^2 & A_{33}A_{32}-A_{23}A_{33} \end{bmatrix}$$

$$= \underbrace{\begin{bmatrix} 0 & -A_{22}(A_{31}+A_{13})+A_{23}A_{21}+A_{32}A_{12} & A_{33}(A_{12}+A_{21})-A_{13}A_{23}-A_{31}A_{32} \\ A_{22}(A_{31}+A_{13})-A_{23}A_{21}-A_{32}A_{12} & 0 & -A_{23}^2-A_{32}^2+2A_{22}A_{33} \\ -A_{33}(A_{12}+A_{21})+A_{13}A_{23}+A_{31}A_{32} & A_{23}^2+A_{32}^2-2A_{22}A_{33} & 0 \end{bmatrix}}_{\widehat{\mathbf{m_1}}}$$

leading to the conclusion that

$$\mathrm{ax}(\widehat{\mathbf{m_1}}) = \begin{Bmatrix} A_{23}^2+A_{32}^2-2A_{22}A_{33} \\ A_{33}(A_{12}+A_{21})-A_{13}A_{23}-A_{31}A_{32} \\ A_{22}(A_{31}+A_{13})-A_{23}A_{21}-A_{32}A_{12} \end{Bmatrix} \Rightarrow \mathbf{m_1} = \mathrm{ax}\,(2\mathrm{skew}(\mathbf{A}\boldsymbol{\epsilon_1}\mathbf{A})). \quad \text{(G.54)}$$

The vector $\mathbf{m_1}$ can be recognized in the derived expression:

$$\boldsymbol{\epsilon} : \left(\mathbf{A}\widehat{\mathbf{b}}\mathbf{A}\right)$$

$$= \begin{bmatrix} A_{23}^2 + A_{32}^2 - 2A_{22}A_{33} & A_{33}(A_{12} + A_{21}) - A_{23}A_{13} - A_{31}A_{32} & A_{22}(A_{13} + A_{31}) - A_{21}A_{23} - A_{32}A_{12} \\ A_{33}(A_{12} + A_{21}) - A_{13}A_{23} - A_{32}A_{31} & A_{13}^2 + A_{31}^2 - 2A_{11}A_{33} & A_{11}(A_{23} + A_{32}) - A_{12}A_{13} - A_{31}A_{21} \\ A_{22}(A_{13} + A_{31}) - A_{12}A_{32} - A_{23}A_{21} & A_{11}(A_{32} + A_{23}) - A_{12}A_{13} - A_{31}A_{21} & A_{12}^2 + A_{21}^2 - 2A_{11}A_{22} \end{bmatrix} \begin{Bmatrix} b_1 \\ b_2 \\ b_3 \end{Bmatrix}$$

as the first column in the matrix. By analogy we obtain

$$\mathbf{m_2} = \begin{Bmatrix} A_{33}(A_{12} + A_{21}) - A_{23}A_{13} - A_{31}A_{32} \\ A_{13}^2 + A_{31}^2 - 2A_{11}A_{33} \\ A_{11}(A_{32} + A_{23}) - A_{12}A_{13} - A_{31}A_{21} \end{Bmatrix}, \quad \mathbf{m_3} = \begin{Bmatrix} A_{22}(A_{13} + A_{31}) - A_{21}A_{23} - A_{32}A_{12} \\ A_{11}(A_{23} + A_{32}) - A_{12}A_{13} - A_{31}A_{21} \\ A_{12}^2 + A_{21}^2 - 2A_{11}A_{22} \end{Bmatrix},$$

where $\mathbf{m_2} = \text{ax}\left(2\text{skew}(\mathbf{A}\boldsymbol{\epsilon_2}\mathbf{A})\right)$ and $\mathbf{m_3} = \text{ax}\left(2\text{skew}(\mathbf{A}\boldsymbol{\epsilon_3}\mathbf{A})\right)$. Finally, we obtain

$$\boldsymbol{\epsilon} : \left(\mathbf{A}\widehat{\mathbf{b}}\mathbf{A}\right) = [\mathbf{m_1} \quad \mathbf{m_2} \quad \mathbf{m_3}]\,\mathbf{b}$$

$$= [\text{ax}(2\text{skew}(\mathbf{A}\boldsymbol{\epsilon_1}\mathbf{A})) \quad \text{ax}(2\text{skew}(\mathbf{A}\boldsymbol{\epsilon_2}\mathbf{A})) \quad \text{ax}(2\text{skew}(\mathbf{A}\boldsymbol{\epsilon_3}\mathbf{A}))]\,\mathbf{b}.$$

Second term in (G.52):

$$-(\mu - \nu)N_i\boldsymbol{\epsilon} : \left(\mathbf{F}\mathbf{Q}^{\mathrm{T}}\text{GRAD}(\Delta\mathbf{u})\mathbf{Q}^{\mathrm{T}}\right) = -(\mu - \nu)N_i\boldsymbol{\epsilon} : \left(\mathbf{F}\mathbf{Q}^{\mathrm{T}}(\Delta\mathbf{u} \otimes \nabla_X)\mathbf{Q}^{\mathrm{T}}\right)$$

$$= -(\mu - \nu)N_i\boldsymbol{\epsilon} : \left(\underbrace{\mathbf{F}\mathbf{Q}^{\mathrm{T}}\Delta\mathbf{u}}_{\text{vector}}\,\underbrace{\nabla_X^{\mathrm{T}}\mathbf{Q}^{\mathrm{T}}}_{\text{vector}^{\mathrm{T}}}\right)$$

$$= -(\mu - \nu)N_i\boldsymbol{\epsilon} : \left((\mathbf{F}\mathbf{Q}^{\mathrm{T}}\Delta\mathbf{u}) \otimes (\mathbf{Q}\nabla_X)\right)$$

$$|\text{by using } \boldsymbol{\epsilon} : (\mathbf{a} \otimes \mathbf{b}) = -\widehat{\mathbf{b}}\mathbf{a} = \widehat{\mathbf{a}}\mathbf{b}|$$

$$= (\mu - \nu)N_i\widehat{\mathbf{Q}\nabla_X}\mathbf{F}\mathbf{Q}^{\mathrm{T}}\Delta\mathbf{u}, \qquad (\text{G.55})$$

where ∇_X in (G.55) operates exclusively on $\Delta\mathbf{u}$.

Finally, we obtain

$$-N_i\boldsymbol{\epsilon} : \left(\mathbf{F}(\mu - \nu)\Delta\mathbf{E}\mathbf{Q}^{\mathrm{T}}\right)$$

$$= -(\mu - \nu)N_i\boldsymbol{\epsilon} : \left(\mathbf{F}\mathbf{Q}^{\mathrm{T}}\widehat{\Delta\boldsymbol{\varphi}}^{\mathrm{T}}\mathbf{F}\mathbf{Q}^{\mathrm{T}}\right) - (\mu - \nu)N_i\boldsymbol{\epsilon} : \left(\mathbf{F}\mathbf{Q}^{\mathrm{T}}\text{GRAD}\Delta\mathbf{u}\mathbf{Q}^{\mathrm{T}}\right)$$

$$= (\mu - \nu)N_i\left[\text{ax}(2\text{skew}(\mathbf{F}\mathbf{Q}^{\mathrm{T}}\boldsymbol{\epsilon_1}\mathbf{F}\mathbf{Q}^{\mathrm{T}})) \quad \text{ax}(2\text{skew}(\mathbf{F}\mathbf{Q}^{\mathrm{T}}\boldsymbol{\epsilon_2}\mathbf{F}\mathbf{Q}^{\mathrm{T}})) \quad \text{ax}(2\text{skew}(\mathbf{F}\mathbf{Q}^{\mathrm{T}}\boldsymbol{\epsilon_3}\mathbf{F}\mathbf{Q}^{\mathrm{T}}))\right]\Delta\boldsymbol{\varphi}$$

$$+ (\mu - \nu)N_i\widehat{\mathbf{Q}\nabla_X}\mathbf{F}\mathbf{Q}^{\mathrm{T}}\Delta\mathbf{u}. \qquad (\text{G.56})$$

G.10.3.3 $-N_i\boldsymbol{\epsilon} : \left(\mathbf{F}\mathbf{B}^{\mathbf{T}}\mathbf{Q}^{\mathbf{T}}\widehat{\Delta\boldsymbol{\varphi}}^{\mathbf{T}}\right)$

By applying (G.49) we obtain:

$$-N_i\boldsymbol{\epsilon} : \left(\mathbf{F}\mathbf{B}^{\mathrm{T}}\mathbf{Q}^{\mathrm{T}}\widehat{\Delta\boldsymbol{\varphi}}^{\mathrm{T}}\right) = N_i\boldsymbol{\epsilon} : \left(\mathbf{F}\mathbf{B}^{\mathrm{T}}\mathbf{Q}^{\mathrm{T}}\widehat{\Delta\boldsymbol{\varphi}}\right) \tag{G.57}$$

$$= N_i\left[\left(\mathbf{F}\mathbf{B}^{\mathrm{T}}\mathbf{Q}^{\mathrm{T}}\right)^{\mathrm{T}} - \mathrm{tr}\left(\mathbf{F}\mathbf{B}^{\mathrm{T}}\mathbf{Q}^{\mathrm{T}}\right)\mathbf{I}\right]\Delta\boldsymbol{\varphi}. \tag{G.58}$$

Now we recall (G.40)

$$\left.\frac{\mathrm{d}}{\mathrm{d}\epsilon}\right|_{\epsilon=0} \left(-N_i\boldsymbol{\epsilon} : \left(\mathbf{F}\mathbf{B}^{\mathrm{T}}\mathbf{Q}^{\mathrm{T}}\right)\right)_\epsilon$$

$$= -N_i\boldsymbol{\epsilon} : \left(\mathrm{GRAD}(\Delta\mathbf{u})\mathbf{B}^{\mathrm{T}}\mathbf{Q}^{\mathrm{T}}\right) - N_i\boldsymbol{\epsilon} : \left(\mathbf{F}(\mathbf{T} : \Delta\mathbf{E})^{\mathrm{T}}\mathbf{Q}^{\mathrm{T}}\right) - N_i\boldsymbol{\epsilon} : \left(\mathbf{F}\mathbf{B}^{\mathrm{T}}\mathbf{Q}^{\mathrm{T}}\widehat{\Delta\boldsymbol{\varphi}}^{\mathrm{T}}\right),$$

and substitute the following derived terms:

$$-N_i\boldsymbol{\epsilon} : \left(\mathrm{GRAD}(\Delta\mathbf{u})\mathbf{B}^{\mathrm{T}}\mathbf{Q}^{\mathrm{T}}\right) = N_i\widehat{\mathbf{Q}\mathbf{B}\nabla_X}\Delta\mathbf{u}, \quad \text{derived in Section (G.10.3.1)}$$

$$- N_i\boldsymbol{\epsilon} : \left(\mathbf{F}(\mathbf{T} : \Delta\mathbf{E})^{\mathrm{T}}\mathbf{Q}^{\mathrm{T}}\right)$$
$$= -N_i\boldsymbol{\epsilon} : \left(\mathbf{F}(\lambda\,\mathrm{tr}(\Delta\mathbf{E})\mathbf{I}\mathbf{Q}^{\mathrm{T}}\right) - N_i\boldsymbol{\epsilon} : \left(\mathbf{F}(\mu+\nu)\Delta\mathbf{E}^{\mathrm{T}}\mathbf{Q}^{\mathrm{T}}\right) - N_i\boldsymbol{\epsilon} : \left(\mathbf{F}(\mu-\nu)\Delta\mathbf{E}\mathbf{Q}^{\mathrm{T}}\right)$$
$$= \underbrace{4\lambda N_i\,\mathrm{ax}(\mathrm{skew}(\mathbf{F}\mathbf{Q}^{\mathrm{T}}))\left[\mathrm{ax}(\mathrm{skew}(\mathbf{F}\mathbf{Q}^{\mathrm{T}}))\right]^{\mathrm{T}}\Delta\boldsymbol{\varphi} + 2\lambda N_i\,\mathrm{ax}(\mathrm{skew}(\mathbf{F}\mathbf{Q}^{\mathrm{T}}))\nabla_X^{\mathrm{T}}\mathbf{Q}^{\mathrm{T}}\Delta\mathbf{u}}_{-N_i\boldsymbol{\epsilon}:(\mathbf{F}(\lambda\,\mathrm{tr}(\Delta\mathbf{E})\mathbf{I}\mathbf{Q}^{\mathrm{T}})}$$
$$\underbrace{-(\mu+\nu)N_i\left(\mathbf{F}\mathbf{F}^{\mathrm{T}} - \mathrm{tr}(\mathbf{F}\mathbf{F}^{\mathrm{T}})\mathbf{I}\right)\Delta\boldsymbol{\varphi} - (\mu+\nu)N_i\widehat{\mathbf{F}\nabla_X}\Delta\mathbf{u}}_{-N_i\boldsymbol{\epsilon}:(\mathbf{F}(\mu+\nu)\Delta\mathbf{E}^{\mathrm{T}}\mathbf{Q}^{\mathrm{T}})}$$
$$+ (\mu-\nu)N_i\left[\mathrm{ax}(2\mathrm{skew}(\mathbf{F}\mathbf{Q}^{\mathrm{T}}\boldsymbol{\epsilon_1}\mathbf{F}\mathbf{Q}^{\mathrm{T}}))\ \mathrm{ax}(2\mathrm{skew}(\mathbf{F}\mathbf{Q}^{\mathrm{T}}\boldsymbol{\epsilon_2}\mathbf{F}\mathbf{Q}^{\mathrm{T}}))\ \mathrm{ax}(2\mathrm{skew}(\mathbf{F}\mathbf{Q}^{\mathrm{T}}\boldsymbol{\epsilon_3}\mathbf{F}\mathbf{Q}^{\mathrm{T}}))\right]\Delta\boldsymbol{\varphi}$$
$$+ (\mu-\nu)N_i\widehat{\mathbf{Q}\nabla_X}\mathbf{F}\mathbf{Q}^{\mathrm{T}}\Delta\mathbf{u}, \quad \text{derived in Section (G.10.3.2)}$$

$$-N_i\boldsymbol{\epsilon} : \left(\mathbf{F}\mathbf{B}^{\mathrm{T}}\mathbf{Q}^{\mathrm{T}}\widehat{\Delta\boldsymbol{\varphi}}^{\mathrm{T}}\right) = N_i\left[\left(\mathbf{F}\mathbf{B}^{\mathrm{T}}\mathbf{Q}^{\mathrm{T}}\right)^{\mathrm{T}} - \mathrm{tr}\left(\mathbf{F}\mathbf{B}^{\mathrm{T}}\mathbf{Q}^{\mathrm{T}}\right)\mathbf{I}\right]\Delta\boldsymbol{\varphi}, \quad \text{derived in Section (G.10.3.3)}.$$

Finally, (G.40) follows as

$$\left.\frac{\mathrm{d}}{\mathrm{d}\epsilon}\right|_{\epsilon=0} \left(-N_i\boldsymbol{\epsilon} : \left(\mathbf{F}\mathbf{B}^{\mathrm{T}}\mathbf{Q}^{\mathrm{T}}\right)\right)_\epsilon$$
$$= N_i\widehat{\mathbf{Q}\mathbf{B}\nabla_X}\Delta\mathbf{u} + 4\lambda N_i\,\mathrm{ax}(\mathrm{skew}(\mathbf{F}\mathbf{Q}^{\mathrm{T}}))\left[\mathrm{ax}(\mathrm{skew}(\mathbf{F}\mathbf{Q}^{\mathrm{T}}))\right]^{\mathrm{T}}\Delta\boldsymbol{\varphi}$$
$$+ 2\lambda N_i\,\mathrm{ax}(\mathrm{skew}(\mathbf{F}\mathbf{Q}^{\mathrm{T}}))\nabla_X^{\mathrm{T}}\mathbf{Q}^{\mathrm{T}}\Delta\mathbf{u} - (\mu+\nu)N_i\left(\mathbf{F}\mathbf{F}^{\mathrm{T}} - \mathrm{tr}(\mathbf{F}\mathbf{F}^{\mathrm{T}})\mathbf{I}\right)\Delta\boldsymbol{\varphi}$$
$$- (\mu+\nu)N_i\widehat{\mathbf{F}\nabla_X}\Delta\mathbf{u}$$

$$+ (\mu - \nu)N_i \left[\mathrm{ax}(2\mathrm{skew}(\mathbf{F}\mathbf{Q}^{\mathrm{T}}\boldsymbol{\epsilon_1}\mathbf{F}\mathbf{Q}^{\mathrm{T}})) \quad \mathrm{ax}(2\mathrm{skew}(\mathbf{F}\mathbf{Q}^{\mathrm{T}}\boldsymbol{\epsilon_2}\mathbf{F}\mathbf{Q}^{\mathrm{T}})) \quad \mathrm{ax}(2\mathrm{skew}(\mathbf{F}\mathbf{Q}^{\mathrm{T}}\boldsymbol{\epsilon_3}\mathbf{F}\mathbf{Q}^{\mathrm{T}})) \right] \Delta\boldsymbol{\varphi}$$

$$+ (\mu - \nu)N_i\widehat{\mathbf{Q}\nabla_X}\mathbf{F}\mathbf{Q}^{\mathrm{T}}\Delta\mathbf{u} + N_i \left[\left(\mathbf{F}\mathbf{B}^{\mathrm{T}}\mathbf{Q}^{\mathrm{T}}\right)^{\mathrm{T}} - \mathrm{tr}\left(\mathbf{F}\mathbf{B}^{\mathrm{T}}\mathbf{Q}^{\mathrm{T}}\right)\mathbf{I} \right] \Delta\boldsymbol{\varphi},$$

where all ∇_X operate on $\Delta\mathbf{u}$.

Appendix H

Validation of the derived formulation

In order to check the validity of the derived formulation we observe the undeformed configuration, i.e.

$$\mathbf{u} = \mathbf{0}, \quad \boldsymbol{\varphi} = \mathbf{0}, \quad \mathbf{B} = \mathbf{0}, \quad \mathbf{G} = \mathbf{0}, \quad \mathbf{F} = \mathbf{I}, \quad \mathbf{Q} = \mathbf{I}, \tag{H.1}$$

leading to

$$\boldsymbol{\ell} = \mathrm{ax}(\mathrm{skew}(\mathbf{F}\mathbf{Q}^{\mathrm{T}})) = \mathrm{ax}(\frac{1}{2}(\mathbf{I} - \mathbf{I}^{\mathrm{T}})) = \mathbf{0}, \tag{H.2}$$

and

$$[\mathbf{m_1}\ \mathbf{m_2}\ \mathbf{m_3}] = [\mathrm{ax}(2\mathrm{skew}(\mathbf{I}\boldsymbol{\epsilon_1}\mathbf{I}))\ \ \mathrm{ax}(2\mathrm{skew}(\mathbf{I}\boldsymbol{\epsilon_2}\mathbf{I}))\ \ \mathrm{ax}(2\mathrm{skew}(\mathbf{I}\boldsymbol{\epsilon_3}\mathbf{I}))]$$

$$\left[\mathrm{ax}(\mathbf{I}\boldsymbol{\epsilon_1}\mathbf{I} - (\mathbf{I}\boldsymbol{\epsilon_1}\mathbf{I})^{\mathrm{T}})\ \ \mathrm{ax}(\mathbf{I}\boldsymbol{\epsilon_2}\mathbf{I} - (\mathbf{I}\boldsymbol{\epsilon_2}\mathbf{I})^{\mathrm{T}})\ \ \mathrm{ax}(\mathbf{I}\boldsymbol{\epsilon_3}\mathbf{I} - (\mathbf{I}\boldsymbol{\epsilon_3}\mathbf{I})^{\mathrm{T}})\right]$$

$$= \left[\mathrm{ax}\left(\begin{bmatrix} 0 & 0 & 0 \\ 0 & 0 & 2 \\ 0 & -2 & 0 \end{bmatrix}\right)\ \ \mathrm{ax}\left(\begin{bmatrix} 0 & 0 & -2 \\ 0 & 0 & 0 \\ 2 & 0 & 0 \end{bmatrix}\right)\ \ \mathrm{ax}\left(\begin{bmatrix} 0 & 2 & 0 \\ -2 & 0 & 0 \\ 0 & 0 & 0 \end{bmatrix}\right)\right]$$

$$= \begin{bmatrix} -2 & 0 & 0 \\ 0 & -2 & 0 \\ 0 & 0 & -2 \end{bmatrix}$$

$$= -2\mathbf{I}$$

Thus, in the undeformed configuration the element incremental nodal residual reduces to

$$
\Delta \mathbf{g}_i^e = \left\{
\begin{array}{c}
-\widehat{\mathbf{I0}(N_i\nabla_X)}\Delta\boldsymbol{\varphi} + \lambda\mathbf{I}(N_i\nabla_X)2\mathbf{0}^{\mathrm{T}}\Delta\boldsymbol{\varphi} + \lambda\mathbf{I}(N_i\nabla_X)\nabla_X^{\mathrm{T}}\mathbf{I}^{\mathrm{T}}\Delta\mathbf{u} + (\mu+\nu)\widehat{\mathbf{I}(N_i\nabla_X)}\Delta\boldsymbol{\varphi} + (\mu+\nu)\nabla_X^{\mathrm{T}}(N_i\nabla_X)\Delta\mathbf{u} - (\mu-\nu)\mathbf{II}^{\mathrm{T}}\widehat{\mathbf{I}(N_i\nabla_X)}\Delta\boldsymbol{\varphi} + (\mu-\nu)\mathbf{I}\nabla_X(N_i\nabla_X^{\mathrm{T}})\mathbf{I}^{\mathrm{T}}\Delta\mathbf{u} \\
-\widehat{\mathbf{I0}(N_i\nabla_X)}\Delta\boldsymbol{\varphi} + \alpha\mathbf{I}(N_i\nabla_X)\nabla_X^{\mathrm{T}}\mathbf{I}^{\mathrm{T}}\Delta\boldsymbol{\varphi} + (\beta+\gamma)\nabla_X^{\mathrm{T}}(N_i\nabla_X)\Delta\boldsymbol{\varphi} + (\beta-\gamma)\mathbf{I}\nabla_X(N_i\nabla_X^{\mathrm{T}})\mathbf{I}^{\mathrm{T}}\Delta\boldsymbol{\varphi} + N_i\widehat{\mathbf{I0}\nabla_X}\Delta\mathbf{u} + 4\lambda N_i\,\mathbf{00}^{\mathrm{T}}\Delta\boldsymbol{\varphi} + 2\lambda N_i\,\mathbf{0}\nabla_X^{\mathrm{T}}\mathbf{I}^{\mathrm{T}}\Delta\mathbf{u} + \dots \\
\dots - (\mu+\nu)N_i\left(\mathbf{II}^{\mathrm{T}} - \mathrm{tr}(\mathbf{II}^{\mathrm{T}})\mathbf{I}\right)\Delta\boldsymbol{\varphi} - (\mu+\nu)N_i\widehat{\mathbf{I}\nabla_X}\Delta\mathbf{u} - 2(\mu-\nu)N_i\mathbf{I}\Delta\boldsymbol{\varphi} + (\mu-\nu)N_i\widehat{\mathbf{I}\nabla_X}\mathbf{II}^{\mathrm{T}}\Delta\mathbf{u} + N_i\left[\left(\mathbf{I0}^{\mathrm{T}}\mathbf{I}^{\mathrm{T}}\right)^{\mathrm{T}} - \mathrm{tr}\left(\mathbf{I0}^{\mathrm{T}}\mathbf{I}^{\mathrm{T}}\right)\mathbf{I}\right]\Delta\boldsymbol{\varphi}
\end{array}
\right\}
$$

$$
= \left\{
\begin{array}{c}
\lambda(N_i\nabla_X)\nabla_X^{\mathrm{T}}\Delta\mathbf{u} + (\mu+\nu)\widehat{(N_i\nabla_X)}\Delta\boldsymbol{\varphi} + (\mu+\nu)\nabla_X^{\mathrm{T}}(N_i\nabla_X)\Delta\mathbf{u} - (\mu-\nu)\widehat{(N_i\nabla_X)}\Delta\boldsymbol{\varphi} + (\mu-\nu)\nabla_X(N_i\nabla_X^{\mathrm{T}})\Delta\mathbf{u} \\
\alpha(N_i\nabla_X)\nabla_X^{\mathrm{T}}\Delta\boldsymbol{\varphi} + (\beta+\gamma)\nabla_X^{\mathrm{T}}(N_i\nabla_X)\Delta\boldsymbol{\varphi} + (\beta-\gamma)\nabla_X(N_i\nabla_X^{\mathrm{T}})\Delta\boldsymbol{\varphi} + 2(\mu+\nu)N_i\mathbf{I}\Delta\boldsymbol{\varphi} - (\mu+\nu)N_i\widehat{\nabla_X}\Delta\mathbf{u} - 2(\mu-\nu)N_i\mathbf{I}\Delta\boldsymbol{\varphi} + (\mu-\nu)N_i\widehat{\nabla_X}\Delta\mathbf{u}
\end{array}
\right\}
$$

$$
= \left\{
\begin{array}{c}
\left(\lambda(N_i\nabla_X)\nabla_X^{\mathrm{T}} + (\mu+\nu)\nabla_X^{\mathrm{T}}(N_i\nabla_X) + (\mu-\nu)\nabla_X(N_i\nabla_X^{\mathrm{T}})\right)\Delta\mathbf{u} + \left((\mu+\nu)\widehat{(N_i\nabla_X)} - (\mu-\nu)\widehat{(N_i\nabla_X)}\right)\Delta\boldsymbol{\varphi} \\
\left((\mu-\nu)N_i\widehat{\nabla_X} - (\mu+\nu)N_i\widehat{\nabla_X}\right)\Delta\mathbf{u} + \left(\alpha(N_i\nabla_X)\nabla_X^{\mathrm{T}} + (\beta+\gamma)\nabla_X^{\mathrm{T}}(N_i\nabla_X) + (\beta-\gamma)\nabla_X(N_i\nabla_X^{\mathrm{T}}) + 2(\mu+\nu)N_i\mathbf{I} - 2(\mu-\nu)N_i\mathbf{I}\right)\Delta\boldsymbol{\varphi}
\end{array}
\right\}
$$

$$
= \begin{bmatrix}
\lambda(N_i\nabla_X)\nabla_X^{\mathrm{T}} + (\mu+\nu)\nabla_X^{\mathrm{T}}(N_i\nabla_X)\mathbf{I} + (\mu-\nu)\nabla_X(N_i\nabla_X^{\mathrm{T}}) & (\mu+\nu)\widehat{(N_i\nabla_X)} - (\mu-\nu)\widehat{(N_i\nabla_X)} \\
(\mu-\nu)N_i\widehat{\nabla_X} - (\mu+\nu)N_i\widehat{\nabla_X} & \alpha(N_i\nabla_X)\nabla_X^{\mathrm{T}} + (\beta+\gamma)\nabla_X^{\mathrm{T}}(N_i\nabla_X)\mathbf{I} + (\beta-\gamma)\nabla_X(N_i\nabla_X^{\mathrm{T}}) + 4\nu N_i\mathbf{I}
\end{bmatrix}
\left\{\begin{array}{c}\Delta\mathbf{u}\\\Delta\boldsymbol{\varphi}\end{array}\right\}
$$

$$
= \begin{bmatrix}
\lambda(N_i\nabla_X)\nabla_X^{\mathrm{T}} + (\mu+\nu)\nabla_X^{\mathrm{T}}(N_i\nabla_X)\mathbf{I} + (\mu-\nu)\nabla_X(N_i\nabla_X^{\mathrm{T}}) & 2\nu\widehat{(N_i\nabla_X)} \\
-2\nu\widehat{(N_i\nabla_X)} & \alpha(N_i\nabla_X)\nabla_X^{\mathrm{T}} + (\beta+\gamma)\nabla_X^{\mathrm{T}}(N_i\nabla_X)\mathbf{I} + (\beta-\gamma)\nabla_X(N_i\nabla_X^{\mathrm{T}}) + 4\nu N_i\mathbf{I}
\end{bmatrix}
\left\{\begin{array}{c}\Delta\mathbf{u}\\\Delta\boldsymbol{\varphi}\end{array}\right\}
$$

Now we introduce the interpolation of the kinematic fields (5.31) and obtain

$$
\Delta\mathbf{g}_i = \sum_{j=1}^{n_{node}} \begin{bmatrix}
\lambda(N_i\nabla_X)(N_j\nabla_X^{\mathrm{T}}) + (\mu+\nu)(N_j\nabla_X^{\mathrm{T}})(N_i\nabla_X)\mathbf{I} + (\mu-\nu)(N_j\nabla_X)(N_i\nabla_X^{\mathrm{T}}) & 2\nu\widehat{(N_i\nabla_X)}N_j \\
-2\nu\widehat{(N_i\nabla_X)}N_j & \alpha(N_i\nabla_X)(N_j\nabla_X^{\mathrm{T}}) + (\beta+\gamma)(N_j\nabla_X^{\mathrm{T}})(N_i\nabla_X)\mathbf{I} + (\beta-\gamma)(N_j\nabla_X)(N_i\nabla_X^{\mathrm{T}}) + 4\nu N_i N_j\mathbf{I}
\end{bmatrix}
\left\{\begin{array}{c}\Delta\mathbf{u}_j^e\\\Delta\boldsymbol{\varphi}_j^e\end{array}\right\},
$$

By introducing the following

$$
(N_i \nabla_X) = \left\{ \begin{array}{c} \frac{\partial N_i}{\partial X_1} \\ \frac{\partial N_i}{\partial X_2} \\ \frac{\partial N_i}{\partial X_3} \end{array} \right\}, \quad (N_j \nabla_X^{\mathrm{T}}) = \left\langle \begin{array}{ccc} \frac{\partial N_j}{\partial X_1} & \frac{\partial N_j}{\partial X_2} & \frac{\partial N_j}{\partial X_3} \end{array} \right\rangle, \quad \widehat{(N_i \nabla_X)} = \begin{bmatrix} 0 & -\frac{\partial N_i}{\partial X_3} & \frac{\partial N_i}{\partial X_2} \\ \frac{\partial N_i}{\partial X_3} & 0 & -\frac{\partial N_i}{\partial X_1} \\ -\frac{\partial N_i}{\partial X_2} & \frac{\partial N_i}{\partial X_1} & 0 \end{bmatrix},
\tag{H.3}
$$

$$
(N_j \nabla_X^{\mathrm{T}})(N_i \nabla_X)\mathbf{I} = \begin{bmatrix} \frac{\partial N_i}{\partial X_1}\frac{\partial N_j}{\partial X_1} + \frac{\partial N_i}{\partial X_2}\frac{\partial N_j}{\partial X_2} + \frac{\partial N_i}{\partial X_3}\frac{\partial N_j}{\partial X_3} & 0 & 0 \\ 0 & \frac{\partial N_i}{\partial X_1}\frac{\partial N_j}{\partial X_1} + \frac{\partial N_i}{\partial X_2}\frac{\partial N_j}{\partial X_2} + \frac{\partial N_i}{\partial X_3}\frac{\partial N_j}{\partial X_3} & 0 \\ 0 & 0 & \frac{\partial N_i}{\partial X_1}\frac{\partial N_j}{\partial X_1} + \frac{\partial N_i}{\partial X_2}\frac{\partial N_j}{\partial X_2} + \frac{\partial N_i}{\partial X_3}\frac{\partial N_j}{\partial X_3} \end{bmatrix},
\tag{H.4}
$$

$$
(N_i \nabla_X)(N_j \nabla_X^{\mathrm{T}}) = \left\{ \begin{array}{c} \frac{\partial N_i}{\partial X_1} \\ \frac{\partial N_i}{\partial X_2} \\ \frac{\partial N_i}{\partial X_3} \end{array} \right\} \left\langle \begin{array}{ccc} \frac{\partial N_j}{\partial X_1} & \frac{\partial N_j}{\partial X_2} & \frac{\partial N_j}{\partial X_3} \end{array} \right\rangle = \begin{bmatrix} \frac{\partial N_i}{\partial X_1}\frac{\partial N_j}{\partial X_1} & \frac{\partial N_i}{\partial X_1}\frac{\partial N_j}{\partial X_2} & \frac{\partial N_i}{\partial X_1}\frac{\partial N_j}{\partial X_3} \\ \frac{\partial N_i}{\partial X_2}\frac{\partial N_j}{\partial X_1} & \frac{\partial N_i}{\partial X_2}\frac{\partial N_j}{\partial X_2} & \frac{\partial N_i}{\partial X_2}\frac{\partial N_j}{\partial X_3} \\ \frac{\partial N_i}{\partial X_3}\frac{\partial N_j}{\partial X_1} & \frac{\partial N_i}{\partial X_3}\frac{\partial N_j}{\partial X_2} & \frac{\partial N_i}{\partial X_3}\frac{\partial N_j}{\partial X_3} \end{bmatrix},
\tag{H.5}
$$

$$
(N_j \nabla_X)(N_i \nabla_X^{\mathrm{T}}) = \left\{ \begin{array}{c} \frac{\partial N_j}{\partial X_1} \\ \frac{\partial N_j}{\partial X_2} \\ \frac{\partial N_j}{\partial X_3} \end{array} \right\} \left\langle \begin{array}{ccc} \frac{\partial N_i}{\partial X_1} & \frac{\partial N_i}{\partial X_2} & \frac{\partial N_i}{\partial X_3} \end{array} \right\rangle = \begin{bmatrix} \frac{\partial N_j}{\partial X_1}\frac{\partial N_i}{\partial X_1} & \frac{\partial N_j}{\partial X_1}\frac{\partial N_i}{\partial X_2} & \frac{\partial N_j}{\partial X_1}\frac{\partial N_i}{\partial X_3} \\ \frac{\partial N_j}{\partial X_2}\frac{\partial N_i}{\partial X_1} & \frac{\partial N_j}{\partial X_2}\frac{\partial N_i}{\partial X_2} & \frac{\partial N_j}{\partial X_2}\frac{\partial N_i}{\partial X_3} \\ \frac{\partial N_j}{\partial X_3}\frac{\partial N_i}{\partial X_1} & \frac{\partial N_j}{\partial X_3}\frac{\partial N_i}{\partial X_2} & \frac{\partial N_j}{\partial X_3}\frac{\partial N_i}{\partial X_3} \end{bmatrix},
\tag{H.6}
$$

we obtain

$$
\Delta \mathbf{g}_i = \sum_{j=1}^{8} \begin{bmatrix} \mathbf{K_{m_{u1}}} & \mathbf{K_{m_\varphi}} \\ \mathbf{K_{m_\varphi}}^{\mathrm{T}} & \mathbf{K_{m_{u2}}} \end{bmatrix} \left\{ \begin{array}{c} \Delta \mathbf{u}_j^e \\ \Delta \boldsymbol{\varphi}_j^e \end{array} \right\},
$$

where

$$\mathbf{K_{m_{u1}}} = \lambda \begin{bmatrix} \frac{\partial N_i}{\partial X_1}\frac{\partial N_j}{\partial X_1} & \frac{\partial N_i}{\partial X_1}\frac{\partial N_j}{\partial X_2} & \frac{\partial N_i}{\partial X_1}\frac{\partial N_j}{\partial X_3} \\ \frac{\partial N_i}{\partial X_2}\frac{\partial N_j}{\partial X_1} & \frac{\partial N_i}{\partial X_2}\frac{\partial N_j}{\partial X_2} & \frac{\partial N_i}{\partial X_2}\frac{\partial N_j}{\partial X_3} \\ \frac{\partial N_i}{\partial X_3}\frac{\partial N_j}{\partial X_1} & \frac{\partial N_i}{\partial X_3}\frac{\partial N_j}{\partial X_2} & \frac{\partial N_i}{\partial X_3}\frac{\partial N_j}{\partial X_3} \end{bmatrix} + (\mu+\nu)\left(\frac{\partial N_i}{\partial X_1}\frac{\partial N_j}{\partial X_1} + \frac{\partial N_i}{\partial X_2}\frac{\partial N_j}{\partial X_2} + \frac{\partial N_i}{\partial X_3}\frac{\partial N_j}{\partial X_3}\right)\begin{bmatrix} 1 & 0 & 0 \\ 0 & 1 & 0 \\ 0 & 0 & 1 \end{bmatrix} + (\mu-\nu)\begin{bmatrix} \frac{\partial N_j}{\partial X_1}\frac{\partial N_i}{\partial X_1} & \frac{\partial N_j}{\partial X_1}\frac{\partial N_i}{\partial X_2} & \frac{\partial N_j}{\partial X_1}\frac{\partial N_i}{\partial X_3} \\ \frac{\partial N_j}{\partial X_2}\frac{\partial N_i}{\partial X_1} & \frac{\partial N_j}{\partial X_2}\frac{\partial N_i}{\partial X_2} & \frac{\partial N_j}{\partial X_2}\frac{\partial N_i}{\partial X_3} \\ \frac{\partial N_j}{\partial X_3}\frac{\partial N_i}{\partial X_1} & \frac{\partial N_j}{\partial X_3}\frac{\partial N_i}{\partial X_2} & \frac{\partial N_j}{\partial X_3}\frac{\partial N_i}{\partial X_3} \end{bmatrix}$$

$$= \begin{bmatrix} (\lambda+2\mu)\frac{\partial N_i}{\partial X_1}\frac{\partial N_j}{\partial X_1} + (\mu+\nu)\left(\frac{\partial N_i}{\partial X_2}\frac{\partial N_j}{\partial X_2} + \frac{\partial N_i}{\partial X_3}\frac{\partial N_j}{\partial X_3}\right) & \lambda\frac{\partial N_i}{\partial X_1}\frac{\partial N_j}{\partial X_2} + (\mu-\nu)\frac{\partial N_i}{\partial X_2}\frac{\partial N_j}{\partial X_1} & \lambda\frac{\partial N_i}{\partial X_1}\frac{\partial N_j}{\partial X_3} + (\mu-\nu)\frac{\partial N_i}{\partial X_3}\frac{\partial N_j}{\partial X_1} \\ \lambda\frac{\partial N_i}{\partial X_2}\frac{\partial N_j}{\partial X_1} + (\mu-\nu)\frac{\partial N_i}{\partial X_1}\frac{\partial N_j}{\partial X_2} & (\lambda+2\mu)\frac{\partial N_i}{\partial X_2}\frac{\partial N_j}{\partial X_2} + (\mu+\nu)\left(\frac{\partial N_i}{\partial X_1}\frac{\partial N_j}{\partial X_1} + \frac{\partial N_i}{\partial X_3}\frac{\partial N_j}{\partial X_3}\right) & \lambda\frac{\partial N_i}{\partial X_2}\frac{\partial N_j}{\partial X_3} + (\mu-\nu)\frac{\partial N_i}{\partial X_3}\frac{\partial N_j}{\partial X_2} \\ \lambda\frac{\partial N_i}{\partial X_3}\frac{\partial N_j}{\partial X_1} + (\mu-\nu)\frac{\partial N_i}{\partial X_1}\frac{\partial N_j}{\partial X_3} & \lambda\frac{\partial N_i}{\partial X_3}\frac{\partial N_j}{\partial X_2} + (\mu-\nu)\frac{\partial N_i}{\partial X_2}\frac{\partial N_j}{\partial X_3} & (\lambda+2\mu)\frac{\partial N_i}{\partial X_3}\frac{\partial N_j}{\partial X_3} + (\mu+\nu)\left(\frac{\partial N_i}{\partial X_1}\frac{\partial N_j}{\partial X_1} + \frac{\partial N_i}{\partial X_2}\frac{\partial N_j}{\partial X_2}\right) \end{bmatrix},$$

$$\mathbf{K_{m_{u2}}} = \alpha \begin{bmatrix} \frac{\partial N_i}{\partial X_1}\frac{\partial N_j}{\partial X_1} & \frac{\partial N_i}{\partial X_1}\frac{\partial N_j}{\partial X_2} & \frac{\partial N_i}{\partial X_1}\frac{\partial N_j}{\partial X_3} \\ \frac{\partial N_i}{\partial X_2}\frac{\partial N_j}{\partial X_1} & \frac{\partial N_i}{\partial X_2}\frac{\partial N_j}{\partial X_2} & \frac{\partial N_i}{\partial X_2}\frac{\partial N_j}{\partial X_3} \\ \frac{\partial N_i}{\partial X_3}\frac{\partial N_j}{\partial X_1} & \frac{\partial N_i}{\partial X_3}\frac{\partial N_j}{\partial X_2} & \frac{\partial N_i}{\partial X_3}\frac{\partial N_j}{\partial X_3} \end{bmatrix} + (\beta+\gamma)\left(\frac{\partial N_i}{\partial X_1}\frac{\partial N_j}{\partial X_1} + \frac{\partial N_i}{\partial X_2}\frac{\partial N_j}{\partial X_2} + \frac{\partial N_i}{\partial X_3}\frac{\partial N_j}{\partial X_3}\right)\begin{bmatrix} 1 & 0 & 0 \\ 0 & 1 & 0 \\ 0 & 0 & 1 \end{bmatrix} + (\beta-\gamma)\begin{bmatrix} \frac{\partial N_j}{\partial X_1}\frac{\partial N_i}{\partial X_1} & \frac{\partial N_j}{\partial X_1}\frac{\partial N_i}{\partial X_2} & \frac{\partial N_j}{\partial X_1}\frac{\partial N_i}{\partial X_3} \\ \frac{\partial N_j}{\partial X_2}\frac{\partial N_i}{\partial X_1} & \frac{\partial N_j}{\partial X_2}\frac{\partial N_i}{\partial X_2} & \frac{\partial N_j}{\partial X_2}\frac{\partial N_i}{\partial X_3} \\ \frac{\partial N_j}{\partial X_3}\frac{\partial N_i}{\partial X_1} & \frac{\partial N_j}{\partial X_3}\frac{\partial N_i}{\partial X_2} & \frac{\partial N_j}{\partial X_3}\frac{\partial N_i}{\partial X_3} \end{bmatrix} + 4\nu N_i N_j \begin{bmatrix} 1 & 0 & 0 \\ 0 & 1 & 0 \\ 0 & 0 & 1 \end{bmatrix}$$

$$= \begin{bmatrix} (\alpha+2\beta)\frac{\partial N_i}{\partial X_1}\frac{\partial N_j}{\partial X_1} + (\beta+\gamma)\left(\frac{\partial N_i}{\partial X_2}\frac{\partial N_j}{\partial X_2} + \frac{\partial N_i}{\partial X_3}\frac{\partial N_j}{\partial X_3}\right) + 4\nu N_i N_j & \alpha\frac{\partial N_i}{\partial X_1}\frac{\partial N_j}{\partial X_2} + (\beta-\gamma)\frac{\partial N_i}{\partial X_2}\frac{\partial N_j}{\partial X_1} & \alpha\frac{\partial N_i}{\partial X_1}\frac{\partial N_j}{\partial X_3} + (\beta-\gamma)\frac{\partial N_i}{\partial X_3}\frac{\partial N_j}{\partial X_1} \\ \alpha\frac{\partial N_i}{\partial X_2}\frac{\partial N_j}{\partial X_1} + (\beta-\gamma)\frac{\partial N_j}{\partial X_2}\frac{\partial N_i}{\partial X_1} & (\alpha+2\beta)\frac{\partial N_i}{\partial X_2}\frac{\partial N_j}{\partial X_2} + (\beta+\gamma)\left(\frac{\partial N_i}{\partial X_1}\frac{\partial N_j}{\partial X_1} + \frac{\partial N_i}{\partial X_3}\frac{\partial N_j}{\partial X_3}\right) + 4\nu N_i N_j & \alpha\frac{\partial N_i}{\partial X_2}\frac{\partial N_j}{\partial X_3} + (\beta-\gamma)\frac{\partial N_i}{\partial X_3}\frac{\partial N_j}{\partial X_2} \\ \alpha\frac{\partial N_i}{\partial X_3}\frac{\partial N_j}{\partial X_1} + (\beta-\gamma)\frac{\partial N_i}{\partial X_1}\frac{\partial N_j}{\partial X_3} & \alpha\frac{\partial N_i}{\partial X_3}\frac{\partial N_j}{\partial X_2} + (\beta-\gamma)\frac{\partial N_i}{\partial X_2}\frac{\partial N_j}{\partial X_3} & (\alpha+2\beta)\frac{\partial N_i}{\partial X_3}\frac{\partial N_j}{\partial X_3} + (\beta+\gamma)\left(\frac{\partial N_i}{\partial X_1}\frac{\partial N_j}{\partial X_1} + \frac{\partial N_i}{\partial X_2}\frac{\partial N_j}{\partial X_2}\right) + 4\nu N_i N_j \end{bmatrix},$$

and

$$\mathbf{K_{m_\varphi}} = 2\nu N_j \begin{bmatrix} 0 & -\frac{\partial N_i}{\partial X_3} & \frac{\partial N_i}{\partial X_2} \\ \frac{\partial N_i}{\partial X_3} & 0 & -\frac{\partial N_i}{\partial X_1} \\ -\frac{\partial N_i}{\partial X_2} & \frac{\partial N_i}{\partial X_1} & 0 \end{bmatrix} = \begin{bmatrix} 0 & -2\nu\frac{\partial N_i}{\partial X_3}N_j & 2\nu\frac{\partial N_i}{\partial X_2}N_j \\ 2\nu\frac{\partial N_i}{\partial X_3}N_j & 0 & -2\nu\frac{\partial N_i}{\partial X_1}N_j \\ -2\nu\frac{\partial N_i}{\partial X_2}N_j & 2\nu\frac{\partial N_i}{\partial X_1}N_j & 0 \end{bmatrix}.$$

It is observed that the obtained element material stiffness matrix coincides with the stiffness matrix derived in the linear analysis, as expected.

Bibliography

[1] R.D. Gauthier and W. E. Jahsman. A Quest for Micropolar Elastic Constants. *Journal of Applied Mechanics*, 42(2):369–374, 1975.

[2] J. Argyris. An excursion into large rotations. *Computer Methods in Applied Mechanics and Engineering*, 32(1-3):85–155, sep 1982.

[3] L. E. Malvern. *Introduction to the mechanics of a continious medium*. Prentice-Hall, Inc, New Jersey, 1969.

[4] W. Nowacki. *Theory of micropolar elasticity*. Springer-Verlag, Vienna, 1972.

[5] R. S. Lakes. Size effects and micromechanics of a porous solid. *Journal of Materials Science*, 18:2572–2580, 1983.

[6] R. S. Lakes. Experimental Microelasticity of two porous solids. *International Journal of Solids and Structures*, 22(1):55–63, 1986.

[7] W. B. Anderson and R. S. Lakes. Size effects due to Cosserat elasticity and surface damage in closed-cell polymethacrylimide foam. *Journal of Materials Science*, 29(24):6413–6419, 1994.

[8] L. Toubal, M. Karama, and B. Lorrain. Stress concentration in a circular hole in composite plate. *Composite Structures*, 68(1):31–36, 2005.

[9] A. R. Hadjesfandiari and G. F. Dargush. Couple stress theory for solids. *International Journal of Solids and Structures*, 48(18):2496–2510, sep 2011.

[10] R. D. Mindlin and N. N. Eshel. On first strain-gradient theories in linear elasticity. *International Journal of Solids and Structures*, 4(1):109–124, 1968.

[11] A. C. Eringen. *Microcontinuum Field Theories: I. Foundations and Solids*. Springer-Verlag, New York, 2012.

[12] E. Cosserat and F. Cosserat. *Théorie des corps déformables*. Herman, Paris, 1909.

[13] H. Neuber. On the general solution of linear-elastic problems in isotropic and anisotropic Cosserat continua. In *Applied Mechanics: Proceedings of the Eleventh International Congress of Applied Mechanics Munich*, pages 153–158. Springer Berlin Heidelberg, Berlin, Heidelberg, 1966.

[14] W. Voigt. Theoretische studien über die elasticitätsverhältnisse der krystalle. *Abhandlungen der Königlichen Gesellschaft der Wissenschaften zu Göttingen*, 34:3–51, 1887.

[15] W. Günther. Zur Statik und Kinematik des Cosseratschen Kontinuums. *Abhandlungen der Braunschweigischen Wissenschaftlichen Gesellschaft*, 10:195–213, 1958.

[16] C. Truesdell and W. Noll. *The Non-Linear Field Theories of Mechanics*. Springer Berlin Heidelberg, Berlin, Heidelberg, 2004.

[17] R. A. Toupin. Theories of elasticity with couple-stress. *Archive for Rational Mechanics and Analysis*, 17(2):85–112, 1964.

[18] H. Schäfer. Das Cosserat kontinuum. *ZAMM - Journal of Applied Mathematics and Mechanics*, 47(8):485–498, 1967.

[19] A. C. Eringen and E. S. Suhubi. Nonlinear theory of simple micro-elastic solids. *International Journal of Engineering Science*, 2(2):189–203, may 1964.

[20] J. Dyszlewicz. *Micropolar Theory of Elasticity*. Springer-Verlag Berlin and Heidelberg GmbH & Co. KG, Berlin, 2004.

[21] V.A. Eremeyev, L.P. Lebedev, and H. Altenbach. *Foundations of Micropolar Mechanics*. Springer-Verlag, Berlin, 2013.

[22] J. F. C. Yang and R. S. Lakes. Transient Study of Couple Stress Effects in Compact Bone: Torsion. *Journal of Biomechanical Engineering*, 103(4):275–279, 1981.

[23] J. F. C. Yang and R. S. Lakes. Experimental study of micropolar and couple stress elasticity in compact bone in bending. *Journal of Biomechanics*, 15(2):91–98, 1982.

[24] R. S. Lakes, S. Nakamura, J. C. Behiri, and W. Bonfield. Fracture mechanics of bone with short cracks. *Journal of Biomechanics*, 23(10):967–975, 1990.

[25] Z. Rueger and R. S. Lakes. Cosserat elasticity of negative Poissons ratio foam: experiment. *Smart Materials and Structures*, 25(5):054004, 2016.

[26] C. P. Chen and R. S. Lakes. Holographic study of conventional and negative Poisson's ratio metallic foams: elasticity, yield and micro-deformation. *Journal of Materials Science*, 26(20):5397–5402, 1991.

[27] Z.P. Bažant and M. Christensen. Analogy between micropolar continuum and grid frameworks under initial stress. *International Journal of Solids and Structures*, 8(3):327–346, 1972.

[28] X. L. Wang and W. J. Stronge. Micropolar theory for two-dimensional stresses in elastic honeycomb. *Proceedings of the Royal Society A, Mathematical, Physical and Engineering Sciences*, 455(1986):2091–2116, 1999.

[29] R. J. Mora, A. M. Waas, and A. Arbor. Evaluation of the Micropolar elasticity constants for honeycombs. *Acta Mechanica*, 192:1–16, 2007.

[30] D. Besdo. Towards a Cosserat-theory describing motion of an originally rectangular structure of blocks. *Archive of Applied Mechanics*, 80(1):25–45, 2010.

[31] A. J. Beveridge, M. A. Wheel, and D. H. Nash. A higher order control volume based finite element method to predict the deformation of heterogeneous materials. *Comput. Struct.*, 129:54–62, 2013.

[32] M. McGregor and M. A. Wheel. On the coupling number and characteristic length of micropolar media of differing topology. *Proceedings of the Royal Society A: Mathematical, Physical and Engineering Sciences*, 470(2169):20140150–20140150, 2014.

[33] M. A. Wheel, J. C. Frame, and P. E. Riches. Is smaller always stiffer? On size effects in supposedly generalised continua. *International Journal of Solids and Structures*, 67-68:84–92, 2015.

[34] S. Hassanpour and G. R. Heppler. Micropolar elasticity theory: a survey of linear isotropic equations, representative notations, and experimental investigations. *Mathematics and Mechanics of Solids*, 22(2):224–242, 2015.

[35] S. Nakamura, R. Benedict, and R. Lakes. Finite element method for orthotropic micropolar elasticity. *International Journal of Engineering Science*, 22(3):319–330, 1984.

[36] E. Providas and M. A. Kattis. Finite element method in plane Cosserat elasticity. *Computers and Structures*, 80(27-30):2059–2069, 2002.

[37] F.-Y. Huang and K.-Z. Liang. Torsional Analysis of micropolar elasticity using the finite element method. *International Journal of Engineering Science*, 32(2):347–358, 1994.

[38] F.-Y. Huang, B.-H. Yan, J.-L. Yan, and D.-U. Yang. Bending analysis of micropolar elastic beam using a 3-D finite element method. *International Journal of Engineering Science*, 38:275–286, 2000.

[39] L. Li and S. Xie. Finite element method for linear micropolar elasticity and numerical study of some scale effects phenomena in MEMS. *International Journal of Mechanical Sciences*, 46(11):1571–1587, 2004.

[40] H. Zhang, H. Wang, and G. Liu. Quadrilateral isoparametric finite elements for plane elastic Cosserat bodies. *Acta Mechanica Sinica*, 21(4):388–394, 2005.

[41] V. V. Korepanov, V. P. Matveenko, and I. N. Shardakov. Finite element analysis of two- and three-dimensional static problems in the asymmetric theory of elasticity as a basis for the design of experiments. *Acta Mechanica*, 223(8):1739–1750, 2012.

[42] M. A. Wheel. A control volume-based finite element method for plane micropolar elasticity. *International Journal for Numerical Methods in Engineering*, 75(8):992–1006, 2008.

[43] P. Steinmann and E. Stein. A unifying treatise of variational principles for two types of micropolar continua. *Acta Mechanica*, 121(1-4):215–232, 1997.

[44] W. Pietraszkiewicz and V . A. Eremeyev. On vectorially parameterized natural strain measures of the non-linear Cosserat continuum. *International Journal of Solids and Structures*, 46(11-12):2477–2480, 2009.

[45] W. Pietraszkiewicz and V. A. Eremeyev. On natural strain measures of the non-linear micropolar continuum. *International Journal of Solids and Structures*, 46(3-4):774–787, 2009.

[46] Paul Steinmann. A micropolar theory of finite deformation and finite rotation multiplicative elastoplasticity. *International Journal of Solids and Structures*, 31(8):1063–1084, 1994.

[47] P. Grammenoudis and Ch. Tsakmakis. Finite element implementation of large deformation micropolar plasticity exhibiting isotropic and kinematic hardening effects. *Int. J. Numer. Meth. Engng*, 62:1691–1720, 2005.

[48] S. Ramezani, R. Naghdabadi, and S. Sohrabpour. Non-linear finite element implementation of micropolar hypo-elastic materials. *Computer Methods in Applied Mechanics and Engineering*, 197:4149–4159, 2008.

[49] S. Bauer, M. Schäfer, P. Grammenoudis, and Ch. Tsakmakis. Three-dimensional finite elements for large deformation micropolar elasticity. *Computer Methods in Applied Mechanics and Engineering*, 199(41-44):2643–2654, 2010.

[50] S. Bauer, W. G. Dettmer, D. Peric, and M. Schäfer. Micropolar hyperelasticity: constitutive model, consistent linearization and simulation of 3D scale effects. *Computational Mechanics*, 50:383–396, 2012.

[51] S. Bauer, W. G. Dettmer, D. Peric, and M. Schäfer. Micropolar hyper-elastoplasticity: constitutive model, consistent linearization, and simulation of 3D scale effects. *International Journal for Numerical Methods in Engineering*, 91:39–66, 2012.

[52] P. Chadwick. *Continuum Mechanics: Concise Theory and Problems.* Dover Publications, Inc., New York, 1999.

[53] R. W. Ogden. *Non-Linear Elastic Deformations.* Dover Publications, Inc., Mineola, New York, 2013.

[54] H. Jeffreys and B. Jeffreys. *Methods of Mathematical Physics.* Cambridge University Press, Cambridge, 1956.

[55] E. H. Moore. A Simple Proof of the Fundamental Cauchy-Goursat Theorem. *Transactions of the American Mathematical Society*, 1(4):499–506, 1900.

[56] A. Ibrahimbegović. *Nonlinear Solid Mechanics: Theoretical Formulations and Finite Element Solution Methods.* Springer, London, 2009.

[57] A. C. Eringen. Linear Theory of Micropolar Elasticity. *Journal of Mathematics and Mechanics*, 15:909–923, 1966.

[58] J. E. Marsden and T. J. R. Hughes. *Mathematical foundations of elasticity.* Dover Publications, Inc., New York, 1994.

[59] R. D. Mindlin and H. F. Tiersten. Effects of couple-stresses in linear elasticity. *Archive for Rational Mechanics and Analysis*, 11(1):415–448, 1962.

[60] H. Jeffreys. *Cartesian Tensors.* Cambridge University Press, Cambridge, 1957.

[61] P. A. Kelly. *Mechanics Lecture Notes: An introduction to Solid Mechanics.* University of Auckland, 2018.

[62] R. S. Lakes. Physical Meaning of Elastic Constants in Cosserat, Void, and Microstretch Elasticity. *Mechanics of Materials and Structures*, 11(3):1–13, 2016.

[63] S. C. Cowin. An incorrect inequality in micropolar elasticity theory. *Zeitschrift fur Angewandte Mathematik und Physikr angewandte Mathematik und Physik ZAMP*, 21(3):494–497, 1970.

[64] S. Grbčić, G. Jelenić, and D. Ribarić. Quadrilateral 2D linked-interpolation finite elements for micropolar continuum. *submitted for publication*, 2018.

[65] S. Grbčić, A. Ibrahimbegović, and G. Jelenić. Variational formulation of micropolar elasticity using 3D hexahedral finite-element interpolation with incompatible modes. *Computers and Structures*, 205:1–14, 2018.

[66] R.L. Taylor. FEAP - Finite Element Analysis Program, 2014.

[67] O. C. Zienkiewicz and R. L. Taylor. *The Finite Element Method Volume 1 : The Basis.* Butterworth-Heinemann, Oxford, 2000.

[68] G. Jelenić and E. Papa. Exact solution of 3D Timoshenko beam problem using linked interpolation of arbitrary order. *Archive of Applied Mechanics*, 81(2):171–183, 2011.

[69] D. Ribarić and G. Jelenić. Higher-order linked interpolation in quadrilateral thick plate finite elements. *Finite Elements in Analysis and Design*, 51:67–80, 2012.

[70] D. Ribarić and G. Jelenić. Higher-order linked interpolation in triangular thick plate finite elements. *Engineering Computations*, 31(1):69–109, 2014.

[71] D. J. Allman. A compatible triangular element including vertex rotations for plane elasticity analysis. *Computers and Structures*, 19(1-2):1–8, 1984.

[72] E. L. Wilson and A. Ibrahimbegović. Use of incompatible displacement modes for the calculation of element stiffnesses or stresses. *Finite Elements in Analysis and Design*, 7(3):229–241, 1990.

[73] E.G. Kirsch. Die Theorie der Elastizität und die Bedürfnisse der Festigkeitslehre. *Zeitschrift des Vereines deutscher Ingenieure*, 42:797–807, 1898.

[74] C. Geuzaine and J.-F. Remacle. Gmsh: a three-dimensional finite element mesh generator with built-in pre- and post-processing facilities. *International Journal for Numerical Methods in Engineering*, 79(11):1309–1331, 2009.

[75] S. Timoshenko and J.N. Goodier. *Theory of Elasticity.* McGraw-Hill, New York, 1951.

[76] A. Ibrahimbegovic and E. L. Wilson. A modified method of incompatible modes. *Communications in Applied Numerical Methods*, 7:187–194, 1991.

[77] E. L. Wilson. The static condensation algorithm. *International Journal for Numerical Methods in Engineering*, 8(1):198–203, 1974.

[78] E.L. Wilson, R.L. Taylor, W.P. Doherty, and J. Ghaboussi. Incompatible displacement models. In *Numerical and Computer Methods in Structural Mechanics*, pages 43–57. Elsevier, 1973.

[79] G. Strang. Variational crimes in the finite element method. In A K Aziz, editor, *The Mathematical Foundations of the Finite Element Method with Applications to Partial Differential Equations*, pages 689–710. Academic Press, 1972.

[80] N. Benkemon, M. Hautefeuille, J.-B. Colliat, and A. Ibrahimbegovic. Failure of heterogeneous materials: 3D meso-scale FE models with embedded discontinuities. *International Journal for Numerical Methods in Engineering*, 82:1671–1688, 2010.

[81] A. Ibrahimbegovic and S. Melnyk. Embedded discontinuity finite element method for modeling of localized failure in heterogeneous materials with structured mesh: An alternative to extended finite element method. *Computational Mechanics*, 40(1):149–155, 2007.

[82] I. Kožar, T. Rukavina, and A. Ibrahimbegović. Method of Incompatible Modes Overview and Application. *Graevinar*, 70:19–29, 2018.

[83] G. N. Watson. *A treatise on the theory of Bessel functions.* Cambridge University Press, Cambridge, 2 edition, 1995.

[84] A. Ibrahimbegovic. On the choice of finite rotation parameters. *Computer Methods in Applied Mechanics and Engineering*, 149(1-4):49–71, 1997.

[85] M. Gaćeša. *Fixed-Pole Concept in 3D Beam Finite Elements - Relationship to Standard Approaches and Analysis of Different Interpolations.* PhD thesis, University of Rijeka, Faculty of Civil Engineering, 2015.

[86] B. Hall. *Lie Grups, Lie Algebras, and representations: An Elementary Introduction.* Springer-Verlag, New York, 2003.

[87] H. Goldstein, C.P. Poole, and J.L. Safko. *Classical Mechanics.* Addison-Wesley, San Francisco, 3rd edition, 2001.

[88] A. Ibrahimbegovic and I. Kozar. Non-linear Wilson's brick element for finite elastic deformations of three-dimensional solids. *Communications in Numerical Methods in Engineering*, 11(8):655–664, 1995.

[89] A. Ibrahimbegović, I. Kožar, and F. Frey. Computational Aspects of Vector-Like Parametrization of Three-Dimensional Finite Rotations. *International Journal for Numerical Methods in Engineering*, 38:3653–3673, 1995.

[90] J. Stuelpnagel. On the Parametrization of the Three-Dimensional Rotation Group. *SIAM Review*, 6(4):422–430, 1964.

[91] Richard A. Spurrier. Comment on " Singularity-Free Extraction of a Quaternion from a Direction-Cosine Matrix". *Journal of Spacecraft and Rockets*, 15(4):255–255, jul 1978.

[92] H. Jeffreys and B. Jeffreys. Change of Variables in an Integral. In *Methods of Mathematical Physics*, pages 32–33. Cambridge University Press, Cambridge, 3rd edition, 1988.

[93] E. Reissner. On one-dimensional finite-strain beam theory: The plane problem. *Zeitschrift für angewandte Mathematik und Physik ZAMP*, 23(5):795–804, sep 1972.

[94] M.A. Crisfield and G. Jelenić. Objectivity of strain measures in geometrically exact 3D beam theory and its finite element implementation. *Proceedings of the Royal Society of London, Series A*, 455:1125–1147, 1999.

[95] R.L. Taylor and S. Govindjee. FEAP – A Finite Element Analysis Program. Technical report, University of California, Berkeley, Berkeley, 2017.

[96] I. Kožar and A. Ibrahimbegović. Finite element formulation of the finite rotation solid element. *Finite Elements in Analysis and Design*, 20(2):101–126, jun 1995.

[97] K. J. Bathe and S. Bolourchi. Large displacement analysis of three-dimensional beam structures. *International Journal for Numerical Methods in Engineering*, 14(7):961–986, jan 1979.

[98] G. Jelenić and M.A. Crisfield. Geometrically exact 3D beam theory: implementation of a strain-invariant finite element for statics and dynamics. *Computer Methods in Applied Mechanics and Engineering*, 171(1-2):141–171, 1999.

List of Figures

List of Tables

Sara Grbčić

Born on 26 May 1991 in Yverdon-les-Bains, Switzerland. Attended high school Gimnazija Andrije Mohorovičića in Rijeka from 2005 to 2009. Attended Faculty of Civil Engineering at the University of Rijeka from 2009 to 2014 and obtained a bachelor and a master's (*suma cum laude*) degree in the field of construction-geotechnical engineering. In 2011 was awarded with a scholarship for a student exchange program given by the University of Rijeka Foundation in association with The Lions Club and took part in a Student Exchange Camp in Japan for one month. Since 2011 was the President of the Student Union of the Faculty of Civil Engineering in Rijeka and in 2013 was awarded with the Dean award for volunteering. During master studies worked as a trainee at the architecture and design company *Dzeta* in Tunisia through an Iaeste internship programme for three months. The last year of her master studies was working for the international turnkey contractor company in the oil and gas industry *Saipem*. Her master thesis entitled *Offshore geotechnical engineering design* represents a feasibility study for constructing offshore and near shore objects needed for pipeline instalation and was made in conjuction with *Saipem*.

After graduation, enrolled the postgraduate doctoral study programme in Civil Engineering in the field of Engineering mechanics and started working full-time as a research assistant at the University of Rijeka, Faculty of Civil Engineering within the scientific projects *Configuration-dependent Approximation in Non-linear Finite-element Analysis of Structures* (HRZZ-IP-11-2013-1631) and *Young Researchers Career Development Project - Training of Doctoral Students* financed by the Croatian Science Foundation under the supervision of Prof. Gordan Jelenić. In May 2016 was awarded with a French Government Scholarship and enrolled a joint PhD programme between Sorbonne Universities, University of Technology of Compiegne and University of Rijeka, Faculty of Civil Engineering and continued research under the supervision of two supervisors, Prof. Gordan Jelenić and Prof. Adnan Ibrahimbegović.